Higgs Couplings and Supersymmetry in the Light of early LHC Results

Dissertation
zur
Erlangung des Doktorgrades (Dr. rer. nat.)
der
Mathematisch-Naturwissenschaftlichen Fakultät
der
Rheinischen Friedrich-Wilhelms-Universität Bonn

von
Tim Stefaniak
aus
Kappeln

Bonn, 22.05.2014

Dieser Forschungsbericht wurde als Dissertation von der Mathematisch-Naturwissenschaftlichen Fakultät der Universität Bonn angenommen und ist auf dem Hochschulschriftenserver der ULB Bonn http://hss.ulb.uni-bonn.de/diss_online elektronisch publiziert.

1. Gutachter:	Prof. Herbert Karl Dreiner, Ph.D.
2. Gutachter:	Prof. Dr. Klaus Desch
Tag der Promotion:	16.07.2014
Erscheinungsjahr:	2014

Higgs Couplings and Supersymmetry in the Light of early LHC Results

Tim Stefaniak

Abstract

We present phenomenological studies investigating the implications of early results from the Large Hadron Collider (LHC) for models beyond the Standard Model (BSM), mostly focusing on Supersymmetry (SUSY). Our work covers different aspects in this wide field of research. We describe the development and basic concepts of the public computer codes `HiggsBounds` (version 4) and `HiggsSignals`. These confront the Higgs sector predictions of BSM models with results from LEP, Tevatron and LHC Higgs searches. While `HiggsBounds` tests the model against experimental null-results, `HiggsSignals` evaluates the model's chi-squared compatibility with the signal rate and mass measurements of the Higgs boson, that was discovered by the LHC in 2012. We then perform a systematic study of potential deviations in the Higgs couplings from their Standard Model (SM) prediction. No significant deviations are found. Future capabilities of Higgs coupling determination at the later LHC stages and at the International Linear Collider (ILC) are explored. We also study the implications of the Higgs discovery for the Minimal Supersymmetric Standard Model (MSSM), considering either the light or the heavy $\mathcal{CP}$-even Higgs boson as the discovered state. We show that both interpretations are viable and discuss their phenomenology. Finally, we study the LHC signatures of resonant scalar lepton production, which may arise in SUSY models with R-parity violation (RPV). These are confronted with early LHC results, yielding constraints on the relevant RPV operators.

Acknowledgements

This dissertation would not have been possible without the help and encouragement I received from many people over the recent years. Here I want to take the opportunity to express my heartfelt thanks for this support.

First of all, special thanks go to my supervisor Herbi Dreiner for having me in his group and for always giving me the freedom to follow my own research interests and ideas. I am grateful for his support in- and outside of the scientific world. I would also like to thank Manuel Drees for interesting discussions while enjoying the daily Mensa lunch ritual. Thanks go also to Klaus Desch for his kind support and for helpful discussions on experimental questions. I am grateful to both of them, as well as to Martin Langer, for refereeing my dissertation.

In my research projects I have had the pleasure to collaborate with very competent and extremely nice people. Most of all, I thank Philip Bechtle and Oscar Stål for lots of helpful and very productive discussions, their endless support, and for all the stuff they have taught me. Moreover, I am grateful for the collaboration and discussions with Sven Heinemeyer and Georg Weiglein, who have always been very supportive. I also want to thank Karina Williams here, not only for her faith in me, when handing over to me the main responsibility for the computer code `HiggsBounds`. For many fruitful discussions and productive collaborations I thank Oliver Brein, John Conley, Sebastian Grab, Florian Staub, Lisa Zeune, as well as Björn Sarrazin, Mathias Hamer and the rest of the `Fittino` group. At this stage, I also want to thank Arnulf Quadt, Gunnar Ingelman, Nazila Mahmoudi as well as Andreas Höcker and Till Eifert for steering me into the direction of particle physics.

Good research can only be performed in a pleasant and productive environment. For that, I cannot think of a better place than the BCTP, and being among the members of Herbi's group. I would like to give a big thank you to all my past and present colleagues over the last five years, most importantly, Nicolás Bernal, Nicki Bornhauser, Stefano Colucci, John Conley, Sebastian Grab, Marja Hanussek, Jong Soo Kim, Suchita Kulkarni, Kilian Nickel, Toby Opferkuch, Daniel Schmeier, Lorenzo Ubaldi and Karina Williams. In particular, I thank Daniel, Toby and Lorenzo for proof-reading parts of the thesis manuscript (and for forcing me to remove unnecessary parentheses).

I want to thank my friends and family for reminding me that there is a world outside physics, and for their great support and understanding of my scientific endeavors. Without your support I would not have made it. Last but not least, I thank Annemarie for being part of my life, and for making me happy every day.

List of Publications

My research during the three years of my PhD studies resulted in the following publications:

1. P. Bechtle, S. Heinemeyer, O. Stål, T. Stefaniak, G. Weiglein, *Probing the Standard Model with Higgs signal rates from the Tevatron, the LHC and a future ILC.*
   Submitted to the Journal of High Energy Physics (JHEP), `arXiv:1403.1582 [hep-ph]`.

2. P. Bechtle, O. Brein, S. Heinemeyer, O. Stål, T. Stefaniak, G. Weiglein, K. Williams, *HiggsBounds-4: Improved Tests of Extended Higgs Sectors against Exclusion Bounds from LEP, the Tevatron and the LHC.*
   Published in **Eur.Phys.J. C74 (2014) 2693**, `arXiv:1311.0055 [hep-ph]`.

3. O. Stål, T. Stefaniak, *Constraining extended Higgs sectors with HiggsSignals.*
   Published in **PoS EPS-HEP2013 (2013) 314**, `arXiv:1310.4039 [hep-ph]`.

4. P. Bechtle, K. Desch, H. K. Dreiner, M. Hamer, M. Krämer, B. O'Leary, W. Porod, X. Prudent, B. Sarrazin, T. Stefaniak, M. Uhlenbrock, P. Wienemann, *Constrained Supersymmetry after the Higgs Boson Discovery: A global analysis with Fittino.*
   Published in **PoS EPS-HEP2013 (2013) 313**, `arXiv:1310.3045 [hep-ph]`.

5. P. Bechtle, S. Heinemeyer, O. Stål, T. Stefaniak, G. Weiglein, *HiggsSignals: Confronting arbitrary Higgs sectors with measurements at the Tevatron and the LHC.*
   Published in **Eur.Phys.J. C74 (2014) 2711**, `arXiv:1305.1933 [hep-ph]`.

6. P. Bechtle, O. Brein, S. Heinemeyer, O. Stål, T. Stefaniak, G. Weiglein, K. Williams, *Recent Developments in HiggsBounds and a Preview of HiggsSignals.*
   Published in **PoS CHARGED (2012) 024**, `arXiv:1301.2345 [hep-ph]`.

7. P. Bechtle, S. Heinemeyer, O. Stål, T. Stefaniak, G. Weiglein, L. Zeune, *MSSM Interpretations of the LHC Discovery: Light or Heavy Higgs?*
   Published in **Eur.Phys.J. C73 (2013) 2354**, `arXiv:1211.1955 [hep-ph]`.

8. H. K. Dreiner, T. Stefaniak, *Bounds on R-parity Violation from Resonant Slepton Production at the LHC.*
   Published in **Phys.Rev. D86 (2012) 055010**, `arXiv:1201.5014 [hep-ph]`.

The work presented in this thesis contains results from all these publications except (4).

Contents

CHAPTER 1

Introduction

The start-up of the Large Hadron Collider (LHC) at CERN at the end of 2009 marks the beginning of an exciting era for particle physics. Until the end of 2011 the LHC experiments recorded proton-proton (pp) collisions at a center-of-mass (CM) energy of 7 TeV. Shortly after, the LHC continued running at a slightly higher CM energy of 8 TeV. Such high collision energies have not been reached by the previous generations of particle accelerators, such as the Tevatron at Fermilab and the Large Electron-Positron Collider (LEP) at CERN. These energies open a new window to great discoveries that may revolutionize our understanding of particle physics. In the beginning of 2013, the LHC began a longer shutdown in order to prepare for the operation at a CM energy of 13 TeV, thus pushing the high-energy frontier even further. The next run will presumably start in early 2015.

In July 2012 the LHC experiments ATLAS [1] and CMS [2] announced the discovery of a new particle with a mass around 125.7 GeV during searches for the Standard Model Higgs boson. This spectacular discovery marks a milestone in an effort that has been ongoing for almost half a century. In ensuing analyses of the new particles' spin, $\mathcal{CP}$ and coupling properties [3–6] convincing experimental evidence was found to identify the new particle as a Higgs boson. The existence of such a particle was postulated in 1964 by François Englert and Robert Brout [7] and shortly after by Peter Higgs [8]. It arises as a consequence of *electroweak symmetry breaking* (EWSB) via the so-called *Higgs mechanism*[1]. This mechanism gives mass to the electroweak gauge bosons without violating the fundamental principle of gauge invariance inherent to gauge quantum field theories. In October 2013 — after the LHC experiments had confirmed the Higgs boson discovery to even higher confidence using the full available experimental data collected during the LHC runs at CM energies of 7 and 8 TeV — the Swedish Royal Academy of Science awarded the Nobel Prize in Physics to François Englert and Peter Higgs[2] for the formulation of the Higgs mechanism.

So far, the properties of the discovered Higgs boson are well in agreement with those predicted

[1] The Higgs mechanism is sometimes also denoted Brout-Englert-Higgs (BEH) mechanism, or even Brout-Englert-Guralnik-Hagen-Higgs-Kibble (BEGHHK) mechanism, to give full tribute to all contributors [9]. Here, we keep it short for simplicity.

[2] Unfortunately, Robert Brout passed away in 2011, before the discovery of the Higgs boson. In a BBC interview [10] Peter Higgs commented the 2013 Nobel Prize award as follows: "*I think it's good that they restricted the prize to the two of us, because, by implication, they're recognizing Robert Brout as the third who couldn't be awarded the prize.*"

by the *Standard Model of Particle Physics* (SM). The SM provides a successful description of three fundamental forces, the strong, weak and electromagnetic interactions, and assembles the elementary particles into a pattern formed by the symmetries of Nature. It has passed an enormous amount of very precise experimental tests making it nowadays one of the most experimentally verified theories in Natural Science. The last missing piece within this model was the Higgs boson and has now been discovered. It is now of paramount interest to determine the properties of the discovered Higgs boson as precisely as possible with current and future experiments. Any significant deviation from the SM expectation may hint to new physics beyond the SM (BSM).

The existence of BSM physics is very well motivated. Despite its remarkable success, there are several theoretical issues and experimental observations suggesting that the SM cannot be the ultimate theory of Nature. This is evident as the SM does not incorporate gravity, the fourth (known) fundamental force of Nature. At very high energies of the order of the so-called Planck mass, $M_P \sim 10^{19}$ GeV, the strengths of all fundamental interactions, including gravity, are anticipated to be of the same order. A unified description of all four fundamental forces at these high energies seems therefore indispensable. But already at lower energies the SM suffers from a naturalness issue commonly known as the *Hierarchy Problem* [11], which is related to the question of why gravity is roughly 10^{32} times weaker than the weak force. This problem manifests in the fact that the Higgs mass is very sensitive to quantum corrections at higher energy scales. Within the SM, it can only be resolved by an unnatural fine-tuning of the model parameters, or by accepting the fact that new physics will appear at the TeV scale, which render a new solution to this problem. Hence, the hierarchy problem is arguably the leading motivation to search for BSM physics at the LHC. However, besides the hierarchy problem, there are other open issues which cannot be explained by the SM, such as the nature of cold dark matter [12], the origin of neutrino masses [13], the observed baryon asymmetry in the Universe [14] and many others.

Many BSM theories have been proposed which can provide solutions to most of these issues. One of the most promising candidates is *Supersymmetry* (SUSY) [15–24], which extends the space-time symmetry of the SM to a symmetry relating fermions and bosons. It predicts the existence of a yet undiscovered superpartner for each SM particle, which differs in spin by 1/2. Thus, in the supersymmetric extension of the SM the particle spectrum is essentially doubled. SUSY provides a solution to many of the aforementioned problems of the SM. In particular, it stabilizes the Higgs mass at the electroweak scale via additional quantum corrections involving the superpartner fields. It furthermore provides a connection to string theories, which are regarded as promising candidates for the ultimate theory of all fundamental interactions, including gravity.

Besides a doubled particle spectrum, realistic supersymmetric models feature also an extended number of Higgs fields. In the minimal supersymmetric extension of the SM (MSSM) the Higgs sector contains two Higgs doublet fields. In the $\mathcal{CP}$ conserving case, this results in two $\mathcal{CP}$-even and one $\mathcal{CP}$-odd neutral physical Higgs states as well as one charged Higgs boson after EWSB. Thus, there are two possible interpretations of the discovered Higgs boson within the MSSM, namely that either the light or the heavy $\mathcal{CP}$-even Higgs boson has been found. The masses and couplings of these Higgs bosons can be predicted quite accurately within the model, and the predicted Higgs decay and production rates may differ significantly to those predicted in the SM. Thus, confronting these model predictions with the measurements of the new particles' properties results in severe constraints on the MSSM parameter space. Further constraints are obtained from direct collider searches for the remaining Higgs states.

In fact, the same reasoning can be applied to *any* BSM model that can predict Higgs boson properties different to those predicted by the SM. A model-independent framework, in which the Higgs sector predictions of *arbitrary* models are confronted with the experimental results from past and present Higgs searches at collider experiments, is therefore very valuable for the particle physics theory community. With such an interface between theory and experiment, a wide range of BSM models can easily be tested against the experimental observations, far beyond the few models investigated directly by the experimental collaborations. The public computer tool `HiggsBounds` [25–28] has constituted such a framework since 2009 by providing the experimental constraints from negative results of Higgs searches at the LEP, Tevatron and LHC experiments to the theory community. With the new discovery, the mass and signal rate measurements from the LHC and Tevatron experiments of the Higgs boson provide another important way to test BSM models. In this thesis we describe the development of the public computer code `HiggsSignals`, which uses these observables to perform BSM model tests by means of a statistical χ^2 measure, employing the model-independent framework of `HiggsBounds`.

With the discovery of the Higgs boson and the measurements of its mass and signal rates at the LHC and Tevatron two important questions arise. Firstly, in a combined picture of all available measurements, are there any hints for deviations from the SM predictions in the coupling structure or production and decay properties of the discovered Higgs state? And secondly, is there any model beyond the SM, such as the MSSM, that can provide a *better* description of the current measurements than the SM? Answering these questions will help to reveal the nature of the discovered Higgs boson, which is one of the prime goals of the particle physics community for the upcoming years (and decades).

We address both questions in this thesis. In the first case, the question can be answered by employing a rather general parametrization of possible SM Higgs coupling deviations via SM Higgs coupling scale factors [29, 30]. By performing a minimum χ^2 fit of these scale factors to the current signal rate measurements we systematically study the room for potential deviations from the SM predictions. Furthermore, we investigate how the precision of the Higgs coupling determination will improve with future signal rate measurements at later stages of the LHC program, assuming $300\,\text{fb}^{-1}$ and $3\,\text{ab}^{-1}$ of data at a CM energy of 14 TeV. We also explore the capabilities for Higgs coupling determination with hypothetical measurements of an anticipated future International Linear Collider (ILC).

The second question is addressed for the case of the MSSM. We perform a detailed global fit analysis taking into account the current Higgs mass and signal rate measurements as well as low-energy observables that are sensitive to new physics contributions. We explore the viability of both potential Higgs signal interpretations, i.e. identifying the discovered state with the light or the heavy $\mathcal{CP}$-even neutral Higgs boson of the MSSM, and discuss the favored MSSM parameter space.

While the discovered Higgs boson opens up new opportunities to probe BSM physics indirectly via the measurement of its production and decay rates, another important endeavor of the LHC is the direct search for new particles predicted by BSM theories. So far, no significant excess beyond the SM expectation has been found in any of these searches. These null-results have been used to constrain the parameter space of BSM models and to derive under simplifying assumptions lower mass limits for the new particles [31].

Searches for supersymmetric particles mainly concentrated on the case where a discrete symmetry called R-parity is conserved. R-parity conservation (RPC) is usually imposed in order to prevent the theory from predicting rapid proton decay, which is unobserved in Nature. This assumption has strong phenomenological consequences for collider experiments, most import-

antly, that SUSY particles can only be produced pairwise and that the lightest SUSY particle (LSP) is stable. However, R-parity does not necessarily have to be conserved to forbid the rapid proton decay if it is replaced by another in some cases less restrictive discrete symmetry. In that case, single production of SUSY particles at colliders may be possible and all SUSY particles, including the LSP, decay.

In the agenda of direct searches for BSM physics it is important to achieve an experimental sensitivity to all possible signatures that may arise in BSM scenarios. In the last part of this thesis we therefore investigate LHC signatures arising from resonant single production and subsequent decay of a lepton superpartner (slepton) within supersymmetric models with R-parity violation (RPV). These signatures have not directly been searched for at the LHC. We study the sensitivity of existing LHC searches to these signatures and derive upper limits on the strength of the relevant R-parity violating operators from the null-results of the relevant searches.

The thesis is organized as follows. Chapter 2 provides the theoretical background for the work presented in this thesis. We give a brief review of the SM, where the emphasis is laid on the Higgs mechanism and its phenomenological implications. We then turn to the discussion of Higgs boson decays, production mechanisms at lepton and hadron colliders, and the main experimental search strategies for the SM Higgs boson at past and present collider experiments. In the second half of Chapter 2 we discuss the shortcomings of the SM and outline possible ways to probe BSM physics. We then give an introduction to the MSSM phenomenology. In Chapter 3 we illustrate how experimental results, i.e. both exclusion limits and measurements, from Higgs collider searches are presented by the experimental collaborations and how these can be compared with the prediction of BSM models. Moreover, we briefly discuss the Higgs boson discovery at the LHC. We present the public computer codes `HiggsBounds` and `HiggsSignals` in Chapter 4. In particular, we describe the new features of the latest version `HiggsBounds-4`, which have been developed within this work. We then introduce the basic concepts of the program `HiggsSignals` and describe how the latest experimental data is implemented. Several performance and validation tests of the `HiggsSignals` procedure are presented. In Chapter 5 we perform the systematic analysis of Higgs coupling scale factor models. We explore potential tendencies and the allowed ranges for coupling deviations from the SM prediction using all presently available signal rate measurements from the Tevatron and LHC as implemented in `HiggsSignals`. We then turn to the discussion of future capabilities for Higgs coupling determination at the LHC and ILC. We study the viability of the two possible MSSM interpretations of the Higgs boson discovery in Chapter 6. First we investigate the compatibility of three MSSM benchmark scenarios with the experimental data. We then go beyond these restricted scenarios and present a global fit of the phenomenological MSSM, taking into account Higgs mass and signal rate as well as low-energy observables. We compare the fit qualities obtained within the SM and the MSSM, considering both Higgs interpretations. We determine the favored regions of the MSSM parameter space and discuss their phenomenology. In Chapter 7 we study the resonant slepton production signature of SUSY models with R-parity violation. We study the implications of early LHC search results from the 7 TeV run for these models by deriving upper bounds on the coupling strengths of the relevant RPV operators. The thesis is summarized in Chapter 8.

In Appendix A we provide additional information on the experimental data that is used in our work. This includes information about the analyses implemented in `HiggsBounds`, lists of expected future LHC and ILC measurements of Higgs signal rates used in Chapter 5 as well as Tevatron and LHC Higgs signal rate measurements from the end of 2012, when the global fit

of the MSSM presented in Chapter 6 was originally performed. In Appendix B.1 we provide a discussion of the $\mathcal{P}$-value that can be derived from the `HiggsSignals` χ^2 value, and give further information about the implementation of correlated theoretical uncertainties in `HiggsSignals`. Appendix C contains additional information for our analysis of resonant slepton production at the LHC, that is presented in Chapter 7.

Notation and Conventions

We use natural units throughout this thesis, i.e. $\hbar = c \equiv 1$. In Chapter 2 we use the Einstein summation convention, i.e. repeated indices are summed over unless explicitly stated otherwise. All other conventions are introduced in the text when they are needed.

CHAPTER 2

Phenomenology of Higgs Bosons

In this chapter we give an introduction to the Standard Model of Particle Physics (SM) as well as to its minimal supersymmetric extension. In particular, we discuss certain phenomenological aspects of the Higgs boson(s) appearing in these models. This will form the theoretical basis of the work presented in this thesis.

In Section 2.1 we briefly review the theoretical structure of the SM and explain how the Higgs boson arises in the mechanism of electroweak symmetry breaking (EWSB) within the SM. We furthermore discuss the theoretical and indirect experimental constraints it has to face. We then turn to the discussion of the SM Higgs boson collider phenomenology in Section 2.2, where we review the decay and production modes as well as the most promising search strategies at lepton and hadron colliders. In Section 2.3, we discuss various phenomena and theoretical considerations, that can not be explained within the SM, thus motivating the search for physics beyond the SM (BSM). The remaining part of this chapter, Section 2.4, is dedicated to the discussion of the phenomenology of the minimal supersymmetric extension of the SM (MSSM).

Excellent reviews of the Higgs phenomenology in the SM and the MSSM can be found in Refs. [32–34] and Ref. [24], respectively. These reviews, as well as the textbook *The Higgs Hunter's Guide* [35] and notes from recent lectures on Higgs physics [36, 37] have been used extensively for the discussion presented in this chapter.

2.1 The Higgs mechanism in the Standard Model

The SM successfully describes the three fundamental forces of strong, weak and electromagnetic interactions in a renormalizable, Lorentz-invariant quantum field theory based on the gauge group $G_{\mathrm{SM}} = \mathrm{SU}(3)_c \otimes \mathrm{SU}(2)_L \otimes \mathrm{U}(1)_Y$. The strong interaction between quarks, as described by the theory of *Quantum Chromodynamics* (QCD) [38], is represented by the non-Abelian gauge group $\mathrm{SU}(3)_c$, where c denotes *color* charge. It is mediated by spin-1 gauge fields G^a_μ ($a = 1, \ldots, 8$) in the adjoint representation called gluons. The remaining gauge group $\mathrm{SU}(2)_L \otimes \mathrm{U}(1)_Y$ represents the electroweak (EW) interaction [39] with gauge fields W^A_μ ($A = 1, 2, 3$) and B_μ in the adjoint representation of $\mathrm{SU}(2)_L$ and $\mathrm{U}(1)_Y$, respectively. Here, L represents the left-chiral structure of the weak interaction and Y denotes the *hypercharge*.

The SM has passed many extremely precise experimental tests and is therefore one of the

Matter fields	G_{SM} representation	electric charge Q	Particle notation
$L_{iL} = \begin{pmatrix} \nu_i \\ \ell_i \end{pmatrix}_L$	$(\mathbf{1}, \mathbf{2}, -\frac{1}{2})$	0 -1	$\begin{pmatrix} \nu_e \\ e_L \end{pmatrix}, \begin{pmatrix} \nu_\mu \\ \mu_L \end{pmatrix}, \begin{pmatrix} \nu_\tau \\ \tau_L \end{pmatrix}$
e_{iR}	$(\mathbf{1}, \mathbf{1}, -1)$	-1	$e_R, \quad \mu_R, \quad \tau_R$
$Q_{iL} = \begin{pmatrix} u_i \\ d_i \end{pmatrix}_L$	$(\mathbf{3}, \mathbf{2}, +\frac{1}{6})$	$+\frac{2}{3}$ $-\frac{1}{3}$	$\begin{pmatrix} u \\ d \end{pmatrix}, \begin{pmatrix} c \\ s \end{pmatrix}, \begin{pmatrix} t \\ b \end{pmatrix}$
u_{iR}	$(\mathbf{3}, \mathbf{1}, +\frac{2}{3})$	$+\frac{2}{3}$	$u_R, \quad c_R, \quad t_R$
d_{iR}	$(\mathbf{3}, \mathbf{1}, -\frac{1}{3})$	$-\frac{1}{3}$	$d_R, \quad s_R, \quad b_R$

Table 2.1: Matter content of the Standard Model (SM). The leptons and quarks are described by left-chiral SU(2) doublets and right-chiral SU(2) singlets and come in three generations ($i = 1, 2, 3$). The second column denotes the representation under the SM gauge group G_{SM}. The electric charge Q is given in the third column. In the last column the notation for the particles of the three generations is given.

most successful theories in Natural Science[1]. Comprehensive introductions to the SM can be found in many textbooks, see e.g. Refs. [40–42]. In this section, we give a brief review of the SM particle content and its gauge interactions. We then discuss how the electroweak symmetry is broken via the *Higgs mechanism* [7–9] in the SM. In the remaining part of this section we discuss theoretical considerations of vacuum stability and perturbativity of the electroweak sector, as well as implications of global fits to electroweak precision data from past collider experiments.

2.1.1 The particle content and gauge interactions of the SM

The matter content of the SM, consisting of lepton and quark fields, is given in Tab. 2.1. The nature of the electroweak interaction forces us to distinguish between left-chiral fields, being doublets under $\text{SU}(2)_L$, and right-chiral $\text{SU}(2)_L$ singlets. The quarks form triplets under the gauge group $\text{SU}(3)_c$ and thus participate in the strong interactions while the leptons, being $\text{SU}(3)_c$ singlets, do not. As will be discussed below, the electroweak gauge symmetry $\text{SU}(2)_L \otimes \text{U}(1)_Y$ is spontaneously broken down to a remnant $\text{U}(1)_{\text{em}}$ gauge symmetry, which describes electromagnetism. Therefore, the electric charge Q is related to the third component of the *weak isospin* T^A and the hypercharge Y, i.e. the associated gauge charges of the two parts of the electroweak gauge group:

$$Q = T^3 + Y. \tag{2.1}$$

Note that, within each generation, the relation $\sum_f Y_f = \sum_f Q_f = 0$ holds, ensuring the cancellation of chiral anomalies [43, 44] and thus preserving renormalizability of the electroweak theory [45].

Given N fermionic matter fields ψ_n ($n = 1, \ldots, N$) plus the requirements of renormalizability and invariance under Lorentz- and the SM gauge transformations, the SM Lagrangian contains

[1] Reasons why the SM is believed not to be the ultimate theory of fundamental forces will be discussed in Section 2.3, along with an overview of some currently observed experimental discrepancies.

the following kinetic terms for the gauge and matter fields:

$$\mathcal{L}_{\text{SM, kinetic}} = -\frac{1}{4}\left[\sum_{a=1}^{8} G^a_{\mu\nu} G^{\mu\nu\ a} + \sum_{A=1}^{3} W^A_{\mu\nu} W^{\mu\nu\ A} + B_{\mu\nu} B^{\mu\nu}\right] + \sum_{n=1}^{N} \overline{\psi}_n i\gamma^\mu D_\mu \psi_n, \tag{2.2}$$

where $\mu, \nu \in \{0, 1, 2, 3\}$ are space-time indices, $\overline{\psi} \equiv \psi^\dagger \gamma^0$, and γ^μ are the Dirac matrices. The field strength tensors of the $\mathrm{SU}(3)_c$, $\mathrm{SU}(2)_L$ and $\mathrm{U}(1)_Y$ gauge fields are given by

$$G^a_{\mu\nu} \equiv \partial_\mu G^a_\nu - \partial_\nu G^a_\mu + g_s f^{abc} G^b_\mu G^c_\nu, \tag{2.3a}$$
$$W^A_{\mu\nu} \equiv \partial_\mu W^A_\nu - \partial_\nu W^A_\mu + g_2 \epsilon^{ABC} W^B_\mu W^C_\nu, \tag{2.3b}$$
$$B_{\mu\nu} \equiv \partial_\mu B_\nu - \partial_\nu B_\mu, \tag{2.3c}$$

where f^{abc} and ϵ^{ABC} are the structure constants and g_s and g_2 the gauge couplings of $\mathrm{SU}(3)_c$ and $\mathrm{SU}(2)_L$, respectively. Depending on the matter field's representation under G_{SM} the gauge covariant derivative D_μ may be comprised of the following terms:

$$D_\mu \equiv \partial_\mu + \underbrace{i g_s \frac{\lambda^a}{2} G^a_\mu}_{\text{only for quark fields}} + \underbrace{i g_2 \frac{\tau^A}{2} W^A_\mu}_{\text{only for left-chiral fields}} + i g_Y \hat{Y} B_\mu. \tag{2.4}$$

Here, the generators of the gauge groups $\mathrm{SU}(3)_c$, $\mathrm{SU}(2)_L$ and $\mathrm{U}(1)_Y$ in the fundamental representation appear, given by the Gell-Mann matrices λ^a, the Pauli-Matrices τ^A (where the weak isospin is $T^A \equiv \tau^A/2$) and the hypercharge operator $\hat{Y}$ (with $\hat{Y}\psi_n = Y_n \psi_n$), respectively. The $U(1)_Y$ coupling strength is denoted as g_Y. It can be checked explicitly that Eq. (2.2) is invariant under local gauge transformations of the matter and gauge fields, given in the infinitesimal form by

$$\psi_n \longrightarrow \exp\left\{i\left[\alpha^a \frac{\lambda^a}{2} + \alpha'^A \frac{\tau^A}{2} + \alpha'' Y_n\right]\right\} \psi_n, \tag{2.5a}$$
$$G^a_\mu \longrightarrow G^a_\mu - \partial_\mu \alpha^a + g_s f^{abc} G^b_\mu \alpha^c, \tag{2.5b}$$
$$W^A_\mu \longrightarrow W^A_\mu - \partial_\mu \alpha'^A + g_2 \epsilon^{ABC} W^B_\mu \alpha'^C, \tag{2.5c}$$
$$B_\mu \longrightarrow B_\mu - \partial_\mu \alpha'', \tag{2.5d}$$

with space-time dependent transformation parameters $\alpha, \alpha', \alpha'' \in \mathbb{R}$ for the $\mathrm{SU}(3)_c$, $\mathrm{SU}(2)_L$ and $\mathrm{U}(1)_Y$ gauge symmetries, respectively.

The principle of gauge symmetry has proven to be extremely powerful and predictive in the history of the SM. Requiring the action $S = \int d^4x \mathcal{L}$ to be invariant under a *local* $\mathrm{SU}(N)$ or $\mathrm{U}(N)$ gauge transformation leads inevitably to the introduction of spin-1 gauge fields, so-called vector bosons, fulfilling the role of force mediators. For the Abelian $U(1)_{\text{em}}$ gauge theory this leads to the photon, in the $\mathrm{SU}(3)_c$ of QCD we obtain eight gluons, and in $\mathrm{SU}(2)_L$ we obtain three W bosons, out of which two are electrically charged and one is neutral. However, at the same time, invariance under the gauge transformations of the SM gauge group, G_{SM}, forbids all mass terms. For instance, a gauge boson mass (GBM) term $\mathcal{L}_{\text{GBM}} = \frac{1}{2} M_B^2 B_\mu B^\mu$ transforms under Eq. (2.5d) to $\mathcal{L}_{\text{GBM}} - M_B^2 B^\mu \partial_\mu \alpha'' + \mathcal{O}(\alpha''^2)$ and is thus not invariant. Similarly, Dirac

fermion mass (DFM) terms,

$$\mathcal{L}_{\text{DFM}} = -m_\psi \overline{\psi}\psi = -m_\psi[\overline{\psi_R}\psi_L + \overline{\psi_L}\psi_R], \tag{2.6}$$

obey neither the $\text{SU}(2)_L$ nor the $\text{U}(1)_Y$ gauge symmetry, since ψ_L is a $\text{SU}(2)_L$ doublet and ψ_R is a $\text{SU}(2)_L$ singlet, and both have different hypercharges, cf. Tab. (2.1). Thus, the presence of Dirac mass terms would break the gauge symmetry of the SM explicitly. However, it is an observational fact that fermions[2] and the vector bosons of the weak interaction, $W^\pm$ and Z, are massive [48, 49], with masses ranging from rather small values like the electron mass of 511 keV to very large values like the top quark mass of around 173 GeV. How can this be reconciled with the gauge principles in the electroweak sector? The solution to this problem is provided by the Higgs mechanism, which introduces scalar fields to the theory.

2.1.2 The Higgs mechanism

In the SM we add a complex $\text{SU}(2)_L$ doublet of scalar fields ϕ to the particle content,

$$\Phi = \begin{pmatrix} \phi^+ \\ \phi^0 \end{pmatrix}, \quad \text{with hypercharge} \quad Y_\Phi = +\frac{1}{2}. \tag{2.7}$$

The previously discussed SM Lagrangian, Eq. (2.2), now needs to be extended by the gauge invariant terms of the scalar field,

$$\mathcal{L}_{\text{scalar}} = (D^\mu \Phi)^\dagger (D_\mu \Phi) - V(\Phi), \tag{2.8}$$

with the scalar potential[3]

$$V(\Phi) = \mu^2 \Phi^\dagger \Phi + \lambda (\Phi^\dagger \Phi)^2, \qquad (\mu, \lambda \in \mathbb{R}). \tag{2.9}$$

For $\mu^2 < 0$ and $\lambda > 0$, $V(\Phi)$ forms the shape of a *Mexican hat*, as illustrated in Fig. 2.1, which features a continuous set of local minima at $|\Phi|^2 = -\mu^2/2\lambda$, corresponding to a non-zero vacuum expectation value (vev) of the scalar doublet field, $\langle\Phi\rangle_0 = \langle 0|\,\Phi\,|0\rangle$. Note that, up to this point, electroweak gauge symmetry is still manifest since $|\Phi|^2$ is gauge invariant. However, both the $\text{SU}(2)_L$ and $\text{U}(1)_Y$ symmetries become *hidden* (or *spontaneously broken*) once we make a specific gauge choice for the vev, e.g.

$$\langle\Phi\rangle_0 = \frac{1}{\sqrt{2}} \begin{pmatrix} 0 \\ v \end{pmatrix} \quad \text{with} \quad v = \left(-\frac{\mu^2}{\lambda}\right)^{1/2} \in \mathbb{R}. \tag{2.10}$$

This is illustrated in Fig. 2.1 for the U(1) part of the gauge symmetry: Before the gauge choice, there is a set of equivalent minima lying on a circle of radius $\sqrt{-\mu^2/(2\lambda)}$. The gauge choice fixes the ground state by choosing one and thus breaks the rotational U(1) symmetry spontaneously. It is important to note that the gauge choice in Eq. (2.10) preserves invariance under a residual

[2] For now, we exclude neutrinos from this discussion. Evidence for (at least two) neutrinos masses is given by the observation of neutrino flavor oscillations [46], however, the exact origin and pattern of neutrino masses is still subject of current research [13]. Fits to current cosmological observations from the Planck satellite constrain the sum of neutrino masses to be tiny, $\sum_i m_{\nu_i} \leq 0.23\,\text{eV}$ (at 95% C.L.) [47].

[3] Note, that μ^2 is of dimension mass-squared. This newly introduced mass scale breaks the scale invariance of the theory explicitly.

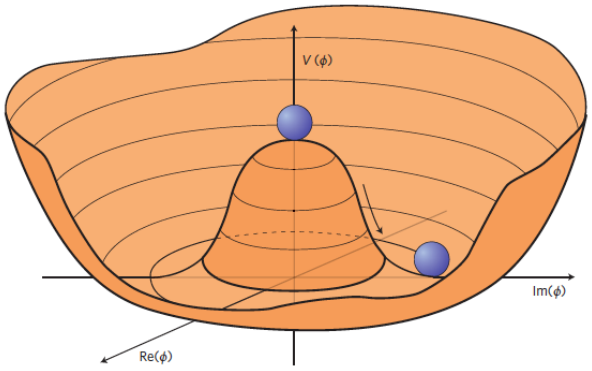

Figure 2.1: Illustration of the Higgs potential $V(\Phi)$, Eq. (2.9), in the case of $\mu^2 < 0$. The minimum is given at $|\Phi|^2 = -\mu^2/(2\lambda)$. The rotational U(1) symmetry is spontaneously broken by a gauge choice, which fixes the ground state to one of the points at the bottom of the potential. Taken from Ref. [36].

U(1) gauge symmetry[4], which is identified with electromagnetism and described by the theory of *Quantum Electrodynamics* (QED). Hence, the existence of one massless gauge boson, the photon, is ensured.

The dynamics induced by the spontaneously broken gauge symmetries follow from studying small perturbations of the scalar field Φ around the chosen ground state,

$$\Phi(x) = \exp\left(\frac{i\xi^A(x)\,\tau^A}{2v}\right)\begin{pmatrix} 0 \\ (v + H(x))/\sqrt{2} \end{pmatrix}, \tag{2.11}$$

where $\xi^A(x)$ and $H(x)$ are real fields. Using the remaining gauge freedom in the $\mathrm{SU}(2)_L$ gauge fields we can rotate away the three real degrees of freedom ξ^A. This is done by the following $\mathrm{SU}(2)_L$ transformation on the scalar, gauge and matter fields, respectively (*unitary gauge*):

$$\Phi \longrightarrow \Phi' = \exp\left(-\frac{i\xi^A\tau^A}{2v}\right)\Phi = \begin{pmatrix} 0 \\ (v + H)/\sqrt{2} \end{pmatrix}, \tag{2.12a}$$

$$\tau^A W_\mu^A \longrightarrow \tau^A W'^A_\mu, \tag{2.12b}$$

$$L \longrightarrow L' = \exp\left(-\frac{i\xi^A\tau^A}{2v}\right)L, \qquad (L = L_{i\,L}, Q_{i\,L}). \tag{2.12c}$$

In this gauge the Lagrangian in Eq. (2.8) takes the form

$$\begin{aligned}\mathcal{L}_{\text{scalar}} = &\frac{1}{2}(\partial_\mu H)(\partial^\mu H) + \frac{v^2}{8}\left[g_2^2|W_\mu^1 - iW_\mu^2|^2 + (g_2 W_\mu^3 - g_Y B_\mu)^2\right] \\ &+ \frac{1}{8}(H^2 + 2vH)\left[g_2^2|W_\mu^1 - iW_\mu^2|^2 + (g_2 W_\mu^3 - g_Y B_\mu)^2\right] \\ &- \frac{1}{4}\lambda H^4 - \lambda v H^3 - \lambda v^2 H^2 + \frac{1}{4}\lambda v^4,\end{aligned} \tag{2.13}$$

[4] Note, that the choice of $\langle\Phi\rangle_0$ presented in Eq. (2.10) is consistent with the choice of the $\mathrm{SU}(2)_L$ structure of the SM fields given in Tab. 2.1. The charged component of the scalar field, ϕ^+, must not acquire a vev in order to preserve the $\mathrm{U}(1)_{\text{em}}$ symmetry of electromagnetism.

where we inserted Eq. (2.10). The term $-\lambda v^2 H^2$ in the last row is a mass term for the H field, the physical *Higgs boson*. In the SM, there is no *a priori* prediction for its mass,

$$m_H = \sqrt{2\lambda v^2} = \sqrt{-2\mu^2}, \tag{2.14}$$

since μ (or λ) are not dictated by any of the other SM parameters.

The remainder of Eq. (2.13) consists of new mass terms for the gauge bosons (first row) as well as terms that describe the Higgs-gauge boson interactions (second row) and Higgs self-interactions (third row).The mass eigenstates of the charged gauge boson fields, $W_\mu^\pm$, and neutral gauge boson fields, A_μ and Z_μ, can be identified as the combinations

$$W_\mu^\pm \equiv \frac{1}{\sqrt{2}}\left(W_\mu^1 \mp i W_\mu^2\right), \tag{2.15}$$

$$A_\mu \equiv \frac{1}{\sqrt{g_2^2 + g_Y^2}}\left(g_Y W_\mu^3 + g_2 B_\mu\right) = \sin\theta_W W_\mu^3 + \cos\theta_W B_\mu \tag{2.16}$$

$$Z_\mu \equiv \frac{1}{\sqrt{g_2^2 + g_Y^2}}\left(g_2 W_\mu^3 - g_Y B_\mu\right) = \cos\theta_W W_\mu^3 - \sin\theta_W B_\mu, \tag{2.17}$$

where we introduced the *weak mixing angle* of the neutral gauge bosons, θ_W, given by

$$\sin\theta_W \equiv \frac{g_Y}{\sqrt{g_2^2 + g_Y^2}}. \tag{2.18}$$

With these definitions, the gauge boson mass and Higgs-gauge boson interaction terms of Eq. (2.13) become

$$\begin{aligned}\mathcal{L}_{\text{scalar}} \supset &+ \frac{v^2 g_2^2}{4} W_\mu^+ W^{-\mu} + \frac{(g_2^2 + g_Y^2)v^2}{8} Z_\mu Z^\mu \\ &+ (H^2 + 2vH)\left[\frac{g_2^2}{4} W_\mu^+ W^{-\mu} + \frac{g_2^2 + g_Y^2}{8} Z_\mu Z^\mu\right].\end{aligned} \tag{2.19}$$

Hence, the weak gauge boson masses are given by

$$M_W = \frac{1}{2} g_2\, v, \qquad M_Z = \frac{1}{2}\sqrt{g_2^2 + g_Y^2}\, v. \tag{2.20}$$

Note, that the photon field, A_μ, is still massless, since it is associated with the remaining unbroken U(1) gauge symmetry, as discussed above.

The W boson mass is related to the Fermi constant, $G_F = \sqrt{2} g_2^2/(8 M_W^2)$, which is determined from very precise measurements of the muon decay lifetime [50, 51]. This fixes the Higgs vev to $v = (\sqrt{2} G_F)^{-1/2} \simeq 246.2\,\text{GeV}$. The so-called *rho parameter*,

$$\rho \equiv \frac{M_W^2}{M_Z^2 \cos^2\theta_W}, \tag{2.21}$$

which corresponds to the relative strength of the charged and neutral currents at small momentum exchange ($q^2 \ll M_W^2$), is equal to unity at tree-level in the SM. This is a direct consequence of the doublet nature of the scalar field Φ, since in this case the model features

a custodial SU(2) global symmetry. In the SM, this symmetry is broken at the loop level by mass splittings of fermions within the same doublet, as well as by $\mathrm{U}(1)_Y$ gauge interactions, both leading to small corrections to the ρ parameter.

With the gauge choice of Eq. (2.12), the three real degrees of freedom ξ^A, the so-called *Goldstone bosons*, have disappeared, while the three weak gauge bosons $W^\pm$ and Z became massive and thus gained each another degree of freedom forming the longitudinal polarization mode. More generally, the *Goldstone theorem* [52] states that we obtain a massless scalar mode for each spontaneously broken generator of a continuous symmetry. In the case of spontaneously broken gauge symmetries, and the choice of the unitary gauge, these Goldstone modes are then absorbed by the gauge bosons, providing the longitudinal polarization of the now massive gauge boson.

With the introduction of the scalar field Φ, Eq. (2.7), we can further write down gauge invariant Yukawa terms for its interactions with the matter fields,

$$\mathcal{L}_{\text{Yukawa}} = -Y^{(\ell)}_{ij}\overline{e_{iR}}\Phi^\dagger L_{jL} - Y^{(d)}_{ij}\overline{d_{iR}}\Phi^\dagger Q_{jL} - Y^{(u)}_{ij}\overline{u_{iR}}\Phi\cdot Q_{jL} + \text{h.c.}, \tag{2.22}$$

where the Yukawa couplings Y_{ij} are 3×3 complex matrices. In the last term we have the anti-symmetric SU(2) product, $\Phi\cdot Q_{jL} = \phi^+ d_{jL} - \phi^0 u_{jL}$. In unitary gauge, Eq. (2.12), this becomes

$$\mathcal{L}_{\text{Yukawa}} = -\frac{(v+H)}{\sqrt{2}}\left[Y^{(\ell)}_{ij}\overline{e_{iR}}\,\ell_{jL} + Y^{(d)}_{ij}\overline{d_{iR}}\,d_{jL} + Y^{(u)}_{ij}\overline{u_{iR}}\,u_{jL}\right] + \text{h.c.}. \tag{2.23}$$

after spontaneous symmetry breaking. We have obtained mass terms for the charged fermions, cf. Eq. (2.6), proportional to the Yukawa coupling matrices Y_{ij}. Due to this proportionality, a bi-unitary rotation in generation space[5], which diagonalizes the mass matrices, automatically diagonalizes the Higgs couplings to the physical mass eigenstates. Hence the fermion masses are given by

$$m_{f_i} = \frac{v}{\sqrt{2}}Y^{(f)}_{ii}, \tag{2.24}$$

and *flavor changing neutral currents* (FCNCs) are absent at tree-level. We will often use the short notation $y_{f_i} \equiv Y^{(f)}_{ii}$ for the Yukawa couplings.

We can read off the coupling strengths of the Higgs interactions to fermions and gauge bosons ($V = W, Z$) from Eqs. (2.23) and (2.19), respectively:

$$g_{Hff} = i\,\frac{m_f}{v}, \quad g_{HVV} = -2i\,\frac{M_V^2}{v}, \quad g_{HHVV} = -2i\,\frac{M_V^2}{v^2}. \tag{2.25}$$

Thus, the Higgs boson preferentially decays to the heaviest particle that is kinematically accessible, as will be discussed in Section 2.2.1. The trilinear and quartic Higgs self-interactions

[5] In the quark sector the physical mass eigenstates are obtained by unitary transformations of the EW interaction (or *flavor*) eigenstates, described by the unitary matrices $V^{u(d)}_{L,R}$ for the left- and right-handed up-type (down-type) quark fields, respectively. The misalignment of mass and flavor eigenstates is described by the unitary *Cabibbo-Kobayashi-Maskawa* (CKM) matrix [53], $V_{\text{CKM}} = (V^u_L)^\dagger V^d_L$, and leads to a remnant flavor structure in the quark charged current interactions. V_{CKM} can be parametrized in terms of three real angles and one complex, $\mathcal{CP}$-violating phase. A similar formulation in the lepton sector with massive neutrinos (after introducing right-handed neutrinos) leads to the *Pontecorvo-Maki-Nakagawa-Sakata* (PMNS) matrix [54].

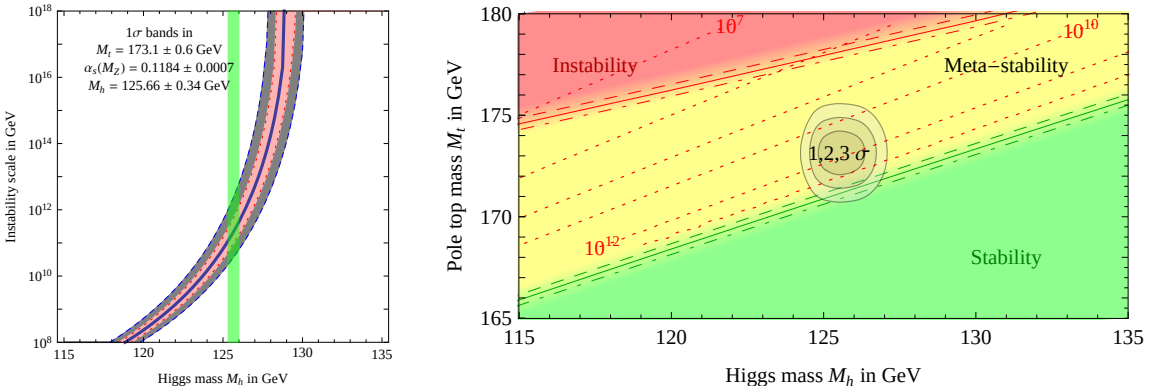

(a) Instability scale Λ_I at which the quartic Higgs coupling λ becomes negative as a function of the Higgs mass.

(b) Regions of absolute stability, meta-stability and instability of the SM vacuum in the plane of the top quark mass, M_t, and Higgs boson mass, M_h. The gray areas indicate the experimentally favored region at 1, 2, and 3σ. The dotted contour-lines show the instability scale Λ_I in GeV.

Figure 2.2: Theoretical constraints on the SM Higgs sector from the vacuum (meta-)stability requirement. Figures are taken from Ref. [56], where more details can be found.

are given by

$$g_{HHH} = 3i\,\frac{m_H^2}{v}, \quad g_{HHHH} = 3i\,\frac{m_H^2}{v^2}. \tag{2.26}$$

At a Higgs mass of 125 GeV, the absolute value of the quartic Higgs coupling strength is ~ 0.78 and thus the Higgs self-interactions are well within the perturbative regime.

On first sight, the Higgs mechanism of the SM may seem rather *ad hoc* [55], however, the mechanism of spontaneous symmetry breaking for giving masses to gauge bosons and fermions is in fact very generic. The introduction of a scalar field Φ and the choice of the coefficient μ^2 in its effective potential being negative suffices to automatically generate the observed fermion and gauge boson masses without violating the principles of renormalizable gauge theories.

2.1.3 Theoretical constraints on the SM Higgs sector

We now briefly review the theoretical constraints on the SM Higgs sector that can be inferred from requiring *(i)* a well-behaved Higgs potential that ensures a stable or meta-stable vacuum as well as perturbativity of the theory, and *(ii)* the restoration of unitarity in scattering processes of the longitudinal modes of massive gauge bosons.

(i) Vacuum (meta-)stability

As we have seen above, the quartic coupling λ is required to be positive for the scalar field to acquire a finite vacuum expectation value. This corresponds to a Higgs potential that is bounded from below and hence to a stable vacuum. The dependence on the energy scale Q (also known as *running*) of the coupling λ is described by the Renormalization

Group (or *Callan-Symanzik*) Equation (RGE) [57],

$$Q^2 \frac{d\lambda}{dQ^2} = \frac{d\lambda}{d\ln Q^2} = \beta(\lambda, g, y_f). \tag{2.27}$$

Note that the β function depends on the gauge and Yukawa couplings in addition to λ. In general, it is calculated from the loop corrections to wave functions and vertices, see e.g. Ref. [40] for an introduction. Here, the main contributions to the β function come from the quartic Higgs self- and Higgs-gauge boson interactions as well as the Higgs-Yukawa interactions with the top quark. At one-loop level, these are given by [58]

$$\beta(\lambda, g_2, g_Y, y_t) \simeq \frac{1}{16\pi^2}\left[12\lambda^2 + 6\lambda y_t^2 - 3y_t^4 - \frac{3}{2}\lambda(3g_2^2 + g_Y^2) + \frac{3}{16}(3g_2^4 + 2g_2^2 g_Y^2 + g_Y^4)\right]. \tag{2.28}$$

For small values of the quartic coupling, $|\lambda| \ll 1$, the top quark contribution, $-3y_t^4$, is dominant, yielding a negative β function that drives the quartic coupling to negative values, $\lambda(Q^2 \geq \Lambda_I^2) \leq 0$, at a high scale Λ_I. Requiring a stable vacuum therefore sets a lower bound on λ and thus on the Higgs mass m_H [32],

$$m_H^2 \gtrsim \frac{v^2}{8\pi^2}\left[-12\frac{m_t^4}{v^4} + \frac{3}{16}(3g_2^4 + 2g_2^2 g_Y^2 + g_Y^4)\right] \ln \frac{\Lambda_I^2}{v^2}, \tag{2.29}$$

which depends on the instability scale Λ_I. Likewise, this can be read as an upper limit on the energy scale where new physics effects appear and change the running of the Higgs quartic coupling. Note, that these constraints feature a strong dependence on the top quark mass m_t.

A weaker but nevertheless equally valid requirement is the meta-stability of the vacuum: The presence of other, deeper minima of the SM effective potential than the electroweak vacuum is allowed, as long as the tunneling time of the transition from the electroweak vacuum to the other vacua exceeds the lifetime of the Universe. In this case, the lower bound on m_H is generally much weaker than Eq. (2.29), although the calculation of the tunneling time is quite involved and relies on various cosmological assumptions.

Results from a recent analysis [56] of the vacuum stability including next-to-next-to-leading order (NNLO) corrections to the effective SM Higgs potential are shown in Fig. 2.2. The measured values of the top quark mass, $m_t \approx 173\,\text{GeV}$, and the Higgs mass, $m_H \approx 125.7\,\text{GeV}$, drive the Higgs quartic coupling to negative values at some scale $\sim 10^{10} - 10^{14}$ GeV, as can be seen in Fig. 2.2(a). However, the lifetime of the vacuum is estimated to be much larger than the age of the Universe, leading to the interesting fact that the experimentally favored parameter region is considered to be meta-stable, as shown in Fig. 2.2(b). However, it should be noted that no definite conclusion on the fate of the SM electroweak vacuum can be drawn yet since the uncertainties in m_H, m_t and, to a lesser extent, the strong coupling α_s are still too large.

An upper limit on the Higgs mass, m_H, can be obtained from requiring the theory to remain perturbative at higher scales. For large values of λ, the β function, Eq. (2.28), can

be approximated by $\beta \approx 3\lambda^2/(4\pi^2)$, leading an approximate solution for Eq. (2.27) of

$$\lambda(Q^2) \approx \lambda(v^2) \left[1 - \frac{3}{4\pi^2}\lambda(v^2) \ln \frac{Q^2}{v^2}\right]^{-1}. \tag{2.30}$$

This leads to a *Landau pole*, $\lambda(Q = \Lambda_C) \to \infty$, at an energy scale

$$\Lambda_C = v \exp\left(\frac{8\pi^2 v^2}{3m_H^2}\right). \tag{2.31}$$

From employing the RGE running of the quartic coupling λ we can determine the energy cut-off scale Λ_C below which λ remains finite and perturbative, or, in other words, the energy domain in which the SM remains valid. Requiring perturbativity up to the Grand Unification (GUT) scale, $\Lambda_C \sim 10^{16}$ GeV, yields an upper limit of $m_H \lesssim 200\,\text{GeV}$, while larger Higgs masses $m_H \lesssim 1\,\text{TeV}$ are allowed if the cut-off scale is $\sim \mathcal{O}(1\,\text{TeV})$. With the mass value of the discovered Higgs boson being at about 125.7 GeV, the SM is well within the perturbative regime at all energy scales.

(ii) **Perturbative unitarity**

If we attempted to calculate scattering processes of the longitudinal modes of massive gauge bosons at tree-level without adding the scalar field Φ (assuming that the Lagrangian could contain explicit mass terms for the gauge bosons), the cross section features a bad energy behavior, i.e. it grows linearly or even quadratically with the CM energy $\sqrt{s}$ of the scattering process, and thus violates unitarity[6]. In the SM the Higgs boson restores this tree-level unitarity if the Higgs boson is not too heavy [59, 60]. For instance, for the charged W boson scattering process $W^+W^- \to W^+W^-$, the tree-level scattering amplitude at high energies is given by

$$A(W^+W^- \to W^+W^-) \xrightarrow{s \gg M_W^2} \frac{m_H^2}{v^2}\left(2 + \frac{m_H^2}{s - m_H^2} + \frac{m_H^2}{t - m_H^2}\right), \tag{2.32}$$

where s and t are Mandelstam variables. For very large Higgs masses, the growing amplitude eventually leads to the violation of unitarity of the cross section[7]. This happens (in the worst case) for roughly

$$m_H \lesssim 700\,\text{GeV}, \tag{2.33}$$

see Ref. [32] for a more detailed discussion. Note, that the restoration of unitarity via the Higgs boson exchange requires the Higgs boson couplings to be *exactly* those as predicted in the SM, Eqs. (2.25) and (2.26), unless the theory contains multiple Higgs bosons (in which case unitarity sum rules have to be fulfilled) [61].

In summary, the picture *before* the Higgs boson discovery was that all theoretical constraints hinted towards a Higgs boson in the mass region of roughly $50\,\text{GeV} \lesssim m_H \lesssim 1\,\text{TeV}$. As we will

[6] Unitarity of the scattering amplitude corresponds to the conservation of probability, which is one of the basic principles of Quantum Mechanics.

[7] Decomposing the scattering amplitude A into partial waves a_ℓ of orbital momentum ℓ and using the optical theorem, the unitarity requirement can be quantified as $|\text{Re}\, a_\ell| < 1/2$ [32].

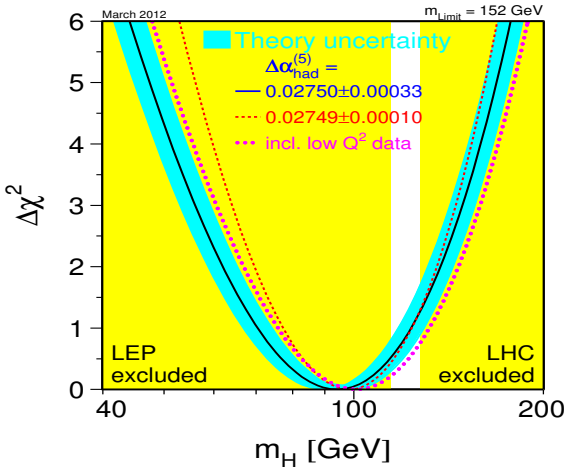

(a) Profiled χ^2 likelihood distribution in the SM Higgs mass, m_H. Taken from Ref. [65].

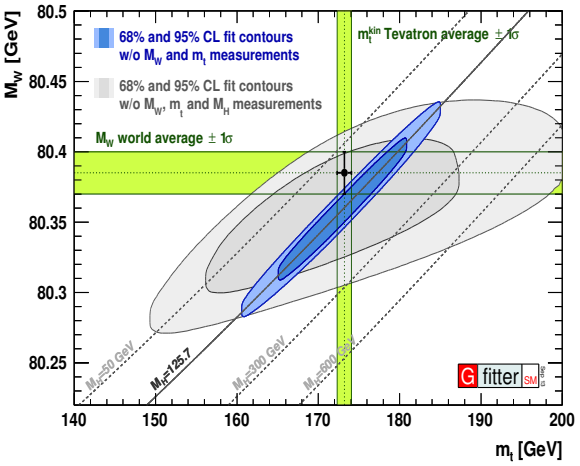

(b) Preferred regions in the top quark-W boson mass plane. Taken from Ref. [66].

Figure 2.3: Global χ^2 fits of the SM parameters to electroweak precision data from the LEP electroweak working group (LEPEWWG) [65] (a) and GFitter [66] (b).

now discuss, this conjecture was supported by results from experimental precision tests of the SM.

2.1.4 Precision tests of the electroweak sector

A large variety of high-precision measurements have been performed at past collider experiments at SLC, LEP-1, LEP-2 and the Tevatron, amongst others the determination of the W, Z and top-quark masses and decay widths [62, 63]. Together with the measurements of cross sections and various asymmetries of the process $e^+e^- \to Z/\gamma^* \to f\bar{f}$ around the Z pole, $\sqrt{s} \sim M_Z$, at LEP and SLC [64], they define the two past decades as the era of electroweak precision physics.

As we have seen above, the electroweak gauge interactions depend only on three quantities at tree-level: The gauge couplings g_2 and g_Y, and the Higgs vev v. These can be accurately determined from measurements of the electromagnetic coupling constant α_{em} at low energies, the Fermi constant G_F from the muon lifetime, and M_Z from the LEP/SLC experiments, although corrections at loop-level as well as the RGE running between different scales introduce some uncertainty.

The sensitivity of the electroweak observables to loop corrections provides indirect indications on the Higgs mass. This sensitivity is reflected, for instance, in the one-loop corrections to the ρ parameter, Eq. (2.21), which depend quadratically on the top-quark mass, m_t, and logarithmically on the Higgs mass, m_H in the heavy Higgs limit, $m_H \gg M_Z$. Global fits of the SM parameters[8] (including the Higgs mass) to the electroweak precision observables thus comprise highly non-trivial tests of the consistency of the SM and, in particular after the measurement of the top quark mass, provide important constraints on the Higgs mass.

[8] The determination of the CKM matrix elements, however, requires dedicated measurements from flavor physics, see e.g. Ref. [67] for a review.

The quality of these global fits is typically very good, indicating that most measurements are highly compatible with the SM. Updated results from two of these fits are shown in Fig. 2.3. The *blue band plot* from the LEP Electroweak Working Group (LEPEWWG) [65] (status of March 2012), as depicted in Fig. 2.3(a), shows the profiled χ^2 likelihood distribution in the Higgs mass together with direct exclusion limits at the 95% confidence level (C.L.) from LEP and LHC experiments. Theoretical uncertainties from various missing higher-order corrections are condensed into the blue band. The best-fit Higgs mass value is $m_H = 94^{+29}_{-24}$ GeV. The predictive power of this plot was impressively demonstrated when the Higgs boson was found in July 2012 at the LHC in exactly the remaining unexcluded mass region, with a mass value compatible with the best-fit value within roughly one standard deviation (1σ).

The electroweak precision observables give rise to strong correlations of the top quark, the W boson and the Higgs mass, as illustrated by the GFitter result [66] (status of *September 2013*) shown in Fig. 2.3(b). Fitting the electroweak precision data with and without taking the observed Higgs mass into account yields in both cases a SM fit that is well compatible with the direct measurements of M_W and m_t. With a Higgs mass of 125.7 GeV, the SM prediction for the top quark [W boson] mass is slightly higher [lower] than the combined direct measurements.

For more details about the electroweak precision tests we refer the reader to Ref. [68]. In summary, both theoretical arguments and indirect implications from electroweak precision measurements strongly suggested the existence of a Higgs boson in the mass range of $\mathcal{O}$(few GeV$-$1 TeV), preferentially, though, rather close to the Z boson mass, $m_H \sim M_Z$. Hence, collider searches at the LEP, Tevatron and LHC experiments focussed on this mass range.

2.2 Collider phenomenology of the SM Higgs boson

In this section we give an overview of the main SM Higgs boson decay modes and production channels at e^+e^- and hadron colliders. After early studies of the Higgs boson collider phenomenology in the 1970's [69], much theoretical effort has gone into precise predictions of the Higgs boson branching ratios and production cross sections over the past three decades, as these are an essential ingredient for Higgs boson searches at collider experiments. Here, these predictions will be discussed on a rather qualitative level, for details on the precision calculations we refer the reader to Refs. [30, 32, 33, 70, 71] and references therein.

In the SM, all parameters in the scalar potential, Eq. (2.9), are fixed once the SM Higgs mass, m_H, is specified. Consequently, the complete phenomenological profile of the SM Higgs boson only depends on this one parameter m_H (besides other rather well-measured SM parameters). This changes in theories beyond the SM (BSM), which feature a larger number of unknown model parameters. Nevertheless, the BSM predictions for the collider phenomenology of the neutral Higgs boson(s) can often be derived to a good approximation by rescaling the SM cross sections and partial widths by effective couplings calculated within the BSM theory. This is often advantageous, as higher-order QCD and EW corrections to the cross sections and partial widths have been calculated to a high accuracy for the SM Higgs boson. These precision calculations are usually not carried out to such a high level of sophistication in phenomenological studies of BSM theories.

2.2.1 Higgs boson decays

Due to the mass dependence of the Higgs couplings, Eq. (2.25), the SM Higgs boson predominantly decays into the heaviest particle-antiparticle pair that is kinematically accessible,

depending on the available energy m_H. From the pole masses[9] of the SM gauge bosons and fermions[10] [74, 75],

$$M_Z = 91.188\,\text{GeV}, \quad M_W = 80.385\,\text{GeV}, \quad m_\mu = 0.106\,\text{GeV}, \quad m_\tau = 1.777\,\text{GeV},$$
$$m_c = (1.67 \pm 0.07)\,\text{GeV}, \quad m_b = (4.78 \pm 0.06)\,\text{GeV}, \quad m_t = (173.34 \pm 0.76)\,\text{GeV}, \tag{2.34}$$

all partial widths, $\Gamma(D_j(H))$, for the Higgs boson decays to these particles can be calculated. Here, the various decay modes of the Higgs boson H are denoted by $D_j(H)$. The branching ratio, which is the probability of the Higgs boson decaying into a certain final state, is then given by

$$\text{BR}(D_j(H)) \equiv \frac{\Gamma(D_j(H))}{\Gamma_{\text{tot}}}, \tag{2.35}$$

with the total decay width $\Gamma_{\text{tot}} = \sum_j \Gamma(D_j(H))$, where the sum runs over *all* possible decay modes $D_j(H)$. For a reliable prediction of the Higgs boson signal rates at colliders, a precise calculation of Γ_{tot}, and hence of all partial widths, is a necessity. Uncertainties in the total width prediction will introduce strongly correlated uncertainties among all the branching ratios.

An overview of the branching ratios of the SM Higgs boson as a function of the Higgs mass is given in Fig. 2.4. The low mass region, $m_H \in [1, 100]$ GeV, depicted in Fig. 2.4(a), was accessible at the e^+e^- collider LEP, while the high mass region, $m_H \in [80, 1000]$ GeV, shown in Fig. 2.4(b), is probed by the hadron collider experiments at the Tevatron and LHC. As expected, the predominant decay modes are those into the heaviest particles allowed by phase space. However, besides the (on-shell) two-body decays in kinematically accessible regions, $m_H > 2m_X$, it is important to also take into account the three- and even four-body Higgs decays via off-shell W and Z bosons below the WW/ZZ thresholds.

Due to the proportionality of the Higgs couplings to the masses of the decay products, the total width ranges over many orders of magnitude, namely from 10^{-4} GeV for $m_H \lesssim 10$ GeV to 1 TeV for $m_H \sim 1$ TeV. The total width for a SM Higgs boson with $m_H \sim 125$ GeV is about 4.1 MeV. Experimentally, this is too small to be resolved in invariant mass distributions of the decay products, as the finite energy resolution of the LHC detectors is much larger[11]. On the theoretical side, the narrow width justifies the approach to factorize the Higgs production process from the subsequent decay in the on-shell region[12] (known as the *narrow-* or *zero-width approximation*). For very large Higgs masses, however, the Higgs boson would manifest itself as a very broad resonance with a width being of around the size of its mass. This requires a careful theoretical treatment beyond the narrow width approximation, taking also interference

[9] The pole mass is defined as the position of the pole in the propagator, which is typically measured by experiment. Quark masses, however, cannot be observed directly since they are (except for the top quark) confined in hadrons. The pole mass can be related to the *running* mass (in the $\overline{\text{MS}}$ renormalization scheme) [72], which corresponds to the mass parameter in the renormalized Lagrangian. Nevertheless, for the top quark delicate issues (and thus uncertainties) in the interpretation of the measured mass remain, see Ref. [73] for a discussion.

[10] The masses of the electron and light quarks, u, d and s, are too small to be relevant for Higgs phenomenology.

[11] Even at a future International Linear Collider (ILC) the width is too small to be measured directly from the line-shape [76]. However, by combining signal rate measurements with the ILC measurement of the total $e^+e^- \to ZH$ cross section, cf. Section 2.2.2, the total width can be unambiguously inferred. This will be discussed in Chapter 5.

[12] Recently, it has been pointed out that even for a Higgs mass of 125 GeV interference effects (in the off-shell region) can still play a role and provide sensitivity for probing the total widths at the LHC [77]. See Chapter 5 for more details.

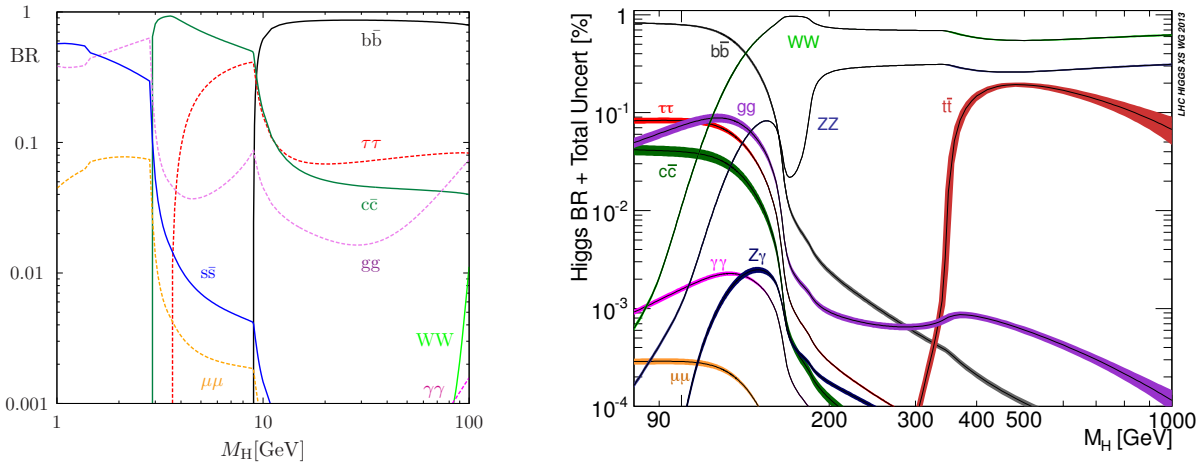

(a) Low mass region. Taken from Ref. [33].

(b) High mass region. Taken from Ref. [30].

Figure 2.4: Branching ratios (BR) of a SM Higgs boson for low (a) and high (b) Higgs boson masses. In (b), the bands indicate the theoretical uncertainty of the BR predictions.

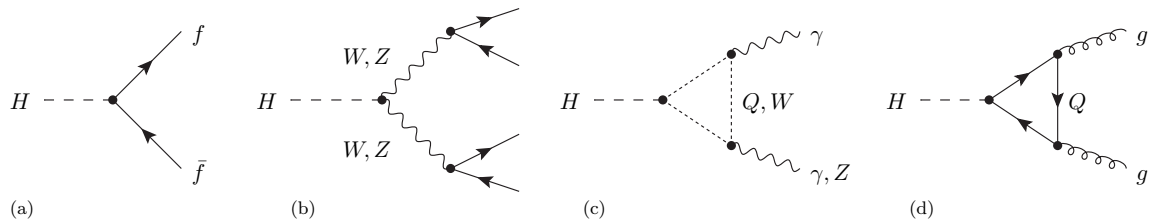

Figure 2.5: Leading-order diagrams for the various SM Higgs boson decay channels into a fermion-antifermion ($f\bar{f}$) pair (a), weak gauge bosons (W,Z) with successive decay to fermions (b), photons and photon-Z boson (c) and gluons (d). Q denotes any heavy quark.

effects between signal and background processes into account, see e.g. Ref. [30] for a discussion of current developments.

The relevant leading-order Feynman diagrams for the various decay modes of the SM Higgs boson are shown in Fig. 2.5. In the following we briefly discuss the main features of the relevant decay channels and give the leading-order expressions for the partial widths.

- ***H* → *f*$\bar{f}$**

  For the Higgs decay into fermion-antifermion ($f\bar{f}$) pairs, the partial width at leading order (LO) is given by

$$\Gamma_{\text{LO}}(H \to f\bar{f}) = \frac{g_2^2 N_c}{32\pi M_W^2} m_H \, m_f^2 \, \beta_f^3, \tag{2.36}$$

  with the fermion velocity $\beta_f = (1 - 4m_f^2/m_H^2)^{1/2}$ and the color factor $N_c = 3$ (1) for quarks (leptons). According to Eq. (2.34) the relevant decay modes are those to $t\bar{t}$ (for heavy Higgs bosons), $b\bar{b}$, $\tau^+\tau^-$, $c\bar{c}$, and, to a lesser extent, $\mu^+\mu^-$. The kinematical factor β_f^3 in Eq. (2.36) leads to a strong suppression near threshold, $m_H \simeq 2m_f$. The suppression is weaker for a pseudoscalar (or $\mathcal{CP}$-odd) Higgs boson, A, where we have

$\Gamma_{\text{LO}}(A \to f\bar{f}) \propto \beta_f$. We often encounter pseudoscalar Higgs bosons in non-minimal Higgs sectors of BSM theories, for instance in the MSSM, see Section 2.4.

For quark final states next-to-leading-order (NLO) QCD corrections are sizable and need to be taken into account. A proper treatment of higher-order corrections requires to base the Yukawa coupling on the running quark mass at the scale of the Higgs mass, $\overline{m}_q(m_H)$, allowing for the resummation of large logarithms [78]. Furthermore, the threshold regime, $m_H \simeq 2m_q$, deserves particular attention as potential mixing between the Higgs boson and $(q\bar{q})$ bound states may play a significant role [79].

- ***H → WW/ZZ → 4f***

  The partial width for a Higgs boson decaying into two on-shell gauge bosons, $H \to VV$ $(V = W, Z)$, is given by [80]

$$\Gamma_{\text{LO}}(H \to VV) = \frac{g_2^2}{128\pi M_W^2}\, m_H^3\, \delta_V \sqrt{1-4x}\,(1-4x+12x^2), \tag{2.37}$$

  where $\delta_W = 2$, $\delta_Z = 1$ due to the symmetry of exchanging the identical Z bosons in the final state, and $x = M_V^2/m_H^2$. Thus, at large Higgs masses, i.e. small x, the decay width to WW is twice the decay width to ZZ.

  Below the WW and ZZ thresholds (as is the case for the discovered Higgs boson at $m_H \sim 125.7\,\text{GeV}$), these decays have to be treated as three- and four-body decays with off-shell gauge bosons and final state fermions[13] [81]. Despite the propagator suppression, these decays can still compete with the decay $H \to b\bar{b}$ due to the smallness of the bottom Yukawa coupling, cf. Fig. 2.4. Furthermore, the kinematical details (energy, angular and invariant-mass distributions) of the four-fermion final state allow for the determination of the spin and $\mathcal{CP}$ properties of a discovered Higgs boson candidate [82, 83].

- ***H → γγ/γZ***

  The Higgs decay into two photons or a photon and a Z boson is mediated at leading order by W boson and charged fermion loops, as depicted in Fig. 2.5(c). The dominant and sub-dominant contributions come for the W boson and top quark loop, respectively. The partial width for the decay $H \to \gamma\gamma$ is given by

$$\Gamma_{\text{LO}}(H \to \gamma\gamma) = \frac{g_2^2 \alpha_{\text{em}}^2}{1024\pi^3 M_W^2}\, m_H^3 \left| \sum_f N_c Q_f^2 A_{1/2}^H(\tau_f) + A_1^H(\tau_W) \right|^2, \tag{2.38}$$

  with the electric charge Q_f and color factor N_c of the fermion in the loop. The form factors for spin-1/2 and spin-1 particles are given by

$$A_{1/2}^H(\tau) = 2[\tau + (\tau-1)f(\tau)]\tau^{-2}, \tag{2.39}$$

$$A_1^H(\tau) = -[2\tau^2 + 3\tau + 3(2\tau-1)f(\tau)]\tau^{-2}. \tag{2.40}$$

[13] Formulae for the leading order three- and four-body decays can e.g. be found in Ref. [32].

The function $f(\tau)$ is defined by

$$f(\tau) = \begin{cases} \arcsin^2(\sqrt{\tau}) & \tau \leq 1 \\ -\frac{1}{4}\left[\log\frac{1+\sqrt{1-\tau^{-1}}}{1-\sqrt{1-\tau^{-1}}} - i\pi\right]^2 & \tau > 1 \end{cases}, \tag{2.41}$$

and the τ parameters are given by $\tau_f = m_H^2/4m_f^2$ and $\tau_W = m_H^2/4M_W^2$. It is important to note that due to the interference terms, the partial width is sensitive to the relative sign of the individual contributions. At a Higgs boson mass of $m_H \sim 125\,\text{GeV}$, the top quark and W boson loop contributions have opposite sign and thus the tW interference term yields a negative contribution to the partial width.

Due to the suppression by the additional electromagnetic coupling constant, the loop decays $H \to \gamma\gamma$ and $H \to Z\gamma$ are only important for light Higgs bosons, $m_H \lesssim 130\,\text{GeV}$, where the total width is rather small. Despite its rather small branching ratio, the $H \to \gamma\gamma$ channel provides an experimentally clean collider signature and thus played a major role in the discovery of the Higgs boson, see Chapter 3. Moreover, these loop-induced decay modes feature a great sensitivity to new heavy charged particles of BSM theories: Due to the proportionality of the Higgs couplings to the particle masses the loop mass suppression is compensated, hence virtual particles do not decouple in the heavy mass limit. A precise measurement of the $H \to \gamma\gamma$ and $H \to Z\gamma$ partial widths thus probes potential effects induced by heavy charged particles, which might be too heavy to be produced directly at current collider experiments[14].

- ***H → gg***

  The Higgs boson decay to two gluons is mediated by heavy quark loops, as depicted in Fig. 2.5(d), with the dominant contribution coming from top quarks and a small contribution from bottom quarks. The partial width at leading order is given by

$$\Gamma_{\text{LO}}(H \to gg) = \frac{g_2^2\alpha_s^2}{288\pi^3 M_W^2} m_H^3 \left|\frac{3}{4}\sum_Q A_{1/2}^H(\tau_Q)\right|^2, \tag{2.42}$$

  with the strong coupling constant α_s, the loop function $A_{1/2}^H$ given by Eq. (2.39) and $\tau_Q = m_H^2/4m_Q^2$. For this process, the NLO QCD corrections (entering at the two-loop level) are very important, leading to an increase of the partial width by up to $\sim 70\%$ for $m_H \lesssim 2M_W$ and at the $t\bar{t}$ threshold [102]. Even beyond NLO [85] the partial width is further increased by about 20% in the light Higgs regime.

The numerical values of the SM Higgs branching ratios and total width for Higgs masses in the proximity of the discovered Higgs boson are listed in Tab. (2.2), taken from Ref. [30]. These values are evaluated with the state-of-the-art tools `HDecay` [86, 87] and `Prophecy4f` [88]. We furthermore list the maximal uncertainty estimates[15] (relative to the quoted branching ratio),

[14] As a nice example, it was shown in Ref. [84] that the $H \to \gamma\gamma$ signal strength measured at the LHC excludes the existence of a fourth generation of fermions (assuming fourth generation fermion masses of $m_{f'} \leq 800\,\text{GeV}$).

[15] Note, that the uncertainty for the total width is derived by adding the partial width uncertainties linearly. Furthermore, PUs and THUs are added linearly [30]. We find this to be an (overly) conservative approach and discuss an alternative approach in Section 4.2.2, which also allows to account for correlations among the branching ratio uncertainties in global Higgs couplings fits.

Higgs mass [GeV]	Branching ratios to fermionic final states $b\bar{b}$	$\tau^+\tau^-$	$c\bar{c}$	$\mu^+\mu^-$	$t\bar{t}$	Total width [GeV]
125.0	$57.7\%\,^{+3.2}_{-3.3}$	$6.32\%\,^{+5.7}_{-5.7}$	$2.91\%\,^{+12.2}_{-12.2}$	$0.0219\%\,^{+6.0}_{-5.9}$	–	$4.07 \cdot 10^{-3}\,^{+4.0}_{-3.9}$
125.5	$56.9\%\,^{+3.3}_{-3.3}$	$6.24\%\,^{+5.7}_{-5.6}$	$2.87\%\,^{+12.2}_{-12.2}$	$0.0216\%\,^{+5.9}_{-5.8}$	–	$4.14 \cdot 10^{-3}\,^{+3.9}_{-3.9}$
126.0	$56.1\%\,^{+3.3}_{-3.4}$	$6.16\%\,^{+5.7}_{-5.6}$	$2.83\%\,^{+12.2}_{-12.2}$	$0.0214\%\,^{+5.9}_{-5.8}$	–	$4.21 \cdot 10^{-3}\,^{+3.9}_{-3.8}$
Higgs mass [GeV]	Branching ratios to bosonic final states gg	WW^*	ZZ^*	$\gamma\gamma$	γZ	Total width [GeV]
125.0	$8.57\%\,^{+10.2}_{-10.0}$	$21.5\%\,^{+4.3}_{-4.2}$	$2.64\%\,^{+4.3}_{-4.2}$	$0.228\%\,^{+5.0}_{-4.9}$	$0.154\%\,^{+9.0}_{-8.8}$	$4.07 \cdot 10^{-3}\,^{+4.0}_{-3.9}$
125.5	$8.52\%\,^{+10.2}_{-9.9}$	$22.3\%\,^{+4.2}_{-4.1}$	$2.76\%\,^{+4.2}_{-4.1}$	$0.228\%\,^{+4.9}_{-4.9}$	$0.158\%\,^{+8.9}_{-8.8}$	$4.14 \cdot 10^{-3}\,^{+3.9}_{-3.9}$
126.0	$8.48\%\,^{+10.1}_{-9.9}$	$23.1\%\,^{+4.1}_{-4.1}$	$2.89\%\,^{+4.1}_{-4.1}$	$0.228\%\,^{+4.9}_{-4.8}$	$0.162\%\,^{+8.8}_{-8.8}$	$4.21 \cdot 10^{-3}\,^{+3.9}_{-3.8}$

Table 2.2: Branching ratios and total width of the SM Higgs boson in the mass region of the discovered Higgs boson. The quoted upper and lower uncertainties are relative to the predicted value and given in percentage. Numbers are taken from Ref. [30].

comprised of parametric uncertainties (PUs) derived from variations of the input parameters (α_s, m_c, m_b, m_t) as well as theoretical uncertainties (THUs) for the missing higher-order corrections [89]. As can be seen from Tab. 2.2 and Fig. 2.4(b), with the mass value of the discovered Higgs boson, $m_H \sim 125.7\,\text{GeV}$, Nature kindly provides us with the opportunity to measure various Higgs decay modes, since all channels except $H \to t\bar{t}$ are accessible with current or future collider experiments. This further allows to probe the various Higgs couplings and thus provides an important test of the SM predictions.

2.2.2 Higgs boson production at lepton colliders

Until 2011 the lower limit on the SM Higgs boson mass, $m_H \geq 114.4\,\text{GeV}$, came from the experiments at the *Large Electron-Positron Collider* (LEP) at CERN [90]. Moreover, LEP provided a plethora of model-independent cross section limits in various Higgs channels (see also Chapter 3). In the future, the next collider experiment beyond the LHC is anticipated to be an e^+e^- linear collider, opening the area of precision measurements of the discovered Higgs state at $\sim 125.7\,\text{GeV}$. Here, we briefly review the most important SM Higgs boson production processes at the e^+e^- colliders at LEP and a future *International Linear Collider* (ILC) [91–93].

The importance of the various Higgs production mechanisms at e^+e^- colliders strongly depends on the CM energy $\sqrt{s}$. Up to LEP energies, $\sqrt{s} \lesssim 209\,\text{GeV}$, the *Higgs-strahlung* process $e^+e^- \to ZH$ with subsequent decays of the Higgs and Z boson to SM fermions was the main search channel. At higher energies of prospective future e^+e^- linear colliders, Higgs production via the fusion of W or Z bosons and in association with top quark pairs becomes relevant. Representative lowest-order diagrams for these processes are depicted in Fig. 2.6. In the following we give a qualitative description of their main features. More details can be found e.g. in Refs. [32, 33, 91].

- **$e^+e^- \to ZH$ (Higgs-strahlung)**

  The Higgs-strahlung process $e^+e^- \to ZH$, depicted in Fig. 2.6(a), is an s-channel process, hence its cross section peaks near the kinematic threshold and falls off $\propto 1/s$ at higher energies $\sqrt{s}$. With a Higgs mass of $\sim 125.7\,\text{GeV}$, the maximum of the leading-order cross

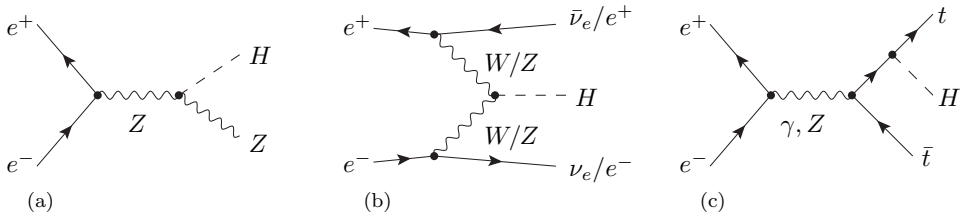

Figure 2.6: Representative lowest-order diagrams for the main Higgs boson production processes at e^+e^- colliders: (a) Higgs-strahlung process, (b) WW and ZZ fusion process and (c) Higgs production in association with a $t\bar{t}$ pair.

section is obtained at $\sqrt{s} \approx 246\,\text{GeV}$, however, collinear photon emissions off the initial state decrease the effective CM energy of the hard process. Therefore, the maximal cross section $\sigma(e^+e^- \to ZH)$ is obtained at slightly higher beam energies.

The Higgs-strahlung cross section is directly proportional to the squared Higgs coupling to Z bosons and is therefore an important means for probing the Higgs mechanism. At the ILC a simultaneous measurement of the Higgs mass and the total Higgs-strahlung cross section is possible using the $e^+e^- \to ZH$ process with subsequent decays of the Z boson to quarks, electrons and, most importantly, muons. The Higgs mass can be determined from the shape of the distribution of the invariant mass recoiling against the reconstructed Z boson, while the normalization of this distribution provides the total cross section $\sigma(e^+e^- \to ZH)$ independently of the Higgs decay mode. As will be discussed in Chapter 5, the total cross section measurement is an essential ingredient for a model-independent Higgs coupling determination.

- **$e^+e^- \to \nu\bar{\nu}H$ (WW-fusion) and $e^+e^- \to e^+e^-H$ (ZZ-fusion)**

  The process $e^+e^- \to \nu\bar{\nu}H$ involves the sum over all three neutrino species, to which the s-channel $e^+e^- \to ZH$ process with $Z \to \nu\bar{\nu}$ contributes. The WW-fusion channel, depicted in Fig. 2.6(b), only yields $\nu_e\bar{\nu}_e$ in the final state, and in this case the s- and t-channels interfere. However, the contributions from the WW-fusion (and similarly the ZZ-fusion) process to the cross section are $\propto \ln(s/m_H^2)/M_W^2$ for large energies. Hence, the WW-fusion channel becomes dominant for sufficiently high CM energies, $\sqrt{s} \gtrsim 450\,\text{GeV}$. The ZZ-fusion channel has a roughly 10 times smaller cross section than the WW fusion process, however, this deficit is partially compensated since the final state electrons allow for a better reconstruction of the kinematics of the process.

- **$e^+e^- \to t\bar{t}H$ (associated Higgs production with a top quark pair)**

  The analysis of the $2 \to 3$ s-channel process $e^+e^- \to t\bar{t}H$ at a future e^+e^- collider is an important means to probe the top quark Yukawa coupling. Due to the high kinematic threshold this process becomes only accessible at CM energies $\sqrt{s} \gtrsim 2m_t + m_H \simeq 470\,\text{GeV}$. The contribution from the diagrams with the Higgs boson being radiated off from the top or anti-top quark, as depicted in Fig. 2.6(c), dominates over the contribution from the diagram, where the Higgs boson couples to the virtual Z boson (not shown). At high energies the cross section falls with $1/s$.

  Due to the $t\bar{t}$ pair in the final state, the cross section receives sizable higher-order QCD corrections [94]. These are particularly large in the threshold region, where the $t\bar{t}$ pair is

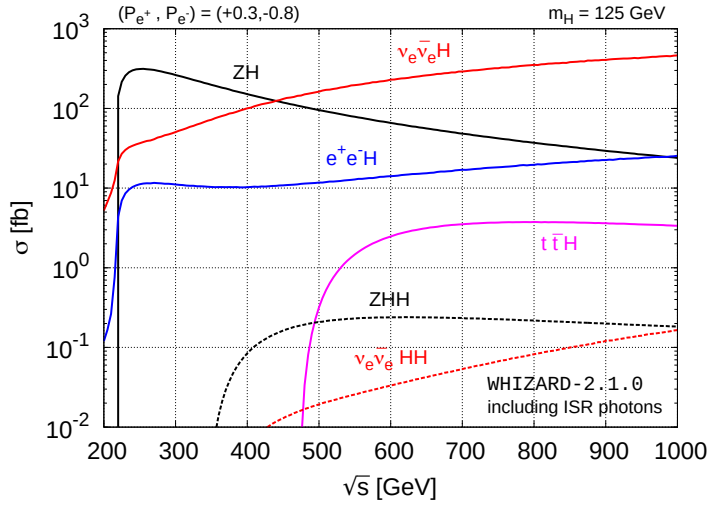

Figure 2.7: Total cross section for various Higgs production processes at an e^+e^- collider with polarized beams as a function of the CM energy $\sqrt{s}$. These results have been evaluated using `Whizard-2.1.0` [97] and include the dominant EW corrections from ISR photons.

produced nearly at rest, due to Coulomb gluon exchange, which can be interpreted as the formation of $t\bar{t}$ bound states. Similar effects arise in differential cross sections in regions where the invariant mass of the $t\bar{t}$ system is $m_{t\bar{t}} \simeq 2m_t$.

The dominant higher-order EW corrections to the total cross sections of these processes come from collinear photonic initial-state ratiation (ISR), which can amount to 10% or more. Further subdominant corrections arise from machine dependent Beamstrahlung effects and genuine EW corrections to the production processes. Note also, that the Higgs production cross sections can be enhanced by a factor of up to two by exploiting the possibility of polarized e^+e^- beams [95].

In addition to the processes discussed above, a future e^+e^- linear collider may feature the possibility of probing the triple Higgs coupling in Higgs-boson pair production [96] if the CM energy is high enough. The relevant processes are Higgs-strahlung and WW-fusion, Fig. 2.6(a) and (b), where the produced Higgs boson splits into a pair of Higgs bosons. However, these processes compete with other Higgs pair production diagrams that are not governed by the triple Higgs coupling and which dominate the overall cross section. Hence, a determination of the triple Higgs coupling is only possible, if at all, with a very high integrated luminosity $\mathcal{L} \gtrsim \mathcal{O}(1\,\text{ab}^{-1})$ and at high energies $\sqrt{s} \gtrsim 500\,\text{GeV}$.

We close the discussion of Higgs boson production processes at e^+e^- colliders by showing in Fig. 2.7 the total cross sections of the relevant production processes for a Higgs boson mass of 125 GeV as a function of the CM energy $\sqrt{s}$. These numbers have been obtained using `Whizard-2.1.0` [97] and include the dominant EW corrections from ISR photons. We further list the cross sections for unpolarized and polarized e^+e^- beams for the CM energies $\sqrt{s} = [250,\ 500,\ 1000]$ GeV in Tab. 2.3. Here, P_{e^-} (P_{e^+}) denotes the longitudinal polarization of the electron (positron) beam, where a value of $+1$ (-1) corresponds to a completely right-handed (left-handed) polarization [95]. The chosen CM energies mark three considered stages of the anticipated future ILC program.

	Total Higgs production cross section (in fb)					
CM energy $\sqrt{s}$	250 GeV		500 GeV		1000 GeV	
Beam polarization (P_{e^+}, P_{e^-})	unpol.	$(+0.3, -0.8)$	unpol.	$(+0.3, -0.8)$	unpol.	$(+0.3, -0.8)$
$e^+e^- \to ZH$	211.5	312.1	64.5	95.2	16.2	23.9
$e^+e^- \to \nu_e\bar{\nu}_e H$	20.6	36.5	70.7	162.2	198.0	462.4
$e^+e^- \to e^+e^- H$	7.67	11.17	8.93	11.73	20.12	25.46
$e^+e^- \to t\bar{t}H$	-	-	0.184	0.318	2.000	3.364
$e^+e^- \to ZHH$	-	-	0.141	0.209	0.123	0.182
$e^+e^- \to \nu_e\bar{\nu}_e HH$	-	-	0.012	0.019	0.073	0.165

Table 2.3: Higgs production cross sections at a future e^+e^- linear collider with and without polarized beams at CM energies of $\sqrt{s} = [250,\ 500,\ 1000]$ GeV for a Higgs mass of 125 GeV. These results have been evaluated using `Whizard-2.1.0` [97] and include the dominant EW corrections from ISR photons.

2.2.3 Higgs boson production at hadron colliders

We now turn to the discussion of Higgs boson production processes at hadron colliders. Past and present hadron colliders are the proton-antiproton ($p\bar{p}$) collider Tevatron at Fermilab, which had been operating at CM energies up to $\sqrt{s} = 1.96$ TeV until September 2011, and the proton-proton (pp) collider LHC at CERN. The LHC has been running at CM energies of $\sqrt{s} = 7$ and 8 TeV, collecting data up to an integrated luminosity of $\mathcal{L} \sim 25\,\text{fb}^{-1}$ per experiment, and is currently preparing the next run at a higher CM energy of 13 TeV.

In hadronic collisions only a fraction of the the total CM energy $\sqrt{s}$ is available to the hard scattering process of the hadron's constituents (gluons, quarks, antiquarks), commonly called *partons*. Hence, only the range of the energy of the hard process $\sqrt{\hat{s}}$ is fixed by the machine. The flux of parton a_i with a momentum fraction x_i of the hadron h_i's momentum P_i, when probed at a certain energy μ_F (the *factorization scale*), is described by the *parton distribution function* (PDF) $f_{a_i/h_i}(x, \mu_F)$ [98–100]. These functions are determined from experiment, mostly from high-precision data from deep-inelastic scattering processes at the HERA collider at DESY (Hamburg). The hadronic cross sections are then calculated in the factorized form (see e.g. Ref. [101] for an introduction)

$$\sigma_{h_1h_2\to f+X} = \sum_{a,b} \int_0^1 dx_1 \int_0^1 dx_2 f_{a/h_1}(x_1, \mu_F) f_{b/h_2}(x_2, \mu_F) \int d\hat{\sigma}_{ab\to f}(x_1P_1, x_2P_2, \mu_F), \quad (2.43)$$

where the partonic cross section $d\hat{\sigma}_{ab\to f}$ contains the full information on the hard scattering process of the partons into the final state f and can be calculated within perturbation theory. Additional contributions to the final state from beam remnants, underlying event, showering, etc. are denoted by X. The factorization scale μ_F defines the scale at which the matching between the perturbative calculation of the matrix elements and the non-perturbative part (described by the PDFs) is performed.

Higher-order QCD corrections to the total cross section are generally important at hadron colliders due to the strongly interacting particles in the initial state. For the Higgs boson production processes these have been calculated up to NNLO, see Ref. [30, 70, 71] and references therein. A residual dependence on the *renormalization scale* μ_R, at which the input parameters

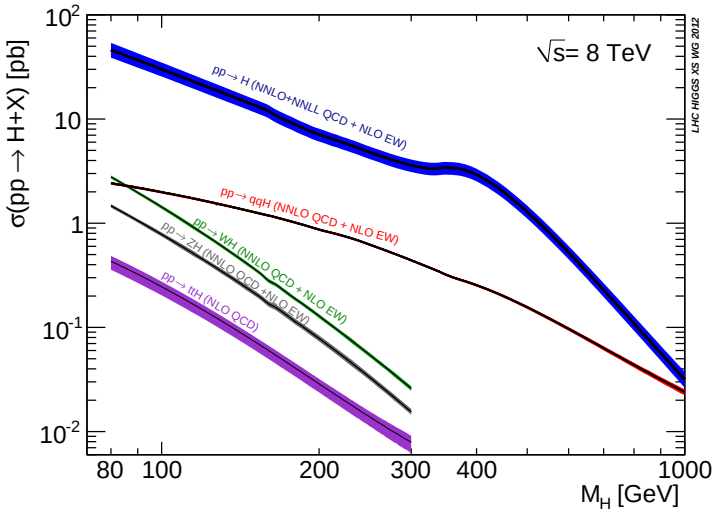

Figure 2.8: Inclusive cross sections for Higgs boson production in the SM at the LHC with a CM energy of $\sqrt{s} = 8\,\text{TeV}$ as a function of the Higgs boson mass. The band indicates the total theoretical uncertainty. Taken from Ref. [30].

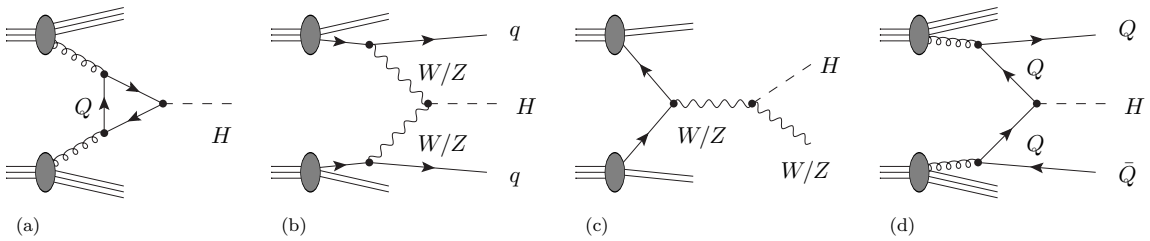

Figure 2.9: Representative leading-order diagrams for the four main SM Higgs boson production mechanisms at hadron colliders: (a) gluon-gluon fusion, (b) vector boson fusion, (c) associate Higgs production with a vector boson (*Higgs-strahlung*) and (d) with a heavy-quark pair. Light and heavy quarks are denoted by q and Q, respectively.

(strong coupling constant, quark masses, etc.) are defined, arises from missing higher order calculations.

In fact, both the factorization and renormalization scale dependence are not physical, but merely a consequence of the limited order of the perturbative expansion to which the calculation is performed. Theoretical uncertainties are usually estimated by varying these scales by factors of 1/2 and 2 from their central values, which are appropriately chosen at a natural scale of the process, where large logarithmic corrections are expected to be absorbed.

We show the currently most precise predictions of the total hadronic cross sections for LHC collisions at $\sqrt{s} = 8\,\text{TeV}$ in Fig. 2.8 (taken from Ref. [30]). Representative leading-order diagrams for the main SM Higgs boson production mechanisms are shown in Fig. 2.9. In the following we will briefly discuss the most relevant features of these production channels. For a more complete listing of higher-order corrections see Ref. [33, 70, 71].

- ***pp*/*pp̄* → *H* + *X* (single Higgs production)**

  In hadron collisions the Higgs boson can be produced resonantly via the gluon-gluon fusion (ggF) production mechanism depicted in Fig. 2.9(a), which is mediated by triangular loops

of heavy quarks. In the SM, owing to the proportionality of the Yukawa couplings to the fermion mass, the top quark loop gives by far the largest contribution. Subdominant contributions $\sim \mathcal{O}(4\%)$ come from the bottom quark loop. The process receives very large NLO [102] and NNLO [103] corrections, increasing the cross section by $\sim 80-100\%$ and another $\sim 25\%$, respectively, indicating a slow convergence of the perturbative expansion. The gluon-gluon fusion process delivers the largest total cross section at the Tevatron and the LHC due to the large gluon flux in high energy $pp/p\bar{p}$ collisions.

Single Higgs production is dominated by Higgs bosons at low transverse momenta p_T, corresponding to the recoil against some hadronic activity. Experimental analyses often categorize events by the number of jets in order to suppress the background and to characterize the signal. Here one should bear in mind that requiring an additional jet (e.g. from real gluon emission) costs one order in the perturbative expansion and hence increases the theoretical uncertainty from scale variation.

- **$pp/p\bar{p} \to H + 2\,\text{jets} + X$ (vector boson fusion)**

  The vector boson fusion (VBF) process, depicted in Fig. 2.9(b), features two accompanying jets, which go preferentially into the forward-backward directions due to the t-channel topology. Special VBF selection cuts on these jets plus a central-jet veto can thus be exploited to suppress the background and identify the signal [104] (see also Section 2.2.4).

  Similarly as for vector boson fusion at e^+e^- colliders, the cross section grows logarithmically with the (partonic) CM energy, $\hat{\sigma} \propto \ln \hat{s}/M_V^2$. Hence, while the VBF channel was of rather minor importance at the Tevatron, it yields the second largest Higgs production cross section at the LHC. The relative contribution to the LO cross section from the WW and ZZ fusion diagrams is roughly $2:1$.QCD [87, 105] and EW [106] NLO corrections are each at the level of $\sim 5-10\%$.

- **$pp/p\bar{p} \to WH/ZH + X$ (associated Higgs production with a vector boson)**

  The Higgs-strahlung processes $pp/p\bar{p} \to WH/ZH + X$ are important production mechanisms for Higgs masses close to the LEP limit, $m_H \gtrsim 114\,\text{GeV}$, and have been the main search channel at the Tevatron. The vector boson in the final state, if decaying leptonically, gives an additional handle to search for difficult Higgs decays like $H \to b\bar{b}$ (using e.g. jet substructure techniques [107]).

  Higher-order QCD corrections have been calculated up to NNLO [108, 109], where Higgs-strahlung is very similar to the Drell-Yan process [110] and thus governed by the corresponding Higgs-vector boson coupling. The NLO and NNLO QCD corrections increase the inclusive cross section in total by up to $30-40\%$. Furthermore, at NNLO the gluon initiated process $gg \to ZH$ contributes at the level of $\sim 8\%$ for an LHC energy of $\sqrt{s} = 8\,\text{TeV}$. Note, that this process also features a slight dependence on the top Yukawa coupling [109]. The NLO EW corrections decrease the total cross section by up to $5-10\%$ [111].

- **$pp/p\bar{p} \to Q\bar{Q}H + X$ (associated Higgs production with heavy quarks)**

  The production processes $pp/p\bar{p} \to Q\bar{Q}H + X$, with the final state quarks Q being either top or bottom quarks, have a rather low total cross section, cf. Fig. 2.8. A representative diagram is depicted in Fig. 2.9(d). Note, that also $q\bar{q}$ initiated diagrams contribute, which dominate the cross section for Tevatron energies, but play a rather minor role at the LHC.

	Total Higgs production cross section (in pb)				
Hadron collider CM energy	Tevatron 1.96 TeV	LHC 7 TeV	LHC 8 TeV	LHC 14 TeV	Theoretical uncertainties[†]
$pp/p\bar{p} \to H$	0.9493	15.13	19.27	50.35	$7.5\% \oplus 7.2\%$
$pp/p\bar{p} \to qqH$	0.0653	1.222	1.578	4.172	$0.2\% \oplus 2.7\%$
$pp/p\bar{p} \to WH$	0.1295	0.5785	0.7046	1.504	$1.0\% \oplus 2.3\%$
$pp/p\bar{p} \to ZH$	0.0785	0.3351	0.4153	0.8830	$3.1\% \oplus 2.5\%$
$pp/p\bar{p} \to t\bar{t}H$	0.0043	0.08632	0.1293	0.6113	$6.6\% \oplus 8.1\%$
$pp/p\bar{p} \to b\bar{b}H$	N/A	0.1613	0.2106	0.5805	$18.0\% \oplus 6.4\%$

[†] The theoretical uncertainties (THUs) refer to the LHC at $\sqrt{s} = 8$ TeV prediction. The first (second) number corresponds to the symmetrized THU derived under QCD scale (PDF+α_s) variation [70].

Table 2.4: Total cross sections for the main Higgs production processes at the Tevatron and LHC for various CM energies $\sqrt{s}$ and a Higgs mass of $m_H = 125$ GeV. Taken from Refs. [30, 70, 114].

The top quark associated Higgs production is phase space suppressed due to the large top quark mass and drops rapidly with increasing Higgs mass. Due to the low production rate and the typically large $t\bar{t} + X$ background, this production mode is experimentally challenging. Hence, $t\bar{t}H$ production has not been expected to play any role for the Higgs boson discovery. However, at a later stage this process provides an important means to probe the top Yukawa coupling without relying on the gluon fusion process, see Chapter 5. NLO QCD corrections to the total cross section are at the level of $10 - 20\%$ [112].

The cross section of the bottom quark associated Higgs production process ($b\bar{b}H$) is slightly larger than for $t\bar{t}H$ production, however, its experimental signature is overwhelmed by QCD background. Nevertheless, the process is relevant in beyond the SM Higgs searches (e.g. in supersymmetry), where the bottom Yukawa coupling can be strongly enhanced (see Section 2.4.3), thus increasing the $b\bar{b}H$ cross section by several orders of magnitude. In the NLO calculation the predictions obtained within the four- and five-flavor PDF schemes need to be matched consistently (using the *Santander matching* prescription) [71, 113].

The most accurate cross section predictions of the discussed production processes for a SM Higgs boson mass of 125 GeV at the Tevatron and at the LHC for CM energies of $\sqrt{s} = 7, 8$ and 14 TeV are summarized in Tab. 2.4, taken from Refs. [30, 70, 114]. We also list the relative theoretical uncertainties estimated from varying the renormalization and factorization scales as well as different PDF sets in the numerical evaluation.

2.2.4 SM Higgs boson searches

After the separate discussion of Higgs production and decay processes, we now turn to the experimental signatures and search strategies for the most important processes. The experimental challenge in searches for the SM Higgs boson is to achieve an improvement of the *a priori* very small signal-to-background ratio by designing a dedicated data analysis. The selection strategies have been evolving over the years, starting from simple cut-based analyses and going to very sophisticated analyses using multivariate techniques such as likelihood ratios,

artificial neural networks or boosted decision trees. In this section we briefly describe the main Higgs boson search channels at the LEP, Tevatron and LHC experiments and outline the basic strategy for the signal selection. For detailed descriptions of the selection strategies and the background processes we refer to the original literature by the experiments, see also Ref. [33] for a review.

Higgs searches at LEP

As already noted in Section 2.2.2, the main Higgs boson production channel at the LEP experiments with CM energies up to 209 GeV is the Higgs-strahlung process $e^+e^- \to ZH$. The experimental searches encompassed the four-jet final state $(Z \to q\bar{q})(H \to b\bar{b})$, the missing energy final state $(Z \to \nu\bar{\nu})(H \to b\bar{b})$, the leptonic final state $(Z \to \ell^+\ell^-)(H \to b\bar{b})$ (with $\ell = e, \mu$) and the tau-lepton final states $(Z \to \tau^+\tau^-)(H \to b\bar{b})$ and $(Z \to q\bar{q})(H \to \tau^+\tau^-)$. These final states cover about 80% of the total rate for a Higgs mass of 115 GeV.

Two b-tagged jets were required to suppress the background in the $H \to b\bar{b}$ event selection. Further sensitivity was gained by a precise reconstruction of the di-jet invariant mass of the jets assigned to the Higgs decay as well as of the jets or leptons assigned to the Z boson. In particular, in signal events with the leptonic Z boson decay, $Z \to \ell^+\ell^-$, the mass of the Higgs boson candidate was reconstructed from the recoil to the di-lepton system. In this way, even potential *invisible* Higgs decays (as predicted in some beyond the SM theories), where the Higgs decay products escape detection, could be constrained [115]. Signal channels with $Z \to \nu\bar{\nu}$ are characterized by large missing energy and momentum. The reconstructed missing mass is then required to be approximately the Z boson mass M_Z. In the tau-lepton channels, two tau-lepton candidates are required and the invariant mass of the di-tau-lepton system is required to reconstruct either the Z boson or Higgs boson mass.

The final SM Higgs search combination of all four LEP experiments ALEPH, DELPHI, L3 and OPAL excluded the SM Higgs boson in the full mass range up to 114.4 GeV at 95% C.L. [90].

Higgs searches at the Tevatron and LHC

The Tevatron experiments CDF and DØ mainly investigated the Higgs boson mass range 100 – 200 GeV (see e.g. Ref. [116] for an overview). The most sensitive channel at low masses, $m_H \lesssim 130$ GeV, is $H \to b\bar{b}$ produced in association with a W or Z boson, which decays leptonically via $W \to \ell\nu$, $Z \to \ell^+\ell^-$ or $Z \to \nu\bar{\nu}$ (with $\ell = e, \mu$). At higher masses, $M_H \gtrsim 130$ GeV, the search for $H \to W^+W^- \to \ell^+\nu\ell^-\bar{\nu}$, with the Higgs boson being produced in gluon fusion, becomes the most sensitive channel. Other Higgs decay modes such as $H \to \gamma\gamma$, $H \to ZZ \to \ell^+\ell^-\ell^+\ell^-$ and $H \to \tau\tau$ as well as Higgs production in vector boson fusion and $t\bar{t}H$ production were also searched for, however, with a much lower sensitivity.

The LHC was designed to explore the full Higgs mass range up to $\lesssim 1$ TeV. The harsh conditions of proton-proton collisions at high CM energies of $\sqrt{s} = 7$ and 8 TeV at a very large instantaneous luminosity of up to 6.8×10^{33} cm^{-2} s^{-1} impose great challenges on the event reconstruction. Higgs searches at the LHC therefore consider only final states that contain at least one photon, electron, muon or reconstructed tau-lepton. We show the LHC production rates of the relevant topologies for a CM energy of $\sqrt{s} = 8$ TeV in Fig. 2.10, taken from Ref. [70]. Due to the high cross section of the gluon fusion process channels with low branching ratios such as $H \to \gamma\gamma$ and $H \to ZZ \to \ell^+\ell^-\ell^+\ell^-$ are also accessible at the LHC. In fact, these two channels provide the highest sensitivity over a large mass range and played a crucial role in the Higgs boson discovery, see Section 3.2.

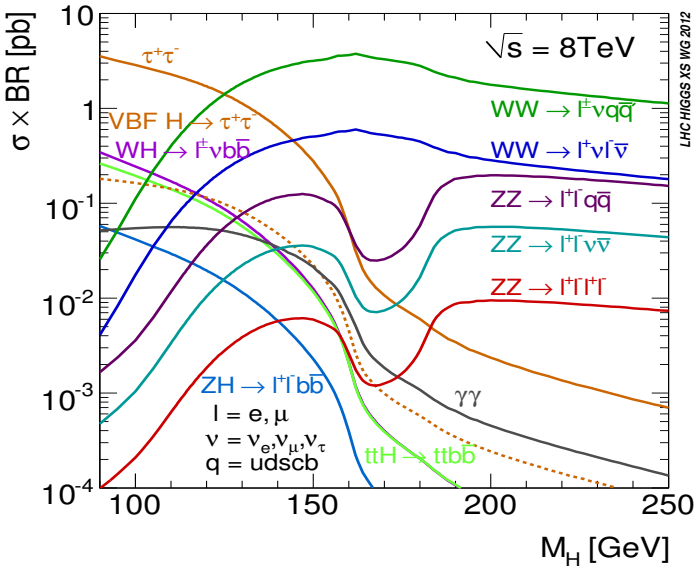

Figure 2.10: SM Higgs boson production rates (i.e. cross section times branching ratio) at a CM energy of 8 TeV. For $H \to \tau\tau$ both the inclusive (solid line) and VBF (dashed line) mode are plotted. Taken from Ref. [70].

In the following we briefly describe the basic strategies for the signal selection of the main search channels at the Tevatron and LHC experiments:

- ***pp/pp̄ → H → γγ***

  In the low mass region, $m_H \lesssim 150\,\text{GeV}$, the $pp \to H \to \gamma\gamma$ channel is one of the most sensitive channels at the LHC. The analysis selects events with two isolated photons with large transverse momenta. The signal reveals itself as a peak on top of a continuum background in the di-photon invariant mass spectrum. The overall sensitivity of the analysis as well as the sensitivity to different production modes is enhanced by dividing the signal sample into various categories, characterized by the number of jets, pseudorapidity of the photons and other technical details of the photon reconstruction. In particular, sensitivity to VBF production is gained by requiring two jets with large separation in pseudorapidity and large di-jet invariant mass. The Higgs boson mass can be determined quite accurately from the di-photon peak with a precision of $\lesssim 1 - 2\%$.

- ***pp/pp̄ → H → ZZ⁽*⁾***

  At the LHC, the $pp \to H \to ZZ \to \ell^+\ell^-\ell^+\ell^-$ channel, albeit its rather small production rate, cf. Fig. 2.10, features the very clean signature of a resonance in the four-lepton invariant mass spectrum over a small continuum background, and is therefore known as the "golden-plated" LHC search channel for Higgs masses up to $\lesssim 150\,\text{GeV}$ and in particular beyond 200 GeV. In the mass range around 180 GeV the sensitivity is decreased due to the $pp \to ZZ$ background. At large Higgs masses, $m_H \gtrsim 200\,\text{GeV}$, the channels $pp \to H \to ZZ \to \ell^+\ell^-\nu\bar{\nu}$ and $pp \to H \to ZZ \to \ell^+\ell^- q\bar{q}$ also become important. Using the four-lepton channel, the mass of the discovered Higgs boson can be determined from the four-lepton invariant mass to better than $1 - 2\%$.

- $\boldsymbol{pp/p\bar{p} \to H \to WW^{(*)}}$

  In the intermediate and high mass region, $m_H \gtrsim 150\,\text{GeV}$, the full leptonic channel $pp/p\bar{p} \to H \to W^+W^- \to \ell^+\nu\ell^-\bar{\nu}$ contributes significantly to the overall sensitivity both at Tevatron and the LHC. In particular, in the intermediate mass region $150\,\text{GeV} \lesssim m_H \lesssim 180\,\text{GeV}$, this topology features a much greater sensitivity than the $pp \to H \to ZZ \to \ell^+\ell^-\ell^+\ell^-$ channel at the LHC [83]. The signature is characterized by two oppositely charged leptons and large missing energy. Discriminating observables are the di-lepton invariant mass, the transverse mass and the azimuthal opening angle between the two leptons, as the signal prefers small values of the opening angle due to spin correlations [83]. The signal can be further categorized into different jet multiplicities to specifically target the Higgs production in vector boson fusion.

  Besides the full leptonic channel, ATLAS and CMS also analyzed the semi leptonic channel $pp/p\bar{p} \to H \to W^+W^- \to \ell\nu q\bar{q}$. This channel is less sensitive, however, it provides a better way to reconstruct the mass of the Higgs candidate via the invariant mass of the $\ell\nu q\bar{q}$ system.

- $\boldsymbol{pp/p\bar{p} \to H \to \tau\tau}$

  In the $H \to \tau^+\tau^-$ analyses the invariant mass of the reconstructed tau-lepton pair is searched for a broad excess [117]. The mass resolution is rather poor with a precision of $\sim 10 - 30\%$. Both leptonically and hadronically decaying tau-leptons are reconstructed, and the signal is divided into exclusive subcategories, depending on the final state, in order to optimize the sensitivity to the VBF, WH, ZH and $t\bar{t}H$ production modes. The VBF category typically features the greatest sensitivity.

- $\boldsymbol{pp/p\bar{p} \to VH \to V(b\bar{b})}$ **(with $\boldsymbol{V = W, Z}$)**

  Analyses of the $H \to b\bar{b}$ channel typically rely on a W or Z boson that is produced in association with the Higgs boson and decays leptonically as $W \to \ell\nu$, $Z \to \ell^+\ell^-$ or $Z \to \nu\bar{\nu}$ (with $\ell = e, \mu$). The charged lepton(s) and/or missing energy from the neutrinos from the gauge boson decay gives important handles to trigger the events, thus enabling the search for the dominant but experimentally challenging Higgs decay mode $H \to b\bar{b}$.

  The mass of the Higgs boson candidate can be reconstructed from the invariant mass of the two b-tagged jets with a resolution of around $10 - 15\%$. The invariant mass and transverse momentum of the b-tagged jet system are important observables to discriminate the signal process from the background processes such as VZ production with $Z \to b\bar{b}$.

2.3 Open paths to physics beyond the Standard Model

With the discovery of the Higgs boson in 2012 the complete particle content of the SM is experimentally confirmed. Nevertheless, and despite its remarkable success in describing most of the phenomena up to thus far probed energy scales, the SM is widely regarded not to be the complete theory of the fundamental forces. In this section we discuss theoretical and experimental arguments for this opinion and mention possible solutions to these issues. In the second part of this section we outline possible ways to experimentally probe effects of physics beyond the SM. Moreover, we will comment on some interesting (but sometimes rather speculative) discrepancies between measurement and the SM expectation, that currently exist in the experimental data.

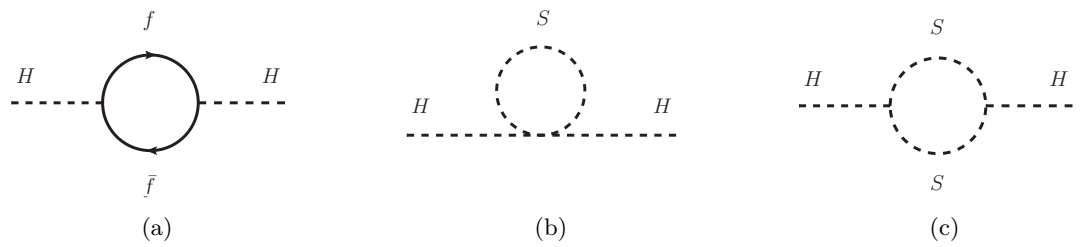

Figure 2.11: One-loop self energy diagrams for a scalar particle H. In the SM, these diagrams lead to a quadratically divergent Higgs mass correction, which lead to the *hierarchy problem*.

- **Gauge coupling unification, Grand Unification, and a theory of everything?**

  A unified description of all fundamental interactions of nature — electromagnetism, weak and strong interactions as well as gravity — is an outstanding goal of theoretical high energy physics. At a very high energy scale, $M_p \simeq 10^{19}$ GeV, the strength of the gravitational force becomes comparable to the gauge forces and hence a quantum description of gravity becomes necessary. However, a successful formulation of such a *Theory of Everything* (TOE) — mostly based on ideas of string theory — has not yet been accomplished.

  On the contrary, the three fundamental gauge forces can successfully be unified at a typical scale $M_{\text{GUT}} \simeq 2 \cdot 10^{16}$ GeV in so-called *Grand Unified Theories* (GUTs) [118]. Here, the SM gauge group is embedded in a larger gauge group, e.g. SU(5) or SO(10). Moreover, these theories predict the unification of the running gauge couplings at the scale of Grand Unification, M_{GUT}.

  From LEP measurements of the gauge couplings at the Z pole, the running up to M_{GUT} can be extrapolated [119, 120]. This running depends sensitively on the particle content of the theory and any new interacting particles between the electroweak and the GUT scale can alter it. It has been shown that the gauge couplings do *not* unify within the SM, whereas they can unify for the extended particle content introduced by the minimal supersymmetric extension of the SM (MSSM) [119].

- **The Hierarchy Problem**

  The most striking argument for expecting new physics effects at scales $\sim \mathcal{O}(\text{TeV})$ is the naturalness or *hierarchy problem* [11]. Consider the one-loop corrections from fermion loops to the SM Higgs mass, shown in Fig. 2.11(a), which is expressed by the self-energy

$$\begin{aligned} i\Pi_H(p^2) &= -\frac{y_f^2}{2} \int \frac{d^4k}{(2\pi)^4} \frac{\text{Tr}[(\not{k} + m_f)(\not{k} - \not{p} + m_f)]}{(k^2 - m_f^2)((k-p)^2 - m_f^2)} \\ &= -2y_f^2 \int \frac{d^4k}{(2\pi)^4} \left[\frac{1}{k^2 - m_f^2} + \frac{2m_f^2}{(k^2 - m_f^2)^2} \right]. \end{aligned} \tag{2.44}$$

  with external momentum p of the Higgs boson and internal momentum k and mass m_f of the fermion in the loop. The first term in Eq. (2.44) is quadratically divergent. Regulating this divergence by introducing the scale of new physics Λ as an ultraviolet momentum

cut-off yields a mass correction of

$$\delta m_{H,f}^2 = \frac{y_f^2}{8\pi^2}\left[-\Lambda^2 + 6m_f^2 \ln\left(\frac{\Lambda}{m_f}\right) + \text{finite terms}\right]. \tag{2.45}$$

Suppose the SM is valid up to typical energy scales of GUTs, $\Lambda \sim M_{\text{GUT}} \simeq 2 \cdot 10^{16}$ GeV, or string theories, $\Lambda \sim M_{\text{P}} \simeq 10^{19}$ GeV, the mass correction would be ~ 30 orders of magnitude larger than the Higgs mass itself, $m_H \sim 125\,\text{GeV}$. Of course, the quadratic divergences could be renormalized away, however, one would need an unnatural amount of fine-tuning between the bare Higgs mass squared $m_{H,0}^2$ and the total mass correction δm_H^2 in order to keep the renormalized squared mass $m_h^2 = m_{H,0}^2 + \delta m_H^2$ at the electroweak scale. Note that, while this problem is demonstrated here only for the fermion contributions, the same problem appears for the gauge boson and (self-coupled) Higgs loop contributions [21].

A solution to this problem is provided if Λ is not too large but rather $\sim \mathcal{O}(\text{TeV})$. New physics then needs to explain why the loop integral cuts off at Λ. Nevertheless, the Higgs mass remains very sensitive to any new particles entering at higher energies, which couple directly or indirectly to the Higgs field.

One of the most elegant solutions[16] to the hierarchy problem is provided by *supersymmetry*[17]. Consider an additional scalar field S that couples to the Higgs field via the Lagrangian terms

$$\mathcal{L} \supset -\sqrt{2}\, y_S^{(1)} H|S|^2 - \frac{1}{2}\, y_S^{(2)} |H|^2 |S|^2. \tag{2.46}$$

Their one-loop corrections to the Higgs mass, as shown in Fig. 2.11(b) and (c), read

$$\delta m_{H,S}^2 = \frac{1}{16\pi^2}\left[y_S^{(2)}\Lambda^2 - \left(4(y_S^{(1)})^2 + 2y_S^{(2)}\right) m_S^2 \ln\left(\frac{\Lambda}{m_S}\right) + \text{finite terms}\right]. \tag{2.47}$$

Note, that the scalar loop contribution, Eq. (2.47), has the opposite sign than the fermionic loop contribution, Eq. (2.45), due to the different spin-statistics of bosons and fermions. In supersymmetry two complex scalar fields are introduced for each Dirac fermion. If furthermore the coupling strength equality $y_S^{(2)} = y_f^2$ holds, then the quadratic divergences in Eqs. (2.45) and (2.47) cancel. This relation is indeed prescribed by supersymmetry. Moreover, if supersymmetry is *unbroken*, in which case even the masses are equal, $m_S = m_f$, also the logarithmic divergences cancel.

- **Dark Matter and Dark Energy**

  Various astrophysical observations, such as the measurement of rotation curves of spiral galaxies, stellar motion in the vicinity of and gravitational lensing effects by galaxy clusters, etc., provide evidence for the existence of a significant amount of clustering, non-baryonic and non-luminous matter, so-called *Dark Matter* (DM), in our Universe (see e.g. Ref. [123] for an introduction). If DM is composed of elementary particles, the SM does not deliver a suitable candidate[18]. Moreover, observations of Type Ia super-

[16] Alternative approaches to solve the hierarchy problem can be found in the literature, postulating for instance the existence of large extra dimensions [121] or another strong force at the TeV scale [122].
[17] The supersymmetric extension of the SM will be described in more detail in Section 2.4.
[18] The only candidates within the SM fulfilling the required weak interaction properties are neutrinos. However,

novae suggest that the expansion of the universe is accelerating [124], which led to the postulation of *Dark Energy*, a new form of energy with negative pressure. Dark energy may be interpreted as the vacuum energy, however, the required value is ~ 120 orders of magnitude smaller than what is predicted by the SM.

Measurements of the anisotropies in the temperature spectrum of the *Cosmic Microwave Background* (CMB) by the WMAP [125] and Planck satellites [47] can be used to infer the energy content of the Universe, yielding 25.8% of Dark Matter, 69.2% of Dark Energy and only 4.9% of known baryonic matter, assuming the *Standard Model of Cosmology* (Λ_{CDM}). The dark matter relic abundance can be predicted in models with a suitable DM candidate. Its observed value [47],

$$\Omega_{\mathrm{DM}} h^2 = 0.1187 \pm 0.0017, \tag{2.48}$$

where Ω_{DM} is the DM mass density normalized to the critical density[19] and $h \approx 0.7$ [126] is the Hubble constant in units of 100 km/(s·Mpc), thus provides a non-trivial constraint for new physics models. And indeed, many extensions of the SM contain good DM candidates, e.g. axions [127, 128], the lightest neutralino [129, 130], gravitino [131] or axino [132] in supersymmetric models, hidden sector particles [133], Higgs singlets [134] and inert doublets [135, 136], lightest Kaluza-Klein states [137], etc. (see Refs. [12] for reviews).

- **The baryon asymmetry in the Universe**

  The puzzle of why we see more matter than antimatter in the visible Universe is still unresolved [14]. Given symmetrical initial conditions in the early Universe, the three Sakharov conditions [138] of baryon number violation, $\mathcal{C}$ and $\mathcal{CP}$ violation and interactions outside of thermal equilibrium have to be fulfilled to generate a baryon asymmetry. The observed baryon asymmetry,

  $$\eta \equiv \frac{n_B - n_{\bar{B}}}{n_\gamma} \sim 10^{-10}, \tag{2.49}$$

  where n_B, $n_{\bar{B}}$ and n_γ are the number densities of baryons, antibaryons and photons, respectively, is much larger than the asymmetry obtained from electroweak baryogenesis [139] in the SM. New sources of $\mathcal{CP}$ violation from physics beyond the SM and/or other mechanisms of baryogenesis [140, 141] are required to generate the observed baryon asymmetry dynamically.

- **Neutrino oscillations**

  Various experiments have observed flavor oscillations of solar, atmospheric, reactor and fixed target neutrinos [46]. The oscillations depend on the mass differences among the neutrino species, indicating that at least two neutrinos are massive (see Refs. [13] for reviews). Fits to current cosmological observations from the Planck satellite constrain the sum of the neutrino masses to be tiny, $\sum_i m_{\nu_i} \leq 0.23\,\mathrm{eV}$ (at 95% C.L.) [47].

due to their very light masses $\leq \mathcal{O}(\mathrm{eV})$, they are highly-relativistic ("hot") and therefore cannot easily explain the galaxy structure formation.

[19] The critical density $\rho_c = 3H^2/8\pi G$, with the Hubble parameter H and Newton's gravitational constant G, corresponds to the energy density of a Universe with spatially flat (Euclidean) geometry, which is favored by current observations [47].

Given the SM particle content as introduced in Section 2.1.1 and the requirement of having only renormalizable and gauge invariant terms in the Lagrangian, the neutrino masses cannot be explained. As we have seen in Section 2.1.2, the generation of fermion masses via the Higgs mechanism requires both left- and right-handed fermions. But even if we simply add right-handed neutrinos to the particle content of the SM, the smallness of the required Yukawa couplings seems unnatural. A very popular explanation for the neutrino masses is the *See-Saw Mechanism* [142], where right-handed neutrinos with a Majorana mass $M_M \sim 10^{12-16}$ GeV are introduced. A small mixing between the left- and right-handed neutrinos then yields neutrino masses of $\lesssim \mathcal{O}(\text{eV})$ with natural Yukawa couplings of $\sim \mathcal{O}(0.1-1)$.

Besides the standard See-Saw mechanism with a very high new physics mass scale M_M, there have been many attempts to connect the generation of neutrino masses also with new physics at the TeV-scale, e.g. by allowing lepton number violating operators in supersymmetric models [143].

These arguments, in particular the hierarchy problem, strongly motivate the search for BSM physics at the TeV-scale (and beyond). Effects of new physics can be probed in two complementary ways: Firstly, in *indirect* searches, i.e. in precise measurements of low-energy observables (LEOs) such as rare B-meson decays, the anomalous magnetic moment of the muon and the W boson mass, where new contributions from BSM physics can significantly alter the predictions of the SM. After the Higgs boson discovery, measurements of the Higgs boson couplings also provide indirect probes of new physics. And secondly, in *direct* searches, where BSM particles are directly produced in collider experiments.

- **Flavor observables**

  New physics effects can be probed indirectly with *flavor observables*, in particular neutral meson mixing processes and rare B meson decays, which occur in the SM only at the loop level. Although the detection of such processes is experimentally challenging, the sensitivity to BSM effects should not be underestimated, since these may give sizable contributions at the same loop-order or even at tree-level. Precise measurements of these processes thus place strong constraints on BSM physics (see e.g. Refs. [144, 145]).

  Important rare B-meson decays are e.g. the FCNC decay[20] $B \to X_s\gamma$, which is (predominantly) mediated by a W boson-top quark loop in the SM, as well as the decays $B_s \to \mu^+\mu^-$ and $B_u \to \tau\nu$. The current measurements and SM predictions of their branching fractions are given in Tab. 2.5. Thus far, no significant discrepancy between measurement and SM prediction has been observed in these processes.

- **The anomalous magnetic moment of the muon**

  Precision studies of the anomalous magnetic moment of the muon, $a_\mu \equiv (g_\mu - 2)/2$, provide an important test of the SM [146]. Large quantum corrections to the magnetic dipole moment of the muon from BSM physics can easily occur, e.g. from light scalar leptons and electroweak gauginos in supersymmetry. Experimentally, the magnetic moment can be measured from the spin precession of muons in a low energy storage ring [147]. There

[20] X_s represents any hadronic system containing a strange quark.

Observable	Experimental value		SM prediction
$\mathrm{BR}(B \to X_s\gamma)$	$(3.43 \pm 0.21 \pm 0.07) \times 10^{-4}$	[149]	$(3.08 \pm 0.22) \times 10^{-4}$
$\mathrm{BR}(B_s \to \mu^+\mu^-)$	$(2.9 \pm 0.7) \times 10^{-9}$	[150, 151]	$(3.87 \pm 0.50) \times 10^{-9}$
$\mathrm{BR}(B_u \to \tau\nu_\tau)$	$(1.14 \pm 0.22) \times 10^{-4}$	[149]	$(0.80 \pm 0.12) \times 10^{-4}$
δa_μ	$(30.2 \pm 9.0) \times 10^{-10}$	[147, 148]	–
M_W	(80.385 ± 0.015) GeV	[65, 152, 153]	(80.361 ± 0.004) GeV

Table 2.5: The experimental values and SM predictions of low-energy observables (LEO) that provide indirect probes of new physics. The SM predictions for the B physics observables (W boson mass) are calculated with `SuperIso-3.3` [154] (`FeynHiggs-2.9.4` [155–157], see also Ref. [158]) for $m_H = 125.7\,\mathrm{GeV}$ and $m_t = 173.2\,\mathrm{GeV}$. These observables are used in the (updated) global fit of the phenomenological MSSM presented in Chapter 6.

is a persisting discrepancy[21] at the 3.6σ level between the measured value, a_μ^{exp}, and the SM prediction, a_μ^{SM}. The unexplained difference, $\delta a_\mu \equiv a_\mu^{\mathrm{exp}} - a_\mu^{\mathrm{SM}}$, given in Tab. 2.5, may be a sign of new physics.

- **The W boson mass**

  As already mentioned in Section 2.1.4, the measured W boson mass is slightly too large than the best-fit value obtained from a global fit to the electroweak precision observables within the SM [66, 159]. M_W is an important indirect probe of new physics due to its sensitivity to radiative corrections from BSM physics. It has been shown that the currently observed mild discrepancy at the $\sim 1.5\sigma$ level can be ameliorated within the MSSM without violating any of the current bounds from direct LHC searches for Higgs bosons and supersymmetric particles [158, 160]. For the future, a significant improvement of the precision of the W boson and top quark mass measurements (as e.g. obtained at a future ILC [91, 92, 161]) would be highly beneficial to test the SM and hence probe effects of new physics [162]. In Tab. 2.5 we give the latest combined measurement [65, 152, 153] of M_W and its SM prediction, evaluated for a top quark mass $m_t = 173.2\,\mathrm{GeV}$ and a Higgs boson mass of $m_H = 125.7\,\mathrm{GeV}$ using `FeynHiggs-2.9.4` [155–157] (see also Ref. [158]).

- **Higgs boson couplings**

  With the discovery of a Higgs boson at the LHC a new era of precision physics has begun, where the Higgs boson's properties, in particular its coupling strengths, need to be accurately determined at present and future collider experiments. The Higgs boson couplings can be significantly different in BSM physics that affects EWSB, as e.g. in the MSSM, see Section 2.4.3. However, most BSM models also feature a *decoupling limit*, where one of the potentially many neutral Higgs bosons takes on the properties of the SM Higgs boson. Hence, high precision measurements at the sub-percent level might be needed to see effects from BSM physics in the Higgs couplings.

  As outlined in the introduction, the determination of Higgs boson couplings and the study of their implications for supersymmetric extensions of the SM is a central theme of this

[21] There is an ongoing debate about the accuracy of the experimental input for the SM prediction of a_μ, which is based on hadronic τ decays. Here, we use the prediction based only on data from e^+e^- annihilation to hadrons, which is regarded to be theoretically cleaner [148].

thesis. We therefore discuss how the Higgs boson couplings can be determined (with or without further model assumptions) in much more detail in Chapter 5.

- **Direct searches at the LHC**

  Many BSM theories predict the existence of new particles with masses $\sim \mathcal{O}(100\,\text{GeV} - \text{few TeV})$. If such particles exist, they can be produced copiously at the LHC, in particular, if they are strongly interacting. Their decays into lighter SM and BSM particles may leave distinct signatures in the detector, potentially comprised of large lepton and jet multiplicities and a significant amount of missing transverse energy. If this is the case, the signal can be discriminated from the otherwise overwhelming SM background by an appropriately designed data analysis.

  Various searches for these signatures have been performed by the LHC experiments, see Refs. [163, 164] and [165, 166] for an overview of current ATLAS and CMS results, respectively. Thus far, no significant deviation has been found in any of these analyses, which were using data up to the full available integrated luminosity of $\mathcal{L} \sim 25\,\text{fb}^{-1}$ per experiment. These negative search results can be translated into constraints on the parameter space of BSM models or effective descriptions of new physics effects (see e.g. Refs. [167] for LHC constraints on effective DM models).

  In the MSSM with conserved R-parity (see Section 2.4), the strongly interacting supersymmetric particles (the *squarks* and *gluinos*) are by now mostly[22] constrained to be heavier than $\gtrsim 1\,\text{TeV}$ (see e.g. Ref. [31] for a review). The exact lower limits on the supersymmetric particle masses are strongly model-dependent. For instance, models with compressed mass spectra typically yield weaker limits due to kinematically softer final state particles and thus decreased signal acceptances of the analyses [168, 169]. Another possibility is that R-parity is not conserved, cf. Section 2.4.1 leading to rather different collider signatures. As early LHC searches mainly focussed on the R-parity conserving case, we study the implications of early LHC results for supersymmetric models with R-parity violating interactions in Chapter 7.

- **Direct and indirect detection of dark matter**

  Besides direct searches for the production of DM candidates in high-energy collisions at the LHC, there are two other important ways to search for DM [12]: Firstly, *direct detection* experiments search for a recoil signature of relic DM particles traversing an underground-based detector with a large volume of absorber material such as germanium or liquid xenon. Various experiments with different detection techniques and absorber materials are currently running. While some of these experiments, DAMA/LIBRA [170], CoGeNT [171] and CRESST [172], have reported the observation of a signal, other experiments, primarily XENON100 [173] and LUX [174], have nominally excluded the parameter regions favored by these signals [175]. Moreover, the signals themselves do not agree among each other [176]. Hence, the current picture is inconclusive, see Ref. [177] for recent reviews. Secondly, *indirect detection* of dark matter is a technique of searching for the radiation produced in dark matter annihilation processes, taking place in dense regions of the galactic halo, e.g. the galactic center, or in the Sun or the Earth. For the current status of indirect DM detection see e.g. Ref. [178].

[22] Note that constraints on the third generation supersymmetric quark masses are much weaker.

If a consistent picture of DM signals emerges, the observed dark matter mass and direct detection scattering cross section will put severe constraints on the BSM parameter space. Moreover, the existence of the suspected DM candidate(s) needs to be confirmed by complementary searches at collider experiments.

It should be kept in mind that with the large number of available experimental tests of the SM from the various areas, more or less significant deviations between observation and the SM expectation are naturally expected for a few of these observables already for purely statistical reasons, i.e. even if the expectation is based on the correct theory. And indeed, currently observed deviations are found for instance in some B-flavor observables: The branching ratio of the decay $B \to D^{(*)}\tau\nu$ measured by BaBar [179] currently disagrees with the SM expectation at the 3.4σ level[23], and another discrepancy is observed in a kinematical distribution of the decay $B^0 \to K^{*0}\mu^+\mu^-$ by the LHCb experiment [181], which amounts to a local discrepancy of 3.7σ.

Another (less significant and rather speculative) discrepancy is found at both ATLAS [182] and CMS [183] in the measurement of the WW production cross section, which appears to be slightly larger than expected in the SM. Possible explanations can e.g. be found within the MSSM [184, 185]. Last but not least, a $\sim 2\sigma$ discrepancy is observed at the Tevatron experiments CDF [186] and DØ [187] in the forward-backward asymmetry in $pp \to t\bar{t}$ events. A possible explanation of this phenomenon may be the existence of a heavy neutral spin-1 gauge boson Z' [188].

2.4 The Minimal Supersymmetric Standard Model

As alluded in the previous section, the supersymmetric extension of the SM provides possible solutions to many of the conceptual and observational issues left unexplained by the SM. For this reason, and because of its appealing theoretical structure, supersymmetry (SUSY) is the most popular and best-studied theory beyond the SM. In this section we give a brief introduction to weak-scale supersymmetry before turning to the discussion of its Higgs sector. We further outline some guiding principles that allow to effectively reduce the number of free parameters of supersymmetric models and therefore enable phenomenological studies.

In the following we mainly concentrate on the concepts and model features that are relevant for the work presented in this thesis. More thorough introductions and reviews of supersymmetry can e.g. be found in Refs. [15–24].

2.4.1 Foundations of the MSSM

Supersymmetry is the only possible way to extend the Lorentz (or Poincaré) space-time symmetry by relating fermionic and bosonic degrees of freedom via spinorial charges [189]. Schematically, a supersymmetric transformation Q acts on a fermionic state $|F\rangle$ by transforming it into a boson $|B\rangle$, and conversely:

$$Q\,|F\rangle = |B\rangle\,, \qquad Q\,|B\rangle = |F\rangle\,. \tag{2.50}$$

[23] See Ref. [180] for a possible explanation within the Two-Higgs Doublet Model (2HDM) with generic flavor structure.

In the supersymmetric extension of the SM (SSM), each SM particle has a superpartner with its spin differing by 1/2. Together they form a *supermultiplet*, which is an irreducible representation of the SUSY algebra and contains equal number of bosonic and fermionic degrees of freedom. The SUSY generator Q commutes both with the generators of the gauge interactions and with $P^2 = M^2$, hence, in exact supersymmetry, the superpartners of the SM fields have the same quantum numbers and mass M. As we have seen in Section 2.3, these equalities lead to the exact cancellation of problematic radiative corrections to the Higgs mass. Thus, supersymmetry protects the light Higgs mass and makes the theory technically natural. However, we have not observed any superpartners of SM particles yet, so SUSY must be a broken symmetry if it indeed exists in nature. We will discuss below how this breaking can be accommodated without spoiling the naturalness.

Two types of supermultiplets are needed to assemble the SM fields and their superpartners: A *chiral* (or *matter*) supermultiplet, which contains a single two-component Weyl fermion (spin 1/2) and a complex scalar field (spin 0), and a *vector* (or *gauge*) supermultiplet with a massless vector boson (spin 1) and a two-component Weyl fermion. In order to include gravity an additional supermultiplet with a graviton (spin 2) and its fermionic superpartner, the gravitino (spin 3/2), is needed. Supermultiplets are most conveniently written using the *superfield formalism*, see e.g. Refs. [15, 22] for an introduction.

The MSSM particle content

The chiral supermultiplets of the MSSM, i.e. the supersymmetric extension of the SM with minimal particle content, are given in Tab. 2.6. They contain the SM fermions and their scalar superpartners, the *sfermions*. We have three generations ($i = 1, 2, 3$) of left-handed (right-handed) up- and down-type *squarks*, $\tilde{u}_{Li}$, $\tilde{d}_{Li}$ ($\tilde{u}_{Ri}$, $\tilde{d}_{Ri}$), which are the spin-0 superpartners of the left-handed (right-handed) up-and down-type quarks, respectively; the superpartners of the left-handed (right-handed) charged leptons are the left-handed (right-handed) charged *sleptons*, $\tilde{\ell}_{Li}$ ($\tilde{e}_{Ri}$); and the *sneutrinos*, $\tilde{\nu}_i$, which are the superpartners of the neutrinos. Conventionally, all SM fermions are described by left-handed Weyl spinors, hence the conjugates of the right-handed quarks and leptons are given in Tab. 2.6.

An important feature of supersymmetric models is the necessity of having at least two Higgs doublet fields. The fermionic partner of a single Higgs doublet, the *Higgsino*, would lead to a gauge anomaly of the electroweak symmetry [20, 190]. With two Higgs doublets of opposite hypercharge, cf. Tab. 2.6, the contributions to the anomaly cancel. Moreover, the superpotential (see below) must be an analytic function of chiral superfields, hence we need (at least) two Higgs doublets to give mass to both the up- and down-type quarks via the Higgs mechanism. The Higgs sector will be discussed in more detail in Section 2.4.3.

The SM gauge bosons and their fermionic superpartners, the *gauginos*, are assembled in the vector supermultiplets presented in Tab. 2.7. We have the *bino*, $\tilde{B}$, the superpartner of the $U(1)_Y$ gauge boson; three *winos*, $\tilde{W}^A$ ($A = 1, 2, 3$), the superpartners of the $\mathrm{SU}(2)_L$ gauge bosons; and the *gluinos*, $\tilde{g}^a$ ($a = 1, \ldots, 8$), the superpartners of the $\mathrm{SU}(3)_C$ gauge bosons, the gluons.

After EWSB, some of the fields in Tab. 2.6 and 2.7 will have the same remaining conserved quantum numbers and can therefore mix. The bino, the third wino component, $\tilde{W}^3$, and the neutral Higgsinos mix and their mass eigenstates are called *neutralinos*, $\tilde{\chi}^0_n$, where $n = 1, \ldots, 4$ denotes an ordering according to an increasing mass hierarchy (i.e. $\tilde{\chi}^0_1$ is the lightest neutralino). The mixing of the winos $\tilde{W}^1$ and $\tilde{W}^2$ and the charged Higgsinos results in the *charginos*, $\tilde{\chi}^\pm_m$

Field names	superfield	spin 0	spin 1/2	$SU(3)_C$, $SU(2)_L$, $U(1)_Y$
squarks, quarks (×3 families)	Q_i	$\tilde{q}_{Li} \equiv \begin{pmatrix} \tilde{u}_{Li} \\ \tilde{d}_{Li} \end{pmatrix}$	$q_{Li} = \begin{pmatrix} u_{Li} \\ d_{Li} \end{pmatrix}$	$(\mathbf{3}, \mathbf{2}, +1/6)$
	$\bar{U}_i$	$\tilde{u}^*_{Ri}$	$u^\dagger_{Ri}$	$(\bar{\mathbf{3}}, \mathbf{1}, -2/3)$
	$\bar{D}_i$	$\tilde{d}^*_{Ri}$	$d^\dagger_{Ri}$	$(\bar{\mathbf{3}}, \mathbf{1}, +1/3)$
sleptons, leptons	L_i	$\tilde{\ell}_{Li} \equiv \begin{pmatrix} \tilde{\nu}_i \\ \tilde{\ell}_{Li} \end{pmatrix}$	$\ell_{Li} \equiv \begin{pmatrix} \nu_i \\ \ell_{Li} \end{pmatrix}$	$(\mathbf{1}, \mathbf{2}, -1/2)$
(×3 families)	$\bar{E}_i$	$\tilde{e}^*_{Ri}$	$e^\dagger_{Ri}$	$(\mathbf{1}, \mathbf{1}, +1)$
Higgs, higgsinos	H_1	$h_1 \equiv \begin{pmatrix} h_1^0 \\ h_1^- \end{pmatrix}$	$\tilde{h}_1 \equiv \begin{pmatrix} \tilde{h}_1^0 \\ \tilde{h}_1^- \end{pmatrix}$	$(\mathbf{1}, \mathbf{2}, -1/2)$
	H_2	$h_2 \equiv \begin{pmatrix} h_2^+ \\ h_2^0 \end{pmatrix}$	$\tilde{h}_2 \equiv \begin{pmatrix} \tilde{h}_2^+ \\ \tilde{h}_2^0 \end{pmatrix}$	$(\mathbf{1}, \mathbf{2}, +1/2)$

Table 2.6: *Chiral* (or *matter*) supermultiplets of the MSSM. $i = 1, 2, 3$ is the generation index. The last column gives the gauge representation under the SM gauge group G_{SM}.

Field names	superfield	spin 1/2	spin 1	$SU(3)_C$, $SU(2)_L$, $U(1)_Y$
bino, B boson	V_1	$\tilde{B}$	B_μ	$(\mathbf{1}, \mathbf{1}, 0)$
winos, W bosons	V_2	$\tilde{W}^A$	W^A_μ	$(\mathbf{1}, \mathbf{3}, 0)$
gluinos, gluons	V_3	$\tilde{g}^a$	G^a_μ	$(\mathbf{8}, \mathbf{1}, 0)$

Table 2.7: *Vector* (or *gauge*) supermultiplets (with their gauge representation) of the MSSM.

$(m = 1, 2)$. Again, $\tilde{\chi}_1^\pm$ denotes the lighter mass eigenstate.

The squarks and sleptons in Tab. 2.6 are given in the flavor basis. In general, these can mix between different generations and right- and left-handed fields after EWSB, leading to 6×6 mass matrices for each the sleptons, down- and up-type squarks. However, the generational mixing is highly restricted by experimental bounds on FCNC processes [191, 192] (see Section 2.4.2 for more details). Furthermore, the mass terms and trilinear scalar interactions[24], which lead to the mixing of left- and right-handed states within one generation, are usually assumed to be proportional to the corresponding SM fermion mass and Yukawa couplings, respectively. In this work, we therefore only consider left-right mixing for the third generation squarks and sleptons. The mass eigenstates are labeled by $\tilde{t}_k$, $\tilde{b}_k$, $\tilde{\tau}_k$, $(k = 1, 2)$, respectively, following the same mass ordering as above.

Note, that so far we have been assuming that lepton-number, L, and baryon number, B, are conserved quantities. In the SM, this is indeed the case, albeit for no apparent deeper reason[25]. In general, supersymmetric models can feature violation of lepton and baryon number (see below). In that case, the mixing of superfields will be more complicated [193].

[24] These terms break supersymmetry explicitly as will be discussed later.

[25] The lepton number and baryon number conservation in the SM are regarded as *accidental* symmetries. It is simply not possible to write down Lorentz- and gauge-invariant renormalizable operators that violate L or B in the SM.

The superpotential

In a renormalizable supersymmetric field theory[26], all interactions and masses of the particles are solely determined by their gauge transformation properties and the *superpotential* W, which is a holomorphic function of the chiral superfields. With the particle content given in Tab. 2.6, the most general gauge invariant and renormalizable superpotential of the SSM is[27] [194, 195]

$$W_{\text{SSM}} = W_{\text{RPC}} + W_{\text{RPV}}, \tag{2.51}$$

$$W_{\text{RPC}} = Y^{(\ell)}_{ij} H_1 \cdot L_i \bar{E}_j + Y^{(d)}_{ij} H_1 \cdot Q_i \bar{D}_j - Y^{(u)}_{ij} H_2 \cdot Q_i \bar{U}_j - \mu H_1 \cdot H_2, \tag{2.52}$$

$$W_{\text{RPV}} = \frac{1}{2}\lambda_{ijk} L_i \cdot L_j \bar{E}_k + \lambda'_{ijk} L_i \cdot Q_j \bar{D}_k + \frac{1}{2}\lambda''_{ijk} \bar{U}_i \bar{D}_j \bar{D}_k - \kappa_i L_i \cdot H_2, \tag{2.53}$$

where $i, j, k = 1, 2, 3$ are generation indices. We use the notation $A \cdot B \equiv \epsilon_{ab} A^a B^b$ for the contraction of two SU(2)-doublet superfields A and B, with the SU(2) indices $a, b = 1, 2$ and the total anti-symmetric tensor ϵ_{ab} with $\epsilon_{12} = -\epsilon_{21} = +1$. We omitted the $SU(3)$ color indices.

The first part of the superpotential, W_{RPC}, includes supersymmetric generalizations of the Yukawa couplings for the leptons, down- and up-type quarks superfields. These contain the Yukawa terms of the SM, cf. Eq. (2.22), which give mass to the fermions after EWSB. Note, that H_1 gives mass to the down-type quarks and charged leptons, while H_2 gives mass to the up-type quarks[28]. The last term in Eq. (2.52) is a supersymmetric generalization of a Higgsino mass term. The parameter μ has the dimension of mass and is required to be $\sim \mathcal{O}(10^2\ \text{GeV})$ for consistent EWSB.

The second part of the superpotential, W_{RPV}, contains baryon-number violating (BNV) and lepton-number violating (LNV) operators. If both types are present simultaneously in the theory the proton decays rapidly [198–200]. This is in contradiction with experiments [201] and the lower limit on the proton lifetime [74] severely constrains the product of LNV and BNV couplings to unnaturally small values [199].

The problem of rapid proton decay can be cured be imposing a *discrete gauge symmetry* [202] that prohibits either the BNV or LNV terms, or both. A very popular choice is *R-parity* [203], R_p, (also called *matter parity*) which prohibits all terms in W_{RPV}, Eq. (2.53). It can be defined as

$$R_p \equiv (-1)^{2S+3B+L} = \begin{cases} +1 & \text{for SM particles} \\ -1 & \text{for SUSY particles} \end{cases}, \tag{2.54}$$

where B and L are the baryon and lepton number of the particle, respectively, and S denotes its spin. This discrete symmetry is usually assumed to be conserved in the MSSM. It features the interesting phenomenological consequence that SUSY particles can only be produced (and annihilated) pairwise. Once SUSY particles are produced they (cascade) decay into the lightest supersymmetric particle (LSP), which cannot further decay due to the symmetry. As it is stable, the LSP is a good candidate for dark matter [12, 129, 130, 204]. For the same reason it is restricted to be color-, flavor- and charge-neutral. In many considered SUSY models the lightest neutralino $\tilde{\chi}^0_1$ is the LSP.

[26] If SUSY is broken there will be additional soft SUSY-breaking terms in the Lagrangian (see below).

[27] The subscripts RPC and RPV are abbreviations for *R-parity conservation* and *R-parity violation* and are explained below.

[28] This pattern of (tree-level) Yukawa interactions corresponds to a Type II Two-Higgs-Doublet-Model (2HDM) [196, 197].

In fact, the phenomenologically equivalent discrete symmetry *proton hexality* [205, 206], P_6, is better suited for protecting the proton from its untimely demise, because it also forbids dangerous dimension-5 proton decay operators.

Another possible discrete symmetry is *baryon triality* [206], B_3, which prohibits the BNV operator $\bar{U}\bar{D}\bar{D}$, but allows the LNV terms in W_{RPV}, Eq. (2.53). It also forbids the aforementioned dimension-5 proton decay operators. Phenomenologically, the LSP is unstable in this case and therefore generally not a good DM candidate. Any SUSY particle can now be the LSP, which potentially leads to interesting and unexpected collider signatures [207]. Furthermore, SUSY particles can be produced singly, possibly at resonance [207–210]. This signature will be investigated in Chapter 7 in order to derive bounds on the R-parity violating couplings from the non-observation in LHC searches. Note also, that the LNV operators are well-suited to generate neutrino masses [143, 211].

Soft SUSY breaking

A realistic weak-scale SUSY model must contain SUSY breaking, since superpartners with equal mass as the SM particles are experimentally excluded. Similarly as in the electroweak sector, the mechanism of SUSY breaking is anticipated to be spontaneous. However, there is no consensus on how exactly the SUSY breaking should be done and many models of spontaneous symmetry breaking have been proposed. For phenomenological studies, it is very useful to parametrize this ignorance by adding extra interaction terms to the supersymmetrized SM Lagrangian, which break SUSY explicitly. The SUSY-breaking couplings should be *soft* (i.e. of positive mass dimension) in order not to reintroduce quadratic divergencies in the radiative corrections to scalar masses spoiling the natural solution of the hierarchy problem, cf. Section 2.3. The most general form of explicit SUSY-breaking consistent with R-parity conservation and the minimal particle content of the SSM is [212]

$$\begin{aligned}
-\mathcal{L}_{\text{soft}} =& \frac{1}{2}\left(M_1\,\tilde{B}\tilde{B} + M_2\,\tilde{W}^A\tilde{W}^A + M_3\,\tilde{g}^a\tilde{g}^a + \text{h.c.}\right) \\
&+ m_{H_1}^2\,h_1^\dagger h_1 + m_{H_2}^2\,h_2^\dagger h_2 - (B\mu\,h_1\cdot h_2 + \text{h.c.}) \\
&+ (M_{\tilde{\ell}}^2)_{ij}\,\tilde{\ell}_{Li}^\dagger\tilde{\ell}_{Lj} + (M_{\tilde{e}}^2)_{ij}\,\tilde{e}_{Ri}^*\tilde{e}_{Rj} + (M_{\tilde{q}}^2)_{ij}\,\tilde{q}_{Li}^\dagger\tilde{q}_{Lj} + (M_{\tilde{u}}^2)_{ij}\,\tilde{u}_{Ri}^*\tilde{u}_{Rj} + (M_{\tilde{d}}^2)_{ij}\,\tilde{d}_{Ri}^*\tilde{d}_{Rj} \\
&+ \left[(A_{\tilde{e}}Y^{(\ell)})_{ij}\,h_1\cdot\tilde{\ell}_{Li}\tilde{e}_{Rj}^* + (A_{\tilde{d}}Y^{(d)})_{ij}\,h_1\cdot\tilde{q}_{Li}\tilde{d}_{Rj}^* - (A_{\tilde{u}}Y^{(u)})_{ij}\,h_2\cdot\tilde{q}_{Li}\tilde{u}_{Rj}^* + \text{h.c.}\right].
\end{aligned} \tag{2.55}$$

The first row contains three (complex) Majorana mass terms for the gauginos. Three soft-breaking mass parameters for the Higgs fields appear in the second row. The third row holds soft-breaking mass terms for the squarks and sleptons, given by five hermitian 3×3 squared-mass matrices. The last row contains the scalar interactions that correspond to the Yukawa couplings in the superpotential, Eq. (2.52). These trilinear scalar interaction terms contribute to the slepton and squark masses and are given by complex 3×3 matrix A-parameters. After EWSB, these terms mix the left- and right-handed sleptons and squarks. It is apparent that $\mathcal{L}_{\text{soft}}$ breaks supersymmetry as it involves only fields without their superpartners.

With the supersymmetrization of the SM, no additional parameters (apart from new parameters in the extended Higgs sector, cf. Section 2.4.3) are introduced. However, $\mathcal{L}_{\text{soft}}$, Eq. (2.55), contains 105 new parameters, which have no counterpart in the SM. Thus, the MSSM contains 124 independent parameters (including the SM parameters) [23]. In this extensive parameter

space, phenomenological studies are very difficult. Thus we need a guiding principle to reduce the amount of free parameters. We address this issue in the next section.

2.4.2 Phenomenological and constrained supersymmetry

Given the $\mathcal{O}(10^2)$ new terms introduced by explicit soft-breaking of SUSY, Eq. (2.55), as *a priori* arbitrary free parameters of the MSSM, the theory suffers from a severe *flavor problem* [213]: Without an underlying ordering principle in the sfermion mass matrices large FCNCs are naturally induced, which are, however, unobserved in experiment [191, 192]. For instance, in the slepton sector the off-diagonal matrix elements that couple the selectron to the smuon are strongly constrained by the non-observation of the process $\mu \to e\gamma$ [214, 215]. In the squark sector, experimental constraints come from neutral meson mixing like $K^0 - \bar{K}^0$, $D^0 - \bar{D}^0$ and $B^0 - \bar{B}^0$ [67, 191, 216–218] as well as rare decay processes like $b \to s\gamma$ [67, 219]. As a result, large parts of the 124-dimensional parameter space of the general MSSM are already ruled out. Note however, that bounds involving third-generation sfermions are in general less restrictive than those involving only sfermions of the first and second generation.

Provided that the SUSY particle masses are not too heavy[29], $\lesssim \mathcal{O}$(few TeV), the large FCNCs can only be avoided by either a (presumably dynamically generated) *alignment* between the fermion and sfermion mass matrices such that they can be made diagonal in the same basis, or by assuming *flavor blind universality* of the mass matrices of sfermions with the same $\mathrm{SU}(2)_L \times \mathrm{U}(1)_Y$ quantum numbers, each proportional to the 3×3 identity matrix in generation space,

$$(M^2_{\tilde{f}})_{ij} = M^2_{\tilde{f}} \times \delta_{ij}, \qquad \text{with} \quad \tilde{f} = \tilde{\ell}, \tilde{e}, \tilde{q}, \tilde{u}, \tilde{d}. \tag{2.56}$$

In this case, the FCNC amplitudes are suppressed by a *super-GIM mechanism* (analogously to the *GIM mechanism* in the SM [221]). Note that, in principle, the MSSM may also contain 40 new physical complex phases that introduce $\mathcal{CP}$-violating effects [23, 213, 222, 223]. These are strongly restricted by experimental observations, in particular from electric dipole moments (EDMs) [222–224]. Here we shall concentrate on the real MSSM where these phases are absent.

The trilinear scalar couplings $(A_{\tilde{e}})_{ij}$, $(A_{\tilde{d}})_{ij}$ and $(A_{\tilde{u}})_{ij}$ in Eq. (2.55) couple left- and right-handed fields to each other. After EWSB, they also contribute to the squark and slepton mass matrices and may induce large FCNCs. This can be avoided by a similar universality assumption,

$$(A_{\tilde{e}})_{ij} = A_\ell \times \delta_{ij}, \quad (A_{\tilde{d}})_{ij} = A_d \times \delta_{ij}, \quad (A_{\tilde{u}})_{ij} = A_u \times \delta_{ij}. \tag{2.57}$$

Due to the proportionality to the respective Yukawa coupling matrix, cf. Eq. (2.55), they will only induce substantial mixing in the third generation sfermion sector.

As we have seen, by using the low energy constraints from FCNCs and EDMs as a guiding principle for assumptions on universality and absence of complex phases, respectively, the number of free model parameters has been greatly reduced. Thus, phenomenological studies become feasible, and two complementary paths can be followed. In a *top-down approach*, assumptions on the SUSY parameters are imposed at a very high energy (e.g. GUT) scale. The RGEs are then employed to obtain the SUSY parameters at the EW scale, which is accessible to collider

[29] The flavor problem can also be avoided if the first and second generation sfermions are very heavy (in the multi-TeV range) and thus essentially decouple from the physics at observable energy scales [220].

experiments. With further assumptions on the underlying SUSY breaking mechanism these models can be highly predictive with only a few free parameters (see below). Alternatively, in a *bottom-up approach*, the SUSY parameters can be chosen directly at the EW scale, only guided by phenomenological arguments (as discussed above) and, optionally, generic parameter relations that are typically obtained in high-scale models.

Constrained (high-scale) MSSM

As briefly mentioned in Section 2.3, one of the motivations for SUSY is the gauge coupling unification at a scale $M_{\text{GUT}} \sim 2 \cdot 10^{16}$ GeV, suggesting that the MSSM is embedded in a grand unified theory. In that case it seems natural to have all gauginos in the same representation of a unifying simple gauge group [118, 225, 226], leading to equal gaugino masses at the GUT scale,

$$M_1 = M_2 = M_3 \equiv m_{1/2} \qquad \text{at} \quad M_{\text{GUT}}. \tag{2.58}$$

In the same way, the universality conditions Eqs. (2.56) and (2.57) should be assumed at M_{GUT}. In minimal high-scale models, further universality of the soft-breaking masses and trilinear couplings is often assumed:

$$M_{\tilde{\ell}}^2 = M_{\tilde{e}}^2 = M_{\tilde{q}}^2 = M_{\tilde{u}}^2 = M_{\tilde{d}}^2 = m_{H_1}^2 = m_{H_2}^2 \equiv m_0 \qquad \text{at} \quad M_{\text{GUT}}, \tag{2.59}$$

$$A_\ell = A_u = A_d \equiv A_0 \qquad \text{at} \quad M_{\text{GUT}}. \tag{2.60}$$

Note that, due to the RGE running, the scalar masses and trilinear interactions are in general not universal at the electroweak scale. This can lead to small contributions to FCNCs, which are however typically consistent with the experimental constraints [227].

In addition to these three universal soft-breaking parameters we need two more parameters to specify the MSSM Higgs sector, see Section 2.4.3. A convenient choice are the parameters $\tan\beta$ and $\text{sgn}(\mu)$, where $\tan\beta$ is the ratio of the vevs of the two Higgs doublets and $\text{sgn}(\mu)$ is the sign of the Higgs mixing parameter μ, cf. Eq. (2.52). The magnitude of μ and the soft-breaking parameter B, cf. Eq. (2.55), are fixed by the minimization of the scalar potential, see Section 2.4.3. Thus, this high-scale SUSY model is completely specified by the five parameters

$$m_0,\ m_{1/2},\ A_0,\ \tan\beta,\ \text{sgn}(\mu). \tag{2.61}$$

This model is known as the constrained MSSM (CMSSM). It can set in relation to the class of supergravity models [228], where supersymmetry is promoted to a local symmetry and thus provides a natural incorporation of gravity. The minimal supergravity (mSUGRA) model, which is a subset of the CMSSM parameter space, can be obtained by imposing certain simplifying assumptions on the supergravity Lagrangian [229], thus this model is also well motivated from a theoretical perspective.

The (experimentally accessible) particle spectrum at the EW scale is obtained from the evolution of the RGEs[30]. An example of the RGE running of the soft-breaking masses from M_{GUT} to the EW scale is shown in Fig. 2.12 for a typical CMSSM parameter point, specified by $m_0 = 80\,\text{GeV}$, $m_{1/2} = 250\,\text{GeV}$, $A_0 = -500\,\text{GeV}$, $\tan\beta = 10$ and $\mu > 0$ at M_{GUT} [22]. Due to the different gauge charges, the squark and slepton masses evolve quite differently, i.e. the squarks

[30] Explicit formulae for the one-loop RGEs can e.g. be found in Ref. [22]

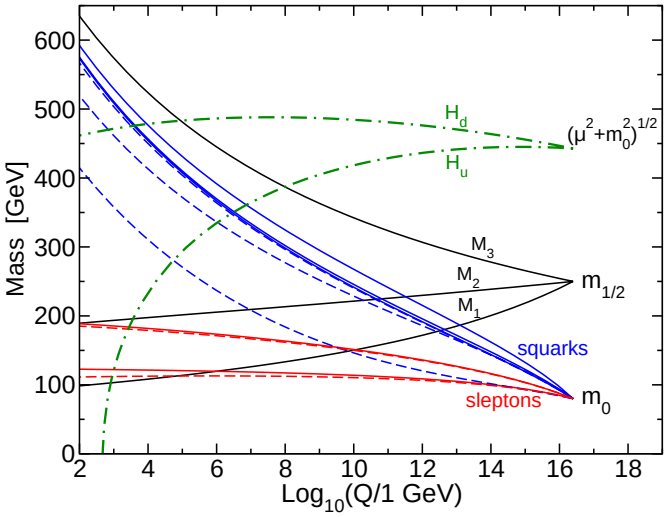

Figure 2.12: Typical RGE running of slepton (red lines), squark (blue lines) and gaugino (black lines) soft-breaking masses from M_{GUT} to M_Z in the CMSSM. Also shown is the running of $(m_{H_1}^2 + \mu^2)$ and $(m_{H_2}^2 + \mu^2)$. The latter runs negative and thus triggers electroweak symmetry breaking. Taken from Ref. [22]. Note the slightly different notation, $H_d \equiv H_1$, $H_u \equiv H_2$.

become much heavier than the sleptons at the EW scale since they are strongly interacting. The RGE running is furthermore influenced by the Yukawa couplings which lower the sparticle masses at the EW scale. Thus, the third generation squarks and sleptons are lighter than those of the first and second generation.

Fig. 2.12 also shows the running of the quantities $(m_{H_1}^2 + \mu^2)$ and $(m_{H_2}^2 + \mu^2)$ which appear in the Higgs scalar potential, see Section 2.4.3. The large top-Yukawa coupling leads to a large decrease of the up-type Higgs mass parameter, m_{H_2}, going from M_{GUT} to the EW scale, such that $(m_{H_2}^2 + \mu^2)$ eventually runs to negative values at the EW scale, leading to EWSB. Thus, SUSY provides a *dynamical mechanism* for EWSB [230, 231].

The gaugino masses feature the same running as the corresponding gauge couplings, hence M_3 increases and M_1 and M_2 decrease when going from M_{GUT} to the EW scale. At every energy scale, we have the relation (up to small two-loop effects [232])

$$\frac{M_1}{g_1^2} = \frac{M_2}{g_2^2} = \frac{M_3}{g_3^2} = \frac{m_{1/2}}{g_{\text{GUT}}^2}, \tag{2.62}$$

with $g_1 = \sqrt{5/3}\, g_Y$, the strong coupling constant $g_3 = g_s$ and the universal gauge coupling $g_{\text{GUT}} \simeq 0.73$ at M_{GUT}. Expressed in terms of the weak mixing angle, we thus have

$$M_1 = \frac{5}{3} \tan^2 \theta_W \, M_2, \tag{2.63}$$

and an approximate relation $M_3 : M_2 : M_1 \simeq 7 : 2 : 1$ at the EW scale.

Before the start-up of the LHC, results from global fit analyses [233, 296] to low-energy and astrophysical observables suggested that the CMSSM, if realized in Nature, features a relatively light SUSY particle spectrum. In particular, these studies predicted a great coverage of the preferred CMSSM parameter space by the discovery potential of the first LHC run. However, no signal has been seen in any of the SUSY searches, excluding the previously preferred parameter

space.

The current status of the CMSSM, taking into account the exclusion limits from SUSY searches from the first LHC run as well as the measurements of the discovered Higgs boson, has been studied extensively in the literature, see e.g. Refs. [233–235, 249, 296]. The remaining allowed parameter space features a rather heavy sparticle spectrum, with masses of the squarks, gluino and the heavier EW gauginos being well above 1 TeV. Furthermore, the lightest $\mathcal{CP}$-even Higgs boson is very SM-like in this parameter region, and the lightest neutralino and scalar tau lepton have similar masses of $\sim 300 - 600\,\text{GeV}$ [234]. Besides these grim prospects for a potential discovery at the LHC, the model looses more and more its attractiveness when naturalness arguments are considered [249] (see Section 2.4.3 for a brief discussion of the so-called *Little Hierarchy Problem*).

The phenomenological MSSM (pMSSM)

In a more phenomenological approach the SUSY parameters are specified directly at the EW scale. In this way, the phenomenology of the full MSSM parameter space can be explored, while constrained high-scale models typically cover only very specific corners of the parameter space. This approach is therefore advantageous from an experimental point of view, where we aim for a full exploration and coverage of possible SUSY signatures at e.g. collider experiments. Moreover, it contains only a minimal amount of theoretical prejudice about the high-scale behavior of the theory and the underlying SUSY breaking mechanism.

One possible choice is to assume the universality of soft-breaking masses and trilinear couplings, Eqs. (2.56) and (2.57), at the EW scale. However, since the third generation sfermion masses are less constrained by flavor processes and, as we have seen above, also can feature a quite different RGE running in high-scale models due to their large Yukawa couplings, we will here only assume the flavor universality, Eq. (2.56) and (2.57), for the first and second generation ($i, j = 1, 2$) and keep the third generation sfermion masses and trilinear couplings separate:

$$M_{\tilde{\tau}_L},\ M_{\tilde{\tau}_R},\ M_{\tilde{q}_3}(= M_{\tilde{t}_L} = M_{\tilde{b}_L}),\ M_{\tilde{t}_R},\ M_{\tilde{b}_R},\ A_t,\ A_b,\ A_\tau. \tag{2.64}$$

Additional parameters are needed to specify the MSSM Higgs sector, which are typically chosen to be

$$\tan\beta,\ m_A,\ \mu, \tag{2.65}$$

where m_A is the mass of the pseudoscalar Higgs boson A, see Section 2.4.3.

We will study the implications of the Higgs boson discovery for the phenomenological MSSM in Chapter 6, also taking into account low energy observables and limits from direct collider searches for Higgs bosons and SUSY particles.

As it will be relevant for the following discussion, we briefly give the formulae for the left-right mixing of the sfermions. This mixing is particularly important for the sfermions of the third generation, while it is usually negligible for the first and second generation. In the basis of current eigenstates $(\tilde{f}_L, \tilde{f}_R)$ within each fermion generation, the sfermion mass matrices read

$$\mathcal{M}^2_{\tilde{f}} = \begin{pmatrix} m_f^2 + m_{LL}^2 & m_f X_f \\ m_f X_f & m_f^2 + m_{RR}^2 \end{pmatrix}. \tag{2.66}$$

Here, we defined

$$m_{LL}^2 \equiv M_{\tilde{f}_L}^2 + (\tfrac{1}{2} - Q_f \sin^2\theta_W) M_Z^2 \cos 2\beta, \tag{2.67}$$

$$m_{RR}^2 \equiv M_{\tilde{f}_R}^2 + Q_f \sin^2\theta_W \, M_Z^2 \cos 2\beta, \tag{2.68}$$

$$X_t \equiv A_f - \mu \cot\beta. \tag{2.69}$$

Q_f denotes the electric charge of the (s)fermion, Eq. (2.1). The mass matrices are diagonalized by 2×2 rotation matrices of angle θ_f,

$$R_f = \begin{pmatrix} \cos\theta_f & \sin\theta_f \\ -\sin\theta_f & \cos\theta_f \end{pmatrix}, \tag{2.70}$$

where the mixing angle is given by

$$\sin(2\theta_f) = \frac{2 m_f X_f}{m_{\tilde{f}_1}^2 - m_{\tilde{f}_2}^2}, \tag{2.71}$$

The resulting sfermion masses read

$$m_{\tilde{f}_{1,2}}^2 = m_f^2 + \frac{1}{2}\left[m_{LL}^2 + m_{RR}^2 + \sqrt{(m_{LL}^2 - m_{RR}^2)^2 + 4 m_f^2 X_f^2}\right]. \tag{2.72}$$

In the stop sector, the mixing is very strong for large values of the stop mixing parameter $X_t = A_t - \mu \cot\beta$ and generates a significant mass splitting between the two mass eigenstates.

2.4.3 The MSSM Higgs sector

The tree-level potential for the two Higgs doublets h_1 and h_2 of the MSSM, cf. Tab. 2.6, follows from the superpotential, Eq. (2.52), and the soft-breaking Lagrangian, Eq. (2.55). It reads

$$\begin{aligned} V_H = &\frac{g_Y^2 + g_2^2}{8}(|h_1|^2 - |h_2|^2)^2 + \frac{g_2^2}{2}|h_1^\dagger h_2|^2 + |\mu|^2(|h_1|^2 + |h_2|^2) \\ &+ m_{H_1}^2 |h_1|^2 + m_{H_2}^2 |h_2|^2 - (B\mu \, h_1 \cdot h_2 + \text{h.c.}). \end{aligned} \tag{2.73}$$

We observe that the quartic Higgs couplings are expressed in terms of the $\mathrm{SU}(2)_L \times \mathrm{U}(1)_Y$ gauge couplings. The tree-level Higgs potential therefore contains only three free parameters, which originate from the soft-breaking Lagrangian, Eq. (2.55). These are often expressed as

$$m_{11}^2 \equiv m_{H_1}^2 + |\mu|^2, \qquad m_{22}^2 \equiv m_{H_2}^2 + |\mu|^2, \qquad m_{12}^2 \equiv B\mu, \tag{2.74}$$

which are the elements of the tree-level mass squared matrix of the scalar potential.

Spontaneous electroweak symmetry breaking is achieved if the minimum of V_H is attained at nonzero values of the Higgs fields,

$$\langle h_1 \rangle = \frac{1}{\sqrt{2}} \begin{pmatrix} v_1 \\ 0 \end{pmatrix}, \qquad \langle h_2 \rangle = \frac{1}{\sqrt{2}} \begin{pmatrix} 0 \\ v_2 \end{pmatrix}, \tag{2.75}$$

with real and positive $v_{1,2}$. The W and Z boson masses are now given by

$$M_W = \frac{g_2}{2}(v_1^2 + v_2^2)^{1/2}, \qquad M_Z = \frac{1}{2}(g_Y^2 + g_2^2)^{1/2}(v_1^2 + v_2^2)^{1/2}, \tag{2.76}$$

i.e. $(v_1^2 + v_2^2)^{1/2} = v \approx 246\,\text{GeV}$. In order for the two vevs to develop non-zero values, at least one mass eigenvalue of the mass squared matrix of V_H has to be negative. This is the case if $m_{11}^2 m_{22}^2 < m_{12}^4$, i.e.

$$(B\mu)^2 > (m_{H_1}^2 + |\mu|^2)(m_{H_2}^2 + |\mu|^2). \tag{2.77}$$

This immediately shows that $m_{H_1}^2 = m_{H_2}^2 = B = 0$ is not a viable option, i.e. SUSY breaking is a prerequisite for EWSB. The ratio of the two vacuum expectation values is commonly denoted by

$$\tan\beta \equiv v_2/v_1, \tag{2.78}$$

and is typically restricted to the range $1.5 \lesssim \tan\beta \lesssim 65$ [236] by radiatively induced EWSB, where one of the eigenvalues of the neutral Higgs mass squared matrix is driven to a negative value by the top Yukawa coupling in the RGE evolution [237]. Further constraints on the $\tan\beta$ range come from the requirement of perturbative couplings up to the GUT scale $\sim 2\times10^{16}$ GeV.

By minimizing the scalar potential at the electroweak minimum, $\partial V/\partial h_i|_{\langle h_i\rangle} = 0$ $(i = 1, 2)$, we obtain two minimization conditions, which can be written as

$$2B\mu = (m_{H_1}^2 - m_{H_2}^2)\tan 2\beta + M_Z^2 \sin 2\beta, \tag{2.79}$$

$$|\mu|^2 = (m_{H_2}\sin^2\beta - m_{H_1}^2\cos^2\beta)/\cos 2\beta - M_Z^2/2. \tag{2.80}$$

If $m_{H_1}^2$ and $m_{H_2}^2$ are known (e.g. from RGE running from a high scale, see Section 2.4.2), the specification of $\tan\beta$ and the sign of μ will fix the parameters B and $|\mu|^2$ via Eqs. (2.79) and (2.80). In order to avoid unnatural cancellations in Eq. (2.80), the soft-breaking mass parameters $|\mu|^2$, $|m_{H_1}|^2$ and $|m_{H_2}|^2$ should be $\sim \mathcal{O}(M_Z^2)$.

Out of the eight degrees of freedom contained in the two complex Higgs doublets only three are absorbed during EWSB to form the longitudinal components of the $W^\pm$ and Z bosons. We are thus left with five physical Higgs states: The real parts of the neutral components, h_1^0 and h_2^0, mix with an angle α to form two $\mathcal{CP}$-even neutral states h and H, where the physical masses are $m_h < m_H$ by definition. The remaining (imaginary) neutral component is the $\mathcal{CP}$-odd (or pseudoscalar) state A with mass m_A. The remaining two degrees of freedom form a charged Higgs boson pair $H^\pm$.

Higgs boson masses and couplings at tree-level

The tree-level masses of these five physical states can be obtained from the scalar potential, Eq. (2.73). The pseudoscalar Higgs mass is given by

$$m_A^2 = -\frac{B\mu}{\sin 2\beta}. \tag{2.81}$$

Note, that $\sin 2\beta$ is restricted to be positive, thus Eq. (2.81) makes only sense if $B\mu < 0$ at the electroweak scale. As has been noted in the previous section, m_A and $\tan\beta$ are often chosen

(besides the well known Z boson mass, M_Z) as input model parameters, which completely fix the MSSM Higgs sector at tree-level via Eqs. (2.79), (2.80) and (2.81). The charged Higgs mass is given by

$$m_{H^\pm}^2 = m_A^2 + M_W^2, \tag{2.82}$$

and is relatively stable under radiative corrections unless $\tan\beta$ becomes very large [238]. The masses of the $\mathcal{CP}$-even neutral Higgs bosons are given by

$$m_{h,H}^2 = \frac{1}{2}\left[m_A^2 + M_Z^2 \mp \sqrt{(m_A^2 + M_Z^2)^2 - 4m_A^2 M_Z^2 \cos^2 2\beta}\right]. \tag{2.83}$$

Here, an important prediction is the upper bound on the light Higgs tree-level mass,

$$m_h \leq \min(m_A, M_Z)|\cos 2\beta| \leq M_Z. \tag{2.84}$$

If the light Higgs boson is considered as a candidate of the discovered Higgs state at $\sim 125.7\,\text{GeV}$, large radiative corrections to m_h are needed to lift the mass to the observed value, as will be discussed below. Note also the sum rule $m_h^2 + m_H^2 = m_A^2 + M_Z^2$ at tree-level.

The mixing angle α of the $\mathcal{CP}$-even Higgs bosons, defined by

$$\begin{pmatrix} H \\ h \end{pmatrix} = \begin{pmatrix} \cos\alpha & \sin\alpha \\ -\sin\alpha & \cos\alpha \end{pmatrix} \begin{pmatrix} h_1^0 \\ h_2^0 \end{pmatrix}, \tag{2.85}$$

is given by

$$\tan 2\alpha = \frac{m_A^2 + M_Z^2}{m_A^2 - M_Z^2} \tan 2\beta, \qquad \text{with} \quad -\frac{\pi}{2} \leq \alpha \leq 0. \tag{2.86}$$

Together with $\tan\beta$, the mixing angle α determines the tree-level couplings of the neutral Higgs bosons to fermions and gauge bosons. These are listed in Tab. 2.8, where the couplings g are normalized to the corresponding SM Higgs coupling, Eq. (2.25). The Higgs couplings to the electroweak gauge bosons, $V = W^\pm, Z$, are shared between the $\mathcal{CP}$-even Higgs bosons, such that their squares add up to the SM Higgs coupling squared[31]:

$$g_{hVV}^2 + g_{HVV}^2 = 1. \tag{2.87}$$

In contrast, there is no tree-level coupling of the pseudoscalar Higgs A to gauge bosons. Due to Eq. (2.87), the tree-level predictions of M_W, M_Z and $\cos^2\theta_W$ are the same as in the SM, and thus also $\rho = 1$ at tree-level.

The tree-level couplings of the neutral Higgs bosons to fermions feature a strong $\tan\beta$ de-

[31] In fact, this sum rule generalizes to arbitrary models with extended Higgs sectors consisting only of $\text{SU}(2)_L$ doublets and singlets, $\sum_i g_{\Phi_i VV}^2 = 1$, with Φ_i denoting the neutral Higgs states.

Higgs boson Φ	$g_{\Phi uu}$	$g_{\Phi dd}$, $g_{\Phi\ell\ell}$	$g_{\Phi VV}$ $(V = W^\pm, Z)$	$g_{\Phi AZ}$	$g_{\Phi H^\pm W^\mp}$
h	$\cos\alpha/\sin\beta$	$-\sin\alpha/\cos\beta$	$\sin(\beta-\alpha)$	$\cos(\beta-\alpha)$	$\mp\cos(\beta-\alpha)$
H	$\sin\alpha/\sin\beta$	$\cos\alpha/\cos\beta$	$\cos(\beta-\alpha)$	$-\sin(\beta-\alpha)$	$\pm\sin(\beta-\alpha)$
A	$\cot\beta$	$\tan\beta$	0	0	1

Table 2.8: Tree-level couplings of the neutral MSSM Higgs bosons $\Phi = h, H, A$. The middle columns give the Higgs couplings to up-type quarks, $g_{\Phi uu}$, down-type quarks and charged leptons, $g_{\Phi dd}$ and $g_{\Phi\ell\ell}$, respectively, and electroweak gauge bosons, $g_{\Phi VV}$ $(V = W^\pm, Z)$. These couplings are normalized to the corresponding coupling of the SM Higgs boson, Eq. (2.25). The pseudoscalar Higgs boson coupling to fermions features also an additional factor of $i\gamma_5$ that is omitted here. The last two columns give the couplings to the pseudoscalar Higgs boson A and a Z boson, $g_{\Phi AZ}$, and to the charged Higgs boson $H^\pm$ and W boson, $g_{\Phi H^\pm W^\mp}$. These are normalized to $g_Z = M_Z/v$ and $g_W = M_W/v$, respectively.

pendence. This can be seen explicitly if we rewrite the expressions given in Tab. 2.8 as

$$\begin{aligned} g_{hdd} = g_{h\ell\ell} &= -\frac{\sin\alpha}{\cos\beta} = \sin(\beta-\alpha) - \tan\beta\cos(\beta-\alpha), \\ g_{huu} &= \frac{\cos\alpha}{\sin\beta} = \sin(\beta-\alpha) + \cot\beta\cos(\beta-\alpha), \\ g_{Hdd} = g_{H\ell\ell} &= \frac{\cos\alpha}{\cos\beta} = \cos(\beta-\alpha) + \tan\beta\sin(\beta-\alpha), \\ g_{Huu} &= \frac{\sin\alpha}{\sin\beta} = \cos(\beta-\alpha) - \cot\beta\sin(\beta-\alpha). \end{aligned} \tag{2.88}$$

The Higgs couplings to down-type quarks and charged leptons is enhanced by a factor $\tan\beta$, depending on the magnitude of $\cos(\beta-\alpha)$, whereas the couplings to up-type quarks is simultaneously suppressed. A similar behavior can be observed for the pseudoscalar Higgs boson A, cf. Tab. 2.8.

We also list in Tab. 2.8 the neutral Higgs boson coupling to the pseudoscalar Higgs boson A and a Z boson, $g_{\Phi AZ}$, as well as the coupling to the charged Higgs boson $H^\pm$ and W boson, $g_{\Phi H^\pm W^\mp}$. These couplings do not exist in the SM. The normalization factors of these couplings are $g_Z = M_Z/v$ and $g_W = M_W/v$, respectively. More details and expressions for the remaining Higgs couplings (e.g. the charged Higgs couplings, self-couplings, couplings to SUSY particles, etc.) can e.g. be found in Refs. [15, 24].

The decoupling limit

An important limit of extended Higgs sectors is the *decoupling limit* [196]. In the MSSM it is obtained by taking m_A very large, $m_A \to \infty$. In practice, the decoupling limit is already approximately reached for $m_A \gtrsim 300\,\text{GeV}$. In this limit we have at tree-level

$$\begin{aligned} m_h^2 &\longrightarrow M_Z^2\cos^2 2\beta, \\ m_H^2 &\longrightarrow m_A^2 + M_Z^2\sin^2 2\beta, \\ |\cos(\beta-\alpha)| &\longrightarrow \frac{M_Z^2}{2m_A^2}|\sin 4\beta|, \end{aligned} \tag{2.89}$$

and thus we are left with one light Higgs boson h, while the other Higgs states are very heavy and degenerate in mass, $m_A \sim m_H \sim m_{H^\pm}$. Moreover, the tree-level couplings of the neutral Higgs bosons to the electroweak gauge bosons, $V = W^\pm, Z$, behave as [24]

$$\begin{aligned} g_{hVV} = \sin(\beta-\alpha) &\xrightarrow{m_A \gg M_Z} 1 - \frac{M_Z^4}{8M_A^4}\sin^2 4\beta \xrightarrow{\tan\beta \gg 1} 1 - \frac{2M_Z^4}{M_A^4 \tan^2\beta} \to 1, \\ g_{HVV} = \cos(\beta-\alpha) &\xrightarrow{m_A \gg M_Z} \frac{M_Z^2}{2M_A^2}\sin 4\beta \xrightarrow{\tan\beta \gg 1} - \frac{2M_Z^2}{M_A^2 \tan\beta} \to 0, \end{aligned} \tag{2.90}$$

i.e. the light $\mathcal{CP}$-even Higgs-gauge boson coupling g_{hVV} approaches the SM value while the heavy $\mathcal{CP}$-even Higgs boson decouples. As can be seen, the decoupling limit is reached more quickly if $\tan\beta$ is large. The behavior of the neutral Higgs couplings to fermions in the decoupling limit can be seen by applying the approximations of Eq. (2.90) in Eq. (2.88), leading to $g_{huu} \to 1$, $g_{hdd} \to 1$ and $g_{Huu} \to -\cot\beta$, $g_{Hdd} \to \tan\beta$. Thus, in the decoupling limit, the light $\mathcal{CP}$-even Higgs boson h of the MSSM becomes indistinguishable from the SM Higgs boson.

Radiative corrections

As stated earlier, large radiative corrections to the light Higgs mass, m_h, are needed to increase its value significantly beyond M_Z, e.g., to the observed Higgs boson mass of $\sim 125.7\,\text{GeV}$. Beyond tree-level, the MSSM Higgs boson masses depend in general on the full MSSM particle spectrum, however, most strongly on the stop and (if $\tan\beta$ is large) the sbottom sector as well as on the gluino mass. In the decoupling limit, $m_A \gg M_Z$, the dominant 1-loop corrections at $\mathcal{O}(y_t^2)$ are given by [239–241]

$$\delta m_h^2 = \frac{3g_2^2\, m_t^4}{8\pi^2 M_W^2}\left[\ln\left(\frac{M_S^2}{m_t^2}\right) + \frac{X_t^2}{M_S^2}\left(1 - \frac{1}{12}\frac{X_t^2}{M_S^2}\right)\right], \tag{2.91}$$

where the stop mixing parameter X_t is given by Eq. (2.69). We furthermore defined $M_S \equiv \sqrt{m_{\tilde{t}_1} m_{\tilde{t}_2}}$ as a representative SUSY mass scale. The first term in Eq. (2.91) contains the logarithmic corrections from the mass difference between the top quark and its superpartner(s), which we already encountered in the discussion of the hierarchy problem, cf. Section 2.3. The second term is introduced from left-right mixing in the stop sector. This 1-loop correction is maximized for $X_t \approx \sqrt{6} M_S$.

Beyond these corrections, leading and subleading parts of the known two-loop calculations have been implemented in public codes. In a Feynman diagrammatic (FD) approach, as e.g. followed by the public computer code `FeynHiggs` [155–157]which we use in this work, generally the on-shell (OS) renormalization scheme is employed. `FeynHiggs` includes all (sub)dominant two-loop corrections to the neutral Higgs boson masses [155–157, 242]. Recently, these fixed-order calculations have been combined with an all-order resummation of the leading and subleading contributions from the stop sector [242] (available in `FeynHiggs-2.10.0` and higher), which becomes important for $M_S \gtrsim$ few TeV. Other codes, e.g. `CPsuperH` [243] and `SPheno` [244], obtain their results using the renormalization group improved effective potential approach [241, 245], where the parameters are defined in the $\overline{\text{MS}}$ renormalization scheme. Hence, the parameters X_t and M_S (which are most relevant for the neutral Higgs boson mass corrections) are scheme-dependent, and this difference must be taken into account when comparing the results[32]. In

[32] Approximate formulae for the conversion of the OS quantities into $\overline{\text{MS}}$ quantities are given in Refs. [241, 246].

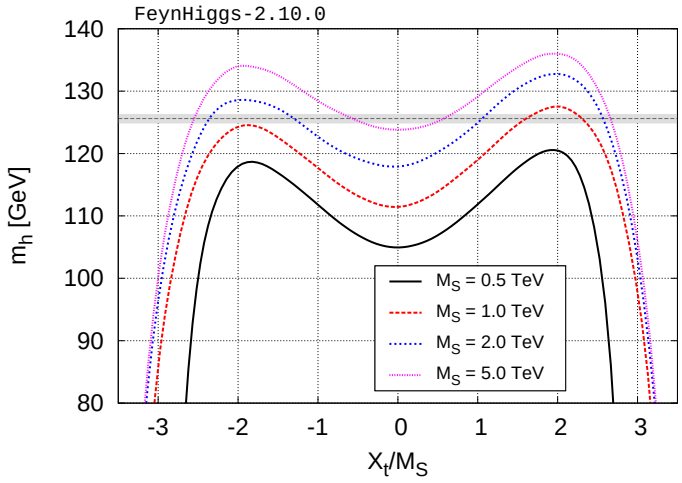

Figure 2.13: Prediction of the light Higgs boson mass, m_h, as a function of the (on-shell) stop mixing parameter X_t/M_S for various values of $M_S = m_{\tilde{t}_L} = m_{\tilde{t}_R} = m_{\tilde{b}_L} = m_{\tilde{b}_R}$, obtained with `FeynHiggs-2.10.0` [155–157, 242]. We furthermore set $\tan\beta = 10$, $\mu = M_2 = m_A = m_{\tilde{\ell}} = 1\,\text{TeV}$ and the gluino and first/second generation squark masses to $m_{\tilde{g}} = m_{\tilde{q}_L} = m_{\tilde{q}_R} = 1.5\,\text{TeV}$. The gray dashed line and area indicate the experimental 2σ range of the Higgs mass measurement, $\hat{m}_H \approx 125.7 \pm 0.7$ GeV.

the on-shell scheme, the full known radiative corrections to the lightest Higgs boson mass are maximized for $X_t^{\text{OS}} \approx 2M_S^{\text{OS}}$ (see below). The theoretical uncertainty of the light neutral Higgs mass prediction is estimated to be $\Delta m_h \lesssim 3\,\text{GeV}$, depending on the SUSY parameter region, and is mainly due to differences in the renormalization schemes [156, 160, 247].

We show the predicted light Higgs mass, m_h, as a function of the stop mixing, X_t/M_S, for various M_S values in Fig. 2.13, as obtained with `FeynHiggs-2.10.0`. Here, we assumed equal third generation squark soft-breaking masses, $M_S = m_{\tilde{t}_L} = m_{\tilde{t}_R} = m_{\tilde{b}_L} = m_{\tilde{b}_R}$, and set $\tan\beta = 10$, $\mu = M_2 = m_A = 1\,\text{TeV}$, and the first and second generation squark and gluino masses to 1.5 TeV. We further assume universal soft-breaking slepton masses of 1 TeV and universality of the trilinear couplings, Eq. (2.57). M_1 is derived from M_2 via the GUT relation in Eq. (2.63).

Fig. 2.13 clearly shows that the Higgs mass is maximized for the on-shell parameters $X_t \approx 2M_S$. For a not too large SUSY mass scale, $M_{\text{SUSY}} \lesssim$ few TeV, the radiative corrections can increase the light Higgs mass up to $m_h \lesssim 135\,\text{GeV}$, thus we can reach Higgs masses that are well compatible with the Higgs discovery (indicated by the gray area). In Fig. 2.13, we need an average stop mass of $M_S \gtrsim 1\,\text{TeV}$ to reach $m_h \sim 125.7\,\text{GeV}$. However, light stop masses, $m_{\tilde{t}_1} \gtrsim 300\,\text{GeV}$, may still be viable if the assumptions on the remaining parameters (in particular on the soft-breaking stop masses) are relaxed, as will be discussed in Chapter 6.

While the radiative corrections to the Higgs mass depend only logarithmically on the stop masses, the minimization condition in Eq. (2.80) receives (1-loop) corrections which are quadratically dependent on the soft-breaking mass parameters [248]. Minimization of the one-loop

In the following numerical results, we will refer to the OS quantities and omit the superscript 'OS'.

effective scalar potential leads to [249]

$$\frac{M_Z^2}{2} = \frac{m_{H_1}^2 + \Sigma_d^d - (m_{H_2}^2 + \Sigma_u^u)\tan^2\beta}{\tan^2\beta - 1} - \mu^2 \tag{2.92}$$

where Σ_u^u and Σ_d^d describe the radiative corrections. They include contributions from (s)particles with sizable Yukawa and/or gauge couplings to the Higgs sector and feature a quadratic dependence on the corresponding soft-breaking mass parameters. In order to obtain a *natural* value of the Z boson mass on the left-hand side of Eq. (2.92), each term on the right-hand side should not be too far from the EW energy scale $\sim M_Z$. The fact that we however need stop masses $\gtrsim 300\,\text{GeV}$ in order to increase m_h to the observed value $125.7\,\text{GeV}$ makes a certain amount of fine-tuning unavoidable[33]. This is sometimes called *Little Hierarchy Problem* [249, 250, 252].

Beyond tree-level the neutral Higgs couplings receive very similar corrections as the neutral Higgs boson masses, Eq. (2.91). The $\mathcal{CP}$-even Higgs mixing angle α, given by Eq. (2.86) at tree-level, is now obtained from diagonalizing the radiatively corrected $\mathcal{CP}$-even Higgs mass matrix. Using this corrected angle, $\alpha \to \alpha_{\text{eff}}$, the expressions of the Higgs-gauge boson couplings in Tab. 2.8 are unchanged.

The radiative corrections to the Higgs-fermion couplings are slightly more complicated. Additional one-loop vertex corrections modify the tree-level Lagrangian, such that small contributions to the top (bottom) quark Yukawa couplings are generated by the 'wrong' Higgs doublet H_1 (H_2). In case of the neutral $\mathcal{CP}$-even Higgs boson couplings to bottom quarks, we can write [253, 254]

$$g_{hbb} = \frac{1}{1+\Delta_b}\left(-\frac{\sin\alpha_{\text{eff}}}{\cos\beta} + \Delta_b\frac{\cos\alpha_{\text{eff}}}{\sin\beta}\right), \tag{2.93}$$

$$g_{Hbb} = \frac{1}{1+\Delta_b}\left(\frac{\cos\alpha_{\text{eff}}}{\cos\beta} + \Delta_b\frac{\sin\alpha_{\text{eff}}}{\sin\beta}\right). \tag{2.94}$$

There are two main contributions to the threshold correction Δ_b, an $\mathcal{O}(\alpha_s)$ correction from a sbottom-gluino loop and an $\mathcal{O}(y_t^2)$ contribution from a stop-higgsino loop. For $M_S \gg m_t$ and $\tan\beta \gg 1$, these two contributions read

$$\Delta_b = \frac{2\alpha_s}{3\pi} m_{\tilde{g}}\mu\tan\beta \times I(m_{\tilde{b}_1}^2, m_{\tilde{b}_2}^2, m_{\tilde{g}}^2) + \frac{y_t^2}{16\pi^2} A_t\mu\tan\beta \times I(m_{\tilde{t}_1}^2, m_{\tilde{t}_2}^2, \mu^2), \tag{2.95}$$

with the function I given by

$$I(a,b,c) = \frac{ab\ln(a/b) + bc\ln(b/c) + ca\ln(c/a)}{(a-b)(b-c)(c-a)} \sim \frac{1}{\max(a,b,c)}. \tag{2.96}$$

The Δ_b corrections can become important for large values of $\tan\beta$ and of μ, A_t and the gluino mass $m_{\tilde{g}}$ (with respect to M_S) [255]. For $\mu, m_{\tilde{g}}, A_t > 0$, the Δ_b correction is positive, leading to a suppression of the bottom Yukawa coupling. However, Δ_b can also be negative, potentially resulting in a strong enhancement of the bottom Yukawa coupling as $\Delta_b \to -1$.

[33] This fine-tuning can be reduced in non-minimal supersymmetric models by e.g. adding Higgs singlet(s) to the theory [250, 251].

Genuine MSSM Higgs processes at colliders

The additional Higgs bosons of the MSSM Higgs sector give rise to a plethora of novel collider processes that are absent in the SM. Moreover, SUSY particles may be directly connected to the Higgs boson phenomenology, both as potential Higgs boson decay products or mother particles, i.e. particles that decay into Higgs bosons. A detailed discussion of this rich collider phenomenology can e.g. be found in Refs. [24, 35]. Here, we only give a brief qualitative survey of the main genuine MSSM Higgs processes relevant to past and present collider experiments.

At e^+e^- colliders, both neutral and charged Higgs bosons can be produced in pairs via the processes

$$e^+e^- \to Z^* \to \Phi A, \quad (\Phi = h, H) \tag{2.97}$$
$$e^+e^- \to \gamma/Z^* \to H^+H^-, \tag{2.98}$$

respectively.

The neutral Higgs boson pair production process, Eq. (2.97), is complementary to the Higgs-strahlung process $e^+e^- \to Z\Phi$ (with $\Phi = h, H$), since the corresponding couplings are $g^2_{hAZ} = \cos^2(\beta-\alpha)$ and $g^2_{hZZ} = \sin^2(\beta-\alpha)$ (and vice versa for the heavy $\mathcal{CP}$-even Higgs boson H), respectively, cf. Tab. 2.8. In the limit $g^2_{hAZ} \simeq 1$, searches for the process in Eq. (2.97) at LEP, focussing on the $4b$, $2b2\tau$ and 4τ final states, resulted in 95% C.L. lower limits on the h and A boson masses,

$$m_h > 91.0\,\text{GeV} \quad \text{and} \quad m_A > 91.9\,\text{GeV}, \tag{2.99}$$

respectively [256]. More importantly, the LEP experiments provided model-independent cross section limits on the pair production process [257]. These limits are very useful to constrain models with extended Higgs sectors beyond those investigated by the experimental collaborations, see e.g. Sections 4.1.4 and 6.1.

The tree-level cross section of the charged Higgs pair production process, Eq. (2.98), only depends on the charged Higgs boson mass, $m^\pm_H$, since the H^+H^-Z tree-level coupling is prescribed solely by the gauge interactions. LEP searches for this process, with the subsequent charged Higgs decays $H^+ \to c\bar{s}$ and $H^+ \to \tau^+\nu_\tau$, yielded a lower 95% C.L. mass bound of [258, 259]

$$m_{H^\pm} > 80.0\,\text{GeV}. \tag{2.100}$$

Charged Higgs bosons can also be searched for at hadron colliders. If the charged Higgs boson mass is below the top quark mass, $m_{H^\pm} \lesssim 170\,\text{GeV}$, it can be produced via the top quark decay $t \to H^+b$. The corresponding coupling is proportional to the combination

$$g_{H^\pm tb} \propto m_b \tan\beta(1+\gamma_5) + m_t \cot\beta(1-\gamma_5), \tag{2.101}$$

such that the $t \to H^+b$ decay can compete with the standard $t \to W^+b$ decay for very small $\tan\beta \sim 1$ and large $\tan\beta \gtrsim 30$. The coupling strength, Eq. (2.101), is minimal at $\tan\beta = \sqrt{m_t/m_b} \simeq 6$.

Searches for a light charged Higgs boson at the LHC experiments ATLAS [260, 261] and CMS [262, 263] mainly focus on top quark pair production, where one top quark decays via $t \to H^+b$ with subsequent decay $H^+ \to \tau^+\nu_\tau$. These searches severely constrain the low m_A

region, in particular, scenarios where the heavier $\mathcal{CP}$-even Higgs boson could be interpreted as the discovered Higgs state, cf. Chapter 6. In the future, at an increased CM energy $\sqrt{s} \sim 13/14\,\text{TeV}$ and higher integrated luminosity, charged Higgs production in association with a top quark or W boson, or even charged Higgs pair production processes become relevant at the LHC to probe charged Higgs boson masses beyond m_t.

Novel collider signatures also appear due to possible Higgs-to-Higgs decays. Assuming that the discovered Higgs state is the lighter Higgs boson h, experimental searches for heavy Higgs boson production with subsequent decays $H \to hh$ and $A \to Zh$ can be performed, see e.g. Ref. [264] for a recent CMS analysis. Furthermore, the possible appearance of the SM-like Higgs boson in SUSY particle decay chains provides novel collider signatures that can be probed at the LHC [265].

Benchmark scenarios for MSSM Higgs searches

The definition of MSSM benchmark scenarios provides a useful framework for presenting experimental results of MSSM Higgs searches at the LEP, Tevatron and LHC experiments. These benchmark scenarios are typically chosen to be two-dimensional slices of the pMSSM parameter space, cf. Section 2.4.2, which represent distinct phenomenological aspects that are interesting for direct searches at colliders. The LEP, Tevatron and LHC experiments have made extensive use of the scenarios suggested in Refs. [255, 266–268], see e.g. Ref. [257]. Recently, updated scenarios have been suggested in Ref. [246] to account for the Higgs boson discovery and improved limits on SUSY particles from direct searches at the LHC. Here, we briefly introduce three of these updated benchmark scenarios, the m_h^{max}, $m_h^{\text{mod+}}$ and low-M_H scenario, as these are used later in this thesis.

In all following benchmark scenarios, the first and second generation squark and slepton soft-breaking masses as well as trilinear couplings are fixed to

$$\begin{aligned} M_{\tilde{q}} = M_{\tilde{u}} = M_{\tilde{d}} &= 1500\,\text{GeV}, \\ M_{\tilde{\ell}} = M_{\tilde{e}} &= 500\,\text{GeV}, \\ A_e = A_u = A_d &= 0\,\text{GeV}, \end{aligned} \tag{2.102}$$

since these have only a minor impact on the MSSM Higgs sector predictions. The bino mass, M_1, is fixed via the GUT relation, Eq. (2.63). Another assumption is the universality of third generation squark soft-breaking masses,

$$M_{\tilde{t}_L} = M_{\tilde{b}_L} = M_{\tilde{t}_R} = M_{\tilde{b}_R} \equiv M_{\text{SUSY}}, \tag{2.103}$$

as well as universality of the trilinear couplings of the third generation squarks and sleptons,

$$A_t = A_b = A_\tau. \tag{2.104}$$

For the top quark mass a value of $m_t = 173.2\,\text{GeV}$ is used[34] [269].

- **The (updated) $\mathbf{m_h^{max}}$-scenario**

  The m_h^{max} scenario was originally defined in Refs. [266, 268]. The stop mixing parameter X_t is chosen such that the radiative corrections to the lightest $\mathcal{CP}$-even Higgs boson mass,

[34] The top quark mass value has recently been updated [75]. The new value is obtained from a combination of Tevatron and LHC results and is given in Eq. (2.34).

cf. Eq. (2.91), are maximized. Given the mass measurement of the discovered Higgs state from the LHC, $\hat{m}_H \sim 125.7\,\text{GeV}$, and assuming that this state is indeed the lightest $\mathcal{CP}$-even Higgs boson of the MSSM, lower bounds on m_A, $m_{H^\pm}$ and $\tan\beta$ can be derived using this scenario [270].

The fixed parameters of the updated m_h^{max} scenario are given by

$$\begin{aligned} M_{\text{SUSY}} = 1000\,\text{GeV}, \quad \mu = 200\,\text{GeV}, \quad M_2 = 200\,\text{GeV}, \quad m_{\tilde{g}} = 1500\,\text{GeV}, \\ M_{\tilde{\tau}_L} = M_{\tilde{\tau}_R} = 1000\,\text{GeV}, \quad X_t^{\text{OS}} = 2\ M_{\text{SUSY}}, \quad (X_t^{\overline{\text{MS}}} = \sqrt{6}\ M_{\text{SUSY}}), \end{aligned} \tag{2.105}$$

leaving m_A and $\tan\beta$ as free parameters. Here, X_t is both given for the on-shell (OS) and $\overline{\text{MS}}$ renormalization schemes.

In fact, this choice of maximal stop mixing, $X_t^{\text{OS}} = 2\ M_{\text{SUSY}}$, can easily lead to a too large prediction of the lightest Higgs mass, m_h, at larger values of $\tan\beta \gtrsim 10$ and moderately large values of $m_A \gtrsim 300\,\text{GeV}$. Hence, only a rather small strip in the $(m_A, \tan\beta)$ plane is consistent with the observed mass value of $\sim 125.7\,\text{GeV}$.

Note, that for large parts of the m_h^{max}-scenario, in particular at relatively low values of $\tan\beta \lesssim 10$, the heavy Higgs boson decay mode $\text{BR}(H \to hh)$ as well as decays into charginos and neutralinos can be sizable. At larger values of $\tan\beta$ the couplings of the heavy $\mathcal{CP}$-even and pseudoscalar Higgs boson to down-type fermions is enhanced and thus the search for $H/A \to \tau\tau$ is most sensitive.

- **The $\mathbf{m_h^{mod+}}$-scenario**

  The $m_h^{\text{mod+}}$-scenario is a slight modification of the m_h^{max}-scenario, where the issue of a too large lightest $\mathcal{CP}$-even Higgs mass is addressed (see above). The scenario is obtained from Eq. (2.105) by a simple change of the stop mixing parameter X_t to

$$X_t^{\text{OS}} = 1.5\ M_{\text{SUSY}}, \quad (X_t^{\overline{\text{MS}}} = 1.6\ M_{\text{SUSY}}), \tag{2.106}$$

  which decreases the radiative corrections to the lightest Higgs mass, Eq. (2.91), cf. also Fig. 2.13. Consequently, large parts of the $(m_A, \tan\beta)$ plane are consistent with the observed mass value of $\sim 125.7\,\text{GeV}$ in this benchmark scenario.

  Note, that there is also a variant called $m_h^{\text{mod-}}$-scenario, where X_t is chosen to be negative. This scenario is very similar to the $m_h^{\text{mod+}}$-scenario in its Higgs phenomenology, however, it has distinct predictions for the low energy observables $(g-2)_\mu$, $\text{BR}(b \to s\gamma)$ and $\text{BR}(B_s \to \mu\mu)$ [271].

- **The low-$\mathbf{M_H}$ scenario**

  In principle, the heavier $\mathcal{CP}$-even Higgs boson H can be identified with the discovered Higgs state at $\sim 125.7\,\text{GeV}$ in the MSSM. This was pointed out in Refs. [270, 272–274] and will be discussed in more detail in Chapter **??**. In this case, the MSSM Higgs sector is very different to the SM case as all five MSSM Higgs bosons would be light. Thus, this interpretation is not possible in the decoupling limit. In fact, the parameter region where the heavier $\mathcal{CP}$-even Higgs bosons obtains SM-like couplings is rather known as the *anti-decoupling regime* [24].

The low-M_H-scenario is designed as a representative benchmark for this alternative interpretation. The parameters are chosen to be

$$M_{\text{SUSY}} = 1500\,\text{GeV}, \quad M_A = 110\,\text{GeV}, \quad M_2 = 200\,\text{GeV}, \quad m_{\tilde{g}} = 1500\,\text{GeV},$$
$$M_{\tilde{\tau}_L} = M_{\tilde{\tau}_R} = 1000\,\text{GeV}, \quad X_t^{\text{OS}} = 2.45\ M_{\text{SUSY}}, \quad (X_t^{\overline{\text{MS}}} = 2.9\ M_{\text{SUSY}}), \tag{2.107}$$

with μ and $\tan\beta$ left as free parameters. In this scenario, the light $\mathcal{CP}$-even Higgs boson h has a rather low mass $\lesssim 100\,\text{GeV}$ and reduced couplings to electroweak gauge bosons. The charged Higgs boson is about 132 GeV, hence the top quark decay mode $t \to H^\pm b$ is kinematically open.

Already at the time of its proposal [246], this benchmark scenario was severely constrained by various MSSM Higgs searches, in particular from $h/H/A \to \tau\tau$ searches[35], light charged Higgs searches in top quark decays, $t \to H^\pm b \to (\tau\nu_\tau)b$ [260, 262], and LEP Higgs searches for the processes $e^+e^- \to Zh$ [90] and $e^+e^- \to Ah$ [257]. We discuss the viability of this scenario in the light of current limits in Chapter 6.

[35] Since all Higgs bosons have very similar masses and MSSM Higgs searches with $\tau\tau$ final states have typically a rather poor mass resolution all three neutral Higgs bosons contribute to the signal.

CHAPTER 3

Experimental Constraints and Evidence from Higgs Boson Collider Searches

In this chapter we give an introduction to how experimental results from Higgs boson collider searches are presented and interpreted. We first discuss the exclusion limits obtained from non-observations in Higgs searches at LEP and the hadron collider experiments at the Tevatron and LHC and then turn to the discussion of the Higgs boson discovery and the mass and signal rate measurements at the LHC.

The exclusion limits and mass/rate measurements from past and present Higgs boson collider searches form the basic experimental input of the computer programs `HiggsBounds` and `HiggsSignals`, respectively, which are presented in Chapter 4.

3.1 Exclusion Limits from Higgs boson collider searches

In the LEP era, important methods for the statistical analysis of null results from Higgs searches (and other collider searches) were developed, most importantly, the CL_s method [275]. It addresses the following question: How should a possible formal signal exclusion be treated, which originates from a statistical downward fluctuation of the observed data with respect to the background expectation, in cases where the sensitivity of the experiment in fact was not high enough to yield this exclusion? This is done by allowing a conservative modification of the statistical coverage by defining the quantity

$$\mathrm{CL}_s \equiv \frac{\mathrm{CL}_{s+b}}{\mathrm{CL}_b}, \tag{3.1}$$

where CL_{s+b} [CL_b] is the confidence of the *signal plus background* $(s+b)$ [*background* (b)] hypothesis. They are truely frequentist probabilities as obtained when the experiment is repeated many times for the underlying hypothesis being true. In contrast, CL_s is not strictly a frequentist confidence as it features over-coverage. In other words, since $\mathrm{CL}_b \leq 1$, we have $\mathrm{CL}_s \geq \mathrm{CL}_{s+b}$. Still, an exclusion at 95% C.L., i.e. the probability of a false signal rejection on the basis of a statistical fluctuation being 5%, is conventionally claimed if $\mathrm{CL}_s < 0.05$, although the actual confidence level of the exclusion may be higher. Nevertheless, in the limit of low signal yields, $s + b \approx b$, a significant downward fluctuation of the data that would cause an exclusion of the

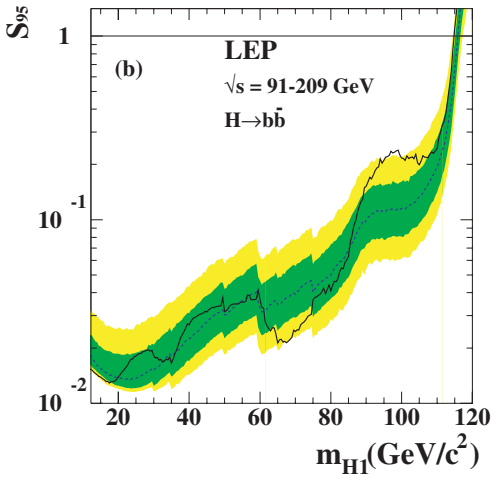

(a) The 95% C.L. upper limit, S_{95}, on the SM normalized cross section of the signal topology $e^+e^- \to ZH \to Z(b\bar{b})$ as a function of the Higgs boson mass [90]. The solid (dashed) line represents the observed (expected) limit. The green (yellow) bands give the 68 (95)% C.L. region around the expected limit. The horizontal line, $S_{95} = 1$, corresponds to the SM prediction.

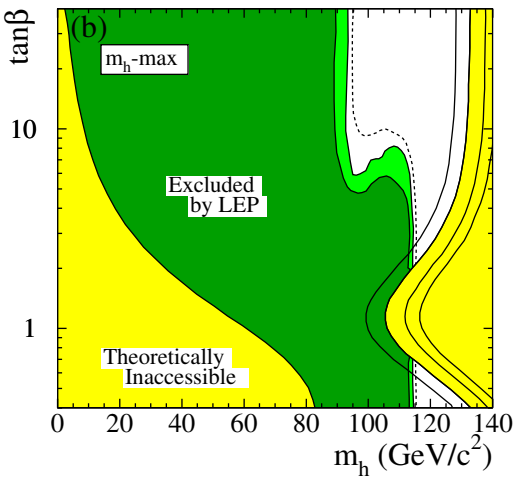

(b) Excluded regions within the $m_h^{\max}$ MSSM benchmark scenario, cf. Section 2.4.3, from a combination of different search channels at LEP. The yellow, light and dark green areas indicate theoretically inaccessible, 95% C.L. and 99% C.L. excluded parameter regions, respectively. The dashed line shows the 95% C.L. expected exclusion. At larger Higgs masses m_h, the different black contours represent different values of the top mass between 165 and 180 GeV.

Figure 3.1: Examples for exclusion limits obtained from the combination of Higgs searches of all four LEP experiments: (a) model-independent cross section limits on the signal topology $e^+e^- \to ZH \to Z(b\bar{b})$; (b) model-dependent interpretation within the $m_h^{\max}$ MSSM benchmark scenario. Figures are taken from Ref. [257].

pure $s+b$ hypothesis, $\mathrm{CL}_{s+b} < 5\%$, cannot exclude the signal anymore, since $\mathrm{CL}_{s+b} \approx \mathrm{CL}_b$ and thus $\mathrm{CL}_s \approx 1$. This is wanted, since in this case the experiment is regarded not to be sensitive to exclude the signal due to the very low expected signal yield. In the experimental analysis, the confidences CL_{s+b} and CL_b are calculated from the probability density functions (pdfs) of $-2\ln(Q)$ for the underlying hypotheses $s+b$ and b, respectively, where the test statistics $Q = \mathcal{L}_{s+b}/\mathcal{L}_b$ is the ratio of the likelihoods for the two tested hypotheses, see Ref. [276] for an introduction.

The exclusion limits from null results in Higgs searches can generally be presented in two ways by the experimental collaborations: In the first type the exclusion is presented as a limit on the topological cross section of the signal process that has been searched for, which is typically normalized to a well known reference cross section, e.g. the cross section predicted for a SM Higgs boson. The limit is then presented as a function of the mass(es) of the involved Higgs boson(s). The signal process may consist of several signal topologies, each comprised of a Higgs production mode $P_j(H)$ and a decay mode $D_j(H)$. Each signal topology then enters with a signal efficiency (or acceptance) ϵ^j that is specific to the experimental analysis. Examples of such *inclusive* analyses are most searches for a SM Higgs boson, in which all relevant production modes are combined in order to maximize the discovery (or exclusion) reach. The limit is then

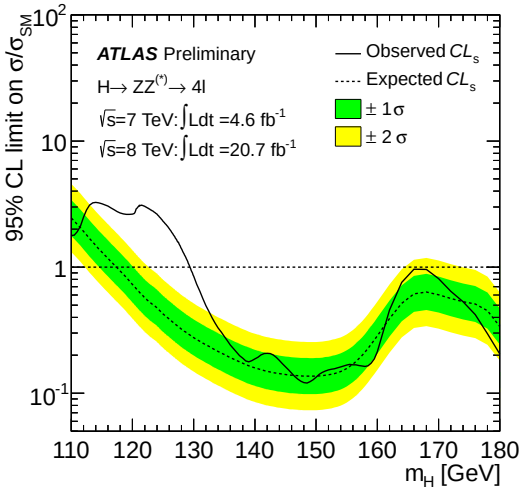

(a) 95% C.L. upper limit on the SM signal strength modifier μ, Eq. (3.2), for the inclusive Higgs channel $pp \to H \to ZZ^{(*)} \to 4\ell$ from ATLAS [277].

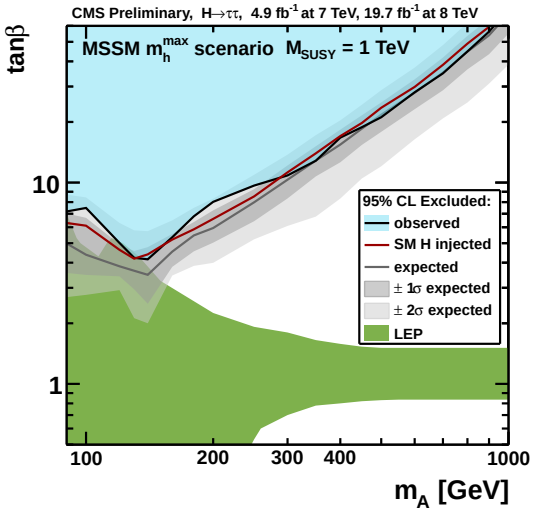

(b) Interpretation within the $m_h^{\max}$ scenario of the CMS MSSM Higgs boson search $h/H/A \to \tau\tau$ [278]. The LEP excluded area (green) corresponds to the 95% C.L. exclusion shown in Fig. 3.1(b).

Figure 3.2: Examples for current LHC 95% C.L. exclusion limits: (a) upper limit on the SM signal strength modifier $\mu = \sigma/\sigma_{SM}$ from the ATLAS SM Higgs search $H \to ZZ^* \to 4\ell$; (b) model-dependent interpretation of the CMS MSSM Higgs search with di-tau-lepton final states, $h/H/A \to \tau\tau$, within the $m_h^{\max}$ MSSM benchmark scenario.

set on a universal scale factor of the SM signal rate, the *signal strength modifier*

$$\mu = \frac{\sum_j \epsilon^j \, \sigma(P_j(H)) \times \mathrm{BR}(D_j(H))}{\sum_j \epsilon^j \, \sigma_{\mathrm{SM}}(P_j(H)) \times \mathrm{BR}_{\mathrm{SM}}(D_j(H))}, \tag{3.2}$$

with the sums running over all considered signal topologies. The 95% C.L. upper limit on μ is sometimes denoted by S_{95} (in LEP results) or μ_{95}.

If all efficiencies ϵ_j are made public with the limit on μ, or if only one signal topology is considered, the presented limit is *model-independent* and can be applied to BSM models straight-forwardly. This is the main purpose of the program `HiggsBounds` which will be discussed in Chapter 4. Unfortunately, the signal efficiencies ϵ_j are rarely quoted in a sufficient way and care has to be taken when applying these limits to models that are different to the one investigated by the experiment. This is discussed in more detail in Section 4.1.2.

An example of this type of exclusion limit is given in Fig. 3.1(a) for the combined LEP searches for $e^+e^- \to ZH \to Z(bb)$ [90, 257], yielding the observed 95% C.L. SM Higgs mass limit of $m_H \geq 114.4\,\mathrm{GeV}$. Besides the observed limit, the experiments also provide the expected 95% C.L. exclusion limit (dashed line), which is evaluated from MC simulation and assumes that the observation is identical to be expected background. Thus, the expected limit indicates the overall sensitivity of the analysis to the signal. Another example is given in Fig. 3.2(a) for the ATLAS SM Higgs search in the process $H \to ZZ^* \to 4\ell$ [277]. Here, the sum in Eq. (3.2) runs over the five LHC Higgs production modes, $P_j(H) \in \{\mathrm{ggf}, \mathrm{VBF}, WH, ZH, t\bar{t}H\}$, cf. Section 2.2.3. This limit excludes the SM Higgs boson in the mass range $m_H \gtrsim 130\,\mathrm{GeV}$. The

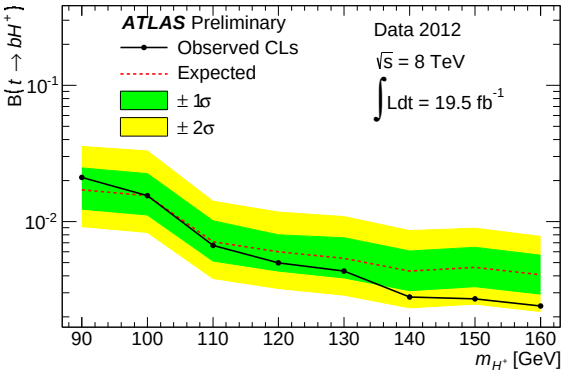

Figure 3.3: Upper 95% C.L. limit on the branching ratio BR($t \to H^+ b$) from the ATLAS light charged Higgs search [261]. The presented exclusion assumes BR($H^+ \to \tau\nu$) = 1.

presence of the Higgs boson signal (cf. Section 3.2) leads to the departure between the expected and observed 95% C.L. upper limit seen in the mass region $m_H \sim 120 - 130\,\text{GeV}$. In fact, after the Higgs boson signal in this region has been established, the underlying background hypothesis of this limit turns out to be a wrong assumption and should be revised to e.g. assuming a SM Higgs boson. The expected exclusion limit, as presented in Fig. 3.2(a), may lead to difficulties if the limit is considered as a constraint on extended Higgs sectors besides other exclusion limits from Higgs searches, see Section 4.1.1 for details.

The second type of how null results from Higgs searches are published by the experiments is the presentation of *model-dependent* interpretations within some of the most popular models, such as the MSSM Higgs benchmark scenarios [257, 259, 279, 280], cf. Section 2.4.3. By performing a full MC simulation of the signal within the investigated model and possibly combining all relevant search channels, the experimental collaborations can set very accurate and powerful exclusions on the considered model parameter space. However, the re-interpretation of these exclusions in terms of *other* models is virtually impossible. Nevertheless, these interpretations are still very useful for the following reasons: Firstly, the observed and expected exclusion limits are indicative for the analyses' sensitivity to the defining phenomenological features of the benchmark models, which represent certain corners of the (higher-dimensional) model parameter space. Based on benchmark studies the experimental analysis can be tuned in order to improve the overall sensitivity to these models. Secondly, the model-dependent limits provide the possibility to study the coverage and performance of model-independent cross section limits by interpreting these within the considered benchmark model and comparing them to the full model analysis.

As examples for model-dependent exclusion limits we give the interpretations within the m_h^{max} scenario in Fig. 3.1(b) for the combined LEP analyses [257] and in Fig. 3.2(b) for the most recent CMS MSSM Higgs search with $\tau\tau$ final states [278].

Besides the few examples of signal channels that have been discussed so far, there exists a plethora of different exclusion limits from the LEP, Tevatron and LHC experiments on the cross sections of the various possible signal channels for various Higgs mass ranges. As briefly discussed in Section 2.4.3, cross section limits also exists for signal processes involving multiple neutral Higgs bosons, for instance from LEP searches for Higgs pair production, $e^+e^- \to h_1 h_2 \to (bb)(bb)$, or Higgs-to-Higgs decays, $e^+e^- \to Zh_2 \to Z(h_1 h_1) \to Z(bb)(bb)$ [257].

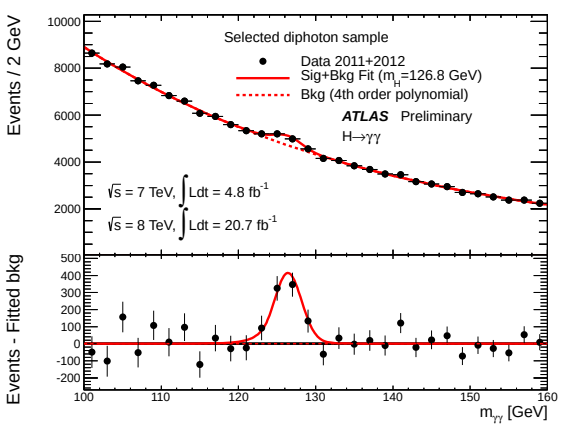

(a) Di-photon invariant mass distribution in the ATLAS $H \to \gamma\gamma$ analysis [3].

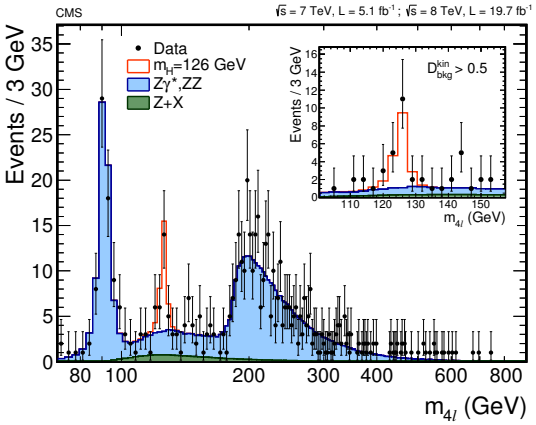

(b) Four-lepton invariant mass distribution in the CMS $H \to ZZ^* \to 4\ell$ analysis [281].

Figure 3.4: Observation of the Higgs boson signal as a narrow resonance in the invariant mass spectrum the $H \to \gamma\gamma$ channel (a) and $H \to ZZ^* \to 4\ell$ channel (b), shown for the ATLAS and CMS result, respectively.

Furthermore, limits on charged Higgs processes come e.g. from LEP searches for charged Higgs pair production [258, 259], Eq. (2.98), or top quark decays into charged Higgs bosons. For the latter, we display in Fig. 3.3 as an example the most recent ATLAS 95% C.L. upper limit[1] on the top quark branching ratio to charged Higgs bosons, $\mathrm{BR}(t \to H^+ b)$. Altogether, these amount to more than 100 different channels that may be still relevant for constraining BSM models. It is the task of the computer program `HiggsBounds` to collect these results and apply them in a consistent way to the Higgs sector predictions of an arbitrary BSM model provided by the user, as will be discussed in Chapter 4.

3.2 The Higgs boson discovery at the LHC

On July 4, 2012 the LHC experiments ATLAS [1] and CMS [2] announced the discovery of a narrow resonance with a mass around 125.7 GeV in the search for the SM Higgs boson. Each experiment quantified the significance of the excess to $\sim 5\sigma$ for the combination of SM Higgs searches, mainly driven by the analyses of the decays modes $H \to \gamma\gamma$, $H \to ZZ^* \to 4\ell$ and, to a lesser extent, $H \to WW^* \to \ell\nu\ell\nu$. Since then, these results have been confirmed and refined using the full 2012 data set, such that the local significance of the excess in ATLAS (CMS) searches has risen to 7.4σ [282] (3.9σ [283]) in the $H \to \gamma\gamma$ channel and 6.6σ [277] (6.8σ [281]) in the $H \to ZZ^* \to 4\ell$ channel. Further excesses found in the $H \to \tau\tau$ channel [284–286], albeit at much lower significances, as well as results from the $H \to bb$ channel from the Tevatron experiments [287] support the findings. Within the current experimental and theoretical uncertainties, both the coupling properties, inferred from the (combination of the) signal strength measurements of individual channels [3, 5, 288], as well as further investigations of the spin and parity properties [4, 6, 277, 281], are in very good agreement with the predictions

[1] In the presented limit the charged Higgs boson is assumed to decay exclusively to tau-leptons, $H^+ \to \tau\nu_\tau$. Nevertheless, the limit can be applied straight-forwardly to the product $\mathrm{BR}(t \to H^+ b) \times \mathrm{BR}(H^+ \to \tau\nu_\tau)$ in the general case.

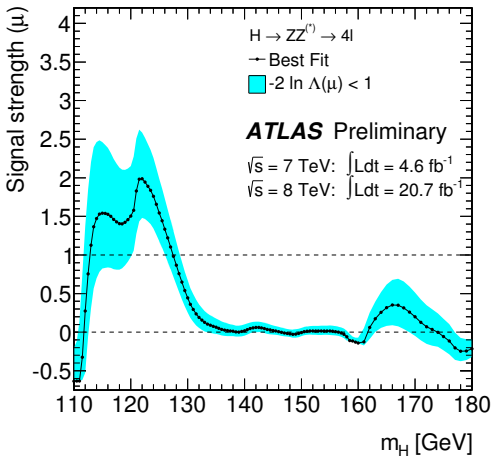

(a) The best-fit signal strength $\hat{\mu}$ for the LHC Higgs process $(pp) \to H \to ZZ^{(*)} \to 4\ell$, given as a function of the assumed Higgs mass m_H. The cyan band gives the 68% C.L. uncertainty of the measurement.

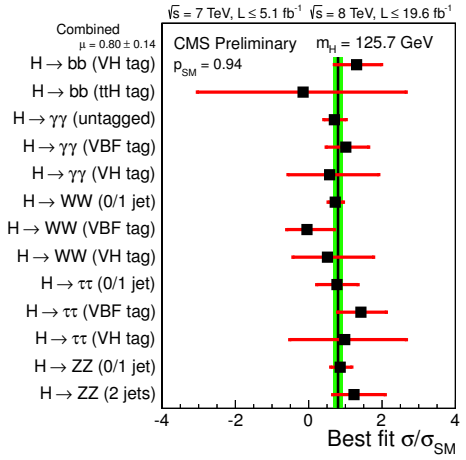

(b) The signal strength of various Higgs channels measured at a fixed hypothetical Higgs mass of $m_H = 125.7\,\text{GeV}$. The combined signal strength scales all Higgs signal rates uniformly and is estimated to $\hat{\mu}_{\text{comb}} = 0.80 \pm 0.14$.

Figure 3.5: Measured signal strength modifiers by ATLAS in the search for $H \to ZZ^{(*)} \to 4\ell$ [277] (a), and the best fit rates (for various Higgs search channels) for a Higgs signal at $m_H = 125.7\,\text{GeV}$ according to CMS [5] (b).

for a SM Higgs boson.

As briefly discussed in Section 2.2.3, the Higgs signal manifests itself as a narrow resonance in the invariant mass spectrum of the final state particles in the $H \to \gamma\gamma$ and $H \to ZZ^{(*)} \to 4\ell$ channels. This is shown in Fig. 3.4 for the latest results from ATLAS [3] and CMS [281], respectively. From the observed resonances the Higgs mass can be determined at the 1% level, yielding the combined results[2] of

$$\hat{m}_H = \begin{cases} 125.5 \pm 0.2\ (\text{stat.})\ {}^{+0.5}_{-0.6}\ (\text{syst.})\ \text{GeV} & \text{from ATLAS [289]}, \\ 125.7 \pm 0.3\ (\text{stat.}) \pm 0.3\ (\text{syst.})\ \text{GeV} & \text{from CMS [5]}. \end{cases} \tag{3.3}$$

Here and in the following, the hat symbol, $\hat{Q}$, always denotes the measurement of a quantity Q, while the un-hatted quantity refers to the model prediction.

Similarly as for the exclusion limits from SM Higgs searches, cf. Section 3.1, the signal rate measurements are presented as best-fit values for the universal scale factor (or signal strength modifier), $\hat{\mu}$, cf. Eq. (3.2), of the SM signal rate prediction. These measurements are, besides the Higgs mass measurements, the basic experimental input of the program `HiggsSignals`, which will be presented in Chapter 4.

Two examples of such measurements (from ATLAS and CMS) are shown in Fig. 3.5. In the ATLAS result shown in Fig. 3.5(a) (taken from Ref. [277]) the measured signal strength modifier, $\hat{\mu}$, in the inclusive $pp \to H \to ZZ^{(*)} \to 4\ell$ process is given as a function of m_H (black line). The cyan band gives a $\pm 1\sigma$ uncertainty on the measured rate. Since the signal strength modifier is measured relative to its SM value ($\hat{\mu} = 1$, displayed in Fig. 3.5 by a dashed line), this

[2] The four individual Higgs mass measurements are given in Section 4.2.3.

contains also the theory uncertainties on the SM Higgs branching ratios and cross sections [70, 71, 89], cf. also Tabs. 2.2 and 2.4, respectively. As can be seen from Fig. 3.5, the measured value of $\hat{\mu}$ is allowed to take on negative values. In the absence of sizable signal-background interference — as is the case for the SM — the signal model would not give $\hat{\mu} < 0$. This must therefore be understood as statistical downward fluctuations of the data with respect to the background expectation (the average background-only expectation is $\hat{\mu} = 0$). To keep $\hat{\mu}$ as an unbiased estimator of the true signal strength, it is however essential that the full range of values is retained.

The second example, this time from CMS, is shown in Fig. 3.5(b) (taken from Ref. [5]). This figure summarizes the measured signal strength modifiers for *all* relevant Higgs decay channels at an interesting value of the Higgs mass, here $m_H = 125.7\,\text{GeV}$. It is important to note that, once a value for m_H has been selected, this plot shows a compilation of information for the separate channels that is also available directly from the mass-dependent plots (as shown in Fig. 3.5(b)). Again, the error bars on the measured $\hat{\mu}$ values correspond to 1σ uncertainties that include both experimental (systematic and statistical) uncertainties, as well as SM theory uncertainties.

Both types of signal strength measurements, i.e. either as a function of m_H or for a fixed value of m_H, are used as experimental input in `HiggsSignals`. However, for many channels only the signal rate measurements for a fixed Higgs mass value exist in the literature, hence we mostly concentrate on using those measurements in the work presented in this thesis.

If we want to test other models than the SM against the signal strength measurement $\hat{\mu}_i$ of a Higgs analysis i, the signal strength modifier has to be evaluated from the cross section and branching ratio predictions in the model. The model-predicted signal strength modifier is then given by

$$\mu_i = \frac{\sum_j \epsilon^{i,j}_{\text{model}}\, \sigma_{\text{model}}(P_j(H)) \times \text{BR}_{\text{model}}(D_j(H))}{\sum_j \epsilon^{i,j}_{\text{SM}}\, \sigma_{\text{SM}}(P_j(H)) \times \text{BR}_{\text{SM}}(D_j(H))}. \tag{3.4}$$

The subscript 'model' ('SM') denote the quantities predicted by the investigated model (SM). In general, the signal efficiencies $\epsilon^{i,j}$ can be different from the SM for models in which the influence of Higgs boson interaction terms with a non-standard (higher-dimensional or CP-odd) tensor-structure cannot be neglected [290]. In that case, the model efficiencies need to be evaluated with a dedicated MC simulation of the signal process j for each Higgs analysis i within the investigated model. However, in many cases the signal efficiencies within the model and the SM can be assumed to be identical, for instance, if the discovered Higgs state is identified with the light or heavy $\mathcal{CP}$-even Higgs boson in the MSSM.

It is obvious from Eq. (3.4) that the information on the signal efficiencies is an essential ingredient to reliably calculate the predicted signal strength. They should therefore always be published with the measurements by the experimental collaborations. The same holds for exclusion limits on the signal strength modifier, see Section 4.1.2 for a further discussion.

For the work presented in Chapter 4 it is convenient to decompose Eq. (3.4) as

$$\mu_i = \sum_j \zeta^{i,j}\, \omega^{i,j}_{\text{SM}}\, c^j. \tag{3.5}$$

Here we introduced the *relative efficiency scale factors*, $\zeta^{i,j} \equiv \epsilon^{i,j}_{\text{model}}/\epsilon^{i,j}_{\text{SM}}$, describing the relative change of the signal efficiency in the model with respect to the SM. Furthermore we define the

SM channel weights and (SM normalized) *channel signal strengths modifiers* as

$$\omega_{\mathrm{SM}}^{i,j} \equiv \frac{\epsilon_{\mathrm{SM}}^{i,j}\,\sigma_{\mathrm{SM}}(P_j(H)) \times \mathrm{BR}_{\mathrm{SM}}(D_j(H))}{\sum_{j'}\epsilon_{\mathrm{SM}}^{i,j'}\,\sigma_{\mathrm{SM}}(P_{j'}(H)) \times \mathrm{BR}_{\mathrm{SM}}(D_{j'}(H))}, \tag{3.6}$$

$$c^j \equiv \frac{\sigma_{\mathrm{model}}(P_j(H)) \times \mathrm{BR}_{\mathrm{model}}(D_j(H))}{\sigma_{\mathrm{SM}}(P_j(H)) \times \mathrm{BR}_{\mathrm{SM}}(D_j(H))}, \tag{3.7}$$

respectively [291, 292].

CHAPTER 4

Tools for BSM Higgs Boson Phenomenology

The search for Higgs bosons is, and has been, a major cornerstone at past, present and future high energy particle colliders. This has become even more important in view of the recent Higgs boson discovery. In the quest for new physics beyond the SM, theorists have proposed numerous different models to solve the present challenges of particle physics, and they are not (yet) tired to come up with even more. However, in order to prove the validity of these models, they need to be confronted with experimental observations. Regarding the Higgs sector, the model must be able to explain the Higgs boson signal seen at the LHC, in particular, it has to be compatible with the observed mass and signal rates. Furthermore, since many BSM theories contain extended Higgs sectors with multiple physical Higgs states, exclusion limits from the non-observation in Higgs boson searches still need to be taken into account.

In this chapter we describe the development of the publicly available `Fortran` codes `HiggsBounds` and `HiggsSignals`. These tools are designed to confront (extended) Higgs sectors of arbitrary BSM models with the experimental results from Higgs searches at the LEP, Tevatron and LHC experiments. While `HiggsBounds` tests the model predictions against the 95% C.L. exclusion limits obtained from non-observations in Higgs collider searches, `HiggsSignals` evaluates the statistical (χ^2) compatibility of the model predictions with the signal rate and mass measurements performed for the recently discovered Higgs state, and possibly other signals of additional Higgs bosons discovered in the future. The full constraining power of past and present experimental results from Higgs boson collider searches on BSM models can thus be exploited by the simultaneous use of `HiggsBounds` and `HiggsSignals`. Both programs will be used extensively in the studies presented in the Chapter 5 and 6 of this thesis.

For both programs, we concentrate here on the description of the concepts, performance and validation. More technical details and a description of how to use these programs can be found in the latest published documentations [28, 291] as well as on the website

`http://higgsbounds.hepforge.org`

where both the `HiggsBounds` and `HiggsSignals` codes can be downloaded.

4.1 `HiggsBounds`

Historically, the first version of `HiggsBounds` was developed in 2009 by P. Bechtle, O. Brein, S. Heinemeyer, G. Weiglein and K. Williams [25]. The main motivation of this code was two-

fold: For phenomenological studies, it had been a very tedious (and sometimes difficult) task to go through the $\mathcal{O}(100)$ Higgs boson search results and to apply them to the model under investigation by hand. Therefore, the first motivation was the convenience of having a common database, where all relevant exclusion limits are collected, and a fast and user-friendly way to apply them to the model. Secondly, many of the phenomenological studies at that time employed questionable statistical techniques to apply the exclusion limits to their model. `HiggsBounds` therefore aimed for a consistent statistical procedure, such that the confidence level of the experimental limit (mostly given at 95% C.L.) is formally preserved for the model exclusion.

Since these early developments, `HiggsBounds` has been proven to be a very useful tool for phenomenological surveys and global fits of the parameter space of various BSM models, see e.g. Refs. [158, 234, 246, 270, 272, 293–296]. It has been continuously developed [26] and is nowadays an established tool in the field of Higgs and SUSY phenomenology. Within this thesis, the version `HiggsBounds-4` [27, 28] was developed, hence the emphasis of the discussion presented here is on these latest developments. Version 4 differs significantly from previous versions of the code in several respects, most notably:

- The code has been extended to fully incorporate the LHC exclusion limits for CM energies of both $\sqrt{s} = 7$ and 8 TeV. This rather straight-forward development required an extension of the model input provided by the user, the internal data structure as well as the implementation of many new LHC results. We will not further discuss these developments here.

- The main algorithm of `HiggsBounds` has been extended to ensure a reliable application of exclusion limits in the presence of a signal (as is now observed in the LHC data). This will be described in Section 4.1.1.

- The *model-likeness test*, which tests whether a given model fulfills the assumptions of a particular Higgs search to a sufficient degree, has been fully rewritten to enable in particular the limits from SM Higgs searches at the LHC to be applied in a wider context. More details will be given in Section 4.1.2.

- A simple algorithm was introduced to take into account theory uncertainties on the Higgs mass predictions. This will be described in Section 4.1.3. These uncertainties are relevant, for instance, for the lightest Higgs boson mass in the MSSM.

- An extension is provided, which offers an alternative statistical treatment of the LEP constraints in the form of a χ^2 likelihood value. This information is very valuable for global fits of models with extended Higgs sectors. We will discuss this extension in Section 4.1.4.

In the following we describe the main `HiggsBounds` procedure and give more details on these latest developments.

4.1.1 General approach of `HiggsBounds-4`

In this section we give a brief introduction to the main structure of the `HiggsBounds` program and the employed statistical procedure. We also describe one conceptual change of the latter with respect to previous `HiggsBounds` versions, which has been prompted by the application

of HiggsBounds to models which feature a Higgs boson with a mass close to the observed LHC Higgs signal. A pictorial overview of the HiggsBounds main structure is given in Fig. 4.1.

The basic input for HiggsBounds (which the user has to provide) are the relevant physical quantities predicted for the Higgs sector of the model under consideration. The necessary predictions for each Higgs boson H_i ($i = 1, \ldots, n_{H^0} + n_{H^\pm}$) in the model are, schematically,

$$M_{H_i}, \quad \Gamma_{\rm tot}(H_i), \quad {\rm BR}_{\rm model}(H_i \to ...), \quad \frac{\sigma_{\rm model}(P(H_i))}{\sigma_{\rm ref}(P(H))}, \tag{4.1}$$

i.e. the Higgs boson mass, its total decay width (it is assumed that the narrow width approximation holds), its decay branching ratios, and the production cross sections, normalized to a particular reference value. Here, P denotes a specific Higgs production process. If P exists in the SM, its cross section, $\sigma^{\rm SM}(P(H))$, evaluated at the same mass value, $M_H = M_{H_i}$, is typically used as the reference cross section, $\sigma_{\rm ref}$. In some cases it can also be necessary to supply additional predictions, such as the BR($t \to bH^+$), the $\mathcal{CP}$ properties of the neutral Higgs bosons or the theoretical uncertainties of the Higgs masses.

The Higgs production cross sections at the LHC and Tevatron can be given in different formats: The user can provide the cross sections either at the hadronic level, e.g. obtained from a full cross section calculation including the PDF convolution, Eq. (2.43), for each experiment and CM energy, at the partonic level, or via an effective coupling (or scale factor) approximation. In the latter case, the production cross sections and partial decay widths are obtained from scaling the corresponding SM quantities, cf. Section 2.2.3, by the provided effective couplings. For more details on the theoretical model input and the approximations employed in the derivation of the hadronic cross sections and branching ratios see Refs. [25, 26, 28].

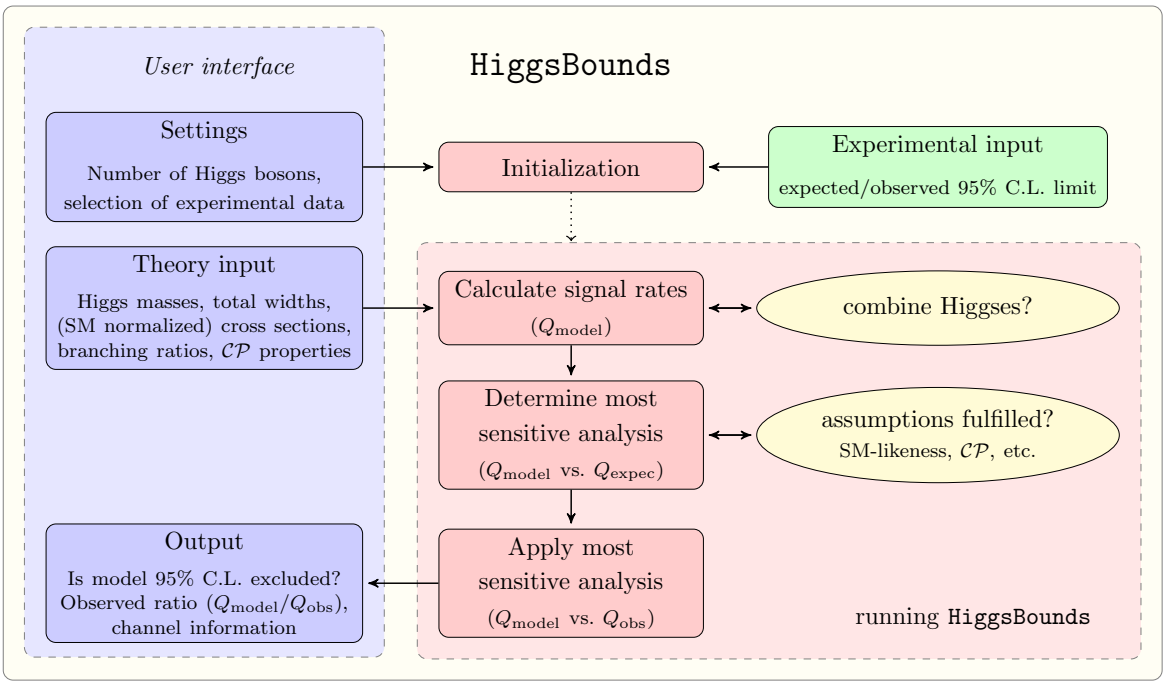

Figure 4.1: Overview of the main HiggsBounds structure and algorithms.

In addition to the model predictions, the other important ingredient of `HiggsBounds` is the experimental data. Exclusion limits obtained from non-observation in Higgs searches, as discussed in Section 3.1, are collected from the experimental publications, with the aim of keeping the code as up-to-date as possible with the latest developments. Currently the code includes results from LEP, the Tevatron and the LHC experiments. More information on which analyses are available in `HiggsBounds` is provided in Appendix **??**. The data for these analyses is contained in tables holding both the expected and observed exclusion limits at 95% C.L. as a function of the Higgs boson mass(es). The list consists both of analyses for which model-independent limits were published, and of dedicated analyses carried out specifically under the assumption of the SM (like most LHC searches to date), or for Higgs bosons with certain $\mathcal{CP}$ properties. These limits can be applied to models with Higgs bosons, which show these characteristics *to a sufficient degree*[1] at the considered parameter point.

We call the application of the limit from a particular Higgs search to one of the Higgs bosons of the model under study (or to two of the Higgs bosons, for searches involving two Higgs bosons) an "analysis application", which we denote by X in the following[2]. Each analysis application has a corresponding signal cross section prediction $\sigma(X)$, which `HiggsBounds` uses to calculate the relevant quantity $Q_{\text{model}}(X)$ for which the experimental limit is given; typically this is a conveniently normalized cross section times a branching ratio, cf. Section 3.1. The corresponding experimental quantities are denoted $Q_{\text{expec}}(X)$ and $Q_{\text{obs}}(X)$ for the expected and observed limits, respectively. If two Higgs bosons have a narrow mass separation, $\delta M = M_{h_i} - M_{h_j}$, then their predicted cross sections are added for certain analyses where the mass resolution is limited and interference effects are expected to be negligible. The settings for the maximal δM_h can be varied by the user separately for LEP, Tevatron, and LHC analyses (the default values are 0 GeV for LEP and 10 GeV for Tevatron/LHC).

`HiggsBounds` operates by considering, for each analysis application, the ratio of the model predictions, $Q_{\text{model}}(X)$, to the experimental limits. To ensure that the result can be interpreted as an exclusion at 95% C.L. (which is the same confidence level as adopted by the individual analyses), it is crucial that the model prediction is only compared to the experimentally *observed* limit for *one* particular analysis application. In a first step, `HiggsBounds` therefore uses the *expected* experimental limits to determine the analysis application X_0 with the highest statistical sensitivity to exclude the model point under consideration,

$$X_0 = X : \max \frac{Q_{\text{model}}(X)}{Q_{\text{expec}}(X)}. \tag{4.2}$$

In the second step, `HiggsBounds` then performs the exclusion test for the Higgs boson and analysis combination represented by X_0, by computing the ratio to the *observed* limit

$$k_0 = \frac{Q_{\text{model}}(X_0)}{Q_{\text{obs}}(X_0)}. \tag{4.3}$$

If $k_0 > 1$, `HiggsBounds` concludes that this parameter point of the tested model is excluded at 95% C.L.[3].

[1] This statement will be quantified in Section 4.1.2.

[2] As an example, suppose that a model with three neutral Higgs bosons (h_1, h_2, h_3) should be checked against the limits from two neutral Higgs searches, A_1 and A_2. Then there are six possible analysis applications, $X \in \{A_1(h_1), A_1(h_2), A_1(h_3), A_2(h_1), A_2(h_2), A_2(h_3)\}$, for this model.

[3] If we had instead compared the predicted cross sections directly to the experimentally observed limits for *all*

The statistical method as described here (in the following referred to as the *classic* method) has been the only mode of operation available in previous HiggsBounds versions. For HiggsBounds-4, we have extended this method to perform better in situations where a Higgs boson signal is present (as is now the case in the LHC data). The problem of the *classic* method arises for models with multiple Higgs bosons. If one of these has a mass close to that of the observed signal (which is likely, since any reasonable model should also explain this signal), its analysis applications will test the model predictions against limits (for various channels) in the signal region. In this region, the *expected* limits (if based on the *background-only* hypothesis) will continue to improve with more experimental data and optimized analysis methods, whereas the *observed* limits can never be expected to reach exclusion at the SM level (provided a true signal of near-SM strength is what is observed), see e.g. Fig. 3.2(a). For model points in which the most sensitive analysis application X_0 is a test of the signal-like Higgs boson, the *classic* HiggsBounds method would therefore never yield exclusion. Moreover, constraints on the remaining Higgs spectrum (with less expected sensitivity) are not applied. Even if the exclusion remains formally valid at 95% C.L., it could be anticipated that this problem would eventually become serious enough to limit the usability of the code.

Among the several possible ways that the HiggsBounds algorithm could be extended to address this problem, all involving different compromises, we have opted for a solution which involves a slight violation of the strict testing of only one experimental limit. We call this the *full* HiggsBounds method. In summary, this method performs the original HiggsBounds test separately for each Higgs boson in the model. In the full HiggsBounds method, the first step is to evaluate the most sensitive analysis application X_i for each Higgs boson H_i according to

$$X_i = X(H_i) : \max \frac{Q_{\text{model}}\left(X(H_i)\right)}{Q_{\text{expec}}\left(X(H_i)\right)}. \tag{4.4}$$

This is followed by a straightforward exclusion test on the individually most sensitive analysis applications

$$k_i = \frac{Q_{\text{model}}(X_i)}{Q_{\text{obs}}(X_i)}. \tag{4.5}$$

The result of these tests contains more information than the single test of HiggsBounds *classic*, such as exclusion/non-exclusion by individual Higgs bosons, and is now part of the program's output (see Ref. [28] for details). A combined HiggsBounds exclusion is also calculated, with the result being interpreted as model exclusion if $k_i > 1$ for *any* of the k_i. The combined (single-number) output is then calculated as

$$k_0 = \max_i k_i, \tag{4.6}$$

$$X_0 = X_i : \max_i k_i. \tag{4.7}$$

By the construction of the *full* method, it follows directly that the two methods are equivalent for models with a single Higgs boson. It is also clear that the *full* method can only give *stronger* exclusion than the *classic* method. This is consistent with the fact that the exclusion

available search channels and considered the model excluded if at least one of them gave exclusion at 95% C.L., the result would in general *not* correspond to an exclusion at 95% C.L.. The combined probability of yielding a false exclusion from any of the individual comparisons of Q_{model} to Q_{obs} would also yield an overall probability for false exclusion higher than that from applying a single limit.

of the *full* method will correspond to a limit at somewhat *lower* statistical confidence level than 95%. Still, the deviation from the strict 95% C.L. should be minor in this approach compared to the alternative (naive) testing of all Higgs bosons versus all observed limits, since the number of Higgs bosons in a model in general is much smaller than the number of implemented experimental analyses. Furthermore, a non-negligible dilution of the 95% C.L. interpretation of the combined result is only expected in the case where more than one test X_i leads to a ratio $k_i \approx 1$.

To illustrate the difference between the *classic* and *full* methods of `HiggsBounds`, we show in Fig. 4.2 the excluded regions in the $m_h^{\text{mod+}}$ benchmark scenario of the MSSM [246], introduced in Section 2.4.3, obtained under both settings. In this scenario the light Higgs boson h can have a mass close to the LHC signal around $M_h \sim 125\,\text{GeV}$ (this region, considering a 2 (3) GeV total uncertainty on M_h is indicated by dark (light) green colour in the figure). The excluded regions, as evaluated by `HiggsBounds`, are shown separately for the LEP (blue) and the LHC (red) exclusion limits. When evaluating the limits in this figure, a theory uncertainty of 3 GeV is taken into account in the evaluation of the lightest Higgs mass, see Sect. 4.1.3 for details on how this is done.

As can be seen from this figure, the *full* method gives the strongest exclusion, corresponding to the most accurate application of the existing limits in this scenario (as also used in Ref. [246]). The difference to the *classic* method can be seen in particular for high M_A and high $\tan\beta$ (the decoupling regime). Here the applicability of the *classic* method is limited, since the globally most sensitive channel is a search for the lightest (SM-like) Higgs boson, which cannot be excluded when is mass its in the signal region, $M_h \simeq 125\,\text{GeV}$. This is in contrast to the results in the *full* method, which can be further illustrated by looking at the contribution of individual Higgs bosons as shown in Fig. 4.3 for the same MSSM example. Fig. 4.3(a) shows the exclusion contributed by the light Higgs boson h. The narrow unexcluded region around $m_A = 135$ GeV results from a particular channel ($pp \to Vh$, $h \to b\bar{b}$) being the most sensitive. For this channel, the observed limit is not strong enough here to exclude the lightest Higgs. Fig. 4.3(b) shows the exclusion from the channel $H/A \to \tau^+\tau^-$ [297]. Both H and A are treated together, since their masses are close to degenerate over most of the parameter space. The dominant exclusion therefore comes from the same search channels and their signal rates are added. Finally, Fig. 4.3(c) shows the exclusion[4] from searches for the charged Higgs boson $H^\pm$ [260, 262, 263]. The exclusion region presented for the *full* method in Fig. 4.2 consists of the union of the three different exclusion regions shown here.

4.1.2 Applying exclusion limits to arbitrary Higgs models

The aim of `HiggsBounds` is to apply limits derived in Higgs collider searches to models which have *not* been directly investigated by the experimental analyses. These models can be *arbitrary* in the sense that they may contain any number of neutral or (singly) charged Higgs bosons, or particles which behave like (elementary) Higgs bosons in Higgs collider searches. Examples of the latter include theories with composite Higgs bosons [298] or dilatons [299]. More specifically, the requirements on the theory in order for the results of `HiggsBounds` to be reliable are the following:

1. The narrow width approximation must be applicable, such that the predictions for each

[4] Note, that the latest charged Higgs boson search result from ATLAS [261] is not included here. We briefly discuss the impact of the updated search in Appendix A.1.

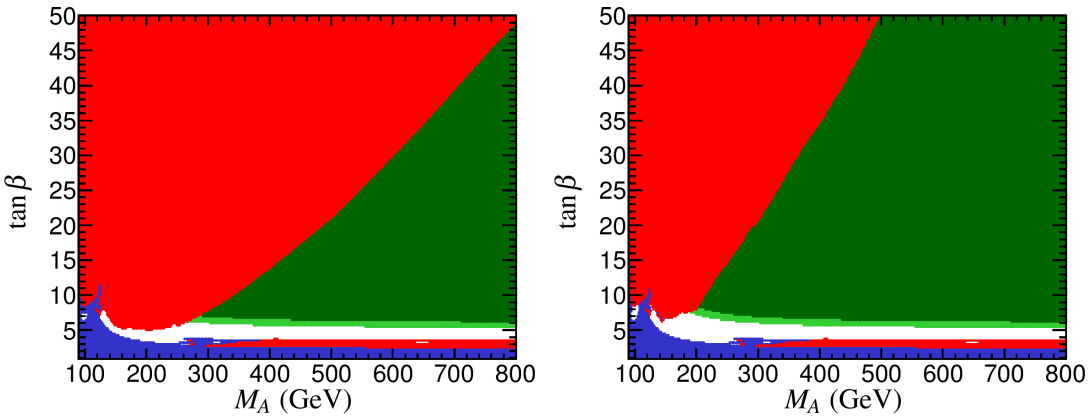

(a) Results from `HiggsBounds` *full*. (b) Results from `HiggsBounds` *classic*.

Figure 4.2: Exclusion regions in the MSSM parameter space for the $m_h^{\text{mod+}}$ benchmark scenario [246]. Results from `HiggsBounds` *full* (a) are compared to the results from `HiggsBounds` *classic* (b). The colours show exclusion by the LHC (red), LEP (blue), and the favored region where $M_h = 125.7 \pm 2$ GeV (dark green), $M_h = 125.7 \pm 3$ GeV (light green).

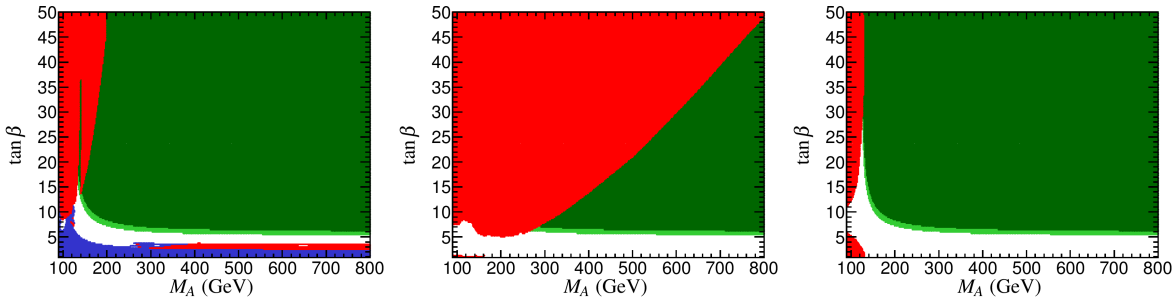

(a) Light Higgs h exclusion. (b) Heavy Higgs H/A exclusion. (c) Charged Higgs $H^{\pm}$ exclusion.

Figure 4.3: Contribution to the *full* `HiggsBounds` exclusion in the MSSM parameter space for the $m_h^{\text{mod+}}$ benchmark scenario [246] from exclusion of the individual Higgs bosons: h (a), H/A (b), and $H^{\pm}$ (c). The colour coding is the same as in Fig. 4.2.

process can be factorized into Higgs production and decay.

2. The investigated model should not change the signature of the background processes considerably. Usually, new physics models which show strong deviations from the SM in the background processes of Higgs searches are not considered in the literature, since this would often put them in conflict with SM electroweak precision data [153, 300]. Hence, they would most likely not be interesting for `HiggsBounds` anymore. The presence of such backgrounds would rather correspond to an opportunity for the discovery of physics beyond the SM in other areas.

3. The investigated model should not significantly change the kinematical distributions of the signal topology X (e.g. the η and p_T distributions of the final state particles) from that assumed in the corresponding analysis. For a more detailed discussion of this requirement, see Refs. [25, 26].

The above requirements are typically sufficient to ensure the applicability of *model-independent* exclusion limits, i.e. limits on a cross section of a certain Higgs signal topology, composed of *one* production and *one* decay process. If further model assumptions have been made in the experimental analysis, for instance on the $\mathcal{CP}$-properties of the Higgs boson or on the top quark branching ratios, `HiggsBounds` checks whether the investigated model fulfills them before applying the analysis.

The application of exclusion limits to arbitrary Higgs models becomes less trivial if the experimental analysis combines several Higgs signal topologies under the assumption of a specific model. This is the case for most of the Tevatron and LHC Higgs searches, where a SM Higgs boson is assumed. As discussed in Section 3.1, the exclusion limit is then set on a common signal scale factor for all considered SM Higgs topologies, the so-called signal strength modifier μ, Eq. (3.2). In `HiggsBounds` the signal efficiencies ϵ^j are generally assumed to be the same for the model and the SM (see requirements (2) and (3) above). If these efficiencies were published together with the exclusion limit posed by an experimental analysis, the predicted signal strength modifier μ could be computed for a given model without further assumptions using Eq. (3.4). However, these efficiencies have so far been made publicly available only in a very few cases[5]. In `HiggsBounds` we therefore neglect the channel efficiencies in Eq. (3.4), leading to an unavoidable model-dependence of the resulting limit, since the calculation of μ via Eq. (3.4) with all $\epsilon_i \equiv 1$, is strictly speaking only valid if the model predictions for all signal topologies of the analysis contribute to the total signal rate in (approximately) the same proportions as in the SM.

In order to ensure that an analysis is applied only when this last requirement is fulfilled by the model, `HiggsBounds` performs a SM-likeness test for every Higgs analysis performed under SM assumptions. A test of this kind has been present in all versions of `HiggsBounds` [25, 26]. However, significant improvements of this test have been implemented in `HiggsBounds-3.8.0` (and higher), which we will discuss here.

Using the decomposition of the predicted signal strength modifier, Eq. (3.5), and neglecting the channel efficiencies ($\epsilon_i \equiv 1$), the predicted signal strength modifier μ can be obtained as $\mu \approx \sum_{j=1}^{N} \omega_j c_j$, where ω_j and c_j are given by Eqs. (3.6) (with $\epsilon_j \equiv 1$) and (3.7), respectively. Note, that the sum runs only over those signal topologies that have been taken into account in the experimental analysis. The requirement that the signal topologies contribute in similar proportions to the total signal rate as in the SM is fulfilled if all channel signal strengths c_i are similar to the total signal strength modifier μ (and thus similar to each other). A possible SM-likeness criterion would therefore be to require

$$\Delta \equiv \max_i \left| \frac{\delta c_i}{\mu} \right| < \xi \tag{4.8}$$

with $\delta c_i = c_i - \mu$ and $\xi \sim \mathcal{O}(\text{few } \%)$, i.e. that the maximal relative deviation of the channel signal strength modifiers from the total signal strength modifier is less than a few percent. In fact, this criterion is very similar to what was used in earlier versions of `HiggsBounds`. However, this choice was found to be too restrictive in some cases, since it may reject an analysis application which is actually justifiable, leading to overly conservative results. In particular, it

[5] These efficiencies usually depend on the tested Higgs boson mass. Using a single number for ϵ_i therefore might appear to be a crude approximation. Nevertheless, for many searches, having access to this information even for one or a few values of the Higgs mass would already provide a better approximation of the full result than in the current situation.

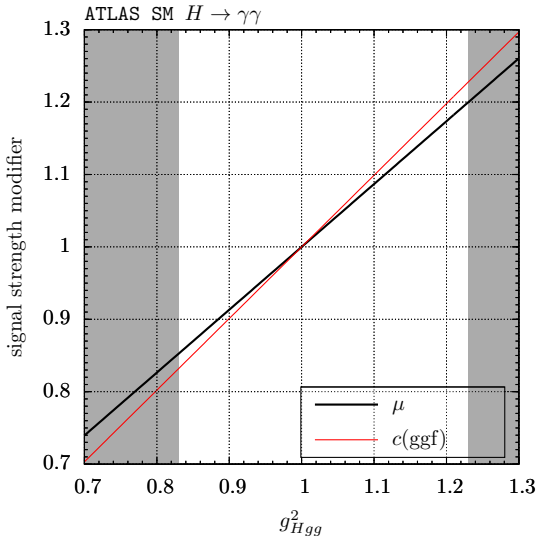

(a) Variation of g^2_{Hgg}.

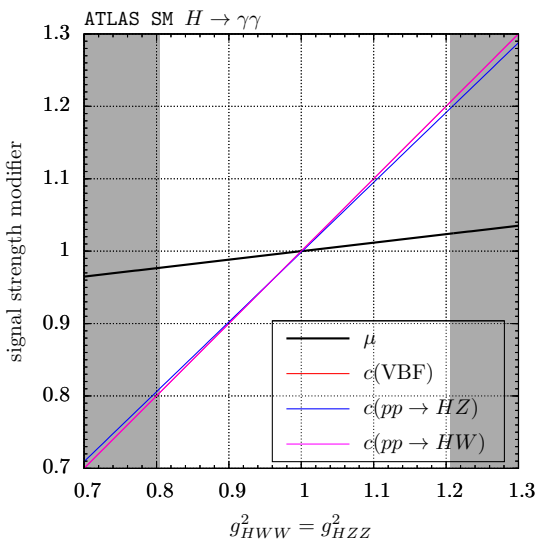

(b) Variation of $g^2_{HWW} = g^2_{HZZ}$.

Figure 4.4: Performance of the SM-likeness test. Total signal strength modifier μ and the relevant individual signal strength modifiers c_i for the ATLAS $H \to \gamma\gamma$ search [301] with modified effective Higgs couplings (relative to the SM) g^2_{Hgg} (a) and g^2_{HVV} $(V = W, Z)$ (b) for a Higgs boson with mass $m = 125\,\text{GeV}$. The remaining couplings are set to their SM values. The gray regions indicate the parameters for which the SM-likeness test fails.

is reasonable that channels contributing only a few percent to the total signal rate should be allowed to deviate more from their SM expectations, since their influence on μ is subdominant. We therefore introduce the SM channel weights ω_i, Eq. (3.6), in an improved SM-likeness test criterion,

$$\Delta \equiv \max_i \; \omega_i \left| \frac{\delta c_i}{\mu} \right| < \xi. \tag{4.9}$$

The default setting in `HiggsBounds` is $\xi = 2\%$. This is a conservative choice, considering that the uncertainties on the rate predictions for individual channels (even in the SM) are generally larger. With the improved SM-likeness test, the maximal *weighted* deviation of an individual signal strength modifier from the total signal strength modifier is required to be less than 2%. Models fulfilling this SM-likeness test for a SM analysis can be safely tested against its exclusion limit.

To illustrate the inclusion of the SM weights ω_i in the SM-likeness test criterion, we consider as an example the ATLAS $H \to \gamma\gamma$ search [301] and test a toy model with a single Higgs boson H with mass $m_H = 125\,\text{GeV}$. We depart from the SM by modifying either the squared effective Higgs coupling to gluons, g^2_{Hgg}, or the coupling to vector bosons, g^2_{HVV} $(V = W, Z)$. Both effective couplings are to be understood as normalized to the corresponding SM coupling. All other effective Higgs couplings, in particular the $H\gamma\gamma$ coupling, are set to their SM values. At $m = 125\,\text{GeV}$, the SM weights for the LHC at $\sqrt{s} = 7\,\text{TeV}$ are

$$\omega \approx (87.7\%,\ 6.8\%,\ 3.2\%,\ 1.8\%,\ 0.5\%) \tag{4.10}$$

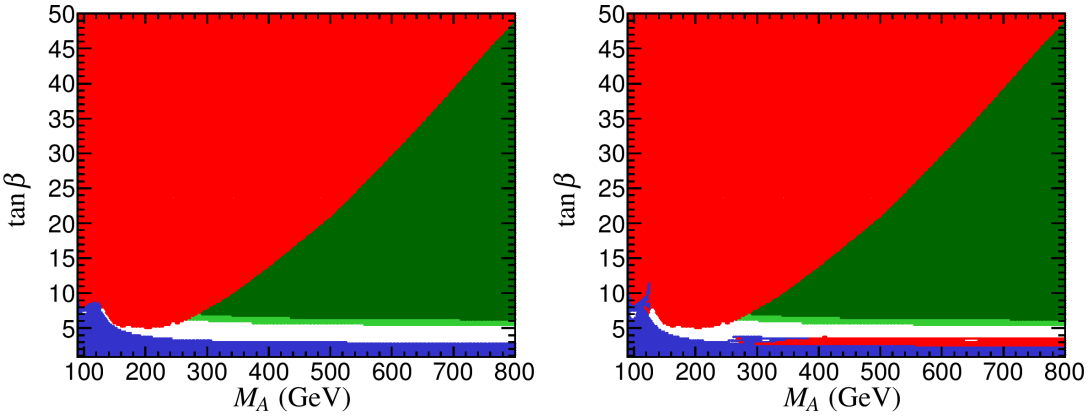

(a) SM-likeness test without weights, Eq. (4.8). (b) SM-likeness test with weights, Eq. (4.9).

Figure 4.5: Combined `HiggsBounds` exclusion in the the $m_h^{\text{mod+}}$ benchmark scenario of the MSSM using a SM-likeness test without weights (a) and using the new SM-likeness test with weights included (b). The colour coding is the same as in Fig. 4.2.

for the production processes ($gg \to H$, VBF, HW, HZ, $Ht\bar{t}$), cf. Tab. 2.4. In Fig. 4.4 we show how the total signal strength modifier μ and the c_i for the signal topologies are influenced by the modified effective Higgs couplings. Varying g^2_{Hgg}, as shown in Fig. 4.4(a), influences only the cross section gluon-gluon fusion (ggf) process, $gg \to H$. However, due to its large SM weight, $\omega_{\text{ggf}} \approx 87.7\%$, the total signal strength modifier μ follows $c(\text{ggf})$ closely. The failure of the SM-likeness test at $g^2_{Hgg} \leq 0.835$ and ≥ 1.225 is therefore eventually caused by the ggf signal topology, although the deviation δc_i for the remaining signal topologies VBF, HW, HZ and $Ht\bar{t}$ is much larger here. However, the SM weights of these channels are much smaller. The same effects can be seen when varying g^2_{HVV} ($V = W, Z$), shown in Fig. 4.4(b). Now, the c_i of the VBF, HW, HZ signal topologies are affected by the modified effective coupling, but the total signal strength modifier μ is only slightly influenced due the small weight of these channels. Again, the deviation between μ and $c(\text{ggf})$ eventually causes the SM-likeness test to fail. Due to the inclusion of the SM weights in Eq. (4.9), subdominant signal topologies are allowed to deviate further from μ.

In comparison with the old SM-likeness test (which was used in `HiggsBounds` up to version `3.7.0`), the new criterion leads to a wider applicability of SM Higgs search results to other Higgs sectors, and thus to a significant improvement of the performance of `HiggsBounds`. This is shown in Fig. 4.5 for the $m_h^{\text{mod+}}$ benchmark scenario of the MSSM [246]. Without SM weights, Fig. 4.5(a), the LHC exclusion approximately follows the results from the dedicated MSSM search for $H/A \to \tau\tau$ [297], and no additional exclusion can be set. In particular there is *no* LHC exclusion from the SM-like Higgs boson h. With the full weighted criterion active (the default setting in `HiggsBounds-4`), shown in Fig. 4.5(b), the lightest MSSM Higgs boson can become sufficiently SM-like at large M_A and small $\tan\beta$ for the combined SM Higgs searches of ATLAS and CMS to be applied, giving additional areas of exclusion. Note, that Fig. 4.5(b) is identical to the previously shown Fig. 4.2(a).

4.1.3 Treatment of Higgs mass uncertainties

In several theories with extended Higgs sectors, the Higgs boson masses are not free parameters but can be predicted as a function of the other model parameters up to a certain theoretical accuracy. This is the case, for example, in the MSSM, where out of the five physical Higgs states typically only one mass, M_A or $M_{H^\pm}$, is used as an (on-shell) input parameter, see Section 2.4.3. The remaining Higgs masses then become predictions of the model, with a theoretical uncertainty that varies within the parameter space and with the sophistication of the theoretical prediction.

We have extended `HiggsBounds` to be able to take this type of theoretical uncertainty into account when evaluating the Higgs exclusion limits. For theories that have no Higgs mass uncertainties, or where they are negligibly small, this new feature can be left deactivated. In `HiggsBounds-4`, the Higgs mass uncertainties are taken into account approximately by varying each mass within a user-defined interval[6]. If the tested Higgs boson is not excluded by the probed limit (in the normal `HiggsBounds` sense) for any mass in this interval, the tested parameter point of the model is regarded as being allowed. This leads to an overall conservative (weaker) result for the exclusion limit when uncertainties are included.

Technically, the number of mass points N considered in the variation can be specified by a variable. The default setting is $N = 3$ (this corresponds to testing the central mass value, M_H, and the two endpoints, $M_H \pm \Delta M_H$, of the specified uncertainty interval). When a sensitive limit varies rapidly with M_H, it is advisable to increase N for best results. The mass variation is performed for each Higgs boson independently. In the *classic* `HiggsBounds` method this variation is also simultaneous, which leads to a multi-dimensional computation grid with a complexity growing as $\mathcal{O}(N^{n_H})$, where n_H is the number of Higgs bosons with a non-zero mass uncertainty[7]. For the *full* method, since the limit from each Higgs boson is already considered independently of the others, the complexity remains managable, i.e. being $\mathcal{O}(n_H N)$. Nevertheless, it is recommended to specify uncertainties only for those Higgs bosons for which it is numerically relevant.

The effects of a theoretical mass uncertainty on the resulting `HiggsBounds` limits are demonstrated in Fig. 4.6, which shows the combined exclusion for a SM-like Higgs boson with $\Delta M_H = 0$ GeV (solid lines), and similarly for a Higgs boson with SM-like couplings but a theory mass uncertainty of $\Delta M_H = 2$ GeV (dashed lines). In this figure, the mass range excluded at 95% C.L. corresponds to where the limit on $\sigma_{\text{model}}/\sigma_{\text{SM}} < 1$. Including the mass uncertainties can be seen here as a broadening of the allowed range for the Higgs mass prediction in the model by ± 2 GeV around the signal region. It can also be seen that for a given mass point the resulting upper limit on the signal rate is always weaker or equal to the upper limit obtained without theoretical mass uncertainty. Including a theory mass uncertainty in `HiggsBounds` therefore produces overall more conservative limits, which is as expected.

This point is further illustrated in Fig. 4.7, which shows the resulting limits from the light (SM-like) MSSM Higgs boson, h, when running `HiggsBounds` *full* for the m_h^{max} benchmark scenario [246], cf. Section 2.4.3. Similar to previous figures, the green band shows the region of parameter space where $M_h = 125.7 \pm 2$ (3) GeV. For large values of M_A and $\tan\beta$, the m_h^{max}

[6] Changes to the relative rates induced by the Higgs mass variation is considered to be "second-order", and are therefore neglected in this procedure. This approximation is valid when the rate predictions vary slowly within the mass uncertainty interval, which sets an upper limit on the reasonable size of the mass uncertainties.

[7] To avoid unnecessary calculations, uncertainties smaller than the minimal mass spacing at which the experimental results are available (currently 0.1 GeV for some channels) are not considered.

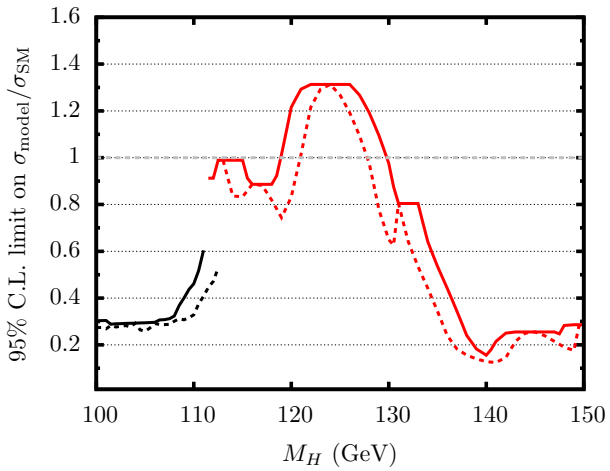

Figure 4.6: Upper limits from `HiggsBounds` (at 95% C.L.) on the relative signal strength versus the Higgs boson mass in the SM, which has zero theoretical uncertainty (dashed lines), and in a model with a SM-like Higgs boson with a theoretical mass uncertainty of 2 GeV (solid lines). The two colours indicate mass ranges where the most sensitive limit is from either LEP (black) or the LHC (red).

scenario gives rise to values of M_h that are *too high* compared to the measured LHC signal. The predicted value for M_h increases with $\tan\beta$. $M_h \gtrsim 128\,\text{GeV}$ is excluded when no theory uncertainty is applied, cf. Fig. 4.6. The three subfigures in Fig. 4.7 show the results when using a mass uncertainty (resulting from the calculation of M_h in the model [156]) of $\Delta M_h = 0$ GeV, $\Delta M_h = 1$ GeV, and $\Delta M_h = 2$ GeV. It can be seen that the exclusion at high M_A from the limit on the lightest Higgs boson goes down to lower $\tan\beta$ values when ΔM_h is small. This illustrates the importance of taking Higgs mass uncertainties into account when interpreting exclusion limits (and compatibility with observed signals, see Section 4.2) in the MSSM and other scenarios for physics beyond the SM.

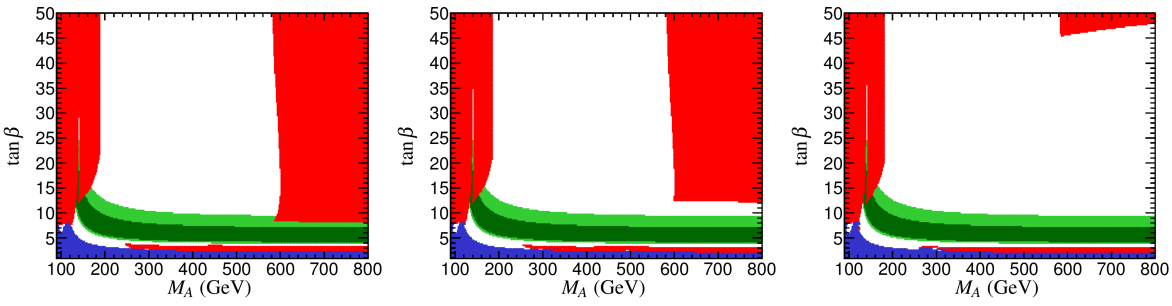

(a) $\Delta m_h = 0\,\text{GeV}$. (b) $\Delta m_h = 1\,\text{GeV}$. (c) $\Delta m_h = 2\,\text{GeV}$.

Figure 4.7: Contribution from the lightest MSSM Higgs boson, h, to the *full* `HiggsBounds` exclusion in the parameter space for the m_h^{max} benchmark scenario [246]. The results are shown for a theory mass uncertainty of $\Delta M_h = 0$ GeV (a), $\Delta M_h = 1$ GeV (b), and $\Delta M_h = 2$ GeV (c). The colour coding is the same as used in Fig. 4.2.

4.1.4 Including the χ^2 information from LEP Higgs searches

An unfortunate limitation of both the model-independent limits implemented in HiggsBounds, as well as the model-dependent search limits presented by the experiments, is that they are available only at one fixed confidence interval, which is 95% C.L. for all searches implemented in HiggsBounds. The result of an exclusion provided by HiggsBounds based on these searches therefore has a confidence limit of *at least* 95% C.L., and in many cases higher. However, the exact level of confidence at which a signal with the properties given to HiggsBounds is either excluded or allowed, is generally unknown.

This has unfortunate consequences for the use of these limits in applications like global fits (see e.g. Ref. [274, 296] for examples of such fits in the MSSM). There, a model point, for which the predicted Higgs signal is excluded for example at 96% C.L., i.e. with a significance of slightly more than 2σ, might still be a very good fit if the other properties of the model point in the global fit match the data well. However, the conventional HiggsBounds output only contains information about whether the parameter point is experimentally excluded at *at least* 95% C.L. and thus can only be treated as a "hard cut" on the validity of a parameter point.

In order to circumvent this problem, at least for the LEP Higgs searches, the full information on CL_{s+b} and CL_s for all Higgs mass combinations in the model-independent LEP searches from Ref. [257] have been re-calculated for varying cross sections [302]. These can be written as $\sigma_i = f_i\,\sigma_{i,\mathrm{ref}}$, with $\sigma_{i,\mathrm{ref}}$ being the reference cross section times branching fraction for search i, motivated by the SM Higgs boson or the corresponding cross section for non-SM Higgs bosons (see Ref. [257] for details), and f_i being an arbitrary scaling parameter. A logarithmic grid in the scaling parameters f_i with 100 points between 10^{-3} and 1 is used. Using an interpolation, the actual CL values can be calculated for every Higgs production mode at LEP for every physically allowed cross section.

The CL_{s+b} can then be transferred into a quantity, whose properties closely follow that of a χ^2 function. This is achieved by assuming that the likelihood distribution of $-2\ln Q$ [257], where Q is the test statistics, cf. Section 3.1, is Gaussian in the asymptotic limit. The one-sided CL_{s+b} can then be transferred into the two-sided calculation of a χ^2 using the formula

$$\chi^2_H = 2\,\mathrm{InvErf}^2(1 - 2\,\mathrm{CL}_{s+b}), \tag{4.11}$$

where InvErf is the inverse of the Gauss error function. The resulting χ^2_H can be used as a continuous expression of the agreement between the result of the LEP Higgs boson searches and the model predictions. Note that, in the case of a strong excess in one of the searches, χ^2_H is not only large for models whose predicted cross section times branching fraction is above the observed limit, but also for predictions much smaller than the observed rate in data.

Examples for the relation between the LEP CL_{s+b} and χ^2_H, also for different values of the scale factor f, are given in Fig. 4.8 for the processes $e^+e^- \to HZ$ (for the SM combination of decay modes) and $e^+e^- \to h_1h_2 \to b\bar{b}b\bar{b}$. For the latter we assume equal Higgs masses, $m_H \equiv m_{h_1} = m_{h_2}$, for illustrational purposes. It can be seen that for $\mathrm{CL}_{s+b} \approx 0.5$, indicating very good agreement of the signal plus background prediction with the data, fluctuations of χ^2_H around 0 are unavoidable, but numerically irrelevant.

In addition, the possibility exists to follow a prescription from Ref. [303] to include a mass uncertainty into χ^2_H by folding the full χ^2 distribution with a Gaussian (normal) distribution $G(M'; M_H, \Delta M_H)$ with central value M_H and the standard deviation given by the mass uncer-

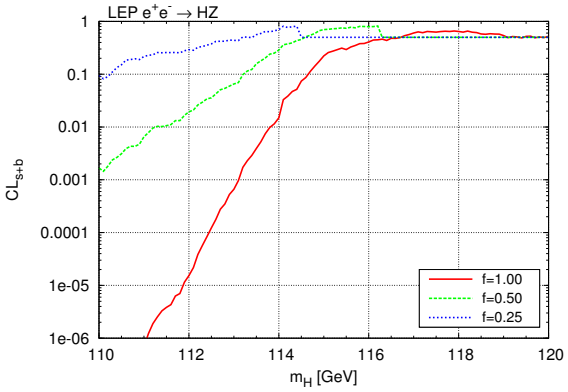

(a) CL_{s+b} result for $e^+e^- \to hZ$ (in the SM).

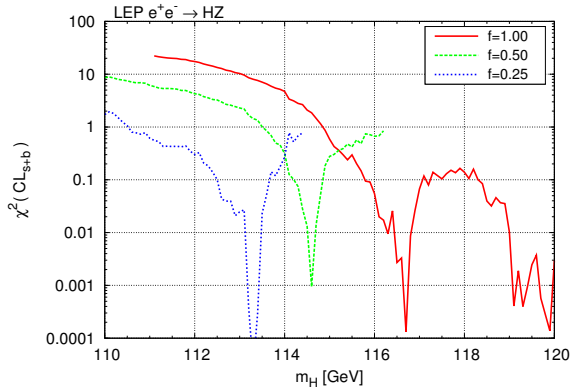

(b) χ^2_H result for $e^+e^- \to hZ$ (in the SM).

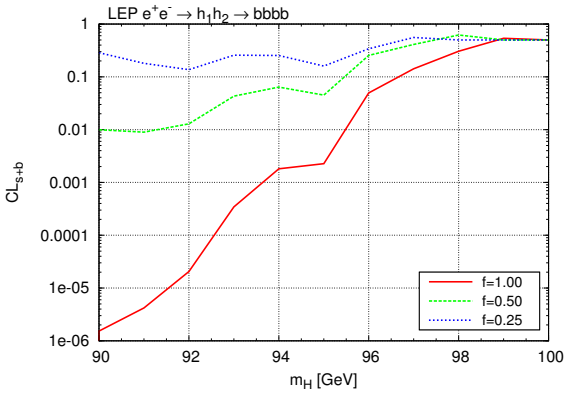

(c) CL_{s+b} result for $e^+e^- \to h_1h_2 \to b\bar{b}b\bar{b}$.

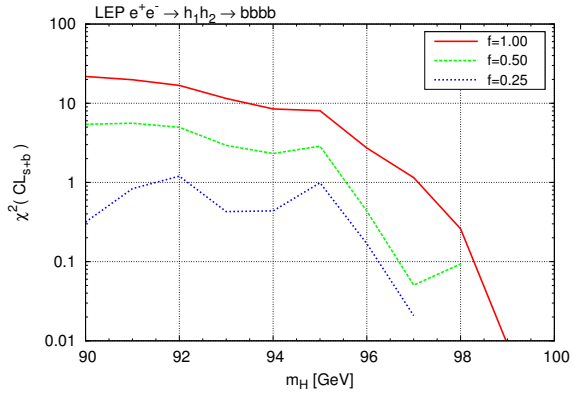

(d) χ^2_H result for $e^+e^- \to h_1h_2 \to b\bar{b}b\bar{b}$.

Figure 4.8: Examples for transferring the LEP CL into a value for χ^2_H using three different values of the scale factor $f = (0.25, 0.5, 1.0)$: LEP CL_{s+b} result for $e^+e^- \to hZ$ in the SM (a), the resulting χ^2_H for the same process (b), LEP CL_{s+b} results for $e^+e^- \to h_1h_2 \to b\bar{b}b\bar{b}$ (c) and the corresponding χ^2_H result (d). For the latter process we set equal masses, $m_H \equiv m_{h_1} = m_{h_2}$, for better illustration.

tainty[8] ΔM_H. This results in

$$\chi^2_{H,\text{bare}}(M_H, \Delta M_H) = -2 \ln \left(\int_{-\infty}^{+\infty} \mathrm{d}M' \ \exp\left(-\frac{1}{2} \chi^2_H(M') \right) G(M'; M_H, \Delta M_H) \right). \qquad (4.12)$$

Since the folding introduces small, but non-zero values $\chi^2_{H,\text{bare}}(M_H, \Delta M_H)$ for $M_H > 116.4\,\text{GeV}$, where no sensitivity is expected for the SM-like Higgs search channels, the final $\chi^2_H(M_H, \Delta M_H)$ is obtained by subtracting $\chi^2_{H,\text{bare}}(116.4\,\text{GeV}, \Delta M_H)$ from $\chi^2_{H,\text{bare}}(M_H, \Delta M_H)$ for the accessible mass region $M_H \leq 116.4\,\text{GeV}$, and by setting $\chi^2_H(M_H, \Delta M_H) = 0$ for $M_H > 116.4\,\text{GeV}$. A similar procedure is adapted for non-SM like searches, where the points of vanishing sensitivity are determined for each search prior to the folding.

This implementation has already been used in global fits of constrained SUSY models [296]. A non-trivial example of how the LEP χ^2 information can be applied is given in Fig. 4.9. This

[8] This mass uncertainty can be specified independently from the uncertainties discussed in Sect. 4.1.3.

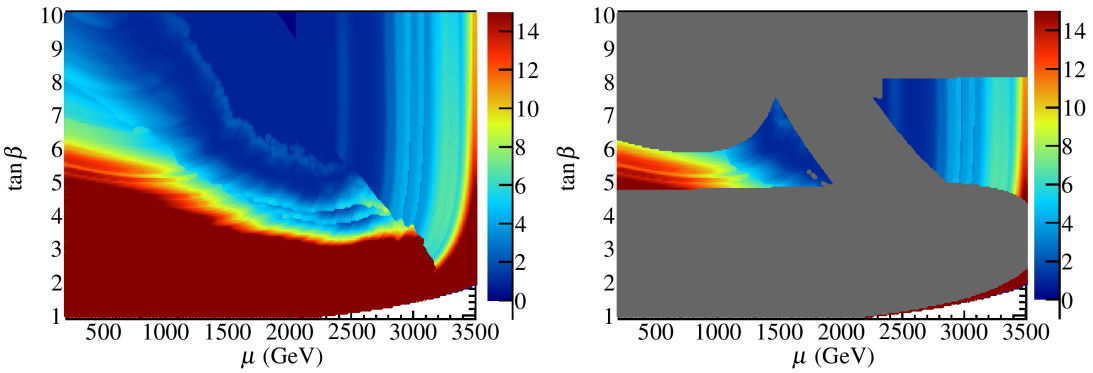

(a) Without LHC exclusions.

(b) With LHC exclusions (gray).

Figure 4.9: HiggsBounds results for the LEP χ^2 (colours) in the low-M_H scenario of the MSSM [246]. The LEP χ^2 information is shown both on its own (a), and with the combined LHC exclusion bounds in gray (b). The latest limit from ATLAS charged Higgs searches [261] is not applied here. These results, which are included from HiggsBounds-4.1, lead to exclusion over the whole parameter space of this benchmark scenario.

figure shows the MSSM low-M_H benchmark scenario [246], in which the heavier $\mathcal{CP}$-even Higgs boson is interpreted as the LHC signal around $M_H \sim 126\,\text{GeV}$, cf. Section 2.4.3. In that case, the lightest Higgs boson, h, is usually below the SM LEP limit and has suppressed couplings to gauge bosons. This is reflected in the figure, showing that a sizable χ^2 penalty is obtained in the parts of the parameter space with low values of m_h, where the couplings to gauge bosons are such that the LEP Higgs searches are sensitive to the production of such a state[9]. The sharp edge in the χ^2 distribution in Fig. 4.9 is obtained at the boundary between two regions of parameter space where the χ^2 contribution comes from the channels $e^+e^- \to hZ$, $h \to b\bar{b}$ and $e^+e^- \to hA \to 4b$, respectively. Using the LEP χ^2 information together with the HiggsBounds exclusion at 95% C.L. from Tevatron/LHC[10], Fig. 4.9 (right) gives the most complete information available from direct Higgs search limits.

Even after the discovery of a SM-like Higgs boson, Higgs boson exclusions still play, and will continue to play a vital role in fitting models of physics beyond the SM with an extended Higgs sector. It would therefore be to great advantage if the Tevatron and LHC collaborations would follow the example of the LEP Higgs working group and provide exclusion limits for varying values of $f\,\sigma_{\text{ref}}$ in addition to the results that are presented at 95% C.L..

4.2 HiggsSignals

The LHC discovery of a Higgs boson in July 2012 initiated the developments of the program HiggsSignals [291, 304]. These form a major part of the work presented in this thesis. In this section we present the program's concepts and functionalities as well as its validation by detailed comparisons of HiggsSignals results with official fit results from ATLAS and CMS.

The purpose of HiggsSignals is to evaluate a statistical (χ^2) measure in order to provide

[9] Note, that we used a mass uncertainty of 2 GeV for the lightest Higgs boson here.

[10] Note, that this figure does not contain the latest charged Higgs search result from ATLAS [261]. Applying this limit excludes the whole plane of the low-M_H benchmark scenario, see Section 6.2.

a quantitative answer to the statistical question of how compatible the model predictions are with the signal strengths and mass measurements from Higgs searches at the Tevatron and LHC experiments. This χ^2 value can be evaluated with two distinct (and to some extend complementary) methods, namely the *peak-centered* and the *mass-centered* χ^2 method.

In the *peak-centered* χ^2 method, the (neutral) Higgs signal rates and masses predicted by the model are tested against the various signal rate measurements published by the experimental collaborations for a fixed Higgs mass hypothesis, as e.g. given in Fig 3.5(b). This hypothetical Higgs mass is typically motivated by the signal "peak" observed in the channels with high mass resolution, i.e. the searches for $H \to \gamma\gamma$ and $H \to ZZ^{(*)} \to 4\ell$. In this way, the model is tested *at the mass position of the observed peak*. In this method, the total χ^2 value is comprised of contributions from both the signal rate observables and the Higgs mass observables. This method is considered to be the default `HiggsSignals` χ^2 procedure.

In the *mass-centered* χ^2 method on the other hand[11], `HiggsSignals` tries to find for every neutral Higgs boson in the model the corresponding signal rate measurements, which are performed under the assumption of a Higgs boson mass equal to the predicted Higgs mass. Thus, the χ^2 is evaluated at the *model-predicted mass position*. For this method to be applicable, the experimental measurements therefore have to be given for a certain mass range, as e.g. shown in Fig. 3.5(a). Unfortunately, this information has only been published for a very few cases, limiting the applicability of this method. In this thesis we will not further discuss the *mass-centered* χ^2 method. A detailed description can be found in Ref. [291].

The model predictions are given by the user in the same form as in `HiggsBounds`, cf. Section 4.1.1, i.e. the predicted Higgs masses, production cross sections and decay rates need to be provided. In addition, theory uncertainties for the Higgs cross section and branching ratio predictions can be provided. The experimental data from Tevatron and LHC Higgs searches is provided with the program, and we aim to keep `HiggsSignals` updated with the latest experimental results. It is however also possible for the user to directly modify or add to the data at will.

The usefulness of a generic code such as `HiggsSignals` has become apparent in the aftermath of the Higgs boson discovery, given the intense work by theorists to use the new Higgs measurements as constraints on the SM and theories for new physics, see e.g. Refs. [270, 272, 274, 305–311]. With `HiggsSignals` we provide a public tool that can be used for both model-independent and model-dependent studies of Higgs masses, couplings, rates, etc. in a consistent framework. The χ^2 output of `HiggsSignals` can also be conveniently used as direct input to global model fits. The code was released in May 2013 and is based on the `HiggsBounds` Fortran library. Since then, it has already been used in various phenomenological studies, see e.g. Refs. [234, 293, 312]. The program forms a major ingredient for the Higgs coupling determinations and global MSSM fits presented in Chapter 5 and 6 of this thesis.

This section is organized as follows. In Section 4.2.1 we discuss the statistical approach followed in `HiggsSignals`, which is based on the Gaussian approximation. In Section 4.2.2 we present the functionality of the peak-centered χ^2 method. The currently implemented experimental data (in the latest version `HiggsSignals-1.2.0`) and its implementation is discussed in Section 4.2.3. These observables are also used in the studies presented in Chapter 5 and 6. In Section 4.2.4 we discuss the performance of the peak-centered χ^2 method and present detailed validation tests, where official ATLAS and CMS fit results are compared with the reproduced `HiggsSignals` results.

[11] `HiggsSignals` also provides the possibility of using the *peak-* and *mass-centered* χ^2 methods simultaneously.

4.2.1 Statistical approach in HiggsSignals

As discussed in Section 3.2, the search results of ATLAS and CMS are reported in the form of the signal strength modifier $\hat{\mu}$, the ratio of the best-fit signal strength to the expected SM strength of a signal in a certain channel, and its uncertainty $\Delta\hat{\mu}$. In the profile likelihood approach [313] used by the experimental collaborations, $\Delta\hat{\mu}$ is derived from the allowed variation of the signal strength multiplier μ around the best fit value $\hat{\mu}$. This is calculated using the likelihood ratio

$$\lambda(\mu) \equiv \mathcal{L}(\mu, \hat{\hat{\theta}})/\mathcal{L}(\hat{\mu}, \hat{\theta}), \tag{4.13}$$

i.e. the likelihood function $\mathcal{L}$ for a given μ with nuisance parameters $\hat{\hat{\theta}}$ optimized at the given value of μ, divided by $\mathcal{L}$ for $\hat{\mu}$ and $\hat{\theta}$ optimized simultaneously, see Ref. [313] for more details. The uncertainty of $\hat{\mu}$ is then calculated using a test statistics based on $-2\ln\lambda(\mu)$. According to Wilks' Theorem [314, 315] (see also Ref. [276]), this can be expressed as

$$-2\ln\lambda(\mu) = \frac{(\mu-\hat{\mu})^2}{\sigma^2} + \mathcal{O}(1/\sqrt{N}), \tag{4.14}$$

with data sample size N. In general, this converges quite quickly to a central or non-central χ^2 distribution, depending on the nuisance parameters [313]. If the test statistics follows a χ^2 distribution, the uncertainties of the measurement can generally be treated as Gaussian, hence we interpret $\Delta\hat{\mu}$ as the Gaussian uncertainty σ, and neglect the $\mathcal{O}(1/\sqrt{N})$ term. Looking at the experimental results used in HiggsSignals, cf. Section 4.2.3, and the available event sample sizes in the current experimental analyses of the full integrated luminosity of $\sim 25\,\text{fb}^{-1}$ from the 7/8 TeV LHC runs, this approximation is justified in almost all analyses. Possible remaining differences to the Gaussian approximation may be still visible in (subcategories of) the $H \to ZZ^* \to 4\ell$ channel, in which the event sample size is still rather small. The largest remaining effects of non-Gaussian distributions are taken into account in HiggsSignals by using asymmetric uncertainties on the measured signal strength in the χ^2 calculation, if published as such by the collaborations.

While the χ^2 calculated in HiggsSignals can be expected to statistically approximate the true $-2\ln\lambda$ distribution, Eq. (4.14), there are three relevant experimental input quantities, which can systematically affect the accuracy of the HiggsSignals output in case they are not presented in a complete form in the publicly disclosed information:

- The signal efficiencies ϵ_i of the various Higgs channels/processes considered in the (categories of a) Higgs analysis, as introduced in Eq. (3.2);

- the correlations of the relevant experimental systematic uncertainties (e.g. of the jet energy scale (JES), $e^{\pm}/\gamma$ identification and energy scale, tagging efficiencies, etc.) between different Higgs search analyses;

- the use of continuous variables for classification of channels/production processes (e.g. by using multivariate techniques), which cannot be mapped directly onto signal strengths measurements for distinct categories used as experimental input for the χ^2 fit in HiggsSignals. An example for this is the CMS $H \to ZZ^* \to 4\ell$ analysis [316]. A comparison of results obtained with the approximated method in HiggsSignals with the official CMS results is given in Section 4.2.4.

While the signal efficiencies ϵ_i could mostly be provided straight-forwardly for every analysis as public information, the communication of the (correlated) systematics, both from experimental and theoretical sources, used in a given analysis is not common. However, within the Gaussian approximation these could in principle be taken into account in `HiggsSignals`. For the future it would be desirable if this information was provided in a model-independent way. We give some ideas on how information on correlated systematic uncertainties in Higgs boson rate measurements could be communicated in Ref. [317]. For a few cases, namely the ATLAS $H \to \tau\tau$ [284] and CMS $H \to \gamma\gamma$ [283, 318], this information could (approximately) be included in `HiggsSignals` given the public information. Details are given in Section 4.2.3. Already with the currently available statistics the ignorance of efficiencies and correlations of experimental systematics are often the dominant effects for the typically small deviations between the official results by the collaborations and the `HiggsSignals` results. The assumption on the parabolic shape of the likelihood, on the other hand, has typically a relatively small impact. More details will be given in Sections 4.2.3 and 4.2.4.

The χ^2 based approach in `HiggsSignals` could in principle be replaced by the use of likelihood curves from the collaborations, which are currently available in $(m_H,\ \hat{\mu})$ grids for a few analyses [5, 283], albeit not for the categories individually. Once they are available for the majority of analyses and for every single (category of an) analysis, the χ^2 could partly be replaced by the use of these likelihoods. However, significant modifications of the final likelihood by a tool like `HiggsSignals` would still be required to make it applicable to arbitrary Higgs sectors, due to potentially different signal compositions and hence changed theoretical rate uncertainties. Moreover, the necessity of incorporating correlated systematics, as mentioned above, remains also in this approach.

An alternative approach for transferring the experimental results into global Higgs coupling or model fits was proposed in Refs. [319] (see also Ref. [307]). This approach suggests that the experiments provide combined (higher-dimensional) likelihood distributions for scale factors of the Higgs boson production modes. On first sight, an appealing feature is that correlations among the combined analyses of the experimental and theoretical uncertainties for the model investigated by the analysis (usually the SM) are automatically taken care of by the collaborations. However, when going beyond the combination of that specific selection of analyses, e.g. when combining ATLAS and CMS results, or already when combining the likelihoods of different decay modes, detailed knowledge of the correlations of common uncertainty sources is again required. Moreover, a careful treatment of these correlations in a combination, as it is done for the simple one-dimensional signal strength measurements in `HiggsSignals`, is far more complicated for higher-dimensional likelihoods.

For these reasons, we recommend the experimental collaborations to continue providing one-dimensional signal strength measurements, including detailed information on signal efficiencies and correlations, since then the amount of model-dependence in the experimental results is rather minimal [317]. Nevertheless, we also support the suggestions made in Refs. [319], since these higher-dimensional likelihoods are still useful on their own and for validation. Note also recently proposed attempts to disentangle theoretical uncertainties from signal strength measurements [320].

4.2.2 The peak-centered χ^2 method

The objective of this method is to perform a χ^2 test for the hypothesis that a local excess, "signal" (or "peak observable"), in the observed data at a specified mass is generated by the

model. In short, this test tries to minimize the total χ^2 by assigning, to each Higgs signal in the used experimental dataset, any number of Higgs bosons of the model. From each signal, the predicted signal strength modifiers and possibly also the corresponding predicted Higgs masses (for channels with good mass resolution) enter the total χ^2 evaluation in a correlated way. Schematically, the total χ^2 is given by

$$\chi^2_{\text{tot}} = \chi^2_\mu + \sum_{i=1}^{N_H} \chi^2_{m_i}, \tag{4.15}$$

where N_H is the number of (neutral) Higgs bosons of the model. The calculation of the individual contributions from the signal strength modifiers, χ^2_μ, and the Higgs masses, $\chi^2_{m_i}$, will be discussed below.

The input data used in this method is based on the prejudice that a Higgs signal has been observed at a particular Higgs mass value, which does not necessarily have to be the exact same value for all observables. Currently, an obvious and prominent application of the peak-centered χ^2 method would be the test of a single Higgs boson against the rate and mass measurements performed at around 125–126 GeV in all available channels reported by the experimental collaborations at the LHC and Tevatron. This will be done in the studies presented in Chapter 5 and 6 of this thesis. However, `HiggsSignals` is implemented in a way that is much more general: Firstly, contributions from other Higgs bosons in the model to the Higgs signals will be considered, and if relevant, included in the test automatically. Secondly, the extension of this test to more Higgs signals (in other mass regions) can simply be achieved by the inclusion of the proper experimental data, or for a phenomenological study, the desired pseudo-data.

Signal rate observables

For N defined signal observables, the total χ^2 contribution from the signal rates is given by

$$\chi^2_\mu = \sum_{\alpha=1}^{N} \chi^2_{\mu,\alpha} = (\hat{\boldsymbol{\mu}} - \boldsymbol{\mu})^T \mathbf{C}_\mu^{-1} (\hat{\boldsymbol{\mu}} - \boldsymbol{\mu}), \tag{4.16}$$

where the observed and predicted signal strength modifiers are contained in the N-dimensional vectors $\hat{\boldsymbol{\mu}}$ and $\boldsymbol{\mu}$, respectively. The predicted signal strength modifiers, $\boldsymbol{\mu}$, are evaluated from the theoretical input on the model according to Eq. (3.4). In contrast to `HiggsBounds` the user has also the possibility to insert the relative efficiency changes $\zeta^{i,j}$ for each analysis and signal topology, if this is of relevance (see Ref. [292] for more details). $\mathbf{C}_\mu$ is the signal strength covariance matrix. In the following we describe how $\mathbf{C}_\mu$ is constructed. We first outline the procedure for the case, in which correlations among theoretical uncertainties of *different* Higgs production cross sections and branching ratios, as e.g. introduced by common parametric dependences, are neglected, and afterwards discuss the generalization to include these correlations.

In the first step, the diagonal elements $(\mathbf{C}_\mu)_{\alpha\alpha}$, corresponding to signal observable α, are filled with the *intrinsic* experimental (statistical and systematic) 1σ uncertainties on the signal strengths squared, denoted by $(\Delta\hat{\mu}^*_\alpha)^2$. These will be treated as uncorrelated uncertainties, since there is no information publicly available on their correlations. We define these uncorrelated uncertainties by subtracting from the total uncertainty $\Delta\hat{\mu}_\alpha$, which is given directly from the 1σ error band in the experimental data, cf. Fig. 3.5, the luminosity uncertainty as well as the theory uncertainties on the predicted signal rate. These will be included at a later stage as

correlated uncertainties. In this subtraction we assume that all uncertainties can be treated as Gaussian errors. This gives

$$(\Delta\hat{\mu}_\alpha^*)^2 = (\Delta\hat{\mu}_\alpha)^2 - (\Delta\mathcal{L}\cdot\hat{\mu}_\alpha)^2 - \sum_{a=1}^{k_\alpha}(\omega_a^\alpha \Delta c_a^{\mathrm{SM}})^2\cdot\hat{\mu}_\alpha^2. \tag{4.17}$$

Here, $\Delta\mathcal{L}$ is the relative uncertainty on the luminosity, and Δc_a^{SM} is the SM channel rate uncertainty for a total of k_α channels contributing to the analysis with signal α. It is given by

$$(\Delta c_a^{\mathrm{SM}})^2 = (\Delta\sigma_a^{\mathrm{SM}})^2 + (\Delta\mathrm{BR}_a^{\mathrm{SM}})^2, \tag{4.18}$$

where $\Delta\sigma_a^{\mathrm{SM}}$ and $\Delta\mathrm{BR}_a^{\mathrm{SM}}$ are the relative systematic uncertainties of the production cross section σ_a and branching ratio BR_a, respectively, of the channel a in the SM. Their recommended values [30, 70, 71] at a Higgs mass around $m_H \sim 125\,\mathrm{GeV}$ have been given in Tabs. 2.2 and 2.4. The SM channel weights, ω_a, have been defined in Eq. (3.6).

The advantage of extracting $(\Delta\hat{\mu}_\alpha^*)^2$ via Eq. (4.17) over using the experimental values $(\Delta\hat{\mu}_\alpha)^2$ directly is that it allows us to take into account the correlations of the theory uncertainties among different signal rates observables. These correlations are inevitably present in signal rate measurements that comprise the same Higgs production and/or decay modes. Furthermore, if other models beyond the SM are investigated, the theory uncertainties on the channel rates can in general be different to those in the SM. Similarly, this construction allows to include the correlations of the relative luminosity uncertainties[12], which can usually be taken equal for all analyses within one collaboration.

In the next step, we insert these correlated uncertainties into the covariance matrix. To each matrix element $(\mathbf{C}_\mu)_{\alpha\beta}$, including the diagonal, we add a term $(\Delta\mathcal{L}_\alpha\hat{\mu}_\alpha)(\Delta\mathcal{L}_\beta\hat{\mu}_\beta)$ if the signals α and β are observed in analyses from the same collaboration. Note, that usually the further simplification $\Delta\mathcal{L}_\alpha = \Delta\mathcal{L}_\beta$ applies in this case. We then add the correlated theory uncertainties of the signal rates, given by

$$\left(\sum_{a=1}^{k_\alpha}\sum_{b=1}^{k_\beta}\left[\delta_{p(a)p(b)}\Delta\sigma_{p(a)}^{\mathrm{model}}\Delta\sigma_{p(b)}^{\mathrm{model}} + \delta_{d(a)d(b)}\Delta\mathrm{BR}_{d(a)}^{\mathrm{model}}\Delta\mathrm{BR}_{d(b)}^{\mathrm{model}}\right]\cdot\omega_{a,\alpha}^{\mathrm{model}}\omega_{b,\beta}^{\mathrm{model}}\right)\mu_\alpha\mu_\beta. \tag{4.19}$$

Here, k_α and k_β are the respective numbers of Higgs (production × decay) channels considered in the experimental analyses, in which the signals α and β are observed. We use the index notation $p(a)$ and $d(a)$ to map the channel a onto its production and decay processes, respectively. In other words, analyses where the signals share a common production and/or decay mode have correlated systematic uncertainties. These channel rate uncertainties are inserted in the covariance matrix according to their relative contributions to the total signal rate *in the model*, i.e. via the channel weight evaluated from the model predictions,

$$\omega_j^{\mathrm{model}} \equiv \frac{\epsilon_j^{\mathrm{model}}\,\sigma^{\mathrm{model}}(P_j(H))\times\mathrm{BR}^{\mathrm{model}}(D_j(H))}{\sum_{j'}\epsilon_{j'}^{\mathrm{model}}\,\sigma^{\mathrm{model}}(P_{j'}(H))\times\mathrm{BR}^{\mathrm{model}}(D_{j'}(H))} \tag{4.20}$$

(cf. Eq. (3.6) for the corresponding weights in the SM). If the theory uncertainties on the Higgs

[12] If the correlations of other experimental systematics are known, they can be taken care of in an analogous way as for the luminosity uncertainty [317]. Currently, this is done for the ATLAS $H\to\tau\tau$ and the CMS $H\to\gamma\gamma$ analyses, see Section 4.2.3 for details.

production and decay rates, as well as the channel weights in the model under investigation, are equal to those in the SM, and also the predicted signal strength matches with the observed signal strength, the uncertainties $(\Delta\hat{\mu}_\alpha)^2$ extracted from the experimental data are exactly restored for the diagonal elements $(\mathbf{C}_\mu)_{\alpha\alpha}$.

We now discuss the generalization, in which correlations among the theoretical uncertainties of the cross section (branching ratio) predictions of *different* production (decay) modes are taken into account. These correlations are induced, for instance, by the dependence of the rate predictions on common parametric uncertainties, like e.g. the uncertainties on the charm, bottom and top quark mass or the strong coupling constant α_s. The relevant information on these correlations can be encoded in (relative) covariance matrices, which can then be fed into HiggsSignals.

If such relative covariance matrices for the production cross sections and branching ratios, denoted in the following by $C^{\text{SM, model}}_{\sigma,ij}$ and $C^{\text{SM, model}}_{\text{BR},ij}$ for the SM and the model, respectively, are known, the contribution to the overall covariance matrix from the theoretical uncertainties of the predicted signal strength, Eq. (4.19), changes to

$$\left(\sum_{a=1}^{k_\alpha}\sum_{b=1}^{k_\beta}\left[C^{\text{model}}_{\sigma,p(a)p(b)} + C^{\text{model}}_{\text{BR},d(a)d(b)}\right]\cdot\omega^{\text{model}}_{a,\alpha}\omega^{\text{model}}_{b,\beta}\right)\mu_\alpha\mu_\beta. \tag{4.21}$$

The theoretical rate uncertainty of the SM, which is subtracted from the quoted $\hat{\mu}$ uncertainty beforehand in order to derive the uncorrelated part of the uncertainty, cf. Eq. (4.17), is now evaluated in a similar way as in Eq. (4.21), but using the covariance matrices $C^{\text{SM}}_{\sigma,ij}$ and $C^{\text{SM}}_{\text{BR},ij}$ and weights ω evaluated for the SM and with μ substituted by $\hat{\mu}$.

The contributions of the major parametric and theoretical (higher-order) uncertainty sources to the total uncertainties of the partial decay widths and production cross sections are given separately by the LHC Higgs Cross Section Working Group (LHCHXSWG) in Refs. [30, 89]. However, there is unfortunately no consensus on how these contributions can be properly combined since the shapes of the underlying probability distributions are unknown. Hence, thus far, the use of conservative maximum error estimates is recommended. Nevertheless, such a prescription is needed in order to properly account for the correlations.

In HiggsSignals we employ covariance matrices evaluated by a Monte Carlo (MC) simulation, which combines the parametric and theoretical uncertainties in a correlated way. The relative parametric uncertainties (PU) on the partial Higgs decay widths, $\Delta\Gamma^i_{\text{PU}}(H \to X_k)$, from the strong coupling, α_s, and the charm, bottom and top quark mass, m_c, m_b and m_t, respectively, as well as the theoretical uncertainties (THU) from missing higher order corrections, $\Delta\Gamma_{\text{THU}}(H \to X_k)$, are taken from Tab. 1 of Ref. [30]. The PUs are provided for each decay mode for both positive and negative variation of the parameter. From this response to the parameter variation we can deduce the correlations among the various decay modes resulting from the PUs. More importantly, correlations between the branching ratio uncertainties are introduced by the total decay width, $\Gamma^{\text{tot}} = \sum_k \Gamma(H \to X_k)$. The covariance matrix for the Higgs branching ratios is then evaluated with a toy MC simulation: all PUs are smeared by a Gaussian of width $\Delta\Gamma^i_{\text{PU}}(H \to X_k)$, with the derived correlations being taken into account. Similarly, the THUs are smeared according to a Gaussian or uniform distribution within their uncertainties. We find that both probability distributions give approximately the same covariance matrix. A detailed description of our procedure is given in Appendix B.2, including a comparison of dif-

ferent implementations and assumptions[13] on the theoretical uncertainties in the light of future data from the high luminosity LHC and the ILC. Overall, we find slightly smaller estimates for the uncertainties than those advocated by the LHCHXSWG, cf. Appendix B.2. This is not surprising, since the (very conservative) recommendation is to combine the uncertainties linearly.

Using the present uncertainty estimates [30], the correlation matrix for the branching ratios in the basis $(H \to \gamma\gamma, WW, ZZ, \tau\tau, bb, Z\gamma, cc, \mu\mu, gg)$ is given by

$$(\rho^{\mathrm{SM}}_{\mathrm{BR},ij}) = \begin{pmatrix} 1 & 0.91 & 0.91 & 0.71 & -0.88 & 0.41 & -0.13 & 0.72 & 0.60 \\ 0.91 & 1 & 0.96 & 0.75 & -0.94 & 0.43 & -0.14 & 0.76 & 0.64 \\ 0.91 & 0.96 & 1 & 0.75 & -0.93 & 0.43 & -0.13 & 0.76 & 0.64 \\ 0.71 & 0.75 & 0.75 & 1 & -0.79 & 0.34 & -0.12 & 0.59 & 0.50 \\ -0.88 & -0.94 & -0.93 & -0.79 & 1 & -0.42 & 0.11 & -0.73 & -0.79 \\ 0.41 & 0.43 & 0.43 & 0.34 & -0.42 & 1 & -0.05 & 0.34 & 0.29 \\ -0.13 & -0.14 & -0.13 & -0.12 & 0.11 & -0.05 & 1 & -0.12 & -0.50 \\ 0.72 & 0.76 & 0.76 & 0.59 & -0.73 & 0.34 & -0.12 & 1 & 0.50 \\ 0.60 & 0.64 & 0.64 & 0.50 & -0.79 & 0.29 & -0.50 & 0.50 & 1 \end{pmatrix}. \tag{4.22}$$

As can be seen, strong correlations are introduced via the total width. As a result, the $H \to b\bar{b}$ channel, which dominates the total width, as well as the $H \to c\bar{c}$ channel are anti-correlated with the remaining decay modes.

For the production modes at the LHC with a center-of-mass energy of 8 TeV the correlation matrix in the basis (ggH, VBF, WH, ZH, $t\bar{t}H$) is given by

$$(\rho^{\mathrm{SM}}_{\sigma,ij}) = \begin{pmatrix} 1 & -2.0 \cdot 10^{-4} & 3.7 \cdot 10^{-4} & 9.0 \cdot 10^{-4} & 0.524 \\ -2.0 \cdot 10^{-4} & 1 & 0.658 & 0.439 & 2.5 \cdot 10^{-4} \\ 3.7 \cdot 10^{-4} & 0.658 & 1 & 0.866 & -9.8 \cdot 10^{-5} \\ 9.0 \cdot 10^{-4} & 0.439 & 0.866 & 1 & 2.8 \cdot 10^{-4} \\ 0.524 & 2.5 \cdot 10^{-4} & -9.8 \cdot 10^{-5} & 2.8 \cdot 10^{-4} & 1 \end{pmatrix}. \tag{4.23}$$

Significant correlations appear between the gluon fusion (ggH) and $t\bar{t}H$ production processes due to common uncertainties from the parton distributions and QCD-scale dependencies, as well as among the vector boson fusion (VBF) and associate Higgs-vector boson production (WH, ZH) channels.

The scripts for the evaluation of the covariance matrices of the production and decay rate uncertainties are included in the `HiggsSignals` package [292]. In this way, they can be re-evaluated for different uncertainty estimates, as e.g. relevant for studies assuming future improvements of these uncertainties, cf. Section 5.3, or if the uncertainties of the model predictions are significantly different than in the SM.

Higgs mass observables

The other type of observables that gives contributions to the total χ^2 in the peak-centered method is the mass measurements performed for the observed signals. Not all observables implemented in `HiggsSignals` feature a mass measurement. In general, a Higgs boson in the model that is not *assigned* to a signal (see below for the precise definition), receives a zero χ^2 contribution from this signal. This would be the case, e.g., for multiple Higgs bosons, whose

[13] The capabilities of Higgs coupling determinations within these future scenarios of prospective theoretical uncertainties and future measurements are investigated in Chapter 5.

mass predictions are not in the vicinity of the observed signal.

HiggsSignals allows the probability density function (pdf) for the Higgs boson masses to be modeled either as a uniform distribution (box), as a Gaussian, or as a box with Gaussian tails. In the Gaussian case, a full correlation in the theory mass uncertainty is taken into account for a Higgs boson that is considered as an explanation for two (or more) signal observables (which include a mass measurement).

Assume that a signal α is observed at measured mass value $\hat{m}_\alpha$, and that a Higgs boson h_i with a predicted mass m_i, potentially with a theory uncertainty Δm_i, is assigned to this signal. Its χ^2 contribution is then simply given by

$$\chi^2_{m_i,\alpha} = \begin{cases} 0 & \text{, for } |m_i - \hat{m}_\alpha| \leq \Delta m_i, \\ \infty & \text{, otherwise} \end{cases} \qquad \text{with} \quad \Delta m_i = \Delta m_i + \Delta \hat{m}_\alpha, \tag{4.24}$$

for a uniform (box) mass pdf, and

$$\chi^2_{m_{H,i},\alpha} = \begin{cases} 0 & \text{, for } |m_i - \hat{m}_\alpha| \leq \Delta m_i, \\ (m_i - \Delta m_i - \hat{m}_\alpha)^2/(\Delta \hat{m}_\alpha)^2 & \text{, for } m_i - \Delta m_i < \hat{m}_\alpha, \\ (m_i + \Delta m_i - \hat{m}_\alpha)^2/(\Delta \hat{m}_\alpha)^2 & \text{, for } m_i + \Delta m_i > \hat{m}_\alpha, \end{cases} \tag{4.25}$$

for a box-shaped pdf with Gaussian tails. Here, we denote the experimental uncertainty of the mass measurement of the analysis associated to signal α by $\Delta \hat{m}_\alpha$. The use of a box-shaped mass pdf, Eq. (4.24), is not recommended in situations where the theory mass uncertainty is small compared to the experimental precision of the mass measurement (and in particular when $\Delta m_i = 0$), since this can lead to overly restrictive results in the assignment of the Higgs boson(s) to high-resolution channels. Moreover, a box-shaped pdf is typically not a good description of the experimental uncertainty of a mass measurement in general. We included this option mostly for illustrational purposes.

In the case of a Gaussian mass pdf the χ^2 calculation is performed in a similar way as the calculation of χ^2_μ in Eq. (4.16). We calculate for each Higgs boson h_i the contribution

$$\chi^2_{m_i} = \sum_{\alpha=1}^{N} \chi^2_{m_i,\alpha} = (\hat{\mathbf{m}} - \mathbf{m}_i)^T \mathbf{C}^{-1}_{\mathbf{m_i}} (\hat{\mathbf{m}} - \mathbf{m}_i). \tag{4.26}$$

Here, the α-th entry of the predicted mass vector $\mathbf{m}_i$ is given by m_i, if the Higgs boson h_i is assigned to the signal α, or $\hat{m}_\alpha$ otherwise (thus leading to a zero χ^2 contribution from *this* observable and *this* Higgs boson). As can be seen from Eq. (4.26), we construct a mass covariance matrix $\mathbf{C}_{\mathbf{m_i}}$ for each Higgs boson h_i in the model. The diagonal elements $(\mathbf{C}_{\mathbf{m_i}})_{\alpha\alpha}$ contain the experimental mass resolution squared, $(\Delta \hat{m}_\alpha)^2$, of the analysis in which the signal α is observed. The squared theory mass uncertainty, $(\Delta m_i)^2$, enters all matrix elements $(\mathbf{C}_{\mathbf{m_i}})_{\alpha\beta}$ (including the diagonal), for which the Higgs boson h_i is assigned to both signal observables α and β. Thus, the theoretical mass uncertainty is treated as fully correlated.

The sign of this correlation depends on the relative position of the predicted Higgs boson mass, m_i, with respect to the two (different) observed mass values, $\hat{m}_{\alpha,\beta}$ (where we assume $\hat{m}_\alpha < \hat{m}_\beta$ for the following discussion): If the predicted mass lies outside the two measurements, i.e. $m_i < \hat{m}_\alpha, \hat{m}_\beta$ or $m_i > \hat{m}_\alpha, \hat{m}_\beta$, then the correlation is assumed to be positive. If it lies in between the two mass measurements, $\hat{m}_\alpha < m_i < \hat{m}_\beta$, the correlation is negative (i.e. we have anti-correlated observables). The necessity of this sign dependence can be illustrated as follows:

Let us assume the predicted Higgs mass is varied within its theoretical uncertainty. In the first case, the deviations of m_i from the mass measurements $\hat{m}_{\alpha,\beta}$ both either increase or decrease (depending on the direction of the mass variation). Thus, the mass measurements are positively correlated. However, in the latter case, a variation of m_i towards one mass measurement always corresponds to a larger deviation of m_i from the other mass measurements. Therefore, the theoretical mass uncertainties for these observables have to be anti-correlated.

Assignment of multiple Higgs bosons

If a model contains an extended (neutral) Higgs sector, it is a priori not clear which Higgs boson(s) give the best explanation of the experimental observations. Moreover, possible superpositions of the signal strengths of the Higgs bosons have to be taken into account. Another (yet hypothetical) complication arises if *more than one* Higgs signal has been discovered in the *same* Higgs search, indicating the discovery of *another* Higgs boson. In this case, care has to be taken that a Higgs boson of the model is only considered as an explanation of one of these signals.

In the peak-centered χ^2 method, these complications are taken into account by the automatic *assignment* of the Higgs bosons in the model to the signal observables. In this procedure, `HiggsSignals` tests whether the combined signal strength of several Higgs bosons might yield a better fit than the assignment of a single Higgs boson to one signal in an analysis. Moreover, based on the predicted and observed Higgs mass values, as well as their uncertainties, the program decides whether a comparison of the predicted and observed signal rates is valid for the considered Higgs boson. A priori, all possible Higgs combinations which can be assigned to the observed signal(s) of an analysis are considered. If more than one signal exists in *one* analysis, it is taken care of that each Higgs boson is assigned to at most one signal to avoid double-counting. A signal to which no Higgs boson is assigned contributes a χ^2 penalty given by Eq. (4.16) with the corresponding model prediction $\mu_\alpha = 0$. This corresponds to the case where an observed signal cannot be explained by any of the Higgs bosons in the model.

For each Higgs search analysis the best Higgs boson assignment is found in the following way: For every possible assignment η of a Higgs boson combination to the signal α observed in the analysis, its corresponding tentative χ^2 contribution, $\chi^2_{\alpha,\eta}$, based on both the signal strength and potentially the Higgs mass measurement, is evaluated. In order to be considered for the assignment, the Higgs combination has to fulfill the following requirements:

- Higgs bosons whose predicted mass m_i lies close enough to the signal mass $\hat{m}_\alpha$, i.e.

$$|m_i - \hat{m}_\alpha| \leq \Lambda\sqrt{(\Delta m_i)^2 + (\Delta\hat{m}_\alpha)^2}, \tag{4.27}$$

  are required to be assigned to the signal α. Here, Λ denotes the *assignment range*, which can be modified by the user (the default setting is $\Lambda = 1$).

- If the χ^2 contribution from the measured Higgs mass is *deactivated* for this signal, i.e. the observable does *not* have a mass measurement, combinations with a Higgs boson that fulfills Eq. (4.27) are taken into account for a possible assignment, and not taken into account otherwise.

- If the χ^2 contribution from the measured Higgs mass is *activated*, combinations with a Higgs boson mass which does not fulfill Eq. (4.27) are still considered. Here, the difference

of the measured and predicted Higgs mass is automatically taken into account by the χ^2 contribution from the Higgs mass, χ^2_m.

In the case where multiple Higgs bosons are assigned to the same signal, the combined signal strength modifier μ is taken as the sum over their predicted signal strength modifiers, corresponding to incoherently adding their rates. The best Higgs-to-signals assignment η_0 in an analysis is that which minimizes the overall χ^2 contribution, i.e.

$$\eta_0 = \eta, \quad \text{for which} \sum_{\alpha=1}^{\mathrm{N_{signals}}} \chi^2_{\alpha,\eta} \text{ is minimal.} \tag{4.28}$$

Here, the sum runs over all signals observed *within this particular analysis*. In this procedure, `HiggsSignals` only considers assignments η where each Higgs boson is not assigned to more than one signal within the same analysis in order to avoid double counting.

There is also the possibility to enforce that a collection of peak observables is either assigned or not assigned in parallel. This can be useful if certain peak observables stem from the same Higgs analysis but correspond to measurements performed for specific tags or categories (e.g. as presently used in $H \to \gamma\gamma$ analyses). See Ref. [291] for a description of these *assignment groups*.

A final remark should be made on the experimental resolution, $\Delta\hat{m}_\alpha$, which enters Eq. (4.27). In case the analysis has an actual mass measurement that enters the χ^2 contribution from the Higgs mass, $\Delta\hat{m}_\alpha$ gives the uncertainty of the mass measurement. If this is not the case, $\Delta\hat{m}_\alpha$ is an estimate of the mass range in which two Higgs boson signals cannot be resolved. This is taken to be the mass resolution quoted by the experimental analysis. Typical values are, for instance, 10% (for $VH \to V(b\bar{b})$ [321]) and 20% (for $H \to \tau\tau$ [322] and $H \to WW^{(*)} \to \ell\nu\ell\nu$ [323]) of the assumed Higgs mass. It should be kept in mind that the `HiggsSignals` procedure to automatically assign (possibly several) Higgs bosons to the signals potentially introduces sharp transitions from assigned to unassigned signals at certain mass values, see Section 4.2.4 for a further discussion. More detailed studies of overlapping signals from multiple Higgs bosons, in which possible interference effects are taken into account, are desirable in case evidence for such a scenario emerges in the future data.

4.2.3 Experimental input from the Tevatron and the LHC

In this section we give an overview of the experimental data that is currently implemented in `HiggsSignals-1.2.0` (status of March 2014) and used by the peak-centered χ^2 method. These observables will be used in the global fits of Higgs couplings and MSSM scenarios presented in Chapter 5 and 6. Moreover, we discuss some details of the implementation, which illustrate the impact of including the major correlations of experimental systematic uncertainties in the χ^2 evaluation on the fit results.

The currently implemented experimental data includes the four Higgs mass measurements from the $H \to ZZ \to 4\ell$ and $H \to \gamma\gamma$ searches at ATLAS [289], and CMS [281, 283],

$$\begin{aligned}
\hat{m}^{ZZ}_{\mathrm{ATL}} &= 124.3\,^{+0.6}_{-0.5}\ (\mathrm{stat.})\,^{+0.5}_{-0.3}\ (\mathrm{syst.})\,\mathrm{GeV},\\
\hat{m}^{\gamma\gamma}_{\mathrm{ATL}} &= 126.8 \pm 0.2\ (\mathrm{stat.}) \pm 0.7\ (\mathrm{syst.})\,\mathrm{GeV},\\
\hat{m}^{ZZ}_{\mathrm{CMS}} &= 125.6 \pm 0.4\ (\mathrm{stat.}) \pm 0.2\ (\mathrm{syst.})\,\mathrm{GeV},\\
\hat{m}^{\gamma\gamma}_{\mathrm{CMS}} &= 125.4 \pm 0.5\ (\mathrm{stat.}) \pm 0.6\ (\mathrm{syst.})\,\mathrm{GeV}.
\end{aligned} \tag{4.29}$$

Following a conservative approach, the (symmetric) mass uncertainty $\Delta\hat{m}$ implemented in `HiggsSignals` is obtained by adding the quoted statistical and systematic uncertainties linearly (and taking the larger value in case of asymmetric uncertainties).

In total, 80 signal strength measurements from the CDF, DØ, ATLAS and CMS experiments are implemented. These are listed in Tabs. 4.1 and 4.2, where also numbers for the assumed signal composition of a SM Higgs boson are provided for all observables. Furthermore, we list the CM energy at which the analyzed data was collected. Measurements based on a combination of 7 and 8 TeV data are implemented as 8 TeV-only data in `HiggsSignals`. Most of the listed observables enter the χ^2 evaluation directly, except for a few cases where a more careful treatment is required as described in detail below.

For the six signal strength category measurements of the ATLAS SM $H \to \tau^+\tau^-$ search we implement additional correlations inspired by the information given in Ref. [284], following the procedure outlined in Ref. [317]. This includes

- correlated uncertainties of $\sim 5-10\%$ $(20-30\%)$ in the VBF (boosted) categories of the gluon gluon fusion (ggF) signal component, mostly representing the uncertainties of the differential p_T distribution of this signal process,
- correlated normalization uncertainties of the top and $Z \to \ell\ell$ background of $\sim 10-15\%$ among the leptonic-leptonic and leptonic-hadronic $\tau\tau$ categories,
- correlated uncertainties from hadronic τ identification of $\sim 4\%$ (12%) in the leptonic-hadronic (hadronic-hadronic) $\tau\tau$ categories,
- correlated di-hadronic τ trigger efficiency uncertainties of 7% among the two hadronic-hadronic $\tau\tau$ channels,
- correlated $Z \to \tau\tau$ background normalization uncertainties of $\sim 10-12\%$ among the hadronic-leptonic and leptonic-leptonic $\tau\tau$ categories.

The effect of including these correlations is shown in Fig. 4.10 for a fit in a two-dimensional scaling model. Here the ggF and $t\bar{t}H$ production cross sections are scaled by $\mu_{\mathrm{ggF+ttH}}$ and the VBF, WH and ZH production cross sections by $\mu_{\mathrm{qqH+VH}}$. The 68% and 95% C.L. regions are shown for both the original ATLAS result [284] and the likelihood reconstructed using `HiggsSignals`. It can clearly be seen that the agreement between the reconstructed and official likelihood is significantly improved if the additional correlations are included.

A similar implementation is done for the CMS $H \to \gamma\gamma$ results [283, 318], since the correlations among the observables introduced by common sources of experimental systematic uncertainties turn out to be non-negligible [291]. Guided by the information given in Ref. [283], we therefore introduce the following correlations for the CMS $H \to \gamma\gamma$ category measurements:

- event migration of 12.5% between neighboring untagged categories for each 7 TeV and 8 TeV results,
- event migration of 15.0% between the loose and tight dijet category at 8 TeV,
- for the dijet categories, we include a dijet tagging efficiency uncertainty, corresponding to an anti-correlated uncertainty among the ggH and VBF channels, of $10-15\%$ and 30%, respectively,

Analysis	energy $\sqrt{s}$	$\hat{\mu} \pm \Delta\hat{\mu}$	SM signal composition [in %]				
			ggH	VBF	WH	ZH	$t\bar{t}H$
ATL $(pp) \to H \to WW \to \ell\nu\ell\nu$ (0/1jet) [289, 324]	7/8 TeV	$0.82^{+0.33}_{-0.32}$	97.2	1.6	0.7	0.4	0.1
ATL $(pp) \to H \to WW \to \ell\nu\ell\nu$ (VBF) [289, 324]	7/8 TeV	$1.42^{+0.70}_{-0.56}$	19.8	80.2	0.0	0.0	0.0
ATL $(pp) \to H \to ZZ \to 4\ell$ (VBF/VH-like) [277, 289]	7/8 TeV	$1.18^{+1.64}_{-0.90}$	36.8	43.1	12.8	7.3	0.0
ATL $(pp) \to H \to ZZ \to 4\ell$ (ggH-like) [277, 289]	7/8 TeV	$1.45^{+0.43}_{-0.37}$	92.5	4.5	1.9	1.1	0.0
ATL $(pp) \to H \to \gamma\gamma$ (unconv.-central-low p_{Tt}) [325]	7 TeV	$0.53^{+1.41}_{-1.48}$	92.9	3.8	2.0	1.1	0.2
ATL $(pp) \to H \to \gamma\gamma$ (unconv.-central-high p_{Tt}) [325]	7 TeV	$0.22^{+1.94}_{-1.95}$	65.5	14.8	10.8	6.2	2.7
ATL $(pp) \to H \to \gamma\gamma$ (unconv.-rest-low p_{Tt}) [325]	7 TeV	$2.52^{+1.68}_{-1.68}$	92.6	3.7	2.2	1.2	0.2
ATL $(pp) \to H \to \gamma\gamma$ (unconv.-rest-high p_{Tt}) [325]	7 TeV	$10.44^{+3.67}_{-3.70}$	64.4	15.2	11.8	6.6	2.0
ATL $(pp) \to H \to \gamma\gamma$ (conv.-central-low p_{Tt}) [325]	7 TeV	$6.10^{+2.63}_{-2.62}$	92.7	3.8	2.1	1.1	0.2
ATL $(pp) \to H \to \gamma\gamma$ (conv.-central-high p_{Tt}) [325]	7 TeV	$-4.36^{+1.80}_{-1.81}$	65.7	14.4	11.0	6.2	2.8
ATL $(pp) \to H \to \gamma\gamma$ (conv.-rest-low p_{Tt}) [325]	7 TeV	$2.74^{+1.98}_{-2.01}$	92.7	3.6	2.2	1.2	0.2
ATL $(pp) \to H \to \gamma\gamma$ (conv.-rest-high p_{Tt}) [325]	7 TeV	$-1.59^{+2.89}_{-2.90}$	64.4	15.1	12.1	6.4	2.0
ATL $(pp) \to H \to \gamma\gamma$ (conv.-trans.) [325]	7 TeV	$0.37^{+3.58}_{-3.79}$	89.2	5.0	3.7	1.9	0.3
ATL $(pp) \to H \to \gamma\gamma$ (2 jet) [325]	7 TeV	$2.72^{+1.87}_{-1.85}$	23.3	75.9	0.5	0.2	0.1
ATL $(pp) \to H \to \gamma\gamma$ (unconv.-central-low p_{Tt}) [282]	8 TeV	$0.87^{+0.73}_{-0.70}$	92.0	5.0	1.7	0.8	0.5
ATL $(pp) \to H \to \gamma\gamma$ (unconv.-central-high p_{Tt}) [282]	8 TeV	$0.96^{+1.07}_{-0.95}$	78.6	12.6	4.7	2.6	1.4
ATL $(pp) \to H \to \gamma\gamma$ (unconv.-rest-low p_{Tt}) [282]	8 TeV	$2.50^{+0.92}_{-0.77}$	92.0	5.0	1.7	0.8	0.5
ATL $(pp) \to H \to \gamma\gamma$ (unconv.-rest-high p_{Tt}) [282]	8 TeV	$2.69^{+1.35}_{-1.17}$	78.6	12.6	4.7	2.6	1.4
ATL $(pp) \to H \to \gamma\gamma$ (conv.-central-low p_{Tt}) [282]	8 TeV	$1.39^{+1.01}_{-0.95}$	92.0	5.0	1.7	0.8	0.5
ATL $(pp) \to H \to \gamma\gamma$ (conv.-central-high p_{Tt}) [282]	8 TeV	$1.98^{+1.54}_{-1.26}$	78.6	12.6	4.7	2.6	1.4
ATL $(pp) \to H \to \gamma\gamma$ (conv.-rest-low p_{Tt}) [282]	8 TeV	$2.23^{+1.14}_{-1.01}$	92.0	5.0	1.7	0.8	0.5
ATL $(pp) \to H \to \gamma\gamma$ (conv.-rest-high p_{Tt}) [282]	8 TeV	$1.27^{+1.32}_{-1.23}$	78.6	12.6	4.7	2.6	1.4
ATL $(pp) \to H \to \gamma\gamma$ (conv.-trans.) [282]	8 TeV	$2.78^{+1.72}_{-1.57}$	92.0	5.0	1.7	0.8	0.5
ATL $(pp) \to H \to \gamma\gamma$ (high mass, 2 jet, loose) [282]	8 TeV	$2.75^{+1.78}_{-1.38}$	45.3	53.7	0.5	0.3	0.2
ATL $(pp) \to H \to \gamma\gamma$ (high mass, 2 jet, tight) [282]	8 TeV	$1.61^{+0.83}_{-0.67}$	27.1	72.5	0.3	0.1	0.0
ATL $(pp) \to H \to \gamma\gamma$ (low mass, 2 jet) [282]	8 TeV	$0.32^{+1.72}_{-1.44}$	38.0	2.9	40.1	16.9	2.1
ATL $(pp) \to H \to \gamma\gamma$ (E_T^{miss} sign.) [282]	8 TeV	$2.97^{+2.71}_{-2.15}$	4.4	0.3	35.8	47.4	12.2
ATL $(pp) \to H \to \gamma\gamma$ (1ℓ) [282]	8 TeV	$2.69^{+1.97}_{-1.66}$	2.5	0.4	63.3	15.2	18.7
ATL $(pp) \to H \to \tau\tau$ (VBF, had-had) [284]	8 TeV	$1.03^{+0.92}_{-0.73}$	25.1	74.9	0.0	0.0	0.0
ATL $(pp) \to H \to \tau\tau$ (boosted, had-had) [284]	8 TeV	$0.77^{+1.17}_{-0.98}$	65.1	16.1	12.5	6.3	0.0
ATL $(pp) \to H \to \tau\tau$ (VBF, lep-had) [284]	8 TeV	$1.61^{+0.77}_{-0.60}$	13.9	86.1	0.0	0.0	0.0
ATL $(pp) \to H \to \tau\tau$ (boosted, lep-had) [284]	8 TeV	$1.21^{+1.07}_{-0.83}$	68.8	16.1	10.1	5.0	0.0
ATL $(pp) \to H \to \tau\tau$(VBF, lep-lep) [284]	8 TeV	$2.19^{+1.23}_{-1.10}$	12.4	87.6	0.0	0.0	0.0
ATL $(pp) \to H \to \tau\tau$ (boosted, lep-lep) [284]	8 TeV	$2.03^{+1.80}_{-1.45}$	66.0	25.6	6.2	2.2	0.0
ATL $(pp) \to VH \to V(bb)$ (0ℓ) [326]	7/8 TeV	$0.46^{+0.88}_{-0.86}$	0.0	0.0	21.2	78.8	0.0
ATL $(pp) \to VH \to V(bb)$ (1ℓ) [326]	7/8 TeV	$0.09^{+1.01}_{-1.00}$	0.0	0.0	96.7	3.3	0.0
ATL $(pp) \to VH \to V(bb)$ (2ℓ) [326]	7/8 TeV	$-0.36^{+1.48}_{-1.38}$	0.0	0.0	0.0	100.0	0.0
ATL $(pp) \to VH \to V(WW)$ [327]	7/8 TeV	$3.70^{+1.90}_{-2.00}$	0.0	0.0	63.8	36.2	0.0
CDF $(p\bar{p}) \to H \to WW$ [328]	1.96 TeV	$0.00^{+1.78}_{-1.78}$	77.5	5.4	10.6	6.5	0.0
CDF $(p\bar{p}) \to H \to \gamma\gamma$ [328]	1.96 TeV	$7.81^{+4.61}_{-4.42}$	77.5	5.4	10.6	6.5	0.0
CDF $(p\bar{p}) \to H \to \tau\tau$ [328]	1.96 TeV	$0.00^{+8.44}_{-8.44}$	77.5	5.4	10.6	6.5	0.0
CDF $(p\bar{p}) \to VH \to Vbb$ [328]	1.96 TeV	$1.72^{+0.92}_{-0.87}$	0.0	0.0	61.9	38.1	0.0
CDF $(p\bar{p}) \to ttH \to ttbb$ [328]	1.96 TeV	$9.49^{+6.60}_{-6.28}$	0.0	0.0	0.0	0.0	100.0

Table 4.1: Signal strength measurements from ATLAS and CDF included in `HiggsSignals-1.2.0`.

Analysis	energy $\sqrt{s}$	$\hat{\mu} \pm \Delta\hat{\mu}$	SM signal composition [in %]				
			ggH	VBF	WH	ZH	$t\bar{t}H$
CMS $(pp) \to H \to WW \to 2\ell 2\nu$ (0/1 jet) [329]	7/8 TeV	$0.74^{+0.22}_{-0.20}$	83.0	11.1	3.8	2.2	0.0
CMS $(pp) \to H \to WW \to 2\ell 2\nu$ (VBF) [329]	7/8 TeV	$0.60^{+0.57}_{-0.46}$	19.8	80.2	0.0	0.0	0.0
CMS $(pp) \to H \to WW \to 2\ell 2\nu$ (VH) [329]	7/8 TeV	$0.39^{+1.97}_{-1.87}$	56.2	4.5	25.1	14.2	0.0
CMS $(pp) \to H \to WW \to 3\ell 3\nu$ (WH) [329]	7/8 TeV	$0.56^{+1.27}_{-0.95}$	0.0	0.0	100.0[1]	0.0	0.0
CMS $(pp) \to VH \to V(WW)$ (hadronic V) [330]	7/8 TeV	$1.00^{+2.00}_{-2.00}$	59.8	4.0	24.2	12.0	0.0
CMS $(pp) \to H \to ZZ \to 4\ell$ (0/1 jet) [316]	7/8 TeV	$0.86^{+0.32}_{-0.26}$	89.8	10.2	0.0	0.0	0.0
CMS $(pp) \to H \to ZZ \to 4\ell$ (2 jet) [316]	7/8 TeV	$1.24^{+0.85}_{-0.58}$	71.2	28.8	0.0	0.0	0.0
CMS $(pp) \to H \to \gamma\gamma$ (untagged 0) [283, 318]	7 TeV	$3.88^{+2.00}_{-1.68}$	61.4	16.9	12.0	6.6	3.1
CMS $(pp) \to H \to \gamma\gamma$ (untagged 1) [283, 318]	7 TeV	$0.20^{+1.01}_{-0.93}$	87.7	6.2	3.6	2.0	0.5
CMS $(pp) \to H \to \gamma\gamma$ (untagged 2) [283, 318]	7 TeV	$0.04^{+1.25}_{-1.24}$	91.4	4.4	2.5	1.4	0.3
CMS $(pp) \to H \to \gamma\gamma$ (untagged 3) [283, 318]	7 TeV	$1.47^{+1.68}_{-2.47}$	91.3	4.4	2.6	1.5	0.2
CMS $(pp) \to H \to \gamma\gamma$ (2 jet) [283, 318]	7 TeV	$4.18^{+2.31}_{-1.78}$	26.7	72.6	0.4	0.2	0.0
CMS $(pp) \to H \to \gamma\gamma$ (untagged 0) [283]	8 TeV	$2.20^{+0.95}_{-0.78}$	72.9	11.7	8.2	4.6	2.6
CMS $(pp) \to H \to \gamma\gamma$ (untagged 1) [283]	8 TeV	$0.06^{+0.69}_{-0.67}$	83.5	8.5	4.5	2.6	1.0
CMS $(pp) \to H \to \gamma\gamma$ (untagged 2) [283]	8 TeV	$0.31^{+0.50}_{-0.47}$	91.5	4.5	2.3	1.3	0.4
CMS $(pp) \to H \to \gamma\gamma$ (untagged 3) [283]	8 TeV	$-0.36^{+0.88}_{-0.81}$	92.5	3.9	2.1	1.2	0.3
CMS $(pp) \to H \to \gamma\gamma$ (2 jet, tight) [283]	8 TeV	$0.27^{+0.69}_{-0.58}$	20.6	79.0	0.2	0.1	0.1
CMS $(pp) \to H \to \gamma\gamma$ (2 jet, loose) [283]	8 TeV	$0.78^{+1.10}_{-0.98}$	46.8	51.1	1.1	0.6	0.5
CMS $(pp) \to H \to \gamma\gamma$ (μ) [283]	8 TeV	$0.38^{+1.84}_{-1.36}$	0.0	0.2	50.4	28.6	20.8
CMS $(pp) \to H \to \gamma\gamma$ (e) [283]	8 TeV	$-0.67^{+2.78}_{-1.95}$	1.1	0.4	50.2	28.5	19.8
CMS $(pp) \to H \to \gamma\gamma$ (E_T^{miss}) [283]	8 TeV	$1.89^{+2.62}_{-2.28}$	22.1	2.6	40.6	23.0	11.7
CMS $(pp) \to H \to \mu\mu$ [331]	7/8 TeV	$2.90^{+2.80}_{-2.70}$	92.5	7.5	0.0	0.0	0.0
CMS $(pp) \to H \to \tau\tau$ (0 jet) [285, 286]	7/8 TeV	$0.40^{+0.73}_{-1.13}$	98.2	1.0	0.5	0.3	0.0
CMS $(pp) \to H \to \tau\tau$ (1 jet) [285, 286]	7/8 TeV	$1.06^{+0.47}_{-0.47}$	76.0	14.9	5.8	3.3	0.0
CMS $(pp) \to H \to \tau\tau$ (VBF) [285, 286]	7/8 TeV	$0.93^{+0.41}_{-0.41}$	17.1	82.9	0.0	0.0	0.0
CMS $(pp) \to VH \to V(\tau\tau)$ [285, 286]	7/8 TeV	$0.98^{+1.68}_{-1.50}$	0.0	0.0	48.6[2]	26.4[2]	0.0
CMS $(pp) \to VH \to V(bb)$ [332]	7/8 TeV	$1.00^{+0.51}_{-0.49}$	0.0	0.0	63.8	36.2	0.0
CMS $(pp) \to ttH \to 2\ell$ (same-sign) [333]	8 TeV	$5.30^{+2.20}_{-1.80}$	0.0	0.0	0.0	0.0	100.0[3]
CMS $(pp) \to ttH \to 3\ell$ [333]	8 TeV	$2.70^{+2.20}_{-1.80}$	0.0	0.0	0.0	0.0	100.0[4]
CMS $(pp) \to ttH \to 4\ell$ [333]	8 TeV	$-4.80^{+5.00}_{-1.20}$	0.0	0.0	0.0	0.0	100.0[5]
CMS $(pp) \to ttH \to tt(bb)$ [334]	7/8 TeV	$1.00^{+1.90}_{-2.00}$	0.0	0.0	0.0	0.0	100.0
CMS $(pp) \to ttH \to tt(\tau\tau)$ [334]	8 TeV	$-1.40^{+6.30}_{-5.50}$	0.0	0.0	0.0	0.0	100.0
CMS $(pp) \to ttH \to tt(\gamma\gamma)$ [335]	8 TeV	$-0.20^{+2.40}_{-1.90}$	0.0	0.0	0.0	0.0	100.0
DØ $(p\bar{p}) \to H \to WW$ [336]	1.96 TeV	$1.90^{+1.63}_{-1.52}$	77.5	5.4	10.6	6.5	0.0
DØ $(p\bar{p}) \to H \to bb$ [336]	1.96 TeV	$1.23^{+1.24}_{-1.17}$	0.0	0.0	61.9	38.1	0.0
DØ $(p\bar{p}) \to H \to \gamma\gamma$ [336]	1.96 TeV	$4.20^{+4.60}_{-4.20}$	77.5	5.4	10.6	6.5	0.0
DØ $(p\bar{p}) \to H \to \tau\tau$ [336]	1.96 TeV	$3.96^{+4.11}_{-3.38}$	77.5	5.4	10.6	6.5	0.0

[1] The signal is contaminated to 15.0% by $WH \to W(\tau\tau)$ in the SM.
[2] The signal is contaminated to 17.2% [9.8%] by $WH \to WWW$ [$ZH \to ZWW$] in the SM.
[3] The $t\bar{t}H \to \ell^\pm\ell^\pm$ signal is comprised of the final states WW (74.5%), ZZ (3.7%) and $\tau\tau$ (21.7%) in the SM.
[4] The $t\bar{t}H \to 3\ell$ signal is comprised of the final states WW (73.0%), ZZ (4.6%) and $\tau\tau$ (22.5%) in the SM.
[5] The $t\bar{t}H \to 4\ell$ signal is comprised of the final states WW (54.1%), ZZ (17.4%) and $\tau\tau$ (28.5%) in the SM.

Table 4.2: Signal strength measurements from CMS and DØ included in `HiggsSignals-1.2.0`.

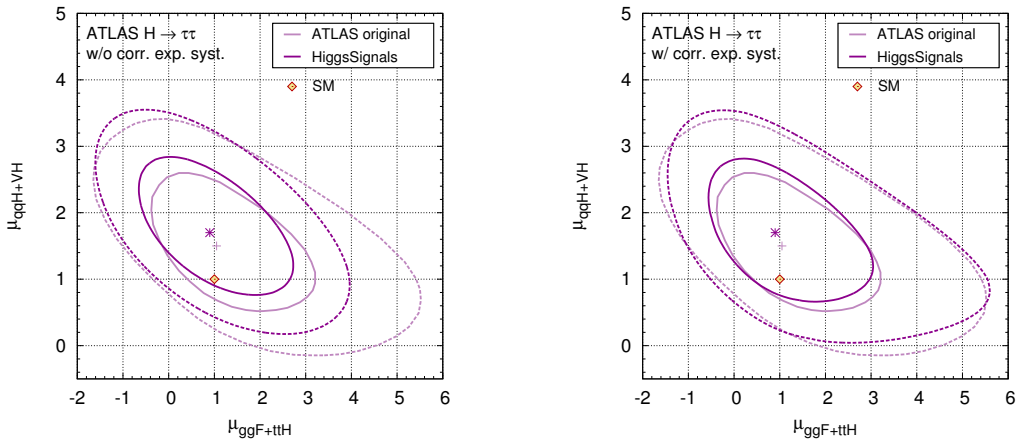

(a) Without correlations of experimental systematic uncertainies.

(b) With correlations of experimental systematic uncertainies.

Figure 4.10: Comparison of our fit results with official ATLAS results for rescaled production cross sections of the gluon fusion (ggF) and $t\bar{t}H$ processes vs. the vector boson fusion (qqH) and VH ($V = W, Z$) processes using the ATLAS $H \to \tau^+\tau^-$ measurements [284]. We compare the effects of neglecting or including correlations of known experimental systematic uncertainties in (a) and (b), respectively. The solid (dashed) curves indicate the 68 (95)% C.L. regions. The asterisk marks the best-fit point. The faint magenta curves and plus sign show the corresponding original ATLAS results.

- E_T^{miss} cut efficiency uncertainty in the E_T^{miss} selection at 8 TeV of 15% for the ggH and VBF channels and 4% for the WH, ZH, $t\bar{t}H$ channels, respectively.

One more complication arises, because the signal rate measurements in the various categories of the $H \to \gamma\gamma$ analysis are only publicly available for a mass value of $m_H = 125.0\,\text{GeV}$. On the contrary, Ref. [5] provides only fit results at 125.7 GeV for the signal strengths

$$\begin{aligned} \hat{\mu}(H \to \gamma\gamma,\ \text{untagged}) &= 0.70^{+0.33}_{-0.29}, \\ \hat{\mu}(H \to \gamma\gamma,\ \text{VBF tag}) &= 1.01^{+0.63}_{-0.54}, \\ \hat{\mu}(H \to \gamma\gamma,\ \text{VH tag}) &= 0.57^{+1.34}_{-1.34}, \end{aligned} \tag{4.30}$$

combining the untagged, dijet and remaining leptonic/missing energy categories, respectively. Furthermore, the official scale factor fit results given by CMS, which can be used to validate our implementation, see Section 4.2.4, assume a Higgs mass of 125.7 GeV [5]. Given the category measurements at 125.0 GeV (based on the MVA analysis), cf. Tab. 4.2, we repeated these fits with `HiggsSignals` to obtain

$$\begin{aligned} \hat{\mu}(H \to \gamma\gamma,\ \text{untagged}) &= 0.64^{+0.32}_{-0.30}, \\ \hat{\mu}(H \to \gamma\gamma,\ \text{VBF tag}) &= 0.79^{+0.58}_{-0.54}, \\ \hat{\mu}(H \to \gamma\gamma,\ \text{VH tag}) &= 0.63^{+1.28}_{-1.14}. \end{aligned} \tag{4.31}$$

We approximate the unknown category measurements at 125.7 GeV by rescaling the category measurements at 125.0 GeV by the ratio of the corresponding combined fit results.

In Fig. 4.11 we show the effects of including the correlations of systematic experimental

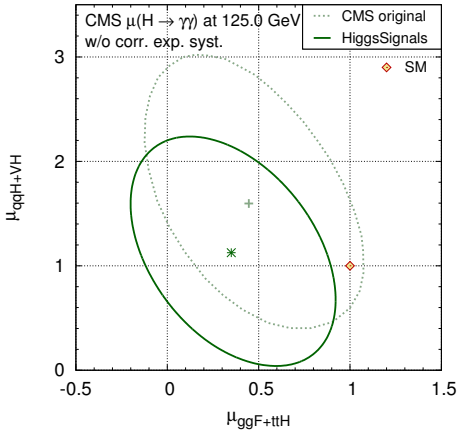

(a) Using original measurements at 125.0 GeV without correlations of experimental systematic uncertainies.

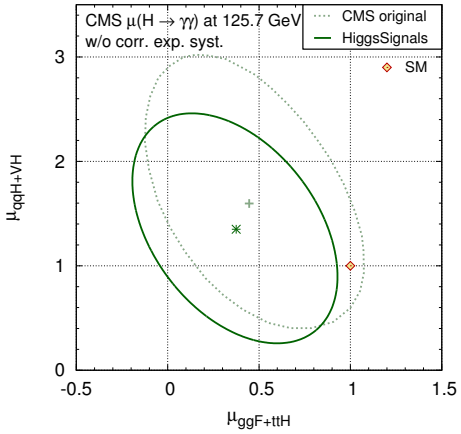

(b) Using approximated measurements at 125.7 GeV without correlations of experimental systematic uncertainies.

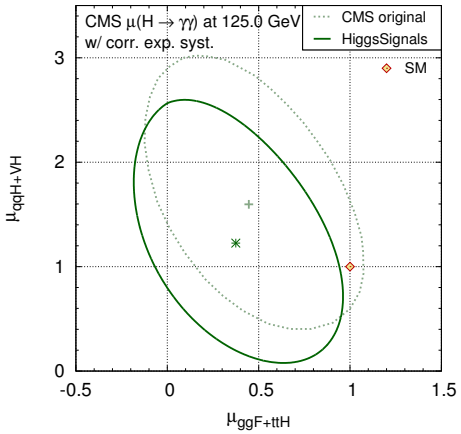

(c) Using original measurements at 125.0 GeV with correlations of experimental systematic uncertainies.

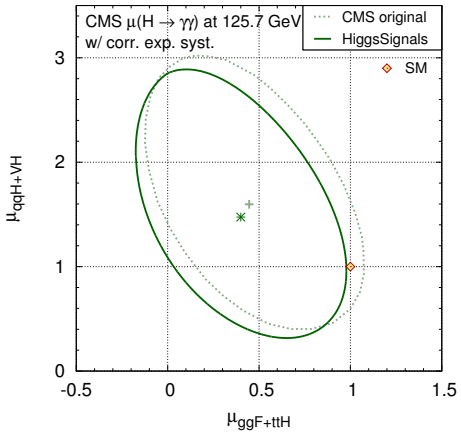

(d) Using approximated measurements at 125.7 GeV with correlations of experimental systematic uncertainies.

Figure 4.11: Comparison of our fit results with official CMS results for rescaled production cross sections of the gluon fusion (ggF) and $t\bar{t}H$ processes vs. the vector boson fusion (qqH) and VH ($V = W, Z$) processes using the CMS $H \to \gamma\gamma$ category measurements [283, 318]. The results have been derived using either the original measurements given at a Higgs mass of 125.0 GeV, shown in (a,c), or approximated (rescaled) measurements at 125.7 GeV, shown in (b,d). We furthermore compare the effects of neglecting or including correlations of known experimental systematic uncertainties in (a,b) and (c,d), respectively. The green contours give the obtained 68% C.L. region, where the dotted faint green curve always indicates the original CMS results obtained for a Higgs boson mass of 125.7 GeV. The corresponding best-fit points are marked by a green asterisk and faint plus sign, respectively.

uncertainties and the rescaling of the category measurements to $m_H = 125.7\,\text{GeV}$ for a 2D fit to common scale factors for the gluon gluon fusion and $t\bar{t}H$ cross section, $\mu_{\text{ggF+ttH}}$, and for the vector boson fusion and VH ($V = W, Z$) cross sections, $\mu_{\text{qqH+VH}}$, using only results from the CMS $H \to \gamma\gamma$ analysis [283, 318]. The original CMS result obtained for $m_H = 125.7\,\text{GeV}$ is overlaid in the figure. It can be seen that both effects have a sizable impact on the result. Acceptable agreement with the official CMS result can be obtained if both the correlations and the rescaling is taken into account, as shown in Fig. 4.11(d). We therefore use this setup of the CMS $H \to \gamma\gamma$ measurements for the fits presented in this thesis. Note however, that the original CMS measurements, as given in Tab. 4.2, are also included in `HiggsSignals-1.2.0` and can be used at will.

4.2.4 Performance and validation

In this section we discuss the performance of the peak-centered χ^2 method for a few illustrative cases. We furthermore validate the procedure by comparing our fit results with official results from the ATLAS and CMS experiments. The quality of agreement of the reproduced `HiggsSignals` results with the official results justifies the Gaussian limit approximation in the statistical approach of `HiggsSignals`. Note that to a certain extent (which is difficult to estimate), the accuracy of the reproduced results suffers from the lack of publicly available information of the analysis efficiencies on the various production modes. Similar performance studies have been done for the mass-centered χ^2 method, see Ref. [291].

Performance of the peak-centered χ^2 method

As a first application we discuss the performance of the peak-centered χ^2 method on a SM-like Higgs boson. As already shown in Fig. 3.5(b), a simple one parameter fit can be performed to the signal strength modifier μ, which scales the predicted signal rates of all investigated Higgs channels uniformly. In this fit the Higgs mass is held fixed at e.g. $m_H = 125.7\,\text{GeV}$. Using the signal strength measurements of the individual search channels obtained by the CMS collaboration [5], as given in Fig. 3.5(b), the best-fit signal strength reconstructed with `HiggsSignals` is $\hat{\mu}_{\text{comb}} = 0.77 \pm 0.14$. This agrees well with the official CMS result, $\hat{\mu}^{\text{CMS}}_{\text{comb}} = 0.80 \pm 0.14$ [5]. Using `HiggsSignals` with similar data from ATLAS [3], where the experimental results for all categories are unfortunately not available at a common value for the Higgs mass, the published value of $\hat{\mu}^{\text{ATLAS}}_{\text{comb}} = 1.30 \pm 0.20$ at $m_H = 125.5\,\text{GeV}$ [3] is nevertheless reproduced reasonably well by $\hat{\mu}_{\text{comb}} = 1.24 \pm 0.20$.

Now we use the full available experimental data, as described in Section 4.2.3. As mentioned in Section 4.2.1, we employ the quoted asymmetric uncertainties to account for the dominant effects of potentially remaining non-Gaussian behavior of the measurements. The $H \to \gamma\gamma$ and $H \to ZZ^{(*)} \to 4\ell$ analyses of ATLAS and CMS come with a mass measurement, which enters the Higgs mass part of the total χ^2, cf. Section 4.2.2. Note however that we choose a rather conservative combination of statistical and systematic mass uncertainties, cf. Section 4.2.3. The Higgs mass can be determined more accurately from a simultaneous fit to the mass and the signal strength, as can be done e.g. with the mass-centered χ^2 method, see Ref. [291]. Note also that the Higgs mass values assumed in the signal strength measurements can differ by up to $\sim 2.5\,\text{GeV}$. In general, it would be desirable if the experiments would present their best-fit signal strengths for all available channels (including specially tagged categories) also for a common Higgs mass (equal or close to the Higgs mass value preferred by the combined data)

once a combination of different channels is performed. In the present case, global fits combining the signal strength measurements performed at different Higgs masses rely on the assumption that these measurements do not vary too much within these mass differences.

It it nevertheless interesting to discuss the total χ^2 distribution obtained in the peak-centered χ^2 method as a function of the Higgs mass, m_H. This serves as a demonstration of the three different Higgs mass uncertainty parametrizations (box, Gaussian, box+Gaussian pdfs), as well as the implications of taking into account the correlations among the systematic uncertainties in the χ^2 calculation. Furthermore, features of the automatic assignment of the Higgs boson to the peak observables can be studied. In the following example, we set the predicted signal strength for all Higgs channels to their SM values ($\mu_i \equiv 1$) and set the production and decay rate uncertainties to the values given in Eqs. (4.22) and (4.23), which are calculated for $m_H \simeq 125\,\text{GeV}$. We then evaluate the total peak-centered χ^2 for each Higgs boson mass $m_H \in [110,\ 140]$ GeV using the full experimental data. In the SM the Higgs mass can be treated as a free parameter, which corresponds to setting the theory mass uncertainty to zero. In order to illustrate the effects of a non-zero theory mass uncertainty, we also consider a model with SM-like Higgs couplings, but which has a 2 GeV theory uncertainty on the predicted Higgs mass. This may approximately represent the lightest $\mathcal{CP}$-even Higgs boson of the MSSM in the decoupling limit.

The total χ^2 mass distribution is shown in Fig. 4.12 for four different cases: In Fig. 4.12(a,b) the correlations among the systematic uncertainties of the signal rates, luminosity and Higgs mass predictions are neglected, whereas they are taken into account in Fig. 4.12(c,d). In order to demonstrate the difference between the three parametrizations of the Higgs mass uncertainty we show the χ^2 distribution assuming a theoretical Higgs mass uncertainty of $\Delta m = 0\,\text{GeV}$ in Fig. 4.12(a,c) and $\Delta m = 2\,\text{GeV}$ in Fig. 4.12(b,d), respectively. Furthermore, Fig. 4.12 includes the number of peak observables, which have been assigned with the Higgs boson, as a function of the Higgs mass. These are depicted by the faint graphs for each Higgs mass uncertainty parametrization.

The discontinuous shape of the χ^2 distribution is caused by changes in the Higgs boson assignment to the individual observables. Recall that, if the Higgs mass m_H is too far away from the implemented mass position of the peak observable, the Higgs boson is not assigned to the signal. This yields a χ^2 contribution corresponding to no predicted signal, $\mu = 0$, cf. Section 4.2.2. Most of the peak observables have different mass resolutions, therefore the χ^2 distribution has a staircase-like shape. At each step, the total number of peak observable assignments changes.

As can be seen in Fig. 4.12 all three parametrizations of the theoretical Higgs mass uncertainty yield the same total χ^2 values if the Higgs mass m_H is far away from the implemented signal mass position, because typically observables which enter the Higgs mass part of the χ^2 in the Gaussian parametrization exhibit a decent mass resolution, and the Higgs boson is only assigned if this χ^2 is low, i.e. $m_H \approx \hat{m}$. Conversely, at the χ^2 minimum at a Higgs mass $m_H \sim 125 - 126\,\text{GeV}$, we obtain slightly different χ^2 values for the three parametrizations: Firstly, assuming that every observable is assigned with the Higgs boson, the minimal χ^2 is in general slightly higher in the Gaussian case than in the box and box+Gaussian case if the Higgs mass measurements do not have the same central values for all (mass sensitive) peak observables. In that case, there will always be a non-zero χ^2 contribution from the Higgs mass measurements for any predicted value of the Higgs mass. Secondly, in the case of no theoretical mass uncertainty, the box parametrization does not exhibit a full assignment of all currently implemented peak observables at any Higgs mass value. This is because the mass measurements

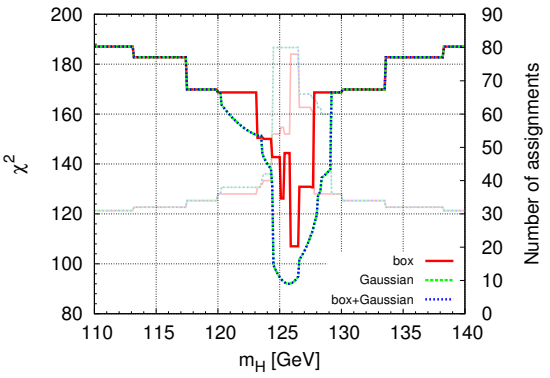

(a) No correlations, $\Delta m = 0\,\text{GeV}$.

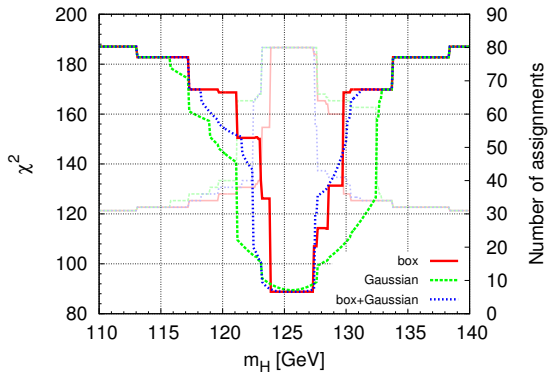

(b) No correlations, $\Delta m = 2\,\text{GeV}$.

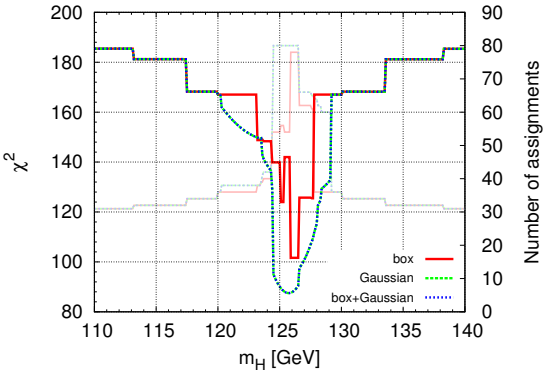

(c) With correlations, $\Delta m = 0\,\text{GeV}$.

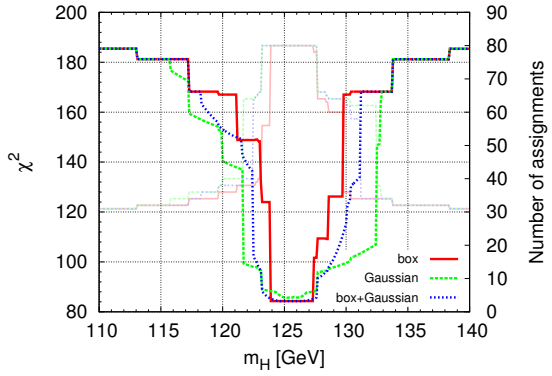

(d) With correlations, $\Delta m = 2\,\text{GeV}$.

Figure 4.12: Total χ^2 distribution obtained from the peak-centered χ^2 method for a SM Higgs boson with mass m_H using the 80 peak observables (containing 80 signal strength measurements and four mass measurements) described in Section 4.2.3. In (a, b), the total χ^2 is evaluated without taking into account the correlations among the systematic uncertainties, whereas they are fully included in (c, d). In (a, c) no theoretical mass uncertainty Δm is assumed (like in the SM) whereas in (b, d) we set $\Delta m = 2\,\text{GeV}$. For each setting, we show the total χ^2 obtained for all three parametrizations of the theoretical Higgs mass uncertainty: box (solid red), Gaussian (dashed green) and box+Gaussian (dotted blue) pdf. For each case, we also give the total number of peak observables, which have been assigned with the Higgs boson, depicted by the corresponding faint lines.

of the ATLAS $H \to \gamma\gamma$ and $H \to ZZ^{(*)} \to 4\ell$ observables [289] have a mass difference of 2.5 GeV, cf. Eq. (4.29), which corresponds to a discrepancy of around 2.5σ [337]. Thus, the Higgs boson is only assigned to either of these (groups of) observables, receiving a maximal χ^2 penalty from the other observable (group). In fact, we observe a double minimum structure in Fig.4.12(a,c), because for a Higgs mass $m_H \in [125.4,\ 125.8]$ GeV, neither the ATLAS $H \to \gamma\gamma$ nor the $H \to ZZ^{(*)} \to 4\ell$ observables are assigned with the Higgs boson, leading to a large total χ^2. This illustrates that the box-shaped pdf is an inappropriate description of the Higgs mass likelihood in the absence of sizable theoretical mass uncertainties.

A difference between the Gaussian and the box+Gaussian parametrization appears only for non-zero Δm. For $\Delta m = 2\,\text{GeV}$ the minimal χ^2 is obtained for a plateau $m_H \approx [124.8 - 126.5]$ GeV in the box+Gaussian case, whereas in the Gaussian case we have a non-degenerate

minimum at $m_H = 125.7\,\text{GeV}$. However, outside this plateau the χ^2 shape of the box+Gaussian increases faster than in the Gaussian case, since the uncertainty governing this Gaussian slope is smaller.

For the Gaussian parametrization of the theoretical Higgs mass uncertainty and no theoretical mass uncertainty the minimal χ^2 at $m_H = 125.7\,\text{GeV}$ changes from 92.0 to 87.5 (for 80 signal strength observables and four mass observables) if we include the correlations among the systematic uncertainties in the χ^2 evaluation. In the case of a non-zero theoretical mass uncertainty, also the shape of the total χ^2 distribution can be affected when the correlations are taken into account. Recall that only in the Gaussian parametrization the correlations of the theoretical mass uncertainties enter the χ^2 evaluation, featuring a sign dependence on the relative position of the predicted Higgs mass value with respect to the two observed Higgs mass values, cf. Sect. 4.2.2. This results in a shallower slope of the χ^2 distribution at Higgs masses larger than all mass measurements, $m_H \gtrsim 126.8\,\text{GeV}$, since all mass observables are positively correlated in this case.

In conclusion we would like to emphasize that, although the direct χ^2 contribution from (the few) mass measurements to the total χ^2 might appear small in comparison to the χ^2 contribution from (many) signal strength measurements, the automatic assignment of Higgs boson(s) to the peak observables introduces a strong mass dependence, even for peak observables without an implemented mass measurement. Hereby, the procedure tries to ensure that a comparison of the predicted and observed signal strength is valid for each observable (depending on the mass resolution of the corresponding Higgs analysis), or otherwise considers the signal as not explainable by the model.

Validation

Both ATLAS [3, 338] and CMS [5, 339] have performed fits of Higgs coupling scale factors in the framework of restricted benchmark models proposed by the LHCHXSWG [29, 30], see Section 5.1.1 for more details. These benchmark scenarios serve as a rather model-independent framework to probe deviations from the Higgs couplings as predicted in the SM and are therefore useful for a generic compatibility test of the SM. Moreover, the experimental results are often presented in the two-dimensional plane of the cross section scale factors $\mu_{\text{ggF+ttH}}$ and $\mu_{\text{qqH+VH}}$ for each Higgs boson decay mode, as already encountered in Section 4.2.3. In this section we focus on the reproduction of some of these official ATLAS and CMS results in order to validate the `HiggsSignals` implementation. Higgs couplings scale factor fits using the combination of all available experimental data will be discussed in detail in Section 5.2.

We validate with the ATLAS and CMS results presented at the Moriond 2013 conference [3, 339]. In this comparison, it should be kept in mind that there are some remaining differences in the underlying experimental data that is publicly available, and the data that went into the official fit results. In the ATLAS fits the Higgs mass is assumed to be 125.5 GeV. However, for this Higgs mass value there are no signal strengths measurements for the $H \to \gamma\gamma$ categories available in the literature. Instead, we use the $H \to \gamma\gamma$ signal strength measurements performed at 126.5 GeV and 126.8 GeV for the 7 and 8 TeV data, respectively [282, 325], keeping in mind that this might lead to some inaccuracies. The ATLAS $H \to WW^{(*)} \to \ell\nu\ell\nu$ and $H \to ZZ^{(*)} \to 4\ell$ signal strength measurements were extracted from Ref. [289]. Note that for the remaining channels, $H \to \tau\tau$ and $VH \to Vb\bar{b}$, only the inclusive $\hat{\mu}$ measurements are available in the literature, whereas the ATLAS fit also includes information of their sub-channels [3]. In the CMS fits of Higgs coupling scaling factors a Higgs mass of 125.7 GeV is assumed. All

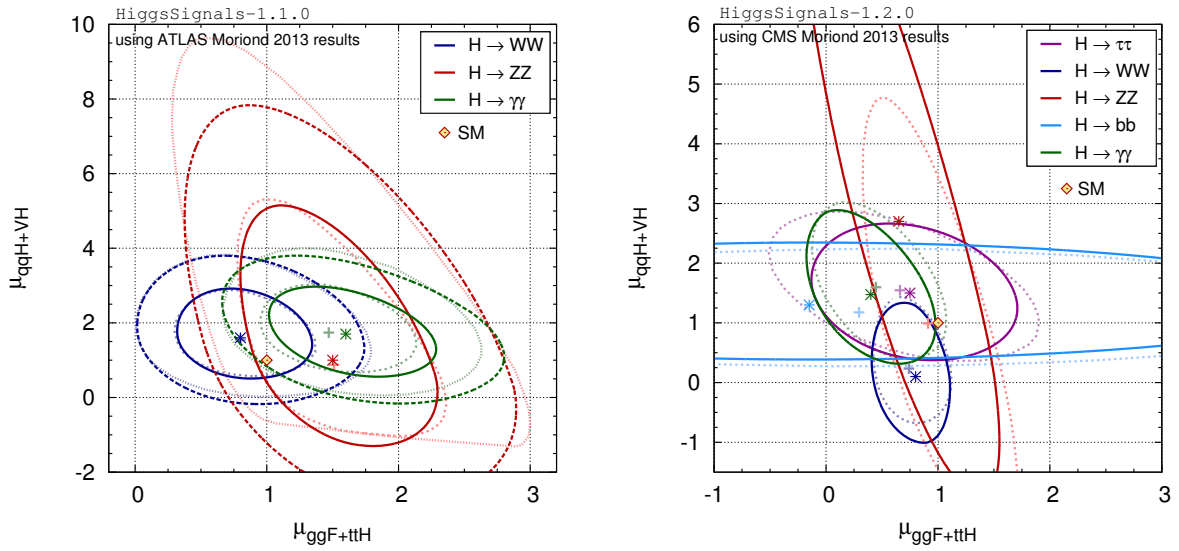

(a) Comparison with ATLAS results [3, 289]. Both the 68% and 95% C.L. regions are shown.

(b) Comparison with CMS results [5]. Only the 68% C.L. regions are shown.

Figure 4.13: Comparison of fit results for the universal scale factors for the production cross sections of gluon-gluon fusion (ggf) and top quark pair associated Higgs production (ttH), $\mu_{\mathrm{ggf+ttH}}$, and of vector boson fusion (qqH) and vector boson associated Higgs production (VH), $\mu_{\mathrm{qqH+VH}}$, using the individual Higgs search channel results from ATLAS [in (a)] and CMS [in (b)]. The 68% (95%) C.L. regions are shown as deep colored, solid (dashed) and faintly colored, dotted (fine-dotted) contours for the `HiggsSignals` results and official ATLAS/CMS result, respectively. The best fit points are given by the asterisk [plus sign] for the `HiggsSignals` [official] result.

signal strength measurements have been performed for this assumed Higgs mass value, except for the $H \to \gamma\gamma$ categories being measured at $m_H = 125.0\,\mathrm{GeV}$. As discussed in Section 4.2.3, we extrapolate these measurements to the mass value of 125.7 GeV.

We first look at ATLAS and CMS fits that explicitly target the different production modes by combining channels with a particular decay mode. Two-parameter fits were performed for each decay mode to a signal strength modifier associated with the gluon gluon fusion (ggF) and $t\bar{t}H$ production mechanisms, $\mu_{\mathrm{ggf+ttH}}$, and a signal strength modifier for the VBF and VH production modes, $\mu_{\mathrm{qqH+VH}}$. These fits allow to investigate sources of potential deviations between the official and the reproduced `HiggsSignals` results separately for each Higgs boson decay mode. Furthermore, unknown channel efficiencies can be adjusted within reasonable ranges, such that the agreement of the fit outcome is optimized.

The results of the same fits performed with `HiggsSignals` are shown in Fig. 4.13 in direct comparison with the results from ATLAS [3, 289] and CMS [5], which are faintly overlaid in the figure. Using the ATLAS results, Fig. 4.13(a), the derived $H \to WW$ ellipse is in perfect agreement with the official result. Also the $H \to \gamma\gamma$ and $H \to ZZ$ ellipses agree reasonably well. The reproduced $H \to \gamma\gamma$ ellipse is slightly shifted towards larger values of $\mu_{\mathrm{ggf+ttH}}$. A potential source of this discrepancy may be the different mass positions at which the measurements are performed. Moreover, the inclusion of correlations among the experimental systematic uncertainties becomes more important, the more the measurements are divided into smaller subsets/categories. These correlations are not publicly known and hence not taken into account

by HiggsSignals. In the $H \to ZZ$ result, a significant difference between the approximations in HiggsSignals and the full profile likelihood (PLL) treatment can be observed. The PLL has a longer tail at large signal strengths, thus leading to extended 68% and 95% C.L. regions at large values of $\mu_{\mathrm{qqH+VH}}$. This is partly due to the Gaussian approximation, which is more constraining at large values than a Poisson distribution with the same central value, as is used in the PLL. This is especially relevant for the very small event count for VBF $H \to ZZ$ candidates. In addition, missing information about correlations of experimental systematics might contribute to the observed difference at large $\mu_{\mathrm{qqH+VH}}$. Note also that one of the two $H \to ZZ$ category measurements that are publicly available [289], cf. Tab. 4.1, is a combination of the VBF and VH production channels, whereas the ATLAS analysis internally treats these channels as separate categories. The requirement of a positive probability density function (pdf) leads to the edge at negative $\mu_{\mathrm{qqH+VH}}$ in the official ATLAS result. We checked that adding the requirement of a positive signal strength modifier in HiggsSignals this edge is reproduced quite well.

Using the CMS results, Fig. 4.13(b), we find reasonably good agreement between HiggsSignals and the official results for $H \to WW$, bb, and $\tau\tau$. The $H \to \gamma\gamma$ ellipses were already discussed in Section 4.2.3, cf. Fig. 4.11, where the inclusion of correlations among the experimental systematic uncertainties led to a significant improvement of the agreement. For the CMS $H \to \tau\tau$ search result a similar implementation of correlations of experimental systematics as performed for ATLAS, cf. Section 4.2.3, may account for the differences observed for the $H \to \tau\tau$ ellipses in Fig. 4.13(b). The $H \to ZZ$ ellipse can only be roughly reproduced using the publicly available data for the two $H \to ZZ$ observables. Even after adjusting their production mode efficiencies, cf. Tab. 4.2, differences remain due to the Gaussian approximation and possibly further (publicly unavailable) information on the VBF-likeness of the observed signal events [316].

Overall, we conclude that the agreement between the HiggsSignals and the official ATLAS and CMS results — after adjusting missing signal efficiencies and (if possible) implementing the major correlated systematics in the most relevant cases — is very good. A more quantitative discussion of the agreement of these results can be found in Ref. [291].

We now turn to the discussion of global fits in the Higgs coupling scale factor benchmark scenarios [29, 30]. We first compare against ATLAS results for two two-dimensional benchmark scenarios[14]. We then turn to the validation with CMS results using a more general parametrization in terms of six coupling scale factors.

Regarding the interpretation of the following benchmark fits using ATLAS results, it should be kept in mind that only two parameters are allowed to deviate from their SM values, while all other Higgs couplings and partial decay widths have been fixed to their SM values. The way an observed deviation from the SM manifests itself in the parameter space of coupling strength modifiers κ_i will sensitively depend on how general the basis of the κ_i is that one has chosen. Furthermore the framework of the coupling strength modifiers κ_i as defined in Ref. [29, 30] is designed for the analysis of relatively small deviations from the SM. In case a firm preference should be established in a parameter region that is very different from the SM case (e.g. a different relative sign of Higgs couplings), the framework of the coupling strength modifiers κ_i would have to be replaced by a more general parametrization. More details on the scale factor framework and its limitations are given in Section 5.1.1.

The first benchmark model we want to investigate is a two-dimensional fit to universal scale

[14] Comparisons for these benchmark scenarios with CMS results can be found in Ref. [291].

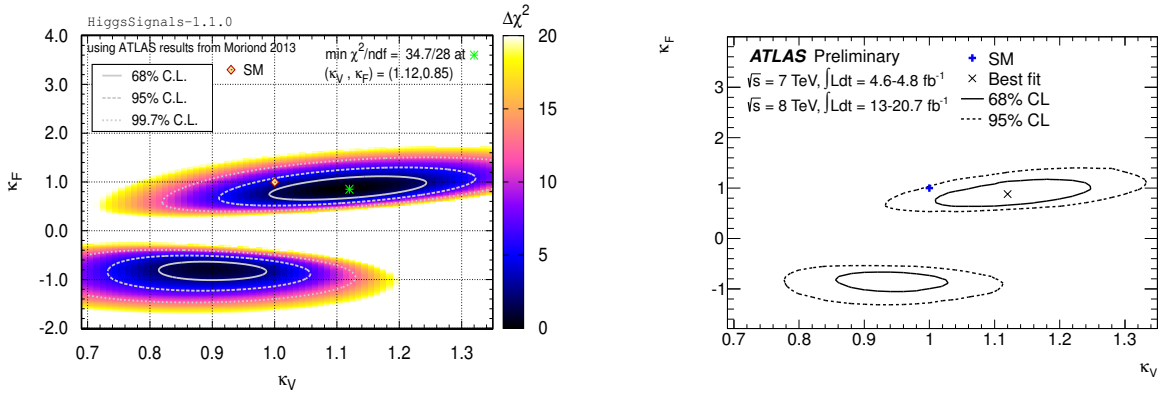

(a) HiggsSignals result.

(b) Official ATLAS result from Ref. [3].

Figure 4.14: Comparison of the two-parameter fits probing different coupling strength scale factors for fermions, κ_F, and vector bosons, κ_V, derived by HiggsSignals (a) and ATLAS [3] (b). The Higgs mass is chosen to be $m_H = 125.5\,\text{GeV}$.

factors for the Higgs coupling to the massive SM vector bosons, κ_V, and to SM fermions, κ_F. In this fit it is assumed that no other modifications to the total width than those induced by the coupling scale factors κ_F and κ_V are present, allowing for a fit to the coupling strength modifiers individually rather than to ratios of the scale factors [29, 30]. Note that the loop-induced effective $H\gamma\gamma$ coupling is derived in this approximation from the (scaled) tree-level couplings $Ht\bar{t}$ and HW^+W^- and thus exhibits a non-trivial scaling behavior, see Section 5.2 for more details. In particular the interference between the t and W boson loops introduces a dependence on the relative sign of the scale factors κ_F and κ_V. In the case of a relative minus sign this interference term gives a positive contribution to the $H\gamma\gamma$ coupling.

The reconstructed ATLAS fit obtained with HiggsSignals is shown in Fig. 4.14(a). For comparison, we show the official ATLAS results [3] in Fig. 4.14(b). We find overall very good agreement. The best point is located at

$$(\kappa_V, \kappa_F) = (1.12, 0.85) \quad \text{with} \quad \chi^2/\text{ndf} = 34.7/28, \tag{4.32}$$

and the (2D) compatibility with the SM hypothesis is 11.1%.

In order to probe the presence of BSM physics in the Higgs boson phenomenology a fit to the loop-induced Higgs couplings to gluons, κ_g, and photons, κ_γ, can be performed. In this fit it is assumed that all other (tree-level) Higgs couplings are as in the SM and no new Higgs boson decay modes exist. Fig. 4.15(a) show the two-dimensional likelihood map in the $(\kappa_\gamma,\ \kappa_g)$ parameter plane for the HiggsSignals result using the ATLAS observables. The corresponding official ATLAS result is given in Fig. 4.15(b). Again, we observe reasonably good agreement with the official result. We find the best fit point at

$$(\kappa_\gamma, \kappa_g) = (1.25, 1.02) \quad \text{with} \quad \chi^2/\text{ndf} = 34.0/28, \tag{4.33}$$

which is (2D) compatible with the SM at the level of 7.6%, respectively. The best-fit region obtained by HiggsSignals is slightly shifted with respect to the official result towards lower

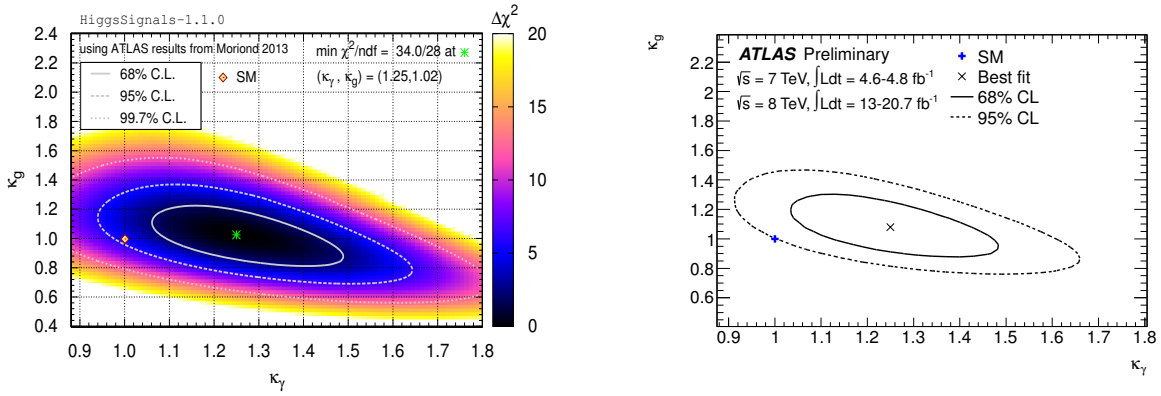

(a) `HiggsSignals` result.

(b) Official ATLAS result from Ref. [3].

Figure 4.15: Comparison of the two-parameter fits probing different coupling strength scale factors to gluons, κ_g, and photons, κ_γ, obtained by `HiggsSignals` (a), and ATLAS [3] (b). It is assumed that no new Higgs boson decay modes are open, $\Gamma_{\text{BSM}} = 0\,\text{GeV}$, and that no other modifications of the couplings occur with respect to their SM values. The Higgs mass is chosen to be $m_H = 125.5\,\text{GeV}$.

values of κ_g by roughly $\Delta\kappa_g \sim 0.05 - 0.10$, whereas the agreement in κ_γ direction is very good.

Finally, we validate the `HiggsSignals` procedure by performing a six-dimensional fit to the CMS Moriond 2013 data and comparing the results to the official fit results presented in Ref. [5]. The fitted scale factors are those for the Higgs couplings to vector bosons, κ_V ($V = W, Z$), up-type quarks, $\kappa_u (\equiv \kappa_t)$, down-type quarks, $\kappa_d (\equiv \kappa_b)$, charged leptons, $\kappa_\ell (\equiv \kappa_\tau)$, gluons, κ_g, and photons, κ_γ. Note, that the total width is obtained from the rescaled partial widths directly, i.e. we assume that no additional Higgs decay modes are present. The CMS fit was performed assuming a Higgs boson mass of 125.7 GeV. The results are shown in Fig. 4.16 in terms of a profiled χ^2 difference to the minimal χ^2 value found[15]. The blue curves indicate the original CMS results [5]. Given the freedom of this very general parametrization, the agreement is remarkably good.

We conclude this section by pointing out that, despite some minor discrepancies observed in fits to single decay modes using subsets of the available measurements, cf. Fig. 4.13, the combination of all available channels from each experiment reproduces the official results very well. We are thus confident that the accuracy of the `HiggsSignals` method is sufficient for a rather precise determination of new physics parameter spaces that are compatible with the Higgs measurements, as well as for Higgs coupling scale factor fits. Nevertheless, the precision of the `HiggsSignals` method strongly depends on the way the experimental results are presented. In particular, it would be highly desirable if the experimental collaborations made information on efficiencies, correlated experimental uncertainties and all category measurements publicly available in a more complete way. We would expect a significant reduction of the observed remaining discrepancies if this information was included in `HiggsSignals`.

[15] More details about the employed profiled likelihood procedure based on the `HiggsSignals` χ^2 output are given in Section 5.1.2.

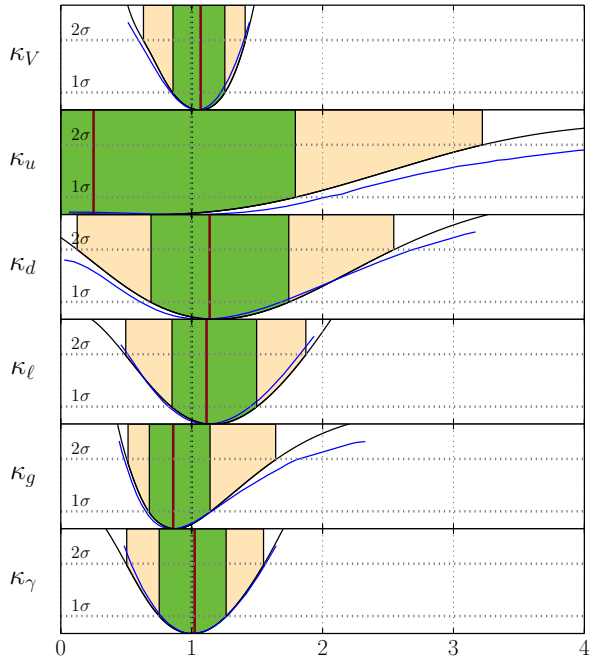

Figure 4.16: One-dimensional $\Delta\chi^2$ profiles of the fitted Higgs coupling scale factors $(\kappa_V, \kappa_u, \kappa_d, \kappa_\ell, \kappa_g, \kappa_\gamma)$ using only the CMS Moriond 2013 results [5]. The blue curves show the original fit result obtained by CMS [5].

4.3 Summary of the Chapter

In this Chapter we introduced the computer tools `HiggsBounds` and `HiggsSignals`. Both programs can be used to confront the Higgs sector predictions of BSM models with the experimental results from direct Higgs searches at the experiments at LEP, the Tevatron and the LHC. While `HiggsBounds` tests the model for a possible 95% C.L. exclusion imposed from null-results in Higgs searches, `HiggsSignals` evaluates the χ^2 compatibility of the model predictions with the Higgs mass and signal strength measurements from the Tevatron and LHC experiments. Both programs are publicly available and free to use. A simultaneous use of both programs provides a rather complete and accurate test of (possibly extended) Higgs sectors of BSM models in a very quick and convenient way.

For the program `HiggsBounds` we concentrated on the description of the latest developments incorporated in version 4 of the program. A slight modification of the main statistical `HiggsBounds` algorithm was introduced, which became necessary with the presence of the Higgs signal and its influence on the exclusion limits in the mass region around 125 GeV. In the case of an extended Higgs sector, the model predictions are now tested against the most sensitive search channel for each Higgs boson of the model.

Another improvement was achieved in the SM-likeness test. In this test, the program checks whether the Higgs boson(s) of the model fulfills to a sufficient degree the assumptions that were made in the experimental search for a SM Higgs boson, and only applies the limit if this is the case. Essentially, the improvement lies in a new definition of the test criterion, where the maximally allowed deviation of the Higgs signal strength between the individual channels and the average is now weighted by the relative contribution of the corresponding signal channel to

the overall signal yield. As a result, subdominant channels are allowed to deviate more from the total signal strength modifier before causing a test failure, leading to a wider applicability of SM Higgs searches to BSM models.

In addition, two new features were in introduced with `HiggsBounds-4`. Firstly, a simple algorithm that takes care of theoretical Higgs mass uncertainties. Hereby, the predicted value is varied within its uncertainty and the most conservative result is given as the program's output. Secondly, the output was extended by the χ^2 likelihood information for the Higgs search results from the LEP experiments. This additional information is useful in global fits of extended Higgs sectors, where the mass of some Higgs states may be within the kinematical reach of the LEP experiments.

The LHC discovery of the Higgs boson triggered the development of the public code `HiggsSignals`. After introducing the basic idea and statistical approach of the program, we described in detail the peak-centered χ^2 method, which is currently the default run mode of `HiggsSignals`. In this method, all available signal strength measurements from the Tevatron and LHC experiments performed for a specific Higgs mass value can be combined in a χ^2 test, which takes into account the major correlations of theoretical and — if known — experimental uncertainties. The total χ^2 value is then comprised of the contribution from these signal rate measurements and a contribution from the mass measurements that have been performed in the $H \to \gamma\gamma$ and $H \to ZZ^* \to 4\ell$ analyses from ATLAS and CMS.

If multiple neutral Higgs bosons exist in the model additional complications may arise. We described how `HiggsSignals` automatically finds the best signal candidate(s) within the model and how it treats a potential signal overlap of multiple Higgs bosons. This is done by assigning the Higgs bosons to the implemented observables if their mass values are close enough to the mass position where the measurement has been performed. The performance of the peak-centered χ^2 method — and in particular of this assignment procedure — was demonstrated by studying the mass dependence of the total χ^2 value for a Higgs boson with SM coupling strengths.

We described in detail the implementation of the signal rate and mass observables from the Tevatron and LHC experiments that are currently included in `HiggsSignals-1.2.0`. We discussed the effects of incorporating the correlations of experimental uncertainties for the ATLAS $H \to \tau\tau$ and CMS $H \to \gamma\gamma$ search in the χ^2 evaluation. Their implementation led to a substantial improvement of the agreement between official and reproduced fit results within simple cross section scaling models. The χ^2 procedure and implementation of experimental results was further validated in several reproductions of fit results within different Higgs coupling or cross section scale factor models. This includes in the most general case a six-dimensional Higgs coupling scale factor fit using CMS results. Comparing the results of these fits to the official fit results from ATLAS and CMS, we find in general a very satisfactory level of agreement.

CHAPTER 5

Determination of Higgs Couplings

With the recent discovery of a Higgs boson at the LHC a new possibility for probing effects of new physics beyond the SM arises. Deviations from the Higgs properties in the SM can arise from an extended structure of the Higgs sector, for instance if there is more than one Higgs doublet. Another source of possible deviations from the SM Higgs properties are loop effects from new particles. A prominent case where both types of coupling modification can occur is the MSSM, see Section 2.4.3. However, a generic property of many theories with extended Higgs sectors is that the lightest scalar can have nearly identical properties to the SM Higgs boson. In this so-called decoupling limit, additional states of the Higgs sector are heavy and may be difficult to detect in collider searches. The potential for deciphering the physics of electroweak symmetry breaking is directly related to the sensitivity for observing deviations from the SM predictions. Given the far-reaching consequences for our understanding of the fundamental structure of matter and the basic laws of nature, it is of the highest priority to probe the properties of the newly discovered particle with a comprehensive set of high-precision measurements. In particular, the determination of its couplings to other particles with the highest possible precision is crucial.

In order to test the compatibility of the newly observed boson with the predictions for the SM Higgs boson based on the data accumulated up to 2012, the LHC Higgs Cross Section Working Group (LHCHXSWG) proposed several benchmark scenarios within an "interim framework", comprised of *Higgs coupling scale factors* [29, 30]. Those have been analyzed by the experimental collaborations [3, 5], as has been partly discussed in the previous Chapter in Section 4.2.4, as well as in further phenomenological studies where Higgs coupling fits have been carried out [291, 307, 308, 312, 340]. Thus far, the results of those analyses show no significant deviations from SM Higgs couplings.

The total Higgs decay width for a Higgs boson mass around 125.7 GeV is not expected to be directly observable at the LHC. In the SM, a total width around 4 MeV is predicted, which is several orders of magnitude smaller than the experimental mass resolution. Suggestions to achieve more sensitive constraints on the total width other than the ones limited by the experimental mass resolution have been made. These are based on the analysis of off-shell contributions above the Higgs resonance in Higgs decays to ZZ^* or WW^* final states [77] and of interference effects between the $H \to \gamma\gamma$ signal and the background continuum [341]. However, the ultimate sensitivities are not expected to reach the value predicted in the SM. A recent CMS analysis of off-shell $H \to ZZ^*$ production yielded an 95% C.L. upper limit of

4.2 times the SM Higgs total width [342]. Nevertheless, the limited access of the LHC to the Higgs width implies that only ratios of couplings can be determined at the LHC, rather than couplings themselves, unless additional theory assumptions are made.

In this chapter we investigate whether there are hints of deviations from the SM Higgs couplings based on a combined picture of all the latest results from the Tevatron and LHC experiments. By investigating a complete selection of possible scale factor parametrizations of Higgs coupling strengths ranging from highly constrained to very generic models, we systematically study potential tendencies in the signal rates and correlations among the fit parameters. In all considered scenarios we allow for additional Higgs decay modes that are either assumed to be altogether *invisible* Higgs decay modes, thus yielding a missing energy collider signature, or considered to be *undetectable* decay modes. In the latter case, additional model assumptions have to be imposed to constrain the total width at the LHC. Based on those assumptions an upper limit on the branching ratio of the undetectable decay modes can be derived for each parametrization.

Going beyond the present status, we analyze the prospects of Higgs coupling determination at future LHC runs with $300\,\text{fb}^{-1}$ and $3000\,\text{fb}^{-1}$ of integrated luminosity, as well as with a future e^+e^- International Linear Collider (ILC). The estimated ILC capabilities are presented both for a model-dependent and model-independent fit framework. In the first case, the total width is constrained by imposing the same assumptions as required for the LHC, and we compare the ILC capabilities directly with those of the high-luminosity LHC (HL–LHC) with $3000\,\text{fb}^{-1}$. In the latter case, the total width is only constrained by the total cross section measurement of the $e^+e^- \to ZH$ process at the ILC, thus enabling measurements of coupling scale factors free from theoretical prejudice.

Finding significant deviations in any Higgs coupling scale factors would provide a strong motivation for studying full models which exhibit a corresponding coupling pattern. However, the fit results obtained within the framework of coupling scale factors can in general *not* be directly translated into realistic new physics models, see Section 5.1.1 for a discussion. Concerning the investigation of particular models of new physics, the most reliable and complete results are obtained by performing a dedicated fit to the Higgs signal rate and mass observables within the considered model. Such BSM model fits, as e.g. presented in Chapter 6, see also Refs. [234, 270, 272, 274, 293, 294, 305–311], can easily be performed with `HiggsSignals`, cf. Section 4.2, which is also used in this study.

This chapter is organized as follows. Section 5.1 introduces the fit methodology and the statistical treatment employed in `HiggsSignals`. In Section 5.2 we present the fit results for the various benchmark parametrizations of Higgs coupling scale factors using all the currently available data from the LHC and the Tevatron. Results for future expectations are presented in Section 5.3. Here the current data is replaced by the projections for the future precisions at the HL–LHC and the ILC, and we discuss the accuracy to which the Higgs coupling scale factors can be determined in the various scenarios. Conclusions of this study are given in Section 5.4.

Relevant additional information to this work is given in the Appendix. In Appendix A.2 we list the estimated future signal rate measurements for the LHC and ILC, which are used in our study. In Appendix B a discussion of the statistical $\mathcal{P}$-value derived from χ^2 fits using Higgs boson signal rates is given. Furthermore, we provide more details on the theoretical uncertainties in the various future scenarios considered in this work.

5.1 Methodology

5.1.1 Scale factor parametrization of Higgs couplings

As discussed in Section 2.1, the SM predicts the couplings of the Higgs boson to all other known particles. These couplings directly influence the rates and kinematic properties of production and decay of the Higgs boson. Therefore, measurements of the production and decay rates of the observed state, as well as their angular correlations, yield information that can be used to probe whether data is compatible with the SM predictions.

In the SM, once the numerical value of the Higgs mass is specified, all the couplings of the Higgs boson to fermions, gauge bosons and to itself are specified within the model. It is therefore in general not possible to perform a fit to experimental data within the context of the SM where Higgs couplings are treated as free parameters [343, 344]. In order to test the compatibility of the newly observed boson with the predictions for the SM Higgs boson and potentially to find evidence for deviations in the 2012 data, the LHCHXSWG proposed several benchmark scenarios containing Higgs coupling scale factors [29, 30]. The idea behind this framework is that all deviations from the SM are computed assuming that there is only one underlying state at $\sim 125.7\,\text{GeV}$. It is assumed that this state is a Higgs boson, and that it is SM-like, in the sense that the experimental results so far are compatible with the SM Higgs boson hypothesis. Also the coupling tensor structures are assumed to be as in the SM, meaning in particular that the discovered state is a $\mathcal{CP}$-even scalar boson. Furthermore, the zero width approximation is assumed to be valid, allowing for a clear separation and simple handling of production and decay of the Higgs particle.

In order to take into account the currently best available SM predictions for Higgs cross sections and partial widths, which include higher-order QCD and EW corrections [30, 70, 71], while at the same time introducing possible deviations from the SM values of the couplings, the predicted SM Higgs cross sections and partial decay widths are dressed with scale factors κ_i. The scale factors κ_i are defined in such a way that the cross sections σ_{ii} or the partial decay widths Γ_{ii} associated with the SM particle i scale with the factor κ_i^2 when compared to the corresponding SM prediction[1]. The most relevant coupling strength modifiers are κ_t, κ_b, κ_τ, κ_W, κ_Z, ... In the various benchmark scenarios defined in Refs. [29, 30] several assumptions are made on the relations of these scale factors in order to investigate certain aspects of the Higgs boson couplings, as will be discussed here in Section 5.2.

One should keep in mind that the inherent simplifications in the κ framework make it rarely possible to directly map the obtained results onto realistic BSM models. The scale factor benchmark scenarios typically have more freedom to adjust the predicted signal rates to the measurements than realistic, renormalizable models. The latter generally feature specific correlations among the predicted rates, which furthermore can depend non-trivially and non-linearly on the model parameters. Moreover, constraints from the electroweak precision data and possibly other sectors, such as dark matter, collider searches, vacuum stability, etc., can further restrict the allowed parameter space and thus the room for Higgs coupling deviations. Preferred values and C.L. regions of the scale factors obtained from profiling over regions in the

[1] Note, that in this interim framework, slight dependencies of the derived collider observables (cross sections σ_{ii}, partial widths Γ_{ii}) on the remaining Higgs coupling scale factors, κ_j ($j \neq i$), are often neglected. For instance, the cross section of the Higgs-strahlung process $pp \to ZH$ features a small dependence on the top-Yukawa coupling scale factor entering via the NNLO process $gg \to Z^* \to HZ$ [109]. However, for scale factor ranges, $\kappa_t \lesssim 3$, this effect is negligible. Hence, the $pp \to ZH$ cross section can be simply rescaled by κ_Z^2.

κ parameter space, which are not covered by the allowed parameter space of the full model, cannot be transferred to the full model. The implications of the Higgs signal rate measurements for the full model can then only be investigated consistently in a dedicated, model-dependent analysis. In that sense, such analyses of realistic BSM models are complementary to the approach followed here, and can easily be performed with the same tools and statistical methods as employed here.

One limitation at the LHC, but not at the ILC, is the fact that the total width cannot be determined experimentally without additional theory assumptions. In the absence of a total width measurement only ratios of κ's can be determined from experimental data. In order to go beyond the measurement of ratios of coupling scale factors to the determination of absolute coupling scale factors κ_i additional assumptions are necessary to remove one degree of freedom. One possible and simple assumption is that there are no new Higgs decay modes besides those with SM particles in the final state. Another possibility is to assume the final state of potentially present additional Higgs decay(s) to be purely invisible, leading to a Z boson recoiling against missing transverse energy in the Higgs-strahlung process at the LHC. By employing constraints from dedicated LHC searches for this signature the total width can be constrained. In both cases, further assumptions need to be imposed on the partial widths of Higgs decays to SM particles which are unobservable at the LHC, like for instance $H \to gg, cc, ss$. As a third possibility, an assumption can be made on the couplings of the Higgs to the SM gauge bosons, $\kappa_{W,Z} \leq 1$ [345, 346]. This assumption is theoretically well-motivated as it holds in a wide class of models. For instance, they hold in any model with an arbitrary number of Higgs doublets, with and without additional Higgs singlets, or in certain classes of composite Higgs models [347]. We will partly make use of these assumptions in our analysis below. More details will be given in Section 5.2.

5.1.2 The profile likelihood analysis using `HiggsSignals`

In this work we use `HiggsSignals-1.2.0`, cf. Section 4.2, to evaluate the statistical χ^2 value obtained from the latest signal rate measurements at the Tevatron and LHC experiments, which have been described in Section 4.2.3. For the studies of prospective Higgs coupling determinations in Section 5.3 we also implement the projected future signal rate measurements at the LHC and ILC experiments, see Section 5.3 and Appendix A.2 for details. In all fits presented in this Chapter we fix the Higgs mass to $m_H = 125.7\,\text{GeV}$. We furthermore assume that the signal efficiencies $\epsilon^{i,j}$ in all experimental analyses, Eq. (3.4), are identical for the SM and the unknown model predicting the rescaled signal rates. This assumption is valid for *small* deviations from the SM Higgs couplings, where kinematic effects changing the efficiencies can be neglected. However, if significant deviations from the SM are found from the analysis, a more careful investigation of anomalous Higgs couplings [348–350] becomes necessary, including a detailed study of their effects on the efficiencies.

In all fits we take into account the correlations among theoretical rate uncertainties, as discussed in Section 4.2.2. The numerical values given in Eqs. (4.22) and (4.23) for the corresponding correlation matrices are used in the fits to current measurements, see Section 5.2, as well as in the conservative future LHC scenario (S1), see Section 5.3.1. For the other future scenarios discussed in Section 5.3, we re-evaluate the covariance matrices based on the assumptions of future improvements of parametric and theoretical higher-order uncertainties. However, while the magnitude of the uncertainties changes in the various scenarios discussed later, we find that the correlations encoded in Eqs. (4.22) and (4.23) are rather universal. A

comparison of uncertainty estimates among all future scenarios we discuss, as well as with the recommended values from the LHCHXSWG, can be found in Appendix B.2.

In this work we employ profile likelihood fits based on the χ^2 value derived from `HiggsSignals`. A "naive" $\mathcal{P}$-value, i.e. the probability of a false model rejection, is quoted based on the agreement between the minimal χ^2 value found in the fit and the number of degrees of freedom (ndf). However, the χ^2 value evaluated by `HiggsSignals` does not generically fulfill the prerequisite for this simple $\mathcal{P}$-value estimation: Firstly, `HiggsSignals` uses asymmetric uncertainties in order to take into account remaining non-Gaussian effects in the measurements. Secondly, the signal rate uncertainties are comprised of constant and relative parts. The latter include the theoretical uncertainties on the cross sections and branching ratios, which are proportional to the signal rate prediction, as well as the luminosity uncertainty, which is proportional to the measured signal rate, cf. Section 4.2.2. These features are necessary in order to effectively reproduce the properties of the full likelihood implementation as done by the experimental collaborations and ensure the correct scaling behavior when testing models different from the SM [291].

These features potentially introduce deviations from the naive χ^2 behavior, which could affect both the extraction of preferred parameter ranges at a certain confidence level from the profiling of the obtained χ^2 distribution, as well as the calculation of the $\mathcal{P}$-value. In order to estimate the impact of these effects, we performed a Monte Carlo (MC) toy study for a simple one-dimensional scale factor model, which is presented in Appendix B.1. From this study two important conclusions can be drawn: Firstly, the central value and uncertainties of the estimated fit parameter extracted from the full toy study do indicate a small variation from the naive values extracted from profiling. However, these variations are each less than 2%. Hence, we are confident that the uncertainties and best fit values quoted later for the profile likelihood scans are valid to a good approximation. Secondly, the $\mathcal{P}$-value obtained in the full MC toy study can be different to the naive χ^2 distribution. For an example of a change in the shape of the observed χ^2 probability density function in toy experiments, see Fig. B.1 in Appendix B.1, which indicates that the actual $\mathcal{P}$-value may be higher than expected when assuming an ideal χ^2 distribution. This effect could be significant and should be taken into account once this technique is used to exclude models, e.g. once the χ^2 probability comes close to 5%. Here, we find naive $\mathcal{P}$-values in the range of 25 – 35%, which are far away from any critical border. Therefore, we are confident that the conclusions drawn from the naive $\mathcal{P}$-values in the remainder of this work would not change in any significant way if a full toy study or, even better, a full likelihood analysis by the experimental collaborations, was done for every fit.

The technical details of the profiled likelihood scans performed in this work are as follows. For an efficient sampling of the parameter space the scans are performed with an adaptive Metropolis (AM) algorithm [351] with flat prior probability distributions using the Markov-Chain Monte Carlo (MCMC) python package `PyMC` [352]. Appropriate initial values for the MCMC chains are found using the maximum a posteriori estimate (MAP) class of `PyMC`. The results are presented in a purely frequentist's interpretation based on the global χ^2 derived from `HiggsSignals` and, optionally, further χ^2 contributions from constraints arising from invisible Higgs searches at the LHC. This higher-dimensional χ^2 distribution is then profiled in order to obtain one- and two-dimensional likelihoods for the fit parameters and related quantities. The $\{1, 2, 3\}\,\sigma$ parameter regions around the best-fit point are then obtained for values of the χ^2 difference to the minimal value, $\Delta\chi^2 = \chi^2 - \chi^2_{\text{min}}$, of $\Delta\chi^2 \leq \{1.0, 4.0, 9.0\}$ for the one-dimensional, and $\Delta\chi^2 \leq \{2.30, 5.99, 11.90\}$ for the two-dimensional profiles, respectively. As

discussed above, we also quote for each benchmark scenario the fit quality at the best-fit point, given by $\chi^2_{\text{min}}/\text{ndf}$, and the corresponding (naively estimated) $\mathcal{P}$-value.

5.2 Current status of the Higgs couplings

In this section we explore the room for possible deviations from the SM Higgs boson couplings in the light of the current signal rate measurements from the Tevatron and LHC experiments. In order to obtain a complete picture, we consider various Higgs coupling scale factor benchmark models, each targeting slightly different aspects of the Higgs sector.

At the Tevatron and LHC experiments, measurements of the signal rates, i.e. the product of a production cross section times the branching ratio to a certain final state, do not provide direct information about the total width of the Higgs boson. As noted in the beginning of this Chapter, the LHC is regarded as being insensitive to directly probe the total Higgs width, Γ_H, unless it features a very broad resonance, $\Gamma_H \sim \mathcal{O}(\text{few GeV})$. The current best limit from such measurements, $\Gamma_H < 3.4\,\text{GeV}$ at 95% C.L., is obtained by CMS using the $H \to ZZ^{(*)} \to 4\ell$ channel [281]. Recently, this limit was significantly improved by CMS to $\Gamma_H < 4.2\ \Gamma_H^{\text{SM}}$ [342], where $\Gamma_H^{\text{SM}} = 4.15\,\text{MeV}$ is the total Higgs width in the SM, following the proposals of Ref. [77] to exploit the ZZ invariant mass spectrum in the process $gg \to ZZ^{(*)} \to 4\ell$ and $2\ell 2\nu$ above the resonance. In the case of an increased total width, $\Gamma_H > \Gamma_H^{\text{SM}}$, enhanced contributions from off-shell Higgs production are expected in this kinematical region[2]. Nevertheless, a total width of that order still allows for a significant branching fraction to undetectable/invisible final states and sizable coupling modifications. SM-like signal rates for a Higgs boson with an increased total width can always be obtained by a simultaneous increase of the branching fraction to undetectable particles and the Higgs couplings to SM particles, if both are allowed to vary and no further assumptions are imposed[3] [307, 345, 346]. Given the signal rate measurements from the experiments at the Tevatron and the LHC, this degeneracy can only be overcome by additional model assumptions and constraints.

In our analysis, we generally allow for an additional branching fraction to new physics, $\text{BR}(H \to \text{NP})$. Concerning the assumptions needed to constrain the total width, we distinguish the two cases of the additional branching fraction being comprised of either *invisible* or *undetectable* Higgs decays. The *invisible* decays are considered to measurable/detectable via e.g. the Higgs-strahlung process, leading to a Z boson recoiling against missing transverse energy at the LHC. Invisible Higgs decays can appear in models where the Higgs boson couples to a light dark matter (DM) candidate, as for instance in light singlet DM models [134] or supersymmetry with a stable neutralino as the lightest supersymmetric particle (LSP). In contrast, the *undetectable* decays cannot be constrained by any present LHC analysis. Possible examples are $H \to gg, cc, ss$ or other light flavored hadronic Higgs decays as these signatures

[2] Note, however, that this method still relies on the model assumption that the coupling strength scales identically in the resonance and off-shell regions. For a discussion and counter-examples of models, where this assumption is not fulfilled, see Ref. [353].

[3] Although the κ scale factor framework technically features a perfect degeneracy between an increasing $\text{BR}(H \to \text{NP})$ and increasing scale factors of the Higgs couplings to SM particles if no additional constraints are imposed, the validity of the underlying model assumptions — in particular the assumption of identical signal efficiencies as in the SM — need to be scrutinized carefully in parameter regions with significant deviations from the SM Higgs couplings. In general, effects leading to such large coupling deviations within the underlying (unknown) model may potentially also lead to different kinematical distributions and hence to changed signal efficiencies. Furthermore, the narrow width approximation will become worse for an increasing total width.

are considered indistinguishable from the background. Other examples can be found in theories beyond the SM, like for instance, decays to supersymmetric particles that further decay via SUSY cascades or via R-parity violating interactions [199] (see Section 2.4.1), which also potentially leading to detached vertices.

In this work we investigate the following two options to overcome this degeneracy:

(i) All additional Higgs decay modes yield an *invisible* final state, i.e.

$$\mathrm{BR}(H \to \mathrm{NP}) \;\equiv\; \mathrm{BR}(H \to \mathrm{inv.}). \tag{5.1}$$

Hence, results from ATLAS and CMS searches measuring the recoil of a Z boson against missing transverse energy in the $pp \to ZH$ production can be used to constrain $\kappa_Z^2\,\mathrm{BR}(H \to \mathrm{NP})$.

(ii) The Higgs-vector boson coupling scale factors are required to be $\kappa_V \leq 1$ ($V = W, Z$). The Higgs production in the VH and VBF channels is then constrained from above [345, 346]. In this case, no assumption on additional Higgs decay modes needs to be imposed. Hence, an upper limit on $\mathrm{BR}(H \to \mathrm{NP})$ can be derived from the fit result. This assumption is valid for models that contain only singlet and doublet Higgs fields. However, in models with higher Higgs field representations [354, 355] this assumption does generally not hold.

As will be discussed in Section 5.3.2, both assumptions become obsolete once the direct cross section measurement for $e^+e^- \to HZ$ becomes available from the ILC.

In the following Sections 5.2.1–5.2.6 we discuss several fits to benchmark parametrizations of Higgs coupling deviations, where we also allow for an additional Higgs boson decay mode $\mathrm{BR}(H \to \mathrm{NP})$ leading to an invisible final state (*i*). In this case, we further constrain the product $\kappa_Z^2\,\mathrm{BR}(H \to \mathrm{NP})$ by adding the profile likelihood, $-2\log\Lambda$, from the ATLAS search[4] $pp \to ZH \to Z(\mathrm{inv.})$ [358] to the global χ^2 obtained from `HiggsSignals`. In Section 5.2.7 we instead employ the theoretical constraint $\kappa_V \leq 1$ (*ii*) to constrain the total width. Under this condition we derive for each benchmark parametrization upper limits on a new Higgs decay mode, which apply irrespectively of whether the final state is truly invisible or just undetectable.

If the individual scale factors for the loop-induced Higgs couplings to gluons and photons, κ_g and κ_γ, respectively, are not treated as individual free parameters in the fit, they can be derived from the fundamental Higgs coupling scale factors. We generally denote such *derived* scale factors as $\overline{\kappa}$. Additional genuine loop contributions from BSM particles to these effective couplings are then assumed to be absent. The Higgs-gluon scale factor is then given in terms of κ_t and κ_b as [29, 30]

$$\overline{\kappa}_g^2(\kappa_b, \kappa_t, m_H) = \frac{\kappa_t^2 \cdot \sigma^{tt}_{\mathrm{ggH}}(m_H) + \kappa_b^2 \cdot \sigma^{bb}_{\mathrm{ggH}}(m_H) + \kappa_t\kappa_b \cdot \sigma^{tb}_{\mathrm{ggH}}(m_H)}{\sigma^{tt}_{\mathrm{ggH}}(m_H) + \sigma^{bb}_{\mathrm{ggH}}(m_H) + \sigma^{tb}_{\mathrm{ggH}}(m_H)}. \tag{5.2}$$

Here, $\sigma^{tt}_{\mathrm{ggH}}(m_H)$, $\sigma^{bb}_{\mathrm{ggH}}(m_H)$ and $\sigma^{tb}_{\mathrm{ggH}}(m_H)$ denote the contributions to the cross section from the top-quark loop, the bottom-quark loop and the top-bottom interference, respectively. For a Higgs mass around 125.7 GeV the interference term is negative for positive scale factors. Details about state-of-the-art calculations have been summarized in Refs. [30, 70, 71]. We use numerical

[4] CMS carried out similar searches for the $pp \to ZH \to Z(\mathrm{inv.})$ process and obtained 95% C.L. upper limits corresponding to $\kappa_Z^2\,\mathrm{BR}(H \to \mathrm{inv.}) \leq 0.75$ (for $Z \to \ell^+\ell^-$) [356] and ≤ 1.82 (for $Z \to b\bar{b}$) [357]. However, unlike ATLAS, CMS does not provide a profile likelihood that can be incorporated into our fit.

values for the different contributions to Eq. (5.2) extracted from `FeynHiggs-2.9.4` [155] for a center-of-mass energy of 8 TeV. These evaluations are based on the calculations presented in Ref. [359, 360]. The top Yukawa contributions are calculated up to NNLO, whereas the bottom Yukawa contributions are evaluated up to NLO. These calculations agree well with the numbers used so far by the experimental collaborations [70].

Similarly to $\overline{\kappa}_g$, the scale factor for the loop-induced Higgs-photon coupling, $\overline{\kappa}_\gamma$, is derived from the coupling scale factors and contributions to the partial width of the involved particles in the loop,

$$\overline{\kappa}^2_\gamma(\kappa_b, \kappa_t, \kappa_\tau, \kappa_W, m_H) = \frac{\sum_{i,j} \kappa_i \kappa_j \cdot \Gamma^{ij}_{\gamma\gamma}(m_H)}{\sum_{i,j} \Gamma^{ij}_{\gamma\gamma}(m_H)}, \tag{5.3}$$

where (i, j) loops over the particles tt, bb, $\tau\tau$, WW, tb, $t\tau$,tW, $b\tau$, bW, τW. The Γ^{ij} have been evaluated with `HDECAY` [86, 87]. The partial widths $\Gamma^{ii}_{\gamma\gamma}$ are derived by setting $\kappa_i = 1$, $\kappa_j = 0$ $(i \neq j)$. Then the cross terms are derived by first calculating $\Gamma_{\gamma\gamma}$ with $\kappa_i = \kappa_j = 1$ and $\kappa_k = 0$ $(k \neq i, j)$, and then subtracting $\Gamma^{ii}_{\gamma\gamma}$ and $\Gamma^{jj}_{\gamma\gamma}$. Despite the absence of a sensitive observable probing the Higgs coupling to $Z\gamma$ directly, we also derive the coupling scale factor $\overline{\kappa}_{Z\gamma}$ in order to infer indirect constraints on this quantity and to evaluate its contribution to the total decay width. This scale factor coupling is derived in complete analogy to $\overline{\kappa}_\gamma$.

In the following benchmark fits, we choose to parametrize our results in terms of the absolute scale factors, κ_i, and an additional branching ratio to new particles, $\mathrm{BR}(H \to \mathrm{NP})$. These parameters can be transformed into the total width scale factor κ^2_H used in the benchmark model proposals from the LHCHXSWG [29, 30],

$$\kappa^2_H = \frac{\overline{\kappa}^2_H(\kappa_i)}{1 - \mathrm{BR}(H \to \mathrm{NP})}, \tag{5.4}$$

where $\overline{\kappa}^2_H(\kappa_i)$ is the derived scale factor for the SM total width as induced by the modified Higgs couplings to SM particles, κ_i (both including the fundamental and loop-induced couplings). For an allowed range $\mathrm{BR}(H \to \mathrm{NP}) \in [0, 1]$, the total width scale factor, κ^2_H, thus ranges from $\overline{\kappa}^2_H$ to infinity.

Before we study potential deviations from the SM Higgs couplings it is worthwhile to look at the fit quality of the SM itself: Tested against the 80 signal rate measurements we find $\chi^2/\mathrm{ndf} = 84.3/80$ which corresponds to a (naive) $\mathcal{P}$-value of $\sim 35.0\%$.[5] Thus, the the measurements are in good agreement with the SM predictions. However, coupling variations may be able to improve the fit quality if the signal rates actually feature systematic under- or over-fluctuations, indicating possible deviations in some of the Higgs couplings from their SM values. It is the goal of the next sections to systematically search for such tendencies as well as to determine the viable parameter space of possible deviations. Note that, if we slightly modify the SM by only adding new Higgs decay modes while keeping the couplings at their SM predictions ($\kappa_i = 1$), we obtain 95% C.L. upper limits of $\mathrm{BR}(H \to \mathrm{inv.}) \leq 17\%$ in the case of purely invisible final states of the additional decay modes, and $\mathrm{BR}(H \to \mathrm{NP}) \leq 20\%$ in the case of undetectable decay modes.

[5] For the SM, where we have no additional invisible or undetectable decay modes, we do not count the ATLAS $\mathrm{BR}(H \to \mathrm{inv.})$ limit into the ndfs.

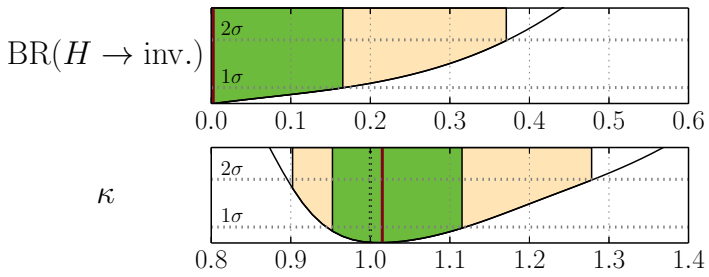

Figure 5.1: One-dimensional $\Delta\chi^2$ profiles for the fit parameters κ and BR($H \to$ inv.) in the universal scale factor fit. The best-fit point is indicated by the red line. The 68% (95%) C.L. regions are illustrated by the green (pale yellow) bands.

Fit parameter	best-fit value	68% C.L. range (1D)	95% C.L. range (1D)
BR($H \to$ inv.)	0.00	$^{+0.17}_{-0.00}$	$^{+0.37}_{-0.00}$
κ	1.01	$^{+0.10}_{-0.08}$	$^{+0.26}_{-0.13}$
κ_H^2	1.03	$^{+0.43}_{-0.13}$	$^{+1.55}_{-0.23}$

Table 5.1: Best-fit values and 68% and 95% C.L. ranges for the fit parameters κ and BR($H \to$ inv.) as well as the derived total width scale factor, κ_H^2, obtained from the one-dimensional $\Delta\chi^2$ profiles in the universal scale factor fit.

5.2.1 Universal coupling modification

The first benchmark model that we consider contains only one universal Higgs coupling scale factor, κ, in addition to the invisible Higgs decay mode. Hence, all Higgs production cross sections and partial widths to SM particles are universally scaled by κ^2. Although this scenario seems to be overly simplistic it actually represents realistic physics models, such as the extension of the SM Higgs sector by a real or complex scalar singlet [134, 361]. In the presence of singlet-doublet mixing κ can be identified with the mixing angle. Both undetectable and invisible Higgs decays are potentially present in these models.

We show the fit results obtained under the assumption of a fully invisible additional Higgs decay mode as one- and two-dimensional profiled $\Delta\chi^2$ distributions in Figs. 5.1 and 5.2(a), respectively. The best fit point is found at $\kappa = 1.01^{+0.10}_{-0.08}$ with a $\chi^2_{\text{min}}/\text{ndf} = 84.3/79$, which corresponds to a $\mathcal{P}$-value of $\sim 32.2\%$. The 68% and 95% C.L. ranges are also listed in Tab. 5.1, along with the corresponding range for the total width scale factor κ_H^2. The two-dimensional $\Delta\chi^2$ distribution in Fig. 5.2(a) shows a strong positive correlation between κ and BR($H \to$ inv.). This reflects the fact that a suppression of the branching ratios to SM particles introduced by an additional invisible decay mode needs to be compensated by an increase of the production rates. The allowed region is however bounded at increasing BR($H \to$ inv.) by the limit from the invisible Higgs search from ATLAS.

In Fig. 5.2(b) we illustrate what happens if this constraint is absent, i.e. if no assumptions on the additional Higgs decay mode or model parameters, such as $\kappa_V \leq 1$, are imposed. The allowed parameter range then extends towards arbitrarily large values of κ, and BR($H \to$ NP) $\to 1$ due to the perfect degeneracy mentioned above. In the same figure we overlay the

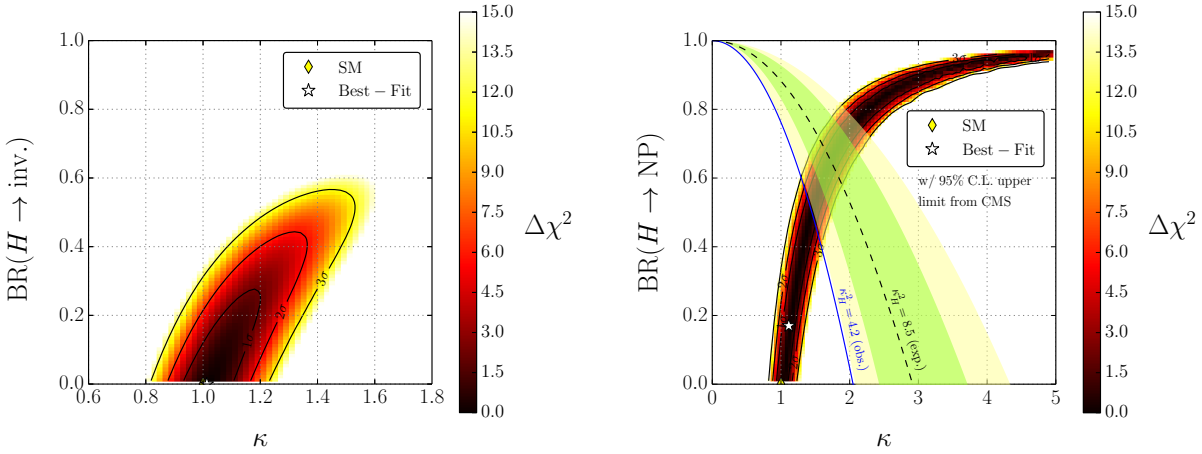

(a) Assuming BR($H \to$ NP) $\equiv$ BR($H \to$ inv.).

(b) No assumptions. We overlay the present observed (expected) CMS upper limit on the total width from off-shell Higgs production [342], given by the solid blue (dashed black) line. The green (yellow) region indicates the 68 (95)% C.L. uncertainty region of the expected CMS limit.

Figure 5.2: Two-dimensional $\Delta\chi^2$ profiles for the fit parameters κ and BR($H \to$ NP) in the universal scale factor fit, assuming purely invisible final states of the additional decay mode (a), or without further assumptions to constrain the total width (b).

present observed (expected) 95% C.L. upper limit from CMS on the total width scale factor, $\kappa^2_H \leq 4.2$ (8.5), that is derived from off-shell Higgs production in the process $gg \to ZZ^{(*)} \to 4\ell$ and $2\ell 2\nu$ [342]. Such upper limits on the total width scale factor, $\kappa^2_{H,\text{limit}}$, can be used to infer indirect bounds on BR($H \to$ NP) and the coupling scale factor κ.[6] Using Eq. (5.4), the limit can be parametrized by

$$\frac{\kappa^2}{1 - \text{BR}(H \to \text{NP})} \leq \kappa^2_{H,\text{limit}}, \tag{5.5}$$

while SM signal rates are obtained for

$$\kappa^2 \cdot [1 - \text{BR}(H \to \text{NP})] = 1. \tag{5.6}$$

For a given upper limit of the total width scale factor, $\kappa^2_{H,\text{limit}}$, we can thus infer the indirect bounds

$$\kappa \leq \sqrt{\kappa_{H,\text{limit}}}, \qquad \text{BR}(H \to \text{NP}) = 1 - \kappa^{-1}_{H,\text{limit}}. \tag{5.7}$$

For the current observed (expected) CMS limit we thus obtain $\kappa \leq 1.43$ (1.71) and BR($H \to$ NP) $\leq 51\%$ (66%). However, even after taking these constraints into account there remains a quite large parameter space with possibly sizable BR($H \to$ NP). Hence, the LHC will not be capable to accurately determine absolute values of the Higgs couplings in a model-independent

[6] Note, that this argument applies also for more general, higher-dimensional scale factor models since all scale factors κ_i are identical in the degenerate case.

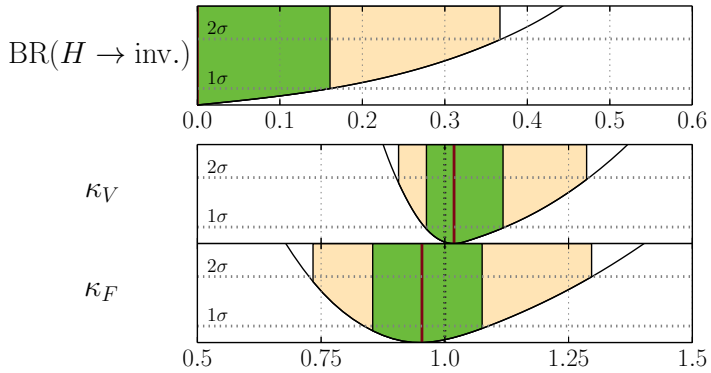

Figure 5.3: One-dimensional $\Delta\chi^2$ profiles for the parameters in the $(\kappa_V, \kappa_F, \mathrm{BR}(H \to \mathrm{inv.}))$ fit.

way. This is reserved for future e^+e^- experiments like the ILC, cf. Section 5.3.2.

Returning to the current fit results displayed in Fig. 5.2, we can also infer from this fit a lower limit on the total signal strength into known final states, normalized to the SM:

$$\kappa^2 \cdot [1 - \mathrm{BR}(H \to \mathrm{NP})] \geq 0.81 \quad (\text{at } 95\% \text{ C.L.}). \tag{5.8}$$

Note, that this limit is irrespective of the final state(s) of the additional Higgs decay mode(s).

5.2.2 Couplings to gauge bosons and fermions

The next benchmark model contains one universal scale factor for all Higgs couplings to fermions, κ_F, and one for the $SU(2)$ gauge bosons, κ_V $(V = W, Z)$. This coupling pattern occurs, for example, in minimal composite Higgs models [347], where the Higgs couplings to fermions and vector bosons can be suppressed with different factors. The loop-induced coupling scale factors are scaled as expected from the SM structure, Eqs. (5.2) and (5.3). Note that $\overline{\kappa}_g$ scales trivially like κ_F in this case, whereas $\overline{\kappa}_\gamma$ depends on the relative sign of κ_V and κ_F due to the W boson-top quark interference term, giving a negative contribution for equal signs of the fundamental scale factors. Due to this sign dependence we allow for negative values of κ_F in the fit,

Fit parameter	best-fit value	68% C.L. range (1D)	95% C.L. range (1D)
$\mathrm{BR}(H \to \mathrm{inv.})$	0.00	$^{+0.16}_{-0.00}$	$^{+0.37}_{-0.00}$
κ_V	1.02	$^{+0.11}_{-0.06}$	$^{+0.27}_{-0.12}$
κ_F	0.95	$^{+0.14}_{-0.12}$	$^{+0.34}_{-0.22}$
κ_H^2	0.95	$^{+0.40}_{-0.20}$	$^{+1.51}_{-0.30}$
$\overline{\kappa}_g$	0.95	$^{+0.14}_{-0.12}$	$^{+0.34}_{-0.23}$
$\overline{\kappa}_\gamma$	1.04	$^{+0.11}_{-0.07}$	$^{+0.28}_{-0.14}$
$\overline{\kappa}_{Z\gamma}$	1.03	$^{+0.10}_{-0.06}$	$^{+0.27}_{-0.12}$

Table 5.2: Best-fit values and 68% and 95% C.L. regions for the fit parameters and derived quantities obtained from the one-dimensional $\Delta\chi^2$ profiles in the $(\kappa_V, \kappa_F, \mathrm{BR}(H \to \mathrm{inv.}))$ fit.

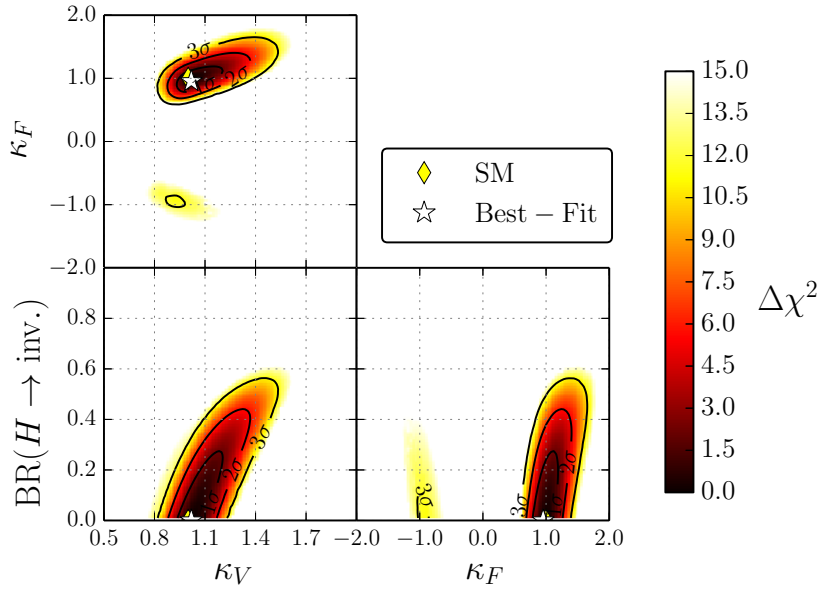

Figure 5.4: Two-dimensional $\Delta\chi^2$ profiles for the fit parameters κ_V, κ_F and BR($H \to$ inv.).

while we restrict $\kappa_V \geq 0$. The assumption of universality of the Higgs-gauge boson couplings, $\kappa_W = \kappa_Z$, corresponds to the (approximately fulfilled) custodial global $SU(2)$ symmetry of the SM Higgs sector. We will explore the possibility of non-universal Higgs-gauge boson couplings in the next section.

We show the one- and two-dimensional profiled $\Delta\chi^2$ distributions in Figs. 5.3 and 5.4, respectively. At the best-fit point we have $\chi^2_{\text{min}}/\text{ndf} = 84.0/78$, corresponding to a $\mathcal{P}$-value of $\sim 30.1\%$. The best-fit values of the fit parameters and the derived scale factors for the total width and loop-induced couplings are listed in Tab. 5.2 including the one-dimensional 68% and 95% C.L. ranges. Both the Higgs-fermion couplings and Higgs-gauge boson couplings are very close to their SM values. At most, κ_F indicates a very weak tendency to a slight suppression. We can obtain 95% C.L. upper limits on the branching ratio to invisible final states, BR($H \to$ inv.) $\leq 37\%$, and the total decay width $\Gamma^{\text{tot}} \leq 2.46 \cdot \Gamma^{\text{tot}}_{\text{SM}} \approx 10.3\,\text{MeV}$.

From the two-dimensional χ^2 profiles, shown in Fig. 5.4, we see that the sector with negative κ_F is disfavored by more than 2σ. In the positive κ_F sector, κ_V and κ_F show a strong positive correlation to preserve SM-like relations among the production cross sections and branching ratios. At this stage, due to the assumed scaling universality of all Higgs couplings to fermions and gauge bosons, the fit does not have enough freedom to resolve small potentially present tendencies in the Higgs signal rates, but rather reflects the overall global picture. Hence, we expect the correlation of κ_V with the Higgs fermion coupling scale factor(s) to diminish once more freedom is introduced in the Yukawa coupling sector. This will be discussed in Section 5.2.4. Furthermore, Fig. 5.4 shows that both κ_V and κ_F are positively correlated with BR($H \to$ inv.), similarly to the case with an overall coupling scale factor (cf. Fig. 5.2).

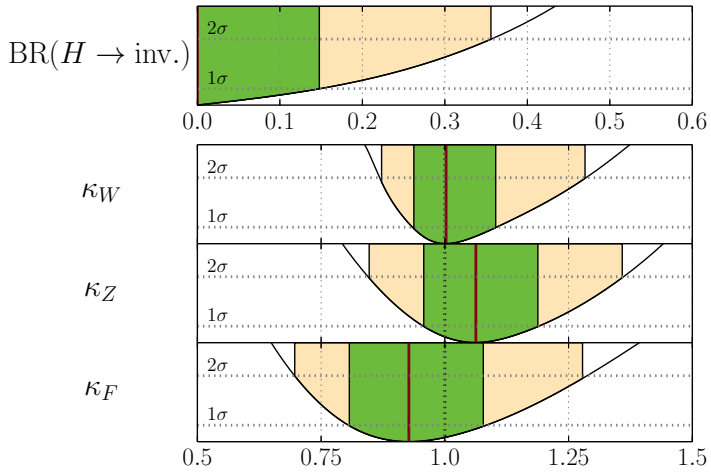

Figure 5.5: One-dimensional $\Delta\chi^2$ profiles for the parameters in the $(\kappa_W, \kappa_Z, \kappa_F, \mathrm{BR}(H \to \mathrm{inv.}))$ fit.

5.2.3 Probing custodial symmetry

As we discussed in Section 2.1.4, deviations from the custodial global $SU(2)$ symmetry are strongly constrained by the ρ parameter, Eq. (2.21), or in an alternative parametrization, the oblique (Peskin-Takeuchi) T parameter [362, 363], obtained in global electroweak fits to the experimental precision data [66, 364]. Nevertheless, as an independent and complementary test, it is important to investigate the universality of the Higgs-gauge boson couplings directly using the signal rate measurements.

Here, we restrict the analysis to the simplest benchmark model probing the custodial symmetry, consisting of individual scale factors for the Higgs couplings to W and Z-bosons, κ_W and κ_Z, respectively, and a universal scale factor for the Higgs-fermion couplings, κ_F. Again, we also allow for an additional invisible decay mode, $\mathrm{BR}(H \to \mathrm{inv.})$. Note that, besides the direct signal rate measurements in the channels $H \to WW^{(*)}$ and $H \to ZZ^{(*)}$, different constraints apply to the scale factors κ_W and κ_Z: The loop-induced coupling scale factors $\overline{\kappa}_\gamma$ and $\overline{\kappa}_{Z\gamma}$ are only affected by κ_W and κ_F, hence κ_Z plays a subdominant role in the important channel $H \to \gamma\gamma$ by only affecting the less important production modes HZ and VBF. In contrast, the invisible Higgs search does not constrain κ_W at all, but only the product $\kappa_Z^2\,\mathrm{BR}(H \to \mathrm{inv.})$. Since the W–Z boson interference term in the VBF channel is neglected, we can impose $\kappa_Z \geq 0$ without loss of information. As in Section 5.2.2, we furthermore impose $\kappa_W \geq 0$ and accommodate the sign dependence in the loop-induced couplings by allowing κ_F to take on negative values.

The results of the fit are shown in Figs. 5.5 and 5.6 as one- and two-dimensional χ^2 profiles in the fit parameters. The best-fit values and the (1D) 68% and 95% C.L. intervals of the fit parameters and derived scale factors are listed in Tab. 5.3. The best fit point features $\chi^2_{\mathrm{min}}/\mathrm{ndf} = 83.7/77$, corresponding to a $\mathcal{P}$-value of $\sim 28.2\%$. Similar as in the previous fit, a very small non-significant suppression of the Higgs-fermion coupling scale factor $\kappa_F \sim 0.93$ can be observed. Furthermore, the fit has a small tendency towards slightly enhanced $\kappa_Z \sim 1.06$, whereas κ_W is very close to the SM value[7]. The Higgs-gauge boson coupling scale factors both

[7] A stronger tendency like this was also seen in the official ATLAS result [3]. Due to the combination with measurements from other experiments, the tendency observed in our fit is much weaker.

Fit parameter	best-fit value	68% C.L. range (1D)	95% C.L. range (1D)
$\mathrm{BR}(H \to \mathrm{inv.})$	0.00	$^{+0.15}_{-0.00}$	$^{+0.36}_{-0.00}$
κ_W	1.00	$^{+0.10}_{-0.07}$	$^{+0.28}_{-0.14}$
κ_Z	1.06	$^{+0.13}_{-0.11}$	$^{+0.30}_{-0.22}$
κ_F	0.93	$^{+0.16}_{-0.12}$	$^{+0.36}_{-0.23}$
κ_H^2	0.90	$^{+0.41}_{-0.18}$	$^{+1.45}_{-0.31}$
$\overline{\kappa}_g$	0.93	$^{+0.15}_{-0.12}$	$^{+0.35}_{-0.23}$
$\overline{\kappa}_\gamma$	1.02	$^{+0.11}_{-0.08}$	$^{+0.29}_{-0.16}$
$\overline{\kappa}_{Z\gamma}$	1.00	$^{+0.11}_{-0.07}$	$^{+0.29}_{-0.13}$

Table 5.3: Best-fit parameter values and 68% and 95% C.L. regions obtained from the one-dimensional $\Delta\chi^2$ profiles in the $(\kappa_W, \kappa_Z, \kappa_F, \mathrm{BR}(H \to \mathrm{inv.}))$ fit.

agree well with the SM predictions, and also with being equal to each other. Since the fit shows excellent agreement of the data with the assumption of custodial symmetry, we will assume $\kappa_W = \kappa_Z \equiv \kappa_V$ in the following fits.

As can be seen from the two-dimensional $\Delta\chi^2$ profiles, Fig. 5.6, the sector with negative κ_F is less disfavored than in the previous fit, albeit still by more than 2σ. Since the connection between κ_W and κ_Z is dissolved, the signal rates of $H \to \gamma\gamma$ can be accommodated more easily in the negative κ_F sector than before. It can be seen in Fig. 5.6 that the least constrained

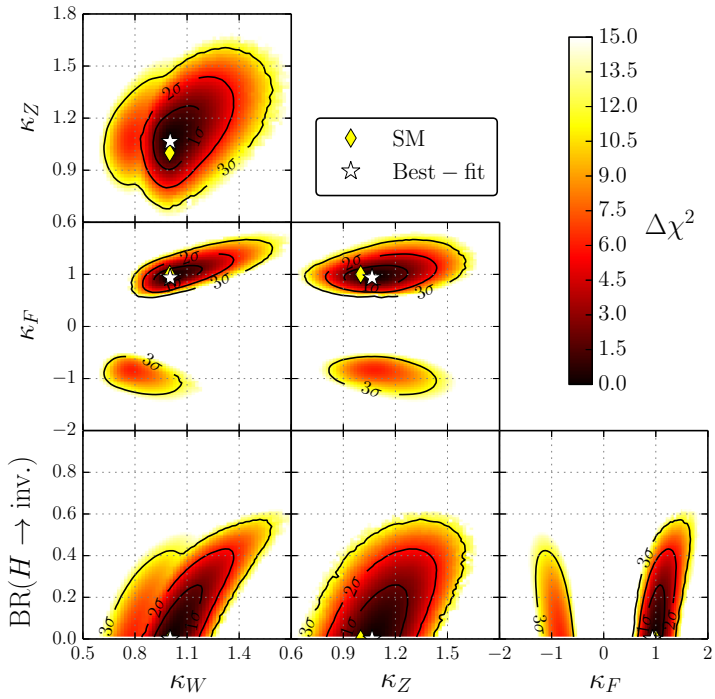

Figure 5.6: Two-dimensional $\Delta\chi^2$ profiles for the parameters in the $(\kappa_W, \kappa_Z, \kappa_F, \mathrm{BR}(H \to \mathrm{inv.}))$ fit.

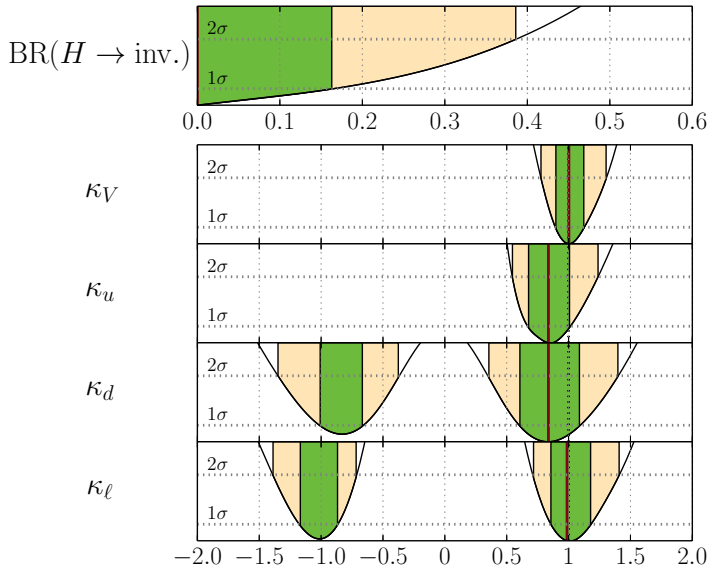

Figure 5.7: One-dimensional $\Delta\chi^2$ profiles for the parameters in the $(\kappa_V, \kappa_u, \kappa_d, \kappa_\ell, \mathrm{BR}(H \to \text{inv.}))$ fit.

region for negative κ_F favors values of $\kappa_W \sim 0.70 - 0.85$ and $\kappa_Z \sim 0.95 - 1.20$, i.e. a much larger discrepancy between κ_W and κ_Z than in the positive κ_F sector, where we found the overall best fit.

5.2.4 Probing the Yukawa structure

We will now have a closer look at the Higgs-fermion coupling structure. In fact, assuming that all Higgs-fermion couplings can be described by one common scale factor—as we have done until now—is motivated in only a few special BSM realizations. A splitting of up- and

Fit parameter	best-fit value	68% C.L. range (1D)	95% C.L. range (1D)
BR($H \to$ inv.)	0.00	$^{+0.17}_{-0.00}$	$^{+0.39}_{-0.00}$
κ_V	1.00	$^{+0.13}_{-0.11}$	$^{+0.31}_{-0.23}$
κ_u	0.84	$^{+0.18}_{-0.17}$	$^{+0.40}_{-0.29}$
κ_d	0.84	$^{+0.26}_{-0.24}$	$^{+0.56}_{-0.49}$
κ_ℓ	0.99	$^{+0.19}_{-0.13}$	$^{+0.42}_{-0.28}$
κ_H^2	0.80	$^{+0.45}_{-0.28}$	$^{+1.53}_{-0.50}$
$\overline{\kappa}_g$	0.84	$^{+0.16}_{-0.12}$	$^{+0.38}_{-0.24}$
$\overline{\kappa}_\gamma$	1.04	$^{+0.15}_{-0.11}$	$^{+0.33}_{-0.24}$
$\overline{\kappa}_{Z\gamma}$	1.01	$^{+0.13}_{-0.10}$	$^{+0.31}_{-0.22}$

Table 5.4: Best-fit values and 68% and 95% C.L. regions for the fit parameters around the best fit point (positive sector only) obtained from the one-dimensional $\Delta\chi^2$ profiles in the $(\kappa_V, \kappa_u, \kappa_d, \kappa_\ell, \mathrm{BR}(H \to \text{inv.}))$ fit.

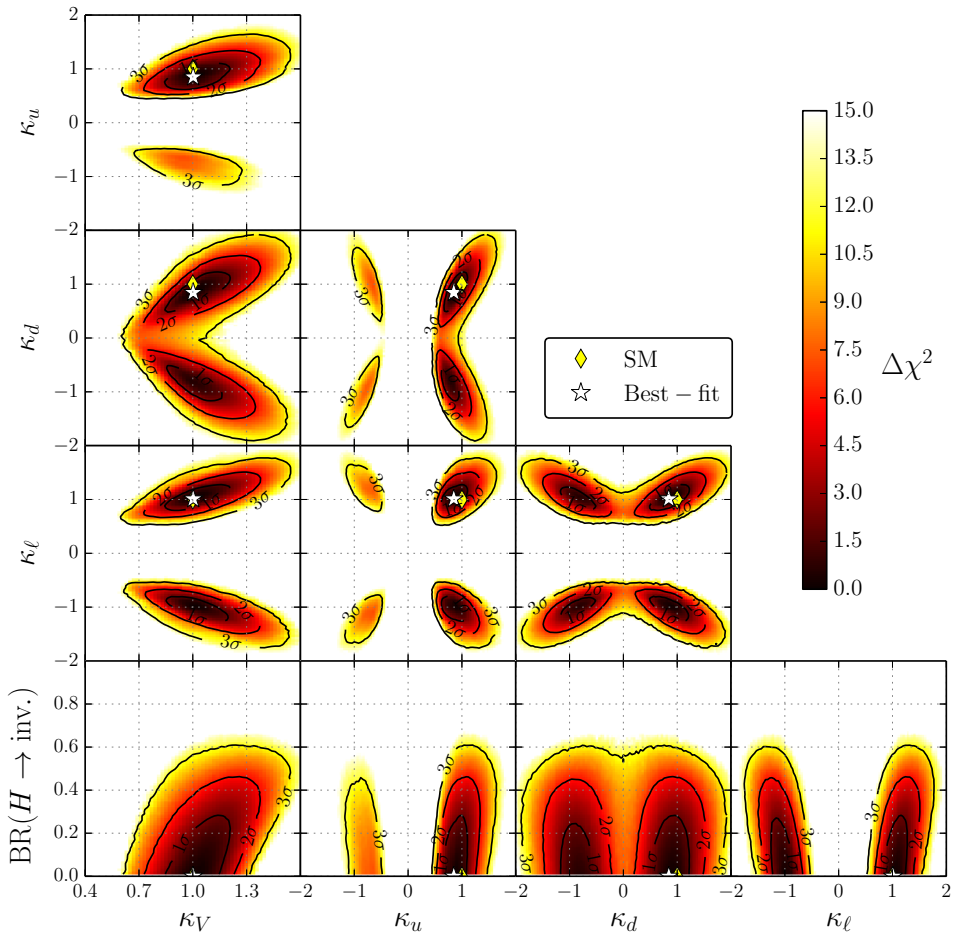

Figure 5.8: Two-dimensional $\Delta\chi^2$ profiles for the parameters in the $(\kappa_V, \kappa_u, \kappa_d, \kappa_\ell, \mathrm{BR}(H \to \text{inv.}))$ fit.

down-type Yukawa couplings appears in many BSM models, e.g. in Two-Higgs-Doublet Models (2HDM) [196, 197] of Type II or in the MSSM, see Section 2.4.3. Moreover, realistic 2HDMs with more generic Yukawa structures featuring additional freedom for the Higgs-charged lepton coupling can be constructed to be consistent with constraints from flavor-changing neutral currents (FCNCs) [145, 180, 197, 365]. Also in the MSSM, as discussed in Section 2.4.3, the degeneracy of bottom-type quarks and leptons can be abrogated by radiative SUSY QCD corrections. Therefore, we now relax the assumption of a universal Higgs-fermion coupling scale factor and introduce common scale factors for all up-type quarks, κ_u, all down-type quarks, κ_d, and all charged leptons, κ_ℓ. All Higgs-fermion coupling scale factors are allowed to take positive and negative values. The parameters κ_V and $\mathrm{BR}(H \to \text{inv.})$ remain from before.

The one-dimensional $\Delta\chi^2$ profiles of the fit parameters are shown in Fig. 5.7. The parameter values of the best-fit point, which is found in the sector with all scale factors being positive, are given in Tab. 5.4 along with the (1D) 68% and 95% C.L. intervals. The fit quality is $\chi^2_{\mathrm{min}}/\mathrm{ndf} = 82.8/76$ corresponding to a $\mathcal{P}$-value of $\sim 27.8\%$. As can be clearly seen in Fig. 5.7, negative values of κ_d and κ_ℓ are still consistent with the measurements within 68% C.L. due to their small influence on the loop-induced Higgs couplings to gluons and/or photons. In particular the sign discrimination of κ_ℓ is very weak. In contrast, negative values of κ_u are

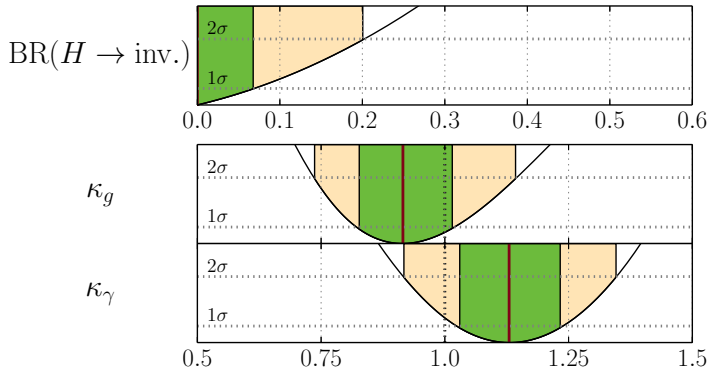

Figure 5.9: One-dimensional $\Delta\chi^2$ profiles for the parameters in the $(\kappa_g, \kappa_\gamma, \mathrm{BR}(H \to \mathrm{inv.}))$ fit.

disfavored by more than 2σ due to the influence on the Higgs-photon effective coupling in the convention $\kappa_V \geq 0$. The fit prefers slightly suppressed values of $\kappa_u \sim 0.84$ since $\kappa_g \simeq \kappa_u$, Eq. (5.2), which is sensitively probed by the LHC measurements via the gluon fusion production mode. Due to the recent $H \to \tau^+\tau^-$ results from ATLAS [284] and CMS [285, 286, 366], κ_ℓ is determined to be very close to its SM value with a precision of $\sim 15\%$. We observe a slight but non-significant suppression of the Higgs-down type quark coupling, $\kappa_d \sim 0.84$. This scale factor has the worst precision of the fitted parameters, about $\sim 30\%$. The sign degeneracy of κ_d is slightly broken via the sensitivity of the Higgs-gluon coupling scale factor to the relative sign of κ_t and κ_b, cf. Eq. (5.2).

The correlation of the fitted coupling scale factors can be seen from the shape of the ellipses in the two-dimensional χ^2 profiles, shown in Fig. 5.8. The slope of the major axis of the ellipse in the positive sector of the $(\kappa_V,\ \kappa_u)$ plane is $\sim 0.6 - 0.7$ and thus much shallower than the slopes in the $(\kappa_V,\ \kappa_d)$ and $(\kappa_V,\ \kappa_\ell)$ planes, approximately given by ~ 1.7 and ~ 1.3, respectively. Therefore, this parameterization exhibits more freedom to adjust the predicted signal rates to the Tevatron and LHC measurements. Nevertheless, the best-fit point and favored region is in perfect agreement with the SM and thus the additional freedom does not improve the fit quality. Once more precise measurements of the $H \to \tau^+\tau^-$ and $H \to b\bar{b}$ channels become available, this parametrization can be expected to provide a good test of the SM due to the different correlations among κ_V and the Higgs-fermion coupling scale factors.

5.2.5 Probing new physics in loop-induced couplings

Up to now we have investigated possible modifications of the fundamental tree-level Higgs boson couplings to SM particles and derived the loop-induced couplings to gluons and photons using Eq. (5.2) and (5.3), respectively. In this section, we modify these coupling scale factors, κ_g and κ_γ, directly. Such modifications could be introduced by unknown new physics loop contributions, while the tree-level Higgs boson couplings are unaffected. Triggered by recent hints in the experimental data for a possible $H \to \gamma\gamma$ enhancement, new physics sources for modifications of the Higgs-photon coupling have been subject to many recent studies. For instance, charged supersymmetric particles such as light staus [246, 274, 367, 385] and charginos [368, 369] could give potentially substantial contributions[8]. In 2HDMs the Higgs-photon

[8] Possible mechanisms for the enhancement of the $H \to \gamma\gamma$ rate in the MSSM are also discussed in Section 6.2.

Fit parameter	best-fit value	68% C.L. range (1D)	95% C.L. range (1D)
$\mathrm{BR}(H \to \mathrm{NP})$	0.00	$^{+0.07}_{-0.00}$	$^{+0.20}_{-0.00}$
κ_g	0.92	$^{+0.11}_{-0.10}$	$^{+0.23}_{-0.18}$
κ_γ	1.14	$^{+0.11}_{-0.11}$	$^{+0.21}_{-0.22}$
κ_H^2	1.01	$^{+0.08}_{-0.03}$	$^{+0.28}_{-0.03}$

Table 5.5: Best-fit values and 68% and 95% C.L. regions for the fit parameters around the best fit point obtained from the one-dimensional $\Delta\chi^2$ profiles in the $(\kappa_g, \kappa_\gamma, \mathrm{BR}(H \to \mathrm{inv.}))$ fit.

coupling can be altered due to contributions from the charged Higgs boson [370], and in the special case of the Inert Doublet Model [135, 136, 371], modifications of κ_γ and $\kappa_{Z\gamma}$ are indeed the only possible change to the Higgs coupling structure. In addition, many of these models can also feature invisible or undetectable Higgs decays. The effective Higgs-gluon coupling can be modified in supersymmetric models by stop contributions, where one can easily find rate predictions for Higgs production in gluon fusion corresponding to $\kappa_g < 1$ [246, 372, 373].

Our fit parametrization represents the case where indirect new physics effects may be visible only in the loop-induced Higgs-gluon and Higgs-photon couplings. Direct modifications to the tree-level couplings, as introduced e.g. if the observed Higgs boson is a mixed state, are neglected. The more general case where all couplings are allowed to vary will be discussed in the next section. Due to the very small branching ratio $\mathrm{BR}(H \to Z\gamma) \times \mathrm{BR}(Z \to \ell\ell)$ in the SM, the LHC is not yet sensitive to probe $\kappa_{Z\gamma}$. We therefore set $\kappa_{Z\gamma} = \kappa_\gamma$. In addition, here we assume that any additional Higgs decays lead to invisible final states. Undetectable Higgs decays are discussed in Section 5.2.7.

The fit results are shown as one- and two-dimensional $\Delta\chi^2$ profiles in the fit parameters

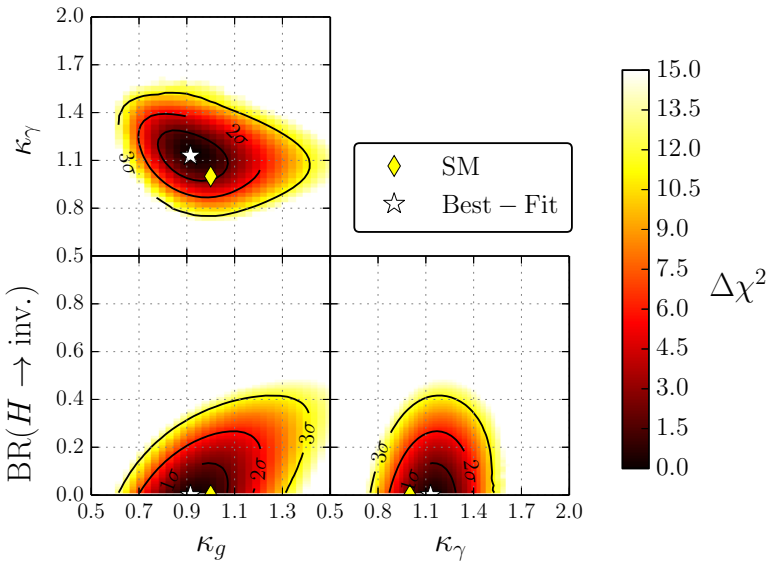

Figure 5.10: Two-dimensional χ^2 profiles for the fit parameters in the $(\kappa_g, \kappa_\gamma, \mathrm{BR}(H \to \mathrm{inv.}))$ fit.

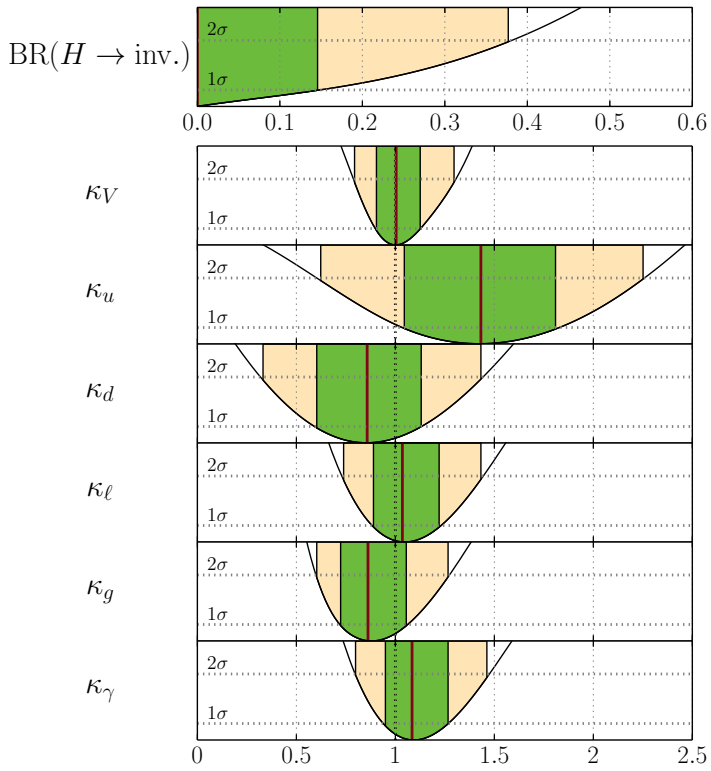

Figure 5.11: One-dimensional $\Delta\chi^2$ profiles for the parameters $\kappa_V, \kappa_u, \kappa_d, \kappa_\ell, \kappa_g, \kappa_\gamma$ and BR($H \to$ inv.) in the general Higgs couplings fit.

in Fig. 5.9 and 5.10, respectively. The (1D) preferred parameter values are also provided in Tab. 5.5. In this scenario, the best fit indicates a slight suppression of the Higgs-gluon coupling, $\kappa_g = 0.92$, with a simultaneous enhancement in the Higgs-photon coupling, $\kappa_\gamma = 1.14$. The anti-correlation of these two parameters can be seen in Fig. 5.10. It is generated by the necessity of having roughly SM-like $gg \to H \to \gamma\gamma$ signal rates. The best fit point, which has $\chi^2_{\text{min}}/\text{ndf} = 82.6/78$, is compatible with the SM expectation at the 1σ level, as can be seen in Fig. 5.10. The estimated $\mathcal{P}$-value is $\sim 33.9\%$. Note that BR($H \to$ inv.) is much stronger constrained to $\leq 20\%$ (at 95% C.L.) in this parametrization than in the previous fits. The reason being that the suppression of the SM decay modes with an increasing BR($H \to$ inv.) cannot be fully compensated by an increasing production cross sections since the tree-level Higgs couplings are fixed. The partial compensation that is possible with an increased gluon fusion cross section is reflected in the strong correlation between κ_g and BR($H \to$ inv.), which can be seen in Fig. 5.10.

5.2.6 General Higgs couplings

We now allow for genuine new physics contributions to the loop-induced couplings by treating κ_g and κ_γ as free fit parameters in addition to a general parametrization of the Yukawa sector as employed in Section 5.2.4. This gives in total seven free fit parameters, κ_V, κ_u, κ_d, κ_ℓ, κ_g, κ_γ and BR($H \to$ inv.). Note, that this parametrization features a sign degeneracy in *all* coupling scale factors, since the only derived scale factor, κ_H^2, depends only on the squared

Fit parameter	best-fit value	68% C.L. range (1D)	95% C.L. range (1D)
$\mathrm{BR}(H \to \text{inv.})$	0.00	$^{+0.15}_{-0.00}$	$^{+0.39}_{-0.00}$
κ_V	1.00	$^{+0.13}_{-0.11}$	$^{+0.31}_{-0.22}$
κ_u	1.42	$^{+0.40}_{-0.39}$	$^{+0.83}_{-0.82}$
κ_d	0.86	$^{+0.28}_{-0.27}$	$^{+0.59}_{-0.54}$
κ_ℓ	1.05	$^{+0.19}_{-0.17}$	$^{+0.40}_{-0.32}$
κ_g	0.88	$^{+0.18}_{-0.16}$	$^{+0.39}_{-0.28}$
κ_γ	1.09	$^{+0.18}_{-0.15}$	$^{+0.38}_{-0.29}$
$\overline{\kappa}_H^2$	0.86	$^{+0.36}_{-0.27}$	$^{+0.90}_{-0.48}$
κ_H^2	0.88	$^{+0.43}_{-0.28}$	$^{+1.56}_{-0.50}$
$\Delta\kappa_\gamma$	0.19	$^{+0.14}_{-0.14}$	$^{+0.30}_{-0.28}$
$\Delta\kappa_g$	−0.63	$^{+0.36}_{-0.32}$	$^{+0.90}_{-0.62}$
$\overline{\kappa}_{Z\gamma}$	0.98	$^{+0.13}_{-0.13}$	$^{+0.29}_{-0.25}$

Table 5.6: Best-fit values and 68% and 95% C.L. regions for the fit parameters (above) and derived scale factors (below) obtained from the one-dimensional $\Delta\chi^2$ profiles in the general Higgs couplings fit.

coupling scale factors. For practical purposes, we thus restrict ourselves to the sector where all scale factors are positive. Furthermore, it can be illustrative to decompose κ_g and κ_γ into scale factors $\overline{\kappa}_i$ for the calculable contributions from SM particles, with rescaled couplings, appearing in the loop, as described by Eqs. (5.2)–(5.3), and a scale factor $\Delta\kappa_i$ for the genuine new physics contributions:

$$\kappa_g = \overline{\kappa}_g + \Delta\kappa_g, \tag{5.9}$$

$$\kappa_\gamma = \overline{\kappa}_\gamma + \Delta\kappa_\gamma. \tag{5.10}$$

This decomposition assumes that the unknown new physics does not alter the loop contributions from SM particles, Eqs. (5.2)–(5.3).

The one-dimensional $\Delta\chi^2$ profiles in the fit parameters are shown in Fig. 5.11. Their best-fit values and preferred parameter ranges are listed together with those of derived scale factors in Tab. 5.6. The best-fit point features a fit quality of $\chi^2_{\text{min}}/\text{ndf} = 79.9/74$ and thus a $\mathcal{P}$-value of $\sim 29.9\%$. Due to the dissolved dependence between the Yukawa couplings and the effective Higgs-gluon and Higgs-photon couplings, κ_u is significantly less accurately determined than in previous more constrained fits. In fact, it is now dominantly influenced by the recent CMS measurements targeting $t\bar{t}H$ production [333–335], which give a combined signal strength of $\hat{\mu}^{t\bar{t}H}_{\text{CMS}} = 2.5^{+1.1}_{-1.0}$ [374]. Hence, the fit prefers slightly enhanced values, $\kappa_u \sim 1.42$, albeit with very large uncertainties. The scale factors κ_g and κ_γ can now be freely adjusted to match the combined rates of Higgs production in gluon fusion and $\mathrm{BR}(H \to \gamma\gamma)$, respectively. Here we observe the same tendencies as in the previous fit, cf. Section 5.2.5. Due to the slight preference for enhanced κ_u and suppressed κ_g, the fitted new physics contribution to the Higgs-gluon coupling is quite sizable and negative, $\Delta\kappa_g \sim -0.63$. In contrast, the Higgs-photon coupling is fairly well described by the rescaled contributions from SM particles alone because the enhanced κ_u also enhances $\overline{\kappa}_\gamma$ slightly. The favored magnitude for the genuine new physics

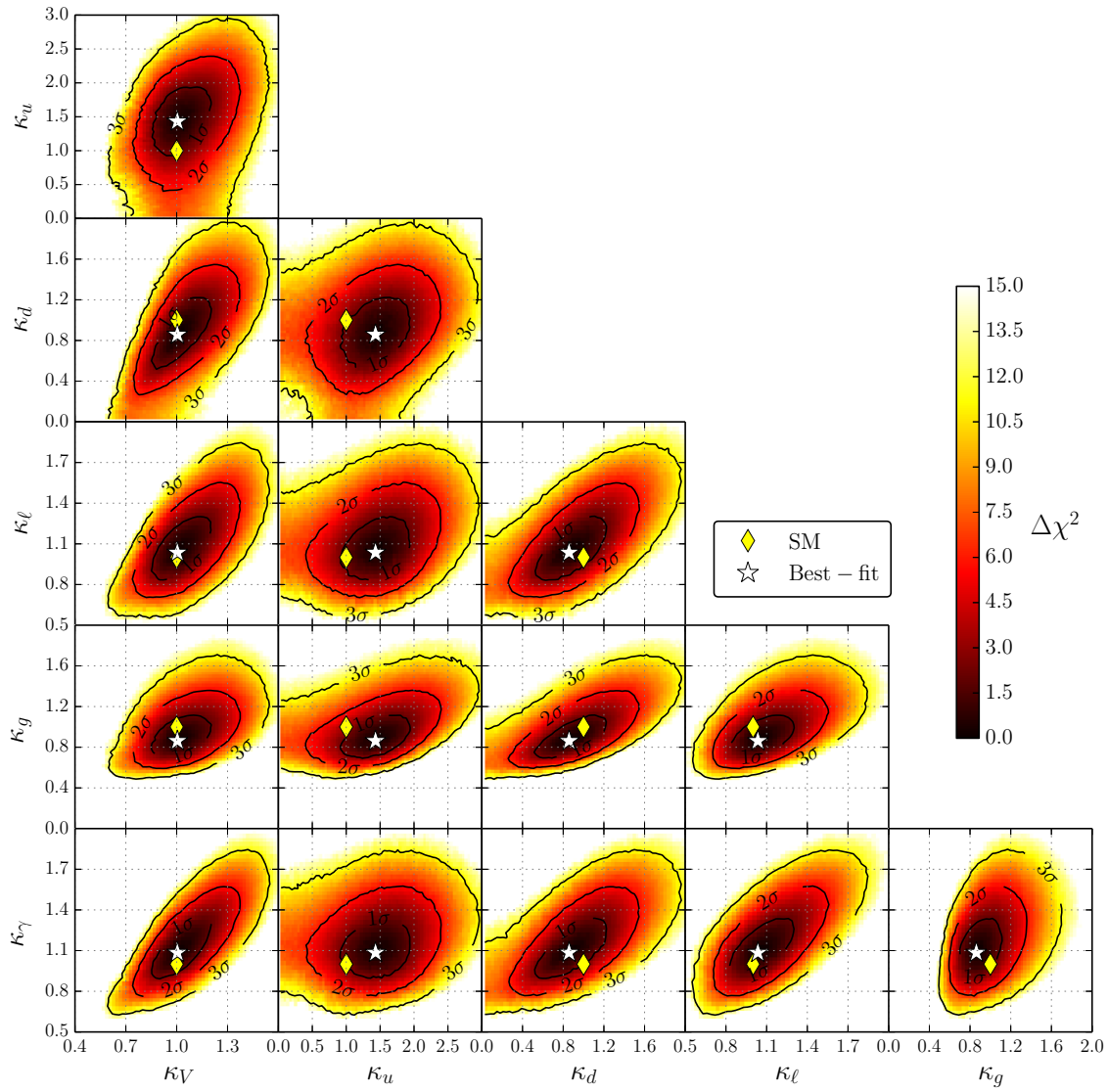

Figure 5.12: Two-dimensional $\Delta\chi^2$ profiles for the fitted Higgs coupling scale factors $\kappa_V, \kappa_u, \kappa_d, \kappa_\ell, \kappa_g, \kappa_\gamma$ and BR($H \to$ inv.) in the general Higgs couplings fit.

contribution to the Higgs-photon coupling is $\Delta\kappa_\gamma \sim 0.19$.

The two-dimensional χ^2 profiles of the fitted Higgs coupling scale factors are shown Fig. 5.12 and their correlations with BR($H \to$ inv.) are given in Fig. 5.13. Similarly as in the fit to the Yukawa structure in Section 5.2.4, all fundamental coupling scale factors are positively correlated. However, the correlations here are much weaker due to the additional freedom introduced for the loop-induced Higgs couplings. In the projection planes for κ_V and the Higgs-fermion coupling scale factors, the ellipses are tilted in comparison to the previous fit in Section 5.2.4, now featuring larger slopes of the major axes, which are roughly given by 7.5, 2.5 and 2.8 for the (κ_V, κ_u), (κ_V, κ_d) and (κ_V, κ_ℓ) planes, respectively. This represents the fact that κ_u, κ_d and κ_ℓ are less accurately determined since they are now only probed by the poorly measured $t\bar{t}H$, $H \to b\bar{b}$ and $H \to \tau^+\tau^-$ rates, respectively, while κ_V is still strongly

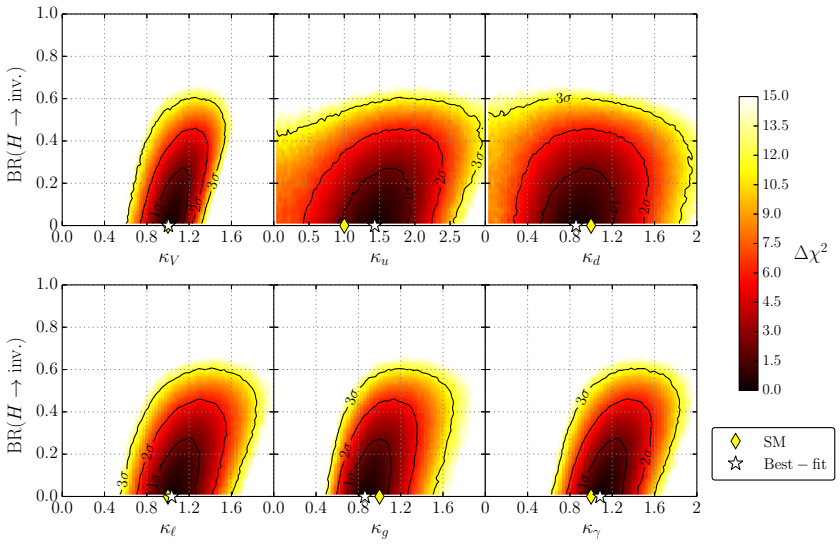

Figure 5.13: Two-dimensional $\Delta\chi^2$ profiles of the fitted Higgs coupling scale factors with the invisible Higgs decay mode, BR($H \to$ inv.), in the general Higgs couplings fit.

constrained by both the VBF and VH production modes and the decay modes $H \to WW^{(*)}$ and $H \to ZZ^{(*)}$.

The correlations of the fundamental coupling scale factors to the loop-induced couplings scale factors κ_g and κ_γ also turn out to be positive. Here the strongest correlation is observed among κ_g and κ_d, which govern the dominant production and decay modes, respectively. Since the decay $H \to b\bar{b}$ is not yet probed to any reasonable accuracy at the LHC, the fit allows for an enhanced decay rate if at the same time the dominant production cross section is also increased in order to compensate for the reduced branching ratios of the remaining decay modes[9]. Nevertheless, the preferred fit region is found for slightly suppressed values of both κ_g and κ_d. A strong positive correlation is also found between κ_V and κ_γ.

It should be noted that the correlation of the loop-induced couplings scale factors κ_g and κ_γ has changed with respect to the previous fit, see Section 5.2.5. They now show a weak positive correlation. This is because the general parametrization features again the degeneracy of increasing scale factors and the additional decay mode, which is only broken by the BR($H \to$ inv.) constraint. This leads to a positive correlation among all κ_i which dominates over the small anti-correlations needed to adjust the small tendencies in the observed signal rates. This is also reflected in Fig. 5.13, where all scale factors show a positive correlation with BR($H \to$ inv.).

Comparing the relative (1σ) precision on the individual scale factors obtained here with the results of an official CMS fit analysis[10] presented at the Moriond 2013 conference [5], we assert the improvements listed in Tab. 5.7. Here only rough symmetrical estimates of the sometimes quite asymmetrical uncertainties are given. With a common interpretation of the latest data from ATLAS, CMS and the Tevatron experiments, a significant improvement of the scale factor

[9] A similar correlation was found in the fit presented in Section 5.2.4 for κ_u and κ_d, because there κ_u was dominantly influencing the derived Higgs-gluon coupling.

[10] The CMS fit parametrizes the Higgs couplings via the same scale factors as used here, however, the fit does not allow for an additional Higgs decay mode. Note, that these CMS fit results were also used to validate the fit procedure and `HiggsSignals` implementation, see Section 4.2.4.

Fit	68% C.L. precision of Higgs coupling scale factors					
	κ_V	κ_g	κ_γ	κ_u	κ_d	κ_ℓ
CMS Moriond 2013	20%	28%	25%	100%	55%	30%
`HiggsSignals` (LHC $\oplus$ Tev.)	12%	20%	15%	30%	35%	18%

Table 5.7: Comparison of the relative 68% C.L. precision of the Higgs coupling scale factors obtained by the CMS combination presented at the Moriond 2013 conference [5] and our results from the (seven-dimensional) general Higgs couplings fit using both LHC and Tevatron measurements. The quoted numbers are rough estimates from the (sometimes asymmetric) likelihood shapes, cf. Ref. [5] and Fig. 5.11.

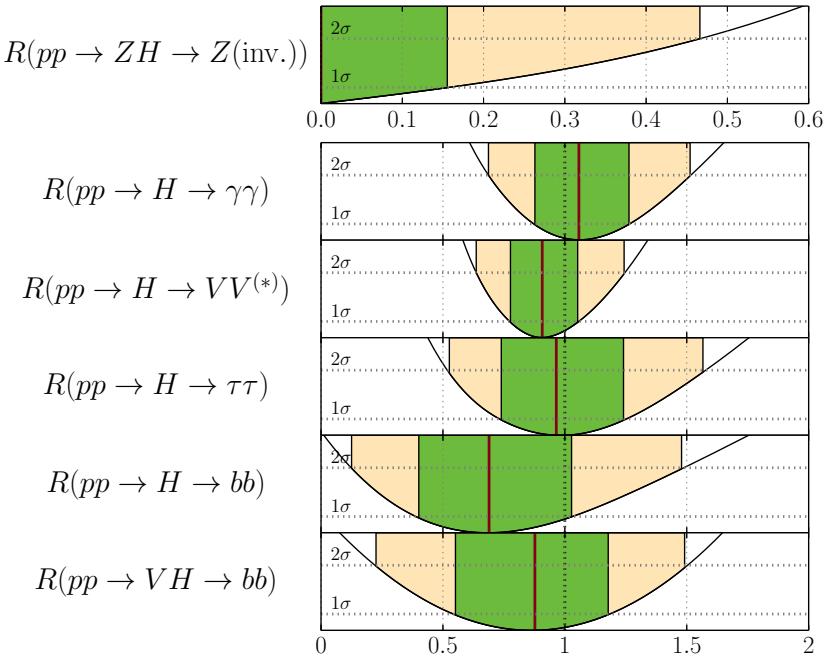

Figure 5.14: One-dimensional $\Delta\chi^2$ profiles from the $(\kappa_V, \kappa_u, \kappa_d, \kappa_\ell, \kappa_g, \kappa_\gamma, \text{BR}(H \to \text{inv.}))$ fit for the (idealized, SM normalized) signal rates at 8 TeV for the main LHC channels.

determination is achieved. Moreover, the strong improvement in the precision of κ_u is due to the dedicated CMS $t\bar{t}H$ tagged analyses [333–335] which had not been included in the CMS fit. With the latest $H \to \tau^+\tau^-$ measurement by ATLAS the precision of κ_ℓ has also improved significantly. Nevertheless, for all scale factors potential deviations within $\sim 10\%$ or even more are still allowed at the 1σ level within this benchmark model.

For this very general fit we also show the predicted signal rates for the preferred parameter space in Fig. 5.14. The rates $R(pp \to H \cdots \to XX)$ are idealized LHC 8 TeV signal rates where all included channels j contribute with the same efficiency ϵ_j, i.e.,

$$R(pp \to H \cdots \to XX) \equiv \mu(pp \to H \cdots \to XX)|_{\epsilon_j=1}\,, \tag{5.11}$$

where μ was defined in Eq. (3.4). The production mode $pp \to H$ denotes inclusive production, i.e. we include all five LHC Higgs production modes at their (rescaled) SM values, whereas the rates denoted by $pp \to ZH$ $[VH]$ include only production through Higgs-strahlung [and WH

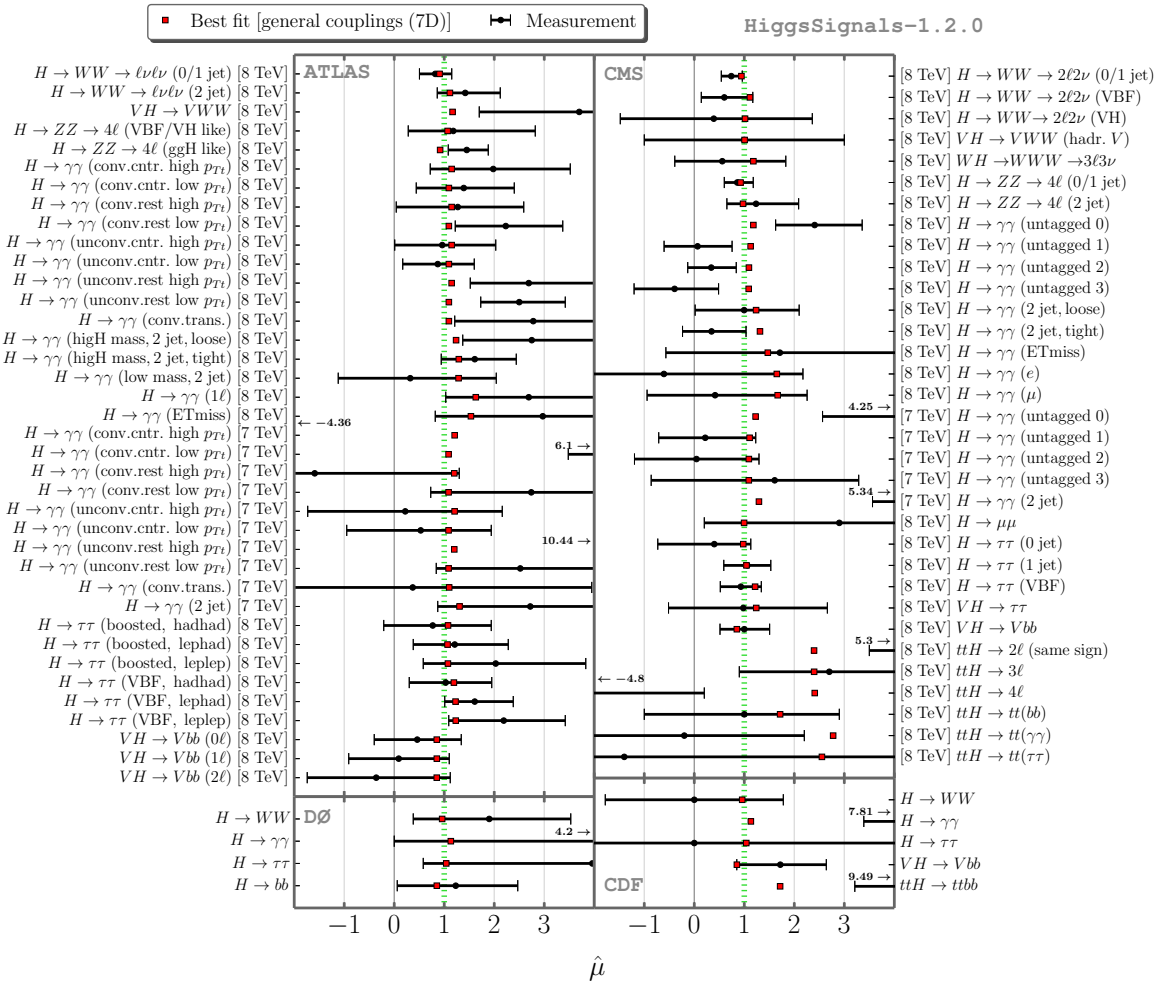

Figure 5.15: Comparison of the predicted signal rates of the best fit point in the general (seven-dimensional) Higgs couplings scale factor benchmark fit with the measurements from the ATLAS, CMS, CDF and DØ collaborations. The green line indicates the prediction for the SM.

production]. It can be seen from the figure that all rates agree with the SM expectation at 68% C.L. A very weak enhancement of the $pp \to H \to \gamma\gamma$ rate is observed, while the remaining channels with fermionic or weak gauge boson final states are slightly suppressed.

Finally, in Fig. 5.15 we show the actual signal rates $\hat{\mu}$ predicted by the best fit point, depicted as red squares, compared to all 80 measurements from the Tevatron and LHC experiments that went into our analysis. The latter are given by the black dots and the error bars indicate the 68% C.L. uncertainty. In the left column we show the ATLAS and DØ results, whereas in the right column the CMS and CDF observables are given. The SM, located at $\hat{\mu} = 1$, is marked as a green dashed line. It can be seen that most signal rates are predicted to be very close to the SM, note however the relatively large range shown for $\hat{\mu}$. An exception can be observed for the channels which comprise a substantial $t\bar{t}H$ component. Moreover, we find a slight enhancement in $H \to \gamma\gamma$ channels with a significant contribution from vector boson fusion and/or associated Higgs-weak gauge boson production. Overall, Fig. 5.15 demonstrates again that despite the large available freedom to adjust the signal rates in this very general parametrization, the

category	SM	Type 1	Type 2	Type 3
Fitted coupling scale factors	-	κ κ_V, κ_F $\kappa_W, \kappa_Z, \kappa_F$	κ_g, κ_γ	$\kappa_V, \kappa_u, \kappa_d, \kappa_\ell$ $\kappa_V, \kappa_u, \kappa_d, \kappa_\ell, \kappa_g, \kappa_\gamma$
BR($H \to$ NP) (68% C.L.)	$\leq 9\%$	$\leq 9\%$	$\leq 10\%$	$\leq 20\%$
BR($H \to$ NP) (95% C.L.)	$\leq 20\%$	$\leq 20\%$	$\leq 26\%$	$\leq 40\%$

Table 5.8: Upper limits at 68% and 95% C.L. on the undetectable Higgs decay mode, BR($H \to$ NP), obtained under the assumption $\kappa_V \leq 1$ ($V = W, Z$). All considered benchmark scenarios can be categorized into three types. The fitted coupling scale factors are given in the middle row.

preferred region agrees remarkably well with the SM. No significant improvement of the fit quality is gained by allowing the additional freedom. This implies that no significant, genuine tendencies of deviations in the SM Higgs coupling structure can be found.

5.2.7 Upper limits on additional undetectable Higgs decay modes

We now discuss the case where the additional Higgs decay mode(s) are not detectable with the current Higgs analyses, i.e. their final states do not lead to the missing transverse energy signature, as discussed in the beginning of Section 5.2. As discussed earlier, SM-like Higgs signal rates can be achieved even with a sizable branching fraction to undetectable final states, if at the same time the Higgs boson production rates are enhanced. In the absence of direct measurements of the Higgs total width or absolute cross sections the degeneracy between simultaneously increasing BR($H \to$ NP) and coupling scale factors κ_i can only be ameliorated with further model assumptions. Requiring that $\kappa_V \leq 1$ (or $\kappa_W \leq 1$ and $\kappa_Z \leq 1$), an upper limit on BR($H \to$ NP) can be derived for each investigated benchmark model without assuming that the additional decay mode leads to a missing energy signature.

Remarkably, we find that some of the six benchmark parametrizations discussed in Section 5.2.1–5.2.6 yield very similar limits on BR($H \to$ NP). We therefore categorize them in

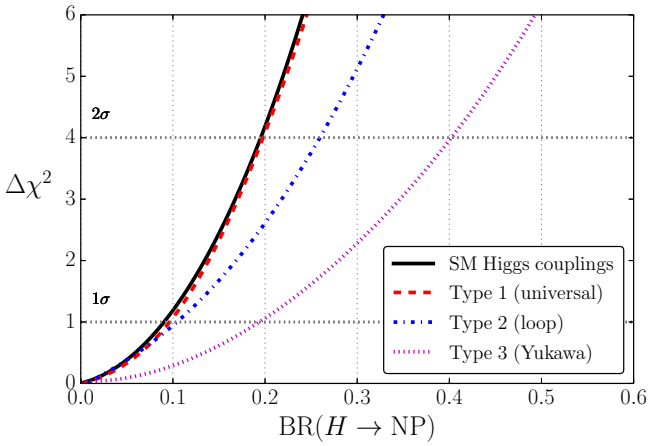

Figure 5.16: One-dimensional χ^2 profiles of BR($H \to$ NP) in all benchmark scenarios with the assumption $\kappa_V \leq 1$ ($V = W, Z$). The three scenario types are defined in the text.

three Types:

Type 1: Benchmark models with universal Yukawa couplings and no additional freedom in the loop-induced couplings. This comprises the fits in Sections 5.2.1–5.2.3.

Type 2: Benchmark models with fixed tree-level couplings but free loop-induced couplings, cf. Section 5.2.5.

Type 3: Benchmark models with non-universal Yukawa couplings, as discussed in Sections 5.2.4 and 5.2.6.

The resulting upper limits on BR($H \to$ NP) are given in Tab. 5.8. The corresponding profiled $\Delta\chi^2$ distributions are displayed in Fig. 5.16. The most stringent limits are obtained for Type 1, where the limit is nearly identical to what is obtained with fixed SM Higgs couplings. The weakest limits are obtained for Type 3. But even in the latter, least restricted case a BR($H \to$ NP) $\leq 40\%$ at the 95% C.L. is found.

5.3 Future precision of Higgs coupling determinations

5.3.1 Prospective Higgs coupling determination at the LHC

The LHC experiments ATLAS and CMS have provided estimates of the future precision for the Higgs signal rate measurements in most of the relevant channels for integrated luminosities of 300 fb^{-1} and 3000 fb^{-1} at $\sqrt{s} = 14$ TeV [375]. The first numbers (from 2012) have recently been updated [376–378]. In this section we use these updated projections to determine the accuracy of future Higgs coupling determination at the LHC. Similar studies based on the updated projections were recently performed in Refs. [379, 380], using a slightly different methodology and parametrization of the Higgs couplings. For earlier studies see also Refs. [340, 345, 346, 381, 382].

Concerning the projected sensitivities for rate measurements from ATLAS, a detailed compilation has been provided in Refs. [376, 377] which in most cases contains information on the signal composition, and the projections are given with and without theoretical uncertainties. ATLAS has also provided projections for sub-channels including tags for the different production modes. Unfortunately, a projection for the important channel $H \to b\bar{b}$ is not yet available. This channel plays an important role in any global fit, since the partial decay width for $H \to b\bar{b}$ dominates the total width in the SM. Moreover, the ATLAS $H \to \tau^+\tau^-$ projection is based on an older analysis, and one could expect a potential improvement from an updated study.

CMS has provided estimates for the capabilities to measure the Higgs signal rates only for inclusive channels [378]. Unfortunately, detailed information about the signal composition is missing. We are therefore forced here to assume typical values for the signal efficiencies guided by present LHC measurements. Moreover, the treatment of theoretical uncertainties in the CMS projections is not very transparent[11]. CMS discusses two scenarios: Scenario 1 uses current systematic and theoretical uncertainties[12]. In Scenario 2 the theoretical uncertainties

[11] See also Ref. [380] for a discussion of this issue.

[12] Note that improvements of systematical uncertainties that can be reduced with increasing statistics in the data control regions are however taken into account. Furthermore, even the assumption that the same systematical uncertainties as at present can be reached for the harsher experimental conditions in future is based on a projection involving a certain degree of improvement.

are reduced by 1/2, whereas the experimental systematic uncertainties are decreased with the square root of the integrated luminosity. No projections without theoretical uncertainties are provided by CMS. However, the Scenario 2 projections appear quite aggressive since they are of the same order as — or even more precise than — the purely experimental projections from ATLAS. Furthermore, our estimates of theoretical uncertainties, rescaled under the assumptions of Scenario 2, yield in some cases, e.g. in the $H \to \gamma\gamma, ZZ^{(*)}$ and $WW^{(*)}$ channels with $3000\,\text{fb}^{-1}$, values that are larger than the CMS estimates of the total (i.e. theoretical and experimental) uncertainties of the measurements, at least when assuming that the main production mechanism for the signal is gluon fusion. Following a conservative approach[13], we therefore use the projected CMS rate measurements given for Scenario 2, but interpret the uncertainties as being purely experimental. However, it should be noted that the dominant effect leading to differences between our results and the official CMS estimates of prospective Higgs coupling determination is the absence of publicly available CMS projections of the category measurements. Using only the inclusive measurements generally leads to lower precision estimates in higher-dimensional scale factor fits.

The ATLAS and CMS estimates of the experimental precision used in our analysis are listed in Tab. A.1 in Appendix A.2, which also gives the assumed signal composition for each channel. For both experiments we assume that the experimental precision includes a 3% systematic uncertainty on the integrated luminosity, which is treated as fully correlated among each experiment.

On top of these experimental precisions we add theoretical rate uncertainties within `HiggsSignals`. We discuss two future scenarios for the LHC-only projections: In the first scenario (S1) we take the current theoretical uncertainties as already used in the previous fits in Section 5.2. This scenario thus represents the rather pessimistic — or conservative — case that no improvement in the theoretical uncertainties can be achieved. With increasing integrated luminosity, however, the uncertainty from the parton density functions (PDF) can be expected to decrease [383]. Future progress can also be expected in calculations of higher-order corrections to the Higgs production cross sections and decay widths, which may further decrease the theoretical uncertainties, in particular the QCD scale dependence and remaining uncertainties from unknown electroweak (EW) corrections. Hence, in the second scenario (S2) we assume that uncertainties from the PDFs, as well as most[14] theoretical uncertainties, are halved. In both scenarios, the parametric uncertainties from the strong coupling constant, α_s, and the heavy quark masses, m_c, m_b and m_t, are unchanged. The different future scenarios considered in our analysis together with the respective assumptions on the future uncertainties and constraints are summarized in Tab. 5.9. The entry "100%" in Tab. 5.9 corresponds to the present value of the considered quantity (and accordingly, "50%" denotes an improvement by a factor of two). More details and estimates of the cross section and branching ratio uncertainties for these scenarios are given in Appendix B.2.

ATLAS and CMS also provide projections for the 95% C.L. upper limit on the rate of an invisibly decaying Higgs boson in the Higgs-strahlung process, $pp \to ZH$. Assuming, like we have done in Section 5.2.1–5.2.6, that additional Higgs decay modes only give rise to purely

[13] Another way to circumvent this problem is discussed in Ref. [380], where an alternative set of projected CMS measurements is proposed.

[14] This includes uncertainties from the QCD scale and unknown EW corrections for the LHC Higgs production modes, as well as the uncertainties of all partial decay widths except the decays to W and Z bosons where higher-order EW corrections are already known with high accuracy.

Future scenario	PDF	α_s	m_c, m_b, m_t	THU†	BR($H \to$ inv.) constraint
LHC300 (S1)	100%	100%	all 100%	100%	conservative, Eq. (5.13)
LHC300 (S2, csv.)	50%	100%	all 100%	50%	conservative, Eq. (5.13)
LHC300 (S2, opt.)	50%	100%	all 100%	50%	optimistic, Eq. (5.15)
HL–LHC (S1)	100%	100%	all 100%	100%	conservative, Eq. (5.14)
HL–LHC (S2, csv.)	50%	100%	all 100%	50%	conservative, Eq. (5.14)
HL–LHC (S2, opt.)	50%	100%	all 100%	50%	optimistic, Eq. (5.16)
ILC250	-	50%	all 50%	50%	$\leq 0.9\%$ (cf. Tab. A.2)
ILC500	-	50%	all 50%	50%	$\leq 0.9\%$ (cf. Tab. A.2)
ILC1000	-	50%	all 50%	50%	$\leq 0.9\%$ (cf. Tab. A.2)
ILC1000 (LumiUp)	-	50%	all 50%	50%	$\leq 0.4\%$ (cf. Tab. A.2)
HL–LHC $\oplus$ ILC250 ($\sigma_{ZH}^{\text{total}}$)‡	50%	50%	all 50%	50%	*
HL–LHC $\oplus$ ILC250	50%	50%	all 50%	50%	*
HL–LHC $\oplus$ ILC500	50%	50%	all 50%	50%	*
HL–LHC $\oplus$ ILC1000	50%	50%	all 50%	50%	*
HL–LHC $\oplus$ ILC1000 (LumiUp)	50%	50%	all 50%	50%	*

† Affects the theoretical uncertainties (THU) of all partial widths except for the decay modes $H \to WW^{(*)}$ and $H \to ZZ^{(*)}$ (kept unchanged) as well as the uncertainties from QCD scale and missing EW corrections for all LHC production modes.
‡ In this scenario only the direct ILC measurement of $\sigma(e^+e^- \to ZH)$ with 250 fb^{-1} at $\sqrt{s} = 250$ GeV is added to the HL–LHC projections to constrain the total width.
* For the HL–LHC $\oplus$ ILC combinations we do not use the assumption BR($H \to$ NP) $\equiv$ BR($H \to$ inv.).

Table 5.9: List of all future scenarios considered. Given are for each scenario the assumptions on uncertainties (relative to the current values, i.e. the entry "100%" denotes the current value, while the entry "50%" denotes an improvement by a factor of two) from parton distribution functions (PDF), the strong coupling α_s, the quark masses (m_c, m_b, m_t), and theoretical uncertainties (THU) on the predictions for the LHC Higgs cross sections and partial decay widths. The last column gives for each scenario the constraint that is employed *if* the additional Higgs decay(s) are assumed to be invisible. The considered integrated luminosities for the three energy stages 250 GeV, 500 GeV and 1 TeV of the ILC for a baseline scenario and for a luminosity upgrade (LumiUp) are specified in Section 5.3.2, based on Ref. [91]. The various ILC scenarios include the projected measurements from the preceding stages.

invisible final states[15], these constraints are incorporated in our fit as ideal χ^2 likelihoods of the form

$$\chi^2 = 4 \cdot \tilde{\sigma}^2 / \tilde{\sigma}^2_{95\%\text{C.L.}}. \tag{5.12}$$

The quantity $\tilde{\sigma}$ corresponds to the product $\kappa_Z^2 \text{BR}(H \to \text{inv.})$, i.e the cross section of $pp \to ZH \to Z(\text{inv.})$ normalized to the SM cross section for $pp \to ZH$. Both ATLAS and CMS consider two scenarios for the projected limits [377, 378]: The conservative (csv.) scenario,

$$\text{LHC } 300\,\text{fb}^{-1}: \quad \tilde{\sigma}_{95\%\text{C.L.}} = 0.32 \text{ (ATLAS)} \qquad \tilde{\sigma}_{95\%\text{C.L.}} = 0.28 \text{ (CMS)} \tag{5.13}$$

$$\text{LHC } 3000\,\text{fb}^{-1}: \quad \tilde{\sigma}_{95\%\text{C.L.}} = 0.16 \text{ (ATLAS)} \qquad \tilde{\sigma}_{95\%\text{C.L.}} = 0.17 \text{ (CMS)} \tag{5.14}$$

[15] We state explicitly in Tab. 5.9 which constraint on the additional decay modes is applied, if purely invisible final states are assumed.

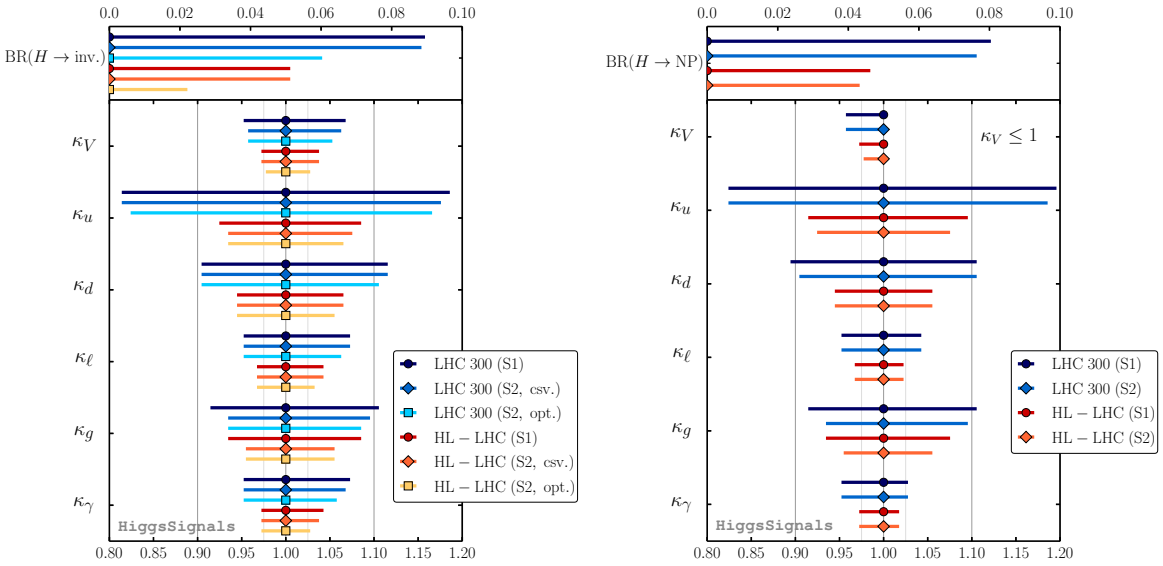

(a) Assuming $\mathrm{BR}(H \to \mathrm{NP}) \equiv \mathrm{BR}(H \to \mathrm{inv.})$.

(b) Assuming $\kappa_V \leq 1$.

Figure 5.17: Projected future precision for the determination of Higgs coupling scale factors at the LHC with integrated luminosities of 300 fb^{-1} and 3000 fb^{-1} (HL–LHC).

and the optimistic (opt.) scenario,

$$\text{LHC } 300\,\mathrm{fb}^{-1}: \quad \tilde{\sigma}_{95\%\text{C.L.}} = 0.23 \text{ (ATLAS)} \qquad \tilde{\sigma}_{95\%\text{C.L.}} = 0.17 \text{ (CMS)} \tag{5.15}$$

$$\text{LHC } 3000\,\mathrm{fb}^{-1}: \quad \tilde{\sigma}_{95\%\text{C.L.}} = 0.08 \text{ (ATLAS)} \qquad \tilde{\sigma}_{95\%\text{C.L.}} = 0.06 \text{ (CMS)}. \tag{5.16}$$

We combine the projected ATLAS and CMS limits by adding their respective χ^2 contributions. For the scenario S1 we only employ the conservative constraints, Eqs. (5.13) and (5.14), whereas for the scenario S2 with reduced uncertainties we compare fits using either the conservative or the optimistic constraint. These cases are denoted by (S2, csv.) and (S2, opt.), respectively.

For the LHC projections we employ the same seven-dimensional scale factor parametrization as discussed in Section 5.2.6. The resulting 68% C.L precision estimates obtained under the assumption that the additional decay mode $\mathrm{BR}(H \to \mathrm{NP}) \equiv \mathrm{BR}(H \to \mathrm{inv.})$ are displayed in Fig. 5.17(a) and listed in Tab. 5.10. The plot includes all six LHC-only scenarios as listed in Tab. 5.9.

In general the obtained 68% C.L. limit on $\mathrm{BR}(H \to \mathrm{inv.})$ is weaker than the limit obtained from a Gaussian combination of the limits in Eqs. (5.13)–(5.16), because the fit has the freedom to adjust $\kappa_Z (\equiv \kappa_V)$ to values < 1. Improvements in the theoretical uncertainties will mostly affect the effective Higgs-gluon coupling. At an integrated luminosity of 300 fb^{-1} we obtain a precision estimate for the scale factor of the effective Higgs-gluon coupling of $\delta\kappa_g \sim 9.5\%$ in the more conservative scenario S1,[16] which is improved to $\delta\kappa_g \sim 7.5\%$ in the most optimistic scenario S2. At the high luminosity LHC with 3000 fb^{-1} the corresponding projections are

[16] Here and in the following the Higgs coupling precision at 68% C.L. is denoted by $\delta\kappa$. The values quoted in the text usually correspond to symmetric averages. For the exact asymmetric values see the corresponding tables, e.g. here Tab. 5.10.

	68% C.L. Higgs coupling scale factor precision [in %]					
	LHC 300			HL–LHC		
Scenario	S1	S2, csv.	S2, opt.	S1	S2, csv.	S2, opt.
BR($H \to$ inv.)	≤ 8.9	≤ 8.8	≤ 6.0	≤ 5.1	≤ 5.1	≤ 2.2
κ_V	$^{+6.8}_{-4.8}$	$^{+6.3}_{-4.3}$	$^{+5.3}_{-4.3}$	$^{+3.8}_{-2.8}$	$^{+3.8}_{-2.8}$	$^{+2.8}_{-2.3}$
κ_u	$^{+18.6}_{-18.6}$	$^{+17.6}_{-18.6}$	$^{+16.6}_{-17.6}$	$^{+8.5}_{-7.5}$	$^{+7.5}_{-6.5}$	$^{+6.5}_{-6.5}$
κ_d	$^{+11.6}_{-9.5}$	$^{+11.6}_{-9.5}$	$^{+10.6}_{-9.5}$	$^{+6.5}_{-5.5}$	$^{+6.5}_{-5.5}$	$^{+5.5}_{-5.5}$
κ_ℓ	$^{+7.3}_{-4.8}$	$^{+7.3}_{-4.8}$	$^{+6.3}_{-4.8}$	$^{+4.3}_{-3.3}$	$^{+4.3}_{-3.3}$	$^{+3.3}_{-3.3}$
κ_g	$^{+10.6}_{-8.5}$	$^{+9.5}_{-6.5}$	$^{+8.5}_{-6.5}$	$^{+8.5}_{-6.5}$	$^{+5.5}_{-4.5}$	$^{+5.5}_{-4.5}$
κ_γ	$^{+7.3}_{-4.8}$	$^{+6.8}_{-4.8}$	$^{+5.8}_{-4.8}$	$^{+4.3}_{-2.8}$	$^{+3.8}_{-2.8}$	$^{+2.8}_{-2.8}$

Table 5.10: Estimates of the future 68% C.L. precision of Higgs coupling scale factors at the LHC under the assumption BR($H \to$ NP) $\equiv$ BR($H \to$ inv.). The values correspond to those in Fig. 5.17(a).

	68% C.L. Higgs coupling scale factor precision [in %]			
	LHC 300		HL–LHC	
Scenario	S1	S2	S1	S2
BR($H \to$ NP)	≤ 8.0	≤ 7.6	≤ 4.6	≤ 4.3
κ_V	$^{+0.0}_{-4.3}$	$^{+0.0}_{-4.3}$	$^{+0.0}_{-2.8}$	$^{+0.0}_{-2.3}$
κ_u	$^{+19.6}_{-17.6}$	$^{+18.6}_{-17.6}$	$^{+9.5}_{-8.5}$	$^{+7.5}_{-7.5}$
κ_d	$^{+10.6}_{-10.6}$	$^{+10.6}_{-9.5}$	$^{+5.5}_{-5.5}$	$^{+5.5}_{-5.5}$
κ_ℓ	$^{+4.3}_{-4.8}$	$^{+4.3}_{-4.8}$	$^{+2.3}_{-3.3}$	$^{+2.3}_{-3.3}$
κ_g	$^{+10.6}_{-8.5}$	$^{+9.5}_{-6.5}$	$^{+7.5}_{-6.5}$	$^{+5.5}_{-4.5}$
κ_γ	$^{+2.8}_{-4.8}$	$^{+2.8}_{-4.8}$	$^{+1.8}_{-2.8}$	$^{+1.8}_{-2.8}$

Table 5.11: Estimates of the future 68% C.L. precision of Higgs coupling scale factors at the LHC under the assumption $\kappa_V \leq 1$. The values correspond to those in Fig. 5.17(b).

$\delta\kappa_g \sim 7.5\%$ for the scenario S1 and $\delta\kappa_g \sim 5\%$ for the scenario S2, irrespective of the assumed precision of the BR($H \to$ inv.) constraint. The assumed improvements of the theoretical uncertainties hence lead to a significant increase of the κ_g precision at the HL–LHC, while the precision at 300 fb^{-1} is still mostly limited by statistics.

The impact of more optimistic limits on the invisible Higgs decays, Eqs. (5.15)–(5.16), can directly be seen in the projected upper 68% C.L. limit on BR($H \to$ inv.) in Fig. 5.17(a). Since this improved constraint also applies to the Higgs–Z boson coupling the precision of the Higgs–vector-boson coupling scale factor, $\delta\kappa_V$, also improves from $\sim 5.3\%$ [3.3%] to $\sim 4.8\%$ [2.6%] at 300 fb^{-1} [3000 fb^{-1}], assuming the improved theoretical uncertainties of Scenario S2. The impact on the remaining scale factors is rather insignificant and results mostly from their positive correlation with κ_V and BR($H \to$ inv.). Hence, these are slightly more constrained from above if a more optimistic limit on the invisible Higgs decays can be achieved.

Taking into account the possibility that an additional Higgs decay mode may result in an undetectable final state, we show the fit results obtained under the assumption $\kappa_V \leq 1$ in

Fig. 5.17(b) and Tab. 5.11. Overall, the achievable precision in the Higgs coupling scale factors with this assumption on the Higgs coupling to gauge bosons is very similar to what was obtained with the assumption of allowing only additional Higgs decays into invisible final states, cf. Fig. 5.17(a). A notable difference is, however, that in particular the scale factors κ_ℓ and κ_γ are more strongly constrained from above due to their positive correlation with κ_V, which is forced to be ≤ 1 by assumption in this case. The obtained 68% C.L. limit projection on $\mathrm{BR}(H \to \mathrm{NP})$ can be regarded as an independent limit projection inferred from the model assumption on κ_V and the chosen parametrization, see also the discussion in Section 5.2.7. Remarkably, the limit projections obtained here are stronger than the allowed range for $\mathrm{BR}(H \to \mathrm{inv.})$ in the previous fits in Fig. 5.17(a) where the constraints from searches for an invisibly decaying Higgs boson have been applied.

Overall, we find estimates of Higgs coupling scale factor precisions within $\sim 5-18\%$ at $300\,\mathrm{fb}^{-1}$ and $\sim 3-10\%$ at $3000\,\mathrm{fb}^{-1}$ obtained under the assumption $\mathrm{BR}(H \to \mathrm{NP}) \equiv \mathrm{BR}(H \to \mathrm{inv.})$. These estimates improve slightly if one assumes $\kappa_V \leq 1$ instead. Comparisons with results in the literature based on the same projections of the future capabilities provided by ATLAS and CMS show that our results agree quite well with those presented in Ref. [379]. A comparison of our results with Ref. [380] would need to take into account the different approaches of implementing the CMS projections. In view of this fact, we also find reasonable agreement with the results presented in Ref. [380].

It should be noted that this seven-parameter fit within the "interim framework" of Higgs-coupling scale factors still contains important simplifying assumptions and restrictions, which one would want to avoid as much as possible in a realistic analysis at the time when $300\,\mathrm{fb}^{-1}$ or $3000\,\mathrm{fb}^{-1}$ of integrated luminosity will have been collected, see the discussion in Refs. [29, 30].

5.3.2 Prospective Higgs coupling determination at the ILC

Looking beyond the LHC, an e^+e^- linear collider (LC) with a center-of-mass energy that can be raised at least up to $\sqrt{s} \sim 500\,\mathrm{GeV}$ is widely regarded to be ideally suited for studying the properties of the discovered new particle with high precision. The Technical Design Report for the International Linear Collider, ILC, has recently been submitted [92], and there are encouraging signs that a timely realisation of this project may become possible due to the strong interest of the Japanese scientific community and the Japanese government to host the ILC.

The ILC offers a clean experimental environment enabling precision measurements of the Higgs boson mass, width, its quantum numbers and $\mathcal{CP}$-properties as well as the signal rates of a variety of production and decay channels, including a high-precision measurement of the decay rate into invisible final states. The Higgs production modes at the ILC have been briefly discussed in Section 2.2.2. The highest statistics can be accumulated at the highest energy, $\sqrt{s} \sim 1\,\mathrm{TeV}$, from the t-channel process where a Higgs boson is produced in WW fusion ($e^+e^- \to \nu\nu H$). At $\sqrt{s} \sim 250\,\mathrm{GeV}$ an absolute measurement of the production cross section can be performed from the Higgs-strahlung process $e^+e^- \to ZH$ near threshold using the recoil of the Higgs boson against the Z boson, decaying via $Z \to \mu^+\mu^-$ or $Z \to e^+e^-$, without having to consider the actual pattern of the Higgs decay. The absolute measurement of the production cross section can be exploited to obtain absolute measurements of the decay branching ratios and of the total width of the decaying particle. Consequently, no additional model assumptions are necessary to constrain the total width and thus the Higgs boson couplings. For $\sqrt{s} \sim 250\,\mathrm{GeV}$

an integrated luminosity of 250 fb^{-1} will result in $\mathcal{O}(10^5)$ Higgs bosons. The ILC will provide high-precision measurements of channels that are known to be difficult (such as $H \to b\bar{b}$) or may even be impossible (such as $H \to c\bar{c}, gg$) at the LHC. At $\sqrt{s} \sim 500$ GeV the weak boson fusion process already dominates over the Higgs-strahlung process for a 125 GeV SM-like Higgs boson, and the two production channels together provide data with very high statistics. Starting from this energy, the top Yukawa coupling and, for sufficiently high luminosity, the trilinear self-coupling will become accessible.

In this section we study the capabilities of Higgs coupling determinations at the ILC. Similar studies have been performed in Ref. [379, 380, 382, 384]. We discuss fit results using prospective ILC measurements both alone and in combination with measurements from the HL–LHC. Since the two major Higgs production modes, Higgs-strahlung and WW fusion, are governed by the Higgs-Z-Z and Higgs-W-W couplings, respectively, from now on we abandon the assumption of custodial symmetry. Instead we fit individual scale factors for these couplings. Thus, we employ an eight-dimensional fit in the parameters κ_W, κ_Z, κ_u, κ_d, κ_ℓ, κ_g, κ_γ and BR($H \to$ NP).

The projected ILC measurements have been presented in Ref. [92] and recently updated in a Snowmass White paper [91]. These updated numbers, which we use in our fits, are summarized in Tab. A.2 in Appendix A.2. In particular, we include the measurements of the total ZH cross section, cf. Tab. A.2, which constrain the total width and enable a *model-independent* determination of the Higgs couplings. An assumed luminosity uncertainty of 0.1% and theoretical uncertainties of the $e^+e^- \to ZH$, $e^+e^- \to \nu\nu H$ and $e^+e^- \to t\bar{t}H$ cross section predictions of 0.5%, 1% and 1%, respectively, are treated as fully correlated in our fit. We assume the same improvements of the theoretical uncertainties for the Higgs decay modes as in Scenario S2 of the LHC projections. In addition, we assume that the parametric uncertainties from dependences on α_s and the heavy quark masses m_c, m_b and m_t can also be reduced by 50% with prospective ILC measurements and lattice calculations [383]. A further reduction of the top quark mass uncertainty — anticipated to improve by a factor of ~ 10 with respect to the current precision [92] — has negligible impact on the partial width uncertainties is and therefore not further considered here. A summary of all future scenarios that we consider in our analysis is given in Tab. 5.9. Estimates of the theoretical uncertainties on the Higgs branching ratios that we apply for the ILC scenarios are provided in Appendix B.2.

In our analysis of the ILC projections we consider three stages of center-of-mass energies, namely 250 GeV (stage 1), 500 GeV (stage 2) and 1 TeV (stage 3). For the integrated luminosities at those energy stages we investigate both a baseline program with integrated luminosities of 250 fb^{-1} at stage 1, 500 fb^{-1} at stage 2 and 1 ab^{-1} at stage 3, as well as a scenario corresponding to a luminosity upgrade (LumiUp). For the latter the integrated luminosities of 1150 fb^{-1} at stage 1, 1600 fb^{-1} at stage 2 and 2.5 ab^{-1} at stage 3 are assumed, see Ref. [91].

In Fig. 5.18 we show the estimated accuracies of the Higgs coupling scale factors at the ILC obtained under *model-dependent* assumptions, in analogy to the analyses performed above for the projections of future accuracies at the LHC: In Fig. 5.18(a) we assume that any additional Higgs decay results in invisible final states; accordingly we also take into account the projected ILC upper limit on BR($H \to$ inv.), cf. Tab. A.2 (or Tab. 5.9). In Fig. 5.18(b) we apply the theoretical constraint $\kappa_W, \kappa_Z \leq 1$. For comparison we also show the fit results for the optimistic HL–LHC scenario (S2, opt) obtained under these assumptions.

Overall, the scale factor precisions achieved under those two assumptions are very similar to each other. Comparing the results of the first ILC stage, where just a 'baseline' value for the integrated luminosity of 250 fb^{-1} is assumed (ILC250), with the ultimate precision that can be reached at the LHC, we see already at this stage a substantial improvement in the precision of

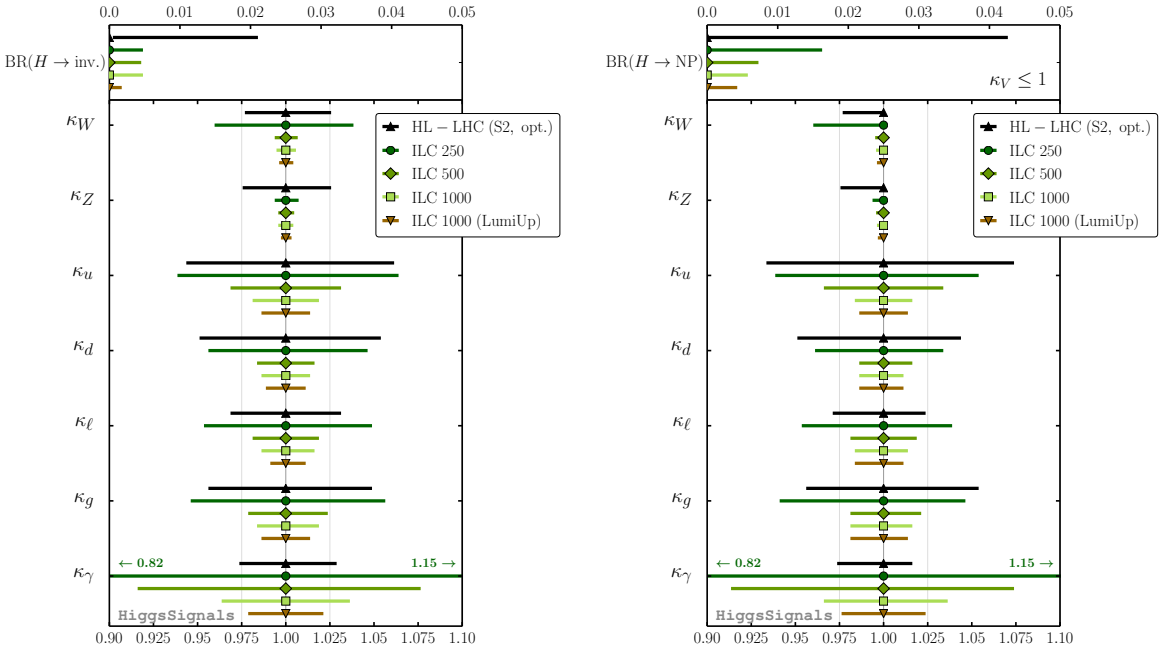

(a) Assuming $\mathrm{BR}(H \to \mathrm{NP}) \equiv \mathrm{BR}(H \to \mathrm{inv.})$.

(b) Assuming $\kappa_W, \kappa_Z \leq 1$.

Figure 5.18: Prospective Higgs coupling scale factor determination at the ILC in comparison with the (optimistic) HL–LHC scenario under the same model assumptions as in Fig. 5.17.

the scale factor κ_Z (from $\sim 2.5\%$ to $\sim 0.7\%$). This is already a crucial improvement since this coupling is of central importance in the experimental test of the electroweak symmetry breaking mechanism. Furthermore, the ILC provides at this stage important measurements that are complementary to the HL–LHC measurements. For instance, the independent determination of the Higgs coupling to gluons via the decay $H \to gg$ is advantageous in order to eliminate the dependence of this quantity on the remaining PDF uncertainties of the LHC gluon fusion process. In addition, the measurement of the rate $\sigma(e^+e^- \to ZH) \times \mathrm{BR}(H \to b\bar{b})$ with 1.2% accuracy, see Tab. A.2, together with the absolute cross section measurement of the ZH production process with a precision of 2.6%, give important constraints on the $H \to b\bar{b}$ decay mode, which dominantly contributes to the total width of a SM-like Higgs boson. However, the corresponding scale factors κ_Z and κ_d are still strongly correlated. Another independent measurement of the $H \to b\bar{b}$ mode with similar precision — as it is provided e.g. at the ILC stage 2 with $\sqrt{s} = 500\,\mathrm{GeV}$ in WW fusion (see below) — is required to abrogate this correlation, thus allowing for a precise determination of κ_d.

The most striking improvement that the ILC already provides at the first stage with $\sqrt{s} = 250\,\mathrm{GeV}$, however, is the *model-independent* measurement of the ZH production process and correspondingly *model-independent* determinations of Higgs branching ratios. Combining this input from the ILC with the measurements performed at the HL–LHC leads to a significant improvement of the latter, as will be discussed below (see Fig. 5.19).

While κ_Z can be probed already quite accurately at the early ILC stage at 250 GeV due to the dominant Higgs-strahlung process, the κ_W determination is less precise, $\delta\kappa_W \sim 4.0\%$. This picture changes at the later stages of the ILC with higher CM energies, denoted as ILC500 and

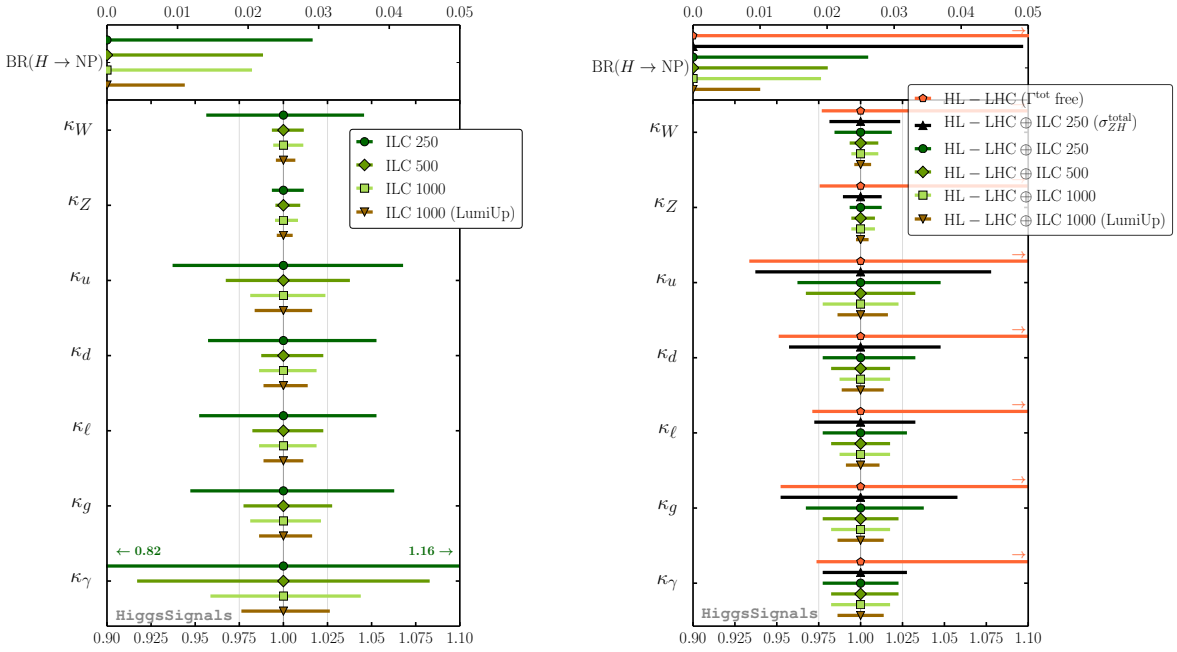

(a) ILC only.

(b) HL–LHC and combination of HL–LHC and ILC.

Figure 5.19: Future prospects of *model-independent* Higgs coupling scale factor determinations at the ILC alone (*a*) and in combination with the HL–LHC (*b*). For comparison, we also show the results obtained at the HL–LHC if the total width is not constrained by any assumptions on additional non-standard Higgs decay modes or limited scale factor ranges (like $\kappa_V \leq 1$).

ILC1000, where the 'baseline' integrated luminosities of 500 fb^{-1} and 1 ab^{-1}, respectively, have been assumed. At ILC500 and ILC1000 the WW fusion becomes the dominant production mode. Here, all scale factors in this parametrization except κ_γ can be determined to a precision of better than 2.5% using only ILC measurements. With the ultimate ILC integrated luminosity, denoted as ILC1000 (LumiUp), even the κ_γ coupling can be probed with an accuracy of $\lesssim 2.5\%$, and the remaining couplings are determined at the $\lesssim 1\%$ level, again using ILC measurements only. In the case where $\kappa_V \leq 1$ is imposed instead of assuming non-standard Higgs decays to result in invisible final states, the sensitivity for setting an upper limit on BR($H \to$ NP) inferred from the fit improves significantly at the ILC from 4.3 (8.5)% to 1.6 (3.3)% at the 68 (95)% C.L..

As stated earlier, the assumptions made in the previous fits are actually unnecessary at the ILC once the total cross section measurement of the $e^+e^- \to ZH$ process is taken into account. Therefore, *model-independent* estimates of the Higgs coupling accuracies can be obtained, which are shown in Fig. 5.19(a) and (b) for the ILC only and HL–LHC $\oplus$ ILC combined measurements, respectively. The values are also listed in Tab. 5.12. The estimated accuracies obtained for the ILC-only measurements in this model-independent approach are only slightly weaker than the ones obtained above under additional model assumptions, cf. Fig. 5.18. At the early ILC stage (ILC250) the sensitivity for setting a *model-independent* 95% C.L. upper limit on BR($H \to$ NP) of $\lesssim 5.8\%$ is obtained from the fit. This sensitivity improves to $\lesssim 4.1-4.4\%$ at the later baseline ILC stages. The more precise measurement of the $e^+e^- \to ZH$ cross section at 250 GeV with

Scenario	68% C.L. Higgs coupling scale factor precision [in %]								
	ILC only				HL–LHC ⊕ ILC				
	250	500	1000	1000 (LumiUp)	250 ($\sigma_{ZH}^{\text{total}}$)	250	500	1000	1000 (LumiUp)
BR($H \to$ NP)	≤ 2.9	≤ 2.2	≤ 2.1	≤ 1.1	≤ 4.9	≤ 2.6	≤ 2.0	≤ 1.9	≤ 1.0
κ_W	$^{+4.6}_{-4.4}$	$^{+1.2}_{-0.7}$	$^{+1.2}_{-0.6}$	$^{+0.7}_{-0.4}$	$^{+2.4}_{-1.9}$	$^{+1.9}_{-1.6}$	$^{+1.1}_{-0.7}$	$^{+1.1}_{-0.6}$	$^{+0.6}_{-0.4}$
κ_Z	$^{+1.3}_{-0.7}$	$^{+1.0}_{-0.6}$	$^{+0.9}_{-0.6}$	$^{+0.5}_{-0.4}$	$^{+1.3}_{-1.1}$	$^{+1.3}_{-0.7}$	$^{+0.9}_{-0.6}$	$^{+0.9}_{-0.6}$	$^{+0.5}_{-0.3}$
κ_u	$^{+6.8}_{-6.3}$	$^{+3.8}_{-3.3}$	$^{+2.3}_{-2.3}$	$^{+1.6}_{-1.6}$	$^{+7.8}_{-6.3}$	$^{+4.8}_{-3.8}$	$^{+3.3}_{-3.3}$	$^{+2.3}_{-2.3}$	$^{+1.6}_{-1.4}$
κ_d	$^{+5.3}_{-4.3}$	$^{+2.3}_{-1.8}$	$^{+1.8}_{-1.3}$	$^{+1.4}_{-1.1}$	$^{+4.8}_{-4.3}$	$^{+3.3}_{-2.3}$	$^{+1.8}_{-1.8}$	$^{+1.8}_{-1.3}$	$^{+1.4}_{-1.1}$
κ_ℓ	$^{+5.3}_{-4.8}$	$^{+2.3}_{-1.8}$	$^{+1.8}_{-1.3}$	$^{+1.9}_{-1.6}$	$^{+3.3}_{-2.8}$	$^{+2.8}_{-2.3}$	$^{+1.8}_{-1.8}$	$^{+1.8}_{-1.3}$	$^{+1.1}_{-0.9}$
κ_g	$^{+6.3}_{-5.3}$	$^{+2.8}_{-2.3}$	$^{+2.3}_{-1.8}$	$^{+1.9}_{-1.6}$	$^{+5.8}_{-4.8}$	$^{+3.8}_{-3.3}$	$^{+2.3}_{-2.3}$	$^{+1.8}_{-1.8}$	$^{+1.4}_{-1.4}$
κ_γ	$^{+15.8}_{-17.8}$	$^{+8.3}_{-8.3}$	$^{+3.8}_{-3.8}$	$^{+2.6}_{-2.6}$	$^{+2.8}_{-2.3}$	$^{+2.3}_{-2.3}$	$^{+2.3}_{-1.8}$	$^{+1.8}_{-1.8}$	$^{+1.4}_{-1.4}$

Table 5.12: 68% C.L. precision estimates and upper limits for the *model-independent* determination of Higgs coupling scale factors and BR($H \to$ NP), respectively, using only ILC measurements or in combination with HL–LHC measurements. These values correspond to those depicted in Fig. 5.19.

the ILC luminosity upgrade improves the sensitivity further, such that BR($H \to$ NP) $\lesssim 2.2\%$ at 95% C.L. can be reached at the ultimate ILC stage at $\sqrt{s} = 1\,\text{TeV}$.

For the combination of HL–LHC and ILC measurements for a model-independent Higgs coupling determination, as shown in Fig. 5.19(b), it is illustrative to consider first the results obtained using the HL–LHC only or with a minimal amount of ILC input, i.e. by only adding the total cross section measurement of the $e^+e^- \to ZH$ process. In the first case, as already demonstrated in Section 5.2.1, the unconstrained fit (HL–LHC (Γ^{tot} free) in Fig. 5.19(b)) features a degeneracy of increasing BR($H \to$ NP) and increasing scale factors κ_i, until the LHC is finally capable to observe broad width effects via off-shell Higgs production. As a result, there is virtually no precision in determining an upper limit for very large values of the scale factors[17].

By adding only the total $e^+e^- \to ZH$ cross section measurement from the baseline ILC250 run to the HL–LHC observables the degeneracy is broken. This leads to a very significant improvement in the determination of all Higgs coupling scale factors. Besides this effect one can see that the combination with this single input value from the ILC leads to further significant improvements affecting also the lower limits on the scale factors. In particular, the precision on the lower limit of κ_Z improves from $\sim 2.5\%$ to $\sim 1.1\%$. Moreover, the 95% C.L. upper limit on BR($H \to$ NP) inferred from this fit, without any additional assumptions, is 9.8%. This is roughly comparable to what has been obtained under the additional model assumptions in the LHC-only fit, cf. Fig. 5.18(b). With the inclusion of the remaining ILC measurements from the baseline 250 GeV run all scale factors except κ_u and κ_g can be measured at the $\sim 2.5\%$ level. κ_u and κ_g can be determined with a precision of $\sim 4.3\%$ and ~ 3.3, respectively. The only scale factor that is dominantly constrained by the LHC data is that for the Higgs-photon coupling, κ_γ, which remains the case even at the later ILC stages at 500 GeV and 1 TeV. With the ultimate ILC luminosity, including the upgrade, and combining all available measurements

[17] The fact that the error bars for the scenario HL–LHC (Γ^{tot} free) extend to values far outside of the right-hand side of Fig. 5.19(b) is indicated by little arrows in the plot.

from the HL–LHC and ILC, all Higgs coupling scale factors are probed to at least a precision of 1.5%. The Higgs-weak gauge boson couplings can even be probed at the per-mille level. At this level the estimated accuracies are dominated by the assumed theory uncertainties. We find that our estimates for the later ILC stages have a slight tendency to be more conservative than those of e.g. Refs. [379, 380], since we include larger theoretical uncertainties for the ILC production cross sections as well as their correlations.

5.4 Summary of the Chapter

In this chapter we have investigated in detail whether the coupling properties of the discovered new particle show any significant deviations from the predictions for a SM Higgs boson at the present level of accuracy. We have further analyzed the room for potential coupling deviations, which remain consistent with the current measurements, and the associated parameter correlations. The study has been carried out within a consistent statistical framework using all available Higgs signal rate measurements from the LHC and Tevatron experiments by employing profile likelihood fits of Higgs coupling scale factors by means of the program `HiggsSignals` (see Section 4.2). The fits have been done both for highly constrained and very generic scale factor parametrizations of the Higgs couplings. All benchmark fits allow for additional Higgs decays to non-standard final states and various assumptions are discussed for constraining the total Higgs decay width at the LHC. In contrast to other investigations in the literature, we have paid particular attention to the treatment of the general case where no constraint on the total Higgs width — or on the branching fraction of Higgs decays to potentially undetectable final states of new physics — is assumed.

We have employed the "interim framework" of Higgs coupling scale factors as a means to parametrize the relations between the physical collider observables (cross sections, branching ratios) and the possible deviations in the couplings of the new state from the predictions for a SM Higgs boson. While the scale factors probe different possible aspects of deviations from the SM predictions, their inherent simplifications and restrictions make it non-trivial to directly map the results obtained in terms of Higgs coupling scale factors onto realistic models of physics beyond the SM. The latter typically predict certain correlations that differ from those assumed within the Higgs coupling scale factor scenarios. The investigation of particular models, such as the MSSM, as will be discussed in Chapter 6, is therefore complementary to the analysis of Higgs coupling scale factors. The tool `HiggsSignals`, which has been used in the present analysis, has been specifically designed for this purpose, and the statistical methods employed here can be directly taken over for fits of realistic new physics models.

For all considered scale factor benchmark models we find very good agreement between the LHC and Tevatron measurements and the signal rates predicted for the SM. For the SM itself, i.e. all scale factors are set to unity, we find a naive $\mathcal{P}$-value of $\sim 35.0\%$, showing good agreement between data and theory. Thus, it is not surprising that the benchmark models achieve similar $\mathcal{P}$-values, which we have found to be typically slightly lower than the SM $\mathcal{P}$-value due to the smaller number of degrees of freedom at similar minimal χ^2. The lowest $\mathcal{P}$-value of $\sim 27.8\%$ is obtained for the fit probing the Yukawa structure in Section 5.2.4, while the best $\mathcal{P}$-value, excluding the SM $\mathcal{P}$-value, is found with $\sim 33.9\%$ for the benchmark fit probing the loop-induced Higgs couplings to gluons and photons, cf. Section 5.2.5.

We find no indicative hint for deviations from the SM in any of the fits. Indeed, all central values of the fitted Higgs coupling scale factors are compatible with their SM values. The fitted

values of an additional Higgs branching fraction, BR($H \to$ NP), are also compatible with zero. Uncertainties on the fitted scale factors range from around 10% in the most constrained case, i.e. a fit of only one universal scaling parameter, up to 40% for the top Yukawa scale factor, κ_u, in the seven-dimensional fit discussed in Section 5.2.6. Comparing these results with the latest official scale factor determination performed by CMS for the Moriond 2013 conference, we find significant improvements in all scale factor precisions. This illustrates the power of a common interpretation of ATLAS and CMS (and Tevatron) measurements, as well as the importance of the recent measurements in the ATLAS $H \to \tau^+\tau^-$ and CMS $t\bar{t}H$-tagged searches.

The corresponding weakest observed limit from the fits on the invisible Higgs decay is BR($H \to$ inv.) < 17 [39]% at the 68% [95%] C.L., also taking into account direct searches for BR($H \to$ inv.) at the LHC. We furthermore find for the total signal strength to known SM final states a lower limit of $\kappa^2 \times (1 - \text{BR}(H \to \text{NP})) > 81\%$ at the 95% C.L., employing the benchmark fit with one universal Higgs coupling scale factor κ. This limit is independent of any further assumption. Moreover, under the assumption that $\kappa_{W,Z} \leq 1$ holds, we find from the most general fit to the present data, which has seven free parameters, the limit BR($H \to$ NP) $< 40\%$ at the 95% C.L., where the final state(s) of such Higgs decay(s) may be undetectable to current LHC experiments.

Beyond the current measurements from the LHC and the Tevatron, we have explored the capabilities of future Higgs coupling determinations using projections of the signal rate measurements for the LHC with 300 fb^{-1} (LHC 300) and 3000 fb^{-1} (HL–LHC) at 14 TeV, as well as for various scenarios of an International Linear Collider (ILC). At the LHC 300 we find estimated precisions for the determination of the Higgs coupling scale factors within $\sim 5 - 18\%$ under the assumption BR($H \to$ NP) $\equiv$ BR($H \to$ inv.). Possible improvements of theoretical uncertainties on the cross sections and branching ratios turn out to have only a marginal effect on those estimated precisions. This changes at the HL–LHC, where the achievable precision of the Higgs-gluon coupling scale factor is significantly limited by the theoretical uncertainty. The precision estimates of the remaining scale factors, however, are hardly affected by varying assumptions on the theoretical uncertainties. Overall, assuming BR($H \to$ NP) $\equiv$ BR($H \to$ inv.), we find scale factor precisions of $\sim 3 - 10\%$ at the HL–LHC. If we make the model assumption $\kappa_V \leq 1$ instead of the assumption that additional non-standard Higgs decays result only in invisible final states, then most of the estimated scale factor precisions marginally improve.

Concerning the prospects at the ILC, we have compared the ILC capabilities of determining Higgs couplings with those of the HL–LHC first for a model-dependent approach, i.e. using the same assumptions as for the HL–LHC analyses, namely assuming either BR($H \to$ NP) $\equiv$ BR($H \to$ inv.) or $\kappa_V \leq 1$ as a means to constrain the total width. We find that already ILC measurements at 250 GeV for 'baseline' assumptions on the integrated luminosity provide significant improvements compared to the most optimistic scenario for the HL–LHC along with complementary measurements that are of similar or slightly worse accuracy compared with the projections for the HL–LHC. Starting from a CM energy of $\sqrt{s} = 500$ GeV for the corresponding 'baseline' luminosity the ILC in fact has the potential to considerably improve upon all measurements of the HL–LHC, apart from the coupling of the Higgs to photons. At $\sqrt{s} = 500$ GeV, the WW fusion channel can be measured significantly better than at 250 GeV, which leads to a significantly higher statistics for all considered quantities and in particular to a further improvement in the determination of the total width. The further improvements from ILC running at 1 TeV and from exploiting the ultimate ILC luminosity (LumiUp) turn out to be rather moderate for the considered case of a model-dependent 8-parameter fit, which is related to our fairly conservative estimates of the future theoretical uncertainties.

The impact of the ILC on improving the determination of the Higgs couplings becomes apparent most strikingly for the model-independent analyses. Without employing additional theoretical assumptions the scale factors at the LHC are essentially unconstrained from above. However, taking into account a single measurement of the ILC — the decay-mode independent recoil analysis of the total Higgs production rate at 250 GeV — in conjunction with the HL–LHC measurements already allows to perform a significantly less model-dependent and more precise fit than with the HL–LHC alone. In particular, with this ILC measurement the assumptions on the additional Higgs decay modes and on κ_V can be dropped.

From prospective measurements at the ILC up to $\sqrt{s} = 1\,\text{TeV}$ with the 'baseline' assumptions for the integrated luminosity together with those from the HL–LHC, we find precision estimates for *all* fitted Higgs coupling scale factors of better than 2.5%. For some scale factors a precision better than 1% is achieved. These estimates are obtained with the least amount of model assumptions and 8 free fit parameters. With the ultimate ILC luminosity (LumiUp) this precision would further increase significantly, reaching a level of better than 1.5% for all scale factors.

The Higgs coupling scale factor benchmark scenarios considered in this study typically have more freedom to adjust the predicted signal rates to the measurements than realistic models. Realistic model generally feature specific correlations among the predicted rates which depend non-trivially on the model parameters. Moreover, limits from the electroweak precision data and other sectors, such as dark matter, collider searches, etc., may further restrict the allowed parameter space and thus the room for Higgs coupling deviations. The fact that the exploration of the Higgs couplings with those rather general parametrizations does not improve the fit quality with respect to the SM is a clear indication of the good agreement of the data with the SM predictions. On the basis of this analysis one would not expect a significant improvement in the description of the data from a realistic model of physics beyond the SM. Thus, the full set of the present public measurements from ATLAS, CMS, CDF and DØ in the Higgs sector does not show any indications for physics beyond the SM.

Despite the lack of a concrete hint for any deviation from the SM in the current measurements, there still is ample room for future discoveries of deviations from the SM predictions for the Higgs couplings. In fact, the current uncertainties are still rather large and thus still allow for sizable deviations from the SM at the level of $\sim \mathcal{O}(10-40\%)$ at the 1σ level, even when making additional theory assumptions, namely $\text{BR}(H \to \text{NP}) \equiv \text{BR}(H \to \text{inv.})$ or $\kappa_V \leq 1$. Comparing those accuracies with the typical deviations expected in realistic models of physics beyond the SM, a large improvement in the experimental precision will be needed in order to sensitively probe the parameter space of the most popular extensions of the SM. The measurements at an ILC-like machine, in conjunction with the HL–LHC, will be crucial in this context for model-independent determinations of absolute Higgs couplings with precisions at the percent level or better, offering great prospects for identifying the underlying mechanism of electroweak symmetry breaking.

CHAPTER 6

Implications of the Higgs Boson Discovery for Supersymmetry

One of the prime goals of the LHC is to explore the origin of electroweak symmetry breaking. The Higgs boson discovery at the LHC marks a milestone in this important scientific quest. As we discussed in Chapter 5, the Higgs signal strengths measured at the LHC experiments are currently in very good agreement with the predictions for the SM Higgs boson. Still, the question arises whether the MSSM (or another model beyond the SM) can give a prediction for the production cross sections and decay widths of the observed Higgs state that yields a better description of the data than the one provided by the SM. The main aim of the work presented in this chapter is to investigate whether, and if so by how much, the MSSM can improve the theoretical description of the current experimental data, and potentially which parts of the parameter space of the MSSM are favored by the current experimental data from the various Higgs search channels.

It was shown that in particular the interpretation of the new state as the light $\mathcal{CP}$-even Higgs boson of the MSSM is a viable possibility (called the "light Higgs case" in the following). The implications and phenomenology of this scenario have been studied in a series of papers [270, 272, 309, 385]. On the other hand, it was also pointed out that the heavy $\mathcal{CP}$-even Higgs boson can have a mass around 125.7 GeV [270, 272] (called the "heavy Higgs case") while maintaining a SM-like behavior. All five MSSM Higgs bosons in this scenario would be rather light, and it would in particular imply the existence of another light Higgs boson with a mass below ~ 125 GeV and suppressed couplings to W and Z bosons. A detailed discussion of the phenomenology of this scenario can also be found in Ref. [273].

In this chapter we study the implications of the Higgs boson mass and signal strength measurements for the MSSM parameter space, considering both interpretations of the discovered Higgs state in terms of the light and the heavy $\mathcal{CP}$-even Higgs boson. In Section 6.1 we study three of the two-dimensional MSSM benchmark planes suggested for interpretation of SUSY Higgs search results at the LHC [246]. In Section 6.2, we go beyond this rather restricted picture of the MSSM by performing a global fit of the seven-dimensional phenomenological MSSM (pMSSM), taking into account also low energy observables. For this study, we present both the published results from November 2012 as well as updated preliminary results.

6.1 MSSM Higgs benchmark scenarios

In this section we investigate the viability of three MSSM Higgs benchmark scenarios [246, 255, 266–268], namely the m_h^{max}, $m_h^{\text{mod+}}$ and low-M_H, in the light of current experimental results from Higgs searches. These scenarios were introduced in Section 2.4.3. They are defined in terms of two free parameters, which are chosen to be $\tan\beta$ and either the $\mathcal{CP}$-odd Higgs boson mass, M_A, or the Higgsino mass parameter, μ. The purpose of these benchmark scenarios is to provide a useful framework for the experimental collaborations to present the results from MSSM Higgs searches in a comparable and, if possible, representative way[1], see Section 3.1. Recently, new MSSM benchmark planes have been proposed in Ref. [246] (see Section 2.4.3) to account for the observed Higgs state with a mass around 125.7 GeV and the improved exclusion limits from direct LHC searches for SUSY particles. However, so far the LHC experiments have presented their results only for the old version of the m_h^{max} scenario [278–280].

The purpose of the following study is twofold: Firstly, by studying the impact of updated constraints from Higgs searches and the mass and signal rate measurements of the discovered Higgs state, we find the parameter regions within these planes that are most compatible with the experimental data. This complements the discussion presented in Ref. [246]. Although such a study gives a first glimpse on the possible MSSM interpretations of the Higgs boson discovery, it should be kept in mind that these two-dimensional fits are rather restricted and do not represent the full pMSSM parameter space. Hence, a more complete study of the (higher-dimensional) pMSSM will be presented in the next section. Secondly, this study serves as a demonstration of the usefulness of the computer codes `HiggsBounds-4` and `HiggsSignals`. These benchmark models provide a comprehensive but non-trivial example to illustrate some important features of these codes.

For each parameter point in these two-dimensional planes we calculated the model predictions with `FeynHiggs-2.9.4` [155–157] and evaluated the total χ^2, comprised of the LEP Higgs exclusion χ^2 value [90, 257], $\chi^2_{\text{LEP,HB}}$, obtained from `HiggsBounds-4`, cf. Section 4.1.4, as well as the total χ^2 from `HiggsSignals-1.2.0` using the peak-centered χ^2 method and the experimental data presented in Section 4.2.3. The 95% C.L. exclusion limits from LHC and Tevatron are applied using[2] `HiggsBounds-4.0.0`. The theoretical mass uncertainty of the lightest Higgs boson is set to 2 GeV when treated as a Gaussian uncertainty (i.e. in the LEP exclusion χ^2 from `HiggsBounds` and in `HiggsSignals`), and to 3 GeV in the evaluation of 95% C.L. excluded regions with `HiggsBounds`, cf. Section 4.1.3.

The results for the updated m_h^{max} scenario are shown in Fig. 6.1 in the (M_A, $\tan\beta$) plane. Besides the colors indicating the $\Delta\chi^2 = \chi^2 - \chi^2_{\text{best-fit}}$ distribution relative to the best fit point (shown as a green star) we also show the parameter regions that are excluded at 95% C.L. by LHC searches for a light charged Higgs boson (dark-green, coarsely striped) [260], neutral Higgs boson(s) in the $\tau\tau$ final state (orange, checkered) [386] and the combination of SM search channels (red, striped) [339], as obtained using `HiggsBounds`[3]. As an indication for the parameter regions that are 95% C.L. excluded by neutral Higgs searches at LEP [90, 257] we include a corresponding contour (black, dashed) for the value $\chi^2_{\text{LEP,HB}} = 4.0$. Conversely, the

[1] As discussed in Section 3.1, a complementary and more usable format to present the null-results from Higgs searches are the model-independent cross section limits for the relevant signal channel(s).

[2] Note, that the latest ATLAS limit from charged Higgs boson searches [261], shown in Fig. 3.3, is not contained in this `HiggsBounds` version. However, we do comment on its implications in the following discussion.

[3] The exclusion regions imposed from these constraints were also shown in Fig. 4.7, albeit, for lower values of the theoretical mass uncertainty for the light $\mathcal{CP}$-even Higgs boson.

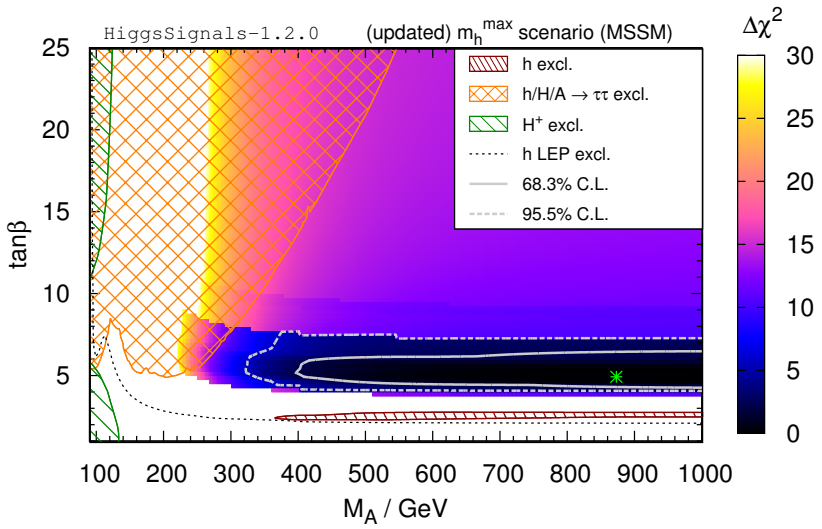

Figure 6.1: Distribution of $\Delta\chi^2$ in the (updated) m_h^{max} benchmark scenario of the MSSM [246]. The result from `HiggsSignals` and the LEP exclusion χ^2 of `HiggsBounds` are added. The patterned areas indicate parameter regions excluded at 95% C.L. from the following LHC Higgs searches: CMS $h/H/A \to \tau\tau$ [386] (orange, checkered), ATLAS $t \to H^+b \to \tau^+\nu_\tau b$ [260] (green, coarsely striped), CMS SM Higgs combination [339] (red, striped). The 95% C.L. LEP excluded region [90, 257], corresponding to $\chi^2_{\text{LEP,HB}} = 4.0$, is below the black dashed line. The best fit point, $(M_A, \tan\beta) = (872\,\text{GeV}, 5.0)$ with $\chi^2/\text{ndf} = 84.9/83$, is indicated by a green star. The 68% and 95% C.L. preferred regions (based on the 2D $\Delta\chi^2$ probability with respect to the best fit point) are shown as solid and dashed gray lines, respectively.

parameter regions favored by the fit are shown as 68% and 95% C.L. regions (based on the two-dimensional $\Delta\chi^2$ compatibility with the best fit point) by the solid and dashed gray lines, respectively.

As can be seen in the figure, the best fit regions are obtained in a strip at relatively small values of $\tan\beta \approx 4.5 - 7$, where in this scenario $m_h \sim 125.7\,\text{GeV}$ is found. At larger $\tan\beta$ values the light Higgs mass in this benchmark scenario, which was designed to maximize m_h for a given $\tan\beta$ in the region of large M_A, turns out to be *higher* than the measured mass of the observed signal, resulting in a corresponding χ^2 penalty. At very low $\tan\beta$ values the light Higgs mass is found to be below the preferred mass region, again resulting in a χ^2 penalty. Here, the χ^2 obtained from `HiggsSignals` steeply rises for $m_h \lesssim 122\,\text{GeV}$, because the mass-sensitive observables from the $H \to \gamma\gamma$ and $H \to ZZ^{(*)} \to 4\ell$ searches cannot be explained by the light Higgs boson anymore, cf. Section 4.2.4. Values of $M_A > 300\,\text{GeV}$ are preferred in this scenario, and thus the light Higgs boson has mainly SM-like couplings. Consequently, the χ^2 contribution from the rate measurements is similar to the one for a SM Higgs boson. In this regime, the Higgs mass dependence of the total χ^2 from `HiggsSignals` is comparable to the results shown in Fig. 4.12(d). We find the best fit point at $(M_A, \tan\beta) = (872\,\text{GeV}, 5.0)$ with a total χ^2 value over the number of degrees of freedom (ndf)[4] of $\chi^2/\text{ndf} = 84.9/83$.

[4] The ndf is calculated here as the sum of 80 Higgs signal strength and four Higgs mass measurements (from

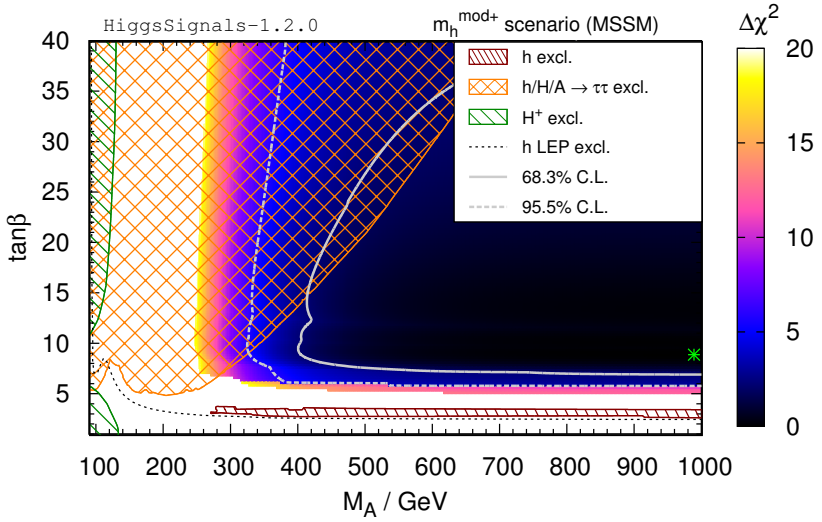

Figure 6.2: $\Delta\chi^2$ distribution (`HiggsSignals` and `HiggsBounds` LEP exclusion χ^2 added) in the $m_h^{\text{mod+}}$ benchmark scenario of the MSSM [246]. The excluded regions and contour lines have the same meaning as in Fig. 6.1. The best fit point (indicated by a green star) is found at $(M_A, \tan\beta) = (988\,\text{GeV}, 9.0)$ with $\chi^2/\text{ndf} = 85.2/83$

.

The second scenario that we discuss here is the $m_h^{\text{mod+}}$ scenario, i.e. a modification of the m_h^{max} scenario with a lower value of X_t, leading to $m_h \sim 125.7\,\text{GeV}$ over nearly the whole $(M_A, \tan\beta)$ plane [246]. The result is shown in Fig. 6.2 (with the same colors and meaning of the contours as for the m_h^{max} scenario, Fig. 6.1). The 95% C.L. excluded regions from `HiggsBounds` have already been discussed in Chapter 4, cf. Figs. 4.2 and 4.3. The best fit point is found at $(M_A, \tan\beta) = (988\,\text{GeV}, 9.0)$ with $\chi^2 = 85.2/83$. Only slightly larger χ^2 values are found over the rest of the plane, except for rather low values $M_A \lesssim 300\,\text{GeV}$ and $\tan\beta \lesssim 6.0$, where m_h is found to be below the preferred mass region. Similar as for the m_h^{max} scenario the lightest Higgs boson is mostly SM-like in the preferred region, and the χ^2 from the signal rates is close to the one found in the m_h^{max} scenario and in the SM.

Finally, we performed a fit in the low-M_H benchmark scenario of the MSSM. This scenario is based on the assumption that the Higgs boson observed at $\sim 125.7\,\text{GeV}$ is the heavy $\mathcal{CP}$-even Higgs boson of the MSSM. In this case the light $\mathcal{CP}$-even Higgs has a mass below the LEP limit for a SM Higgs boson of 114.4 GeV [90], but is effectively decoupled from the SM gauge bosons. The other states of the Higgs spectrum are also rather light, with masses around $\sim 130\,\text{GeV}$, thus this scenario is also very sensitive to searches for additional Higgs bosons. Since M_A must be relatively small in this case the $(\mu, \tan\beta)$ plane is scanned [246], where only $\tan\beta \lesssim 10$ is considered. The $\mathcal{CP}$-odd Higgs boson mass is fixed to $M_A = 110\,\text{GeV}$. Our results are shown in Fig. 6.3. The 95% C.L. excluded regions are obtained from the same Higgs searches as in Fig. 6.1, except for the red patterned region, which results from applying the limit from the CMS SM Higgs search $H \to ZZ^{(*)} \to 4\ell$ [316] to the SM-like, heavy $\mathcal{CP}$-even Higgs boson.

`HiggsSignals`) plus one LEP exclusion observable (from `HiggsBounds`) minus two free fit parameters.

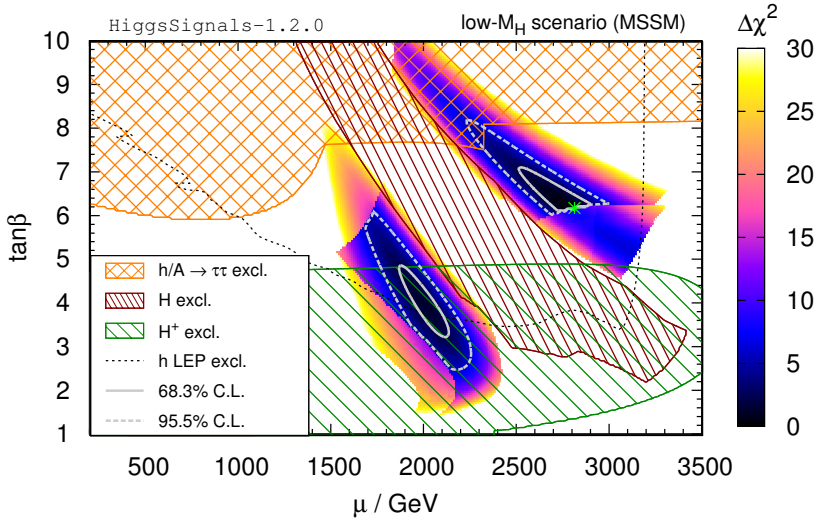

Figure 6.3: $\Delta\chi^2$ distribution (`HiggsSignals` and `HiggsBounds` LEP exclusion χ^2 added) in the low-M_H benchmark scenario of the MSSM [246]. The excluded regions and contour lines have the same meaning as in Fig. 6.1, except the red, finely striped region, which gives the 95% C.L. exclusion from the CMS Higgs search $H \to ZZ^{(*)} \to 4\ell$ [316], applied to the SM-like heavy $\mathcal{CP}$ even Higgs boson. The best fit point (indicated by a green star) is found at $(\mu, \tan\beta) = (2810\,\text{GeV}, 6.2)$ with $\chi^2/\text{ndf} = 91.6/83$.

Two distinct best fit regions are found [246]: The parameter space with $\mu \sim (1.7 - 2.2)$ TeV and $\tan\beta \sim 3 - 6$ predicts a heavy $\mathcal{CP}$-even Higgs boson with a well compatible mass value $m_H \approx 125.7\,\text{GeV}$ and SM-like couplings. However, large parts of this region (with $\tan\beta \lesssim 4.9$) favored by the rate and mass measurements are severely constrained by charged Higgs searches[5]. The second region favored by the fit is located at large values of $\mu \sim (2.3 - 2.9)$ TeV and $\tan\beta \sim 6-8$. Here, the masses of the $\mathcal{CP}$-even Higgs bosons are generally lower. For instance, at the best fit point at $(\mu,\ \tan\beta) \sim (2810\,\text{GeV}, 6.2)$, we have $m_h \approx 83.1\,\text{GeV}$ and $m_H \approx 123.1\,\text{GeV}$. For slightly larger (lower) values of μ ($\tan\beta$) we find a steep edge in the `HiggsSignals` χ^2 distribution, because m_H becomes too low to allow for an assignment of the heavy $\mathcal{CP}$-even Higgs boson to all mass-sensitive peak observables, cf. the results shown in Fig. 4.12(d) in Section 4.2.4. The constraints from LEP Higgs searches for this scenario have already been shown in Fig. 4.9. Due to the low mass of the light $\mathcal{CP}$-even Higgs boson in this region, the LEP channel $e^+e^- \to hA$ [257] is kinematically accessible and contributes a non-negligible χ^2 which increases with μ. The parameter space between the two preferred regions suffers a rather large χ^2 penalty, since in particular the predicted rates for the $H \to ZZ^*, WW^*$ channels are above the rates measured at the LHC, as can also be seen from the 95% C.L. exclusion by `HiggsBounds` in this region.

At the best fit point we find a $\chi^2/\text{ndf} = 91.6/83$. Compared with the light $\mathcal{CP}$-even Higgs interpretation of the observed signal, as discussed in the m_h^{max} and $m_h^{\text{mod+}}$ scenarios, the fit

[5] The excluded region shown in Fig. 6.3 is obtained from an old limit from the ATLAS charged Higgs search [260], based on an integrated luminosity of $4.6\,\text{fb}^{-1}$ collected at $\sqrt{s} = 7\,\text{TeV}$. We discuss the implications of the updated ATLAS limit [261] below.

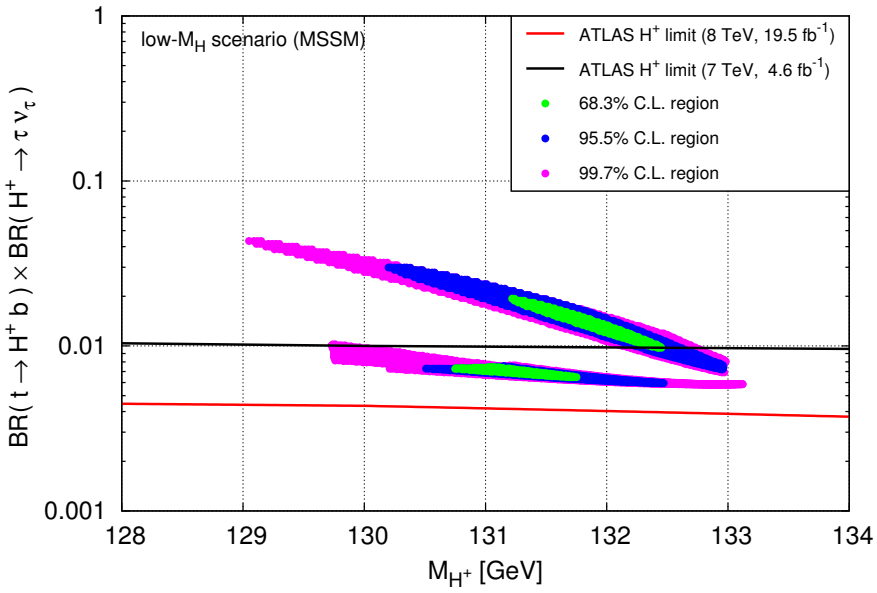

Figure 6.4: Branching ratio for the charged Higgs boson signature in top quark decays, BR($t \to H^+b \to (\tau\nu_\tau)b$), as a function of the charged Higgs mass, M_{H^+}, as predicted for the favored (1σ, 2σ and 3σ) regions of the low-M_H benchmark scenario. The 95% C.L. upper limits from the old and new ATLAS charged Higgs search analysis [260, 261] are overlaid as black and red lines, respectively.

quality is only slightly worse. However, the recently published update of the ATLAS search for light charged Higgs bosons in top quark decays [261], which is based on the full integrated luminosity from the 8 TeV run, leads to an exclusion (at 95% C.L.) of the entire benchmark scenario. This is illustrated in Fig. 6.4, where we show the prediction of BR($t \to H^+b \to (\tau\nu_\tau)b$) as a function of the charged Higgs mass, M_{H^+}, for the low-M_H parameter regions favored by the previous fit. The upper (lower) branch corresponds to the left (right) best fit region in Fig. 6.3. The old [260] and new upper limit [261] from the ATLAS charged Higgs search are included in Fig. 6.4 as black and red lines, respectively.

6.2 Interpretations within the phenomenological MSSM

A first glimpse on the implications of the Higgs measurements for the MSSM parameter space could be gained in Section 6.1 by the study of the rather restricted two-dimensional MSSM benchmark scenarios. However, in order to investigate the potentially favored regions of the MSSM parameter space in a more complete way a scan over the relevant SUSY parameters has to be performed. A complete scan over the more than a hundred free parameters of the MSSM parameter space is neither technically feasible nor does the available experimental information provide sufficient sensitivity to simultaneously constrain a large number of parameters. One therefore needs to focus on a certain subset of parameters. The most ambitious scans performed up to now were done [305, 306] for the phenomenological MSSM with 19 free parameters (pMSSM–19, see Ref. [387] for details). However, on the one hand it is difficult to sample such a multi-dimensional parameter space sufficiently well, on the other hand it is well known that several of the parameters of the pMSSM–19 hardly affect Higgs phenomenology. We therefore

focus in this paper on a smaller set of parameters, namely the real phenomenological MSSM with the seven free parameters that we regard as most relevant for the phenomenology of Higgs and flavor physics (pMSSM–7, see below for details on these parameters).

In our analysis we perform fits in the MSSM both for the interpretation of the LHC signal in terms of the light and the heavy $\mathcal{CP}$-even Higgs of the MSSM and we compare the fit results with the SM case. In the original analysis published in November 2012 [274] we took into account all available individual search channels at ATLAS and CMS at CM energies of 7 and 8 TeV that were publicly available at that time. We furthermore included the Higgs signal rate measurements from the Tevatron experiments. Here, we also present an update for the light Higgs case, where all currently available experimental Higgs measurements are included via `HiggsSignals`. These observables are mostly based on the full integrated luminosity of $\sim 25\,\text{fb}^{-1}$) and have been presented in Section 4.2.3. Besides the Higgs mass and signal rate measurements we took into account the 95% C.L. exclusion limits from Higgs searches using `HiggsBounds`, limits on the SUSY particle masses, as well as the most relevant set of low-energy observables, $\text{BR}(b \to s\gamma)$, $\text{BR}(B_s \to \mu^+\mu^-)$, $\text{BR}(B_u \to \tau\nu_\tau)$, $(g-2)_\mu$ and the mass of the W boson, M_W.

In the following discussion of the analysis framework we first describe the original 2012 analysis and then briefly comment on changes within the updated analysis compared to the old setup. Everything not explicitly mentioned in the description of the updated analysis is to be understood to be unchanged with respect to the original analysis. A similar presentation of the original and updated results can be found in Ref. [388].

6.2.1 Analysis framework

Original 2012 analysis

In the following we briefly describe the fit setup and define the seven fit parameters for our scan. The phenomenological MSSM with real parameters has been introduced in Section 2.4.2. The restriction to seven free/independent parameters is based on the intention to sample the *full* parameter space with $\mathcal{O}(10^7)$ scan points, while ensuring that the most important effects in the MSSM Higgs sector and flavor physics are covered. The tree-level values for the predictions of the MSSM Higgs sector quantities are determined by $\tan\beta$ and the $\mathcal{CP}$-odd Higgs-boson mass M_A. Hence, we chose these two parameters as free parameters. Beyond tree-level, the main correction to the Higgs boson masses stems from the $t/\tilde{t}$ sector, and for large values of $\tan\beta$ also from the $b/\tilde{b}$ sector. We assume universality of the left/right-handed sfermion soft-breaking mass terms of the third generation. The trilinear couplings A_f are assumed to be universal for all generations. Thus, the free parameters describing the sfermion sector are (cf. also Eq. (2.64))

$$M_{\tilde{q}_3} = M_{\tilde{u}_3} = M_{\tilde{d}_3}, \tag{6.1}$$

$$M_{\tilde{l}_3} = M_{\tilde{e}_3}, \tag{6.2}$$

$$A_f. \tag{6.3}$$

Furthermore, the Higgsino mass parameter μ, which also appears in the off-diagonal entry of the sfermion mass matrices, cf. Eq.(2.69), is taken as a free scan parameter. As the last scan parameter we chose the EW gaugino mass parameter M_2 and fix the other EW gaugino mass parameter, M_1, via the GUT relation, Eq. (2.63).

Parameter	Minimum	Maximum
M_A [GeV]	90	1000
$\tan\beta$	1	60
μ [GeV]	200	3000
$M_{\tilde{q}_3}$ [GeV]	200	1500
$M_{\tilde{l}_3}$ [GeV]	200	1500
A_f [GeV]	-3 $M_{\tilde{q}_3}$	3 $M_{\tilde{q}_3}$
M_2 [GeV]	200	500

Table 6.1: Ranges used for the free parameters in the pMSSM–7 scan.

The remaining MSSM parameters are fixed to

$$M_{\tilde{q}_{1,2}} = M_{\tilde{u}_{1,2}} = M_{\tilde{d}_{1,2}} = 1000\,\text{GeV}, \tag{6.4}$$

$$M_{\tilde{l}_{1,2}} = M_{\tilde{e}_{1,2}} = 300\,\text{GeV}, \tag{6.5}$$

$$M_3 (= m_{\tilde{g}}) = 1000\,\text{GeV}. \tag{6.6}$$

The choice for the first and second generation squarks and gluino places their masses roughly at the level currently probed at the LHC. Somewhat larger values would have only a minor impact on our analysis. The values for the first and second generation slepton mass parameters were chosen to provide rough agreement with the anomalous magnetic moment of the muon.

The pMSSM–7 parameter space is sampled by performing random scans (using uniform distributions) over the seven input parameters in the ranges given in Tab. 6.1. The two cases, where either h or H corresponds to the observed signal, are treated in two separate scans, and the results are discussed in parallel below. Each scan starts with $\mathcal{O}(10^7)$ randomly chosen points with a flat distribution over the parameter ranges. A dedicated, smaller, sampling is then performed to map the interesting regions of parameter space[6]. In practice, the full parameter ranges from Tab. 6.1 are taken only for the light Higgs case, while for the heavy Higgs case we limit $M_A < 200\,\text{GeV}$ and $\tan\beta < 30$ (still using the full ranges for the other parameters), which improves the sampling efficiency in the relevant mass region for M_H. In addition, the top quark pole mass is sampled from a Gaussian distribution with $m_t = (173.2 \pm 0.9)$ GeV, using a cutoff at $\pm 2\sigma$. Effects of other parametric uncertainties from SM quantities are estimated to be small, and are therefore neglected.

For the evaluation of the sparticle and Higgs masses we use the code `FeynHiggs` (version 2.9.4) [155–157]. The residual Higgs mass uncertainty from this calculation is estimated to be around $2-3\,\text{GeV}$, depending on the considered region of parameter space [156]. We are interested in parameter points that give a Higgs mass prediction, for either M_h or M_H, close to the observed LHC signal. We therefore constrain the analysis in a first step to points with M_h or M_H in the region $121-129\,\text{GeV}$. In order to avoid configurations in parameter space that give an unstable perturbative behavior in the Higgs mass calculation, we use a criterion based on the **Z**-matrix (as defined in Ref. [155]) and exclude points for which $\left||Z_{k1}^{2\text{L}}| - |Z_{k1}^{1\text{L}}|\right| / |Z_{k1}^{1\text{L}}| > 0.1$ (see Ref. [272] for a similar treatment). Here $k = 1$ (2) is set for a SM-like light (heavy) Higgs, and the superscripts refer to the same quantity evaluated with 1-loop (1L) or 2-loop (2L) precision.

[6] The reader should keep in mind here (and in the following) that the point density has no statistical meaning.

Updated analysis

In the updated analysis of the light Higgs case, we assume universality of the soft-breaking slepton masses of all three generations,

$$M_{\tilde{l}_{1,2}} = M_{\tilde{e}_{1,2}} = M_{\tilde{l}_3} = M_{\tilde{e}_3}, \tag{6.7}$$

in contrast to the old choice of fixed first and second generation slepton masses, Eq. (6.5). Leaving the slepton masses as a universal free parameter is particularly relevant for the fit of the anomalous magnetic moment of the muon, as will be discussed later. Furthermore, we increase the fixed mass values for the first and second generation squarks and the gluino to 1500 GeV in order to evade the improved limits on the sparticle masses from the LHC. The scan contains $\sim 5 \times 10^6$ randomly generated points over the same pMSSM parameters as in the original work. The scan range of μ was extended to $100 - 4000$ GeV. We select scan points for which the lightest $\mathcal{CP}$-even Higgs boson features a mass of 125.7 ± 3 GeV.

6.2.2 Constraints on the parameter space

Original 2012 analysis

Since we are mainly interested in the Higgs sector, we do not exploit the full possibilities in the low-energy MSSM to vary the soft-breaking parameters of the first two generations or the gluino mass. Consequently, it is not relevant to apply LHC exclusion bounds from supersymmetry searches in this analysis, since these can be avoided by adjusting the additional parameters to sufficiently high values with only small effects on the Higgs sector. We do, however, apply the model-independent lower limits on sfermion and chargino masses, typically at the level of ~ 100 GeV from direct searches at LEP, as summarized in Ref. [74]. Furthermore, we require that the lightest supersymmetric particle (LSP) is the lightest neutralino. The 95% C.L. exclusion limits from Higgs searches at the LEP, Tevatron and LHC experiments are taken into account using `HiggsBounds-3.8.0`, which included all relevant limits from the 7 TeV LHC run. Note, that the new `HiggsBounds` features described in Section 4.1 — except for the improved SM likeness test — were not present in this `HiggsBounds` version.

Updated analysis

For the updated analysis we use a yet unpublished `HiggsBounds` version `4.2.0beta`, which contains a preliminary implementation of the 95% C.L. exclusion limit from the latest CMS search for neutral Higgs bosons decaying into τ pairs [278]. Needless to say, this version contains all the new features described in Section 4.1 and the experimental results quoted in Appendix A.1, including the ATLAS result from the charged Higgs search [261]. A theoretical uncertainty of 3 GeV on the light Higgs mass is taken into account in `HiggsBounds` via the procedure described in Section 4.1.3.

As the limits on third generation squark masses have been improving with recent LHC analyses of the full available dataset [163, 165, 389, 390], these should be taken into account within the updated analysis. The implementation of these limits has been beyond the scope of the preliminary analysis update presented here. However, we plan to incorporate these constraints in a future update.

6.2.3 Observables and statistical procedure

Original 2012 analysis

In order to evaluate the compatibility of the MSSM (and the SM) with the observed data and to obtain an indication of what the favored regions of the MSSM parameter space are, we use a simple statistical treatment of the data where the different observables are taken into account by calculating, for every parameter point in the scan, a global χ^2 function

$$\chi^2 = \sum_{i=1}^{n_{\rm LHC}} \frac{(\mu_i - \hat{\mu}_i)^2}{\sigma_i^2} + \sum_{i=1}^{n_{\rm Tev}} \frac{(\mu_i - \hat{\mu}_i)^2}{\sigma_i^2} + \frac{(M_{h,H} - \hat{M}_H)^2}{\sigma^2_{\hat{M}_H}} + \sum_{i=1}^{n_{\rm LEO}} \frac{(O_i - \hat{O}_i)^2}{\sigma_i^2}. \tag{6.8}$$

Quantities with a hat denote experimental measurements, and unhatted quantities the corresponding model predictions for Higgs signal strength modifiers, μ_i, and low-energy observables (LEO), O_i. The different observables entering Eq. (6.8) will be described in more detail below. The combined uncertainties σ_i contain the known theory and experimental uncertainties. Correlations are neglected throughout, since they are for most cases not publicly available. The total number of degrees of freedom, ν, is counted in the naive way as $\nu = n_{\rm obs} - n_{\rm para}$, where $n_{\rm obs}$ is the number of observables, $n_{\rm obs} = n_{\rm LHC} + n_{\rm Tev} + 1 + n_{\rm LEO}$ (for LHC, Tevatron, the Higgs boson mass, and low-energy observables), and $n_{\rm para}$ is the number of model parameters. In the SM we have $n_{\rm para} = 1$ (the Higgs mass), whereas $n_{\rm para} = 7$ for both MSSM analyses.

The measured signal strength modifiers, $\hat{\mu}_i$, for the observed Higgs-like state around 125.7 GeV are taken into account in our fit directly in the χ^2 evaluation, Eq. (6.8). The data for all included channels is given[7] in Tab. A.3 in Appendix A.3, with the corresponding experimental signal strengths and their (asymmetric) $1\,\sigma$ error bands. These rates provide the main dataset to which we fit the MSSM Higgs sector. In total we include 37 observables, where 34 are from the LHC experiments and 3 provide supplementary information from the Tevatron. The observed rate in the $\gamma\gamma$ channel turns out to be considerably above the expectation for a Standard Model (SM) Higgs both for ATLAS [325] and CMS [318], whereas the $b\bar{b}$ and the $\tau^+\tau^-$ channels appear to be somewhat low in the LHC measurements [391, 392].

It should be noted that the best fit signal strength modifiers of ATLAS and CMS are given for different Higgs masses, corresponding to the values measured by the individual experiments, i.e. we interpret the experimental discoveries as being compatible, and due to a single new state. The Tevatron data, which does not admit a mass measurement from the observed excess on its own, is evaluated assuming a Higgs mass of 125 GeV. All values are extracted directly from the quoted experimental references, with one exception: ATLAS has not provided a measurement for the signal strength modifier of $H \to ZZ^{(*)}$ separately for the 7 and 8 TeV data, but only for the combination (the 7 TeV values are available from a previous analysis). To compare to our 8 TeV predictions, these values are therefore calculated from the 7 TeV and $7+8$ TeV data under the assumption of independent Gaussian measurements, following the procedure outlined in Ref. [307]. This should lead to an uncertainty on the estimated 8 TeV rate of the same order as the overall uncertainty from neglecting the (unknown) correlations.

The MSSM predictions for the signal strength modifiers are evaluated in the same way as in

[7] The measured values can also be seen in Figs. 6.5 and 6.7, where the best fit predictions are compared to these measurements, see below.

Eq. (3.4), i.e.

$$\mu_i = \frac{\sum_j \epsilon_{ij}\, \sigma(P_j(h/H)) \times \mathrm{BR}(D_j(h/H))}{\sum_j \epsilon_{ij}\, \sigma_{\mathrm{SM}}(P_j(h/H)) \times \mathrm{BR}_{\mathrm{SM}}(D_j(h/H))}, \tag{6.9}$$

where $\sigma(P_j(h/H))$ denotes the contribution to the production cross section of the light/heavy $\mathcal{CP}$-even Higgs boson from the partonic subprocess P_j, evaluated at the predicted Higgs mass. The production modes considered are gluon-gluon fusion (ggF), vector boson fusion (VBF), associated Higgs production with a vector boson (Vh/H), and with a top quark pair ($t\bar{t}h/H$). The experimental efficiencies ϵ_{ij} are assumed to be the same within the SM and the MSSM. They have only been published by ATLAS and CMS for the $\gamma\gamma$ analysis; for CMS in the case of the subcategories, and for ATLAS also the inclusive result. We make use of these numbers when they are available. For all other channels we have to use the "naive" efficiencies deducible from the analysis description (e.g. for a VBF-type analysis tagging two forward jets, we set $\epsilon = 1$ for the VBF cross section, whereas all other modes have $\epsilon = 0$). In channels where the mass resolution is not good enough to separate contributions from different Higgs bosons, we approximate the contributions from H and the $\mathcal{CP}$-odd Higgs A by adding their signal rates incoherently. We do not add the rates of the $\mathcal{CP}$-even Higgs bosons, whose joint contributions to the signal could also include interference effects. Our analysis is therefore limited to the case with a single $\mathcal{CP}$-even Higgs boson close to the observed signal, and we leave a more detailed treatment of the case when $M_h \sim M_H \sim 126\,\mathrm{GeV}$ to a dedicated analysis. Since the $\mathcal{CP}$-odd Higgs does not have tree-level couplings to vector bosons and hence also a reduced coupling to photons, it gives a negligible contribution to the channels with vector bosons in the Higgs production and/or decay. Effectively, the $\mathcal{CP}$-odd Higgs therefore only plays a role for the inclusive (0/1 jet) $\tau^+\tau^-$ channels. In these channels it can easily dominate over the H contribution for large values of $\tan\beta$. In the light Higgs case, we find that the masses of h and A differ by $M_A - M_h \gtrsim 50\,\mathrm{GeV}$ in the favored region (see below). Thus we do not take any contributions to the h rates from the $\mathcal{CP}$-odd Higgs into account.

The cross section predictions entering Eq. (6.9) are calculated, both in the MSSM and the SM, using `FeynHiggs-2.9.4` [155–157]. For the SM cross sections the results from the LHC Higgs Cross Section Working Group (LHCHXSWG) are implemented [30, 70, 71], where the gluon-gluon fusion (ggF) production cross sections are taken from Ref. [393]. The corresponding MSSM production cross sections are obtained in the effective-coupling approximation [394]. The ggF production cross section follows the description in Ref. [157], where results of Refs. [248, 359, 360, 395] were used. The decay width evaluation includes a full one-loop correction for the decay to fermions [396, 397]; see Ref. [157] for more details on the other channels.

In addition to the signal strength modifiers, we include a χ^2 contribution from the measured Higgs mass $\hat{M}_H$. Averaging the ATLAS and CMS measurements we obtain $\hat{M}_H = 125.7\,\mathrm{GeV}$. We use a total mass uncertainty of $\sigma_{\hat{M}_H} = 3\,\mathrm{GeV}$, which accounts for both the experimental uncertainty and the theoretical uncertainies from missing higher orders [156].

Besides the measurements related to the LHC Higgs signal, we include five low-energy observables (LEO) that are sensitive to new physics effects, cf. Section 2.3. These are listed in Tab. 6.2, which summarizes the experimental values[8] and the corresponding SM theory pre-

[8] Note that the Belle Collaboration has reported a new, lower measurement of $\mathrm{BR}(B_u \to \tau\nu_\tau)$ that is in better agreement with the SM and also with models with two Higgs doublets, like the MSSM [398]. The measurement of $\mathrm{BR}(B_s \to \mu^+\mu^-)$[150, 151] became public shortly after this analysis was performed. Thus, we only use the upper limit on $\mathrm{BR}(B_s \to \mu^+\mu^-)$ here. Both measurements are included in the updated analysis (see below).

Observable	Experimental value		SM value
$\mathrm{BR}(B \to X_s\gamma)$	$(3.43 \pm 0.21 \pm 0.07) \times 10^{-4}$	[149]	$(3.08 \pm 0.22) \times 10^{-4}$
$\mathrm{BR}(B_s \to \mu^+\mu^-)$	$< 4.2 \times 10^{-9}$	[406]	$(3.55 \pm 0.38) \times 10^{-9}$
$\mathrm{BR}(B_u \to \tau\nu_\tau)$	$(1.66 \pm 0.33) \times 10^{-4}$	[149]	$(1.01 \pm 0.29) \times 10^{-4}$
δa_μ	$(30.2 \pm 9.0) \times 10^{-10}$	[147, 148]	–
M_W	(80.385 ± 0.015) GeV	[65, 152, 153]	(80.363 ± 0.004) GeV

Table 6.2: *Original 2012 analysis:* The experimental values and (SM) theory predictions for low-energy observables (LEO) used to constrain the MSSM parameter space.

dictions, evaluated for $M_H^{\rm SM} = 125.7\,\text{GeV}$ and $m_t = 173.2\,\text{GeV}$. The flavor physics observables are evaluated (both in the SM and the MSSM) using `SuperIso` (version 3.2) [154], which in particular contains the results for $\mathrm{BR}(B \to X_s\gamma)$ based on the NNLO calculation of Ref. [399]. Our fit includes also the anomalous magnetic moment of the muon, $a_\mu = \frac{1}{2}(g-2)_\mu$. We use `SuperIso` to calculate the MSSM contribution δa_μ to the anomalous magnetic moment of the muon including the dominant two-loop contributions [400–402], see Ref. [403] for a review.

As a final observable we also include the MSSM prediction of the W boson mass into the fit. As discussed in Section 2.3, the SM prediction shows a $\sim 1.5\sigma$ deviation from the latest experimental value. Our MSSM evaluation of M_W is done using `FeynHiggs`, where the full SM result [159] is supplemented with the leading corrections from the $\tilde{t}/\tilde{b}$ sector [160, 404, 405]. A comparison with the best available MSSM evaluation [158, 160] shows that corrections larger than 10 MeV can be missed if some uncolored SUSY particles are light[9]. We assign a theory uncertainty of 15 MeV to our M_W evaluation and conservatively combine it linearly with the experimental uncertainty. Thus in total we take an uncertainty of ± 30 MeV into account.

Updated analysis

In the updated analysis a major change of the analysis setup is the substitution of the (naive) χ^2 calculation from the Higgs mass and signal rates in Eq. (6.8) by the total χ^2 calculated with `HiggsSignals-1.2.0`, cf. Section 4.2. We use the experimental data presented in Section 4.2.3, thus we have in total 80 signal strength observables (71 from the LHC and 9 from the Tevatron experiments) and 4 Higgs mass measurements, cf. Eq. (4.29). In addition, we include the five low-energy observables as in the original analysis, albeit, with updated experimental and theoretical values. The theory predictions of the B physics observables for the SM and the MSSM as well as δa_μ are calculated with `SuperIso-3.3` for a Higgs mass of 125.7 GeV and a top quark pole mass of $m_t = 173.2\,\text{GeV}$. The W boson mass is obtained from `FeynHiggs-2.9.4` using the same input values. A summary of these experimental and theoretical values has already been given in Section 2.3 in Tab. 2.5. In the updated analysis the combined CMS and LHCb measurement of $\mathrm{BR}(B_s \to \mu^+\mu^-)$ [150, 151] as well as the updated combined value for $\mathrm{BR}(B_u \to \tau\nu_\tau)$ [149], containing the latest Belle result [398], is included.

[9] The contributions from light sleptons and charginos can even be significantly larger ~ 60 MeV if their masses are just above the LEP limits. However, due to the chosen scan parameter ranges and fixed values, cf. Tab. 6.1 and Eq. (6.5) (or Eq. (6.7) for the updated analysis), such large corrections from sleptons and charginos are absent in our analysis.

	LHC only			LHC+Tevatron			LHC+LEO			LHC+Tevatron+LEO		
	χ^2/ν	χ^2_ν	$\mathcal{P}$	χ^2/ν	χ^2_ν	$\mathcal{P}$	χ^2/ν	χ^2_ν	$\mathcal{P}$	χ^2/ν	χ^2_ν	$\mathcal{P}$
SM	27.6/34	0.81	0.77	31.0/37	0.84	0.74	41.6/39	1.07	0.36	45.3/42	1.08	0.34
h	23.3/28	0.83	0.72	26.8/31	0.86	0.68	26.7/33	0.81	0.77	30.4/36	0.84	0.73
H	26.0/28	0.93	0.57	33.1/31	1.07	0.37	35.5/33	1.08	0.35	42.4/36	1.18	0.21

Table 6.3: *Original 2012 analysis*: Global χ^2 results with ν degrees of freedom from the fits of the SM and the MSSM with either h or H as the LHC signal, the reduced $\chi^2_\nu \equiv \chi^2/\nu$, and the corresponding $\mathcal{P}$-values. The number of degrees of freedom are evaluated naively as $\nu = n_{\text{obs}} - n_{\text{param}}$.

	LHC+Tevatron			LHC+Tevatron+LEO		
	χ^2/ν	χ^2_ν	$\mathcal{P}$	χ^2/ν	χ^2_ν	$\mathcal{P}$
SM	87.5/83	1.05	0.35	102.8/88	1.17	0.17
h	84.3/77	1.09	0.27	87.2/82	1.06	0.33

Table 6.4: *Updated analysis*: Global χ^2 results with ν degrees of freedom from the fits of the SM and the MSSM light Higgs case, the reduced $\chi^2_\nu \equiv \chi^2/\nu$, and the corresponding $\mathcal{P}$-values.

6.2.4 Results

We now turn to the discussion of the fit results. We discuss the results from the original analysis and the updated analysis in parallel. Typically, each part starts with the original 2012 results for the light Higgs case, followed by the updated results for this interpretation. Afterwards we discuss the original 2012 results for the heavy Higgs case, for which we have not updated the analysis yet.

In Tab. 6.3 we present the results of the original 2012 fits in terms of total χ^2 values (with ν degrees of freedom), the reduced $\chi^2_\nu \equiv \chi^2/\nu$, and the corresponding $\mathcal{P}$-values. Since ν is derived via the naive counting, the *absolute* numbers of the $\mathcal{P}$-values should not be overinterpreted; the *relative* numbers, however, give a good impression of the *relative* goodness of the fits. For each MSSM intrepretation (the cases of either h or H as the 125.7 GeV signal) we present four different fits: one taking the complete dataset (LHC+Tevatron+LEO) into account, one where the low-energy observables (LEO) are left out, one where the Tevatron data are left out, and finally the fit where only LHC observables are considered. When the fit is performed using only the high-energy collider data, both with and without the Tevatron results, the obtained χ^2 values of the best fit points are quite similar between the SM and the two MSSM interpretations, where the fit in the heavy Higgs case becomes slightly worse after the inclusion of the Tevatron data. When low energy observables are included, the SM and the heavy Higgs case fits become somewhat worse. In the latter case this can be understood from the potentially larger contributions of light Higgs bosons to B-physics observables. For the SM fit the reason lies in the fact that the SM prediction for $(g-2)_\mu$ differs by more than $3\,\sigma$ from the experimental value. Still we find that the SM provides a good fit to the full dataset, with $\mathcal{P}_{\text{SM}} = 0.34$. On the other hand, concerning the MSSM it should be kept in mind that we did not fit the second generation slepton masses, which could potentially further improve the a_μ fit. For the complete fit, the corresponding $\mathcal{P}$-values in the MSSM cases are $\mathcal{P}_h = 0.73$ ($\mathcal{P}_H = 0.21$) for the h (H) interpretations, respectively, which are both acceptable $\mathcal{P}$-values. Thus the light Higgs

interpretation of the MSSM provides a slightly better fit to the combined Higgs and low-energy observables than the SM.

The fit results of the updated analysis are presented in Tab. 6.4, this time given only for the case of using the full experimental data (LHC+Tevatron+LEO) and the case of leaving out the low-energy observables (LHC+Tevatron). With the updated Higgs and B physics observables, we generally find a somewhat lower fit quality of the SM and the MSSM (light Higgs case) with respect to the previous results. As we have seen in Chapter 5, the SM provides a very good description of the current Higgs signal rate measurements, and its fit quality cannot be beaten even in very general models with coupling scale factor modifications. Consequently, when taking only the Higgs observables into account, the MSSM (light Higgs case) does not yield a better fit quality than that obtained in the SM either. Without taking into account the low-energy observables, both the SM and the MSSM yield acceptable $\mathcal{P}$-values of $\mathcal{P}_{\rm SM} = 0.35$ and $\mathcal{P}_h = 0.27$, respectively. Once they are included, the fit quality of the SM becomes worse, resulting in a $\mathcal{P}$-value of $\mathcal{P}_{\rm SM} = 0.17$, while it slightly improves for the MSSM (light Higgs case), yielding $\mathcal{P}_h = 0.33$. The largest χ^2 contribution in the SM arises from the $(g-2)_\mu$ discrepancy, which is unchanged with respect to the original 2012 analysis. Overall, the data shows no clear preference for the MSSM over the SM at this point. While the MSSM fit for the light Higgs case yields a lower total χ^2 value than the SM, this comes at the expense of additional parameters, so that the difference in the $\mathcal{P}$-values is rather moderate.

Starting with the best fit for the light Higgs case, we show in Fig. 6.5 the different best fit points of the original 2012 analysis using all available data (LHC, Tevatron, LEO) (blue solid squares), leaving out LEO (red diamonds) or leaving out the Tevatron data (blue open squares). The comparison of these three different types of results allows to trace the origin of trends in the fitted parameters. The experimental data on the signal strength modifiers in the different channels (as indicated in the figure) is shown as black dots, with the error bars corresponding to $\pm 1\sigma$ uncertainties on $\hat{\mu}$. The values for the best fit point of the complete fit (LHC, Tevatron, LEO) are also listed in Tab. 6.5. From here we can determine some characteristics of the best fit point, such as a significantly enhanced rate in the $\gamma\gamma$ final state and nearly SM rates for the other channels. Leaving out the Tevatron data a small suppression of the fermionic final states can be observed. The fitted rates demonstrate that the pMSSM–7 is able to accommodate the main trends in the LHC and Tevatron data. Comparing the best fit points with and without LEO, we find a qualitatively very similar behavior of the Higgs signal rates.

In Tab. 6.5 we also give the details on the results for the low-energy observables. In the light Higgs case, the only relevant contribution to the total χ^2 comes from $\mathrm{BR}(B_u \to \tau\nu_\tau)$. The best fit value of $\mathrm{BR}(B_s \to \mu^+\mu^-)$ lies below the SM prediction. This feature is indeed found for most of our favored region. We have checked that this trend is present already without taking the χ^2 contribution of $\mathrm{BR}(B_s \to \mu^+\mu^-)$ itself into account, see also the discussion in Ref. [385]. Interestingly, the $\mathrm{BR}(B_s \to \mu^+\mu^-)$ value predicted for the best fit point in the MSSM (light Higgs case) is in very good agreement with the recent combined CMS/LHCb measurement [151], which was not included here in the original 2012 analysis.

The Higgs signal rates predicted for the best fit point of the MSSM (light Higgs case) that we obtain in the full fit (LHC+Tevatron+LEO) of the updated analysis are shown in Fig. 6.6, along with the experimental results as included in `HiggsSignals-1.2.0` (cf. Section 4.2.3). We find that most predicted signal rates are rather close to the SM value ($\mu_{\rm SM} = 1$, indicated by the green line in Fig. 6.6). The only visible exception are the $H \to \gamma\gamma$ channels, where we find an enhancement of the signal rate of $\sim 20\%$ with respect to the SM value. Due to the assumed slepton mass universality, Eq. (6.7), light staus are favored indirectly by $(g-2)_\mu$ in the fit, since

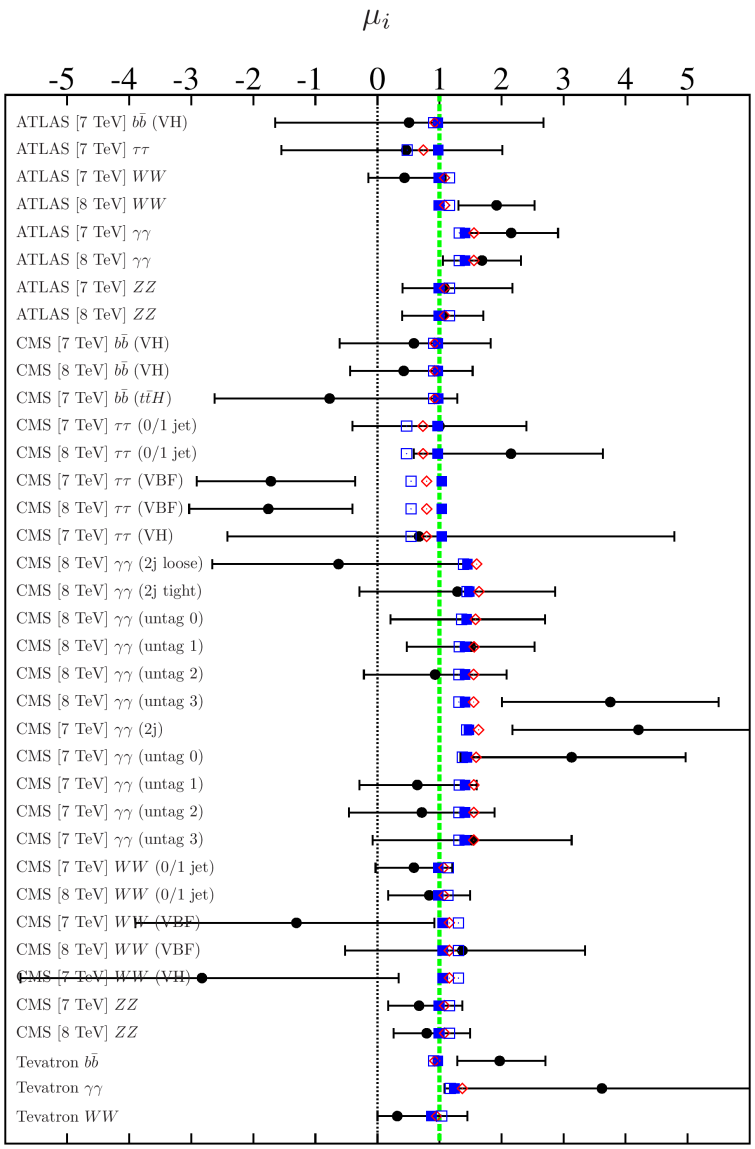

Figure 6.5: *Original 2012 analysis:* Fit results for the signal strength modifiers, μ_i, in the case that the light $\mathcal{CP}$-even Higgs is interpreted as the observed Higgs state ("light Higgs case"). The experimental data is shown as black dots (with error bars). The other symbols show best fit points, corresponding to the full fit (LHC+Tevatron+LEO) (blue solid squares), without the Tevatron data (blue open squares), and without LEO (red diamonds).

sizable contributions can be obtained from light smuons. As will be discussed below, these light staus lead to an enhancement of the $\gamma\gamma$ rate. We checked that a slight $\gamma\gamma$ enhancement of $\sim 10\%$ still persists if the low-energy observables are excluded from the fit. This is consistent with the slight tendency for a $\gamma\gamma$ enhancement found in Section 5.2.6.

In Tab. 6.6 we list the low-energy observables predicted by the best fit point of the full fit (LHC+Tevatron+LEO), along with the individual χ^2 contributions and pull values. With the inclusion of the new Belle result [149, 398] the χ^2 contribution from $\mathrm{BR}(B_u \to \tau\nu_\tau)$ is slightly reduced (in comparison to the previous results), however, it still accounts for the largest χ^2

Channel		$\sqrt{s}$ [TeV]	μ_h	χ^2_h	Pull	μ_H	χ^2_H	Pull
ATLAS	$b\bar{b}$	7	0.98	0.05	0.22	0.83	0.02	0.15
ATLAS	$\tau\tau$	7	0.98	0.11	0.33	2.46	1.67	1.29
ATLAS	WW	7	0.99	0.69	0.83	1.25	1.50	1.22
ATLAS	WW	8	0.99	2.31	-1.52	1.25	1.19	-1.09
ATLAS	$\gamma\gamma$	7	1.41	0.95	-0.98	1.10	1.94	-1.39
ATLAS	$\gamma\gamma$	8	1.42	0.18	-0.43	1.10	0.87	-0.93
ATLAS	ZZ	7	0.99	0.02	-0.13	1.25	0.02	0.16
ATLAS	ZZ	8	0.99	0.01	-0.09	1.25	0.09	0.31
CMS	$b\bar{b}$ (VH)	7	0.98	0.10	0.32	0.83	0.04	0.19
CMS	$b\bar{b}$ (VH)	8	0.98	0.25	0.50	0.83	0.13	0.36
CMS	$b\bar{b}$ (ttH)	7	0.98	0.72	0.85	0.83	0.61	0.78
CMS	$\tau\tau$ (0/1 jets)	7	0.97	0.00	-0.02	2.72	1.43	1.20
CMS	$\tau\tau$ (0/1 jets)	8	0.97	0.57	-0.76	2.81	0.20	0.44
CMS	$\tau\tau$ (VBF)	7	1.04	4.12	2.03	0.61	2.92	1.71
CMS	$\tau\tau$ (VBF)	8	1.04	4.24	2.06	0.61	3.03	1.74
CMS	$\tau\tau$ (VH)	7	1.04	0.01	0.09	0.61	0.00	-0.02
CMS	$\gamma\gamma$ (Dijet loose)	8	1.45	1.04	1.02	1.15	0.76	0.87
CMS	$\gamma\gamma$ (Dijet tight)	8	1.48	0.01	0.12	1.19	0.00	-0.06
CMS	$\gamma\gamma$ (Untagged 0)	8	1.44	0.00	-0.02	1.13	0.07	-0.26
CMS	$\gamma\gamma$ (Untagged 1)	8	1.42	0.01	-0.09	1.10	0.16	-0.39
CMS	$\gamma\gamma$ (Untagged 2)	8	1.41	0.18	0.42	1.09	0.02	0.14
CMS	$\gamma\gamma$ (Untagged 3)	8	1.41	1.80	-1.34	1.09	2.32	-1.52
CMS	$\gamma\gamma$ (Dijet)	7	1.48	1.80	-1.34	1.19	2.21	-1.49
CMS	$\gamma\gamma$ (Untagged 0)	7	1.44	0.89	-0.94	1.14	1.24	-1.11
CMS	$\gamma\gamma$ (Untagged 1)	7	1.41	0.65	0.81	1.10	0.23	0.48
CMS	$\gamma\gamma$ (Untagged 2)	7	1.41	0.35	0.59	1.09	0.10	0.32
CMS	$\gamma\gamma$ (Untagged 3)	7	1.41	0.01	-0.07	1.09	0.07	-0.27
CMS	WW (0/1 jets)	7	0.98	0.40	0.64	1.23	1.09	1.04
CMS	WW (0/1 jets)	8	0.98	0.05	0.22	1.23	0.36	0.60
CMS	WW (VBF)	7	1.05	1.12	1.06	1.39	1.47	1.21
CMS	WW (VBF)	8	1.05	0.03	-0.17	1.39	0.00	0.01
CMS	WW (VH)	7	1.05	1.50	1.22	1.39	1.78	1.33
CMS	ZZ	7	0.99	0.21	0.45	1.25	0.69	0.83
CMS	ZZ	8	0.99	0.08	0.28	1.25	0.43	0.65
LHC	Higgs mass [GeV]		126.1	0.02	0.13	125.8	0.00	0.03
Tevatron	$b\bar{b}$	1.96	0.98	2.13	-1.46	0.83	2.82	-1.68
Tevatron	$\gamma\gamma$	1.96	1.24	0.88	-0.94	0.97	1.08	-1.04
Tevatron	WW	1.96	0.87	0.24	0.49	1.11	0.49	0.70
LEO	$\mathrm{BR}(B \to X_s\gamma) \times 10^4$		3.41	0.00	-0.03	4.38	2.12	1.46
LEO	$\mathrm{BR}(B_s \to \mu^+\mu^-) \times 10^9$		2.79	0.00	0.00	2.24	0.00	0.00
LEO	$\mathrm{BR}(B_u \to \tau\nu_\tau) \times 10^4$		0.98	2.37	-1.54	0.80	3.78	-1.94
LEO	$\delta a_\mu \times 10^9$		2.58	0.24	-0.49	1.34	3.48	-1.87
LEO	M_W [GeV]		80.379	0.04	-0.19	80.383	0.00	-0.05

Table 6.5: *Original 2012 analysis:* Best fit results (for the complete fit) with corresponding χ^2 contributions and pulls for each observable. The pull values are defined as (predicted value - observed value)/(uncertainty). The middle (right) column gives the results for the light (heavy) Higgs interpretation of the observed Higgs state.

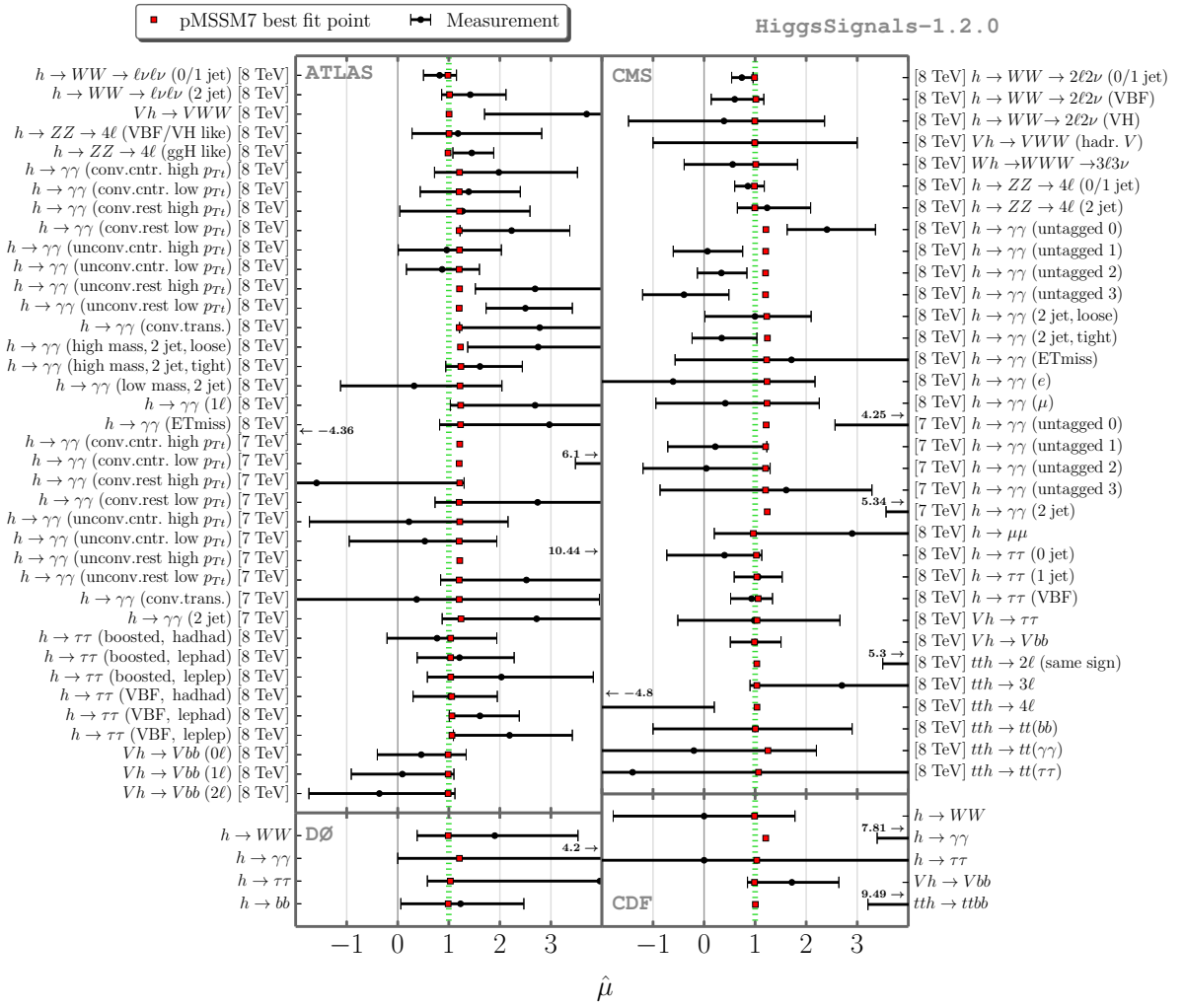

Figure 6.6: *Updated analysis:* Comparison of the observed Higgs signal strength modifiers with those predicted by the best fit point found in the updated analysis of the light Higgs interpretation in the MSSM. The experimental data is shown as black dots (with error bars). The red solid squares indicate the prediction of the best fit point obtained in the full fit (LHC+Tevatron+LEO).

LEO	O_i	χ^2_h	Pull
$\mathrm{BR}(B \to X_s\gamma) \times 10^4$	3.55	0.03	0.18
$\mathrm{BR}(B_s \to \mu^+\mu^-) \times 10^9$	3.66	0.77	0.88
$\mathrm{BR}(B_u \to \tau\nu_\tau) \times 10^4$	0.78	2.00	−1.41
$\delta a_\mu \times 10^9$	2.76	0.09	−0.29
M_W [GeV]	80.382	0.01	−0.10

Table 6.6: *Updated analysis:* Best fit results (for the complete fit) with corresponding χ^2 contributions and pulls for the low-energy observables (LEO).

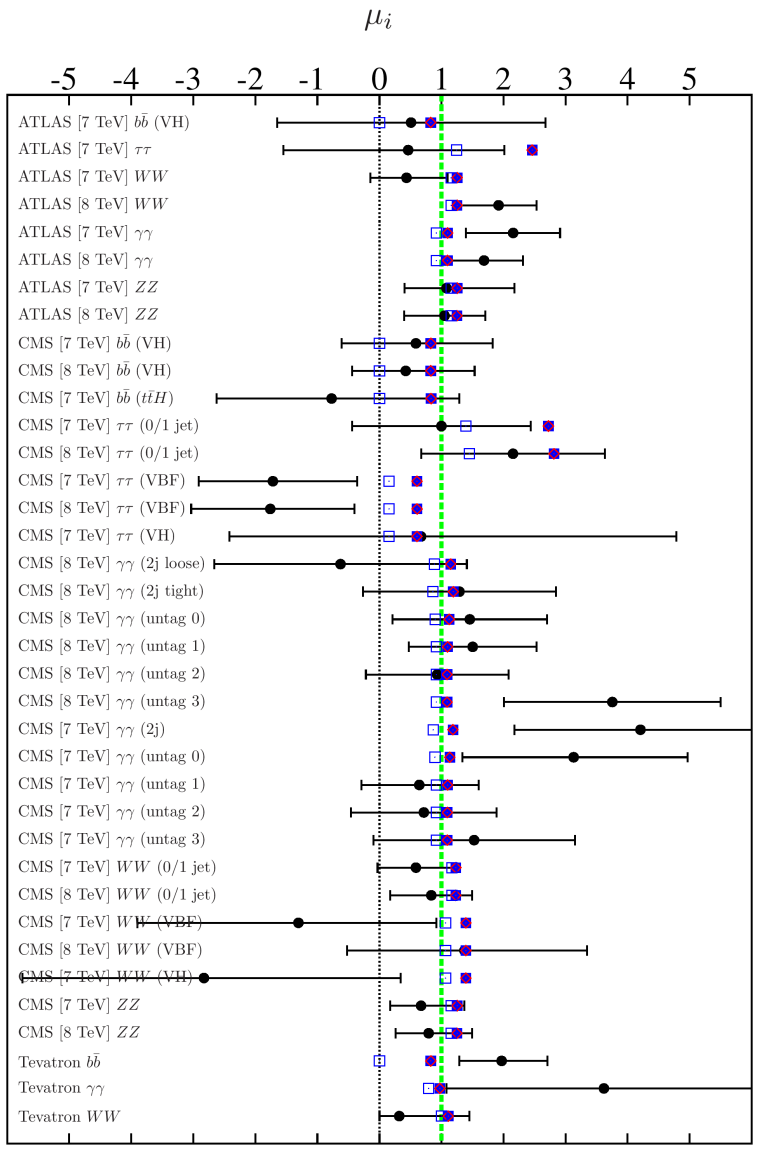

Figure 6.7: *Original 2012 analysis:* Fit results for the signal strength modifiers, μ_i, in the case that the heavy $\mathcal{CP}$-even Higgs is interpreted as the observed Higgs state ("heavy Higgs case"). The experimental data is shown as black dots (with error bars). The other symbols show best fit points, corresponding to the full fit (LHC+Tevatron+LEO) (blue solid squares), without the Tevatron data (blue open squares), and without LEO (red diamonds).

contribution from the the low-energy observables. If we used *only* the Belle result, $\mathrm{BR}(B_u \to \tau\nu_\tau) = (0.96 \pm 0.26) \times 10^{-4}$ [398], instead of the world-average, the χ^2 contribution would be reduced substantially, leading to a better MSSM fit. A moderate χ^2 contribution is also obtained from using the $\mathrm{BR}(B_s \to \mu^+\mu^-)$ measurement, instead of the upper limit that was used in the original analysis. The agreement with $(g-2)_\mu$ improved with respect to the original 2012 analysis, since the smuon mass can now be adjusted in the fit according to Eq. (6.7). In total, the χ^2 contribution from all low-energy observables together is roughly the same as in the original 2012 analysis.

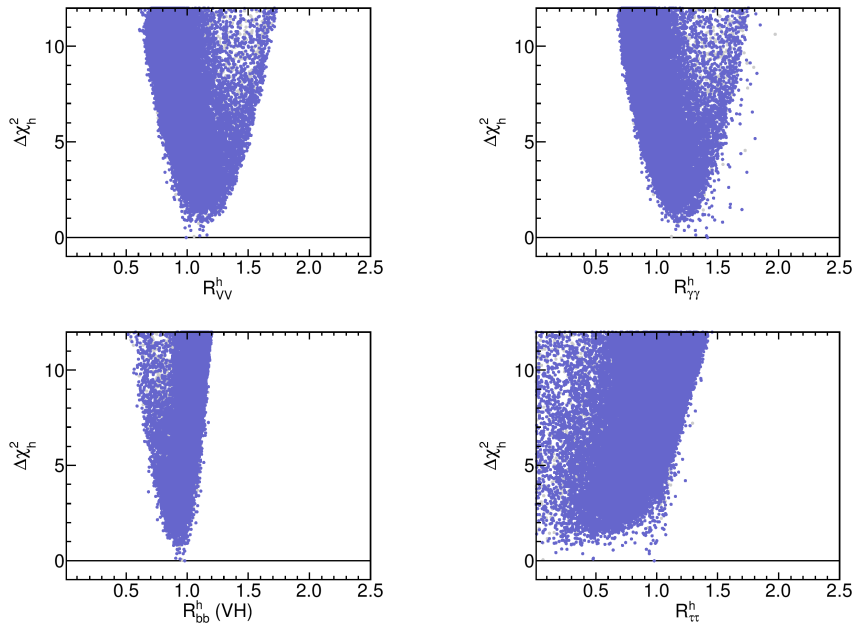

Figure 6.8: *Original 2012 analysis:* Distributions of $\Delta\chi^2_h$ versus the different signal rates (defined in the text) for the light Higgs case, including the full experimental data from Tevatron, LHC and LEOs. The colors show all points in the scan (gray), and points that pass the direct Higgs search constraints from `HiggsBounds-3.8.0` (blue).

The best fit points for the heavy Higgs case are presented in Fig. 6.7, with the numerical values given in Tab. 6.5. As the figure shows, essentially the same best fit point, albeit with different total χ^2, is obtained for the different cases with/without LEO. Leaving out the Tevatron data, however, has a larger qualitative impact on the results, and rates close to zero are allowed in the $b\bar{b}$ channel. In Tab. 6.5 we also give the results for the low-energy observables in the heavy Higgs case. One can see that the relatively small value of the Higgs mass scale in this case leads to non-negligible χ^2 contributions from $\mathrm{BR}(B \to X_s\gamma)$ and $\mathrm{BR}(B_u \to \tau\nu_\tau)$, where the latter would substantially improve for a value close to the new Belle result. Also the SUSY contribution to a_μ turns out to be relatively small, giving a sizable contribution to the total χ^2. However, this is affected by our choice in the original analysis to keep the slepton mass parameters fixed. Concerning $\mathrm{BR}(B_s \to \mu^+\mu^-)$ it should be noted that, as in the light Higgs case, the preferred value is *below* the SM result, which again holds for most of the favored region.

We now turn from the global fit properties and the best fit points to a more detailed analysis of the scan results. From here on we will only consider the results from the full fit, which includes LHC, Tevatron and low-energy observables. For the original analysis, Fig. 6.8 shows distributions of $\Delta\chi^2_h = \chi^2_h - \chi^2_{h,\mathrm{min}}$ for the MSSM (light Higgs case) for the different (idealized) signal rates. The color coding is as follows: all points analyzed in the scan that pass theoretical consistency checks and have one $\mathcal{CP}$-even Higgs boson in the Higgs signal region, cf. Section 6.2.1, are shown in gray. The blue points in addition fulfill constraints at 95% CL from direct Higgs searches applied by `HiggsBounds-3.8.0`.

The signal rates are calculated as the inclusive LHC Higgs production cross section at $\sqrt{s} =$

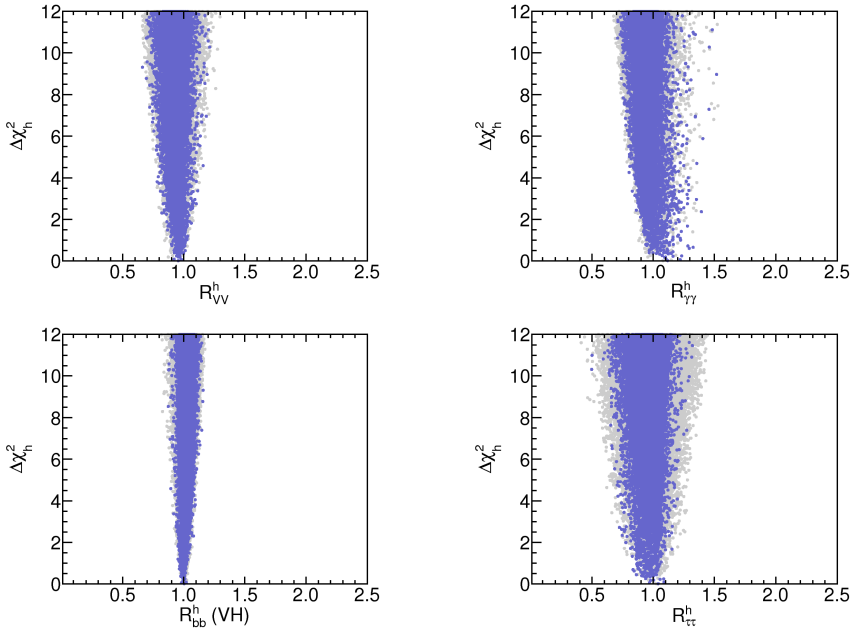

Figure 6.9: *Updated analysis:* Distributions of $\Delta\chi^2_h$ versus the different signal rates (defined in the text) for the light Higgs case, including the full experimental data from Tevatron, LHC and LEOs. The colors show all points in the scan (gray), and points that pass the direct Higgs search constraints from `HiggsBounds-4.2.0beta` (blue).

8 TeV times the decay rate, normalized to the SM predictions (cf. also Eq. (5.11)),

$$R_X^{h,H} = \frac{\sum_i \sigma_i(pp \to h, H) \times \mathrm{BR}(h, H \to X)}{\sum_i \sigma_i^{\mathrm{SM}}(pp \to h, H) \times \mathrm{BR}^{\mathrm{SM}}(h, H \to X)}. \tag{6.10}$$

The only final state for which we consider a different observable than the fully inclusive Higgs production is $b\bar{b}$, where the sum is only taken over the cross sections for $(h, H)Z$ and $(h, H)W^\pm$ associated production. As described above, for the inclusive $\tau^+\tau^-$ channels we consider the contribution of both H and A when these are close in mass. To make it clear when this is the case, we denote the joint (inclusive) rate as $R_{\tau\tau}^{H/A}$. We also define a common rate for vector boson final states $R_{VV} := R_{WW} = R_{ZZ}$. We do not include the experimental efficiencies for the $\gamma\gamma$ channel in Eq. (6.10), since the efficiencies are different for the two experiments. These are however used for the different predictions entering the fit, cf. Eq. (6.9). From the $\Delta\chi^2$ distributions we can extract best fit intervals of the signal rates,

$$R^h_{VV} = 0.99^{+0.22}_{-0.02}, \quad R^h_{\gamma\gamma} = 1.42^{+0.12}_{-0.38}, \quad R^h_{bb} = 0.98^{+0.03}_{-0.10}, \quad R^h_{\tau\tau} = 0.98^{+0.01}_{-0.94}. \tag{6.11}$$

where the quoted uncertainty is given by the distribution of points with $\Delta\chi^2_h < 1$, corresponding to 68% confidence intervals in the Gaussian limit. For $R^h_{\tau\tau}$ we observe a distribution which is very flat near the minimum. This indicates a low sensitivity in the fit to constraints from $\tau^+\tau^-$ final states, and it permits substantially reduced $\tau^+\tau^-$ rates at a very low additional χ^2 contribution.

The results from the updated analysis are shown in Fig. 6.9. It is clearly visible that including the latest experimental measurements from ATLAS and CMS leads to significantly narrower

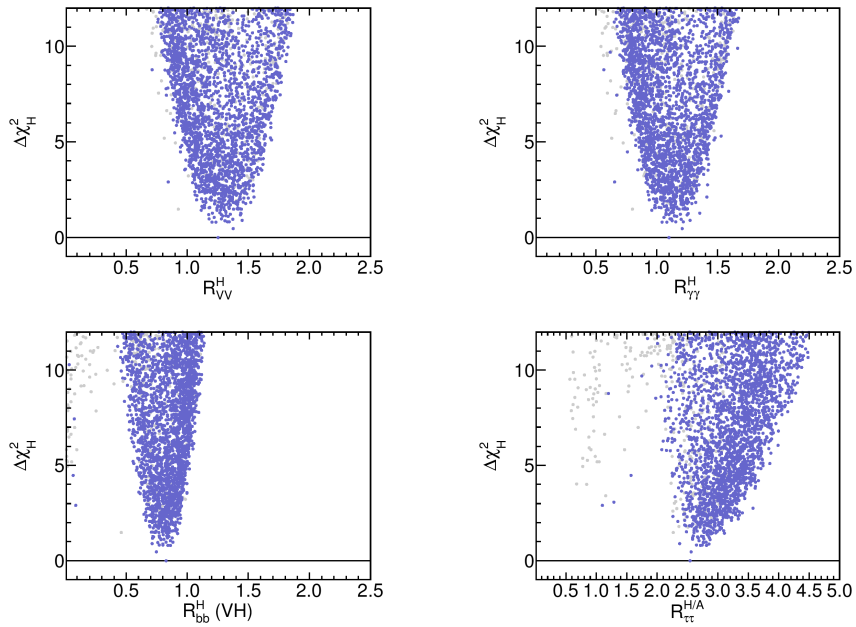

Figure 6.10: *Original 2012 analysis:* Distributions of $\Delta\chi^2_H$ versus the different signal rates (defined in the text) for the heavy Higgs case, including the full experimental data from Tevatron, LHC and LEOs. The color coding is the same as in Fig. 6.8.

$\Delta\chi^2_h$ distributions for all considered signal rates. In particular, the latest $H \to \tau\tau$ measurements from ATLAS [284] and CMS [285, 286] lead to a major improvement of the sensitivity on $R^h_{\tau\tau}$. The 1σ preferred signal rates are

$$R^h_{VV} = 0.99^{+0.04}_{-0.10}, \quad R^h_{\gamma\gamma} = 1.21^{+0.11}_{-0.28}, \quad R^h_{bb} = 0.97^{+0.06}_{-0.02}, \quad R^h_{\tau\tau} = 1.03^{+0.05}_{-0.20}. \tag{6.12}$$

Results for the heavy Higgs case are shown in Fig. 6.10. The resulting $\Delta\chi^2_H$ distributions for individual R_X are similar to those for $\Delta\chi^2_h$ of the original analysis, cf. Fig 6.8, except for $R_{\tau\tau}$, where the additional contribution from the pseudoscalar Higgs boson A strongly enhances this quantity over the corresponding result in the light Higgs case. Extracting the results for the minimal χ^2 in the same way as for the light Higgs case, we obtain

$$R^H_{VV} = 1.25^{+0.30}_{-0.07}, \quad R^H_{\gamma\gamma} = 1.10^{+0.18}_{-0.06}, \quad R^H_{bb} = 0.83^{+0.05}_{-0.12}, \quad R^{H/A}_{\tau\tau} = 2.54^{+0.31}_{-0.17}. \tag{6.13}$$

More information about the phenomenology of the pMSSM–7 Higgs sector can be found from the correlations between the different rates. This is shown in Fig. 6.11 for the light Higgs case. Compared to the one-dimensional χ^2 distributions of Fig. 6.8, this figure introduces two new colors that are used in the following to show regions close to the minimum χ^2. We highlight points for which $\Delta\chi^2_{h,H} < 2.3$ (red) and $\Delta\chi^2_{h,H} < 5.99$ (yellow). In the Gaussian limit these correspond to 68% (95%) confidence regions with two degrees of freedom. We shall refer to these points simply as the *favored region/points*, or sometimes *most favored region/points* when $\Delta\chi^2_{h,H} < 2.3$ is discussed. Here, and in all figures from here on, we refer to the χ^2 of the complete fit, including LHC, Tevatron and LEO. The best fit point is indicated in the figures by a black star.

The left plot of Fig. 6.11 shows the strong, positive, correlation between R^h_{VV} and $R^h_{\gamma\gamma}$. In

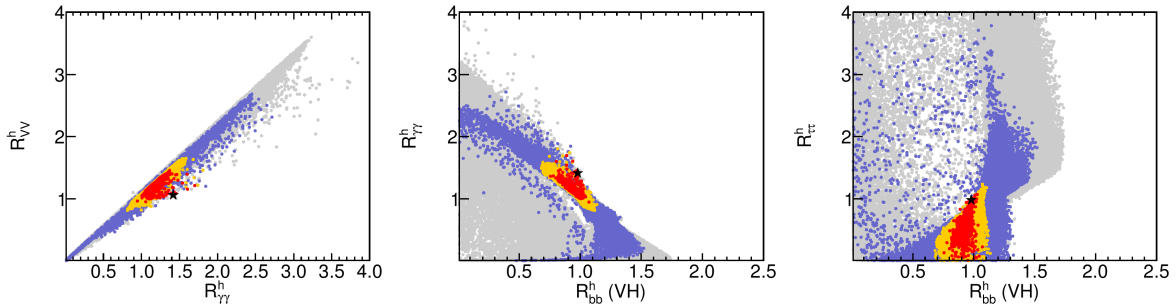

Figure 6.11: *Original 2012 analysis:* Correlations between signal rates for the light Higgs case. The color coding follows that of Fig. 6.8, with the addition of the favored regions with $\Delta\chi^2_h < 2.3$ (red) and $\Delta\chi^2_h < 5.99$ (yellow). The best fit point is indicated by a black star.

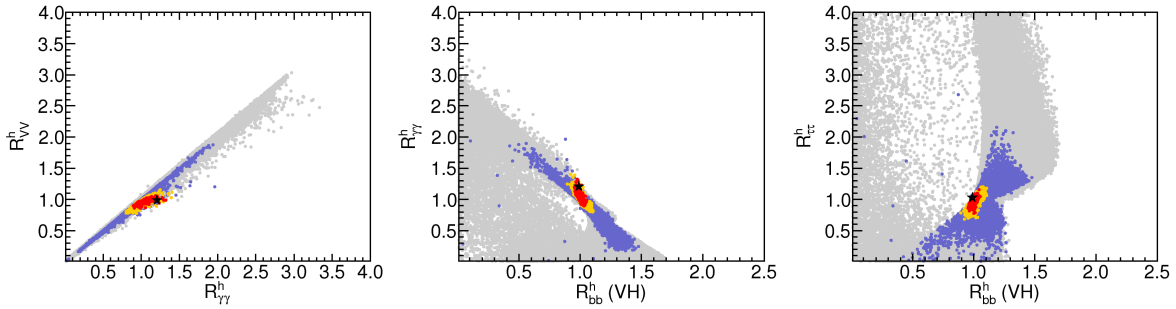

Figure 6.12: *Updated analysis:* Correlations between signal rates for the light Higgs case. The color coding follows that of Fig. 6.8, with the addition of the favored regions with $\Delta\chi^2_h < 2.3$ (red) and $\Delta\chi^2_h < 5.99$ (yellow). The best fit point is indicated by a black star.

most of the viable parameter space we find $R^h_{\gamma\gamma} > R^h_{VV}$. The favored region contains points with fully correlated rates in the interval $0.9 \lesssim R^h_{\gamma\gamma,VV} \lesssim 1.6$, but also solutions with lower degree of correlation, where a $\gamma\gamma$ enhancement of up to $R^h_{\gamma\gamma} \sim 1.8$ is accompanied by a much smaller or even no enhancement of R^h_{VV}. In the second plot of Fig. 6.11 we compare the results of $R^h_{\gamma\gamma}$ and R^h_{bb} (we remind the reader that the latter rate is calculated using the VH production mode only). We find an anticorrelation between these two rates. This can be understood from the fact that the $h, H \to b\bar{b}$ decay gives the largest contribution to the total width for a Higgs boson in this mass range, both in the SM and typically also in the MSSM, cf. Section 2.2.1. A reduction of the $h, H \to b\bar{b}$ partial width is therefore effectively a reduction of the total decay width, which leads to a simultaneous enhancement of the branching ratios into the subdominant final states. This has been pointed out in Ref. [272, 385] as an important mechanism to enhance the $\gamma\gamma$ rate in the MSSM. We shall see below how these effects on the Higgs decay widths affect the parameters in our global fit. The third (right) plot in Fig. 6.11 shows the weak correlation of $R^h_{\tau\tau}$ to R^h_{bb}, where in principle any value of $R^h_{\tau\tau} < 1$ is found in the favored region for $R^h_{bb} \lesssim 1$. Consequently, it is possible to find a strong reduction of the $\tau^+\tau^-$ mode while maintaining a SM-like $b\bar{b}$ rate.

We show the correlations of Higgs signal rates for the updated analysis in Fig. 6.12. The main correlations as noted above are also present here. As expected from the previous discussion of the one-dimensional $\Delta\chi^2$ profiles in the Higgs signal rates, Fig. 6.9, the area of the favored regions in Fig. 6.12 is clearly reduced with respect to the original results due to the updated

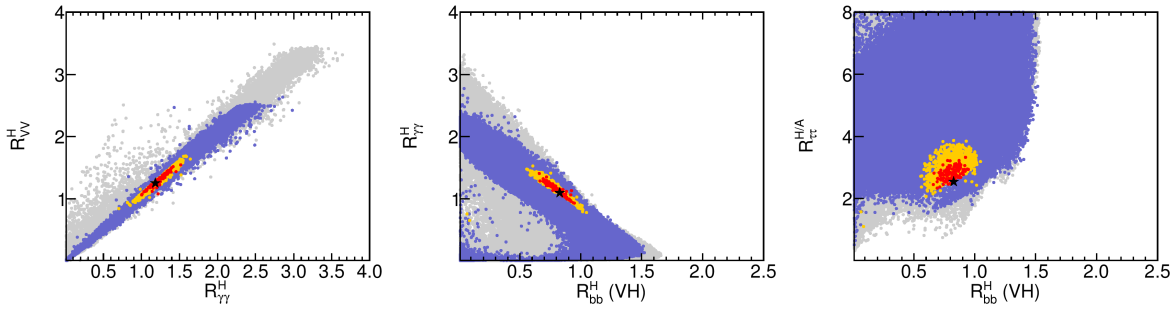

Figure 6.13: *Original 2012 analysis:* Correlations between signal rates in the heavy Higgs case. colors similar to Fig. 6.11, but here representing $\Delta\chi^2_H < 2.3$ (red) and $\Delta\chi^2_H < 5.99$ (yellow). The black star indicates the best fit point for the heavy Higgs case.

experimental data supplied by `HiggsSignals`. Signal rates of $R^h_{\gamma\gamma} \lesssim 1.4$ are still viable, whereas the other rates preferred to be close to 1.0. In particular, we see that the updated ATLAS [284] and CMS [285, 286] measurements in the $\tau\tau$ channel exclude the possibility of low $R^h_{\tau\tau}$ found in the original analysis.

Turning to Fig. 6.13, we show the rate correlations for the heavy Higgs case (of the original analysis). Similar trends as in the light Higgs case are visible in the heavy Higgs data, with the notable difference in the $\tau^+\tau^-$ rate, mainly due to the inclusion of the contribution from the $\mathcal{CP}$-odd Higgs A. The favored regions are found at values for $R^{H/A}_{\tau\tau}$ between 2 and 4, while R^H_{bb} remains below 1.

We now briefly discuss what mechanisms can alter the branching ratios in the manner observed, and what the consequences are for the favored regions of MSSM parameter space. In Fig. 6.14 we show the scan results in the plane of the Higgs sector tree-level parameters $(M_A, \tan\beta)$, where the results for the light Higgs case are shown for the original (updated) analysis in the left (right) plot. Starting with the original analysis (left plot), we find the region at low M_A and high $\tan\beta$ being excluded by direct MSSM Higgs searches (mainly $H/A \to \tau^+\tau^-$). The excluded region appears smaller in this plane than the corresponding results published by the experiments [407, 408], since their results are shown only for one the m_h^{max} benchmark scenario [268]). In an inclusive scan of the pMSSM–7 parameter space, points are found where higher order corrections to the bottom Yukawa coupling lead to suppressed production rates for the heavy MSSM Higgs bosons, and a larger fraction of the parameter space in the $(M_A, \tan\beta)$ plane therefore opens up, see also Refs. [255, 409]. Sizable branching ratios of H/A to SUSY particles also reduce the sensitivity of the searches in the $\tau^+\tau^-$ final state. We see that the regions of very high $\tan\beta \gtrsim 40$, and also low $\tan\beta \lesssim 8$, are disfavored by the fit. At high $\tan\beta$ this results from a poor fit to $(g-2)_\mu$ and flavor observables, whereas for low $\tan\beta$ the fit to the LHC Higgs observables becomes worse. For low $\tan\beta$ it also becomes increasingly difficult to fit the relatively high Higgs mass value of 125.7 GeV, although viable solutions down to $\tan\beta \sim 4$ can be found [270]. Low values of M_A are disfavored by the fit results in the light Higgs case, with the (most) preferred region starting at $M_A \gtrsim 170$ (230) GeV. Taking the rate information into account therefore suggests somewhat higher mass scales for the MSSM Higgs sector than what is required by the $\hat{M}_H \sim 125.7$ GeV Higgs mass measurement alone [270]. For the light Higgs case the lower limits on M_A in the favored regions of the fit exclude the possibility of $M_{H^\pm} < m_t$, where the charged Higgs boson can be produced in the decay of the top quark. On the other hand, the region favored by the fit does not show any upper limit for M_A, which

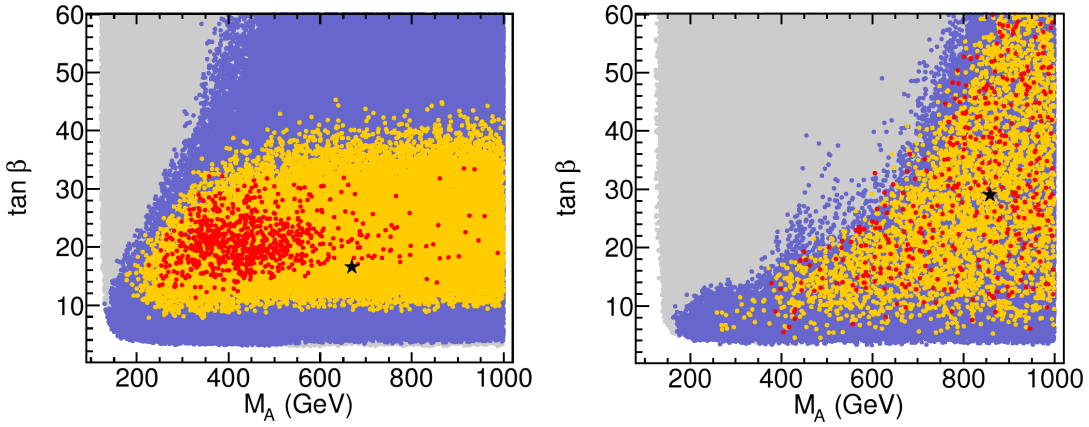

Figure 6.14: Higgs sector tree-level parameters (M_A, $\tan\beta$) in the light Higgs case in the *original 2012 analysis* (left) and the *updated analysis* (right). The color coding is the same as in previous figures.

demonstrates that the decoupling limit ($M_A \gg M_Z$), where the light Higgs boson becomes very SM-like, cf. Section 2.4.3, is a possible scenario. Note also, that the tendency towards the decoupling limit is already a consequence of the relatively large observed Higgs mass. Hence it is natural not to expect large deviations from the SM predictions in the signal rates. This agrees with the findings at the LHC and is reflected in the high quality of the SM fit to the signal rates. Consequently, the rate observables give further support of the decoupling limit solution.

In the updated analysis, shown in the right plot in Fig. 6.14, a significantly larger part of the MSSM parameter space at low M_A and high $\tan\beta$ is excluded by the experimental limits implemented in `HiggsBounds-4.2.0beta`. The dominant exclusion comes from the CMS MSSM Higgs search for $\tau^+\tau^-$ final states [278], which uses the full available integrated luminosity of the 7/8 TeV LHC run. The updated signal rate observables included in `HiggsSignals-1.2.0` drive the MSSM fit even further into the decoupling limit than in the original analysis. For the (most) favored parameter region we find $M_A \gtrsim 250$ (400) GeV. In contrast to the original

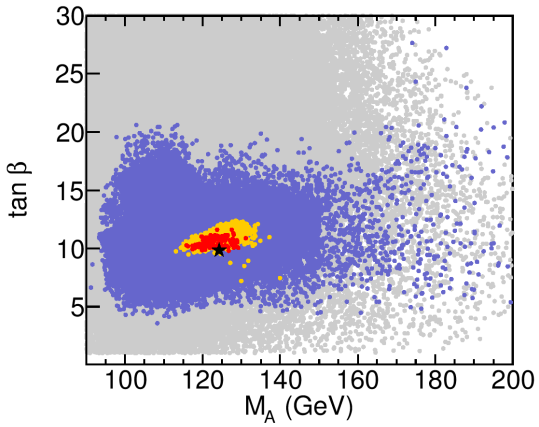

Figure 6.15: *Original 2012 analysis:* Higgs sector tree-level parameters (M_A, $\tan\beta$) in the heavy Higgs case. The color coding is the same as in previous figures.

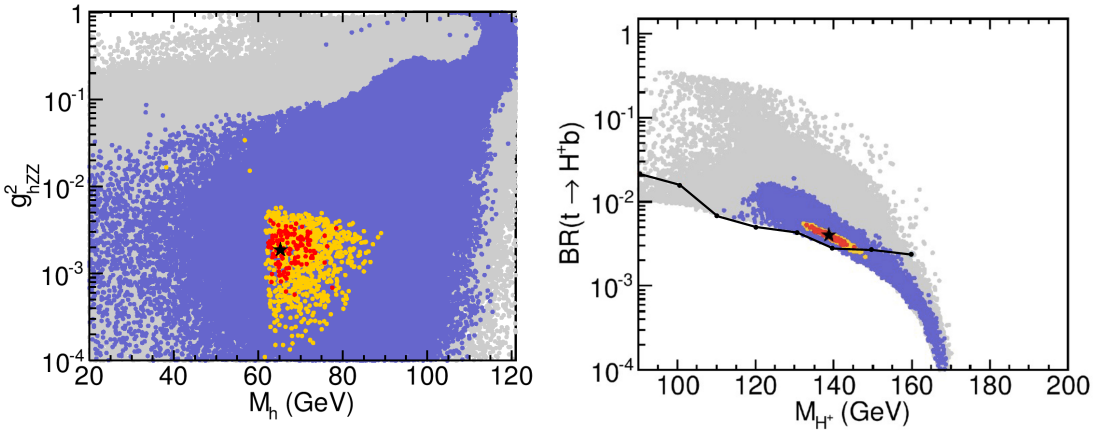

Figure 6.16: *Original 2012 analysis* of the heavy Higgs case: Effective coupling squared g^2_{hZZ} of the lightest MSSM Higgs boson to Z bosons as a function of the lightest Higgs mass M_h (left) and branching ratio of the top quark into a charged Higgs boson and a bottom quark (right). The observed 95% C.L. exclusion limit from the latest ATLAS $t \to H^{\pm}b$ search [261] (taken from Fig. 3.3) is indicated as black line.

2012 results, we find that the updated fit allows a wider range of $\tan\beta$ in the large M_A region, with most favored points found even beyond $\tan\beta \sim 40$. In the original analysis, where we had a fixed smuon mass of 300 GeV, Eq. (6.5), we found these points predicting a too large $(g-2)_\mu$ contribution to accommodate the observed discrepancy between measurement and SM prediction of the anomalous magnetic moment of the muon. In the updated analysis, a better compatibility with $(g-2)_\mu$ is achieved at large values of $\tan\beta$ by adjusting the slepton masses to larger values.

For the heavy Higgs case, as shown in Fig. 6.15, the situation is very different. Low values for M_A are preferred, and the favored region in $(M_A, \tan\beta)$ is much smaller than for the light Higgs case: $110\,\text{GeV} \lesssim M_A \lesssim 140\,\text{GeV}$ and $7 \lesssim \tan\beta \lesssim 13$. Even though the H can be very SM-like in this scenario, this situation is very different from the decoupling limit in the light Higgs case since it implies that all five MSSM Higgs bosons are light.

While in the heavy Higgs scenario the low preferred values for M_A typically lead to a situation where H, A, and $H^{\pm}$ are rather close in mass, the lightest Higgs boson, h, can have a significantly lower mass, as illustrated in the left plot of Fig. 6.16. As we see from this figure, points with $M_h < 90\,\text{GeV}$ have a very small effective coupling to vector bosons, $g^2_{hZZ} \ll 1$, which explains why such light Higgs bosons are compatible with the Higgs search limits from LEP. The bulk of the favored region is found for $60\,\text{GeV} \lesssim m_h \lesssim 90\,\text{GeV}$, with an effective coupling squared to vector bosons at the sub-percent level. Another feature which is clearly visible in the `HiggsBounds` allowed points (blue) is the degradation of the limit around $m_h \sim 98\,\text{GeV}$, which was caused by a slight excess of events observed at LEP in that mass region. While a scenario with $m_H \sim 125.7\,\text{GeV}$ and $m_h \sim 98\,\text{GeV}$ is certainly possible (see also Ref. [270, 273]), it is clearly not favored by our rate analysis. In an updated analysis of the heavy Higgs case, which is not presented here, the χ^2 information of the LEP Higgs search results provided with `HiggsBounds-4`, cf. Section 4.1.4, could be included to provide a more accurate description of the constraints on the light Higgs boson.

In the heavy Higgs case only values of the charged Higgs boson mass below the top mass $(M_{H^{\pm}} < m_t)$ are found, which offers the possibility to test this scenario with LHC searches for

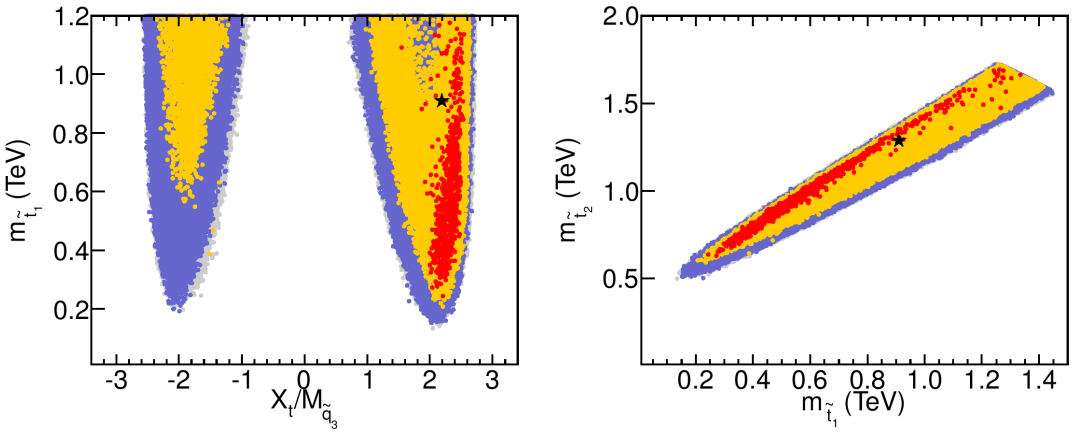

Figure 6.17: *Original 2012 analysis:* Stop mixing parameter $X_t/M_{\tilde{q}_3}$ vs. the light stop mass (left), and the light vs. heavy stop masses (right) in the light Higgs case.

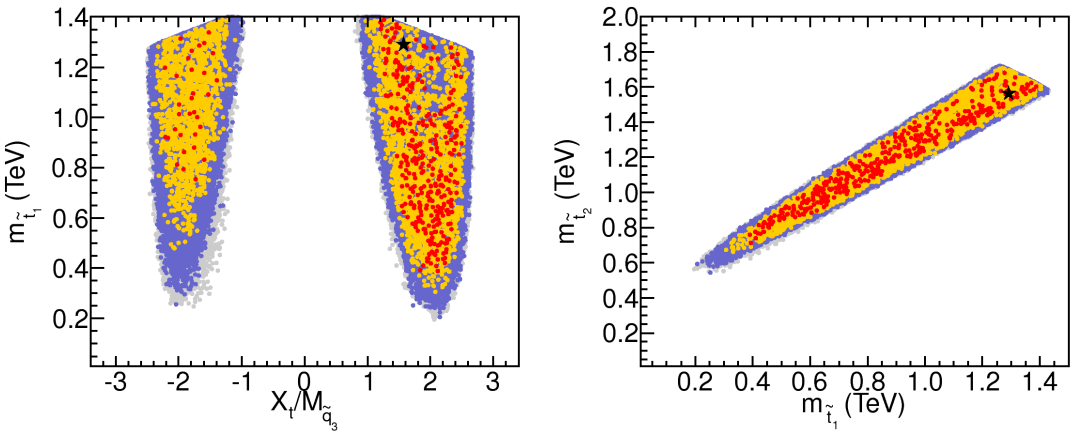

Figure 6.18: *Updated analysis:* Stop mixing parameter $X_t/M_{\tilde{q}_3}$ vs. the light stop mass (left), and the light vs. heavy stop masses (right) in the light Higgs case.

charged Higgs bosons in top quark decays. We therefore show in the right plot of Fig. 6.16 the results for $\mathrm{BR}(t \to bH^+)$ as a function of $M_{H^\pm}$. The currently most stringent upper limit on this decay mode[10], shown in Fig. 3.3 and published by ATLAS [261] after this analysis was performed, is overlaid as a black line in the Fig. 6.16 (right). This limit sets very stringent constraints on this interpretation, excluding the most favored region at the 95% C.L.. However, as can be seen from the figure, there still remain unexcluded parameter points with charged Higgs masses $M_{H^\pm} \gtrsim 145\,\mathrm{GeV}$ within this interpretation. Hence, it remains to be seen within a future update of this analysis, whether the heavy $\mathcal{CP}$-even Higgs interpretation of the MSSM is still viable in the light of updated observables and constraints from LHC Higgs searches.

The most relevant parameters for higher-order corrections in the MSSM Higgs sector are the soft SUSY-breaking parameters in the stop sector. As it was shown in Ref. [270], light scalar top masses down to 150 GeV are in agreement with a light $\mathcal{CP}$-even Higgs mass around $\sim 125\,\mathrm{GeV}$, provided the mixing in the scalar top sector is sufficiently strong. Here we show the

[10] Note, that the displayed exclusion limit assumes $\mathrm{BR}(H^+ \to \tau^+\nu_\tau) = 1$.

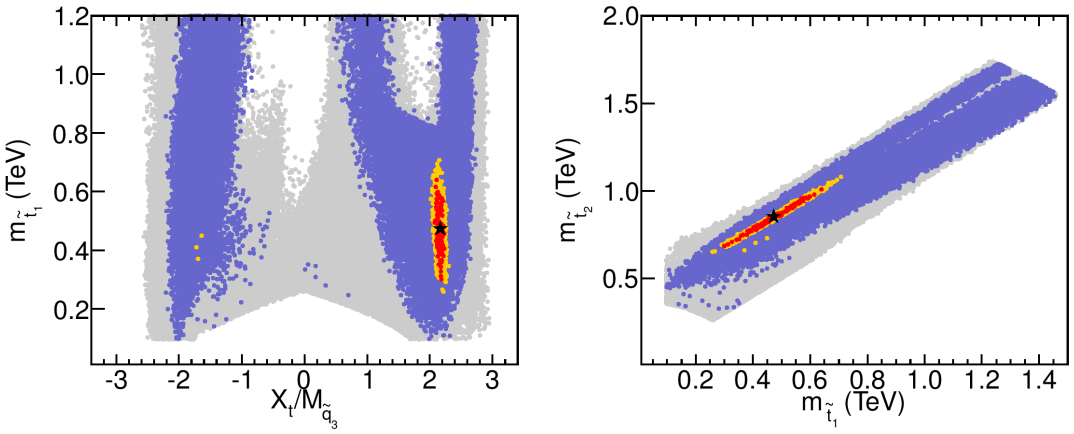

Figure 6.19: *Original 2012 analysis:* Stop mixing parameter $X_t/M_{\tilde{q}_3}$ vs. the light stop mass (left), and the light vs. heavy stop masses (right) in the heavy Higgs case.

corresponding results including the rate analysis. In Fig. 6.17 we show for the original analysis the parameter $X_t/M_{\tilde{q}_3}$ vs. the light stop mass (left plot) and the light vs. the heavy stop mass (right plot) in the light Higgs case. In the left plot one can see that the case of zero stop mixing in the MSSM is excluded by the observation of a light Higgs at $M_h \sim 125.7\,\text{GeV}$ (unless $M_{\tilde{q}_3}$ is extremely large), and that values of $|X_t/M_{\tilde{q}_3}|$ between ~ 1 and ~ 2.5 must be realized if $M_{\tilde{q}_3}$ is at the TeV scale. For the most favored region we find $X_t/M_{\tilde{q}_3} = 2 - 2.5$. It should be noted here that large values of $|A_t| \gtrsim \sqrt{6}\, M_{\tilde{q}_3}$ could potentially lead to charge and color breaking minima [410]. We checked that applying a cut at $|A_t| \gtrsim \sqrt{6}\, M_{\tilde{q}_3}$ would still leave most points of the favored region. Concerning the value of the lightest scalar top mass, the overall smallest values are found at $m_{\tilde{t}_1} \sim 200\,\text{GeV}$, in agreement with the results in Ref. [270]. Even taking the rate information into account, the (most) favored values start at $m_{\tilde{t}_1} \gtrsim 200\,\text{GeV}$ for positive X_t. Such a light $\tilde{t}_1$ is accompanied by a somewhat heavier $\tilde{t}_2$, as can be seen in the right plot of Fig. 6.17. Still, values of $m_{\tilde{t}_1} \sim 200\,\text{GeV}$ are realized for $m_{\tilde{t}_2} \sim 600\,\text{GeV}$, which would mean that both stop masses are rather light, offering interesting possibilities for the LHC. The highest favored $m_{\tilde{t}_1}$ values we find are $\sim 1.4\,\text{TeV}$. These are the maximal values reached in our scan, but from Fig. 6.17 it appears plausible that the favored region extends to larger values of both stop masses. Such a scenario would be extremely difficult to access at the LHC. For the interpretation of these results it is important to remember that we have assumed a universal value for the soft mass parameters in the scalar top and bottom sector. Relaxing this assumption would potentially lead to larger regions of parameter space in which all applied constraints can be satisfied.

We present the same plots for the updated analysis of the light Higgs case in Fig. 6.18. Here, the most favored parameter points (in red) can be found for $|X_t/M_{\tilde{q}_3}| = 1 - 2.5$ as well as for negative X_t. This is connected to the fact that in the updated analysis a suppression of the $b\bar{b}$ decay rate is no longer favored, as will be discussed below. The best fit point features heavy stops with masses close to the upper scan limit, however, the (most) favored region goes down to light stops with masses around $m_{\tilde{t}_1} \gtrsim 300$ (400) GeV, i.e. somewhat higher values than those found in the original analysis.

The results for the scalar top masses in the heavy Higgs case (original analysis) look in principle similar to the light Higgs case, but with substantially smaller favored regions, which

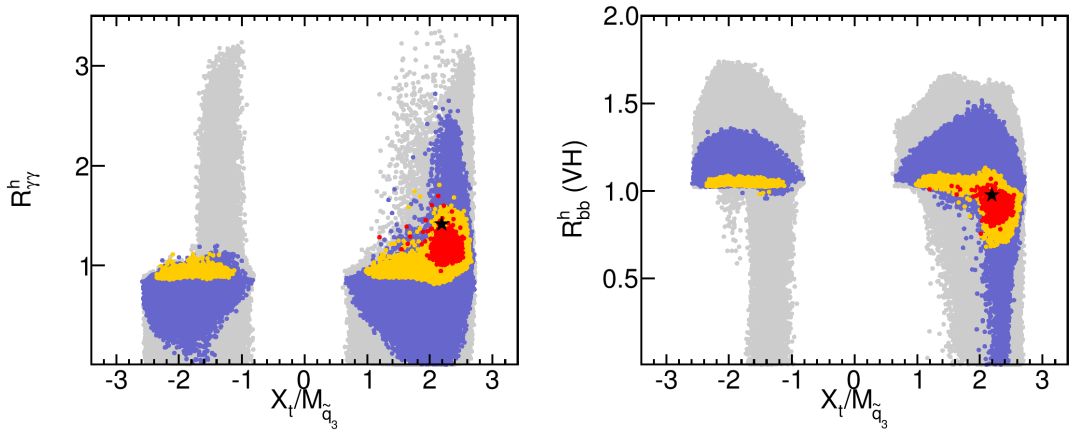

Figure 6.20: *Original 2012 analysis:* Dependence of the rates $R^h_{\gamma\gamma}$ and R^h_{bb} (VH) on the stop mixing parameter $X_t/M_{\tilde{q}_3}$ for the light Higgs case.

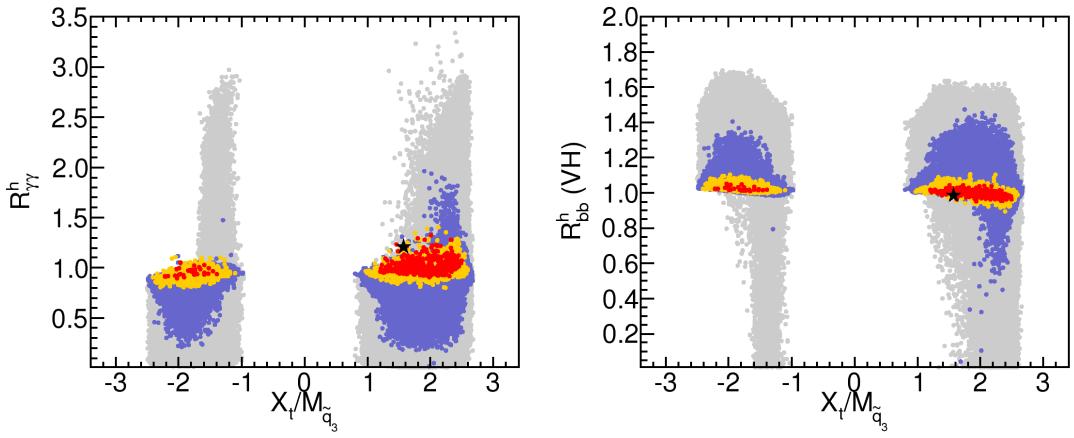

Figure 6.21: *Updated analysis:* Dependence of the rates $R^h_{\gamma\gamma}$ and R^h_{bb} (VH) on the stop mixing parameter $X_t/M_{\tilde{q}_3}$ for the light Higgs case.

are nearly solely realized for positive X_t with $X_t/M_{\tilde{q}_3} = 2$–2.3, as can be seen in Fig. 6.19. The favored values of $m_{\tilde{t}_1}$ range between $\sim 250\,\text{GeV}$ and $\sim 700\,\text{GeV}$ in this case, whereas the preferred range of the heavy stop extends from $m_{\tilde{t}_2} \sim 650\,\text{GeV}$ to $m_{\tilde{t}_2} \sim 1100\,\text{GeV}$.

We now turn to the analysis of rates as a function of the underlying MSSM parameters. This comparison allows to analyze the various mechanisms that are responsible for the observed differences in the decay rates with respect to the SM values.

Starting with the original analysis, we show in Fig. 6.20 the correlation between the ratio $X_t/M_{\tilde{q}_3}$ and $R^h_{\gamma\gamma}$ (left) or R^h_{bb} (VH) (right) for the light Higgs case. It can be seen that the enhancement in the $\gamma\gamma$ channel is only substantial for $X_t/M_{\tilde{q}_3} \gtrsim 2$, where values of up to $R^h_{\gamma\gamma} \sim 1.7$ can be reached in the favored region. Such an enhancement can have two sources: a suppression of $\Gamma(h \to b\bar{b})$, as the by far largest contribution to the total width, or a direct enhancement of $\Gamma(h \to \gamma\gamma)$. That the first mechanism is indeed responsible for a substantial part of the scenarios with an enhancement of $R^h_{\gamma\gamma}$ can be seen in the right plot of Fig. 6.20, which together with the middle plot of Fig. 6.11 illustrates that the enhancement in the $\gamma\gamma$

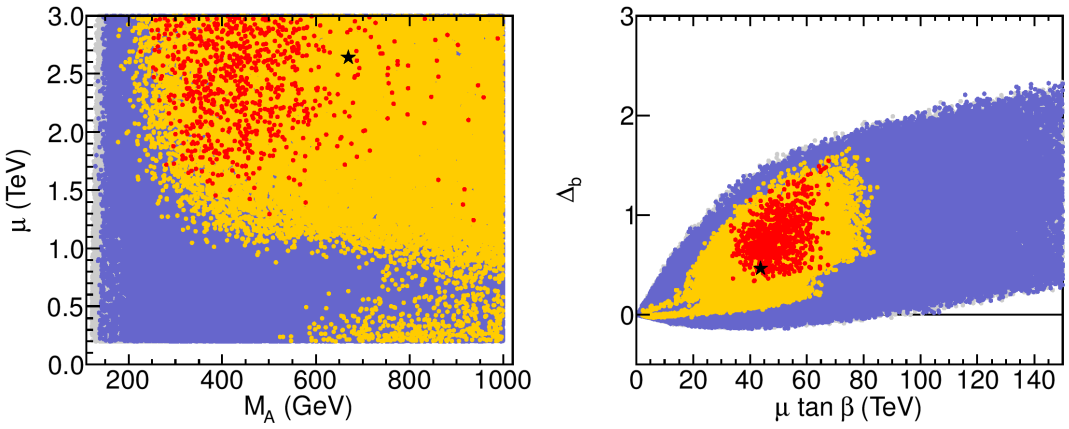

Figure 6.22: *Original 2012 analysis:* Correlation of the μ parameter to the value of M_A (left), and dependence of Δ_b corrections on $\mu \tan\beta$ (right), both in the light Higgs case.

channel in the favored regions is accompanied by some suppression of the $b\bar{b}$ channel. This suppression/enhancement is realised for large values of $X_t/M_{\tilde{q}_3}$.

The corresponding results for the updated analysis are displayed in Fig. 6.21. The most favored points feature $\gamma\gamma$ rates in the range $0.9 \lesssim R^h_{\gamma\gamma} \lesssim 1.3$, however, in contrast to the results of the original 2012 analysis, this possible enhancement is essentially not due to a suppression of the $b\bar{b}$ rate.

A suppression of the $b\bar{b}$ channel can happen in two different ways. As discussed in Section 2.4.3, the (effective) coupling $g_{hb\bar{b}}$ is given by (cf. Eq. (2.93))

$$\frac{g_{hb\bar{b}}}{g_{H_{\rm SM}b\bar{b}}} = \frac{1}{1+\Delta_b}\left(-\frac{\sin\alpha_{\rm eff}}{\cos\beta} + \Delta_b \frac{\cos\alpha_{\rm eff}}{\sin\beta}\right), \tag{6.14}$$

where α is the mixing angle in the $\mathcal{CP}$-even Higgs sector. Higher-order contributions from Higgs propagator corrections can approximately[11] be included via the introduction of an effective mixing angle, corresponding to the replacement $\alpha \to \alpha_{\rm eff}$ [396]. A suppression of the $h \to b\bar{b}$ channel thus occurs for scenarios with small $\alpha_{\rm eff}$. Furthermore, genuine corrections to the $hb\bar{b}$ vertex enter Eq. (6.14) via the threshold correction[12] $\Delta_b \propto \mu \tan\beta$ [253]. The dominant contributions to Δ_b have been given in Eq. (2.95).

While the loop-corrected coupling $g_{hb\bar{b}}$, as given in Eq. (6.14), approaches the SM coupling in the decoupling limit ($M_A \gg M_Z$), a suppression of $g_{hb\bar{b}}$ is still possible for moderately large M_A provided that Δ_b is numerically sizable and positive. We analyze this in Fig. 6.22 for original analysis of the light Higgs case. The left plot in this figure shows that the most favored regions are obtained for $\mu > 1\,\text{TeV}$, and that the combination of small μ and $M_A < 500\,\text{GeV}$ is disfavored. The corresponding Δ_b values are shown in the right plot as a function of $\mu \tan\beta$. The most favored regions here are found in the range $0.3 \lesssim \Delta_b \lesssim 1.5$, for correspondingly large values of $\mu \tan\beta \sim 30 - 70\,\text{TeV}$. Note that the large values for the Δ_b corrections do not pose problems with perturbativity, since they tend to reduce the bottom Yukawa coupling. It

[11] In our numerical analysis we treat propagator-type corrections of the external Higgs bosons in a more complete way, which is based on wave function normalisation factors that form the $\mathbf{Z}$ matrix [155].

[12] The dominant contributions to Δ_b beyond one-loop order are the QCD corrections, given in Ref. [411]. Those two-loop contributions are not included in our analysis.

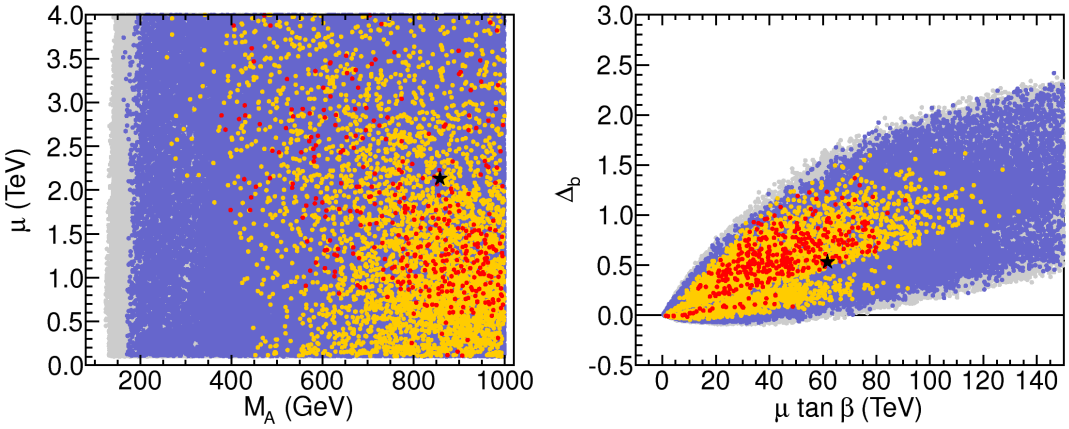

Figure 6.23: *Updated analysis:* Correlation of the μ parameter to the value of M_A (left), and dependence of Δ_b corrections on $\mu \tan\beta$ (right), both in the light Higgs case.

should be noted that the Δ_b corrections in Eq. (6.14) have another important effect: while in the absence of those contributions a small value of α_{eff} would give rise to a simultaneous suppression of the Higgs couplings to $b\bar{b}$ and to $\tau^+\tau^-$, the Δ_b corrections differ from the corresponding contributions to the $g_{h\tau^+\tau^-}$ coupling. This implies in particular that the $g_{h\tau^+\tau^-}$ coupling may be suppressed while the $g_{hb\bar{b}}$ coupling remains unsuppressed (and vice versa), see the discussion of Fig. 6.11 above.

We show the corresponding results for the updated analysis in Fig. 6.23. We find no longer a strong preference for large values of Δ_b. The most favored region features Δ_b values in the range from 0 to ~ 1.3. Consequently, there is also no strong preference for large μ values, as can be seen in the left plot of Fig. 6.23, and large, positive $X_t/M_{\tilde{q}_3}$ values (see e.g. Fig. 6.21).

For the second mechanism, a direct enhancement of the $\Gamma(h \to \gamma\gamma)$ width, it is known that other SUSY particles can play an important role. One possibility that has been discussed recently is to have very light scalar taus [385]. The effect of light scalar taus can also be observed in our analysis, as can be seen in Fig. 6.24 and Fig. 6.25. Here we show $\Gamma(h, H \to \gamma\gamma)/\Gamma(h, H \to \gamma\gamma)_{\text{SM}}$ as a function of $m_{\tilde{\tau}_1}$. In the light Higgs case of the original analysis, shown in the left plot of Fig. 6.24, the enhancement over the SM width reaches 50% for at low stau masses, $m_{\tilde{\tau}_1} \sim 100\,\text{GeV}$, in the favored region. Even lower values of $m_{\tilde{\tau}_1}$, which are allowed regarding the limits from direct searches [74], are forbidden in our scan from the requirement that the LSP is the lightest neutralino, together with the lower limit of $M_2 \geq 200\,\text{GeV}$ and the GUT relation between M_1 and M_2. Relaxing these assumptions would allow for a larger enhancement of $\Gamma(h \to \gamma\gamma)/\Gamma(h \to \gamma\gamma)_{\text{SM}}$, as is clear from the sharp rise of this rate seen in Fig. 6.24 for low $m_{\tilde{\tau}_1}$. For $m_{\tilde{\tau}_1} \gtrsim 300\,\text{GeV}$ a decoupling to the SM rate is observed. Through the contributions of light scalar taus it is thus possible to accommodate enhanced values of $R^h_{\gamma\gamma}$, while maintaining R^h_{bb} and R^h_{VV} at the SM level. Although the best fit point has $m_{\tilde{\tau}_1} \sim 100\,\text{GeV}$, the most favored region covers the entire $m_{\tilde{\tau}_1}$ range.

The preference for light staus is also clearly visible in the updated analysis, shown in the right plot of Fig. 6.24. As the latest measurements of the $b\bar{b}$ rate constraints $R^h_{b\bar{b}}$ to values close to 1, light staus are the dominant source of the $\gamma\gamma$ enhancement. In contrast to the previous results, the fit shows a tendency towards light staus with $m_{\tilde{\tau}_1} \lesssim 600\,\text{GeV}$. This is connected to the fact that we assume the slepton mass universality, Eq. (6.7), and that $(g-2)_\mu$ prefers

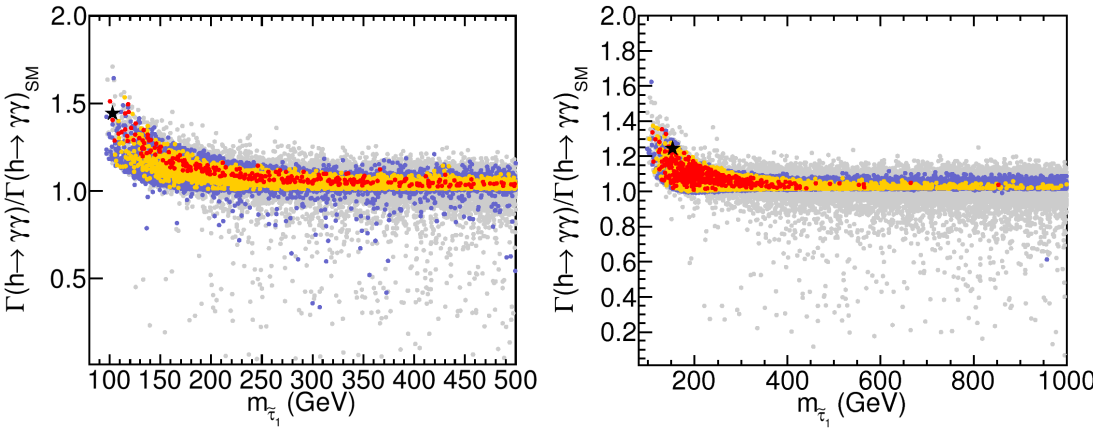

Figure 6.24: Enhancement of the $h \to \gamma\gamma$ partial width in the presence of light staus for the light Higgs case in the *original 2012 analysis* (left) and the *updated analysis* (right).

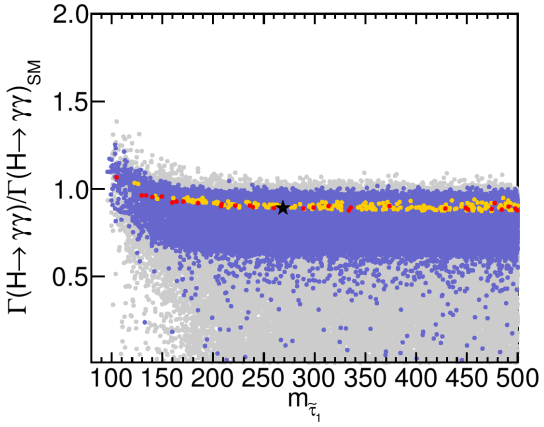

Figure 6.25: *Original 2012 analysis:* Enhancement of the $h \to \gamma\gamma$ partial width in the presence of light staus for heavy Higgs case.

rather light smuons over large regions of the parameter space.

In the heavy Higgs case, on the other hand, as shown in the right plot of Fig. 6.24, the favored region is located close to one, and light staus essentially do not contribute to a possible enhancement of $R^H_{\gamma\gamma}$.

Similarly to the light Higgs case, we investigate the dependence of the rates on the stop sector parameters for the heavy Higgs case. The results are shown in Fig. 6.26. As already seen in Fig. 6.19, the favored regions are given for large and positive $X_t/M_{\tilde{q}_3}$, where we find $0.8 \lesssim R^H_{\gamma\gamma} \lesssim 1.6$ and a corresponding suppression of $0.6 \lesssim R^H_{bb} \lesssim 1.0$. The Δ_b corrections, that enter analogously to Eq. (6.14) (cf. Eq. (2.94)), can also in this case be largely responsible for the suppression of the $R^H_{b\bar{b}}$ rate, as we show in Fig. 6.27. Here one can see that in the heavy Higgs scenario only values of Δ_b between ~ 0.3 and ~ 0.6 are favored, which are realized for $10\,\text{TeV} \lesssim \mu \tan\beta \lesssim 35\,\text{TeV}$, i.e. smaller values than in the light Higgs case in the original analysis.

To summarize the discussion on favored MSSM parameter regions, we list in Tab. 6.7 the parameter values for the best fit points of the complete fit with all observables. We also give

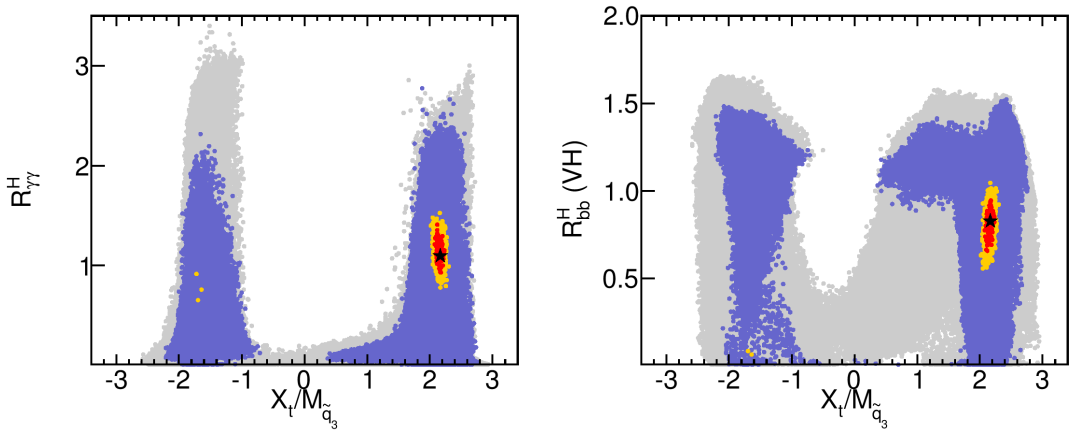

Figure 6.26: *Original 2012 analysis:* Dependence of the rates $R^H_{\gamma\gamma}$ and R^H_{bb} (VH) on the stop mixing parameter $X_t/M_{\tilde{q}_3}$ for the heavy Higgs case.

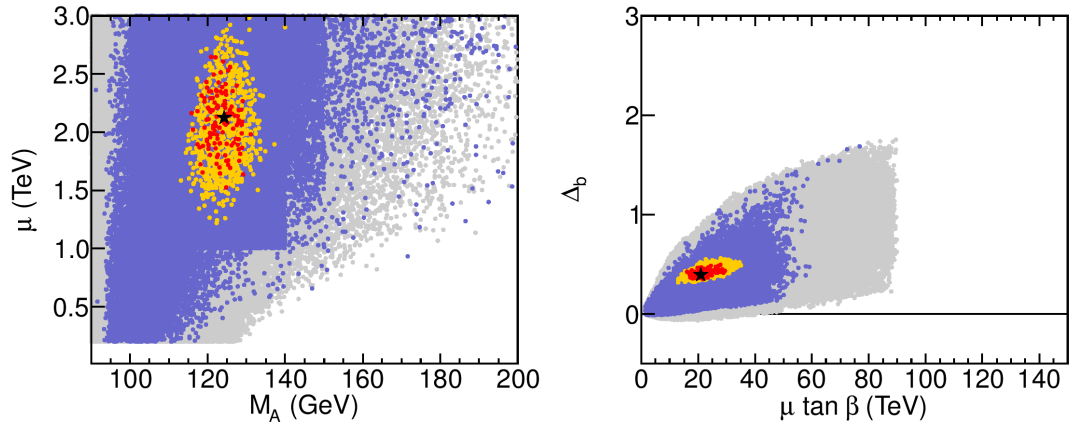

Figure 6.27: *Original 2012 analysis:* Correlation of the μ parameter to the value of M_A (left), and dependence of Δ_b corrections on $\mu \tan\beta$ (right), both in the heavy Higgs case.

the parameter ranges corresponding to $\Delta\chi^2_{h,H} < 1$. For several of the parameters this range extends to the limits of our scanned interval. Cases like this have been indicated in Tab. 6.7 with parentheses around the corresponding numbers. One can see that in most cases the ranges, even evaluated for $\Delta\chi^2_{h,H} < 1$, are quite wide. In the original analysis, one exception is $\tan\beta$, which is relatively tightly constrained (at least at the 1σ level) in the light Higgs case, and even more so in the heavy Higgs case. However, in the updated analysis, the allowed range for $\tan\beta$ became again wider. In the new results we observe a preference for low values of $m_{\tilde{\tau}_1}$, which is driven mostly by $(g-2)_\mu$. In the heavy Higgs case, as discussed above, also the masses of the additional Higgs bosons are relatively tightly constrained. More precise experimental data would be needed to achieve tighter constraints on the other fitted parameters, which enter the MSSM Higgs phenomenology via loop corrections. The fact that even in the more exotic scenario, where the signal at $\sim 125.7\,\text{GeV}$ is interpreted in terms of the heavier $\mathcal{CP}$-even Higgs of the MSSM, the values of individual SUSY parameters are only moderately constrained by the fit illustrates that a reasonably good description of the data can be achieved without the need of tuning certain parameters to specific values. It remains to be seen whether this is still

Parameter	Light Higgs case Original 2012 analysis Best fit			Light Higgs case Updated analysis Best fit			Heavy Higgs case Original 2012 analysis Best fit		
M_A [GeV]	300	669	860	398	858	(1000)	120.5	124.2	128.0
$\tan\beta$	15	16.5	26	9.8	29	(60)	9.7	9.8	10.8
μ [GeV]	1900	2640	(3000)	845	2128	3824	1899	2120	2350
$M_{\tilde{q}_3}$ [GeV]	450	1100	(1500)	637	1424	1481	580	670	740
$M_{\tilde{l}_3}$ [GeV]	250	285	(1500)	230	356	463	(200)	323	(1500)
A_f [GeV]	1100	2569	3600	1249	2315	3524	1450	1668	1840
M_2 [GeV]	(200)	201	450	(200)	229	(500)	(200)	304	370
M_h [GeV]	122.2	126.1	127.1	124.6	125.5	126.4	63.0	65.3	72.0
M_H [GeV]	280	665	860	386	858	(1000)	123.9	125.8	126.4
$M_{H^\pm}$ [GeV]	310	673	860	405	858	(1000)	136.5	138.8	141.5

Table 6.7: Best fit parameter values (in the respective middle column) and (1σ) ranges for $\Delta\chi^2_{h,H} < 1$. Values in parentheses indicate that the limit of the scan range has been reached.

the case after reanalyzing the heavy Higgs case with updated observables and constraints in a future update.

6.3 Summary of the Chapter

In this chapter we analyzed the compatibility of the Minimal Supersymmetric Standard Model (MSSM) with the recent Higgs boson discovery at the LHC. The extended Higgs sector of the MSSM allows — at least in principle — to interpret the discovered Higgs state as the light or the heavy $\mathcal{CP}$-even MSSM Higgs boson, and we considered both cases. We studied the real phenomenological MSSM (pMSSM) in two steps: First, we investigated three of the two-dimensional MSSM Higgs benchmark scenarios proposed in Ref. [246]. Second, we performed a detailed analysis of the seven-dimensional pMSSM (pMSSM–7) parameter space, where the chosen parameters are regarded as the most relevant ones for the Higgs and flavor phenomenology. The computer codes `HiggsBounds` and `HiggsSignals` (albeit, not in the original analysis of the pMSSM–7), which have been discussed in Chapter 4, formed an essential ingredient of these studies.

The two considered MSSM benchmark models with the light $\mathcal{CP}$-even Higgs boson considered as explanation of the discovered Higgs state, namely the m_h^{max} and $m_h^{\text{mod+}}$ scenario, yield a very good fit (comparable to the SM) to the current mass and signal strengths measurements of the Higgs boson at $\sim 125.7\,\text{GeV}$. While the preferred region in the m_h^{max} scenario is found only for restricted values of $\tan\beta \sim 4.5-7$ due to the predicted Higgs mass, a much larger range of $\tan\beta$ is allowed in the $m_h^{\text{mod+}}$ scenario. Both scenarios show a strong preference for the decoupling limit, where the light Higgs boson has nearly SM-like couplings. We find $M_A \gtrsim 400\,\text{GeV}$ for the most favored region in both scenarios.

As a third MSSM benchmark model we considered the low-M_H scenario, where the heavy $\mathcal{CP}$-even Higgs boson is interpreted as the discovered Higgs boson at $\sim 125.7\,\text{GeV}$. Taking into account both the signal strength measurements from Tevatron and LHC experiments as well as

the constraints from LEP Higgs searches, we find a fit quality that is only slightly worse than in the other two scenarios and hence still acceptable. However, this scenario is severely challenged by the negative results from light charged Higgs searches in top quark decays, and we showed that the latest results from the ATLAS search [261] fully exclude this benchmark scenario.

In the study of the pMSSM–7 a random parameter scan with $\mathcal{O}(10^7)$ scan points over the seven parameters most relevant for the Higgs and flavor phenomenology has been performed. For each scan point, a χ^2 function was evaluated, taking into account the measured Higgs signal rates in the individual Higgs search channels from ATLAS, CMS, and the Tevatron experiments, the best fit mass values of the LHC experiments, as well as the following low-energy observables: $\mathrm{BR}(B \to X_s\gamma)$, $\mathrm{BR}(B_s \to \mu^+\mu^-)$, $\mathrm{BR}(B_u \to \tau\nu_\tau)$, $(g-2)_\mu$ and M_W. We presented results from the original analysis performed in the end of 2012, where 37 Higgs signal rate measurements were taken into account. We also showed the results of an updated preliminary analysis of the light Higgs interpretation, where new Higgs boson exclusion limits and measurements of the mass and signal strengths were taken into account via `HiggsBounds-4` and `HiggsSignals`, respectively.

In the original 2012 analysis, we find that the SM yields a good fit to the data, with a χ^2 per degree of freedom (dof) around unity. The precise value depends on whether low-energy observables and/or the Tevatron data are included in the fit. Turning to the MSSM, we find that the pMSSM–7 provides an excellent fit to the Higgs data in the case that the light $\mathcal{CP}$-even Higgs is interpreted as the new state at $\sim 125.7\,\mathrm{GeV}$. In the case that the heavy $\mathcal{CP}$-even Higgs boson is interpreted as the newly discovered state the fit is still acceptable, but somewhat worse than in the light Higgs case once Tevatron and low-energy data is included. The two MSSM best fit points have a total χ^2/ν of 30.4/36 (42.4/36) for the light (heavy) Higgs case after the inclusion of LHC, Tevatron and low-energy data. This translates into $\mathcal{P}$-values of 73% and 21%, respectively. The corresponding SM value for χ^2/ν is 45.3/42, resulting in a fit probability of 34%. In the updated analysis the fit quality for both the SM and the MSSM (light Higgs case) becomes slightly worse but still remains acceptable with χ^2/ν values of 102.8/88 and 87.2/82, respectively, when all Higgs and low-energy observables are included. Thus, both the SM and the light Higgs case of the MSSM are compatible with the data, the overall fit quality of the MSSM interpretation is even slightly better than in the SM due to a better description of the low-energy observables.

The largest χ^2 contribution in the SM comes from the inclusion of $(g-2)_\mu$, which shows a more than 3σ deviation from the SM prediction. Regarding the comparison of the results for the light Higgs case and the heavy Higgs case in the MSSM it should be noted that a sizable part of the additional χ^2 contribution in the heavy Higgs case results from the $\mathrm{BR}(B_u \to \tau\nu_\tau)$ measurement and from $(g-2)_\mu$. The agreement between theory and experiment (both for the MSSM and the SM) for $\mathrm{BR}(B_u \to \tau\nu_\tau)$ would improve with the inclusion of the new Belle measurement. The χ^2 contribution arising from $(g-2)_\mu$ for the heavy Higgs case of the MSSM could potentially be improved if the second generation slepton parameters would be treated as free fit parameters or be set equal to the third generation slepton parameters, as done in the updated analysis of the light Higgs case. This would essentially select the slepton mass parameters yielding the lowest χ^2 value from $(g-2)_\mu$ for each point in parameter space without affecting the rest of the phenomenology in a significant way.

Thus, while the best description of the data is achieved if the new state at $\sim 125.7\,\mathrm{GeV}$ is interpreted as the light $\mathcal{CP}$-even Higgs boson of the MSSM, the more "exotic" interpretation in terms of the heavier $\mathcal{CP}$-even Higgs of the MSSM is also permitted by the data (at the time when the original analysis was performed), even if the results from the Higgs searches at the

LHC are supplemented with results from the Tevatron Higgs searches and with results from flavor physics and electroweak precision data. The latter interpretation would imply that also the other four Higgs bosons of the MSSM are rather light. As no additional Higgs bosons have been found at the LHC after this analysis was conducted, new stringent constraints on this interpretations became available, in particular from the light charged Higgs searches in top quark decays. We compared the latest ATLAS exclusion limit with the charged Higgs predictions in the favored parameter points found in the original analysis. We find large parts of the favored parameter space being excluded. Nevertheless, the limit does not entirely rule out the heavy Higgs interpretation. A detailed update of our analysis is therefore needed to arrive at a more profound conclusion on whether this interpretation is still viable in the light of current experimental data.

In the light Higgs case we find for the best fit point in the full fit an enhancement of production times branching ratio for the $\gamma\gamma$ channels with respect to the SM prediction of about 40% in the original analysis, and 20% in the updated analysis. The rates for the other gauge boson channels are found to be similar as in the SM, and the same holds for the fermionic channels ($b\bar{b}$ and $\tau^+\tau^-$). In the original analysis the $\gamma\gamma$, VV, and $b\bar{b}$ rates show a clear χ^2 minimum, while the $\tau^+\tau^-$ channel has a very broad distribution close to the minimum, and no strong preference can be attributed to the actual best fit value. In the updated analysis the favored ranges for the rates R^h_{VV}, R^h_{bb} and $R^h_{\tau\tau}$ became significantly narrower due to the more precise experimental data, and all rates feature best fit values very close to 1 (the SM value).

In the heavy Higgs case the best fit point has a somewhat smaller enhancement of the $\gamma\gamma$ channel, an enhancement of the gauge boson channels, and a suppression of the $\tau^+\tau^-$ (VBF) and $b\bar{b}$ channels, where the signal contributions of the heavy $\mathcal{CP}$-even and $\mathcal{CP}$-odd Higgs boson have not been added. On the contrary, the inclusive $\tau^+\tau^-$ channel is enhanced due to the contribution of the CP-odd Higgs boson to the signal rate.

For the light Higgs case, as well as for the heavy Higgs case, the rates in the $\gamma\gamma$ and VV channels are strongly correlated, however in most cases with the possibility of a stronger enhancement (or smaller suppression) in the $\gamma\gamma$ channel. Between the $\gamma\gamma$ channel and the $b\bar{b}$ channel an anti-correlation can be observed. This shows that a $\gamma\gamma$ enhancement can arise from a suppression of the $b\bar{b}$ channel. A suppression of the $b\bar{b}$ channel can be caused by a large value of the threshold correction Δ_b, which can reach values exceeding unity. In both MSSM fits of the original analysis, large parts of the favored regions feature such a suppression of the $b\bar{b}$, whereas in the updated analysis a preference for suppressed $b\bar{b}$ could not be observed.

In the light Higgs case, the $\gamma\gamma$ channel can be enhanced by the contribution of light scalar taus to the decay process. When the lightest scalar tau mass is as low as about 100 GeV, we find an enhancement of up to 50% from this mechanism. In the updated analysis, light scalar taus are almost entirely responsible for the $\gamma\gamma$ enhancement. Since we assume mass universality among the three generations of scalar leptons in the updated scan, light scalar taus are also favored since the observed value of the anomalous magnetic moment of the muon, $(g-2)_\mu$, gives rise to a preference of light scalar muons in large parts of the parameter space.

For the scalar top masses, we find that the favored regions start at $m_{\tilde{t}_1} \sim 200\,\text{GeV}$ and $m_{\tilde{t}_2} \sim 600\,\text{GeV}$ in the light Higgs case and at somewhat larger values in the updated analysis. If scalar top masses are required to be at the TeV scale, the mixing in the scalar top sector must exceed $|X_t/M_{\tilde{q}_3}| \sim 1$, where the most favored regions have $X_t/M_{\tilde{q}_3} \simeq 2-2.5$. The most favored region is less restricted in the updated analysis since a $b\bar{b}$ suppression is no longer favored. It extends over $|X_t/M_{\tilde{q}_3}| \simeq 1-2.5$, and includes both positive and negative X_t values. Similar values for the lower bounds on the scalar top masses are found in the heavy Higgs case.

However, for this case we find that the favored regions are also bounded from above by roughly $m_{\tilde{t}_2} \lesssim 1\,\text{TeV}$.

It is evident from our analysis, as demonstrated e.g. by Figs. 6.5, 6.6 and 6.7, that the fitted rates in the MSSM interpretations are not significantly different from the SM predictions. Therefore, very precise measurements of the rates of the observed Higgs boson in all possible signal channels will be needed to gain sensitivity in order to distinguish between a MSSM and the SM Higgs boson. Furthermore, in a complementary approach, experimental searches for additional (non-SM like) Higgs states need to be continued in the future. These are the most direct ways to probe the extended structure of the MSSM Higgs sector, and, as we have seen in particular in the case of the heavy Higgs interpretation, put severe constraints on the MSSM parameter space. If such additional states were found, these would provide a clear way to distinguish between the light and the heavy Higgs interpretation within the MSSM, as these cases have inherently different predictions for the remaining Higgs spectrum.

In the next year, the LHC will start collecting data at a new energy frontier with CM energies $\sim 13/14\,\text{TeV}$. Confronting the upcoming results with predictions in the MSSM will show whether this model, whose unambiguous prediction of a light and potentially SM-like Higgs boson seems to be well supported by the data, will continue to provide a viable description of nature also in the future.

CHAPTER 7

Bounds on R-Parity Violation from Resonant Slepton Production

One of the primary goals of the LHC program is — besides the direct search for Higgs boson(s) to explore the origin of electroweak symmetry breaking — the search for new particles predicted in BSM physics. Various LHC analyses concentrate on the search for the typical SUSY collider signatures, in particular those predicted by the R-parity conserving (RPC) MSSM [203], where the lightest supersymmetric particle (LSP) is stable as well as electrically and color neutral. These analyses thus employ strict cuts on the missing transverse energy (MET), E_T^{miss}, and typically require multiple hard jets and/or isolated leptons in addition, see e.g. Refs. [412, 413] for early LHC searches at a CM energy of 7 TeV (see also Refs. [163, 165] for recent results and Ref. [31] for a review). Unfortunately, no significant excess beyond the SM expectation has been found in any of these searches, resulting in strict lower mass bounds on the new SUSY particles in the simplest SUSY models, see also Ref. [296].

As discussed in Section 2.4.1, SUSY with R-parity violation (RPV) is a viable alternative to the RPC case, as long as the proton stability is still protected by e.g. another discrete symmetry such as baryon triality, B_3. In these SUSY models significantly different LHC signatures may arise, e.g. from the production of single SUSY particles and their subsequent decay. However, such signatures have barely been considered by the experimental collaborations during the first LHC run.

In this chapter we discuss the implications for SUSY models with RPV arising from null results from early LHC searches at a CM energy of 7 TeV. We focus on the collider signatures originating from the resonant production of a single scalar lepton. We consider the ATLAS and CMS searches for dijet resonances, as well as the ATLAS search for like–sign dimuon pairs at the LHC in order to derive bounds on the RPV couplings and relevant sparticle masses.

The work presented here was published in January 2012, i.e. shortly after the first LHC run at a CM energy of 7 TeV was completed, and is therefore based on very early LHC data with integrated luminosities of $\sim 1-2$ fb^{-1}. We briefly comment on the current experimental status of relevant searches and their implications for these SUSY models at the end of the chapter.

7.1 Introduction

Supersymmetry with R-parity violation is theoretically equally well motivated [193, 199, 200, 206] to the R-parity conserving case. It has the same particle content and the same number of imposed symmetries, see Section 2.4.1. In particular it automatically includes light neutrinos [143, 211], without adding a new see-saw energy scale or right-handed neutrinos [142]. If R-parity is replaced by baryon-triality [206], the superpotential must be extended by (cf. Eq. (2.53))

$$W_{B_3} = \frac{1}{2}\lambda_{ijk} L_i \cdot L_j \bar{E}_k + \lambda'_{ijk} L_i \cdot Q_j \bar{D}_k - \kappa_i L_i \cdot H_2. \tag{7.1}$$

These operators all violate lepton number. At a hadron collider the terms $\lambda'_{ijk} L_i Q_j \bar{D}_k$ can lead to resonant slepton and sneutrino production [208],

$$\bar{d}_j + d_k \to \tilde{\nu}_{Li}, \tag{7.2}$$

$$\bar{u}_j + d_k \to \tilde{\ell}^-_{Li}, \tag{7.3}$$

and the corresponding charge conjugate processes. This is our focus here, as opposed to squark and gluino pair production typically considered in the R-parity conserving case. The sleptons can decay via R-parity violating operators

$$\tilde{\nu}_i \to \begin{cases} \ell^+_j \ell^-_k, & L_i L_j \bar{E}_k, \quad \text{(a)} \\ d_j \bar{d}_k, & L_i Q_j \bar{D}_k, \quad \text{(b)} \end{cases} \tag{7.4}$$

$$\tilde{\ell}^-_i \to \begin{cases} \bar{\nu}_j \ell^-_k, & L_i L_j \bar{E}_k, \quad \text{(a)} \\ \bar{u}_j d_k, & L_i Q_j \bar{D}_k. \quad \text{(b)} \end{cases} \tag{7.5}$$

The sleptons can also decay to neutralinos and charginos

$$\tilde{\nu}_i \to \begin{cases} \nu_i \chi^0_j, & \text{(a)} \\ \ell^-_i \chi^+_j, & \text{(b)} \end{cases} \tag{7.6}$$

$$\tilde{\ell}^-_i \to \begin{cases} \ell^-_i \chi^0_j, & \text{(a)} \\ \nu_i \chi^-_j, & \text{(b)} \end{cases}, \tag{7.7}$$

if kinematically accessible. It is the purpose of this paper to investigate resonant slepton production at the LHC via an operator $LQ\bar{D}$. We first consider the decays via the same operator, resulting in resonant dijet production. We go beyond previous work by comparing with the ATLAS [414] and CMS [415] search results, and thus setting relevant bounds on the underlying R-parity violating supersymmetric model. We then consider the decay of the slepton to a neutralino, Eq. (7.7)(d). As we show below this can lead to like–sign dileptons in the final state, due to the Majorana nature of the neutralinos. We then focus on the case of resonantly produced scalar muons and compare to the ATLAS like–sign dimuon search [416].

The phenomenology of resonant slepton production was first studied in Ref. [208]. A detailed discussion focusing on the supersymmetric gauge decays resulting in a like-sign dilepton signature was presented in Refs. [209, 417–419]. Specific benchmark points were investigated in

Ref. [420]. A trilepton signature via the chargino mode in Eq. (7.6) was discussed in Refs. [421, 422]. Since then various aspects have been investigated. Single (squark and) slepton production leading to single top quark production was discussed in Refs. [423, 424]. Resonant slepton production with a 4th family was discussed in Ref. [425], with an ultra light gravitino in [426]. All but the latter assumed a neutralino LSP. Resonant slepton production was also considered in the context of a $\tilde{\tau}$-LSP in Ref. [207]. Resonant squark and slepton production were suggested as an explanation of the CDF Wjj anomaly [427] in Ref. [428].

Resonant slepton production has been directly searched for at the Tevatron by the DØ [429–431] and CDF experiments [432–435], setting bounds on the relevant parameters. DØ [429, 430] focused on the resonant production and decay of smuons ($\tilde{\mu}$) and muon-sneutrinos ($\tilde{\nu}_\mu$) via λ'_{211}. The results were presented as upper limits on λ'_{211} in the $(\tilde{\chi}^0_1, \tilde{\mu})$ mass plane within the minimal supergravity (mSUGRA) / CMSSM framework, see Section 2.4.2. The limits are roughly $\lambda'_{211} < 0.04$ (0.2) for smuon masses $m_{\tilde{\mu}} \lesssim 200 - 300$ (550) GeV. As we will see, our study of the LHC data greatly improves these limits.

CDF [436] and DØ [437] also searched for R-parity violation assuming the (R-parity conserving) pair production of neutralinos and/or charginos. Furthermore, CDF investigated R-parity violation in stop pair production [438]. Implications on R-parity violating models from R-parity conserving SUSY searches at the Tevatron have been studied in [207, 439, 440].

The $LQ\bar{D}$ operator could also lead to resonant squark production at HERA [441, 442]. This has been searched for by both HERA experiments H1 [443–445] and ZEUS [446–448]. They obtained limits in terms of a squark mass. For example for a R-parity violating coupling of electromagnetic strength, $\lambda'_{11k} = 0.3$ ($k \in \{1, 2\}$), the mass bound on the corresponding right-handed down-type squark is $m_{\tilde{d}_k} \gtrsim 280\,\text{GeV}$ [444].

There have also been a few dedicated searches for R-parity violation at the LHC during the 7 TeV run. The ATLAS collaboration has searched for resonant tau sneutrino ($\tilde{\nu}_\tau$) production followed by the R-parity violating decay to an $e\mu$ final state, cf. Eq. (7.4a) [449]. Furthermore, a search for displaced vertices arising from R-parity violating decays of a long-lived neutralino has been performed by ATLAS [450]. The CMS collaboration has considered hadronic supersymmetric pair production followed by cascade decays to a neutralino. The neutralino then decays to a purely leptonic final state [451, 452]. The ATLAS collaboration has furthermore interpreted a generic search in terms of bounds on a bilinear R-parity violating model [412]. These are models where λ_{ijk}, $\lambda'_{ijk} = 0$ and $\kappa_i \neq 0$, *cf.* Eq. (7.1). In general at any given energy scale κ_i can be rotated to zero [143, 453], and we prefer to work in this basis.

The combined mass limits from LEP, assuming the R-parity violating decay of pair-produced gauginos or sleptons via $LQ\bar{D}$ couplings, are $m_{\tilde{\chi}^0_1} \geq 39\,\text{GeV}$, $m_{\tilde{\chi}^\pm_1} \geq 103\,\text{GeV}$, $m_{\tilde{\nu}_{\mu,\tau}} \geq 78\,\text{GeV}$ and $m_{\tilde{\mu}} \geq 90\,\text{GeV}$ [199, 454]. Note however, that the gaugino mass limits are formally only valid in the supersymmetric parameter region investigated by LEP, i.e. for a ratio of the Higgs vacuum expectation values of $1 \leq \tan\beta \leq 35$, a universal soft-breaking scalar mass parameter $m_0 \leq 500\,\text{GeV}$, a Higgs mixing parameter $|\mu| \leq 200\,\text{GeV}$, a $SU(2)$ gaugino mass parameter $M_2 \leq 500\,\text{GeV}$ and a R-parity violating coupling larger than 10^{-4}.

Upper bounds on single $LQ\bar{D}$ couplings from flavor physics and/or from atomic parity violation have been derived and summarized in Refs. [199, 455–457]. These bounds usually scale with the up- or down-type squark mass and thus basically do not constrain R-parity violating effects in the case where the squarks are decoupled from the low energy spectrum, which is the case in our analyses.

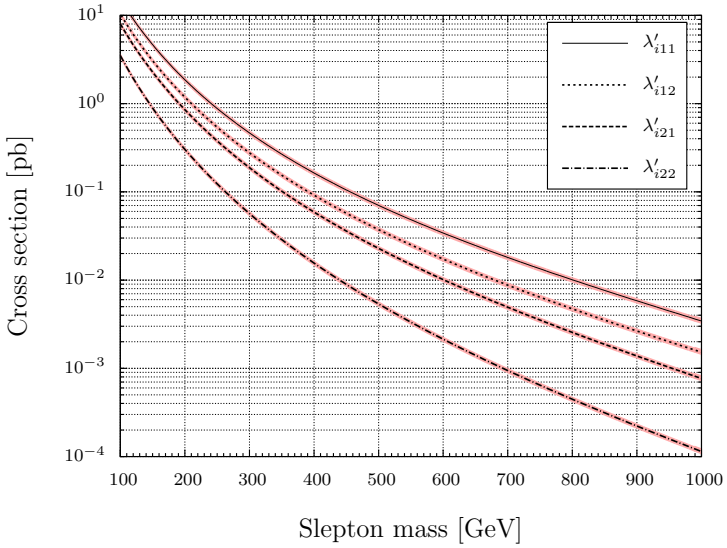

Figure 7.1: Single slepton production cross section including QCD NLO corrections at the LHC for $\sqrt{s} = 7\,\text{TeV}$ as a function of the slepton mass, $m_{\tilde{\ell}}$, for $(\lambda'_{i11}, \lambda'_{i12}, \lambda'_{i21}, \lambda'_{i22}) = 0.01$. The CTEQ6M PDFs have been used, and renormalization and factorization scales have been identified with the slepton mass $m_{\tilde{\ell}}$. The red bands correspond to an estimated 7% systematic uncertainty including PDF and renormalization/factorization scale uncertainties.

7.2 Resonant sleptons at the LHC

7.2.1 Production process

We consider the single production of a slepton at the LHC, Eqs. (7.2) and (7.3). Note that only the $SU(2)$ doublet left-handed component of the slepton field couples to this operator. We assume the singly produced slepton to be purely left-handed. We therefore omit the subscript L in the following. The case of non-negligible mixing of the weak eigenstates — as usually relevant for the third generation slepton, the stau — will be briefly discussed below.

For resonant production, the next-to-leading order (NLO) calculations including QCD and supersymmetric QCD corrections have been performed in Ref. [420, 458–460]. They increase the LO cross section at the 14 TeV LHC by up to 35% for slepton masses less than 2 TeV, while reducing the uncertainty from the renormalization and factorization scale dependence[1] to less than 5% [420]. Further, the authors of Ref. [420] have shown that the dependence on the parton density function (PDF) parametrization is less than 5% by comparing the cross sections obtained by the CTEQ6M [461] and the MRST04 [462, 463] fits. We do not expect these uncertainties to change dramatically for the LHC at a CM energy of $\sqrt{s} = 7\,\text{TeV}$ and therefore adopt these numbers for this study.

The single slepton ($\tilde{\nu}^{(*)}$ and $\tilde{\ell}^{\pm}$) production cross section at the 7 TeV LHC, including NLO QCD corrections (as employed here) is shown in Fig. 7.1, as a function of the joint slepton mass, $\tilde{m}$. We used the CTEQ6M [461] PDFs and set the renormalization and factorization scale equal to the slepton mass, $\mu_R = \mu_F = \tilde{m}$. The red bands in Fig. 7.1 indicate the total theoretical

[1] We checked this by varying the factorization scale, μ_F, and renormalization scale, μ_R, over the range $\tilde{m}/2 \leq \mu_F,\ \mu_R \leq 2\tilde{m}$ for the 7 TeV cross section estimate. The deviations from the value obtained at $\mu_R = \mu_F = \tilde{m}$ are less than 3%.

λ'_{ijk}	$\tilde{m}$ [GeV]	$\tilde{\ell}^+$	$\tilde{\ell}^-$	$\tilde{\nu}+\tilde{\nu}^*$	total
$\lambda'_{i11}=0.01$	250	365	194	428	987
	500	32.6	14.4	33.8	80.8
	800	4.9	1.8	4.5	11.2
$\lambda'_{i12}=0.01$	250	275	47.8	309	632
	500	21.8	2.3	21.7	45.8
	800	2.9	0.2	2.6	5.7
$\lambda'_{i21}=0.01$	250	40.2	122	211	373
	500	1.8	7.6	13.7	23.1
	800	0.1	0.8	1.6	2.5
$\lambda'_{i22}=0.01$	250	25.0	25.0	71.5	122
	500	1.1	1.1	3.3	5.5
	800	0.06	0.06	0.3	0.42

Table 7.1: Number of single slepton events for an integrated luminosity of 1 fb^{-1} at $\sqrt{s}=7$ TeV using the QCD NLO cross section. The first column shows the relevant $L_iQ_j\bar{D}_k$ coupling. The second column gives the slepton mass, $\tilde{m}$. The third, fourth and fifth column contain the number of $\tilde{\ell}^+$, $\tilde{\ell}^-$ and $\tilde{\nu}+\tilde{\nu}^*$ events. The last column shows the sum.

uncertainty of 7%, including both scale uncertainties and PDF parametrization which are added in quadrature.

In Fig. 7.1 we present the cross sections $\sigma(\lambda',\tilde{m})$ for the R-parity violating couplings $\lambda'_{ijk}=0.01$ which couple to the first and second generation quarks ($j,k\in\{1,2\}$). The highest cross section is obtained for λ'_{i11} since it involves valence quarks in all cases. The rate for second generation quarks is suppressed, due to the lower parton luminosity of the sea quarks. $\sigma(\lambda'_{i12})$ is slightly larger than $\sigma(\lambda'_{i21})$ due to the large u quark flux.

Exemplary event rates are shown in Tab. 7.1 for 1 fb^{-1} of LHC data at 7 TeV. Here we set $\lambda'=0.01$; the cross section scales with $(\lambda')^2$. We further list the number of singly produced $\tilde{\ell}^+$, $\tilde{\ell}^-$ and $\tilde{\nu}+\tilde{\nu}^*$ separately. For instance, for a slepton mass $\tilde{m}=500$ GeV and an R-parity violating coupling $\lambda'_{i11}=0.01$ (0.005), we expect in total 80.8 (20.2) signal events, of which the production of a charged slepton comprises 58%. The $\tilde{\ell}^+$ rate differs from the $\tilde{\ell}^-$ rate, since they involve different parton fluxes. In the case of single stau production, where the right-handed component of the lightest stau, $\tilde{\tau}_1$, cannot be neglected, the cross section is suppressed by $\cos^2\theta_{\tilde{\tau}}$, where $\theta_{\tilde{\tau}}$ is the stau mixing angle.

Although SUSY-QCD corrections can be large in specific regions of the supersymmetric parameter space [420], we do not include them in order to stay as model-independent as possible. Next-to-NLO (NNLO) QCD corrections [464], increase the LHC cross section by 3.4-4% compared to the NLO result. We do not include the gluon-gluon fusion production process for sneutrinos, which is only relevant for λ'_{i33} [460].

7.2.2 Slepton decay and signatures

We consider three possible decays of the sleptons. We first analyze the R-parity violating decay to two jets via the production operator, *cf.* Eqs. (7.4)(b) and (7.5)(b). The signature is a narrow

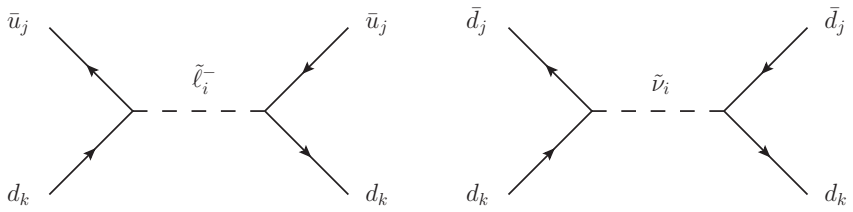

Figure 7.2: Resonant production of a charged slepton, $\tilde{\ell}_i^-$, (left) and a sneutrino, $\tilde{\nu}_i$, (right), followed by the direct decay into two quarks via the R-parity violating coupling λ'_{ijk}. This process leads to a narrow dijet resonance.

dijet resonance. We then consider the decay via a neutralino or a chargino, *cf.* Eqs. (7.6) and (7.7). The former can lead to a like-sign dilepton final state signature. For both analyses, we shall compare our results directly with the relevant ATLAS [414, 416] and CMS [415] results.

Since we can not perform a detailed analysis within the entire supersymmetric parameter space we restrict ourselves to three specific (simplified) lightest neutralino scenarios:

S1 *bino-like* $\tilde{\chi}_1^0$: The wino mass M_2 and the Higgs mixing parameter μ are much larger than the bino and the slepton mass ($M_2, \mu \gg M_1, \tilde{m}$). $\tilde{\chi}_1^0$ therefore has a large bino component. The masses of $\tilde{\chi}_{2,3,4}^0$, and $\tilde{\chi}_{1,2}^{\pm}$, are much larger than $m_{\tilde{\chi}_1^0}$, and $\tilde{m}$.

S2 *wino-like* $\tilde{\chi}_1^0$: $M_1, \mu \gg M_2, \tilde{m}$. Here, $\tilde{\chi}_1^0$ has a large wino component and it is nearly mass degenerate with the (wino-like) $\tilde{\chi}_1^{\pm}$. $\tilde{\chi}_{2,3,4}^0$ and $\tilde{\chi}_2^{\pm}$ are again decoupled from the relevant mass spectrum.

S3 *Higgsino-like* $\tilde{\chi}_1^0$: $M_1, M_2 \gg \mu, \tilde{m}$. Here, $\tilde{\chi}_{1,2}^0$ and $\tilde{\chi}_1^{\pm}$ are nearly mass degenerate and have a large Higgsino component. Hence, gauge interactions of these sparticles are suppressed. The heavier neutralinos, $\tilde{\chi}_{3,4}^0$, and the heavy chargino, $\tilde{\chi}_2^{\pm}$, are decoupled from the relevant mass spectrum.

Note that all model parameters in this study are defined at the weak scale.

Within the framework of the CMSSM, the lightest neutralino is typically dominated by its bino component. Thus, our first simplified scenario *S1* can be seen as a good approximation to wide regions of the CMSSM, where the resonantly produced slepton is lighter than the wino-like $\tilde{\chi}_2^0$ and $\tilde{\chi}_1^{\pm}$. In contrast, in anomaly mediated SUSY breaking scenarios (AMSB) [465–468] the lightest neutralino is rather wino-like. For these scenarios our simplified model *S2* can be considered as an approximation. Note that this discussion neglects the influence of the Higgs mixing parameter μ. In the case of a very small value of μ the $\tilde{\chi}_1^0$ becomes Higgsino-like and thus the scenario takes on the properties of our simplified model *S3*. See also Ref. [469].

The resonant dijet processes via the operator λ'_{ijk}, Eqs. (7.2) and (7.3), and the decays Eqs. (7.4)) and (7.5), are depicted in Fig. 7.2. At tree level, the decay width is $\Gamma(\tilde{\ell}_i^- \to \bar{u}_j d_k) \approx 75\,\text{MeV}$, for $\tilde{m} = 500\,\text{GeV}$ and $\lambda' = 0.05$ [417]. At hadron colliders, this process leads to a very narrow resonance in the invariant mass spectrum of the dijet system. However, due to the large QCD background at the LHC it will only be visible for large slepton masses $\tilde{m} \gtrsim 1\,\text{TeV}$ and reasonably large R-parity violating couplings $\lambda' \gtrsim \mathcal{O}(10^{-2})$.

If the slepton or sneutrino is the LSP, the dijet channel is the only kinematically allowed decay mode. For a $\tilde{\chi}_1^0$ LSP, the slepton decay to dijets is competing with the R-parity conserving decay $(\tilde{\ell}/\tilde{\nu}) \to (\ell/\nu) + \tilde{\chi}_1^0$ and possibly other decays to lighter sparticles, Eqs. (7.6), (7.7). A typical

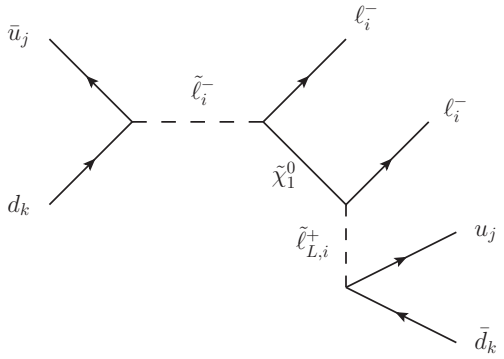

Figure 7.3: Resonant production of a charged slepton, $\tilde{\ell}_i$, with successive decay into the lightest neutralino, $\tilde{\chi}_1^0$, and a charged lepton ℓ_i. The subsequent decay of the $\tilde{\chi}_1^0$ can lead to another lepton of the same charge due to the Majorana nature of the neutralino. Thus, this process gives rise to a like–sign dilepton signature.

value for the kinematically unsuppressed ($m_{\tilde{\chi}_1^0} \ll \tilde{m}$) decay width is $\Gamma(\tilde{\ell} \to \ell\tilde{\chi}_i^0) \approx 1\,\text{GeV}$, for $\tilde{m} = 500\,\text{GeV}$ [19, 470]. This broadens the dijet resonance, and reduces the dijet branching ratio. The exact branching ratios depend on the R-parity violating coupling strength λ', the composition of the light gauginos and on the details of the mass spectrum. The gauge decays are basically absent in *S3* for the first and second generation sleptons, but can be relevant for a scalar tau.

If χ_1^0 is the LSP it decays via the operator $L_iQ_j\bar{D}_k$ as

$$\chi_1^0 \to \begin{cases} \ell_i^- u_j \bar{d}_k \\ \nu_i d_j \bar{d}_k \end{cases} + \text{c.c.} \tag{7.8}$$

The charge conjugate (c.c.) decays are equally likely, due to the Majorana nature of the neutralino. The neutrino and charged lepton decay modes can have different branching ratios depending on the admixture of the lightest neutralino. The decay $\chi_1^0 \to \nu_i\gamma$ for $L_iQ_j\bar{D}_k$ is only possible for $j = k$ [143] but is typically highly suppressed and not relevant for collider signatures [471].

Within the framework of the three decoupled scenarios *S1*-*S3*, only the process

$$\begin{aligned} \bar{u}_j d_k \to \tilde{\ell}^- &\to \ell^- \tilde{\chi}_1^0 \\ &\overset{\lambda'}{\hookrightarrow} \ell^- u_j \bar{d}_k \end{aligned} \tag{7.9}$$

(and its charge conjugate), can lead to a like–sign dilepton signature. One diagram contributing to this process is also illustrated in Fig. 7.3. The sneutrino production

$$d_j \bar{d}_k \to \tilde{\nu}^* \to \ell^+ \tilde{\chi}_1^- \tag{7.10}$$

followed by the decay of the chargino $\tilde{\chi}_1^- \to \ell_i^- \bar{d}_j d_k$ (via $L_iQ_j\bar{D}_k$) leads to an opposite-sign

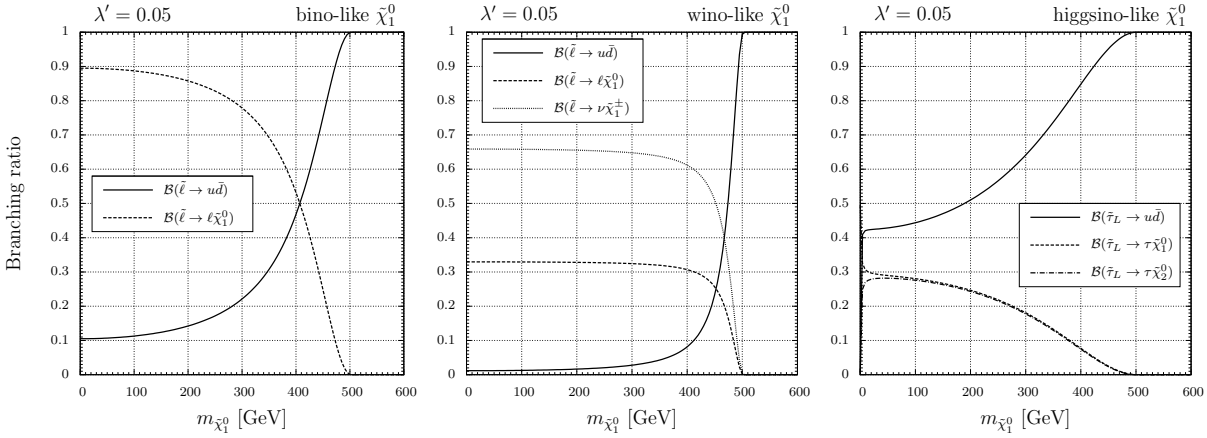

Figure 7.4: Neutralino mass dependence of the branching ratios for the slepton decay modes in the bino-like (left panel), wino-like (middle) and Higgsino-like (right) $\tilde{\chi}_1^0$ scenario. We chose a coupling strength of $\lambda' = 0.05$. The slepton mass is set to $\tilde{m} = 500\,\text{GeV}$. The decays are calculated with `ISAJET7.64` [472]. In the bino- and wino-like $\tilde{\chi}_1^0$ scenario, the (purely left-handed) slepton can be $\tilde{\ell} = \tilde{e}_L, \tilde{\mu}_L, \tilde{\tau}_L$, while in the Higgsino-like $\tilde{\chi}_1^0$ scenario we only show the decays of a (purely left-handed) $\tilde{\tau}_L$. We set $\tan\beta = 10$.

dilepton signature. The cascade decay of the chargino via the neutralino

$$\begin{aligned} d_j\bar{d}_k \to \tilde{\nu}^* \to \ell^+\tilde{\chi}_1^- \\ \hookrightarrow W^-\tilde{\chi}_1^0 \\ \overset{\lambda'}{\hookrightarrow} \ell^+\bar{u}_j d_k \end{aligned} \tag{7.11}$$

in the wino-like scenario is kinematically suppressed since $\tilde{\chi}_1^-$ and $\tilde{\chi}_1^0$ are nearly mass degenerate.

In *S3*, $\tilde{\chi}_1^0$ can be replaced by $\tilde{\chi}_2^0$ in Eq. (7.9). The $\tilde{\chi}_1^0$ and $\tilde{\chi}_2^0$ have similar couplings due to their large Higgsino component and are again nearly mass degenerate. Thus, this process contributes with a similar rate to the like–sign dilepton signature as the process in Eq. (7.9). In addition, the rate is enhanced by roughly a factor of 2 compared to the bino- and wino-like $\tilde{\chi}_1^0$ scenario because the neutral decay $\tilde{\chi}_{1,2}^0 \to \nu_i d_j \bar{d}_k$ in Eq. (7.8) is suppressed for a Higgsino $\tilde{\chi}_{1,2}^0$.

In Fig. 7.4 and 7.5 we show the dependence of the charged slepton branching ratios corresponding to the decays Eq. (7.5b) and (7.7), on the lightest neutralino mass, $m_{\tilde{\chi}_1^0}$, and coupling strength, λ', respectively. In both figures we chose a slepton mass of $\tilde{m} = 500\,\text{GeV}$. In Fig. 7.4 the R-parity violating coupling strength is set to $\lambda' = 0.05$. In Fig. 7.5 we fixed the lightest neutralino mass to 250 GeV.

As $m_{\tilde{\chi}_1^0}$ increases[2], the phase space in the gauge decays of the slepton, Eq. (7.7), decreases and leads to a suppression of the R-parity conserving decays, Eq. (7.5)(b). For $m_{\tilde{\chi}_1^0} \geq 500\,\text{GeV}$, the slepton becomes the LSP and only the dijet decay channel remains accessible. Note that there are extensive regions in R-parity violating CMSSM parameter space where the slepton is indeed the LSP [207].

For the bino- and wino-like $\tilde{\chi}_1^0$ scenario (the left and middle panels in Fig. 7.4 and 7.5, respectively), we show the branching ratios $\mathcal{B}(\tilde{\ell}^+ \to u\bar{d})$, $\mathcal{B}(\tilde{\ell} \to \ell\tilde{\chi}_1^0)$ and $\mathcal{B}(\tilde{\ell}^+ \to \bar{\nu}\tilde{\chi}_1^+)$, where

[2] Computationally, we increase M_1, M_2 or μ in the bino-, wino- or Higgsino-like $\tilde{\chi}_1^0$ scenario, respectively, while setting the decoupled mass parameters to 5 TeV.

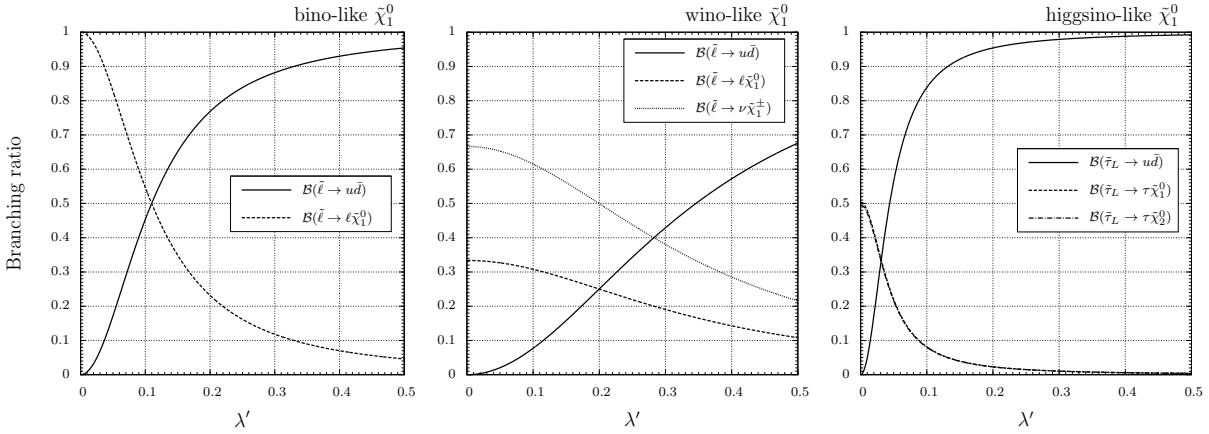

Figure 7.5: λ' dependence of the branching ratios of the slepton decay modes in the bino-like (left panel), wino-like (middle) and Higgsino-like (right) $\tilde{\chi}_1^0$ scenario. We chose a slepton mass of $\tilde{m} = 500\,\text{GeV}$ and a lightest neutralino mass of $m_{\tilde{\chi}_1^0} = 250\,\text{GeV}$. The decays are obtained with `ISAJET7.64` [472]. As in Fig. 7.4 the (purely left-handed) slepton can be $\tilde{\ell} = \tilde{e}_L, \tilde{\mu}_L, \tilde{\tau}_L$, in the bino- and wino-like $\tilde{\chi}_1^0$ scenario, while in the Higgsino-like $\tilde{\chi}_1^0$ scenario we only show the decays of a (purely left-handed) $\tilde{\tau}_L$. We set $\tan\beta = 10$.

the charged slepton is the left-handed slepton of any of the three generations, $\tilde{\ell} = \tilde{e}_L, \tilde{\mu}_L, \tilde{\tau}_L$.

In *S1*, the only kinematically allowed slepton decays are $\tilde{\ell}^+ \to u\bar{d}$ and $\tilde{\ell} \to \ell\tilde{\chi}_1^0$. Recall M_2 is very large and thus the lightest chargino is heavy. *S1* can be viewed as the best-case scenario for the like–sign dilepton signature because the gauge decay of the charged slepton leads in roughly 25% of the cases to the like–sign dilepton signature. The decay $\tilde{\ell} \to \ell\tilde{\chi}_1^0$ dominates for $\lambda' \lesssim 0.05$ (0.1) given a sufficiently large phase space of $\tilde{m} - m_{\tilde{\chi}_1^0} \gtrsim 100$ (250) GeV.

In the wino-like $\tilde{\chi}_1^0$ scenario, we have the three competing decays $\tilde{\ell}^+ \to u\bar{d}$, $\tilde{\ell} \to \ell\tilde{\chi}_1^0$ and $\tilde{\ell}^+ \to \bar{\nu}\tilde{\chi}_1^+$. The slepton decays twice as often to the chargino as to the neutralino, $\mathcal{B}(\tilde{\ell}^+ \to \bar{\nu}\tilde{\chi}_1^+) \approx 2\mathcal{B}(\tilde{\ell} \to \ell\tilde{\chi}_1^0)$. The gauge decays of the charged slepton therefore yield a like–sign dilepton signature only around 1/12 of the time. They dominate for $\lambda' \lesssim 0.05$ (0.35) for a mass difference of $m_{\tilde{\ell}} - m_{\tilde{\chi}_1^0} \gtrsim 50$ (250) GeV and are slightly stronger than in the bino-like $\tilde{\chi}_1^0$ case due to the larger gauge coupling.

In the Higgsino-like $\tilde{\chi}_1^0$ scenario (the right panel in Fig. 7.4 and 7.5), we only give the branching ratios of the (left-handed[3]) third generation slepton, $\tilde{\tau}_L$, because of the non-negligible Higgs Yukawa couplings. The gauge decays of the first and second generation sleptons are negligible, such that these only decay to dijets. We chose a moderate value of $\tan\beta = 10$, which influences the τ Yukawa coupling, cf. see Section 2.4.3. The branching ratios $\mathcal{B}(\tilde{\tau} \to \tau\tilde{\chi}_{1,2}^0)$ are roughly equal. 50% of the gauge decays of the stau yield a like–sign tau pair. However, they dominate the slepton decay modes only for a coupling $\lambda' \lesssim 0.01$ (0.04) for a given mass difference of $m_{\tilde{\ell}} - m_{\tilde{\chi}_1^0} \gtrsim 50$ (250) GeV.

In the case of the lightest stau, $\tilde{\tau}_1$, having a non-negligible right-handed component the branching ratios get more complicated. The right-handed component does not couple to the R-parity violating operator but via Yukawa interactions to the chargino, leading to the decay $\tilde{\tau}_R^+ \to \bar{\nu}_\tau\tilde{\chi}_1^+$. Therefore, with increasing right-handedness of the $\tilde{\tau}_1$, the R-parity violating decay

[3] Here, we decoupled the soft-breaking right-handed stau mass parameter, $(m_{\tilde{\mathbf{E}}})_{33} = 5\,\text{TeV}$, which leads to the lightest stau being purely left-handed.

mode to two jets on the one hand gets suppressed while on the other hand the additional decay mode to the chargino decreases the (like–sign) dilepton rate. Recall that the production is also suppressed for a right-handed stau.

We do not further consider the Higgsino-like $\tilde{\chi}_1^0$ scenario. However, this analysis and the following results in Section 7.3.2 show that a search for like–sign tau pairs would be able to probe resonantly produced tau sleptons with λ'_{3jk} $(j,k=1,2)$ even if the light gauginos, $\tilde{\chi}_{1,2}^0$ and $\tilde{\chi}_1^\pm$, are dominated by their Higgsino component.

7.3 Implications from LHC searches

In this section we use both the dijet and the like–sign dilepton signatures of resonant slepton production to constrain the R-parity violating couplings λ'_{ijk} and the relevant slepton mass. For the calculation of both the R-parity conserving and violating sparticle decays we use `ISAJET7.64` [472] and `ISAWIG1.200` [473]. The `ISAWIG` output is fed into `Herwig6.510` [474–476] for the MC simulation at particle level. We simulate the response of the ATLAS and CMS detector using the general purpose detector simulation package `Delphes1.9` [477]. Jets are reconstructed using the anti-k_T algorithm [478, 479]. In the dijet resonance search in Section 7.3.1, the distance parameter is set to $R=0.6$ (ATLAS) and $R=0.5$ (CMS), while we use $R=0.4$ for the ATLAS like–sign dimuon search in Section 7.3.2. These jet definitions are in accordance with Refs. [414–416].

7.3.1 Search for dijet resonances

Both the ATLAS [414] and the CMS [415] experiment have searched for resonances in the dijet invariant mass spectrum using pp collision data corresponding to an integrated luminosity of 1.0 fb^{-1} at a CM energy of $\sqrt{s}=7\,\text{TeV}$. The non-observation of new resonances led the experiments to derive limits for several new physics models including string resonances, exited quarks, axigluons and colour octet scalar resonances. In the following, we use the model-independent limits on a fiducial signal cross section provided by ATLAS [414] and CMS [415] to constrain the resonant R-parity violating production of sleptons, Eqs. (7.2) and (7.3), with subsequent decay to two jets, Eqs. (7.4)(b) and (7.5)(b). The mass region in the ATLAS (CMS) search ranges from 0.9 TeV (1.0 TeV) to 4.0 TeV (4.1 TeV). Therefore, these searches can only constrain the resonant production of very heavy sleptons. Constraints for lower slepton masses have been derived from CDF and `UA2` searches in Ref. [428].

In order to evaluate the acceptance of the analyses, we simulated 25,000 signal events for the process $pp\to\tilde{\ell}_i/\tilde{\nu}_i\to q_jq_k$ for each slepton mass, $\tilde{m}$. For the ATLAS search, we followed closely the prescription given in the Appendix of Ref. [414]. There, the limits are presented assuming a certain width to mass ratio of the resonance, σ_G/m_G. In our study we determined σ_G/m_G with Gaussian fits of the dijet invariant mass distribution in the region between $0.8\tilde{m}$ and $1.2\tilde{m}$. It ranges from 8% to 5% for slepton masses from 0.9 TeV to 4 TeV. The acceptance $\mathcal{A}$ is given by the fraction of events lying in the region $0.8\tilde{m}$ to $1.2\tilde{m}$ (after all other kinematic requirements are applied) and ranges from 8.1% to 18.6% for slepton masses from 0.9 TeV to 4.0 TeV.

Both $\mathcal{A}$ and σ_G/m_G are fairly independent of λ'_{ijk} $(j,k\in\{1,2\})$ for values between 0.001 and 1.0, since the resonance shape is dominated by the jet smearing of the detector simulation. Thus, we can easily derive upper limits on the R-parity violating coupling squared times the

branching ratio to dijets of the resonant slepton, $\lambda'^2 \times \mathcal{B}(\tilde{\ell}_i/\tilde{\nu}_i \to jj)$, for a given resonant slepton mass, $\tilde{m}$. These limits[4] are shown in Fig. 7.6 for the four types of couplings λ'_{i11}, λ'_{i12}, λ'_{i21} and λ'_{i22} $(i = 1, 2, 3)$. In the case of an intermediate third generation slepton $(i = 3)$, the limit has to be multiplied by $\cos^2\theta_\tau$, cf. Eq. (2.71), to account for possible mixing in the stau sector. To be conservative, we reduced the signal by 7% to take into account the theoretical uncertainty of the NLO cross section prediction. The statistical uncertainty of the acceptance estimate is negligible.

The upper bounds on the four investigated R-parity violating couplings, as derived from the ATLAS search, are listed together with $\mathcal{A}$ and σ_G/m_G in Tab. C.1 in Appendix C.1. We only show upper limits for coupling values in the perturbative regime, i.e. $\lambda' < 1$. For instance, assuming the decay to dijets being the only accessible decay mode, we can derive the upper bounds $\lambda'_{i11} \leq 0.07$ (0.09) and $\lambda'_{i22} \leq 0.38$ (0.64) for a slepton mass $\tilde{m} = 1000\,\text{GeV}$ (1500 GeV).

In the CMS search [415], so–called wide jets are constructed based on anti-k_T jets with distance parameter $R = 0.5$. This allows to distinguish between a quark–quark (qq), quark–gluon (qg) and a gluon–gluon (gg) dijet system. Here, we employ the 95% CL upper limits on $\sigma \times \mathcal{A}$ derived for a qq dijet system. These limits only assume the natural resonance width to be small compared to the CMS dijet mass resolution.

We adopt the CMS construction of wide jets and apply the kinematic requirements to the jets. The acceptance is defined by the fraction of events with dijet invariant mass $m_{jj} > 838\,\text{GeV}$. It ranges from 33.8% to 44.8% for slepton masses from 1.0 TeV to 4.1 TeV. Again, we take into account a 7% systematic uncertainty on the signal.

In Fig. 7.7 we present the upper bounds on $\lambda'^2 \times \mathcal{B}(\tilde{\ell}_i/\tilde{\nu}_i \to jj)$ for the same couplings as before, but now derived from the CMS search. These results are given in detail in Tab. C.2 in Appendix C.1. For a pure dijet decay of the slepton, $\mathcal{B}(\tilde{\ell}_i/\tilde{\nu}_i \to jj) \approx 100\%$, the upper bounds obtained are $\lambda'_{i11} \leq 0.03$ (0.05) and $\lambda'_{i22} \leq 0.18$ (0.37) for a slepton mass $\tilde{m} = 1000\,\text{GeV}$ (1500 GeV). Due to the higher acceptance of the CMS search, these limits are considerably stricter than those obtained from the ATLAS search.

7.3.2 Search for prompt like–sign dimuons

We now turn to the discussion of the constraints from the like–sign dilepton signature. In Ref. [416] ATLAS searched for anomalous production of prompt like–sign muon pairs, using data corresponding to an integrated luminosity of $1.6\,\text{fb}^{-1}$ at a CM energy of $\sqrt{s} = 7\,\text{TeV}$. No significant excess was observed and upper limits on the anomalous production of prompt like–sign muon pairs were derived. In the following, we use these results to constrain the R-parity violating couplings λ'_{2jk}, $j, k \in \{1, 2\}$, assuming the resonant production of a left-handed smuon, $\tilde{\mu}_L$ via Eq. (7.3), and its subsequent decay into the lightest neutralino, $\tilde{\chi}^0_1$, and a muon via Eq. (7.7)(a). The neutralino then decays as in Eq. (7.8) to the lepton with the same sign charge.

In the ATLAS search [416], the signal region is subdivided into four bins. The signal yield is defined by the number of like–sign muon pairs whose invariant mass, $m_{\mu\mu}$, is greater than 15 GeV, 100 GeV, 200 GeV and 300 GeV, respectively. The main requirements on the muons are the following: The transverse momentum of the first (second) muon is larger then 20 (10) GeV. Both muons are in the central region of the detector with pseudorapidity $|\eta| < 2.5$. They are separated from jets by $\Delta R(\mu, \text{jet}) > 0.4$, where $\Delta R(a, b) \equiv \sqrt{(\eta_a - \eta_b)^2 + (\phi_a - \phi_b)^2}$ quantifies

[4] This analysis assumes that the sneutrino and the charged slepton resonance are not distinct. This is generally the case as long as the mass splitting is not too large, i.e. $m_{\tilde{\ell}} - m_{\tilde{\nu}} \lesssim \sigma_G \lesssim 10\%\, m_{\tilde{\ell}}$.

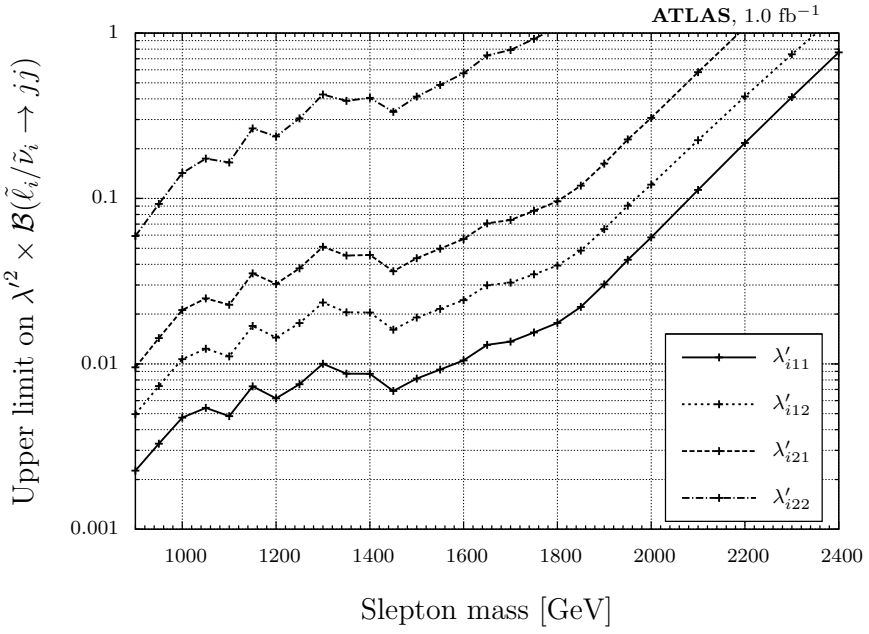

Figure 7.6: Upper bounds on $\lambda'^2 \times \mathcal{B}(\tilde{\ell}_i/\tilde{\nu}_i \to jj)$ derived from the ATLAS dijet resonance searches with 1 fb^{-1} of data.

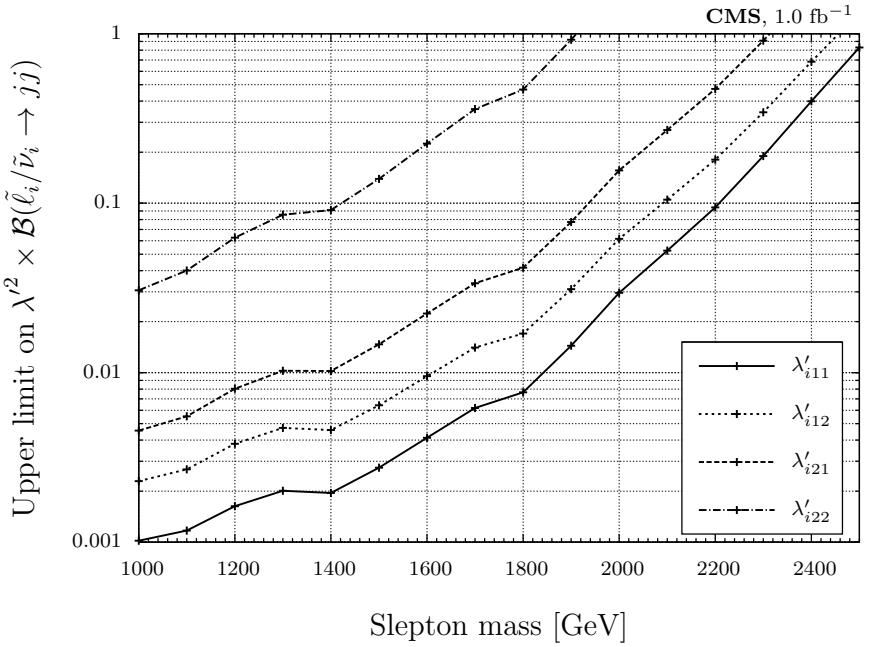

Figure 7.7: Upper bounds on $\lambda'^2 \times \mathcal{B}(\tilde{\ell}_i/\tilde{\nu}_i \to jj)$ derived from the CMS dijet resonance searches with 1 fb^{-1} of data.

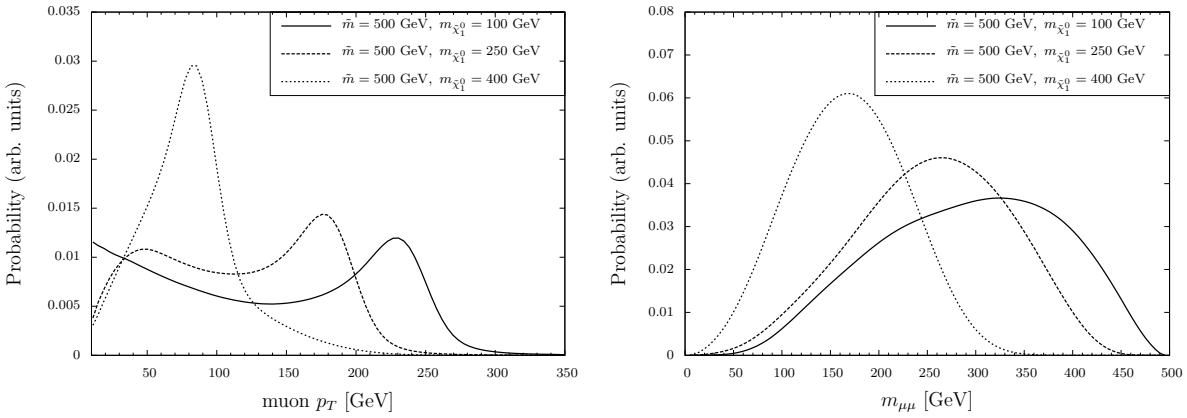

(a) p_T distribution of the isolated muons.

(b) Invariant mass distribution of the like–sign dimuon pairs.

Figure 7.8: Kinematic properties of the single slepton production process $pp \to \tilde{\ell}^*/\tilde{\nu}^* \to \mu/\nu\tilde{\chi}_1^0$ via λ'_{2jk} at the LHC with a CM energy of 7 TeV: (a) Transverse momentum distribution of the muons passing the object selection (isolation, $p_T > 10\,\text{GeV}$) of Ref. [416]; (b) Invariant mass distribution of the like–sign dimuon pairs which pass the full event selection. The slepton mass is set to $\tilde{m} = 500\,\text{GeV}$. We show the shapes for three different neutralino masses, $m_{\tilde{\chi}_1^0} = (100, 250, 500)$ GeV.

the angular distance of two objects a and b, and ϕ is the azimuthal angle. Jets are defined by the anti-k_t algorithm with a distance parameter of $R = 0.4$ and minimal transverse momentum $p_T(\text{jet}) > 7\,\text{GeV}$. The muons have to be prompt, i.e. originating from the primary vertex. This translates in our case into a requirement on the slepton lifetime to be less then $\tau < 10^{-14}$ s. Furthermore, we employ the same cone isolation criteria for the muons as in the ATLAS note [416].

We now discuss the kinematic properties of single slepton production at the LHC with 7 TeV CM energy. The slepton is forced to decay into the lightest neutralino, i.e. we consider the process[5] $pp \to \tilde{\ell}^*/\tilde{\nu}^* \to (\mu/\nu)\tilde{\chi}_1^0$. In Fig. 7.8(a) we provide the transverse momentum (p_T) distribution of the muons passing the isolation, pseudorapidity, jet separation and minimal transverse momentum ($p_T \geq 10\,\text{GeV}$) constraints, whereas Fig. 7.8(b) gives the invariant mass distribution[6] of the like-sign dimuon pairs after the full event selection (except the final $m_{\mu\mu}$ requirement). We give these distributions for three example models with different lightest neutralino masses $m_{\tilde{\chi}_1^0} = (100, 250, 400)$ GeV, slepton mass $\tilde{m} = 500\,\text{GeV}$ and a non-zero R-parity violating coupling λ'_{2jk}.

For large mass splittings between the slepton and the neutralino, $\Delta m = \tilde{m} - m_{\tilde{\chi}_1^0}$, we can identify two distinct peaks in the muon-p_T spectrum. In the first model considered ($\tilde{m} = 500\,\text{GeV}$, $m_{\tilde{\chi}_1^0} = 100\,\text{GeV}$), we have hard muons with typical p_T values around $200 - 250\,\text{GeV}$. These muons origin from the slepton decay. In contrast, the soft muons accumulating at the low end of the distribution stem from the three-body decay of the neutralino (and the chargino in the wino–like scenario). For larger neutralino masses (second and third model) the phase space for the muons from the gaugino decay increases on the one hand, leading to the migration

[5] We must include the sneutrino production even though it does not lead to like–sign dileptons. Both production processes are jointly encoded in `Herwig6.510`.

[6] Both distributions in Fig. 7.8 are obtained from Monte-Carlo simulation using the bino–like $\tilde{\chi}_1^0$ scenario, normalized to unity for a bin size of 2 GeV and then smoothened for better visualization.

of the left peak in the p_T distribution towards higher values. On the other hand, the muons from the slepton decay become softer due to the smaller Δm. In the third model considered ($\tilde{m} = 500\,\text{GeV}$, $m_{\tilde{\chi}_1^0} = 400\,\text{GeV}$), the peaks overlap at a p_T value of around $80 - 90\,\text{GeV}$. For even smaller Δm, the muons from the slepton decay will constitute the low end of the p_T spectrum.

The invariant mass distribution of the like–sign dimuon pairs shown in Fig. 7.8(b) exhibits a broad peak of approximately Gaussian shape. The peak value increases for larger mass splitting Δm.

From this discussion, we can already predict that the acceptance of the ATLAS like–sign dimuon search will decrease for (*i*) small neutralino masses and (*ii*) in the small Δm region, where the slepton and the neutralino are close in mass. In both cases, one of the muons is rather soft due to reduced phase space and thus may not fulfill the minimum p_T requirement. This is especially important for (*i*) since the neutralino decays via a three-body decay. On the other hand, in (*ii*), the invariant mass $m_{\mu\mu}$ tends to be small, thus reducing in particular the acceptance of the high $m_{\mu\mu}$ signal regions.

The (normalized) distributions in Fig. 7.8 are to a good approximation independent of the choice of j, k and the value of λ'_{2jk} (as long as it is a prompt neutralino decay). Furthermore, they are independent of whether we have a bino– or wino–like $\tilde{\chi}_1^0$ scenario[7]. However, note that the absolute number of like–sign dimuon pairs is different for the scenarios *S1* and *S2*, Section 7.2.2.

The signal acceptance $\mathcal{A}$ of the like–sign prompt dimuon search is evaluated by simulating the process $pp \to \tilde{\ell}^*/\tilde{\nu}^* \to (\mu/\nu)\tilde{\chi}_1^0$ in `Herwig6.510`. We simulated 5000 events for each point in the $(m_{\tilde{\chi}_1^0}, \tilde{m})$ mass plane, where we use step sizes of $\Delta\tilde{m} = 10\,\text{GeV}$ and $\Delta m_{\tilde{\chi}_1^0} = 20\,\text{GeV}$. For $m_{\tilde{\chi}_1^0} \leq 40\,\text{GeV}$ (light neutralino) and $m_{\tilde{\chi}_1^0} \in \{\tilde{m} - 40\,\text{GeV},\ \tilde{m}\}$ (boundary region), we decrease the neutralino mass step size to $\Delta m_{\tilde{\chi}_1^0} = 5\,\text{GeV}$ since the acceptance is rapidly changing in these regions. The acceptance maps of the four signal regions with $m_{\mu\mu} > 15\,\text{GeV},\ 100\,\text{GeV},\ 200\,\text{GeV},\ 300\,\text{GeV}$ are given in Fig. C.1 in Appendix C.2. For large parts of the $(m_{\tilde{\chi}_1^0}, \tilde{m})$ mass plane the acceptance $\mathcal{A}$ lies between 2% and 7%. However, in the regions with low neutralino masses, $m_{\tilde{\chi}_1^0} \lesssim (100 - 200)$ GeV, and in the region with small $\Delta m = \tilde{m} - m_{\tilde{\chi}_1^0}$, the search becomes insensitive ($\mathcal{A} \lesssim 2\%$), as expected from the discussion above. More details are given in Appendix C.2. The branching ratios $\mathcal{B}(\tilde{\ell} \to \ell\tilde{\chi}_1^0)$ and $\mathcal{B}(\tilde{\nu} \to \nu\tilde{\chi}_1^0)$ are calculated with `ISAJET7.64` in the same grid for different values of λ' for both the bino- and wino-like $\tilde{\chi}_1^0$ scenario.

The expected signal rate for a given coupling λ'_{2jk} and masses $\tilde{m}$, $m_{\tilde{\chi}_1^0}$ is calculated by

$$\left[\sigma^{\text{NLO}}(\tilde{\ell} \to \ell\tilde{\chi}_1^0) \times \mathcal{B}(\tilde{\ell} \to \ell\tilde{\chi}_1^0) + \sigma^{\text{NLO}}(\tilde{\nu} \to \nu\tilde{\chi}_1^0) \times \mathcal{B}(\tilde{\nu} \to \nu\tilde{\chi}_1^0)\right] \times \mathcal{A}(\tilde{m}, m_{\tilde{\chi}_1^0}), \tag{7.12}$$

where the branching ratios encode the model dependence (on the bino- or wino-like $\tilde{\chi}_1^0$ scenario). The 95% C.L. upper limits on the fiducial cross section for like–sign dimuon production provided by ATLAS are 170.24 fb, 15.68 fb, 4.76 fb and 2.8 fb for the signal regions $m_{\mu\mu} > 15\,\text{GeV},\ 100\,\text{GeV},\ 200\,\text{GeV},\ 300\,\text{GeV}$, respectively [416]. If the signal rate, Eq. (7.12), exceeds the limit in at least one of the signal regions, we consider the model as excluded.

We estimate the total uncertainty of the theory prediction to be 10%, taking into account a 5% systematic uncertainty for the parton density functions, 3% from factorization and renormalization scale uncertainties of the NLO cross section [420] and an averaged statistical uncertainty

[7] In the case of a Higgsino–like $\tilde{\chi}_1^0$, one of the peaks in the lepton-p_T spectrum would be more pronounced since we get twice as many leptons from the neutralino decays compared to the bino– and wino–like $\tilde{\chi}_1^0$ scenarios.

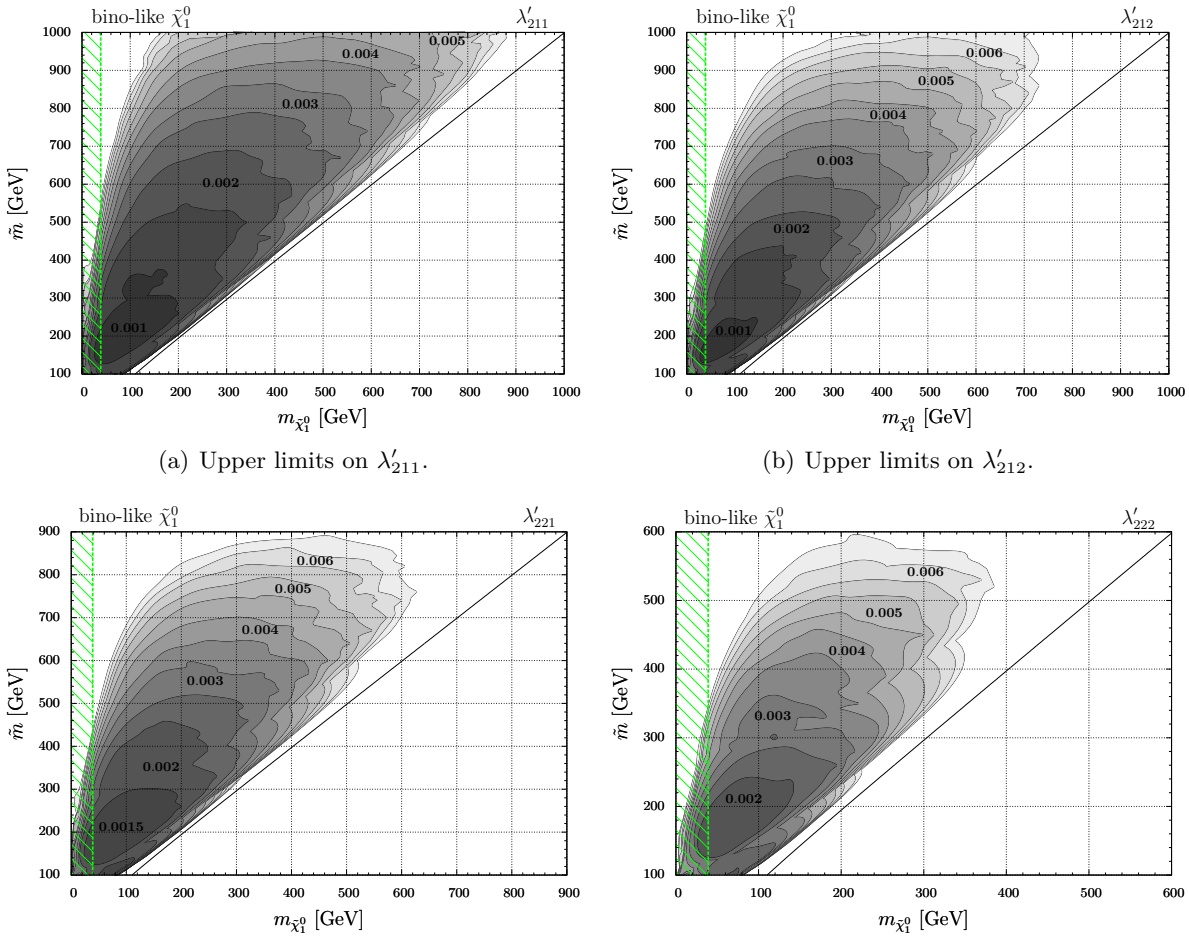

(a) Upper limits on λ'_{211}.

(b) Upper limits on λ'_{212}.

(c) Upper limits on λ'_{221}.

(d) Upper limits on λ'_{222}.

Figure 7.9: Upper bounds on λ'_{2jk} $(j,k \in \{1,2\})$ in the $(m_{\tilde{\chi}_1^0}, \tilde{m})$ mass plane in the bino-like $\tilde{\chi}_1^0$ scenario, derived from the ATLAS prompt like–sign dimuon search. The contour levels are given in steps of 0.0005. The green striped region is excluded due to the lower mass bound from LEP on the lightest neutralino, $m_{\tilde{\chi}_1^0} \geq 39\,\text{GeV}$ [199, 454].

of the acceptance estimate[8]. In order to be conservative, we reduce our signal estimate by the 10% uncertainty in the limit setting procedure.

We present the upper limits[9] on the four investigated R-parity violating couplings λ'_{2jk} $(j,k \in \{1,2\})$ within the bino–like $\tilde{\chi}_1^0$ scenario (*S1*) in Fig. 7.9. They are presented as contours in the $(m_{\tilde{\chi}_1^0}, \tilde{m})$ mass plane. The green striped region indicates the LEP lower mass limit on the lightest neutralino, $m_{\tilde{\chi}_1^0} \geq 39\,\text{GeV}$ [199, 454]. Note, that this limit is parameter dependent, see Section 7.1. The derived upper bounds on λ' range from 0.001 (dark) to 0.0065 (bright) and are displayed in steps of 0.0005 in grayscale. Since the single slepton production cross section

[8] With 5000 simulated events, the relative statistical uncertainty on a typical value of the acceptance $\mathcal{A} = 1\%$ (7%) is $\Delta\mathcal{A} = 14\%$ (5%).

[9] Due to our rather simple treatment of the systematic uncertainties of the signal we cannot claim our upper limits to be exactly at 95% C.L.. In fact, due to the conservative approach of subtracting the systematic uncertainty from the signal yield, we expect our upper limit to be "at 95% C.L. or more".

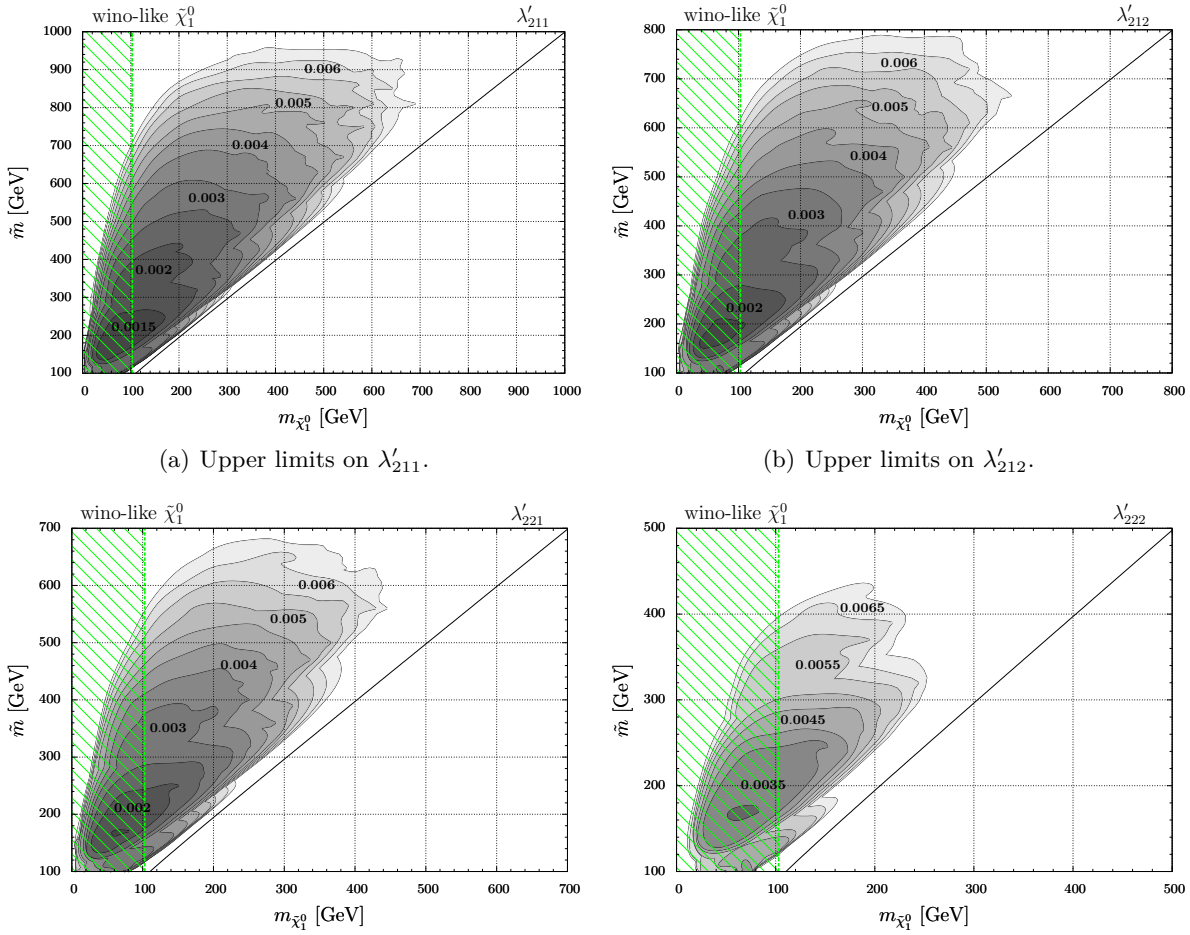

(a) Upper limits on λ'_{211}.

(b) Upper limits on λ'_{212}.

(c) Upper limits on λ'_{221}.

(d) Upper limits on λ'_{222}.

Figure 7.10: Upper bounds on λ'_{2jk} ($j,k \in \{1,2\}$) in the $(m_{\tilde{\chi}_1^0}, \tilde{m})$ mass plane in the wino-like $\tilde{\chi}_1^0$ scenario, derived from the ATLAS prompt like–sign dimuon search. The contour levels are given in steps of 0.0005. The green shaded region is excluded due to the lower mass bound from LEP on the lightest chargino, $m_{\tilde{\chi}_1^\pm} \geq 103\,\text{GeV}$ [199, 454], which is nearly mass degenerate with the lightest neutralino in these scenarios.

decreases with the slepton mass, the bounds become weaker for heavier smuons. Also, due to the insensitivity of the like–sign dimuon search in the regions of low neutralino mass and low $\Delta m = \tilde{m} - m_{\tilde{\chi}_1^0}$, we cannot obtain upper bounds on λ' in these regions.

The most stringent limits are obtained for the coupling λ'_{211} due to the larger cross section, Fig. 7.1. For a roughly elliptic region with $m_{\tilde{\chi}_1^0} \sim \tilde{m} - 100\,\text{GeV}$ and $\tilde{m} \sim (150 - 300)$ GeV, we obtain $\lambda'_{211} \leq 0.001$. Even for large smuon masses of $\lesssim \mathcal{O}(1\,\text{TeV})$, we can still derive bounds down to $\lambda'_{211} \lesssim 0.0045$. The other couplings are less constrained due to the smaller cross section, see Section 7.2.1. The weakest bounds are therefore set on λ'_{222}, ranging from 0.002 for $(m_{\tilde{\chi}_1^0}, \tilde{m}) \sim (100, 200)$ GeV to 0.0065 for smuon masses $\tilde{m} \lesssim 550\,\text{GeV}$.

We now turn to the discussion of the results in the wino–like $\tilde{\chi}_1^0$ scenario (*S2*) shown in Fig. 7.10. The LEP lower mass limit on the chargino, $m_{\tilde{\chi}_1^\pm} \geq 103\,\text{GeV}$ [199, 454], is indicated by the green striped region. As discussed in Section 7.2.2, we expect only 1/12 of the time like-sign dimuon events from the charged slepton gauge decays. Thus, the upper limits on

the R-parity violating coupling λ' are weaker. For instance, for light smuon and neutralino masses, $(m_{\tilde{\chi}_1^0}, \tilde{m}) = (100, 200)$ GeV, the upper bounds obtained in the wino–like $\tilde{\chi}_1^0$ scenario are $\lambda'_{211}, \lambda'_{212} \leq 0.0015$, $\lambda'_{221} \leq 0.002$ and $\lambda'_{222} \leq 0.0035$.

The bino-like and wino-like $\tilde{\chi}_1^0$ limits can be interpreted as the best-case and worst-case scenarios for the like–sign dilepton signature, respectively. These new limits improve current limits from the Tevatron [429, 430] on λ'_{211} by a factor $\mathcal{O}(40)$ or more.

We do not consider a Higgsino-like lightest neutralino (*S3*). As discussed in Section 7.2.2, the slepton decay to the Higgsino-like $\tilde{\chi}_1^0$, $\tilde{\chi}_2^0$ and $\tilde{\chi}_1^\pm$ is highly suppressed due to the small Yukawa coupling, and the competing R-parity violating decay $\tilde{\mu} \to jj$ would dominate, leading to an overall suppression of the like–sign dimuon signature. However, we want to remark that exploring the Higgsino-like $\tilde{\chi}_1^0$ scenario with R-parity violating couplings λ'_{3jk} and a resonantly produced (left-handed) $\tilde{\tau}_1$ would be feasible with a like–sign ditau search.

7.4 Summary of the Chapter

We have investigated the impact of early LHC data from the 7 TeV run on the resonant production of single sleptons in R-parity violating models. We presented the NLO production cross section for resonant sleptons in pp collisions at 7 TeV CM energy. We then discussed the decay modes of the slepton for three simplified models, where the lightest neutralino is either bino– (*S1*), wino–(*S2*), or Higgsino–like (*S3*). We estimated the event yield with a like–sign dilepton final state. Although these scenarios are simplified, they still represent wide regions of (realistic) GUT-based SUSY breaking scenarios like e.g. the CMSSM or the AMSB, as long as the assumed (relevant) sparticle mass hierarchy is fulfilled.

The main part of this work focused on the derivation of upper bounds on the R-parity violating couplings from recently published LHC results. First we considered the dijet signature of resonant sleptons. Using ATLAS and CMS dijet searches each with 1 fb^{-1} of data, we derived upper bounds on the R-parity violating coupling squared, λ'^2_{ijk} $(i = 1, 2, 3,\ j, k = 1, 2)$, times the branching fraction of the slepton to dijets. These limits only depend on the mass of the resonant slepton, $\tilde{m}$, and are thus complementary to low–energy upper bounds, which usually scale with the squark masses. The limits derived from the CMS search turn out to be considerably stricter than those of ATLAS. If the dijet channel is the dominant decay mode, $\mathcal{B}(\tilde{\ell}_i/\tilde{\nu}_i \to jj) \approx 100\%$, the upper bounds obtained are for instance $\lambda'_{i11} \leq 0.03$ (0.05) and $\lambda'_{i22} \leq 0.18$ (0.37) for a slepton mass $\tilde{m} = 1000$ GeV (1500 GeV). The complete ATLAS and CMS results are listed in Tab. C.1 and C.2, respectively. However, these limits from LHC dijet resonance searches only apply for a very massive spectrum where the slepton mass is in the range 0.9 TeV $\leq \tilde{m} \leq$ 2.5 TeV, since a dijet resonance search in the lower mass region is still insensitive due to the overwhelming QCD background.

We then studied the like–sign dilepton signature, which is a very promising channel for resonant slepton production due to the small SM background. Using an ATLAS search for anomalous like-sign dimuon pairs with 1.6 fb^{-1} of data, we set limits on λ'_{211}, λ'_{212}, λ'_{221} and λ'_{222} in the lightest neutralino–slepton mass plane, $(m_{\tilde{\chi}_1^0}, \tilde{m})$, assuming a bino–like (*S1*) or wino–like (*S2*) lightest neutralino LSP. These bounds range from 0.001 (for low slepton and neutralino masses $\sim (100 - 300)$ GeV in *S1*) to 0.0065 (heavier slepton and lightest neutralino masses up to 1 TeV). The strictest bounds are obtained for the λ'_{211} coupling for a bino–like lightest neutralino (*S1*). Our results improve the bounds on λ'_{211} obtained from the Tevatron by a factor $\gtrsim \mathcal{O}(40)$. For instance, for a slepton mass $\tilde{m} = 300$ (400) GeV and a neutralino

mass $m_{\tilde{\chi}_1^0} = 150$ (200) GeV, the upper bound $\lambda'_{211} < 0.04$ (0.08) obtained by DØ [429, 430] has improved to 0.001 (0.0015) by our analysis of the LHC data.

Furthermore, we discussed in some detail the performance of the ATLAS like–sign dimuon search on the resonant slepton signal. For this, we presented the p_T distribution of the isolated muons and the like-sign dimuon invariant mass distribution for three different mass configurations [$\tilde{m} = 500\,\text{GeV}$, $m_{\tilde{\chi}_1^0} = (100, 250, 400)$ GeV]. The signal acceptance is reduced for (*i*) small neutralino masses and (*ii*) for a low mass difference between the slepton and the lightest neutralino. In either case one of the muons has a rather low transverse momentum.

We want to remark that scalar leptoquark searches at ATLAS [480] and CMS [481, 482] are also sensitive to resonant slepton production. These analyses searched for two jets associated with either two leptons or one lepton and missing energy (coming from a neutrino). As discussed in Section 7.2.2, this is also a typical signature of resonant slepton production. Furthermore, the analyses with one final state lepton should perform better than the (like–sign) dilepton search in the parameter region of small mass difference between the slepton and the lightest neutralino, where the lepton detection efficiency is low due to reduced phase-space.

ATLAS and CMS collaborations are encouraged to perform (in a similar manner) searches for anomalous production of like–sign ditau pairs. This would shed new light on the RPV couplings λ'_{3ij} $(i, j = 1, 2)$ assuming a resonantly produced $\tilde{\tau}_1$ with non-negligible left-handed component.

Comment on the current experimental status

After this study was published, ATLAS and CMS collaborations presented updated results for the dijet and like-sign dimuon searches using larger datasets. No significant deviation from the SM expectation was found in any of these updated analyses. Upper cross section limits from the ATLAS dijet resonances search were obtained for the full 7 TeV dataset of $4.8\,\text{fb}^{-1}$ [483], and later also for $13.0\,\text{fb}^{-1}$ of data from the 8 TeV run [484]. Roughly estimated (and ignoring potential statistical fluctuations), the derived limits on $\lambda'^2 \times \mathcal{B}(\tilde{\ell}_i/\tilde{\nu}_i \to jj)$ improve by $\sim 35\%$ with respect to the limits presented in Fig. 7.6 in the light of the full 7 TeV dataset. The limits from the 8 TeV run have only been presented for resonance masses ≥ 1.5 TeV and yield a further improvement of the limit by $\sim 20\%$.

A similar (or even greater) improvement of the upper limits on $\lambda'^2 \times \mathcal{B}(\tilde{\ell}_i/\tilde{\nu}_i \to jj)$ for slepton masses ≥ 1.0 TeV can also be derived from the updated results of the CMS dijet resonances search [485], which is based on the full 8 TeV dataset of $19.6\,\text{fb}^{-1}$. Roughly estimated, the upper limit on λ'_{i11} for a slepton mass of $\tilde{m} = 1$ TeV and $\mathcal{B}(\tilde{\ell}_i/\tilde{\nu}_i \to jj) \approx 100\%$ improves from 0.03 to ~ 0.02.

ATLAS published results based on the full 7 TeV dataset of $4.8\,\text{fb}^{-1}$ for the search for anomalous production of like–sign lepton pairs, considering both electrons and muons [486]. Due to a refined search analysis and more statistics, the fiducial cross section limits on the different dilepton invariant mass bins improved roughly by a factor of 10. Ignoring possible changes in the signal acceptance between the old and new analysis, the presented limits on λ'_{2jk} $(j, k \in \{1, 2\})$ would improve by a factor of $\sim 1/\sqrt{10} \approx 0.3$. Moreover, similar limits could be derived on the *R*-parity violating couplings λ'_{1jk} $(j, k \in \{1, 2\})$ by using the like–sign dielectron results and assuming a resonantly produced left-handed selectron.

Searches for anomalous production of like–sign lepton pairs with or without additional *b*-jets have also been carried out by CMS [487, 488] using the full available dataset from the 7 and 8 TeV run. These searches are also sensitive to resonant slepton production.

CHAPTER 8

Conclusions

Understanding the origin of EWSB is one of the major challenges of modern particle physics. A connection of the EWSB mechanism to BSM physics is strongly motivated by the hierarchy problem. The direct search for new particles predicted by these BSM theories is one of the primary goals of collider experiments.

The progress towards these research goals has been drastically increased in the LHC era. Already the LHC data from the first running phase at CM energies of 7 and 8 TeV led to the long-awaited discovery of a Higgs boson. This initiated a new era of particle physics, in which accurate measurements of the Higgs boson signal rates at present and future colliders need to be performed. These are crucial to test the SM predictions of the Higgs couplings. At the same time, such measurements probe indirectly the effects of new physics beyond the SM, as these can lead to significantly different Higgs boson production and decay rates.

Another lesson learned from the first LHC run is that BSM physics, in particular constrained supersymmetric models like the CMSSM, is not just "around the corner" as has been anticipated from global fit analyses of low-energy and astrophysical observables before the LHC start-up. The non-observation in the large class of direct searches for SUSY particles have led to severe constraints on the SUSY parameter space.

In this thesis we have presented phenomenological studies investigating the implications of early LHC results for models beyond the SM, mostly focusing on supersymmetric models. The presented work covers different aspects in this wide field of research. Extensive summaries of these studies have been given at the end of the each chapter.

We described the development and basic concepts of the public computer codes `HiggsBounds` and `HiggsSignals`. These tools provide a quick and convenient framework, in which the Higgs sector predictions of arbitrary BSM models are confronted with the experimental results from Higgs boson searches at the LEP, Tevatron and LHC experiments. While `HiggsBounds` tests the model predictions against upper limits on the Higgs boson signal cross sections, `HiggsSignals` evaluates the χ^2 compatibility of the model with the Higgs mass and signal rate measurements from the Tevatron and LHC experiments. Great insights into the experimental validity of BSM models can be gained by employing these two codes in parameter scans or global fit analyses.

The χ^2 output from `HiggsSignals` can be used to probe for possible deviations from the SM predictions of the Higgs couplings in the current experimental data. We presented a systematic analysis of benchmark scenarios, in which the SM predicted Higgs production cross sections and partial widths are modified by scale factors. Going from highly constrained to very general

selections of free Higgs coupling scale factors, we found no clear hint for deviations from the SM prediction. In fact, due to the smaller degrees of freedom in these models, all considered scenarios yield slightly lower $\mathcal{P}$-values than the SM $\mathcal{P}$-value of $\sim 35.0\%$. Thus, the SM is in remarkable agreement with the current data. However, there is still ample room for possible deviations from the SM Higgs couplings at the order of $10 - 40\%$ in the current data. We studied how this precision can be improved with future data from upcoming LHC runs as well as with future measurements from the ILC. Considering the fact that the LHC has not found any signs of new physics in the first run of the LHC, potential deviations from the SM Higgs boson couplings are anticipated to be small. Thus, precisions at the sub-percent level in the determination of Higgs couplings, which can only be reached at the later stages of the anticipated ILC program, might be needed to see effects of new physics in the Higgs couplings.

We furthermore studied the implications of the Higgs boson measurements for the MSSM by performing a global fit with of the phenomenological MSSM with seven free parameters. We showed that the MSSM provides an excellent fit to the current data if the discovered Higgs state is interpreted to be the light $\mathcal{CP}$-even Higgs boson of the MSSM. In this case, large values of the pseudoscalar Higgs boson mass, m_A, are preferred, i.e. the decoupling regime of the MSSM is favored. In this case, the light $\mathcal{CP}$-even Higgs boson has automatically SM-like couplings. Very light stops with masses $\lesssim 300\,\text{GeV}$ are disfavored within this interpretation, and a large mixing in the stop sector is required if the lighter stop mass is not too far above 1 TeV. We furthermore investigated the possibility of interpreting the discovered Higgs state in terms of the heavy $\mathcal{CP}$-even Higgs boson of the MSSM. In our fit analysis from November 2012 we found an acceptable fit quality within this rather exotic scenario. It is challenged by various BSM Higgs boson searches, in particular $H \to \tau\tau$ as well as light charged Higgs boson searches, since all MSSM Higgs states are light. We showed that the latest ATLAS results from charged Higgs boson searches in top quark decays excludes the entire low-M_H benchmark scenario at the 95% C.L.. It remains to be seen in a future analysis, whether this limit, together with other updated constraints and observables, is sufficient to fully exclude the heavy Higgs interpretation of the MSSM.

In the last study presented in this thesis, we investigated the LHC collider signatures arising from resonant slepton production in supersymmetric models with R-parity violation. We confronted these models with the null-results from early LHC searches from the 7 TeV run for dijet resonances and anomalous production of like–sign muon pairs. We derived bounds on the coupling strengths of the relevant R-parity violating operators. These bounds exceed the previously existing limits from the Tevatron experiment by a factor of $\mathcal{O}(40)$.

In 2015 the LHC will continue to explore the new physics landscape with a significantly increased CM energy. The new data may open our eyes to what lies beyond the SM.

Let's stay excited!

Appendix

APPENDIX A

Experimental Data

A.1 Experimental Data in HiggsBounds

The program HiggsBounds is continuously updated with the latest experimental results as they become available. Older results, which have been surpassed in sensitivity by newer analyses, are removed. For a detailed list of references for the currently implemented experimental results, we refer the reader to the latest HiggsBounds documentation [28].

Here, we briefly comment on the impact of the latest ATLAS results from light charged Higgs searches [261], shown in Fig. 3.3, on the results shown in Section 4.1, in which this limit has not been applied. As also discussed in other parts of this thesis, this limit is interesting for constraining the MSSM (and other models with multiple Higgs doublets) in the region $M_{H^\pm} < 160$ GeV. In Fig. A.1 we show an updated version of the results from charged Higgs exclusion in the $m_h^{\text{mod+}}$ scenario presented in Fig. 4.3(c). The new limit excludes small values of M_A for all $\tan\beta$. Moreover, it also excludes the whole parameter space of the MSSM low-M_H scenario, as has been discussed in Section 6.1. This new ATLAS charged Higgs limit is included in HiggsBounds version 4.1.0.

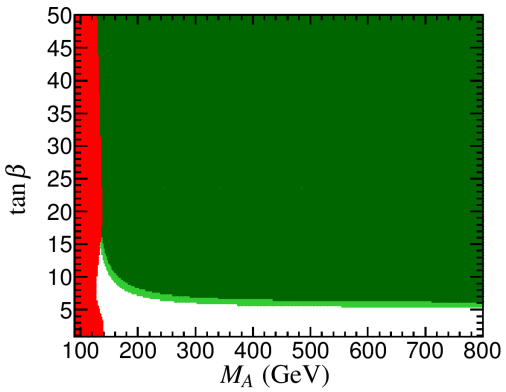

Figure A.1: Updated exclusion region from charged Higgs boson searches in the $m_h^{\text{mod+}}$ scenario using HiggsBounds-4.1. This figure should be compared to Fig. 4.3 (right).

A.2 Projected sensitivity of future signal rate measurements

The future estimates of signal strength measurements in various channels at the LHC for integrated luminosities of $300\,\text{fb}^{-1}$ and $3000\,\text{fb}^{-1}$ are given in Tab. A.1 for ATLAS [377] and CMS [378]. In Tab. A.2 we list the estimated cross section and signal rate measurements at the ILC [91]. These values are used for the study of the LHC and ILC capabilities of Higgs coupling determination presented in Section 5.3.

Analysis	68% C.L. precision		Assumed signal composition [in %]				
	$300\,\text{fb}^{-1}$	$3000\,\text{fb}^{-1}$	ggH	VBF	WH	ZH	$t\bar{t}H$
ATL $(pp) \to h \to \gamma\gamma$ (0jet) [377]	0.12	0.05	91.6	2.7	3.2	1.8	0.6
ATL $(pp) \to h \to \gamma\gamma$ (1jet) [377]	0.14	0.05	81.8	13.2	2.9	1.6	0.5
ATL $(pp) \to h \to \gamma\gamma$ (VBF-like) [377]	0.43	0.16	39.2	58.4	1.4	0.8	0.3
ATL $(pp) \to h \to \gamma\gamma$ (VH-like) [375]	0.77	0.25	2.5	0.4	63.3	15.2	18.7
ATL $(pp) \to h \to \gamma\gamma$ ($t\bar{t}H$-like) [375]	0.54	0.16	0.0	0.0	0.0	0.0	100.0
ATL $(pp) \to h \to WW$ (0jet) [377]	0.08	0.05	98.2	1.8	0.0	0.0	0.0
ATL $(pp) \to h \to WW$ (1jet) [377]	0.17	0.10	88.4	11.6	0.0	0.0	0.0
ATL $(pp) \to h \to WW$ (VBF-like) [375]	0.20	0.09	8.1	91.9	0.0	0.0	0.0
ATL $(pp) \to h \to ZZ$ (ggF-like) [377]	0.06	0.04	88.7	7.2	2.0	1.4	0.7
ATL $(pp) \to h \to ZZ$ (VBF-like) [377]	0.31	0.16	44.7	53.2	0.7	0.4	1.0
ATL $(pp) \to h \to ZZ$ (VH-like) [377]	0.31	0.12	30.1	9.0	34.8	12.1	14.0
ATL $(pp) \to h \to ZZ$ ($t\bar{t}H$-like) [377]	0.44	0.16	8.7	1.7	1.7	3.1	84.8
ATL $(pp) \to h \to Z\gamma$ [377]	1.45	0.54	87.6	7.1	3.1	1.7	0.6
ATL $(pp) \to h \to \mu\mu$ [377]	0.45	0.15	87.6	7.1	3.1	1.7	0.6
ATL $(pp) \to h \to \mu\mu$ ($t\bar{t}H$) [375]	0.72	0.23	0.0	0.0	0.0	0.0	100.0
ATL $(pp) \to h \to \tau\tau$ (VBF-like) [377]	0.16	0.12	19.8	80.2	0.0	0.0	0.0
CMS $(pp) \to h \to \gamma\gamma$ [378]	0.06	0.04	87.6	7.1	3.1	1.7	0.6
CMS $(pp) \to h \to WW$ [378]	0.06	0.04	88.1	7.1	3.1	1.7	0.0
CMS $(pp) \to h \to ZZ$ [378]	0.07	0.04	88.1	7.1	3.1	1.7	0.0
CMS $(pp) \to h \to Z\gamma$ [378]	0.62	0.20	87.6	7.1	3.1	1.7	0.6
CMS $(pp) \to h \to bb$ [378]	0.11	0.05	0.0	0.0	57.0	32.3	10.7
CMS $(pp) \to h \to \mu\mu$ [378]	0.40	0.20	87.6	7.1	3.1	1.7	0.6
CMS $(pp) \to h \to \tau\tau$ [378]	0.08	0.05	68.6	27.7	2.4	1.4	0.0

Table A.1: Projected experimental precision (i.e. without theory uncertainty) of signal strength measurements from ATLAS and CMS at $\sqrt{s} = 14\,\text{TeV}$ for $300\,\text{fb}^{-1}$ and $3000\,\text{fb}^{-1}$ (HL–LHC). The numbers from CMS correspond to Scenario 2 of their projections, however, we treat them as purely experimental precisions, see the discussion in Section 5.3.1.

$\mathcal{L}$ and $\sqrt{s}$	250 fb^{-1} at 250 GeV		500 fb^{-1} at 500 GeV			1 ab^{-1} at 1 TeV	
	ZH	$\nu\bar{\nu}H$	ZH	$\nu\bar{\nu}H$	$t\bar{t}H$	$\nu\bar{\nu}H$	$t\bar{t}H$
$\Delta\sigma/\sigma$	2.6%	-	3.0%	-	-	-	-
BR($H \to$ inv.)	$< 0.9\%$	-	-	-	-	-	-
mode	$\Delta(\sigma \cdot \text{BR})/(\sigma \cdot \text{BR})$						
$H \to b\bar{b}$	1.2%	10.5%	1.8%	0.7%	28%	0.5%	6.0%
$H \to c\bar{c}$	8.3%	-	13.0%	6.2%	-	3.1%	-
$H \to gg$	7.0%	-	11%	4.1%	-	2.6%	-
$H \to WW^{(*)}$	6.4%	-	9.2%	2.4%	-	1.6%	-
$H \to \tau^+\tau^-$	4.2%	-	5.4%	9.0%	-	3.1%	-
$H \to ZZ^{(*)}$	18%	-	25%	8.2%	-	4.1%	-
$H \to \gamma\gamma$	34%	-	34%	23%	-	8.5%	-
$H \to \mu^+\mu^-$	100%	-	-	-	-	31%	-
$\mathcal{L}$ and $\sqrt{s}$	1150 fb^{-1} at 250 GeV		1600 fb^{-1} at 500 GeV			2.5 ab^{-1} at 1 TeV	
	ZH	$\nu\bar{\nu}H$	ZH	$\nu\bar{\nu}H$	$t\bar{t}H$	$\nu\bar{\nu}H$	$t\bar{t}H$
$\Delta\sigma/\sigma$	1.2%	-	1.7%	-	-	-	-
BR($H \to$ inv.)	$< 0.4\%$	-	-	-	-	-	-
mode	$\Delta(\sigma \cdot \text{BR})/(\sigma \cdot \text{BR})$						
$H \to b\bar{b}$	0.6%	4.9%	1.0%	0.4%	16%	0.3%	3.8%
$H \to c\bar{c}$	3.9%	-	7.2%	3.5%	-	2.0%	-
$H \to gg$	3.3%	-	6.0%	2.3%	-	1.4%	-
$H \to WW^{(*)}$	3.0%	-	5.1%	5.1%	-	1.0%	-
$H \to \tau^+\tau^-$	2.0%	-	3.0%	3.0%	-	2.0%	-
$H \to ZZ^{(*)}$	8.4%	-	14.0%	14.0%	-	2.6%	-
$H \to \gamma\gamma$	16.0%	-	19.0%	13.0%	-	5.4%	-
$H \to \mu^+\mu^-$	46.6%	-	-	-	-	20.0%	-

Table A.2: Expected accuracies for the measurements of signal rates and absolute production cross sections at various ILC stages of the baseline program (*above*) and after a luminosity upgrade (*below*) for a Higgs boson with mass $m_H = 125\,\text{GeV}$. Upper limits on BR($H \to$ inv.) are given at 95% C.L.. The numbers are taken from Ref. [91], cf. also Ref. [92].

A.3 Higgs signal rate observables of the original pMSSM–7 fit

In Tab. A.3 we list the signal strength measurements from the Tevatron and LHC experiments, which were used as observables in the original analysis from 2012 of the phenomenological MSSM (presented in Section 6.2).

Channel	$\sqrt{s}$ [TeV]	$\hat{\mu}_{\text{low}}$	$\hat{\mu}$	$\hat{\mu}_{\text{up}}$	Reference
ATLAS data at $\hat{M}_H = 126.5\,\text{GeV}$					
$b\bar{b}$	7	-1.646	0.510	2.680	[391]
$\tau\tau$	7	-1.550	0.464	2.011	[391]
WW	7	-0.164	0.438	1.103	[489]
WW	8	1.308	1.920	2.536	[490]
$\gamma\gamma$ (inclusive)	7	1.397	2.155	2.903	[325]
$\gamma\gamma$ (inclusive)	8	1.054	1.685	2.326	[325]
ZZ	7	0.405	1.080	2.177	[491]
ZZ	8	0.400	1.049	1.708	[492]
CMS data at $\hat{M}_H = 125.0\,\text{GeV}$					
$b\bar{b}$ (VH)	7	-0.606	0.588	1.824	[392]
$b\bar{b}$ (VH)	8	-0.441	0.424	1.535	[392]
$b\bar{b}$ ($t\bar{t}H$)	7	-2.624	-0.771	1.288	[392]
$\tau\tau$ (0/1 jet)	7	-0.400	1.000	2.441	[392]
$\tau\tau$ (0/1 jet)	8	0.588	2.153	3.635	[392]
$\tau\tau$ (VBF)	7	-2.912	-1.718	-0.359	[392]
$\tau\tau$ (VBF)	8	-3.035	-1.759	-0.400	[392]
$\tau\tau$ (VH)	7	-2.418	0.671	4.788	[392]
$\gamma\gamma$ (Dijet loose)	8	-2.660	-0.626	1.409	[318]
$\gamma\gamma$ (Dijet Tight)	8	-0.267	1.289	2.868	[318]
$\gamma\gamma$ (Untagged 3)	8	2.007	3.754	5.549	[318]
$\gamma\gamma$ (Untagged 2)	8	-0.195	0.930	2.080	[318]
$\gamma\gamma$ (Untagged 1)	8	0.475	1.504	2.533	[318]
$\gamma\gamma$ (Untagged 0)	8	0.212	1.456	2.701	[318]
$\gamma\gamma$ (Dijet)	7	2.174	4.209	6.243	[318]
$\gamma\gamma$ (Untagged 3)	7	-0.099	1.528	3.132	[318]
$\gamma\gamma$ (Untagged 2)	7	-0.434	0.715	1.887	[318]
$\gamma\gamma$ (Untagged 1)	7	-0.291	0.643	1.600	[318]
$\gamma\gamma$ (Untagged 0)	7	1.337	3.132	4.974	[318]
WW (0/1 jet)	7	-0.029	0.588	1.206	[392]
WW (0/1 jet)	8	0.176	0.835	1.494	[392]
WW (VBF)	7	-3.900	-1.306	0.918	[392]
WW (VBF)	8	-0.523	1.371	3.347	[392]
WW (VH)	7	-5.753	-2.829	0.341	[392]
ZZ	7	0.176	0.671	1.371	[392]
ZZ	8	0.259	0.794	1.494	[392]
Tevatron data at $\hat{M}_H = 125.0\,\text{GeV}$					
$b\bar{b}$	1.96	1.290	1.970	2.710	[493]
$\gamma\gamma$	1.96	1.080	3.620	6.580	[493]
WW	1.96	0.000	0.320	1.450	[493]

Table A.3: Experimentally measured values for the Higgs signal strength modifiers, and their corresponding uncertainties (lower/upper edges of $1\,\sigma$ error bars), in the various channels.

APPENDIX B

Additional Information on HiggsSignals

B.1 Studies of the $\mathcal{P}$-value of χ^2 fits to Higgs signal rate observables

As explained in detail in Section 4.2, HiggsSignals employs a χ^2 approximation to allow for a very fast evaluation of the model compatibility with public results from Higgs rate and mass measurements in arbitrary models. Comparisons to the results from ATLAS and CMS show that this implementation yields a good approximation to the official results, cf. Section 4.2.4. This allows for a reliable phenomenological analysis of a very large variety of models of new physics against the Higgs search results.

In such studies, the $\mathcal{P}$-value, i.e. the statistical agreement of the measured results with the predictions from a theory, is of high interest. This can be evaluated by means of toy Monte Carlo (MC) techniques. In this section we study to what extent the specific implementation of the χ^2 evaluation in HiggsSignals impacts the $\mathcal{P}$-value calculation. This is also of interest for other implementations of χ^2 tests against Higgs mass and rate measurements [234, 270, 272, 274, 293, 294, 305–311], which employ different levels of detail concerning the implementation of uncertainties (correlated/uncorrelated, relative/absolute, symmetric/asymmetric, etc.). In order to evaluate the impact of the calculation of uncertainties and correlations on the χ^2, we investigate the $\mathcal{P}$-value of a SM-like Higgs boson modified by a global scale parameter κ. It is tested against the latest rate measurements from ATLAS, CMS, CDF and DØ, as presented in Section 4.2.3. Using a toy MC technique the $\mathcal{P}$-value is then evaluated from the HiggsSignals calculated χ^2 for sets of pseudo-measurements thrown around the best fit point and according to the covariance matrix, which we obtain at the best fit point. The exact $\mathcal{P}$-value based on the full likelihood distribution can of course only be calculated by the experimental collaborations. However, no combination of the experiments at LHC and the Tevatron is available, such that an approximate calculation is of interest.

The default treatment of uncertainties in HiggsSignals suggests a deviation from the ideal χ^2 distribution in both the signal strength part, χ^2_μ, and the Higgs mass part, χ^2_m. Therefore, the $\mathcal{P}$-value can only approximately be extracted from the observed χ^2 at the best fit point and the number of degrees of freedom (ndf) assuming an ideal χ^2 distribution. Instead, toy measurements have to be employed to take into account the following effects in the $\mathcal{P}$-value evaluation:

1. The usage of asymmetric (upper and lower) uncertainties in the rate measurements instead

of averaged (symmetric) uncertainties. The choice for the observed rate uncertainty entering the χ^2 evaluation, $\Delta\hat{\mu}$, is dependent on the relative position of the model-predicted signal rate μ with respect to the observed value $\hat{\mu}$:

$$\Delta\hat{\mu} = \begin{cases} \Delta\hat{\mu}^{\text{up}} & , \quad \text{if} \quad \mu > \hat{\mu} \\ \Delta\hat{\mu}^{\text{low}} & , \quad \text{if} \quad \mu < \hat{\mu} \end{cases} . \tag{B.1}$$

2. The usage of relative instead of absolute rate uncertainties. The luminosity uncertainty is scaled with the observed $\hat{\mu}$ value, while the theoretical rate uncertainties are scaled with the predicted μ value in HiggsSignals. Where the experimental systematics can not be attributed to either signal or background, they are treated as background-related and kept constant. This combination generally provides a good approximation of the experimental results.

In case that the mass is also fitted, two additional effects arise:

3. Theoretical mass uncertainties can be treated as (anti-)correlated Gaussian errors in the χ^2_m evaluation. The theory mass uncertainty of two mass observables, $\hat{m}_i$, $\hat{m}_j$, is anti-correlated if the predicted mass lies in between these measurements, $\hat{m}_i < m < \hat{\mu}_j$.

4. The automatic assignment of the Higgs boson to the observables introduces a highly non-trivial deviation from the ideal χ^2 shape in both χ^2_μ and χ^2_m. This procedure takes care that the comparison of the predicted signal rate μ (at mass m) with the measured signal strength $\hat{\mu}$ (at mass $\hat{m}$) is still approximately valid, or otherwise adds a χ^2 penalty to χ^2_μ. In the latter case, the mass measurement associated with the unassigned observable does not enter χ^2_m anymore. This issue is of course only relevant if a model with more than one Higgs boson is studied. It is not further studied in the examples below.

The items (1, 2) lead to a dependence of the covariance matrix C_μ in the χ^2_μ calculation on both the observed signal rate values, $\hat{\mu}$, and the model-predicted signal rate values, μ. Hence, it changes for each set of pseudo-measurements and depends on the tested model. The items (3, 4) are of relevance only in the case of a non-trivial model prediction of the Higgs mass. Here, we choose a fixed Higgs mass of $m_H = 125.7\,\text{GeV}$. We ensure a full assignment of all observables within HiggsSignals, while the actual constant χ^2 contribution from the Higgs mass measurements is of no further relevance in this study. It should be noted, however, that we hereby make the approximation/assumption, that all signal rates measured by the experiments for the Higgs signal at various mass positions between 124.3 GeV and 126.8 GeV can be compared with the hypothesized Higgs state at $m_H = 125.7\,\text{GeV}$.

As a simple generic toy model we employ a fit with only one free parameter, namely a global Higgs coupling scale factor κ affecting all Higgs couplings to bosons and fermions in the same way, thus the SM predictions for the Higgs boson signal rates are universally scaled by κ^2. The toy data is created using the covariance matrix constructed under the principles outlined above and evaluated at the best fit point. The resulting distributions of the minimal χ^2 from the toy experiments thrown around the best fit point in μ is shown in Fig. B.1. In Fig. B.1(a), the main effects leading to a deviation from the naive χ^2-distribution are deactivated: Absolute rate uncertainties are used instead of relative ones for all statistical and systematic errors, and the experimental uncertainties are symmetrized. As expected, a nearly perfect χ^2 shape is obtained. The original best fit point is located at $\kappa^{\text{BF}} = 0.977$ with $\chi^2_{\text{BF,abs/sym}} = 80.3$. The

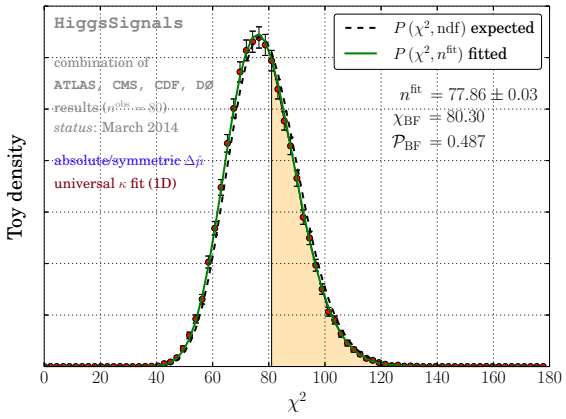

(a) Absolute and symmetrical rate uncertainties.

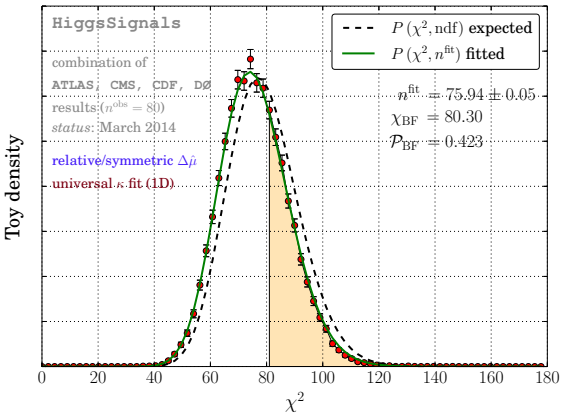

(b) Relative and symmetrical rate uncertainties

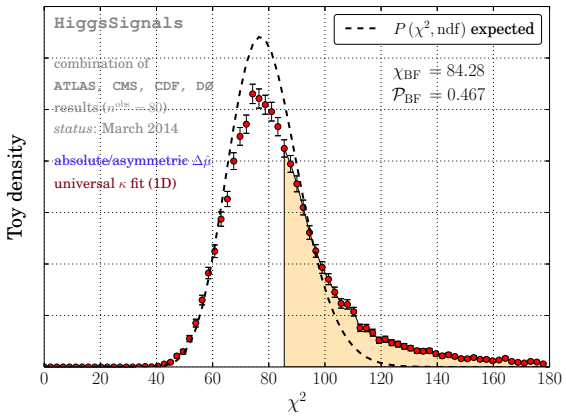

(c) Absolute and asymmetric rate uncertainties.

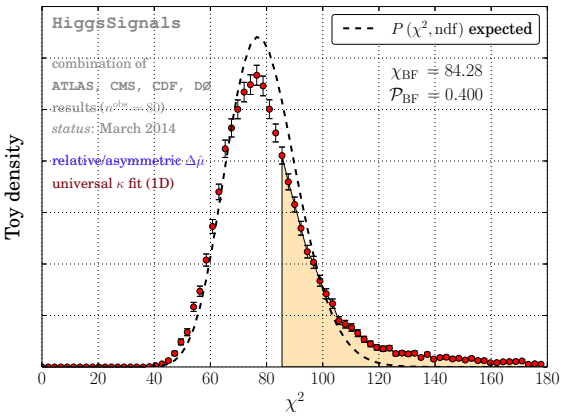

(d) Relative and asymmetric rate uncertainties.

Figure B.1: χ^2 outcomes of the SM predicted Higgs rates tested against pseudo signal rate measurements in a fit setup with 80 rate measurements and one free parameter, a global scale factor κ for all Higgs couplings. The fits are performed with different `HiggsSignals` settings: In (a,c) the luminosity and theory rate uncertainties are kept at their absolute values whereas in (b,d) they are taken relative to the (pseudo-)measured signal rates as evaluated from the original measurements. In (a,b) the signal rate uncertainties $\Delta\hat{\mu}$ are implemented as averaged (symmetrical) values, while (c,d) asymmetrical upper and lower uncertainties as given in the original measurements are employed. The black dashed line shows the expected χ^2 distribution for 80 signal rate observables and one parameter. The solid, green graph shows the best-fitting χ^2 probability function to the toy outcomes. The yellow area underneath this curve as calculated from the observed best-fit χ^2 value (obtained from the original measurements) to ∞ corresponds to the $\mathcal{P}$-value.

$\mathcal{P}$-value is given by the area under the obtained χ^2 distribution for $\chi^2 \geq \chi^2_{\text{BF}}$. In this treatment we obtain $\mathcal{P}^{\text{BF}}_{\text{abs/sym}} = 48.7\%$, indicating very good agreement of all Higgs rate measurements with the toy model chosen here. Note, that the best fit point is extremely close to the SM (with $\kappa = 1$), which features a $\chi^2_{\text{SM,abs/sym}} = 80.4$ in this treatment and thus a very similar $\mathcal{P}$-value.

The more realistic treatment of the uncertainties, however, has significant impact on the $\mathcal{P}$-value, as shown in Fig. B.1(d). The full model dependence of the covariance matrix is used including relative errors and asymmetric experimental uncertainties. This is the most accurate

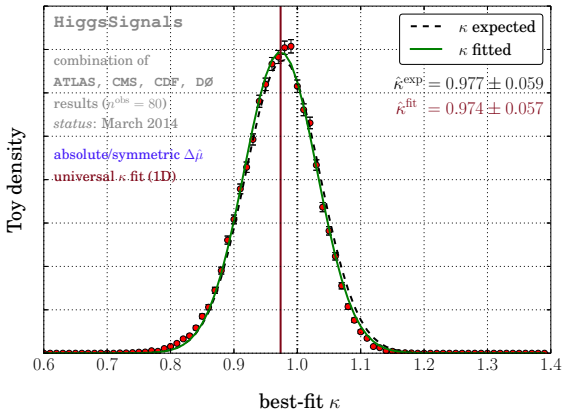

(a) Absolute and symmetrical rate uncertainties.

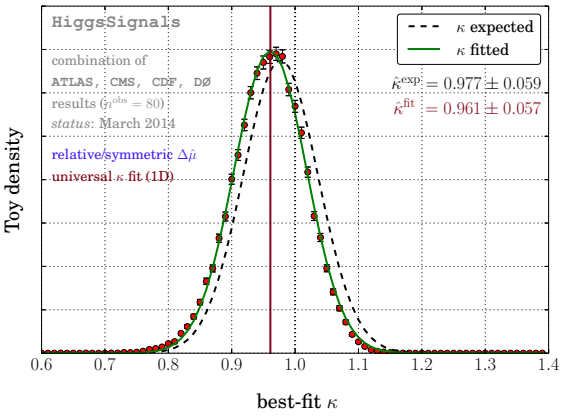

(b) Relative and symmetrical rate uncertainties

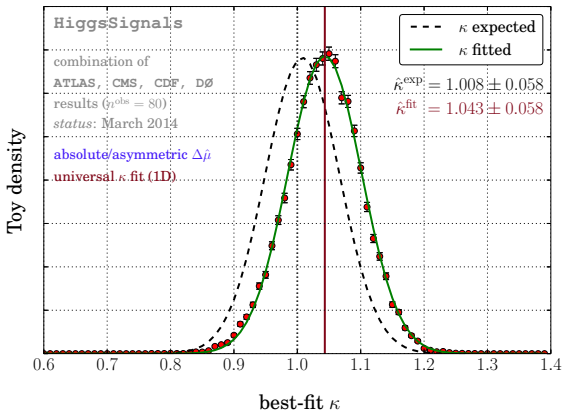

(c) Absolute and asymmetric rate uncertainties.

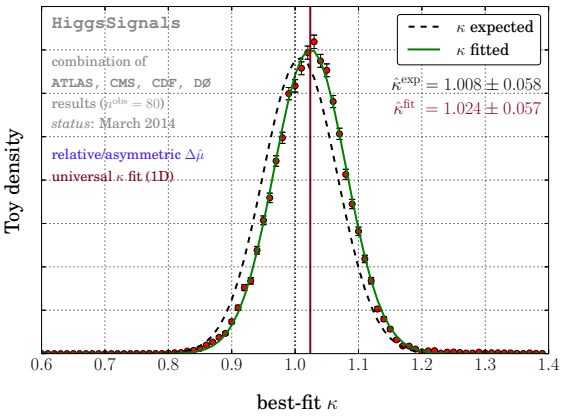

(d) Relative and asymmetric rate uncertainties.

Figure B.2: Best fit values μ of the same toy fits and HiggsSignals settings as discussed in Fig. B.1. The black dashed line shows the expected Gaussian distribution for the original best fit point and 1σ uncertainties extracted at $\Delta\chi^2 = \chi^2 - \chi^2_{\text{BF}} = 1$. The solid, green curve shows the fit of a Gaussian to the toy outcomes.

approximation to the real likelihood distribution and thus provides a more accurate guess of the $\mathcal{P}$-value than the naive calculation above, where these effects have been ignored. The result $\mathcal{P}^{\text{BF}}_{\text{rel/asym}} = 40.0\%$ differs from the previously obtained $\mathcal{P}^{\text{BF}}_{\text{abs/sym}}$. More importantly, the shape of the histogram of the obtained χ^2_{min} values from the toy fits does not follow an ideal χ^2 distribution anymore. More toy outcomes accumulate in the tail of the distribution at larger χ^2 values, thus leading to a slightly improved $\mathcal{P}$-value of the original best fit point than expected when assuming an ideal χ^2 shape. Toy MC studies like this will be of greater importance once the data is more precise, and in particular if significant deviations between the SM and the data emerge. χ^2 analyses that do not take into account the effects described above might thus lead to conclusion significantly deviating from the full results.

In order to show the origin of the deviation of the $\mathcal{P}$-value from the idealized implementation, Fig. B.1(a), the two major effects yielding deviations from the naive expectation are singled out in Fig. B.1(b) and (c). In Fig. B.1(b), only the effect of relative errors, cf. item (2) above,

is applied while the uncertainties are kept symmetrized. It can be seen that the treatment of relative uncertainties by itself has rather small effects. This is because the preferred range of the global scale factor κ is with $\Delta\kappa \sim 6\,\%$ already quite narrow. Hence, κ varies only in a small range and the impact from uncertainties varying with κ is rather insignificant. However, the picture will change in more complex models with more freedom in the variation of individual rates, including some of the benchmark scale factor fits that are discussed in Section 5.2.

In Fig. B.1(c) the effect of asymmetric errors, cf. item (1) above, is studied. In this case we hold the values of the uncertainties fixed for every toy measurement (absolute uncertainties). It can be seen that for the $\mathcal{P}$-value this effect fully dominates the full implementation in Fig. B.1(d) and should not be omitted in any implementation, since it could have a significant effect on the conclusion.

In Fig. B.2 we show the toy distribution of the best fit global scale factor κ for the four different settings discussed above. Again, Fig. B.2(a) shows the idealized result with absolute and symmetrized uncertainties and (d) shows the result from the full implementation of relative and asymmetric uncertainties. The same variations as explained for the $\mathcal{P}$-value can also be observed in the distribution of the best fit points. A small negative bias of about -1.6% in the universal coupling scale factor estimator κ is introduced by the relative uncertainties, as can be seen in Fig. B.2(b). A much larger positive bias of the order of 3.5%, however, results from the correct treatment of asymmetric errors, cf. Fig. B.2(c). This stems from the fact that the experimental uncertainties are typically larger for variations in the upward direction as a direct consequence of the likelihood shape. As expected the full result in Fig. B.2(d) is in between (b) and (c) since both biases apply, leading to an upward shift between expected and fitted universal scale factor of $\sim 1.6\%$. Note also, that the best-fit μ distribution happens to be systematically slightly narrower than what is expected from the naive χ^2 comparison, but in this case by only $\sigma_{\text{fit}}/\sigma_{\text{exp}} = 0.057/0.058$, which corresponds to a change of only $\lesssim 2\%$. We thus conclude that the Gaussian shape of the uncertainties is approximately preserved, and that the uncertainties derived from the profile likelihood in the main part of this paper are expected to be reliable estimates of the uncertainties obtained in a full MC toy based treatment, or even the full likelihood analysis in the experimental collaborations.

In summary, this simple toy model study shows that there are potentially significant effects affecting the evaluation of $\mathcal{P}$-values of arbitrary Higgs models tested against the signal rate measurements. These effects stem from non-Gaussian likelihood effects such as asymmetric uncertainties as well as different scaling behavior of systematic uncertainties with either the measured or predicted rates. Both effects are approximately accounted for in the χ^2 evaluation in `HiggsSignals`, leading to an outcome that does not strictly follow the naive expectation of an ideal χ^2 probability distribution with $n^{\text{dof}} = n^{\text{obs}} - n^{\text{par}}$ due to visible changes in the χ^2_{min} probability density function. In a detailed evaluation of the $\mathcal{P}$-value we therefore advice to take these effects into account by using toy experiments.

B.2 Theoretical uncertainties of Higgs production and decay modes

The (correlated) uncertainties of the Higgs production and decay rates induced by the dependence on (common) parameters are evaluated as follows. We introduce a random variable x_i

following a Normal distribution,

$$P_i(x_i;\alpha) = \frac{1}{\sqrt{2\pi}\alpha} \cdot e^{-\frac{x_i^2}{2\alpha^2}}, \tag{B.2}$$

for each common parametric dependence i. In particular, the following common parametric dependencies are of relevance:

- $i \in \{\alpha_s, m_c, m_b, m_t\}$ for the partial width uncertainties of *all* Higgs decay modes,
- $i = \text{PDF} + \alpha_\text{s}$ for the ggH and $t\bar{t}H$ cross section uncertainties,

The smearing of the common parameter, described by x_i, thus affects the resulting uncertainties of the corresponding production or decay modes in a fully correlated way (see also below). For the remaining parametric dependencies j, individual Normal-distributed random variables x_j^a are introduced per production or decay mode a, thus these uncertainty sources are regarded as uncorrelated. Similarly, the theoretical uncertainties corresponding to estimates of the missing higher-order corrections are described by individual (and thus uncorrelated) Normal-distributed variations, x_th^a, except in the case of WH and ZH production which are treated as fully correlated.

In Eq. (B.2), α is introduced as an artificial scale factor of the standard deviation of the parametric uncertainties. Usually, we choose $\alpha = 1$, corresponding to a 68% C.L. interpretation of the quoted uncertainties. For comparison, however, we define the setting 'LHCHXSWG-matched', where we adjust $\alpha = 1.5$ [1.7] for the cross section [partial width] uncertainties in order to approximately match with the uncertainty estimates given by the LHCHXSWG. Note that all (theoretical, correlated or uncorrelated parametric) variations are described by Eq. (B.2), hence, for simplicity, the scale factor α affects all variations in the same way.

We now employ a Monte-Carlo (MC) calculation, where each iteration k (also called "toy") is defined by throwing random numbers for the parametric and theoretical uncertainty variations, $k \equiv \{x_i, x_j^a, x_\text{th}^a\}_k$. Then, the production cross sections and partial widths predicted for this toy are evaluated as

$$\sigma_k^a = \overline{\sigma}^a + \sum_i x_i \Delta\sigma_i^a + \sum_j x_j^a \Delta\sigma_j^a + x_\text{th}^a \Delta\sigma_\text{th}^a, \tag{B.3}$$

$$\Gamma_k^a = \overline{\Gamma}^a + \sum_i x_i \Delta\Gamma_i^a + \sum_j x_j^a \Delta\Gamma_j^a + x_\text{th}^a \Delta\Gamma_\text{th}^a, \tag{B.4}$$

where $\overline{\sigma}^a$ and $\overline{\Gamma}^a$ are the central values of the production cross sections and partial widths in the SM, respectively, and $\Delta\sigma$ and $\Delta\Gamma$ their parametric or theoretical uncertainties as given in Ref. [30]. We take into account possibly asymmetric uncertainties:

$$\Delta\sigma, \Delta\Gamma = \begin{cases} \Delta\sigma^\text{upper}, \Delta\Gamma^\text{upper} & \text{for} \quad x > 0, \\ \Delta\sigma^\text{lower}, \Delta\Gamma^\text{lower} & \text{for} \quad x < 0. \end{cases} \tag{B.5}$$

Note, that $\Delta\sigma$ and $\Delta\Gamma$ can also be negative, depending on the response of the calculated quantity to the parameter variation. From the partial widths we can simply derive for each toy k the total decay width, $\Gamma_k^\text{tot} = \sum_a \Gamma_k^a$, and branching ratios, $\text{BR}_k^a = \Gamma_k^a / \Gamma_k^\text{tot}$. The covariance

Mode	LHCHXSWG[1] from Ref. [30]	LHCHXSWG matched[2]	LHC-S1	LHC-S2	ILC
$\sigma(gg \to H)$ (ggH)	15.3%	15.6%	10.4%	5.2%	-
$\sigma(qq \to qqH)$ (VBF)	6.9%	5.6%	3.7%	1.9%	-
$\sigma(pp \to WH)$	3.3%	4.0%	2.7%	1.3%	-
$\sigma(pp \to ZH)$	5.7%	6.3%	4.2%	2.1%	-
$\sigma(pp \to t\bar{t}H)$	17.4%	15.6%	10.4%	5.2%	-
$\sigma(e^+e^- \to ZH)$	-	-	-	-	0.5%
$\sigma(e^+e^- \to \nu\bar{\nu}H)$	-	-	-	-	1.0%
$\sigma(e^+e^- \to t\bar{t}H)$	-	-	-	-	1.0%
Using a Gaussian-shaped parameter variation					
$\mathrm{BR}(H \to \gamma\gamma)$	4.9%	4.5%	2.7%	2.3%	1.3%
$\mathrm{BR}(H \to WW^{(*)})$	4.2%	4.3%	2.5%	2.3%	1.3%
$\mathrm{BR}(H \to ZZ^{(*)})$	4.1%	4.3%	2.5%	2.3%	1.3%
$\mathrm{BR}(H \to \tau^+\tau^-)$	5.7%	5.3%	3.1%	2.4%	1.6%
$\mathrm{BR}(H \to b\bar{b})$	3.3%	3.6%	2.1%	1.9%	1.1%
$\mathrm{BR}(H \to Z\gamma)$	8.9%	9.5%	5.6%	3.4%	2.8%
$\mathrm{BR}(H \to c\bar{c})$	12.2%	15.3%	9.0%	8.8%	4.5%
$\mathrm{BR}(H \to \mu^+\mu^-)$	5.9%	5.4%	3.2%	2.5%	1.6%
$\mathrm{BR}(H \to gg)$	10.1%	10.9%	6.4%	5.9%	3.2%

[1] Taken from Ref. [30], using (always the larger) uncertainty estimates for $\sqrt{s} = 8\,\mathrm{TeV}$, $m_H = 125.7\,\mathrm{GeV}$. Theoretical and parametric uncertainties are added linearly. In our *naive* fit, we use these numbers as maximum error estimates and neglect all correlations of common parametric uncertainty sources, total width, etc..

[2] Using an artificially enlarged range for the parametric variation of $\alpha = 1.5$ and 1.7 for the production cross section and partial width uncertainties, respectively.

Table B.1: Relative theoretical uncertainties of LHC and ILC production cross sections and Higgs branching ratios for various implementations and future scenarios discussed in Tab. 5.9.

matrices are then given by

$$\mathrm{cov}(X)_{ab} = \langle X_a X_b \rangle - \langle X_a \rangle \langle X_b \rangle, \tag{B.6}$$

where $\langle \cdot \rangle$ denotes the arithmetic mean for the full toy MC sample and $X = \sigma, \Gamma$ or BR.

In Tab. B.1 we give the relative uncorrelated uncertainties, given by $\mathrm{cov}(X)_{aa}/\overline{X_a}^2$, for the LHC production cross sections and Higgs branching ratios for the future scenarios 'LHC-S1', 'LHC-S2' and 'ILC' discussed in Tab. 5.9. These are compared with the uncertainty estimates given by the LHCHXSWG [30], where the parametric and theoretical uncertainties for a Higgs mass of $m_H = 125.7\,\mathrm{GeV}$ and a (pp) center-of-mass energy of $\sqrt{s} = 8\,\mathrm{TeV}$ are added linearly. For the scenario 'LHCHXSWG-matched' we employ the toy MC procedure with the artificial scale factor $\alpha = 1.5$ and 1.7 for the uncertainties of the production cross sections and branching ratios, respectively. We furthermore compared these uncertainty estimates with those obtained when using a uniform (box-shaped) smearing of the parametric and theoretical uncertainties instead of B.2. The deviations found are rather small, being typically $\lesssim \mathcal{O}(10\%)$.

In order to investigate the impact of the different theoretical uncertainty implementations on the precision estimates of the Higgs coupling scale factors we perform the seven-dimensional scale factor fit, cf. Section 5.2.6 and 5.3.1, to the same combined future projections for the high-

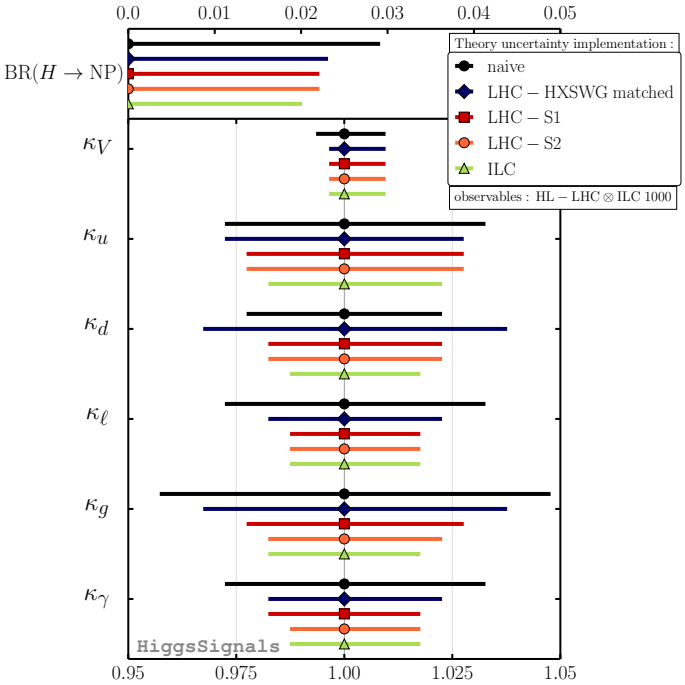

Figure B.3: Comparison of Higgs coupling precision estimates obtained for various implementations of theoretical rate uncertainties. The comparison uses all available measurements from the HL–LHC and the ultimate ILC stage at 1 TeV with $1\,\text{ab}^{-1}$ of data (and including measurements of previous ILC stages).

luminosity LHC and all baseline ILC stages up to 1 TeV, $1\,\text{ab}^{-1}$, for all implementations. The result is shown in Fig. B.3. Comparing the 'naive' implementation, where simply the estimates from the LHCHXSWG are taken (cf. Tab. B.1) and all correlations among the cross section and branching ratio predictions are neglected, with the 'LHC-HXSWG matched' implementation, we see that for the latter, BR($H \to$ NP) and all scale factors except κ_d can be determined more precisely. Note, however, that the major effect causing these differences is actually the remaining mismatch of the uncertainty estimates, cf. Tab. B.1, and not the inclusion of correlations. Nevertheless, as we have argued in this work, we find it more consistent to evaluate the covariances of the cross section and branching ratio predictions directly via the toy MC outlined above, leading to the uncertainty estimates denoted by 'LHC-S1'. Here, we find the largest differences to the 'naive' implementation in the achievable precisions of κ_d, κ_ℓ, κ_g and κ_γ, being $\mathcal{O}(1-2\%)$. As expected, in the scenarios with improved theoretical uncertainties the Higgs coupling precision is further improved, indicating that in this high-statistics scenario the theoretical uncertainties are a dominant limiting factor for the achievable precision.

APPENDIX C

Additional information on Chapter 7

C.1 Tables for the dijet resonance search results

The results of the dijet resonance study in Sect. 7.3.1 are listed in Tab. C.1 and C.2 for the ATLAS and CMS analyses, respectively. The upper bounds on the R-parity violating coupling squared times the branching ratio of the slepton to dijets, ${\lambda'_{ijk}}^2 \times \mathcal{B}(\tilde{\ell}_i/\tilde{\nu}_i \to jj)$, are presented for all $j, k \in \{1, 2\}$ seperately up to the perturbativity bound. We also give the signal acceptance $\mathcal{A}$ for each slepton mass $\tilde{m}$, which has been evaluated with our MC simulation. For the ATLAS results, Tab. C.1, we also provide the resonance width to mass ratio, σ_G/m_G, as derived from a Gaussian fit to the resonance.

C.2 Signal acceptance of the prompt like–sign dimuon search

In Fig. C.1 we give the signal acceptance in the $(m_{\tilde{\chi}_1^0}, \tilde{m})$ mass plane for each signal region, $m_{\mu\mu} > 15\,\text{GeV}$, $100\,\text{GeV}$, $200\,\text{GeV}$, $300\,\text{GeV}$, of the ATLAS prompt like–sign dimuon search [416] for the simulated process $pp \to \tilde{\ell}^*/\tilde{\nu}^* \to (\mu/\nu)\tilde{\chi}_1^0$.

For most of the parameter space, the acceptance ranges between 2% and 7%, where the highest largest values are obtained for models with $m_{\tilde{\chi}_1^0} \approx \tilde{m}/2$. In that case, neither the slepton nor the neutralino decay are kinematically suppressed, leading to sizable transverse momenta of the two leptons. In contrast, the regions with either a low neutralino mass or a low mass difference between slepton and lightest neutralino, $\Delta m = \tilde{m} - m_{\tilde{\chi}_1^0}$, feature a very small acceptance. Here, one of the leptons is soft due to reduced phase space, as discussed in Sect. 7.3.2, and therefore fails to pass the minimum p_T requirement.

The insensitive region at low neutralino masses does not depend on the specific $m_{\mu\mu}$ requirement, since it typically features higher values of $m_{\mu\mu}$, Fig. 7.8(b). In contrast, the acceptance in the low Δm region highly depends on the $m_{\mu\mu}$ cut. Decreasing the mass difference Δm leads to a shift of the $m_{\mu\mu}$ distribution towards lower values. Thus, only the $m_{\mu\mu} > 15\,\text{GeV}$ signal region is capable of exploring the parameter region with Δm down to $\approx 10\,\text{GeV}$, while the other signal regions with $m_{\mu\mu} > (100,\ 200,\ 300)$ GeV require a mass difference of $\Delta m \gtrsim (20,\ 75,\ 150)$ GeV, respectively, to become sensitive (i.e.to obtain $\mathcal{A} \gtrsim 2\%$).

Furthermore, in order to obtain a large $m_{\mu\mu}$ value, the slepton mass $\tilde{m}$ has to be sufficiently large. Thus, the signal regions with $m_{\mu\mu} > (15,\ 100,\ 200,\ 300)$ GeV become sensitive for

$\tilde{m}$ [GeV]	$\mathcal{A}$ (in %)	σ_G/m_G (in %)	Upper limits on $\lambda'^2_{ijk} \times \mathcal{B}(\tilde{\ell}_i/\tilde{\nu}_i \to jj)$ $i11$	$i12$	$i21$	$i22$
900	8.1	8.1	0.00226	0.00497	0.00953	0.05931
950	8.0	7.2	0.00329	0.00734	0.01432	0.09274
1000	7.9	7.5	0.00473	0.01067	0.02117	0.14252
1050	8.2	7.3	0.00542	0.01234	0.02490	0.17413
1100	7.9	6.3	0.00483	0.01110	0.02275	0.16507
1150	8.6	7.9	0.00731	0.01694	0.03524	0.26513
1200	8.8	6.8	0.00619	0.01442	0.03045	0.23733
1250	8.8	6.5	0.00754	0.01764	0.03779	0.30482
1300	8.6	7.5	0.01002	0.02349	0.05104	0.42574
1350	9.0	7.0	0.00873	0.02051	0.04516	0.38927
1400	9.0	7.5	0.00871	0.02044	0.04560	0.40587
1450	9.1	6.4	0.00686	0.01608	0.03634	0.33384
1500	9.1	6.5	0.00815	0.01904	0.04358	0.41282
1550	9.3	6.3	0.00924	0.02149	0.04976	0.48586
1600	9.5	6.3	0.01050	0.02426	0.05683	0.57162
1650	9.4	6.4	0.01303	0.02987	0.07077	0.73286
1700	9.8	6.3	0.01364	0.03098	0.07419	0.79059
1750	9.4	6.1	0.01547	0.03478	0.08418	0.92254
1800	9.6	6.4	0.01769	0.03929	0.09605	-
1850	9.8	5.9	0.02210	0.04840	0.11951	-
1900	9.8	7.0	0.03023	0.06522	0.16255	-
1950	10.0	6.6	0.04261	0.09040	0.22733	-
2000	10.0	6.0	0.05815	0.12116	0.30730	-
2100	10.2	6.5	0.11257	0.22523	0.58045	-
2200	10.4	5.9	0.21673	0.41398	-	-
2300	10.5	6.3	0.41049	0.74428	-	-
2400	10.6	5.7	0.76454	-	-	-

Table C.1: Upper limits on $\lambda'^2 \times \mathcal{B}(\tilde{\ell}_i/\tilde{\nu}_i \to jj)$ derived from the ATLAS search for dijet resonances. The first column gives the resonant slepton mass, $\tilde{m}$ (in GeV), the second and the third column show the acceptance $\mathcal{A}$ (in %) and the width-to-mass ratio, σ_G/m_G (in %), of the gaussian resonance fit, respectively. The other columns contain the upper limits on $\lambda'^2 \times \mathcal{B}(\tilde{\ell}_i/\tilde{\nu}_i \to jj)$, where the indices of λ' are indicated in the table header ($i = 1, 2, 3$).

slepton masses $\tilde{m} \gtrsim (125,\ 200,\ 330,\ 500)$ GeV, respectively.

Although the $m_{\mu\mu} \geq 15\,\text{GeV}$ selection has the best acceptance coverage, it is still important to use also the other signal regions, because they have less SM background and thus stricter upper limits on the fiducial cross section. In parameter regions with heavier sleptons $\tilde{m} \gtrsim \mathcal{O}(600\,\text{GeV})$ and neutralino masses around $\tilde{m}/2$, the signal region with $m_{\mu\mu} > 300\,\text{GeV}$ typically poses the strictest limits on the R-parity violating couplings.

$\tilde{m}$ [GeV]	$\mathcal{A}$ (in %)	Upper limits on $\lambda'^2_{ijk} \times \mathcal{B}(\tilde{\ell}_i/\tilde{\nu}_i \to jj)$			
		$i11$	$i12$	$i21$	$i22$
1000	33.8	0.00102	0.00229	0.00455	0.03064
1100	34.8	0.00117	0.00269	0.00552	0.04007
1200	35.7	0.00163	0.00380	0.00803	0.06254
1300	35.7	0.00201	0.00472	0.01026	0.08555
1400	36.6	0.00195	0.00458	0.01023	0.09103
1500	36.6	0.00275	0.00642	0.01469	0.13914
1600	37.3	0.00413	0.00954	0.02235	0.22478
1700	37.3	0.00619	0.01407	0.03370	0.35911
1800	38.1	0.00766	0.01701	0.04160	0.46863
1900	37.6	0.01441	0.03108	0.07747	0.92097
2000	38.2	0.02956	0.06159	0.15622	-
2100	38.6	0.05246	0.10497	0.27053	-
2200	38.2	0.09454	0.18058	0.47210	-
2300	39.0	0.18974	0.34403	0.91070	-
2400	39.1	0.39971	0.68404	-	-
2500	39.1	0.82990	-	-	-

Table C.2: Upper limits on $\lambda'^2 \times \mathcal{B}(\tilde{\ell}_i/\tilde{\nu}_i \to jj)$ derived from the CMS search for narrow dijet resonances. The first column gives the resonant slepton mass, $\tilde{m}$ (in GeV) and the second shows the acceptance $\mathcal{A}$ (in %). The other columns contain the upper limits on $\lambda'^2 \times \mathcal{B}(\tilde{\ell}_i/\tilde{\nu}_i \to jj)$, where the indices of λ' are indicated in the table header ($i = 1, 2, 3$).

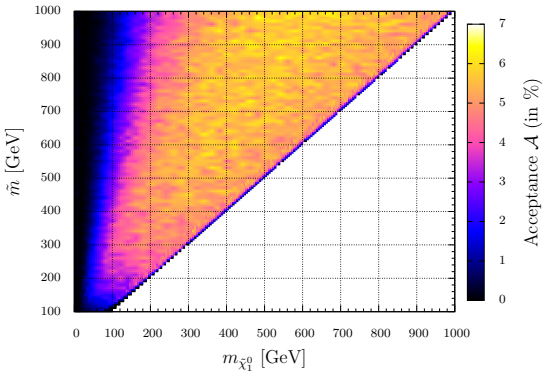

(a) $m_{\mu\mu} > 15\,\text{GeV}$ signal region.

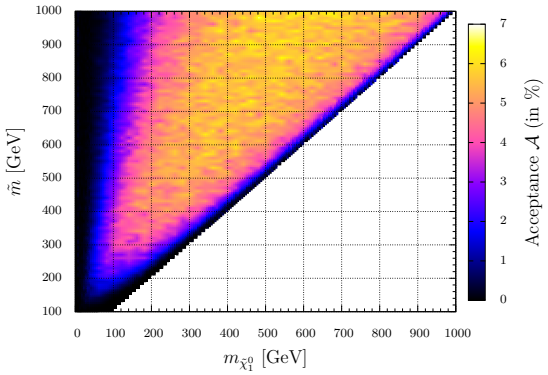

(b) $m_{\mu\mu} > 100\,\text{GeV}$ signal region.

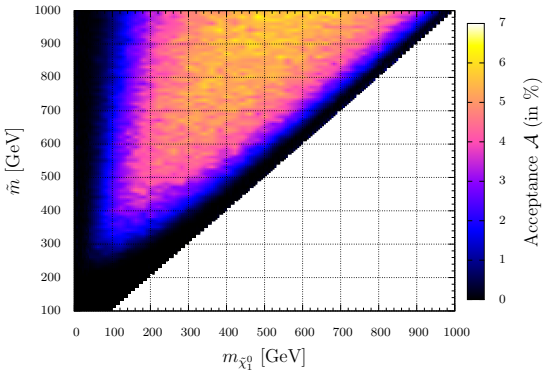

(c) $m_{\mu\mu} > 200\,\text{GeV}$ signal region.

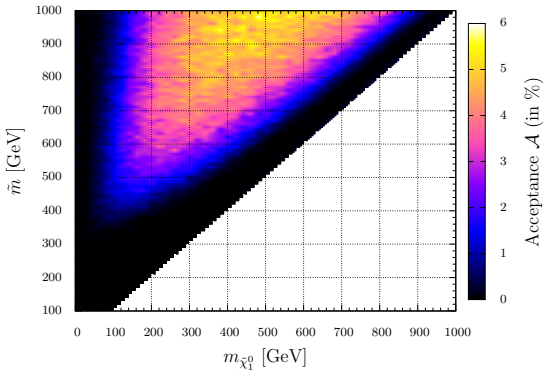

(d) $m_{\mu\mu} > 300\,\text{GeV}$ signal region.

Figure C.1: Signal acceptance $\mathcal{A}$ of the ATLAS same-sign prompt dimuon search for the resonant slepton production process $pp \to \tilde{\ell}^*/\tilde{\nu}^* \to (\mu/\nu)\tilde{\chi}_1^0$. The subfigures (a,b,c,d) show the four signal regions with $m_{\mu\mu} > (15,\ 100,\ 200,\ 300)$ GeV, respectively.

Bibliography

[1] G. Aad et al., *Phys.Lett.* B716 (2012) 1–29, arXiv:1207.7214 [hep-ex].

[2] S. Chatrchyan et al., *Phys.Lett.* B716 (2012) 30–61, arXiv:1207.7235 [hep-ex].

[3] ATLAS Collaboration,
(2013), ATLAS-CONF-2013-034, ATLAS-COM-CONF-2013-035.

[4] ATLAS Collaboration,
(2013), ATLAS-CONF-2013-040, ATLAS-COM-CONF-2013-048.

[5] CMS Collaboration, (2013), CMS-PAS-HIG-13-005.

[6] CMS Collaboration, (2013), CMS-PAS-HIG-13-016.

[7] F. Englert and R. Brout, *Phys. Rev. Lett.* 13 (1964) 321–322.

[8] P. W. Higgs, *Phys. Lett.* 12 (1964) 132–133; P. W. Higgs,
Phys. Rev. Lett. 13 (1964) 508–509; P. W. Higgs, *Phys. Rev.* 145 (1966) 1156–1163.

[9] G. Guralnik, C. Hagen and T. Kibble, *Phys. Rev. Lett.* 13 (1964) 585–587; T. Kibble,
Phys. Rev. 155 (1967) 1554–1561.

[10] Interview with Peter Higgs on BBC's *The Life Scientific.*, 2014,
URL: http://www.bbc.co.uk/programmes/b03vdx7m.

[11] E. Witten, *Nucl.Phys.* B188 (1981) 513; M. Veltman,
Acta Phys.Polon. B12 (1981) 437; H. P. Nilles, *Phys.Lett.* B115 (1982) 193.

[12] G. Jungman, M. Kamionkowski and K. Griest, *Phys.Rept.* 267 (1996) 195–373,
arXiv:hep-ph/9506380 [hep-ph]; G. Bertone, D. Hooper and J. Silk,
Phys.Rept. 405 (2005) 279–390, arXiv:hep-ph/0404175 [hep-ph]; L. Bergström,
New J.Phys. 11 (2009) 105006, arXiv:0903.4849 [hep-ph]; J. L. Feng,
Ann.Rev.Astron.Astrophys. 48 (2010) 495–545, arXiv:1003.0904 [astro-ph.CO].

[13] M. Gonzalez-Garcia and M. Maltoni, *Phys.Rept.* 460 (2008) 1–129,
arXiv:0704.1800 [hep-ph]; A. de Gouvea et al., (2013), arXiv:1310.4340 [hep-ex];
S. King, *Contemp.Phys.* (2007), arXiv:0712.1750 [physics.pop-ph].

[14] M. Trodden, *Rev.Mod.Phys.* 71 (1999) 1463–1500, arXiv:hep-ph/9803479 [hep-ph];
M. Dine and A. Kusenko, *Rev.Mod.Phys.* 76 (2003) 1,
arXiv:hep-ph/0303065 [hep-ph]; J. M. Cline, (2006),
arXiv:hep-ph/0609145 [hep-ph]; D. E. Morrissey and M. J. Ramsey-Musolf,
New J.Phys. 14 (2012) 125003, arXiv:1206.2942 [hep-ph].

[15] M. Drees, R. Godbole and P. Roy, *Theory and phenomenology of Sparticles: an account of four-dimensional N=1 supersymmetry in high-energy physics*, Singapore: World Scientific, 2004.

[16] H. W. Baer and X. Tata, *Weak scale supersymmetry: from superfields to scattering events*, Cambridge: Cambridge Univ. Press, 2006.

[17] J. Wess and J. Bagger, *Supersymmetry and Supergravity*, Princeton series in physics, Princeton University Press, 1992,

[18] H. P. Nilles, *Phys.Rept.* 110 (1984) 1–162.

[19] H. E. Haber and G. L. Kane, *Phys.Rept.* 117 (1985) 75–263.

[20] H. E. Haber, (1993), arXiv:hep-ph/9306207 [hep-ph].

[21] M. Drees, (1996), arXiv:hep-ph/9611409 [hep-ph].

[22] S. P. Martin, (1997), arXiv:hep-ph/9709356 [hep-ph].

[23] H. E. Haber, *Nucl.Phys.Proc.Suppl.* 62 (1998) 469–484, arXiv:hep-ph/9709450 [hep-ph].

[24] A. Djouadi, *Phys. Rept.* 459 (2008) 1–241, arXiv:hep-ph/0503173.

[25] P. Bechtle et al., *Comput.Phys.Commun.* 181 (2010) 138–167, arXiv:0811.4169 [hep-ph].

[26] P. Bechtle et al., *Comput.Phys.Commun.* 182 (2011) 2605–2631, arXiv:1102.1898 [hep-ph].

[27] P. Bechtle et al., *PoS* CHARGED2012 (2012) 024, arXiv:1301.2345 [hep-ph].

[28] P. Bechtle et al., *Eur.Phys.J.* C74 (2014) 2693, arXiv:1311.0055 [hep-ph].

[29] The LHC Higgs Cross Section Working Group: A. David et al., (2012), arXiv:1209.0040 [hep-ph].

[30] The LHC Higgs Cross Section Working Group: S. Heinemeyer et al., (2013), arXiv:1307.1347 [hep-ph], See also https://twiki.cern.ch/twiki/bin/view/LHCPhysics/CrossSections.

[31] N. Craig, (2013), arXiv:1309.0528 [hep-ph].

[32] A. Djouadi, *Phys. Rept.* 457 (2008) 1–216, arXiv:hep-ph/0503172 [hep-ph].

[33] S. Dittmaier and M. Schumacher, *Prog. Part. Nucl. Phys.* 70 (2013) 1–54, arXiv:1211.4828 [hep-ph].

[34] M. Carena et al., *Status of Higgs boson physics*, review appeared in Ref. [74].

[35] J. F. Gunion et al., *The Higgs Hunter's Guide*, 2nd ed., Cambridge, MA: Perseus Publishing, 1990.

[36] J. Ellis, (2013), arXiv:1312.5672 [hep-ph].

[37] M. Drees, "Physics of Higgs Bosons", Unpublished notes from the lecture given in the winter term 2013/14 at Bonn University, Germany.

[38] H. Fritzsch, M. Gell-Mann and H. Leutwyler, *Phys.Lett.* B47 (1973) 365–368; H. D. Politzer, *Phys.Rev.Lett.* 30 (1973) 1346–1349; D. J. Gross and F. Wilczek, *Phys.Rev.Lett.* 30 (1973) 1343–1346; D. Gross and F. Wilczek, *Phys.Rev.* D8 (1973) 3633–3652; D. Gross and F. Wilczek, *Phys.Rev.* D9 (1974) 980–993; M. Gell-Mann, *Phys.Lett.* 8 (1964) 214–215.

[39] S. Glashow, *Nucl.Phys.* 22 (1961) 579–588; S. Weinberg, *Phys.Rev.Lett.* 19 (1967) 1264–1266; A. Salam and J. C. Ward, *Phys.Lett.* 13 (1964) 168–171.

[40] M. E. Peskin and D. V. Schroeder, (1995).

[41] F. Halzen and A. Martin, *Quarks & Leptons: An introductory course in modern particle physics*, John Wiley & Sons, 1984.

[42] D. Griffiths, *Introduction to Elementary Particles*, John Wiley & Sons, 1987.

[43] S. L. Adler and W. A. Bardeen, *Phys.Rev.* 182 (1969) 1517–1536.

[44] S. Treiman, R. Jackiw and D. Gross, *Lectures on Current Algebra and Its Applications*, Princeton Series in Physics, Princeton University Press, 1972,

[45] G. 't Hooft, *Nucl.Phys.* B33 (1971) 173–199; G. 't Hooft, *Nucl.Phys.* B35 (1971) 167–188; G. 't Hooft and M. Veltman, *Nucl.Phys.* B44 (1972) 189–213.

[46] Y. Fukuda et al., *Phys.Rev.Lett.* 82 (1999) 2644–2648, arXiv:hep-ex/9812014 [hep-ex]; Y. Fukuda et al., *Phys.Rev.Lett.* 81 (1998) 1158–1162, arXiv:hep-ex/9805021 [hep-ex]; Q. Ahmad et al., *Phys.Rev.Lett.* 89 (2002) 011301, arXiv:nucl-ex/0204008 [nucl-ex]; M. Apollonio et al., *Eur.Phys.J.* C27 (2003) 331–374, arXiv:hep-ex/0301017 [hep-ex]; B. Cleveland et al., *Astrophys.J.* 496 (1998) 505–526; D. Michael et al., *Phys.Rev.Lett.* 97 (2006) 191801, arXiv:hep-ex/0607088 [hep-ex]; K. Abe et al., *Phys.Rev.Lett.* 107 (2011) 041801, arXiv:1106.2822 [hep-ex]; F. An et al., *Phys.Rev.Lett.* 108 (2012) 171803, arXiv:1203.1669 [hep-ex].

[47] P. Ade et al., (2013), arXiv:1303.5076 [astro-ph.CO].

[48] G. Arnison et al., *Phys.Lett.* B122 (1983) 103–116.

[49] G. Arnison et al., *Phys.Lett.* B126 (1983) 398–410.

[50] D. Webber et al., *Phys.Rev.Lett.* 106 (2011) 041803, arXiv:1010.0991 [hep-ex]; V. Tishchenko et al., *Phys.Rev.* D87.5 (2013) 052003, arXiv:1211.0960 [hep-ex].

[51] J. Erler and P. Langacker, *Electroweak Model and Constraints on New Physics*, review appeared in Ref. [74].

[52] J. Goldstone, *Nuovo Cim.* 19 (1961) 154–164; J. Goldstone, A. Salam and S. Weinberg, *Phys.Rev.* 127 (1962) 965–970; Y. Nambu and G. Jona-Lasinio, *Phys.Rev.* 122 (1961) 345–358; Y. Nambu and G. Jona-Lasinio, *Phys.Rev.* 124 (1961) 246–254.

[53] N. Cabibbo, *Phys.Rev.Lett.* 10 (1963) 531–533; M. Kobayashi and T. Maskawa, *Prog.Theor.Phys.* 49 (1973) 652–657.

[54] Z. Maki, M. Nakagawa and S. Sakata, *Prog.Theor.Phys.* 28 (1962) 870–880; B. Pontecorvo, *Sov.Phys.JETP* 6 (1957) 429; B. Pontecorvo, *Sov.Phys.JETP* 26 (1968) 984–988.

[55] S. Friederich, R. V. Harlander and K. Karaca, (2013), arXiv:1305.5110 [physics.hist-ph].

[56] G. Degrassi et al., *JHEP* 1208 (2012) 098, arXiv:1205.6497 [hep-ph].

[57] J. Callan Curtis G., *Phys.Rev.* D2 (1970) 1541–1547; K. Symanzik, *Commun.Math.Phys.* 18 (1970) 227–246; K. Symanzik, *Commun.Math.Phys.* 23 (1971) 49–86.

[58] T. Cheng, E. Eichten and L.-F. Li, *Phys.Rev.* D9 (1974) 2259; B. Pendleton and G. G. Ross, *Phys.Lett.* B98 (1981) 291; C. T. Hill, *Phys.Rev.* D24 (1981) 691; M. Beg, C. Panagiotakopoulos and A. Sirlin, *Phys.Rev.Lett.* 52 (1984) 883.

[59] B. W. Lee, C. Quigg and H. Thacker, *Phys.Rev.* D16 (1977) 1519.

[60] M. Lüscher and P. Weisz, *Phys.Lett.* B212 (1988) 472.

[61] J. Gunion, H. Haber and J. Wudka, *Phys.Rev.* D43 (1991) 904–912.

[62] The ALEPH, DELPHI, L3, OPAL Collaborations, the LEP Electroweak Working Group, *Phys. Rept.* 532 (2013) 119, arXiv:1302.3415 [hep-ex].

[63] The Tevatron Electroweak Working Group, CDF, D0 Collaborations, (2013), arXiv:1305.3929 [hep-ex].

[64] The ALEPH, DELPHI, L3, OPAL, SLD Collaborations, the LEP Electroweak Working Group, the SLD Electroweak and Heavy Flavour Groups, *Phys. Rept.* 427 (2006) 257, eprint: hep-ex/0509008.

[65] The LEP Electroweak Working Group, URL: http://lepewwg.web.cern.ch/LEPEWWG/.

[66] M. Baak et al., *Eur.Phys.J.* C72 (2012), Update (dated: Sept. 2013) available at http://gfitter.desy.de. 2205, arXiv:1209.2716 [hep-ph].

[67] M. Antonelli et al., *Phys.Rept.* 494 (2010) 197–414, arXiv:0907.5386 [hep-ph].

[68] D. Bardin and G. Passarino, *The Standard Model in the Making: Precision Study of the Electroweak Interactions*, Clarendon Press, 1999.

[69] L. Resnick, M. Sundaresan and P. Watson, *Phys.Rev.* D8 (1973) 172–178; J. R. Ellis, M. K. Gaillard and D. V. Nanopoulos, *Nucl.Phys.* B106 (1976) 292; M. A. Shifman et al., *Sov.J.Nucl.Phys.* 30 (1979) 711–716.

[70] The LHC Higgs Cross Section Working Group: S. Dittmaier et al., (2011), arXiv:1101.0593 [hep-ph].

[71] The LHC Higgs Cross Section Working Group: S. Dittmaier et al., (2012), arXiv:1201.3084 [hep-ph].

[72] N. Gray et al., *Z.Phys.* C48 (1990) 673–680;
D. J. Broadhurst, N. Gray and K. Schilcher, *Z.Phys.* C52 (1991) 111–122;
K. Chetyrkin and M. Steinhauser, *Phys.Rev.Lett.* 83 (1999) 4001–4004,
arXiv:hep-ph/9907509 [hep-ph]; K. Chetyrkin and M. Steinhauser,
Nucl.Phys. B573 (2000) 617–651, arXiv:hep-ph/9911434 [hep-ph];
K. Melnikov and T. v. Ritbergen, *Phys.Lett.* B482 (2000) 99–108,
arXiv:hep-ph/9912391 [hep-ph].

[73] A. Hoang et al., *Eur.Phys.J.direct* C2 (2000) 1, arXiv:hep-ph/0001286 [hep-ph];
A. Quadt, *Eur.Phys.J.* C48 (2006) 835–1000; U. Langenfeld, S. Moch and P. Uwer,
Phys.Rev. D80 (2009) 054009, arXiv:0906.5273 [hep-ph];
T. M. Liss, F. Maltoni and A. Quadt, *The Top Quark*, review appeared in Ref. [74].

[74] J. Beringer et al.,
Phys.Rev. D86 (2012) 010001 and 2013 partial update for the 2014 edition.

[75] The ATLAS, CDF, CMS and DØ Collaborations, (2014), arXiv:1403.4427 [hep-ex].

[76] S. Heinemeyer et al., (2005), arXiv:hep-ph/0511332 [hep-ph].

[77] J. M. Campbell, R. K. Ellis and C. Williams, *JHEP* 1110 (2011) 005,
arXiv:1107.5569 [hep-ph]; F. Caola and K. Melnikov, *Phys.Rev.* D88 (2013) 054024,
arXiv:1307.4935 [hep-ph]; J. M. Campbell, R. K. Ellis and C. Williams,
Phys.Rev. D89 (2014) 053011, arXiv:1312.1628 [hep-ph];
J. M. Campbell, R. K. Ellis and C. Williams, *JHEP* 1404 (2014) 060,
arXiv:1311.3589 [hep-ph].

[78] E. Braaten and J. Leveille, *Phys.Rev.* D22 (1980) 715; N. Sakai,
Phys.Rev. D22 (1980) 2220; T. Inami and T. Kubota, *Nucl.Phys.* B179 (1981) 171;
M. Drees and K.-i. Hikasa, *Phys.Lett.* B240 (1990) 455.

[79] M. Drees and K.-i. Hikasa, *Phys.Rev.* D41 (1990) 1547.

[80] T. G. Rizzo, *Phys.Rev.* D22 (1980) 722; W.-Y. Keung and W. J. Marciano,
Phys.Rev. D30 (1984) 248.

[81] E. N. Glover, J. Ohnemus and S. S. Willenbrock, *Phys.Rev.* D37 (1988) 3193.

[82] C. A. Nelson, *Phys.Rev.* D37 (1988) 1220; A. Soni and R. Xu,
Phys.Rev. D48 (1993) 5259–5263, arXiv:hep-ph/9301225 [hep-ph];
D. Chang, W.-Y. Keung and I. Phillips, *Phys.Rev.* D48 (1993) 3225–3234,
arXiv:hep-ph/9303226 [hep-ph]; A. Skjold and P. Osland,
Phys.Lett. B311 (1993) 261–265, arXiv:hep-ph/9303294 [hep-ph]; V. D. Barger et al.,
Phys.Rev. D49 (1994) 79–90, arXiv:hep-ph/9306270 [hep-ph]; C. Buszello et al.,
Eur.Phys.J. C32 (2004) 209–219, arXiv:hep-ph/0212396 [hep-ph]; S. Choi et al.,
Phys.Lett. B553 (2003) 61–71, arXiv:hep-ph/0210077 [hep-ph].

[83] M. Dittmar and H. K. Dreiner, *Phys.Rev.* D55 (1997) 167–172,
arXiv:hep-ph/9608317 [hep-ph].

[84] O. Eberhardt et al., *Phys.Rev.Lett.* 109 (2012) 241802, arXiv:1209.1101 [hep-ph].

[85] K. Chetyrkin, B. A. Kniehl and M. Steinhauser, *Phys.Rev.Lett.* 79 (1997) 353–356, arXiv:hep-ph/9705240 [hep-ph]; K. Chetyrkin, B. A. Kniehl and M. Steinhauser, *Nucl.Phys.* B510 (1998) 61–87, arXiv:hep-ph/9708255 [hep-ph]; M. Schreck and M. Steinhauser, *Phys.Lett.* B655 (2007) 148–155, arXiv:0708.0916 [hep-ph].

[86] A. Djouadi, J. Kalinowski and M. Spira, *Comput.Phys.Commun.* 108 (1998) 56–74, arXiv:hep-ph/9704448 [hep-ph].

[87] M. Spira, *Fortsch.Phys.* 46 (1998) 203–284, arXiv:hep-ph/9705337 [hep-ph].

[88] A. Bredenstein et al., *Phys.Rev.* D74 (2006) 013004, arXiv:hep-ph/0604011 [hep-ph]; A. Bredenstein et al., *JHEP* 0702 (2007) 080, arXiv:hep-ph/0611234 [hep-ph].

[89] A. Denner et al., *Eur.Phys.J.* C71 (2011) 1753, arXiv:1107.5909 [hep-ph].

[90] R. Barate et al., *Phys.Lett.* B565 (2003) 61–75, arXiv:hep-ex/0306033 [hep-ex].

[91] D. Asner et al., (2013), arXiv:1310.0763 [hep-ph].

[92] H. Baer et al., (2013), arXiv:1306.6352 [hep-ph].

[93] J. E. Brau et al., (2012), arXiv:1210.0202 [hep-ex].

[94] S. Dittmaier et al., *Phys.Lett.* B441 (1998) 383–388, arXiv:hep-ph/9808433 [hep-ph]; S. Dawson and L. Reina, *Phys.Rev.* D59 (1999) 054012, arXiv:hep-ph/9808443 [hep-ph]; G. Belanger et al., *Phys.Lett.* B571 (2003) 163–172, arXiv:hep-ph/0307029 [hep-ph]; A. Denner et al., *Nucl.Phys.* B680 (2004) 85–116, arXiv:hep-ph/0309274 [hep-ph]; Y. You et al., *Phys.Lett.* B571 (2003) 85–91, arXiv:hep-ph/0306036 [hep-ph]; C. Farrell and A. H. Hoang, *Phys.Rev.* D72 (2005) 014007, arXiv:hep-ph/0504220 [hep-ph]; C. Farrell and A. H. Hoang, *Phys.Rev.* D74 (2006) 014008, arXiv:hep-ph/0604166 [hep-ph].

[95] G. Moortgat-Pick et al., *Phys.Rept.* 460 (2008) 131–243, arXiv:hep-ph/0507011 [hep-ph].

[96] G. Gounaris, D. Schildknecht and F. Renard, *Phys.Lett.* B83 (1979) 191; F. Boudjema and E. Chopin, *Z.Phys.* C73 (1996) 85–110, arXiv:hep-ph/9507396 [hep-ph]; V. Ilyin et al., *Phys.Rev.* D54 (1996) 6717–6727, arXiv:hep-ph/9506326 [hep-ph]; A. Djouadi et al., *Eur.Phys.J.* C10 (1999) 27–43, arXiv:hep-ph/9903229 [hep-ph]; D. Miller and S. Moretti, *Eur.Phys.J.* C13 (2000) 459–470, arXiv:hep-ph/9906395 [hep-ph]; U. Baur, *Phys.Rev.* D80 (2009) 013012, arXiv:0906.0028 [hep-ph].

[97] M. Moretti, T. Ohl and J. Reuter, (2001), arXiv:hep-ph/0102195 [hep-ph]; W. Kilian, T. Ohl and J. Reuter, *Eur.Phys.J.* C71 (2011) 1742, arXiv:0708.4233 [hep-ph].

[98] D. Duke and J. Owens, *Phys.Rev.* D30 (1984) 49–54; M. Gluck, E. Reya and A. Vogt, *Z.Phys.* C67 (1995) 433–448; H. Lai et al., *Phys.Rev.* D55 (1997) 1280–1296, arXiv:hep-ph/9606399 [hep-ph]; H. Lai et al., *Eur.Phys.J.* C12 (2000) 375–392, arXiv:hep-ph/9903282 [hep-ph]; J. Pumplin et al., *JHEP* 0207 (2002) 012, arXiv:hep-ph/0201195 [hep-ph]; A. Martin et al., *Eur.Phys.J.* C63 (2009) 189–285, arXiv:0901.0002 [hep-ph].

[99] M. Dittmar et al., (2009), arXiv:0901.2504 [hep-ph].

[100] S. Alekhin et al., (2011), arXiv:1101.0536 [hep-ph]; M. Botje et al., (2011), arXiv:1101.0538 [hep-ph].

[101] R. Ellis, W. Stirling and B. Webber, *QCD and Collider Physics*, Cambridge Monographs on Particle Physics, Nuclear Physics and Cosmology, Cambridge University Press, 2003, URL: http://books.google.de/books?id=TqrPVoS6s0UC.

[102] D. Graudenz, M. Spira and P. Zerwas, *Phys.Rev.Lett.* 70 (1993) 1372–1375; M. Spira et al., *Nucl.Phys.* B453 (1995) 17–82, arXiv:hep-ph/9504378 [hep-ph].

[103] R. V. Harlander, *Phys.Lett.* B492 (2000) 74–80, arXiv:hep-ph/0007289 [hep-ph]; S. Catani, D. de Florian and M. Grazzini, *JHEP* 0105 (2001) 025, arXiv:hep-ph/0102227 [hep-ph]; R. V. Harlander and W. B. Kilgore, *Phys.Rev.* D64 (2001) 013015, arXiv:hep-ph/0102241 [hep-ph]; R. V. Harlander and W. B. Kilgore, *Phys.Rev.Lett.* 88 (2002) 201801, arXiv:hep-ph/0201206 [hep-ph]; C. Anastasiou and K. Melnikov, *Nucl.Phys.* B646 (2002) 220–256, arXiv:hep-ph/0207004 [hep-ph]; V. Ravindran, J. Smith and W. L. van Neerven, *Nucl.Phys.* B665 (2003) 325–366, arXiv:hep-ph/0302135 [hep-ph]; J. Blumlein and V. Ravindran, *Nucl.Phys.* B716 (2005) 128–172, arXiv:hep-ph/0501178 [hep-ph].

[104] V. D. Barger, R. Phillips and D. Zeppenfeld, *Phys.Lett.* B346 (1995) 106–114, arXiv:hep-ph/9412276 [hep-ph]; D. L. Rainwater and D. Zeppenfeld, *JHEP* 9712 (1997) 005, arXiv:hep-ph/9712271 [hep-ph]; D. L. Rainwater, D. Zeppenfeld and K. Hagiwara, *Phys.Rev.* D59 (1998) 014037, arXiv:hep-ph/9808468 [hep-ph]; D. L. Rainwater and D. Zeppenfeld, *Phys.Rev.* D60 (1999) 113004, arXiv:hep-ph/9906218 [hep-ph]; V. Del Duca et al., *JHEP* 0610 (2006) 016, arXiv:hep-ph/0608158 [hep-ph].

[105] T. Han, G. Valencia and S. Willenbrock, *Phys.Rev.Lett.* 69 (1992) 3274–3277, arXiv:hep-ph/9206246 [hep-ph]; T. Figy, C. Oleari and D. Zeppenfeld, *Phys.Rev.* D68 (2003) 073005, arXiv:hep-ph/0306109 [hep-ph]; T. Figy and D. Zeppenfeld, *Phys.Lett.* B591 (2004) 297–303, arXiv:hep-ph/0403297 [hep-ph].

[106] M. Ciccolini, A. Denner and S. Dittmaier, *Phys.Rev.Lett.* 99 (2007) 161803, arXiv:0707.0381 [hep-ph]; M. Ciccolini, A. Denner and S. Dittmaier, *Phys.Rev.* D77 (2008) 013002, arXiv:0710.4749 [hep-ph].

[107] J. M. Butterworth et al., *Phys.Rev.Lett.* 100 (2008) 242001, arXiv:0802.2470 [hep-ph].

[108] T. Han and S. Willenbrock, *Phys.Lett.* B273 (1991) 167–172; H. Baer, B. Bailey and J. Owens, *Phys.Rev.* D47 (1993) 2730–2734; J. Ohnemus and W. J. Stirling, *Phys.Rev.* D47 (1993) 2722–2729.

[109] O. Brein et al., *Eur.Phys.J.* C72 (2012) 1868, arXiv:1111.0761 [hep-ph]; L. Altenkamp et al., *JHEP* 1302 (2013) 078, arXiv:1211.5015 [hep-ph]; R. V. Harlander, S. Liebler and T. Zirke, (2013), arXiv:1307.8122 [hep-ph].

[110] S. Drell and T.-M. Yan, *Phys.Rev.Lett.* 25 (1970) 316–320.

[111] M. Ciccolini, S. Dittmaier and M. Krämer, *Phys.Rev.* D68 (2003) 073003, arXiv:hep-ph/0306234 [hep-ph].

[112] W. Beenakker et al., *Phys.Rev.Lett.* 87 (2001) 201805, arXiv:hep-ph/0107081 [hep-ph]; L. Reina and S. Dawson, *Phys.Rev.Lett.* 87 (2001) 201804, arXiv:hep-ph/0107101 [hep-ph]; L. Reina, S. Dawson and D. Wackeroth, *Phys.Rev.* D65 (2002) 053017, arXiv:hep-ph/0109066 [hep-ph]; S. Dawson et al., *Phys.Rev.* D67 (2003) 071503, arXiv:hep-ph/0211438 [hep-ph]; S. Dawson et al., *Phys.Rev.* D68 (2003) 034022, arXiv:hep-ph/0305087 [hep-ph].

[113] R. Harlander, M. Krämer and M. Schumacher, (2011), arXiv:1112.3478 [hep-ph].

[114] The Tevatron New Physics Higgs Working Group, CDF Collaboration, DØ Collaboration, (2012), arXiv:1207.0449 [hep-ex].

[115] ALEPH Collaboration, DELPHI Collaboration, L3 Collaboration, OPAL Collaboration, The LEP working group for Higgs boson searches, (2001), arXiv:hep-ex/0107032 [hep-ex].

[116] K. J. Knoepfel, *Mod.Phys.Lett.* A29 (2014) 1430009, arXiv:1404.2951 [hep-ex].

[117] R. K. Ellis et al., *Nucl.Phys.* B297 (1988) 221; A. Elagin et al., *Nucl.Instrum.Meth.* A654 (2011) 481–489, arXiv:1012.4686 [hep-ex].

[118] H. Georgi and S. Glashow, *Phys.Rev.Lett.* 32 (1974) 438–441; H. Fritzsch and P. Minkowski, *Annals Phys.* 93 (1975) 193–266; P. Langacker, *Phys.Rept.* 72 (1981) 185; S. Dimopoulos, S. Raby and F. Wilczek, *Phys.Rev.* D24 (1981) 1681–1683.

[119] J. R. Ellis, S. Kelley and D. V. Nanopoulos, *Phys.Lett.* B249 (1990) 441–448; P. Langacker, (1990); U. Amaldi, W. de Boer and H. Furstenau, *Phys.Lett.* B260 (1991) 447–455.

[120] J. R. Ellis, S. Kelley and D. V. Nanopoulos, *Phys.Lett.* B260 (1991) 131–137; S. Dimopoulos, S. Raby and F. Wilczek, *Phys.Today* 44N10 (1991) 25–33; P. Langacker and M.-x. Luo, *Phys.Rev.* D44 (1991) 817–822; P. Langacker and N. Polonsky, *Phys.Rev.* D47 (1993) 4028–4045, arXiv:hep-ph/9210235 [hep-ph]; G. G. Ross and R. Roberts, *Nucl.Phys.* B377 (1992) 571–592.

[121] N. Arkani-Hamed, S. Dimopoulos and G. Dvali, *Phys.Rev.* D59 (1999) 086004, arXiv:hep-ph/9807344 [hep-ph]; I. Antoniadis et al., *Phys.Lett.* B436 (1998) 257–263, arXiv:hep-ph/9804398 [hep-ph]; N. Arkani-Hamed, S. Dimopoulos and G. Dvali, *Phys.Lett.* B429 (1998) 263–272, arXiv:hep-ph/9803315 [hep-ph].

[122] E. Farhi and L. Susskind, *Phys.Rept.* 74 (1981) 277; D. B. Kaplan, H. Georgi and S. Dimopoulos, *Phys.Lett.* B136 (1984) 187; M. J. Dugan, H. Georgi and D. B. Kaplan, *Nucl.Phys.* B254 (1985) 299; H. Georgi and D. B. Kaplan, *Phys.Lett.* B145 (1984) 216; C. T. Hill, *Phys.Lett.* B345 (1995) 483–489, arXiv:hep-ph/9411426 [hep-ph].

[123] E. Kolb and 1. Michael Turner, *The Early Universe*, Frontiers in physics, Westview Press, 1994, URL: http://books.google.de/books?id=Qwijr-HsvMMC.

[124] S. Perlmutter et al., *Astrophys.J.* 517 (1999) 565–586, arXiv:astro-ph/9812133 [astro-ph].

[125] G. Hinshaw et al., *Astrophys.J.Suppl.* 208 (2013) 19, arXiv:1212.5226 [astro-ph.CO].

[126] O. Lahav and A. Liddle, *The Cosmological Parameters*, review appeared in Ref. [74].

[127] L. Covi et al., *JHEP* 0105 (2001) 033, arXiv:hep-ph/0101009 [hep-ph].

[128] J. E. Kim and G. Carosi, *Rev.Mod.Phys.* 82 (2010) 557–602, arXiv:0807.3125 [hep-ph].

[129] J. R. Ellis et al., *Nucl.Phys.* B238 (1984) 453–476.

[130] M. Drees and M. M. Nojiri, *Phys.Rev.* D47 (1993) 376–408, arXiv:hep-ph/9207234 [hep-ph].

[131] M. Bolz, A. Brandenburg and W. Buchmüller, *Nucl.Phys.* B606 (2001) 518–544, arXiv:hep-ph/0012052 [hep-ph].

[132] A. Brandenburg and F. D. Steffen, *JCAP* 0408 (2004) 008, arXiv:hep-ph/0405158 [hep-ph].

[133] J. March-Russell et al., *JHEP* 0807 (2008) 058, arXiv:0801.3440 [hep-ph]; J. L. Feng, H. Tu and H.-B. Yu, *JCAP* 0810 (2008) 043, arXiv:0808.2318 [hep-ph]; J. L. Feng et al., *JCAP* 0907 (2009) 004, arXiv:0905.3039 [hep-ph]; T. Cohen et al., *Phys.Rev.* D82 (2010) 056001, arXiv:1005.1655 [hep-ph].

[134] J. M. Cline et al., *Phys.Rev.* D88 (2013) 055025, arXiv:1306.4710 [hep-ph].

[135] L. Lopez Honorez and C. E. Yaguna, *JHEP* 1009 (2010) 046, arXiv:1003.3125 [hep-ph].

[136] A. Goudelis, B. Herrmann and O. Stål, *JHEP* 1309 (2013) 106, arXiv:1303.3010 [hep-ph].

[137] G. Servant and T. M. Tait, *Nucl.Phys.* B650 (2003) 391–419, arXiv:hep-ph/0206071 [hep-ph]; H.-C. Cheng, J. L. Feng and K. T. Matchev, *Phys.Rev.Lett.* 89 (2002) 211301, arXiv:hep-ph/0207125 [hep-ph]; D. Hooper and S. Profumo, *Phys.Rept.* 453 (2007) 29–115, arXiv:hep-ph/0701197 [hep-ph].

[138] A. Sakharov, *Pisma Zh.Eksp.Teor.Fiz.* 5 (1967) 32–35.

[139] A. G. Cohen, D. B. Kaplan and A. E. Nelson, *Phys.Lett.* B245 (1990) 561–564; A. G. Cohen, D. B. Kaplan and A. E. Nelson, *Nucl.Phys.* B349 (1991) 727–742; G. W. Anderson and L. J. Hall, *Phys.Rev.* D45 (1992) 2685–2698; V. Rubakov and M. Shaposhnikov, *Usp.Fiz.Nauk* 166 (1996) 493–537, arXiv:hep-ph/9603208 [hep-ph]; T. Konstandin, *Phys.Usp.* 56 (2013) 747–771, arXiv:1302.6713 [hep-ph].

[140] I. Affleck and M. Dine, *Nucl.Phys.* B249 (1985) 361.

[141] M. Fukugita and T. Yanagida, *Phys.Lett.* B174 (1986) 45; M. Luty, *Phys.Rev.* D45 (1992) 455–465; R. Barbieri et al., *Nucl.Phys.* B575 (2000) 61–77, arXiv:hep-ph/9911315 [hep-ph]; W. Buchmüller, P. Di Bari and M. Plumacher, *Nucl.Phys.* B643 (2002) 367–390, arXiv:hep-ph/0205349 [hep-ph].

[142] P. Minkowski, *Phys.Lett.* B67 (1977) 421; R. N. Mohapatra and G. Senjanovic, *Phys.Rev.Lett.* 44 (1980) 912; J. Schechter and J. Valle, *Phys.Rev.* D22 (1980) 2227; T. Yanagida, *Prog.Theor.Phys.* 64 (1980) 1103.

[143] L. J. Hall and M. Suzuki, *Nucl.Phys.* B231 (1984) 419; F. Borzumati et al., *Phys.Lett.* B384 (1996) 123–130, arXiv:hep-ph/9606251 [hep-ph]; Y. Grossman and H. E. Haber, *Phys.Rev.Lett.* 78 (1997) 3438–3441, arXiv:hep-ph/9702421 [hep-ph]; Y. Grossman and H. E. Haber, *Phys.Rev.* D59 (1999) 093008, arXiv:hep-ph/9810536 [hep-ph]; Y. Grossman and H. E. Haber, (1999), arXiv:hep-ph/9906310 [hep-ph]; S. Davidson and M. Losada, *JHEP* 0005 (2000) 021, arXiv:hep-ph/0005080 [hep-ph]; M. Hirsch et al., *Phys.Rev.* D62 (2000) 113008, arXiv:hep-ph/0004115 [hep-ph].

[144] J. L. Hewett and J. D. Wells, *Phys.Rev.* D55 (1997) 5549–5560, arXiv:hep-ph/9610323 [hep-ph]; K. Babu and C. F. Kolda, *Phys.Rev.Lett.* 84 (2000) 228–231, arXiv:hep-ph/9909476 [hep-ph]; G. Buchalla, G. Hiller and G. Isidori, *Phys.Rev.* D63 (2000) 014015, arXiv:hep-ph/0006136 [hep-ph]; M. Ciuchini et al., *Phys.Rev.* D67 (2003) 075016, arXiv:hep-ph/0212397 [hep-ph]; E. Golowich et al., *Phys.Rev.* D76 (2007) 095009, arXiv:0705.3650 [hep-ph]; W. Altmannshofer et al., *Nucl.Phys.* B830 (2010) 17–94, arXiv:0909.1333 [hep-ph].

[145] F. Mahmoudi and O. Stål, (2009), arXiv:0907.1791 [hep-ph].

[146] F. Jegerlehner and A. Nyffeler, *Phys.Rept.* 477 (2009) 1–110, arXiv:0902.3360 [hep-ph].

[147] G. Bennett et al., *Phys. Rev. Lett.* 92 (2004) 161802, arXiv:hep-ex/0401008 [hep-ex]; G. Bennett et al., *Phys. Rev.* D73 (2006) 072003, arXiv:hep-ex/0602035 [hep-ex].

[148] M. Davier et al., *Eur. Phys. J. C* 71 (2011) 1515, arXiv:1010.4180 [hep-ph].

[149] Y. Amhis et al., (2012), arXiv:1207.1158 [hep-ex].

[150] R. Aaij et al., *Phys.Rev.Lett.* 110 (2013) 021801, arXiv:1211.2674 [hep-ex].

[151] CMS and LHCb Collaborations, (2013), CMS-PAS-BPH-13-007, LHCb-CONF-2013-012, CERN-LHCb-CONF-2013-012.

[152] Tevatron Electroweak Working Group for the CDF and DØ Collaborations, (2012), arXiv:1204.0042 [hep-ex].

[153] S. Schael et al., *Phys.Rept.* 427 (2006) 257–454, arXiv:hep-ex/0509008 [hep-ex].

[154] F. Mahmoudi, *Comput. Phys. Commun.* 178 (2008) 745–754, arXiv:0710.2067 [hep-ph]; F. Mahmoudi, *Comput. Phys. Commun.* 180 (2009) 1579–1613, arXiv:0808.3144 [hep-ph]; F. Mahmoudi, *Comput. Phys. Commun.* 180 (2009) 1718–1719.

[155] S. Heinemeyer, W. Hollik and G. Weiglein, *Eur.Phys.J.* C9 (1999) 343–366, arXiv:hep-ph/9812472 [hep-ph]; S. Heinemeyer, W. Hollik and G. Weiglein, *Comput.Phys.Commun.* 124 (2000) 76–89, arXiv:hep-ph/9812320 [hep-ph]; M. Frank et al., *JHEP* 0702 (2007) 047, arXiv:hep-ph/0611326 [hep-ph]; T. Hahn et al., *Comput.Phys.Commun.* 180 (2009) 1426–1427; T. Hahn et al., (2014), arXiv:1404.0186 [hep-ph].

[156] G. Degrassi et al., *Eur. Phys. J. C* 28 (2003) 133–143, arXiv:hep-ph/0212020 [hep-ph].

[157] T. Hahn et al., *Nucl. Phys. Proc. Suppl.* 205-206 (2010) 152–157, arXiv:1007.0956 [hep-ph].

[158] S. Heinemeyer et al., *JHEP* 1312 (2013) 084, arXiv:1311.1663 [hep-ph].

[159] M. Awramik et al., *Phys.Rev.* D69 (2004) 053006, arXiv:hep-ph/0311148 [hep-ph].

[160] S. Heinemeyer, W. Hollik and G. Weiglein, *Phys.Rept.* 425 (2006) 265–368, arXiv:hep-ph/0412214 [hep-ph]; S. Heinemeyer et al., *Eur. Phys. J.* C37 (2004) 481–493, arXiv:hep-ph/0403228 [hep-ph]; S. Heinemeyer et al., *JHEP* 0608 (2006) 052, arXiv:hep-ph/0604147 [hep-ph].

[161] S. Heinemeyer and G. Weiglein, (2010), arXiv:1007.5232 [hep-ph].

[162] M. Baak et al., (2013), arXiv:1310.6708 [hep-ph].

[163] ATLAS Collaboration, *Overview of public results of ATLAS Supersymmetry (SUSY) searches*, https://twiki.cern.ch/twiki/bin/view/AtlasPublic/SupersymmetryPublicResults.

[164] ATLAS Collaboration, *Overview of Exotics Public results*, https://twiki.cern.ch/twiki/bin/view/AtlasPublic/ExoticsPublicResults.

[165] CMS Collaboration, *Overview of public results of CMS Supersymmetry (SUSY) searches*, https://twiki.cern.ch/twiki/bin/view/CMSPublic/PhysicsResultsSUS.

[166] CMS Collaboration, *Overview of Exotics public results*, https://twiki.cern.ch/twiki/bin/view/CMSPublic/PhysicsResultsEXO.

[167] H. Dreiner, D. Schmeier and J. Tattersall, *Europhys.Lett.* 102 (2013) 51001, arXiv:1303.3348 [hep-ph]; O. Buchmueller, M. J. Dolan and C. McCabe, *JHEP* 1401 (2014) 025, arXiv:1308.6799 [hep-ph]; G. Busoni et al., *Phys.Lett.* B728 (2014) 412–421, arXiv:1307.2253 [hep-ph]; G. Busoni et al., (2014), arXiv:1402.1275 [hep-ph]; G. Busoni et al., (2014), arXiv:1405.3101 [hep-ph].

[168] S. P. Martin, *Phys.Rev.* D75 (2007) 115005, arXiv:hep-ph/0703097 [HEP-PH]; H. Baer et al., *JHEP* 0708 (2007) 060, arXiv:0707.0618 [hep-ph]; H. K. Dreiner, M. Krämer and J. Tattersall, *Europhys.Lett.* 99 (2012) 61001, arXiv:1207.1613 [hep-ph].

[169] C. F. Berger et al., *JHEP* 0902 (2009) 023, arXiv:0812.0980 [hep-ph]; J. A. Conley et al., *Eur.Phys.J.* C71 (2011) 1697, arXiv:1009.2539 [hep-ph]; J. A. Conley et al., *Physical Review D* (2011), arXiv:1103.1697 [hep-ph].

[170] R. Bernabei et al., *Eur.Phys.J.* C67 (2010) 39–49, arXiv:1002.1028 [astro-ph.GA].

[171] C. Aalseth et al., *Phys.Rev.Lett.* 106 (2011) 131301, arXiv:1002.4703 [astro-ph.CO].

[172] G. Angloher et al., *Eur.Phys.J.* C72 (2012) 1971, arXiv:1109.0702 [astro-ph.CO].

[173] E. Aprile et al., *Phys.Rev.Lett.* 109 (2012) 181301, arXiv:1207.5988 [astro-ph.CO].

[174] D. Akerib et al., (2013), arXiv:1310.8214 [astro-ph.CO].

[175] M. I. Gresham and K. M. Zurek, *Phys.Rev.* D89 (2014) 016017, arXiv:1311.2082 [hep-ph].

[176] R. Catena and P. Gondolo, (2014), arXiv:1405.2637 [hep-ph].

[177] K. Freese, M. Lisanti and C. Savage, *Rev.Mod.Phys.* 85 (2013) 1561–1581, arXiv:1209.3339 [astro-ph.CO]; R. Catena and L. Covi, (2013), arXiv:1310.4776 [hep-ph]; M. Schumann, (2013), arXiv:1310.5217 [astro-ph.CO].

[178] C. Rott, *Nucl.Phys.Proc.Suppl.* 235-236 (2013) 413–420, arXiv:1210.4161 [astro-ph.HE]; A. Ibarra, *Acta Phys.Polon.* B43 (2012) 2199–2224; S. Funk, (2013), arXiv:1310.2695 [astro-ph.HE]; B. Burch and R. Cowsik, *Astrophys.J.* 779 (2013) 35, arXiv:1306.1920 [astro-ph.GA]; P. Salati, (2014), arXiv:1403.4495 [astro-ph.HE].

[179] J. Lees et al., *Phys.Rev.Lett.* 109 (2012) 101802, arXiv:1205.5442 [hep-ex].

[180] A. Crivellin, C. Greub and A. Kokulu, *Phys.Rev.* D86 (2012) 054014, arXiv:1206.2634 [hep-ph].

[181] R. Aaij et al., *Phys.Rev.Lett.* 111 (2013) 191801, arXiv:1308.1707 [hep-ex].

[182] G. Aad et al., *Phys.Rev.* D87.11 (2013) 112001, arXiv:1210.2979 [hep-ex].

[183] C. Collaboration, (2012); S. Chatrchyan et al., *Phys.Lett.* B721 (2013) 190–211, arXiv:1301.4698 [hep-ex].

[184] D. Curtin, P. Jaiswal and P. Meade, *Phys.Rev.* D87.3 (2013) 031701, arXiv:1206.6888 [hep-ph].

[185] K. Rolbiecki and K. Sakurai, *JHEP* 1309 (2013) 004, arXiv:1303.5696 [hep-ph].

[186] T. Aaltonen et al., *Phys.Rev.* D83 (2011) 112003, arXiv:1101.0034 [hep-ex]; T. A. Aaltonen et al., *Phys.Rev.* D88 (2013) 072003, arXiv:1308.1120 [hep-ex].

[187] V. M. Abazov et al., *Phys.Rev.* D84 (2011) 112005, arXiv:1107.4995 [hep-ex]; V. M. Abazov et al., *Phys.Rev.* D88 (2013) 112002, arXiv:1308.6690 [hep-ex].

[188] E. L. Berger et al., *Phys.Rev.Lett.* 106 (2011) 201801, arXiv:1101.5625 [hep-ph]; B. Bhattacherjee, S. S. Biswal and D. Ghosh, *Phys.Rev.* D83 (2011) 091501, arXiv:1102.0545 [hep-ph]; M. Duraisamy, A. Rashed and A. Datta, *Phys.Rev.* D84 (2011) 054018, arXiv:1106.5982 [hep-ph].

[189] R. Haag, J. T. Lopuszanski and M. Sohnius, *Nucl.Phys.* B88 (1975) 257.

[190] J. Gunion and H. E. Haber, *Nucl.Phys.* B272 (1986) 1; J. Gunion and H. E. Haber, *Nucl.Phys.* B278 (1986) 449.

[191] F. Gabbiani et al., *Nucl.Phys.* B477 (1996) 321–352, arXiv:hep-ph/9604387 [hep-ph].

[192] S. Jäger, *Eur.Phys.J.* C59 (2009) 497–520, arXiv:0808.2044 [hep-ph].

[193] B. Allanach, A. Dedes and H. Dreiner, *Phys.Rev.* D69 (2004) 115002, arXiv:hep-ph/0309196 [hep-ph].

[194] S. Weinberg, *Phys.Rev.* D26 (1982) 287.

[195] N. Sakai and T. Yanagida, *Nucl.Phys.* B197 (1982) 533.

[196] T. D. Lee, *Phys. Rev.* D8 (1973) 1226–1239; S. L. Glashow and S. Weinberg, *Phys. Rev.* D15 (1977) 1958; N. G. Deshpande and E. Ma, *Phys. Rev.* D18 (1978) 2574; J. F. Gunion and H. E. Haber, *Phys.Rev.* D67 (2003) 075019, arXiv:hep-ph/0207010 [hep-ph].

[197] T. P. Cheng and M. Sher, *Phys. Rev.* D35 (1987) 3484.

[198] S. Dimopoulos, S. Raby and F. Wilczek, *Phys.Lett.* B112 (1982) 133; A. Y. Smirnov and F. Vissani, *Nucl.Phys.* B460 (1996) 37–56, arXiv:hep-ph/9506416 [hep-ph]; G. Bhattacharyya and P. B. Pal, *Phys.Rev.* D59 (1999) 097701, arXiv:hep-ph/9809493 [hep-ph].

[199] H. K. Dreiner, (1997), arXiv:hep-ph/9707435 [hep-ph]; R. Barbier et al., *Phys.Rept.* 420 (2005) 1–202, arXiv:hep-ph/0406039 [hep-ph].

[200] H. K. Dreiner and M. Thormeier, *Phys.Rev.* D69 (2004) 053002, arXiv:hep-ph/0305270 [hep-ph].

[201] Y. Hayato et al., *Phys.Rev.Lett.* 83 (1999) 1529–1533, arXiv:hep-ex/9904020 [hep-ex]; M. Shiozawa et al., *Phys.Rev.Lett.* 81 (1998) 3319–3323, arXiv:hep-ex/9806014 [hep-ex].

[202] M. Bento, L. J. Hall and G. G. Ross, *Nucl.Phys.* B292 (1987) 400; L. M. Krauss and F. Wilczek, *Phys.Rev.Lett.* 62 (1989) 1221; L. E. Ibanez and G. G. Ross, *Phys.Lett.* B260 (1991) 291–295; L. E. Ibanez and G. G. Ross, *Nucl.Phys.* B368 (1992) 3–37.

[203] G. R. Farrar and P. Fayet, *Phys.Lett.* B76 (1978) 575–579.

[204] H. Goldberg, *Phys. Rev. Lett.* 50 (1983) 1419.

[205] H. K. Dreiner et al., *Nucl.Phys.* B795 (2008) 172–200, arXiv:0708.0989 [hep-ph].

[206] H. K. Dreiner, C. Luhn and M. Thormeier, *Phys.Rev.* D73 (2006) 075007, arXiv:hep-ph/0512163 [hep-ph]; H. K. Dreiner et al., *Nucl.Phys.* B774 (2007) 127–167, arXiv:hep-ph/0610026 [hep-ph]; H.-S. Lee, *Phys.Lett.* B704 (2011) 316–321, arXiv:1007.1040 [hep-ph]; H. K. Dreiner, M. Hanussek and C. Luhn, *Phys.Rev.* D86 (2012) 055012, arXiv:1206.6305 [hep-ph].

[207] H. Dreiner, S. Grab and M. Trenkel, *Phys.Rev.* D79 (2009) 016002, arXiv:0808.3079 [hep-ph]; M. Bernhardt et al., *Phys.Rev.* D79 (2009) 035003, arXiv:0810.3423 [hep-ph]; H. K. Dreiner and S. Grab, *Phys.Lett.* B679 (2009) 45–50, arXiv:0811.0200 [hep-ph]; K. Desch et al., *Phys.Rev.* D83 (2011) 015013, arXiv:1008.1580 [hep-ph]; H. Dreiner, S. Grab and T. Stefaniak, *Phys.Rev.* D84 (2011) 035023, arXiv:1102.3189 [hep-ph]; H. Dreiner, S. Grab and T. Stefaniak, *Phys.Rev.* D84 (2011) 015005, arXiv:1103.1883 [hep-ph].

[208] S. Dimopoulos et al., *Phys.Rev.* D41 (1990) 2099; J. Hewett and T. Rizzo, (1998), arXiv:hep-ph/9809525 [hep-ph]; H. K. Dreiner, P. Richardson and M. H. Seymour, (1998), arXiv:hep-ph/9903419 [hep-ph].

[209] H. K. Dreiner, P. Richardson and M. H. Seymour, *Phys.Rev.* D63 (2001) 055008, arXiv:hep-ph/0007228 [hep-ph].

[210] N. Desai and B. Mukhopadhyaya, *JHEP* 1010 (2010) 060, arXiv:1002.2339 [hep-ph].

[211] H. K. Dreiner, J. Soo Kim and M. Thormeier, (2007), arXiv:0711.4315 [hep-ph]; H. Dreiner, M. Hanussek and S. Grab, *Phys.Rev.* D82 (2010) 055027, arXiv:1005.3309 [hep-ph]; H. K. Dreiner et al., *Phys.Rev.* D84 (2011) 113005, arXiv:1106.4338 [hep-ph].

[212] L. Girardello and M. T. Grisaru, *Nucl.Phys.* B194 (1982) 65.

[213] S. Dimopoulos and D. W. Sutter, *Nucl.Phys.* B452 (1995) 496–512, arXiv:hep-ph/9504415 [hep-ph].

[214] F. Gabbiani and A. Masiero, *Nucl.Phys.* B322 (1989) 235.

[215] M. Brooks et al., *Phys.Rev.Lett.* 83 (1999) 1521–1524, arXiv:hep-ex/9905013 [hep-ex].

[216] M. Ciuchini et al., *JHEP* 9810 (1998) 008, arXiv:hep-ph/9808328 [hep-ph].

[217] D. Becirevic et al., *Nucl.Phys.* B634 (2002) 105–119, arXiv:hep-ph/0112303 [hep-ph].

[218] J. Foster, K.-i. Okumura and L. Roszkowski, *Phys.Lett.* B641 (2006) 452–460, arXiv:hep-ph/0604121 [hep-ph].

[219] G. Degrassi, P. Gambino and G. Giudice, *JHEP* 0012 (2000) 009, arXiv:hep-ph/0009337 [hep-ph]; M. E. Gomez et al., *Phys.Rev.* D74 (2006) 015015, arXiv:hep-ph/0601163 [hep-ph]; L. Silvestrini, *Ann.Rev.Nucl.Part.Sci.* 57 (2007) 405–440, arXiv:0705.1624 [hep-ph]; M. Artuso et al., *Eur.Phys.J.* C57 (2008) 309–492, arXiv:0801.1833 [hep-ph].

[220] A. G. Cohen, D. Kaplan and A. Nelson, *Phys.Lett.* B388 (1996) 588–598, arXiv:hep-ph/9607394 [hep-ph]; J. D. Wells, (2003), arXiv:hep-ph/0306127 [hep-ph]; N. Arkani-Hamed and S. Dimopoulos, *JHEP* 0506 (2005) 073, arXiv:hep-th/0405159 [hep-th]; Y. Nir and N. Seiberg, *Phys.Lett.* B309 (1993) 337–343, arXiv:hep-ph/9304307 [hep-ph].

[221] S. Glashow, J. Iliopoulos and L. Maiani, *Phys.Rev.* D2 (1970) 1285–1292.

[222] J. R. Ellis, S. Ferrara and D. V. Nanopoulos, *Phys.Lett.* B114 (1982) 231.

[223] W. Buchmüller and D. Wyler, *Phys.Lett.* B121 (1983) 321.

[224] J. Polchinski and M. B. Wise, *Phys.Lett.* B125 (1983) 393; F. del Aguila et al., *Phys.Lett.* B126 (1983) 71; D. V. Nanopoulos and M. Srednicki, *Phys.Lett.* B128 (1983) 61; T. Ibrahim and P. Nath, *Rev.Mod.Phys.* 80 (2008) 577–631, arXiv:0705.2008 [hep-ph]; T. Falk et al., *Nucl.Phys.* B560 (1999) 3–22, arXiv:hep-ph/9904393 [hep-ph].

[225] S. Dimopoulos and H. Georgi, *Nucl.Phys.* B193 (1981) 150.

[226] R. Mohapatra, (1999) 336–394, arXiv:hep-ph/9911272 [hep-ph].

[227] P. H. Chankowski, O. Lebedev and S. Pokorski, *Nucl.Phys.* B717 (2005) 190–222, arXiv:hep-ph/0502076 [hep-ph].

[228] R. L. Arnowitt, P. Nath and B. Zumino, *Phys.Lett.* B56 (1975) 81; P. Nath and R. L. Arnowitt, *Phys.Lett.* B56 (1975) 177; S. Deser and B. Zumino, *Phys.Lett.* B62 (1976) 335; D. Z. Freedman, P. van Nieuwenhuizen and S. Ferrara, *Phys.Rev.* D13 (1976) 3214–3218; E. Cremmer et al., *Nucl.Phys.* B147 (1979) 105; E. Cremmer et al., *Nucl.Phys.* B212 (1983) 413.

[229] A. H. Chamseddine, R. L. Arnowitt and P. Nath, *Phys.Rev.Lett.* 49 (1982) 970; R. Barbieri, S. Ferrara and C. A. Savoy, *Phys.Lett.* B119 (1982) 343; L. J. Hall, J. D. Lykken and S. Weinberg, *Phys.Rev.* D27 (1983) 2359–2378; L. Alvarez-Gaume, J. Polchinski and M. B. Wise, *Nucl.Phys.* B221 (1983) 495; S. K. Soni and H. A. Weldon, *Phys.Lett.* B126 (1983) 215.

[230] L. E. Ibanez and G. G. Ross, *Phys.Lett.* B110 (1982) 215–220.

[231] M. Drees and M. M. Nojiri, *Nucl.Phys.* B369 (1992) 54–98.

[232] S. P. Martin and M. T. Vaughn, *Phys.Rev.* D50 (1994) 2282, arXiv:hep-ph/9311340 [hep-ph].

[233] O. Buchmueller et al., *Eur.Phys.J.* C71 (2011) 1583, arXiv:1011.6118 [hep-ph].

[234] P. Bechtle et al., (2013), arXiv:1310.3045 [hep-ph].

[235] O. Buchmueller et al., *Eur.Phys.J.* C71 (2011) 1634, arXiv:1102.4585 [hep-ph]; O. Buchmueller et al., *Eur.Phys.J.* C71 (2011) 1722, arXiv:1106.2529 [hep-ph]; A. Dighe et al., *Int.J.Mod.Phys.* A28 (2013) 1350134, arXiv:1303.0721 [hep-ph]; T. Cohen and J. G. Wacker, *JHEP* 1309 (2013) 061, arXiv:1305.2914 [hep-ph].

[236] H. E. Haber, (1997), arXiv:hep-ph/9707213 [hep-ph].

[237] B. Schrempp and M. Wimmer, *Prog.Part.Nucl.Phys.* 37 (1996) 1–90, arXiv:hep-ph/9606386 [hep-ph].

[238] J. Gunion and A. Turski, *Phys.Rev.* D39 (1989) 2701; J. Gunion and A. Turski, *Phys.Rev.* D40 (1989) 2333; A. Brignole et al., *Phys.Lett.* B271 (1991) 123–132; A. Brignole, *Phys.Lett.* B277 (1992) 313–323; M. A. Diaz and H. E. Haber, *Phys.Rev.* D45 (1992) 4246–4260; P. H. Chankowski, S. Pokorski and J. Rosiek, *Phys.Lett.* B274 (1992) 191–198; M. Frank et al., *Phys.Rev.* D88 (2013) 055013, arXiv:1306.1156 [hep-ph].

[239] Y. Okada, M. Yamaguchi and T. Yanagida, *Prog.Theor.Phys.* 85 (1991) 1–6; J. R. Ellis, G. Ridolfi and F. Zwirner, *Phys.Lett.* B257 (1991) 83–91; H. E. Haber and R. Hempfling, *Phys.Rev.Lett.* 66 (1991) 1815–1818.

[240] H. E. Haber, R. Hempfling and A. H. Hoang, *Z.Phys.* C75 (1997) 539–554, arXiv:hep-ph/9609331 [hep-ph].

[241] M. S. Carena et al., *Nucl.Phys.* B580 (2000) 29–57, arXiv:hep-ph/0001002 [hep-ph].

[242] T. Hahn et al., (2013), arXiv:1312.4937 [hep-ph].

[243] J. Lee et al., *Comput.Phys.Commun.* 156 (2004) 283–317, arXiv:hep-ph/0307377 [hep-ph]; J. Lee et al., *Comput.Phys.Commun.* 180 (2009) 312–331, arXiv:0712.2360 [hep-ph]; J. Lee et al., *Comput.Phys.Commun.* 184 (2013) 1220–1233, arXiv:1208.2212 [hep-ph].

[244] W. Porod, *Comput.Phys.Commun.* 153 (2003) 275–315, arXiv:hep-ph/0301101 [hep-ph]; W. Porod and F. Staub, *Comput.Phys.Commun.* 183 (2012) 2458–2469, arXiv:1104.1573 [hep-ph].

[245] J. Casas et al., *Nucl.Phys.* B436 (1995) 3–29, arXiv:hep-ph/9407389 [hep-ph]; M. S. Carena et al., *Phys.Lett.* B355 (1995) 209–221, arXiv:hep-ph/9504316 [hep-ph]; M. S. Carena, M. Quiros and C. Wagner, *Nucl.Phys.* B461 (1996) 407–436, arXiv:hep-ph/9508343 [hep-ph].

[246] M. Carena et al., *Eur. Phys. J.* C73 (2013) 2552, arXiv:1302.7033 [hep-ph].

[247] B. Allanach et al., *JHEP* 0409 (2004) 044, arXiv:hep-ph/0406166 [hep-ph].

[248] A. Dedes and P. Slavich, *Nucl. Phys.* B657 (2003) 333–354, arXiv:hep-ph/0212132 [hep-ph].

[249] H. Baer et al., *Phys.Rev.* D87.3 (2013) 035017, arXiv:1210.3019 [hep-ph]; H. Baer et al., *Phys.Rev.* D87.11 (2013) 115028, arXiv:1212.2655 [hep-ph].

[250] R. Dermisek and J. F. Gunion, *Phys.Rev.Lett.* 95 (2005) 041801, arXiv:hep-ph/0502105 [hep-ph]; A. Birkedal, Z. Chacko and M. K. Gaillard, *JHEP* 0410 (2004) 036, arXiv:hep-ph/0404197 [hep-ph]; K. Babu et al., *Phys.Rev.* D78 (2008) 055017, arXiv:0807.3055 [hep-ph].

[251] M. Drees, *Int.J.Mod.Phys.* A4 (1989) 3635.

[252] R. Barbieri and A. Strumia, (2000), arXiv:hep-ph/0007265 [hep-ph].

[253] T. Banks, *Nucl.Phys.* B303 (1988) 172; R. Hempfling, *Phys.Rev.* D49 (1994) 6168–6172; L. J. Hall, R. Rattazzi and U. Sarid, *Phys.Rev.* D50 (1994) 7048–7065, arXiv:hep-ph/9306309 [hep-ph]; M. S. Carena et al., *Nucl.Phys.* B426 (1994) 269–300, arXiv:hep-ph/9402253 [hep-ph]; D. M. Pierce et al., *Nucl.Phys.* B491 (1997) 3–67, arXiv:hep-ph/9606211 [hep-ph]; M. S. Carena et al., *Nucl. Phys.* B577 (2000) 88–120, arXiv:hep-ph/9912516.

[254] M. S. Carena and H. E. Haber, *Prog. Part. Nucl. Phys.* 50 (2003) 63–152, arXiv:hep-ph/0208209.

[255] M. S. Carena et al., *Eur. Phys. J.* C45 (2006) 797–814, arXiv:hep-ph/0511023 [hep-ph].

[256] ALEPH Collaboration, DELPHI Collaboration, L3 Collaboration, OPAL Collaboration, The LEP working group for Higgs boson searches, (2001), arXiv:hep-ex/0107030 [hep-ex].

[257] S. Schael et al., *Eur.Phys.J.* C47 (2006) 547–587, arXiv:hep-ex/0602042 [hep-ex].

[258] ALEPH Collaboration, DELPHI Collaboration, L3 Collaboration, OPAL Collaboration, The LEP working group for Higgs boson searches, (2001), arXiv:hep-ex/0107031 [hep-ex].

[259] G. Abbiendi et al., *Eur.Phys.J.* C73 (2013) 2463, arXiv:1301.6065 [hep-ex].

[260] G. Aad et al., *JHEP* 1206 (2012) 039, arXiv:1204.2760 [hep-ex].

[261] ATLAS collaboration, (2013), ATLAS-CONF-2013-090, ATLAS-COM-CONF-2013-107.

[262] CMS Collaboration, *JHEP* 1207 (2012) 143, arXiv:1205.5736 [hep-ex].

[263] CMS Collaboration, (2012), CMS-PAS-HIG-12-052.

[264] CMS Collaboration, (2013), CMS-PAS-HIG-13-025.

[265] K. Huitu et al., *Eur.Phys.J.* C58 (2008) 591–608, arXiv:0808.3094 [hep-ph]; O. Stål and G. Weiglein, *JHEP* 1201 (2012) 071, arXiv:1108.0595 [hep-ph]; S. Gori, P. Schwaller and C. E. Wagner, *Phys.Rev.* D83 (2011) 115022, arXiv:1103.4138 [hep-ph]; D. Ghosh, M. Guchait and D. Sengupta, *Eur.Phys.J.* C72 (2012) 2141, arXiv:1202.4937 [hep-ph].

[266] S. Heinemeyer, W. Hollik and G. Weiglein, *JHEP* 0006 (2000) 009, arXiv:hep-ph/9909540 [hep-ph].

[267] M. S. Carena et al., (1999), arXiv:hep-ph/9912223.

[268] M. S. Carena et al., *Eur. Phys. J. C* 26 (2003) 601–607, arXiv:hep-ph/0202167.

[269] M. Lancaster, (2011), arXiv:1107.5255 [hep-ex].

[270] S. Heinemeyer, O. Stål and G. Weiglein, *Phys. Lett. B* 710 (2012) 201–206, arXiv:1112.3026 [hep-ph].

[271] W. Altmannshofer et al., *JHEP* 1301 (2013) 160, arXiv:1211.1976 [hep-ph].

[272] R. Benbrik et al., *Eur. Phys. J. C* 72 (2012), arXiv:1207.1096 [hep-ph].

[273] M. Drees, *Phys. Rev. D* 86 (2012) 115018, arXiv:1210.6507 [hep-ph].

[274] P. Bechtle et al., *Eur. Phys. J. C* 73 (2013) 2354, arXiv:1211.1955 [hep-ph].

[275] T. Junk, *Nucl.Instrum.Meth.* A434 (1999) 435–443, arXiv:hep-ex/9902006 [hep-ex]; A. L. Read, (2000), CERN-OPEN-2000-205; A. L. Read, *Journal of Physics G: Nuclear and Particle Physics* 28.10 (2002) 2693.

[276] R. J. Barlow, *Statistics: A Guide to the Use of Statistical Methods in the Physical Sciences (Manchester Physics Series)*, Reprint, WileyBlackwell, 1989.

[277] ATLAS Collaboration, (2013), ATLAS-CONF-2013-013, ATLAS-COM-CONF-2013-018.

[278] CMS Collaboration, (2013), CMS-PAS-HIG-13-021.

[279] S. Chatrchyan et al., (2011), arXiv:1104.1619 [hep-ex].

[280] G. Aad et al., *JHEP* 1302 (2013) 095, arXiv:1211.6956 [hep-ex].

[281] S. Chatrchyan et al., (2013), arXiv:1312.5353 [hep-ex].

[282] ATLAS Collaboration, (2013), ATLAS-CONF-2013-012, ATLAS-COM-CONF-2013-015.

[283] CMS Collaboration, (2013), CMS-PAS-HIG-13-001.

[284] ATLAS collaboration, (2013), ATLAS-CONF-2013-108, ATLAS-COM-CONF-2013-095.

[285] CMS Collaboration, (2013), CMS-PAS-HIG-13-004, updated results (dated Dec 2013) taken from https://twiki.cern.ch/twiki/bin/view/CMSPublic/Hig13004TWikiUpdate.

[286] S. Chatrchyan et al., (2014), arXiv:1401.5041 [hep-ex].

[287] T. Aaltonen et al., *Phys.Rev.* D88.5 (2013) 052014, arXiv:1303.6346 [hep-ex].

[288] ATLAS collaboration, (2014), ATLAS-CONF-2014-009, ATLAS-COM-CONF-2014-013.

[289] G. Aad et al., *Phys.Lett.* B726 (2013) 88–119, arXiv:1307.1427 [hep-ex].

[290] S. Banerjee, S. Mukhopadhyay and B. Mukhopadhyaya, *Phys.Rev.* D89 (2014) 053010, arXiv:1308.4860 [hep-ph]; I. Anderson et al., *Phys.Rev.* D89 (2014) 035007, arXiv:1309.4819 [hep-ph]; A. Azatov and A. Paul, *JHEP* 1401 (2014) 014, arXiv:1309.5273 [hep-ph]; E. Boos et al., *Phys.Rev.* D89 (2014) 035001, arXiv:1309.5410 [hep-ph]; M. Chen et al., *Phys.Rev.* D89 (2014) 034002, arXiv:1310.1397 [hep-ph]; G. Buchalla, O. Cata and G. D'Ambrosio, (2013), arXiv:1310.2574 [hep-ph].

[291] P. Bechtle et al., *Eur.Phys.J.* C74 (2014) 2711, arXiv:1305.1933 [hep-ph].

[292] P. Bechtle et al., *Release Note for HiggsSignals-1.1*, *available at* http://higgsbounds.hepforge.org.

[293] A. Bharucha, A. Goudelis and M. McGarrie, (2013), arXiv:1310.4500 [hep-ph]; J. Cao et al., (2013), arXiv:1311.0678 [hep-ph]; L. Wang and X.-F. Han, (2013), arXiv:1312.4759 [hep-ph]; J. Fan and M. Reece, (2014), arXiv:1401.7671 [hep-ph]; K. Kowalska et al., *JHEP* 1404 (2014) 166, arXiv:1402.1328 [hep-ph]; G. Belanger, V. Bizouard and G. Chalons, (2014), arXiv:1402.3522 [hep-ph]; S. Porto, G. A. Moortgat-Pick and K. Rolbiecki, (2014), arXiv:1404.1053 [hep-ph].

[294] N. D. Christensen, T. Han and S. Su, *Phys.Rev.* D85 (2012) 115018, arXiv:1203.3207 [hep-ph]; D. A. Vasquez et al., *Phys.Rev.* D86 (2012) 035023, arXiv:1203.3446 [hep-ph]; M. Hirsch et al., *Phys.Rev.* D86 (2012) 093018, arXiv:1206.3516 [hep-ph]; J. Rathsman and T. Rossler, *Adv.High Energy Phys.* 2012 (2012) 853706, arXiv:1206.1470 [hep-ph]; J. Cao et al., *JHEP* 1211 (2012) 039, arXiv:1206.3865 [hep-ph]; N. D. Christensen, T. Han and T. Li, *Phys.Rev.* D86 (2012) 074003, arXiv:1206.5816 [hep-ph]; C. Han et al., *JHEP* 1310 (2013) 216, arXiv:1308.5307 [hep-ph]; J. Kozaczuk and S. Profumo, (2013), arXiv:1308.5705 [hep-ph]; K. Benakli et al., (2014), arXiv:1403.5122 [hep-ph].

[295] E. Alvarez, E. C. Leskow and J. Zurita, *Phys.Rev.* D83 (2011) 115024, arXiv:1104.3496 [hep-ph]; S. Sekmen et al., *JHEP* 1202 (2012) 075, arXiv:1109.5119 [hep-ph]; A. Arbey, M. Battaglia and F. Mahmoudi, *Eur.Phys.J.* C72 (2012) 1847, arXiv:1110.3726 [hep-ph]; A. Azatov and J. Galloway, *Phys.Rev.* D85 (2012) 055013, arXiv:1110.5646 [hep-ph].

[296] P. Bechtle et al., *Eur.Phys.J.* C66 (2010) 215–259, arXiv:0907.2589 [hep-ph]; P. Bechtle et al., *Phys.Rev.* D84 (2011) 011701, arXiv:1102.4693 [hep-ph]; P. Bechtle et al., *JHEP* 1206 (2012) 098, arXiv:1204.4199 [hep-ph].

[297] CMS Collaboration, (2012), CMS-PAS-HIG-12-050.

[298] J. Espinosa, C. Grojean and M. Muhlleitner, *JHEP* 1005 (2010) 065, arXiv:1003.3251 [hep-ph].

[299] Y. Bai, M. Carena and J. Lykken, *Phys.Rev.Lett.* 103 (2009) 261803, arXiv:0909.1319 [hep-ph].

[300] J. Alcaraz et al., (2006), arXiv:hep-ex/0612034 [hep-ex].

[301] G. Aad et al., *Phys.Rev.Lett.* 108 (2012) 111803, arXiv:1202.1414 [hep-ex].

[302] P. Kemenes, private communication.

[303] J. R. Ellis et al., *JHEP* 0708 (2007) 083, arXiv:0706.0652 [hep-ph].

[304] O. Stål and T. Stefaniak, *PoS* EPS-HEP2013 (2013) 314, arXiv:1310.4039 [hep-ph].

[305] A. Arbey, M. Battaglia and F. Mahmoudi, *Eur. Phys. J. C* 72 (2012) 2169, arXiv:1205.2557 [hep-ph].

[306] A. Arbey et al., *JHEP* 1209 (2012) 107, arXiv:1207.1348 [hep-ph].

[307] A. Azatov et al., *Phys. Rev. D* 86 (2012) 075033, arXiv:1206.1058 [hep-ph]; D. Carmi et al., (2012), arXiv:1206.4201 [hep-ph]; I. Low, J. Lykken and G. Shaughnessy, *Phys. Rev. D* 86 (2012) 093012, arXiv:1207.1093 [hep-ph]; T. Corbett et al., *Phys. Rev. D* 86 (2012) 075013, arXiv:1207.1344 [hep-ph]; P. P. Giardino et al., *Phys. Lett. B* 718 (2012) 469–474, arXiv:1207.1347 [hep-ph]; J. Ellis and T. You, *JHEP* 1209 (2012) 123, arXiv:1207.1693 [hep-ph]; J. Espinosa et al., *JHEP* 1212 (2012) 045, arXiv:1207.1717 [hep-ph]; D. Carmi et al., *JHEP* 1210 (2012) 196, arXiv:1207.1718 [hep-ph]; S. Banerjee, S. Mukhopadhyay and B. Mukhopadhyaya, *JHEP* 1210 (2012) 062, arXiv:1207.3588 [hep-ph]; F. Bonnet et al., *Phys. Rev. D* 86 (2012) 093014, arXiv:1207.4599 [hep-ph]; B. A. Dobrescu and J. D. Lykken, *JHEP* 1302 (2013) 073, arXiv:1210.3342 [hep-ph]; G. Cacciapaglia et al., *JHEP* 1303 (2013) 029, arXiv:1210.8120 [hep-ph]; T. Corbett et al., *Phys. Rev. D* 87 (2013) 015022, arXiv:1211.4580 [hep-ph]; E. Masso and V. Sanz, *Phys. Rev. D* 87 (2013) 033001, arXiv:1211.1320 [hep-ph]; A. Azatov and J. Galloway, *Int. J. Mod. Phys. A* 28 (2013) 1330004, arXiv:1212.1380 [hep-ph]; G. Belanger et al., *JHEP* 1302 (2013) 053, arXiv:1212.5244 [hep-ph]; K. Cheung, J. S. Lee and Y. Tseng, (2013), arXiv:1302.3794 [hep-ph]; G. Belanger et al., (2013), arXiv:1302.5694 [hep-ph]; A. Falkowski, F. Riva and A. Urbano, (2013), arXiv:1303.1812 [hep-ph]; A. Djouadi and G. Moreau, (2013), arXiv:1303.6591 [hep-ph]; F. Chang, W.-P. Pan and F. Xu, (2013), arXiv:1303.7035 [hep-ph]; B. Dumont, S. Fichet and G. von Gersdorff, (2013), arXiv:1304.3369 [hep-ph]; T. Alanne, S. Di Chiara and K. Tuominen, (2013), arXiv:1303.3615 [hep-ph]; P. P. Giardino et al., (2013), arXiv:1303.3570 [hep-ph]; A. Djouadi, (2012), arXiv:1208.3436 [hep-ph]; T. Plehn and M. Rauch, *Europhys. Lett.* 100 (2012) 11002, arXiv:1207.6108 [hep-ph]; G. Belanger et al., *Phys.Rev.* D88 (2013) 075008, arXiv:1306.2941 [hep-ph].

[308] A. Azatov, R. Contino and J. Galloway, *JHEP* 1204 (2012) 127, arXiv:1202.3415 [hep-ph]; J. Espinosa et al., *JHEP* 1205 (2012) 097, arXiv:1202.3697 [hep-ph]; M. Montull and F. Riva, *JHEP* 1211 (2012) 018, arXiv:1207.1716 [hep-ph].

[309] J. R. Espinosa et al., *JHEP* 1212 (2012) 077, arXiv:1207.7355 [hep-ph]; A. Arbey et al., *Phys. Lett. B* 720 (2013) 153–160, arXiv:1211.4004 [hep-ph]; A. Arbey, M. Battaglia and F. Mahmoudi, (2013), arXiv:1303.7450 [hep-ph]; S. Scopel, N. Fornengo and A. Bottino, (2013), arXiv:1304.5353 [hep-ph]; S. Moretti, S. Munir and P. Poulose, (2013), arXiv:1305.0166 [hep-ph].

[310] W. Altmannshofer, S. Gori and G. D. Kribs, *Phys. Rev. D* 86 (2012) 115009, arXiv:1210.2465 [hep-ph]; S. Chang et al., (2012), arXiv:1210.3439 [hep-ph]; A. Celis, V. Ilisie and A. Pich, (2013), arXiv:1302.4022 [hep-ph]; R. Enberg, J. Rathsman and G. Wouda, *JHEP* 1308 (2013) 079, arXiv:1304.1714; R. Enberg, J. Rathsman and G. Wouda, (2013), arXiv:1311.4367 [hep-ph]; B. Coleppa, F. Kling and S. Su, (2013), arXiv:1305.0002 [hep-ph].

[311] X.-F. Han et al., (2013), arXiv:1301.0090 [hep-ph]; J. Cao et al., (2013), arXiv:1303.2426 [hep-ph].

[312] B. Holdom, (2013), arXiv:1306.1564 [hep-ph]; B. Holdom, (2014), arXiv:1404.6229 [hep-ph].

[313] G. Cowan et al., *Eur. Phys. J. C* 71 (2011) 1554, arXiv:1007.1727 [physics.data-an].

[314] S. Wilks, English, *Annals of Mathematical Statistics* 9 (1938) 60–62.

[315] A. Wald, *Transactions of The American Mathematical Society* 54 (3 1943).

[316] CMS Collaboration, (2013), CMS-PAS-HIG-13-002.

[317] P. Bechtle and T. Stefaniak, *On the presentation of correlated systematic uncertainties in Higgs boson rate measurements*, *available at* http://higgsbounds.hepforge.org.

[318] CMS Collaboration, (2012), CMS-PAS-HIG-12-015.

[319] F. Boudjema et al., (2013), arXiv:1307.5865 [hep-ph].

[320] K. Cranmer et al., (2013), arXiv:1401.0080 [hep-ph].

[321] CMS Collaboration, (2012), CMS-PAS-HIG-12-044.

[322] CMS Collaboration, (2013), CMS-PAS-HIG-13-004.

[323] CMS Collaboration, (2013), CMS-PAS-HIG-13-003.

[324] ATLAS Collaboration, (2013), ATLAS-CONF-2013-030, ATLAS-COM-CONF-2013-028.

[325] ATLAS Collaboration, (2012), ATLAS-CONF-2012-091, ATLAS-COM-CONF-2012-109.

[326] ATLAS collaboration, (2013), ATLAS-CONF-2013-079, ATLAS-COM-CONF-2013-080.

[327] ATLAS collaboration, (2013), ATLAS-CONF-2013-075, ATLAS-COM-CONF-2013-069.

[328] T. Aaltonen et al., (2013), arXiv:1301.6668 [hep-ex].

[329] S. Chatrchyan et al., (2013), arXiv:1312.1129 [hep-ex].

[330] CMS Collaboration, (2013), CMS-PAS-HIG-13-017.

[331] CMS Collaboration, (2013), CMS-PAS-HIG-13-007.

[332] CMS Collaboration, (2013), CMS-PAS-HIG-13-012.

[333] CMS Collaboration, (2013), CMS-PAS-HIG-13-020.

[334] CMS Collaboration, (2013), CMS-PAS-HIG-13-019.

[335] CMS Collaboration, (2013), CMS-PAS-HIG-13-015.

[336] V. M. Abazov et al., *Phys.Rev.* D88 (2013) 052011, arXiv:1303.0823 [hep-ex].

[337] ATLAS Collaboration, (2013), ATLAS-CONF-2013-014, ATLAS-COM-CONF-2013-025.

[338] ATLAS Collaboration, (Sept. 2012), ATLAS-CONF-2012-127.

[339] CMS Collaboration, (2012), CMS-PAS-HIG-12-045.

[340] R. Lafaye et al., *JHEP* 0908 (2009) 009, arXiv:0904.3866 [hep-ph]; M. Klute et al., *Phys. Rev. Lett.* 109 (2012) 101801, arXiv:1205.2699 [hep-ph].

[341] L. J. Dixon and Y. Li, *Phys.Rev.Lett.* 111 (2013) 111802, arXiv:1305.3854 [hep-ph].

[342] CMS Collaboration, (2014), CMS-PAS-HIG-14-002.

[343] J. M. Cornwall, D. N. Levin and G. Tiktopoulos, *Phys.Rev.Lett.* 30 (1973) 1268–1270.

[344] C. Llewellyn Smith, *Phys.Lett.* B46 (1973) 233–236.

[345] M. Duhrssen et al., *Phys. Rev.* D70 (2004) 113009, arXiv:hep-ph/0406323.

[346] M. Duhrssen et al., (2004), arXiv:hep-ph/0407190 [hep-ph].

[347] K. Agashe, R. Contino and A. Pomarol, *Nucl. Phys. B* 719 (2005) 165, arXiv:hep-ph/0412089 [hep-ph]; R. Contino, L. Da Rold and A. Pomarol, *Phys. Rev. D* 75 (2007) 055014, arXiv:hep-ph/0612048 [hep-ph]; G. Giudice et al., *JHEP* 0706 (2007) 045, arXiv:hep-ph/0703164 [hep-ph].

[348] W. Buchmüller and D. Wyler, *Nucl.Phys.* B268 (1986) 621–653.

[349] R. Contino et al., *JHEP* 1307 (2013) 035, arXiv:1303.3876 [hep-ph].

[350] A. Pomarol and F. Riva, *JHEP* 1401 (2014) 151, arXiv:1308.2803 [hep-ph].

[351] H. Haario, E. Saksman and J. Tamminen, *Bernoulli* 7.2 (2001) 223.

[352] A. Patil, D. Huard and C. J. Fonnesbeck, *Journal of Statistical Software* 35.4 (2010) 1, ISSN: 1548-7660, URL: http://www.jstatsoft.org/v35/i04.

[353] C. Englert and M. Spannowsky, (2014), arXiv:1405.0285 [hep-ph].

[354] H. Georgi and M. Machacek, *Nucl. Phys. B* 262 (1985) 463; M. S. Chanowitz and M. Golden, *Phys. Lett. B* 165 (1985) 105; J. Gunion, R. Vega and J. Wudka, *Phys. Rev. D* 42 (1990) 1673; S. Chang, *JHEP* 0312 (2003) 057, arXiv:hep-ph/0306034 [hep-ph].

[355] A. Falkowski, S. Rychkov and A. Urbano, *JHEP* 1204 (2012) 073, arXiv:1202.1532 [hep-ph]; S. Chang et al., *Phys. Rev. D* 86 (2012) 095015, arXiv:1207.0493 [hep-ph]; J. Hisano and K. Tsumura, *Phys. Rev. D* 87 (2013) 053004, arXiv:1301.6455 [hep-ph]; S. Kanemura, M. Kikuchi and K. Yagyu, *Phys. Rev. D* 88 (2013) 015020, arXiv:1301.7303 [hep-ph].

[356] CMS Collaboration, (2013), CMS-PAS-HIG-13-018.

[357] CMS Collaboration, (2013), CMS-PAS-HIG-13-028.

[358] G. Aad et al., (2014), arXiv:1402.3244 [hep-ex]; ATLAS Collaboration, (2013), ATLAS-CONF-2013-011, ATLAS-COM-CONF-2013-013.

[359] U. Aglietti et al., *JHEP* 0701 (2007) 021, arXiv:hep-ph/0611266 [hep-ph].

[360] R. Bonciani, G. Degrassi and A. Vicini, *JHEP* 0711 (2007) 095, arXiv:0709.4227 [hep-ph].

[361] R. Schabinger and J. D. Wells, *Phys. Rev. D* 72 (2005) 093007, arXiv:hep-ph/0509209 [hep-ph]; B. Patt and F. Wilczek, (2006), arXiv:hep-ph/0605188 [hep-ph]; V. Barger et al., *Phys. Rev. D* 77 (2008) 035005, arXiv:0706.4311 [hep-ph]; V. Barger et al., *Phys. Rev. D* 79 (2009) 015018, arXiv:0811.0393 [hep-ph]; G. Bhattacharyya, G. C. Branco and S. Nandi, *Phys. Rev. D* 77 (2008) 117701, arXiv:0712.2693 [hep-ph]; S. Bock et al., *Phys. Lett. B* 694 (2010) 44, arXiv:1007.2645 [hep-ph]; C. Englert et al., *Phys. Lett. B* 703 (2011) 298, arXiv:1106.3097 [hep-ph]; C. Englert et al., *Phys. Lett. B* 707 (2012) 512, arXiv:1112.3007 [hep-ph]; G. M. Pruna and T. Robens, *Phys. Rev. D* 88 (2013) 115012, arXiv:1303.1150 [hep-ph].

[362] G. Altarelli and R. Barbieri, *Phys. Lett.* B253 (1991) 161–167.

[363] M. E. Peskin and T. Takeuchi, *Phys. Rev.* D46 (1992) 381–409.

[364] M. Ciuchini et al., *JHEP* 1308 (2013) 106, arXiv:1306.4644 [hep-ph].

[365] A. Crivellin, A. Kokulu and C. Greub, *Phys.Rev.* D87.9 (2013) 094031, arXiv:1303.5877 [hep-ph].

[366] S. Chatrchyan et al., (2014), arXiv:1401.6527 [hep-ex].

[367] L. Basso and F. Staub, *Phys. Rev. D* 87 (2013) 015011, arXiv:1210.7946 [hep-ph].

[368] K. Schmidt-Hoberg and F. Staub, *JHEP* 1210 (2012) 195, arXiv:1208.1683 [hep-ph].

[369] M. Hemeda, S. Khalil and S. Moretti, (2013), arXiv:1312.2504 [hep-ph].

[370] P. Posch, *Phys. Lett. B* 696 (2011) 447, arXiv:1001.1759 [hep-ph]; A. Drozd et al., *JHEP* 1305 (2013) 072, arXiv:1211.3580 [hep-ph]; A. Cordero-Cid et al., (2013), arXiv:1312.5614 [hep-ph].

[371] A. Arhrib, R. Benbrik and N. Gaur, *Phys. Rev. D* 85 (2012) 095021, arXiv:1201.2644 [hep-ph]; M. Krawczyk et al., *JHEP* 1309 (2013) 055, arXiv:1305.6266 [hep-ph]; M. Krawczyk et al., *Acta Phys. Polon. B* 44 (2013) 2163, arXiv:1309.7880 [hep-ph].

[372] A. Djouadi, *Phys. Lett. B* 435 (1998) 101, arXiv:hep-ph/9806315 [hep-ph].

[373] M. S. Carena et al., *Eur. Phys. J. C* 26 (2003) 601, arXiv:hep-ph/0202167 [hep-ph].

[374] https://twiki.cern.ch/twiki/bin/view/CMSPublic/ttHCombinationTWiki, Combination of Search Results for Higgs Boson Production in Association with a Top-Quark Pair.

[375] European Strategy for Particle Physics Preparatory Group, (2013), CERN-ESG-005.

[376] ATLAS Collaboration, (2013), arXiv:1307.7292 [hep-ex].

[377] ATLAS Collaboration, (Oct. 2013), ATL-PHYS-PUB-2013-014.

[378] CMS Collaboration, (2013), arXiv:1307.7135 [hep-ex].

[379] S. Dawson et al., (2013), arXiv:1310.8361 [hep-ex].

[380] M. E. Peskin, (2013), arXiv:1312.4974 [hep-ph].

[381] D. Zeppenfeld et al., *Phys. Rev. D* 62 (2000) 013009, arXiv:hep-ph/0002036 [hep-ph].

[382] M. Klute et al., *Europhys. Lett.* 101 (2013) 51001, arXiv:1301.1322 [hep-ph].

[383] J. Campbell et al., (2013), arXiv:1310.5189 [hep-ph].

[384] T. Han, Z. Liu and J. Sayre, (2013), arXiv:1311.7155 [hep-ph].

[385] H. Baer, V. Barger and A. Mustafayev, *Phys. Rev.* D85 (2012) 075010, arXiv:1112.3017 [hep-ph]; A. Arbey et al., *Phys. Lett. B* 708 (2012) 162–169, arXiv:1112.3028 [hep-ph]; M. Kadastik et al., *JHEP* 1205 (2012) 061, arXiv:1112.3647 [hep-ph]; J. Cao et al., *Phys. Lett. B* 710 (2012) 665–670, arXiv:1112.4391 [hep-ph]; F. Brümmer and W. Buchmüller, *JHEP* 1205 (2012) 006, arXiv:1201.4338 [hep-ph]; D. Carmi et al., *JHEP* 1207 (2012) 136, arXiv:1202.3144 [hep-ph]; J. Ellis and K. A. Olive, *Eur. Phys. J. C* 72 (2012) 2005, arXiv:1202.3262 [hep-ph]; N. Desai, B. Mukhopadhyaya and S. Niyogi, (2012), arXiv:1202.5190 [hep-ph]; T. Cheng et al., (2012), arXiv:1202.6088 [hep-ph]; M. Asano et al., *Phys. Rev.* D86 (2012) 015020, arXiv:1202.6318 [hep-ph]; J.-J. Cao et al., *JHEP* 1206 (2012) 145, arXiv:1203.0694 [hep-ph]; A. Choudhury and A. Datta, *JHEP* 1206 (2012) 006, arXiv:1203.4106 [hep-ph]; P. P. Giardino et al., *JHEP* 1206 (2012) 117, arXiv:1203.4254 [hep-ph]; M. A. Ajaib et al., *Phys. Lett. B* 713 (2012) 462–468, arXiv:1204.2856 [hep-ph]; F. Brümmer, S. Kraml and S. Kulkarni, *JHEP* 1208 (2012) 089, arXiv:1204.5977 [hep-ph]; J. L. Evans, M. Ibe and T. T. Yanagida, *Phys. Rev.* D86 (2012) 015017, arXiv:1204.6085 [hep-ph]; A. Fowlie et al., (2012), arXiv:1206.0264 [hep-ph]; M. R. Buckley and D. Hooper, (2012), arXiv:1207.1445 [hep-ph]; S. Akula, P. Nath and G. Peim, *Phys. Lett. B* 717 (2012) 188–192, arXiv:1207.1839 [hep-ph]; J. Cao et al., *JHEP* 1210 (2012) 079, arXiv:1207.3698 [hep-ph]; M. Hirsch, F. Joaquim and A. Vicente, (2012), arXiv:1207.6635 [hep-ph]; O. Buchmueller et al., *Eur.Phys.J.* C72 (2012) 2243, arXiv:1207.7315; K. Howe and P. Saraswat, *JHEP* 1210 (2012) 065, arXiv:1208.1542 [hep-ph]; C. Wymant, (2012), arXiv:1208.1737 [hep-ph]; Z. Kang et al., (2012), arXiv:1208.2673 [hep-ph]; T. Kitahara, (2012), arXiv:1208.4792 [hep-ph]; Z. Heng, (2012), arXiv:1210.3751 [hep-ph]; M. Carena et al., *JHEP* 1207 (2012) 175, arXiv:1205.5842 [hep-ph]; M. Carena et al., *JHEP* 1203 (2012) 014, arXiv:1112.3336 [hep-ph]; U. Haisch and F. Mahmoudi, (2012), arXiv:1210.7806 [hep-ph].

[386] S. Chatrchyan et al., *Phys. Lett. B* 713 (2012) 68–90, arXiv:1202.4083 [hep-ex].

[387] S. AbdusSalam et al., *Eur. Phys. J. C* 71 (2011) 1835, arXiv:1109.3859 [hep-ph].

[388] L. Zeune, "Constraining supersymmetric models using Higgs physics, precision observables and direct searches", PhD Thesis: University of Hamburg, 2014.

[389] G. Aad et al., *JHEP* 1310 (2013) 189, arXiv:1308.2631 [hep-ex]; G. Aad et al., (2014), arXiv:1403.5222 [hep-ex].

[390] S. Chatrchyan et al., *Eur.Phys.J.* C73 (2013) 2677, arXiv:1308.1586 [hep-ex]; CMS Collaboration, (2013), CMS-PAS-SUS-13-015.

[391] ATLAS Collaboration, (2012), ATLAS-CONF-2012-093, ATLAS-COM-CONF-2012-120.

[392] CMS Collaboration, (2012), CMS-PAS-HIG-12-020.

[393] D. de Florian and M. Grazzini, *Phys. Lett.* B674 (2009), See `http://theory.fi.infn.it/grazzini/hcalculators.html` 291–294, arXiv:0901.2427 [hep-ph].

[394] T. Hahn et al., (2006), arXiv:hep-ph/0607308 [hep-ph].

[395] A. Dedes, G. Degrassi and P. Slavich, *Nucl. Phys.* B672 (2003) 144–162, arXiv:hep-ph/0305127 [hep-ph].

[396] S. Heinemeyer, W. Hollik and G. Weiglein, *Eur. Phys. J.* C16 (2000) 139–153, arXiv:hep-ph/0003022 [hep-ph].

[397] K. E. Williams, H. Rzehak and G. Weiglein, *Eur. Phys. J. C* 71 (2011) 1669, arXiv:1103.1335 [hep-ph].

[398] I. Adachi et al., *Phys.Rev.Lett.* 110.13 (2013) 131801, arXiv:1208.4678 [hep-ex].

[399] M. Misiak and M. Steinhauser, *Nucl. Phys. B* 764 (2007) 62–82, arXiv:hep-ph/0609241 [hep-ph].

[400] G. Degrassi and G. Giudice, *Phys. Rev.* D58 (1998) 053007, arXiv:hep-ph/9803384 [hep-ph].

[401] S. Heinemeyer, D. Stöckinger and G. Weiglein, *Nucl. Phys.* B690 (2004) 62–80, arXiv:hep-ph/0312264 [hep-ph].

[402] S. Heinemeyer, D. Stöckinger and G. Weiglein, *Nucl. Phys.* B699 (2004) 103–123, arXiv:hep-ph/0405255 [hep-ph].

[403] D. Stöckinger, *J. Phys.* G34 (2007) R45–R92, arXiv:hep-ph/0609168 [hep-ph].

[404] A. Djouadi et al., *Phys. Rev. Lett.* 78 (1997) 3626–3629, arXiv:hep-ph/9612363 [hep-ph].

[405] A. Djouadi et al., *Phys. Rev.* D57 (1998) 4179–4196, arXiv:hep-ph/9710438 [hep-ph].

[406] ATLAS, CMS and LHCb Collaborations, (2012), ATLAS-CONF-2012-061, CMS-PAS-BPH-12-009, LHCb-CONF-2012-017.

[407] ATLAS Collaboration, (2012), ATLAS-CONF-2012-094, ATLAS-COM-CONF-2012-113.

[408] CMS Collaboration, (2011), CMS-PAS-HIG-11-029.

[409] S. Gennai et al., *Eur. Phys. J.* C52 (2007) 383–395, arXiv:0704.0619 [hep-ph].

[410] J. Frere, D. Jones and S. Raby, *Nucl.Phys.* B222 (1983) 11; M. Claudson, L. J. Hall and I. Hinchliffe, *Nucl.Phys.* B228 (1983) 501; C. Kounnas et al., *Nucl.Phys.* B236 (1984) 438; J. Gunion, H. Haber and M. Sher, *Nucl.Phys.* B306 (1988) 1; J. Casas, A. Lleyda and C. Munoz, *Nucl.Phys.* B471 (1996) 3–58, arXiv:hep-ph/9507294 [hep-ph]; P. Langacker and N. Polonsky, *Phys.Rev.* D50 (1994) 2199–2217, arXiv:hep-ph/9403306 [hep-ph]; A. Strumia, *Nucl.Phys.* B482 (1996) 24–38, arXiv:hep-ph/9604417 [hep-ph].

[411] D. Noth and M. Spira, *Phys. Rev. Lett.* 101 (2008) 181801, arXiv:0808.0087 [hep-ph].

[412] G. Aad et al., *Phys.Lett.* B710 (2012) 67–85, arXiv:1109.6572 [hep-ex]; G. Aad et al., *Phys.Rev.* D85.1 (2012) 012006, arXiv:1109.6606 [hep-ex]; G. Aad et al., *JHEP* 1111 (2011) 099, arXiv:1110.2299 [hep-ex]; G. Aad et al., *Phys.Lett.* B709 (2012) 137–157, arXiv:1110.6189 [hep-ex]; G. Aad et al., *Phys.Lett.* B710 (2012) 519–537, arXiv:1111.4116 [hep-ex]; G. Aad et al., *Phys.Rev.Lett.* 108 (2012) 181802, arXiv:1112.3832 [hep-ex].

[413] S. Chatrchyan et al., *Phys.Rev.Lett.* 106 (2011) 211802, arXiv:1103.0953 [hep-ex]; S. Chatrchyan et al., *JHEP* 1106 (2011) 026, arXiv:1103.1348 [hep-ex]; S. Chatrchyan et al., *JHEP* 1106 (2011) 077, arXiv:1104.3168 [hep-ex]; S. Chatrchyan et al., *JHEP* 1106 (2011) 093, arXiv:1105.3152 [hep-ex]; S. Chatrchyan et al., *JHEP* 1107 (2011) 113, arXiv:1106.3272 [hep-ex]; S. Chatrchyan et al., *JHEP* 1108 (2011) 155, arXiv:1106.4503 [hep-ex]; S. Chatrchyan et al., *Phys.Rev.* D85 (2012) 012004, arXiv:1107.1279 [hep-ex]; S. Chatrchyan et al., *JHEP* 1108 (2011) 156, arXiv:1107.1870 [hep-ex]; S. Chatrchyan et al., *Phys.Rev.Lett.* 107 (2011) 221804, arXiv:1109.2352 [hep-ex].

[414] G. Aad et al., *Phys.Lett.* B708 (2012) 37–54, arXiv:1108.6311 [hep-ex].

[415] S. Chatrchyan et al., *Phys.Lett.* B704 (2011) 123–142, arXiv:1107.4771 [hep-ex].

[416] ATLAS Collaboration, (2011), ATLAS-CONF-2011-126, ATLAS-COM-CONF-2011-151. During finalization of the study presented in Chapter 7, ATLAS published a similar analysis with a slightly modified event selection in Ref. [494].

[417] P. Richardson, (2000), arXiv:hep-ph/0101105 [hep-ph].

[418] H. K. Dreiner, P. Richardson and M. H. Seymour, (2000), arXiv:hep-ph/0001224 [hep-ph].

[419] F. Deliot, G. Moreau and C. Royon, *Eur.Phys.J.* C19 (2001) 155–181, arXiv:hep-ph/0007288 [hep-ph].

[420] H. Dreiner et al., *Phys.Rev.* D75 (2007) 035003, arXiv:hep-ph/0611195 [hep-ph].

[421] G. Moreau et al., *Phys.Lett.* B475 (2000) 184–189, arXiv:hep-ph/9910341 [hep-ph].

[422] G. Moreau, E. Perez and G. Polesello, *Nucl.Phys.* B604 (2001) 3–31, arXiv:hep-ph/0003012 [hep-ph].

[423] R. J. Oakes et al., *Phys.Rev.* D57 (1998) 534–540, arXiv:hep-ph/9707477 [hep-ph].

[424] M. Bernhardt et al., *Phys.Rev.* D78 (2008) 015016, arXiv:0802.1482 [hep-ph].

[425] O. Cakir et al., *Acta Phys.Polon.* B43 (2012) 63–70, arXiv:1103.5087 [hep-ph].

[426] B. Allanach, M. Guchait and K. Sridhar, *Phys.Lett.* B586 (2004) 373–381, arXiv:hep-ph/0311254 [hep-ph].

[427] T. Aaltonen et al., *Phys.Rev.Lett.* 106 (2011) 171801, arXiv:1104.0699 [hep-ex].

[428] C. Kilic and S. Thomas, *Phys.Rev.* D84 (2011) 055012, arXiv:1104.1002 [hep-ph].

[429] V. Abazov et al., *Phys.Rev.Lett.* 97 (2006) 111801, arXiv:hep-ex/0605010 [hep-ex].

[430] C. T. Autermann, "Resonant second generation slepton production at the Tevatron", FERMILAB-THESIS-2006-46, PhD Thesis, 2006.

[431] V. Abazov et al., *Phys.Rev.Lett.* 100 (2008) 241803, arXiv:0711.3207 [hep-ex].

[432] A. Abulencia et al., *Phys.Rev.Lett.* 96 (2006) 211802, arXiv:hep-ex/0603006 [hep-ex].

[433] T. Aaltonen et al., *Phys.Rev.Lett.* 105 (2010) 191801, arXiv:1004.3042 [hep-ex].

[434] A. Abulencia et al., *Phys.Rev.Lett.* 95 (2005) 252001, arXiv:hep-ex/0507104 [hep-ex].

[435] D. Acosta et al., *Phys.Rev.Lett.* 95 (2005) 131801, arXiv:hep-ex/0506034 [hep-ex].

[436] A. Abulencia et al., *Phys.Rev.Lett.* 98 (2007) 131804, arXiv:0706.4448 [hep-ex].

[437] V. Abazov et al., *Phys.Lett.* B638 (2006) 441–449, arXiv:hep-ex/0605005 [hep-ex].

[438] T. Aaltonen et al., *Phys.Rev.Lett.* 101 (2008) 071802, arXiv:0802.3887 [hep-ex].

[439] S. Chakrabarti, M. Guchait and N. Mondal, *Phys.Lett.* B600 (2004) 231–238, arXiv:hep-ph/0404261 [hep-ph].

[440] S. P. Das, A. Datta and S. Poddar, *Phys.Rev.* D73 (2006) 075014, arXiv:hep-ph/0509171 [hep-ph].

[441] J. Butterworth and H. K. Dreiner, *Nucl.Phys.* B397 (1993) 3–34, arXiv:hep-ph/9211204 [hep-ph].

[442] H. K. Dreiner and P. Morawitz, *Nucl.Phys.* B503 (1997) 55–78, arXiv:hep-ph/9703279 [hep-ph].

[443] T. Ahmed et al., *Z.Phys.* C64 (1994) 545–558.

[444] A. Aktas et al., *Eur.Phys.J.* C36 (2004) 425–440, arXiv:hep-ex/0403027 [hep-ex].

[445] S. Aid et al., *Z.Phys.* C71 (1996) 211–226, arXiv:hep-ex/9604006 [hep-ex].

[446] J. Breitweg et al., *Eur.Phys.J.* C16 (2000) 253–267, arXiv:hep-ex/0002038 [hep-ex].

[447] S. Chekanov et al., *Phys.Rev.* D68 (2003) 052004, arXiv:hep-ex/0304008 [hep-ex].

[448] S. Chekanov et al., *Eur.Phys.J.* C50 (2007) 269–281, arXiv:hep-ex/0611018 [hep-ex].

[449] G. Aad et al., *Eur.Phys.J.* C71 (2011) 1809, arXiv:1109.3089 [hep-ex].

[450] G. Aad et al., *Phys.Lett.* B707 (2012) 478–496, arXiv:1109.2242 [hep-ex].

[451] S. Chatrchyan et al., *Phys.Lett.* B704 (2011) 411–433, arXiv:1106.0933 [hep-ex].

[452] CMS Collaboration, (2011), CMS-PAS-EXO-11-045.

[453] T. Banks et al., *Phys.Rev.* D52 (1995) 5319–5325, arXiv:hep-ph/9505248 [hep-ph].

[454] A. Heister et al., *Eur.Phys.J.* C31 (2003) 1–16, arXiv:hep-ex/0210014 [hep-ex].

[455] G. Bhattacharyya, *Nucl.Phys.Proc.Suppl.* 52A (1997) 83–88, arXiv:hep-ph/9608415 [hep-ph].

[456] B. Allanach, A. Dedes and H. K. Dreiner, *Phys.Rev.* D60 (1999) 075014, arXiv:hep-ph/9906209 [hep-ph].

[457] Y. Kao and T. Takeuchi, (2009), arXiv:0910.4980 [hep-ph].

[458] D. Choudhury, S. Majhi and V. Ravindran, *Nucl.Phys.* B660 (2003) 343–361, arXiv:hep-ph/0207247 [hep-ph].

[459] L. L. Yang et al., *Phys.Rev.* D72 (2005) 074026, arXiv:hep-ph/0507331 [hep-ph].

[460] Q. Chen, T. Han and Z.-G. Si, *JHEP* 0705 (2007) 068, arXiv:hep-ph/0612076 [hep-ph].

[461] J. Pumplin et al., *JHEP* 0602 (2006) 032, arXiv:hep-ph/0512167 [hep-ph].

[462] A. Martin et al., *Phys.Lett.* B531 (2002) 216–224, arXiv:hep-ph/0201127 [hep-ph].

[463] A. Martin et al., *Phys.Lett.* B604 (2004) 61–68, arXiv:hep-ph/0410230 [hep-ph].

[464] S. Majhi, P. Mathews and V. Ravindran, *Nucl.Phys.* B850 (2011) 287–320, arXiv:1011.6027 [hep-ph].

[465] L. Randall and R. Sundrum, *Nucl.Phys.* B557 (1999) 79–118, arXiv:hep-th/9810155 [hep-th].

[466] G. F. Giudice et al., *JHEP* 9812 (1998) 027, arXiv:hep-ph/9810442 [hep-ph].

[467] J. A. Bagger, T. Moroi and E. Poppitz, *JHEP* 0004 (2000) 009, arXiv:hep-th/9911029 [hep-th].

[468] H. Baer et al., *JHEP* 1005 (2010) 069, arXiv:1002.4633 [hep-ph].

[469] K. Choi and H. P. Nilles, *JHEP* 0704 (2007) 006, arXiv:hep-ph/0702146 [HEP-PH].

[470] H. K. Dreiner, H. E. Haber and S. P. Martin, *Phys.Rept.* 494 (2010) 1–196, arXiv:0812.1594 [hep-ph].

[471] H. K. Dreiner and G. G. Ross, *Nucl.Phys.* B365 (1991) 597–613.

[472] F. E. Paige et al., (2003), arXiv:hep-ph/0312045 [hep-ph].

[473] B. Webber, K. Odagiri and P. Richardson, *ISAWIG1.200*, See http://www.hep.phy.cam.ac.uk/~richardn/HERWIG/.

[474] G. Corcella et al., *JHEP* 0101 (2001) 010, arXiv:hep-ph/0011363 [hep-ph].

[475] G. Corcella et al., (2002), arXiv:hep-ph/0210213 [hep-ph].

[476] S. Moretti et al., *JHEP* 0204 (2002) 028, arXiv:hep-ph/0204123 [hep-ph].

[477] S. Ovyn, X. Rouby and V. Lemaitre, (2009), arXiv:0903.2225 [hep-ph].

[478] M. Cacciari, G. P. Salam and G. Soyez, *JHEP* 04 (2008) 063, arXiv:0802.1189 [hep-ph].

[479] M. Cacciari and G. P. Salam, *Phys.Lett.* B641 (2006) 57–61, arXiv:hep-ph/0512210 [hep-ph].

[480] G. Aad et al., *Phys.Rev.* D83 (2011) 112006, arXiv:1104.4481 [hep-ex].

[481] S. Chatrchyan et al., *Phys.Lett.* B703 (2011) 246–266, arXiv:1105.5237 [hep-ex].

[482] S. Chatrchyan et al., *Phys.Rev.* D86 (2012) 052013, arXiv:1207.5406 [hep-ex].

[483] G. Aad et al., *JHEP* 1301 (2013) 029, arXiv:1210.1718 [hep-ex].

[484] ATLAS Collaboration, (2012), ATLAS-CONF-2012-148, ATLAS-COM-CONF-2012-180.

[485] CMS Collaboration, (2013), CMS-PAS-EXO-12-059.

[486] G. Aad et al., *JHEP* 1212 (2012) 007, arXiv:1210.4538 [hep-ex].

[487] S. Chatrchyan et al., *JHEP* 1208 (2012) 110, arXiv:1205.3933 [hep-ex].

[488] S. Chatrchyan et al., *JHEP* 1401 (2014) 163, arXiv:1311.6736.

[489] ATLAS Collaboration,
(2012), ATLAS-CONF-2012-012, ATLAS-COM-CONF-2012-019.

[490] ATLAS Collaboration,
(2012), ATLAS-CONF-2012-098, ATLAS-COM-CONF-2012-138.

[491] G. Aad et al., *Phys. Rev. D* 86 (2012) 032003, arXiv:1207.0319 [hep-ex].

[492] ATLAS Collaboration,
(2012), ATLAS-CONF-2012-092, ATLAS-COM-CONF-2012-106.

[493] TEVNPH Working Group for the CDF and DØ Collaborations, (2012),
arXiv:1207.0449 [hep-ex].

[494] G. Aad et al., *Phys.Rev.* D85 (2012) 032004, arXiv:1201.1091 [hep-ex].